The Eurasia Proceedings of Science, Technology, Engineering & Mathematics (EPSTEM)
ISSN: 2602-3199

ICBASET 2026

International Conference on Basic Sciences, Engineering and Technology (ICBASET)

Proceedings Book

Editor

Mehmet Ozaslan
Gaziantep University, Türkiye

ISBN: 978-625-92435-9-7

Copyright 2026

Published by the ISRES Publishing

Address: Askan Mah. Akinbey Sok. No: 5-A/Konya/TÜRKİYE

Web: www.isres.org

Contact: isrespublishing@gmail.com

Dates: September 17- 18, 2026

Location: İstanbul, Türkiye

https://2026.icbaset.net

This work is licensed under a Creative Commons Attribution-NonCommercial-ShareAlike 4.0 International License.

About Editor

Prof Dr. Mehmet Ozaslan
Department of Biology, Gaziantep University, Türkiye
Website: mehmetozaslan.com
E-mail: ozaslanmd@gantep.edu.tr

Language Editor

Lecturer Ceren Dogan
School of Foreign Languages, Necmettin Erbakan University, Türkiye
Email: cerendogan@erbakan.edu.tr

CONFERENCE PRESIDENT
Prof. Dr. Mehmet Ozaslan - Gaziantep University, Türkiye
Prof. Dr. Csaba Antonya - Transilvania University of Brasov, Romania

SCIENTIFIC BOARD

Besnik Hajdari - University "isa Boletini" Mitrovica, Kosovo
Bogdan Patrut - Alexandru Ioan Cuza Üniversitesi, Romania
Chalavadi Sulochana - Gulbarga University, India
Csaba Antonya - Transilvania University of Brasov, Romania
Dariusz Jacek Jakobczak - Technical University of Koszalin, Poland
Dehini Rachid - University of Bechar, Algeria
Eleonora Guseinoviene - Klaipeda University, Lithuania
Elena Krelja Kurelovic - Polytechnic of Rijeka, Croatia
Elżbieta Patkowska - University of Life Sciences in Lublin, Poland
Eva Trnova - Masaryk University, Czech Republic
Farhad Balash - Kharazmi University, Iran
Fundime Miri - University of Tirana, Albania
Gabriel Delgado-Toral - Universidad Nacional Autónoma de México, Mexico
Gordana Savic - University of Belgrade, Serbia
Hasan Mlinaku, VUZF, Sofia in Bulgaria
Ibrahim Krasniqi - University of Peja, Kosovo
Irina Andreeva - Peter The Great St. Petersburg Polytechnic University, Russia
Isti Hidayah - Semarang State University, Indonesia
Jose Manuel Lopez Guede - University of Basque Country, Spain
Kamil Yurtkan - Cyprus International University, Cyprus
Katsina Christopher Bala - Federal University of Technology, Minna, Nigeria
Khitam Shraim - Palestine Technical University, Palestine
Marija Stanic - University of Kragujevac, Serbia
M. Hanefi Calp - Karadeniz Technical University, Turkey
Mohamed Ahmed - Mansoura University, Egypt
Mousa Attom- American University of Sharjah, U.A.E.
Nicu Bızon - Pitesti University, Romania
Pandian Vasant - Teknology Petronas University, Romania
Rajnalkar Laxman - Gulbarga University, India
Sanaa Al-Delaımy - Mosul University, Iraq
Shadi Aljawarneh - Jordan University of Science and Technology, Jordan
Shynar Baımaganbetova - Nazarbayev University, Kazakhstan
Svetlana Khan - Almaty University of Power Engineering and Telecommunications, Kazakhstan
Yiyang Chen - Soochow University (CN), China
Zairi Ismael Rizman - MARA University of Technology, Malaysia
Zipporah Pewat Duguryil - Federal College of Education, Nigeria

ORGANIZING COMMITTEE

Besnik Hajdari - University "isa Boletini" Mitrovica, Kosovo
Cemil Aydogdu - Hacettepe University, Türkiye
Csaba Antonya - Transilvania University of Brasov, Romania
Danielle Gonçalves de Oliveira Prado-Federal Technological University of Paraná, Brazil

Dariusz Jacek Jakóbczak - Technical University of Koszalin, Poland
Elman Iskender - Central Botanical Garden of Anas, Azerbaijan
Halil Snopce - South East European University, Macedonia
Hasan Mlinaku, VUZF, Sofia in Bulgaria
Ibrahim Krasniqi - University of Peja, Kosovo
Ishtar Imad - Uruk University, Iraq
Jaya Bishnu Pradhan-Tribhuvan University, Mahendra Ratna Campus, Nepal
Kamil Yurtkan - Cyprus International University, Cyprus
Mehmet Özaslan - Gaziantep University, Türkiye
Mohammad Sarwar - Scialert, Dubai, United Arab Emirates
Murat Beytur - Kafkas University, Türkiye
Samire Bagırova - Institute of Dendrology of Anas, Azerbaijan
Suhail Bayati - Hadi University College, Iraq
Zairi Ismael Rizman - MARA University of Technology, Malaysia

Editorial Policies

ISRES Publishing follows the steps below in the procedings book publishing process.
In the first stage, the papers sent to the conferences organized by ISRES are subject to editorial oversight. In the second stage, the papers that pass the first step are reviewed by at least two international field experts in the conference committee in terms of suitability for the content and subject area. In the third stage, it is reviewed by at least one member of the organizing committee for the suitability of references. In the fourth step, the language editor reviews the language for clarity.

Review Process

Abstracts and full-text reports uploaded to the conference system undergo a review procedure. Abstracts will be evaluated on the basis of abstracts/proposals. The conference system allows the full text to be sent if the abstract is accepted. Participants must wait for the evaluation results after uploading their article abstracts to the conference system. If their abstracts are accepted, they can upload their full texts to the conference system. The full texts are then sent to at least two reviewers for review. The conference has a double-blind peer-review process. Any paper submitted for the conference is reviewed by at least two international reviewers with expertise in the relevant subject area. Based on the reviewers' comments, papers are accepted, rejected or accepted with revision. If the comments are not addressed well in the improved paper, then the paper is sent back to the authors to make further revisions. The accepted papers are formatted by the conference for publication in the proceedings.

Aims & Scope

Engineering, technology and basic sciences are closely related fields. Developments and innovations in one of them affect the others. Therefore, the focus of the conference is on studies related to these three fields. Studies in the fields of engineering, technology and basic science are accepted to the conference even if they are not associated with other fields. The conference committee thinks that a study in only one field (for example, mathematics, physics, etc.) will contribute to other fields (for example, engineering, technology, etc.) in future studies, even if it is not associated with the presentation at the conference. In line with this perspective, studies in the following fields are accepted to the conference: Biology, Chemistry, Engineering, Mathematics, Physics and Technology.

The aim of the conference is to bring together researchers and administrators from different countries, and to discuss theoretical and practical issues in all fields of Engineering, Technology and Basic Sciences.

The Eurasia Proceedings of Science, Technology, Engineering & Mathematics (EPSTEM)
ISSN: 2602-3199

Articles: 1-22

CONTENTS

1-Determination of Fracture Parameters of Lime-Pumice Composites Using the Double-K Fracture Model/Pages: 1-10
Ragip Ince, Erkin Eren

2-Evaluation of the Crack Resistance of Hot Mix Asphalt Mixtures Modified with Enprene 611 Elastomer/Pages: 11-18
Esma Bakir, Erkut Yalcin

3-The Role of Participatory Agricultural Extension in Mitigating the Adverse Effects of Climate Change on Agricultural Production/Pages: 19-29
Hashim Saeed Murad, Bawer Taher Mohammad, Salah Jasim Amin

4-Performance Evaluation of Machine Learning Models for Gas Classification Under Sensor Drift on ESP32-S3/Pages: 30-38
Gonca Uslu- Ozkucuk

5-Lengthwise Fracture Analysis of a Moving Thin-Walled Elliptical Cylinder/Pages: 39-48
Victor Rizov

6-A Multiphysics Neural Network Framework for Microdamage Evolution with A Shadow Plasticity Observer/Pages: 49-58
Utku Kaftancioglu, Cagatay Kasar

7-Effect of Hollow Channel Cross-Section Shape on the Damage Mechanism of Reinforced Concrete Slabs Under Near-Field Blast Loading/Pages: 59-66
Dursun Bakir

8-Response of Potato (Salanum Tuberosum L.) and Green Bean (Phaseolus Vulgaris L.) Crops to Mycorrhizal, NPK and Sheep Manure Fertilization in Soil/Pages: 67-75
Mohammed Ayad Harbawi, Fatih Abed Hasan, Hesham Saadaldeen Younes, Aziz Rana Saadallah

9-Assessment of Thymus numidicus and Lavandula stoechas Essential Oils Effects on Deltamethrin-Induced Toxicity in Female Rabbits/Pages: 76-84
Farida Fernane, Nacira Daoudi - Zerrouki, Ouardia Chaouchi, Hakima Aitissad

10-Pedogenic Development and Mineralogical Characteristics of Sedimentary Soil Pedons/Pages: 85-96
Radhwan A. Alkiki, Khalid Anwar Khalid, Abd Al-Kader A. Alhadede

11-Digital Transformation, Cocoa Downstreaming and Export Competitiveness/Pages: 97-127
Dwi Putri Jeng Ivo Nurun Nisa, Jamhari Jamhari, Dwidjono Hadi Darwanto, Arini Wahyu Utami

12-Low-Temperature Fatigue Performance of Polymer-Modified Asphalt Mixtures Evaluated by Cyclic SCB Testing/Pages: 128-135
Abdullah Demirbag, Erkut Yalcin

13-Why Two's Complement Became the Standard: A Comparative Analysis of Unsigned, Sign-Magnitude, One's Complement, and Two's Complement Representations/Pages: 136-151
Bojken Shehu

14-GCD Matrices Associated with Nathanson's Totient Function/Pages: 152-161
Yahia Awad, Haissam Chehade, Wiam Zeid

15-DBSCAN-Based Spatial Hotspot Detection of Motorcycle and Three-Wheeled Vehicle Crashes/Pages: 162-175
Ghaidaa A. Majeed, Abeer K. Jameel

16-BIM Technologies at Structural Design/Pages: 176-183
Ahmet Cagatay Tahaoglu, Yasin Fahjan

17-Machine Learning-Based Pollution Risk Classification in Industrial Wastewater Treatment/Pages: 184-190
Mustafa Ozan Ozkok

18-Integrating Mean Weight Diameter and Environmental Sensitivity Index for Modeling Soil Erosion Risk and Land Degradation in Soils under Different Agricultural Land Uses/Pages: 191-210
Tayseer Thaker Mohammed, Khaled Anwar Khaled

19-Efficiency of Nano and Mineral Iron in Sustaining Faba Bean (Vicia Faba L.) Productivity Within Different Soil Orders/Pages: 211-222
Maryam Abdulkader Albadranie, Rana Saadallah Aziz

20-3D Printing in Shipbuilding and Ship Repair Industry: Challenges and Opportunities/Pages: 223-228
Yordan Denev

21-Deep Learning-Based Classification of Archaeological Artifacts Using Image Processing/Pages: 229-236
Fatma Ozge Ozkok

22-Tetra Neutrosophic Alpha Star Generalized #Ψ Mappings in TetraNeutrosophic Topological Spaces/Pages: 237-259
Raja Mohammad Latif

23-Mid-Infrared (FTIR) Spectroscopy for Urinary Stone Identification: Clinical Relevance in an Industrial Region/Pages:260-267
Volodymyr Sulyma, Kostyantyn BARANNIK, Serhij Malinovskyj, Oleksandr Balalaev

24-Value-Enhanced Oat Breeding for High-Quality Biscuit Production/Pages:268-274
Hayati Akman, Aysegul Soyakil, Yasar Karaduman

25-The Impacts of Capitalism on the Transformation of Cultural Identity: The Case of the Clock Tower in Makkah/Pages:275-284
Bushra Zalloom

The Eurasia Proceedings of Science, Technology, Engineering and Mathematics (EPSTEM)
ISSN: 2602-3199

The Eurasia Proceedings of Science, Technology, Engineering and Mathematics (EPSTEM), 2026

Volume 42, Pages 1-10

ICBASET 2026: International Conference on Basic Sciences, Engineering and Technology

Determination of Fracture Parameters of Lime-Pumice Composites Using the Double-K Fracture Model

Ragip Ince
Firat University

Erkin Eren
Firat University

Abstract: Experimental studies on concrete beams have demonstrated that there are three distinct phases of crack development in cement-based materials: the initiation of cracks, stable crack growth, and unstable fracture. In light of these phases, the Double-K model necessitates two fracture parameters, specifically the unstable stress intensity factor and the initiation stress intensity factor, to effectively simulate the fracture-dominated failure of concrete structures. Particularly, the initiation fracture toughness is crucial in the assessment of certain structures, including nuclear power plants, reservoirs, and water-resource facilities. Roman mortars are considered the initial type of concrete, made from lime, water, sand, and volcanic tuff, enabling the construction of structures that have lasted for nearly two millennia, with prominent examples such as the Pantheon and the Colosseum. The Pantheon temple remains in use as an exhibition hall in the present day. In this study, beams and square prismatic samples featuring three different initial crack lengths were created to determine the fracture characteristics of lime-pumice mixtures containing various aggregate sizes (4 and 16 mm) and subjected to three-point bending tests at fracture test days (28 and 90). The two-parameter model and the double-K fracture model were employed for simulating the results of the fracture test.

Keywords: Double-K fracture model, Lime, Pumice, Two-parameter model

Introduction

Because of its internal structure and the variations in mechanical qualities it undergoes based on its size, concrete is a non-linear building material. When analyzing concrete using fracture mechanics, its non-linear behavior is equally crucial. For over 50 years, a number of academics proposed non-linear fracture models that used at least two size-independent fracture parameters to simulate cracked concrete structures (Hillerborg et al., 1976; Bazant and Oh, 1983; Jenq & Shah, 1985; Nallathambi & Karihaloo, 1986; Bazant & Kazemi, 1990; Xu & Reinhardt, 1999; Hu & Duan, 2008). The non-Hookean fracture models have used specimens with edge notches, such as beams, compact tension specimens, wedge-splitting specimens, and compact compression specimens, to calculate these size-independent fracture characteristics. Additionally, over the past thirty years, square and cylindrical prismatic specimens with central notches have been extensively used to assess the fracture properties of concrete.

Certain fracture metrics, like fracture toughness or fracture energy, have been extensively employed in the design of quasi-brittle materials, including rocks and concrete, based on fracture mechanics. The phrases "fracture toughness" and "fracture energy" are understood in concrete fracture literature as "unstable fracture toughness" or "unstable fracture energy" in relation to the aforementioned factors. In concrete constructions, however, the initiation fracture toughness a measure of crack initiation is just as significant as the fracture toughness a measure of unstable crack propagation. In particular, the analysis of specific structures, like nuclear power plants, pools, and water-resource structures, depends heavily on the initiation fracture toughness. One of

- This is an Open Access article distributed under the terms of the Creative Commons Attribution-Noncommercial 4.0 Unported License, permitting all non-commercial use, distribution, and reproduction in any medium, provided the original work is properly cited.

- Selection and peer-review under responsibility of the Organizing Committee of the Conference

© 2026 Published by ISRES Publishing: www.isres.org

the two design parameters of the Double-K fracture model for which RILEM has recently recommended technical standards is the initial fracture toughness (Xu et al., 2021).

Roman mortars, which are constructed of lime, water, sand, and volcanic tuff, are thought to have been the first concrete. They allowed for the construction of buildings that have stood for almost two millennia, including the Colosseum and the Pantheon. Even now, the Pantheon temple is still utilized as an exhibition space. The fracture characteristics of lime-pumice mixtures with different aggregate sizes (4 and 16 mm) were investigated in this study using beams and square prismatic samples with three different initial crack lengths. These samples were then put through three-point bending tests on fracture test days (28 and 90). The fracture test results were simulated using the double-K fracture model and the two-parameter model.

Fracture Mechanics of Cementitious Composites

Building components made from quasi-brittle substances, such as rock and cement-based materials, demonstrate a three-phase behavior leading up to failure. As illustrated in a beam with an initial crack length a_0, whose load versus crack mouth opening displacement relationship is depicted in Figure 1, these phases consist of: (1) crack initiation, which corresponds to the interval between the initial state and the first cracking load (P_i); (2) stable crack propagation, which corresponds to the interval between the first cracking load and the peak load (P_c); and (3) unstable crack propagation following the peak load. The beam, which behaves nearly in a linearly elastic manner due to material defects until the first cracking load, exhibits non-linear behavior beyond this point due to the development of a fracture process zone (FPZ) behind the free crack (Figure 1c).

A number of non-linear fracture models that utilized at least two size-independent fracture parameters to model cracked concrete members. These approaches generally utilize the fracture toughness parameter (K_{Ic}), which is the fundamental parameter in analysis of the cracked structures (Ince & Bildik, 2021). In Among the various elastic fracture models that are considered equivalent, the two-parameter model (TPM) is capable of predicting solely the unstable crack propagation at the peak load in quasi-brittle structures. This is achieved through the use of two critical parameters that relate to the critical crack length ($a_c=a_0+\Delta a_c$): the fracture toughness (K^s_{Ic}) and the crack tip opening displacement ($CTOD_c$), which effectively characterizes the blunting at the crack tip, as previously defined:

$$K_{Ic}^{s} = \sigma_{Nc}\sqrt{\pi a_c}\,Y\left(g,l\right) \tag{1}$$

$$CTOD_c = \frac{\lambda \sigma_{Nc} a_c}{E} V_1\left(g,l\right) M\left(g,l\right) \tag{2}$$

Where, σ_{Nc} is the nominal strength, E is Young's modulus of the material, and Y, V_1, and M are dimensionless functions of both the structural geometry (g) and the loading configuration (l). In Eq. (2), the coefficient λ takes the value of π for split-tension specimens with central cracks, 4 for beams, and 1 for semi-circular bending specimens and splitting specimens with edge cracks (Ince, 2025a; Ince et al. 2024; Ince, 2021). The term Y is widely referred to as the geometry factor, while M is obtained from the ratio $COD(a_c)/CMOD_c$, where $CMOD_c$ corresponds to the critical crack mouth opening displacement.

Fracture parameters can be deduced using one of two distinct test techniques: the compliance method introduced by RILEM (Shah, 1990) and the peak load method established by Tang et al. (1996) in this approach. In the first technique, these parameters are determined from the relationship between load and crack mouth opening displacement (P-CMOD) of three-point bending specimens that feature a central edge notch, as illustrated in Figure 1a, employing closed-loop testing apparatus. The critical crack length a_c is calculated from two measurements taken from the P-CMOD curve: the initial compliance (C_i) and the unloading compliance (C_u), which is recorded at approximately 95% of the peak load during the descending phase, as depicted in Figure 1b.

Conversely, the peak-load method eliminates the need for complex closed-loop apparatus, thus providing a more straightforward alternative to the RILEM compliance-based procedure for determining fracture parameters in TPM. Nevertheless, this method still requires a minimum of three specimens to account for the variability inherent in concrete. The test specimens may either have identical geometrical dimensions but differ in their initial notch lengths, or they may maintain consistent notch sizes while varying in overall dimensions. For each specimen, the governing equations of TPM can be expressed as outlined by Jenq & Shah (1985).

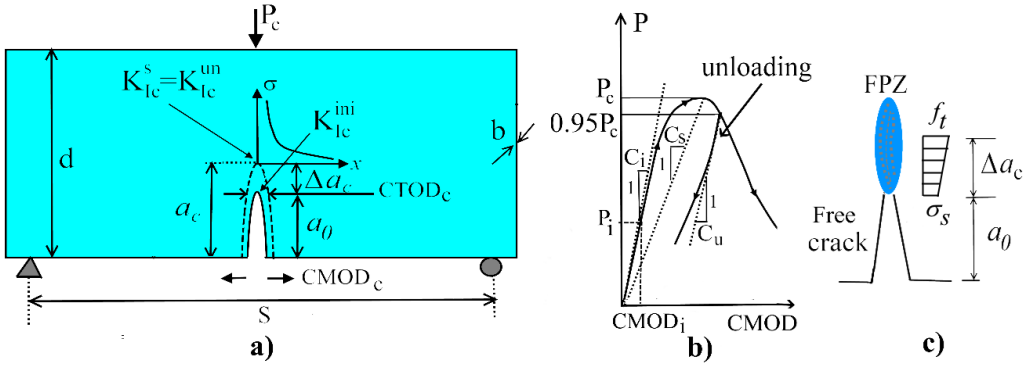

Figure 1. a) A typical concrete beam b) P-CMOD curve c) FPZ formation behind the crack

$$K_I^i\left(\sigma_{Nc}^i, a_c^i\right) = K_{Ic}^s \qquad , i = 1,2$$
$$CTOD^i\left(\sigma_{Nc}^i, a_c^i\right) = CTOD_c \tag{3}$$

In which, *i* refers to the *i*th sample. Consequently, the parameters associated with fractures can be ascertained by simultaneously resolving four non-linear equations. However, it is crucial to evaluate three or more distinct specimens to ensure statistically reliable results, given that random errors are consistently found in the measured values of σ^1_{Nc} and σ^2_{Nc}. As a result, this system, comprising several equations yet containing merely two unknowns, can solely be addressed through an optimization-based methodology. To facilitate this, Tang et al. (1996) suggested that the K^s_{Ic} and $CTOD_c$ curves relevant to particular notch depths should initially be established for each specimen with a unique a_0. Subsequently, the sample standard deviation (s) values associated with the identical K^s_{Ic} value are computed utilizing Eq. (4):

$$s\left(K_{Ic}^s\right) = \sqrt{\sum_{i=1}^{n}\left(CTOD_{cm} - CTOD_{ci}\right)^2 \Big/ \left(n-1\right)}, \qquad i = 1,2,...,n \tag{4}$$

Where, $CTOD_{cm}$ refers to the mean value of $CTOD_{ci}$ values. Consequently, K^s_{Ic} and $CTOD_c$ values corresponding to the minimum value of $s(K^s_{Ic})$ can be assumed to be the parameters of the model.

Ince (2025b) has recently presented a modified peak load method that uses an optimization algorithm to ascertain K^s_{Ic} and $CTOD_c$. This approach relies on the concurrent resolution of Eq. (3), which acts as a failure criterion for concrete structures, taking into account solely the critical crack extension (Δa_c) at peak load for each specimen. Eren & Ince (2025) and Ince & Eren (2026a) applied this modified approach to lime–pumice composites.

The double-K fracture model simulates a concrete structure including free crack via two-parameter: the initiation fracture toughness K^{ini}_{Ic} according to the initial cracking load and the unstable fracture toughness K^{un}_{Ic} according to the peak load. The parameter K^{un}_{Ic} is computed by using the secant compliance (C_s), as shown in Figure 1b. Therefore, an unloading and reloading procedure is not required, and a closed-loop system is not necessary in this model. In the way proposed by the RILEM TC265-TDK (Xu et al. 2021), the initial cracking load in the computation of can be determined from the turning point between the linear and nonlinear parts of the ascending P-CMOD curve, as shown in Figure 1b. However, K^{ini}_{Ic} can also be computed via the inverse method, which has widely been used since the method was initially suggested by Xu & Reinhardt (1999), which was presented below in detail.

$$K_{Ic}^{ini} = K_{Ic}^{un} - K_{Ic}^{c} \tag{5}$$

Where, K^c_{Ic} refers to the cohesive fracture toughness, which is determined by utilizing the trapezoidal cohesive stress function at peak load, in which the value of the upper stress is equal to the tensile strength of the materials (f_t). The analysis results according to the compliance method of wedge-splitting tests and beam tests by Xu et al. (2003) indicated that the parameters K^s_{Ic} and $CTOD_c$ that were computed for the TPM were coherent with K^{un}_{Ic} and $CTOD_c$ that were computed for the double-K model. Moreover, tests by Ince (2012) on cubical and cylindrical split-tension specimens revealed that both K^s_{Ic} and K^{un}_{Ic} could also be determined by adopting the peak-load method based on the TPM.

Experimental Program

In this research, the pozzolanic activity tests of pumice material were initially conducted using CL-80-S type lime, in accordance with TS 25 (1975). To achieve this, lime-pumice mortar was poured into cement molds measuring 40 × 40 × 160 mm, which contained three standard prismatic cavities, following the mixing ratios specified in TS 25 (1975). The samples were then covered with a hard mica material, wrapped in stretch film, and allowed to set for one day, after which they were placed in an oven at 55°C for a duration of one week. Four hours prior to the bending test, the samples were taken out of the oven and permitted to cool. Subsequently, they underwent a three-point bending test using a cement testing machine with a capacity of 30 kN and a support span of 100 mm. Six samples, derived from the three bending specimens that were divided in half, were subjected to a compression test in a cement press with a capacity of 40 kN on a loading area of 40 × 40 mm. Consequently, the flexural-tensile strength of the lime-pumice mortar was determined to be 2.3 MPa, exceeding the threshold of 1.0 MPa, while the compressive strength was found to be 4.4 MPa, surpassing the minimum requirement of 4.0 MPa. It was concluded that the pozzolanic activity of the pumice material is in compliance with TS 25 (1975).

The mixtures containing a maximum aggregate diameter of 4 mm were formulated with a water: lime: pumice: aggregate ratio of 1.53:1.00:1.00:6.00, whereas the mixture with a maximum aggregate diameter of 16 mm was prepared with a water: lime: pumice: aggregate ratio of 1.42:1.00:1.00:6.00. Two types of lime were utilized in the mixtures: CL-80-S lime, which has a specific gravity of 2.08, and CL-90-S lime, with a specific gravity of 2.09. The aggregate was air-dried before the mixing process commenced. The Fuller parabola was employed to ascertain the percentages of the aggregate gradation. Young's modulus of mixtures was determined by utilizing ultrasonic testing techniques. In this study, by using the following formulas, the dynamic the dynamic Young's modulus was determined at the test day for prismatic specimens and cubical specimens, respectively:

$$E_d = 10^3 V^2 \Delta, \quad \text{MPa} \tag{6}$$

$$E_d = 10^3 \frac{V^2 \Delta (1+\nu)(1-2\nu)}{1-\nu}, \quad \text{MPa} \tag{7}$$

In this context, V represents the velocity (km/s) and Δ denotes the unit weight (kg/lt). The Poisson ratio (ν) was assumed to be 0.3 for this research, as lime-pumice mixtures are classified as low strength materials (Erdogan, 2003). It is important to note that the dynamic modulus of the material exceeds the static modulus (E_s). The equation: E_s=6/7×E_d was applied for lime-pumice mixtures in this investigation (Lydon, 1984).

In this study, beams, single-notch cube bending (SNCB) specimens, and splitting specimens with edge cracks (SPEC) containing three distinct initial crack lengths were fabricated to determine the fracture parameters of lime-pumice mixtures. All specimens were kept by wrapping in stretch film in the mold until the test day. The specimens were notched with a diamond saw blade of 1.5 mm thickness on the day of the fracture test. For each mixture, cubes with 100 mm were also produced to determine compressive strength. The specimens were notched with a diamond saw blade of 1.5 mm thickness on the day of the fracture test. Then, the compression tests and the bending tests were conducted by employing a digital compression machine with a capacity of 100 kN. The specimens were loaded monotonically until final failure, and care was taken to apply a constant loading rate (Figure 2). Typically, approximately 2 min (± 30 sec) elapsed before the maximum load capacity for each specimen was reached.

Crack patterns observed at the failure of the notched specimens are illustrated in Figure 3. Four of the SNCB specimens exhibited shear fractures rather than bending fractures along the crack line, and these were not presented in Figure 3. The primary reason for this behavior is that SNCB specimens function similarly to deep beams, where the depth of the compression zone exceeds that of the beam subjected to three-point bending loading (Ince & Eren, 2026b).

Table 1 summarizes specimen types, lime types used in the mixtures, the maximum aggregate size (d_{max}), unit weight of the mixtures (Δ), fracture test age (T), compressive strength (f_c), Young's modulus (E_s), and specimen size (d) of the mixtures. In this table, by denoting n_s, the number of specimens in the group, the mean nominal strength values (σ_{Nc}) are also reported according to the grouped relative notch depths (α_0=a_0/d), respectively.

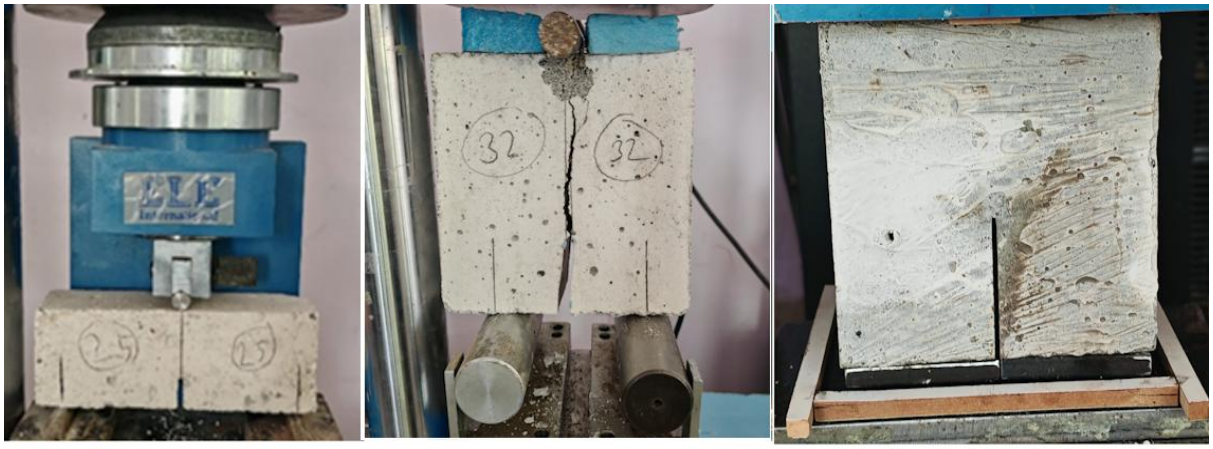

Figure 2. Test setup of the notched specimens

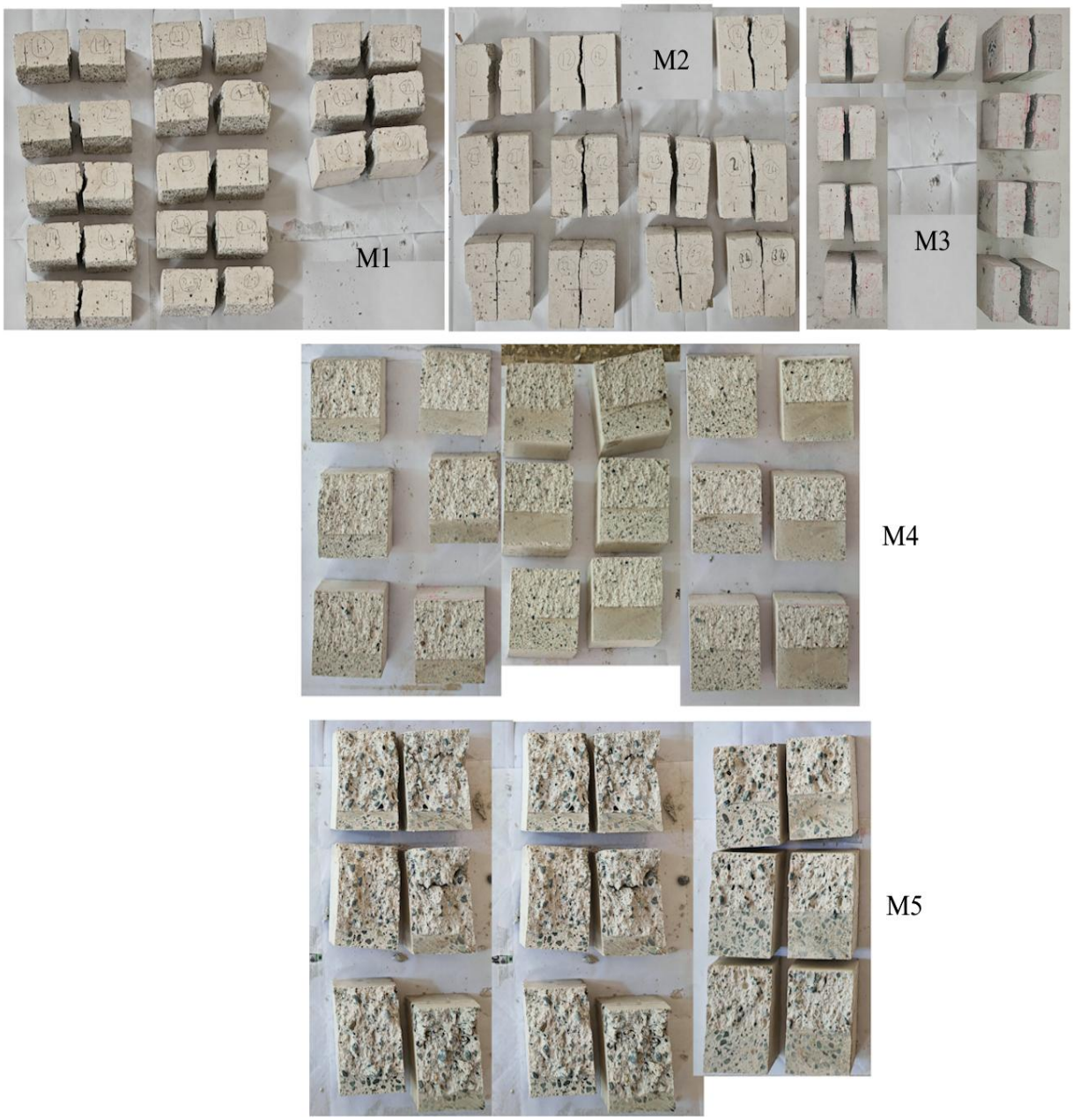

Figure 3. Crack patterns and failure mechanisms of the notched specimens

Table 1. Test results of the notched specimens

Series	Specimen	Lime	d_{max} mm	Δ g/cm^3	T Days	f_c MPa	E_s MPa	d mm	n_s	α_0	σ_{Nc} MPa
M1	Beam	CL-80-S	4	1.93	28	3.79	13384	50	5	0.191	0.821
									5	0.294	0.614
									3	0.449	0.424
M2	SNCB	CL-80-S	4	1.93	28	3.79	13384	150	3	0.316	0.302
									4	0.395	0.268
									4	0.477	0.237
M3	SNCB	CL-90-S	16	2.03	28	3.75	12537	100	4	0.308	0.458
									1	0.399	0.269
									4	0.509	0.303
M4	SPEC	CL-90-S	4	2.01	90	9.82	14216	100	3	0.291	0.611
									3	0.398	0.421
									3	0.48	0.327
M5	SPEC	CL-90-S	16	2.09	90	10.82	20382	150	3	0.188	1.041
									3	0.309	0.886
									3	0.437	0.442

Analysis of Lime-Pumice Composites According to the Double-K Fracture Model

In this study, the experimental results of lime–pumice composites were initially analyzed according to the two-parameter model using the peak-load method developed by Tang et al. (1996). As explained in detail below, this method is based on a specific statistical analysis procedure. Based on Eq. (3), this approach determines the fracture parameters of the material (K^s_{Ic} and $CTOD_c$) using only the peak loads of the specimens. In this method, at least two different groups of specimens are required. Accordingly, the specimen groups should be selected either as specimens having the same dimensions but two different notch lengths or as specimens with the same relative notch length (α_0) but different sizes. However, as previously stated, random errors are always present in the measured nominal strength values (σ_{Nc}). Therefore, in order to obtain statistically valid results, it is recommended that at least three specimen groups be tested.

As shown in Table 1, for the five series, the lime–pumice specimens used in this study were designed as three groups having the same dimensions but three different notch lengths. The applications of the analysis performed according to the peak-load method are presented in Figure 4. First, the K^s_{Ic} - $CTOD_c$ relationships for each group were plotted using Eqs. (1) and (2). Subsequently, the average K^s_{Ic} - $CTOD_c$ relationship for these groups was determined. The statistical procedure of the classical peak-load method is based on the calculation of the sample standard deviation of the groups according to Eq. (4). The following formulas were applied to beams with a span/depth ratio of 2.5 in this study (Yang et al., 1997):

$$Y(\alpha) = \frac{1.83 - 1.65\alpha + 4.76\alpha^2 - 5.3\alpha^3 + 2.51\alpha^4}{\sqrt{\pi}(1+2\alpha)(1-\alpha)^{1.5}} \tag{8}$$

$$V_1(\alpha) = 0.65 - 1.88\alpha + 3.02\alpha^2 - 2.69\alpha^3 + \frac{0.68}{(1-\alpha)^2} \tag{9}$$

$$M(\beta = \alpha_0/\alpha_c, \alpha_c) = \sqrt{(1-\beta)^2 + (1.081 - 1.149\alpha_c)(\beta - \beta^2)} \tag{10}$$

For the SNCB specimens with span/depth=0.6, the LEFM formulas were given by Ince & Eren (2026b):

$$Y(\alpha) = \frac{2.854 - 16.967\alpha + 60.766\alpha^2 - 102.025\alpha^3 + 84.581\alpha^4 - 27.245\alpha^5}{(1+2\alpha)(1-\alpha)^{1.5}} \tag{11}$$

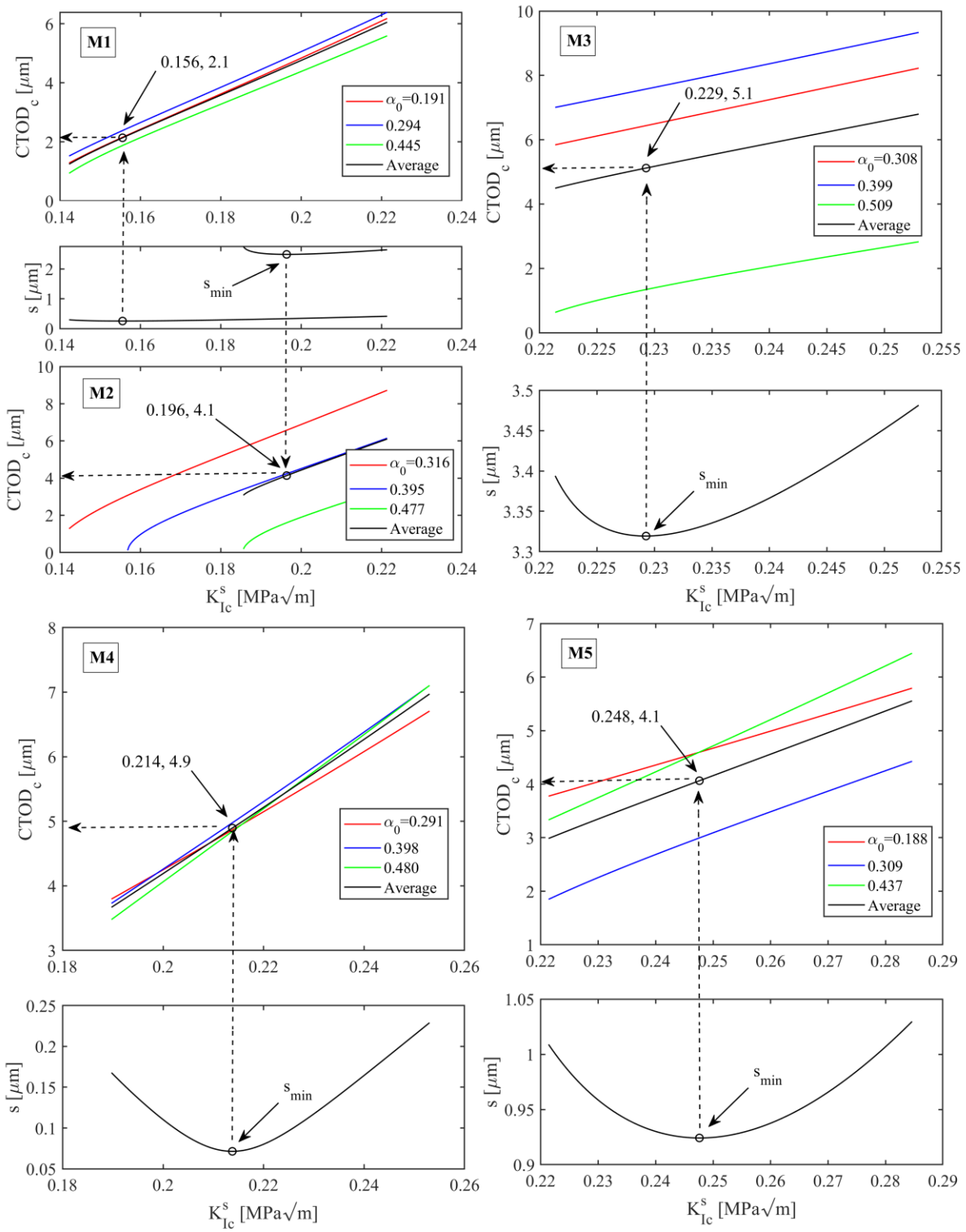

Figure 4. Application of the peak load method to the notched specimens

$$V_1(\alpha) = 8.691 - 27.46\alpha + 5.715\alpha^2 + 74.589\alpha^3 - 101.024\alpha^4 + \frac{4.476}{(1-\alpha)^2} \tag{12}$$

$$M(\beta = \alpha_0/\alpha_c, \alpha_c) = \sqrt{(1-\beta)^2 + (1.007 - 2.747\alpha_c + 2.018\alpha_c^2)(\beta - \beta^2)} \tag{13}$$

For the SPEC specimens subjected to the splitting loading used in Table 2, by denoting γ, the ratio of the width of the distributed load to the specimen depth (γ is 0.1 and 0.2 for the mixtures of M4 and M5, respectively), the LEFM formulas are given by (Ince, 2021):

$$Y\left(\alpha\right) = 0.3691 + 0.4492\alpha + 1.3284\alpha^2 + 2.4467\alpha^3 \quad \text{for}\,\gamma{=}0.1 \tag{14}$$

$$Y\left(\alpha\right) = 0.3341 + 0.0101\alpha + 2.5609\alpha^2 + 0.4067\alpha^3 \quad \text{for}\,\gamma{=}0.2 \tag{15}$$

$$V_1\left(\alpha\right) = 0.3722 + 2.0219\alpha - 6.6125\alpha^2 + 14.3038\alpha^3 \quad \text{for}\,\gamma{=}0.1 \tag{16}$$

$$V_1\left(\alpha\right) = 0.3040 + 1.7717\alpha - 5.3749\alpha^2 + 12.2420\alpha^3 \quad \text{for}\,\gamma{=}0.2 \tag{17}$$

$$M\left(\beta = \alpha_0/\alpha_c\,, \alpha_c\right) = \sqrt{\left(1-\beta\right)^2 + \left(2.16 - 4.02\alpha_c\left(1{-}\gamma\right)^{-0.23}\alpha_c^{3.67}\beta^{1.15}\right)\left(\beta-\beta^2\right)} \tag{18}$$

The cohesive fracture toughness of the material (K^c_{Ic}) in Eq. (5) must be computed to determine the imitation fracture toughness (K^{ini}_{Ic}) at first. For this, the following formula proposed by Xu & Reinhardt (1999), which is valid for an infinitely large specimen, was used in this study:

$$K^c_{Ic} = \sqrt{\frac{8\Delta a_c^{\infty}}{9\pi}}\left[2f_t + \sigma_s\left(CTOD_c\right)\right], \qquad \Delta a_c^{\infty} = \frac{\pi}{32}\left(\frac{CTOD_c E_c}{K^s_{Ic}}\right)^2 \tag{19}$$

Where Δa^{∞}_c is the crack extension in an infinitely large specimen. f_t and σ_s are the upper and lower limit stress values, respectively, as shown in Figure 1c. In this study, the direct tensile strengths of the mixtures (f_t), which is valid for an infinitely large specimen and proposed by Ince & Fenerli (2022), and the values of σ_s were determined by using Eqs. (20) and (21), as follows:

$$f_t = 0.356\frac{K^s_{Ic}}{\sqrt{\Delta a_c^{\infty}}} \tag{20}$$

$$\sigma_s\left(CTOD_c\right) = f_t\left(1 - \frac{CTOD_c}{w_0}\right), \qquad w_0 = \frac{2G_f}{f_t} \tag{21}$$

In which G_f (=$(K^s_{Ic})^2/E_c$), is the fracture energy of the material. For each series, the computed above fracture properties are summarized in Table 2.

Table 2. Analysis results of the notched specimens

Series	$K^s_{Ic} = K^{un}_{Ic}$ MPa√m	$CTOD_c$ mm	G_f N/m	Δa^{∞}_c mm	f_t MPa	σ_s MPa	K^{ini}_{Ic} MPa√m
M1	0.156	0.0021	1.809	3.32	0.961	0.415	0.084
M2	0.196	0.0041	2.881	7.80	0.791	0.342	0.106
M3	0.229	0.0051	4.193	7.70	0.930	0.402	0.124
M4	0.214	0.0049	3.215	10.40	0.746	0.322	0.115
M5	0.248	0.0041	3.008	10.99	0.840	0.363	0.134

Conclusion

The presented work investigated the fracture behavior of lime-pumice mixtures using the peak load method based on the double-K fracture model in fracture mechanics of concrete. The results of this work are detailed below:

The fracture toughness and strength values of the lime-pumice mixtures are approximately one-fifth of those found in normal cementitious mixtures. This reduction may be attributed to the low strength of the lime-pozzolan binder phase. The mechanism at play is that cracks tend to travel around the aggregate, as clearly illustrated in the M4 and M5 series specimens shown in Figure 4. Naturally, this process results in minimal energy absorption.

The initiation and unstable fracture toughness values (K^{ini}_{Ic} and K^{un}_{Ic}) of 90-day mortar are approximately 20% greater than those of 28-day mortar. The fracture toughness values of the lime-pumice mixture with a maximum aggregate size of 16 mm are approximately 30% greater than those of the mixture with a maximum aggregate size of 4 mm after 90 days. Additionally, for the 28-day samples, the fracture toughness values of the mixture with a maximum aggregate size of 16 mm are about 10% greater than those of the mortar.

Recommendations

Further works can come up with more reliable results by scrutinizing various types and sizes of aggregates and specimen types to verify the above findings.

Scientific Ethics Declaration

* The authors declare that the scientific ethical and legal responsibility of this article published in EPSTEM Journal belongs to the authors.

Conflict of Interest

* The authors declare that they have no conflicts of interest

Funding

* The authors declare that no external funding was received for this study.

Acknowledgements or Notes

* This article was presented as an oral presentation at the International Conference on Basic Sciences, Engineering and Technology (www.icbaset.net) held in Istanbul/Türkiye on September 17-18, 2026.

* This article is extracted from the second author's doctorate dissertation entitled "Investigation of Structures Produced from Historical Mortars Using Fracture Mechanics Principles", supervised by Ragip Ince.

* Erkin Eren would like to thank the Scientific and Technological Research Council of Turkey (TÜBİTAK) for supporting his doctoral education with the Domestic General Doctoral Scholarship Program (2211-A).

References

Bažant, Z. P. & Kazemi, M. T. (1990). Determination of fracture energy, process zone length, and brittleness number from size effect with application to rock and concrete. *International Journal of Fracture*, *44(2)*, 111-131.

Bažant, Z. P. & Oh, B. H. (1983). Crack band theory for fracture concrete. *Materials & Structures (RILEM)*, *16(93)*, 155-157.

Erdogan, T. Y. (2003). *Concrete*. METU Press. (in Turkish)

Eren, E. & Ince, R. (2025). Evaluation of nonlinear fracture quantities in lime-pumice mixtures. *The Eurasia Proceedings of Science, Technology, Engineering and Mathematics (EPSTEM), 38,* 672-681.

Hillerborg, A., Modeer, M. & Petersson, P. E. (1976). Analysis of crack formation and crack growth in concrete by means of fracture mechanics and finite elements. *Cement & Concrete Research*, *6*, 773-782.

Hu, X. & Duan K. (2008). Size effect and quasi-brittle fracture: the role of FPZ. *International Journal of Fracture*, *154*, 3–14.

Ince, R. & Bildik, A. T. (2021). A preliminary concrete mixture design based on fracture toughness. *Materials and Structures*, *54*:11.

Ince, R. & Eren, E. (2026a). Assessment of fracture properties in lime-pumice mortars through the utilization of various specimen types. *The Eurasia Proceedings of Science, Technology, Engineering and Mathematics (EPSTEM), 39,* 30-39.

Ince, R. & Eren E. (2026b). Utilizing cylindrical and cubical specimens with edge notch to determine size-independent fracture quantities of rock materials. *Fracture and Structural Integrity*, *75*, 435-462.

Ince, R. & Fenerli, C. (2022). Determination of tensile strength of cementitious composites using fracture parameters of two-parameter model for concrete fracture. *Construction and Building Materials 344*: 128222.

Ince, R. (2012). Determination of the fracture parameters of the Double-K model using weight functions of split-tension specimens. *Engineering Fracture Mechanics*, *96*, 416-432.

Ince, R. (2021). Utilization of splitting strips in fracture mechanics tests of quasi-brittle materials. *Archive of Applied Mechanics*, *91*, 2661–2679.

Ince, R. (2025a). Using SCB specimens to quantify nonlinear fracture characteristics in concrete and rock materials. *Engineering Fracture Mechanics*, *318*, 110951.

Ince, R. (2025b). A modified peak load method based on the two-parameter fracture model in concrete fracture. *The Eurasia Proceedings of Science, Technology, Engineering and Mathematics (EPSTEM), 36,* 141-150.

Ince, R., Yalcin, E. & Yilmaz, M. (2024). Quantifying nonlinear fracture parameters in bituminous SCB specimens: A compliance-based approach. *Case Studies in Construction Materials*, *21*, e03437.

Jenq, Y. S. & Shah, S. P. (1985). Two-parameter fracture model for concrete. *ASCE Journal of Engineering Mechanics*, *111(10)*, 1227-1241.

Lydon, F. D. (1984). *Concrete Mix Design*. Applied Science publishers.

Nallathambi, P. & Karihaloo, B. L. (1986). Determination of the specimen size independent fracture toughness of plain concrete. *Magazine of Concrete Research*, *38(135)*, 67-76.

Shah, S. P. (1990). Determination of fracture parameters (K^s_{Ic} sand $CTOD_c$) of plain concrete using three-point bend tests. *Materials and Structures (RILEM), 23,* 457-460.

Tang, T., Ouyang, C. & Shah, S. P. (1996). A simple method for determining material fracture parameters from peak loads. *ACI Materials Journal*, *93(2)*, 143-157.

TS 25 (1975). *Natural pozzolan (trass) for use in cement and concrete- definitions, requirements and conformity criteria*. Turkish Standard Institute. (in Turkish)

Xu, S. & Reinhardt, H. W. (1999). Determination of double-K criterion for crack propagation in quasi-brittle fracture, Part I: experimental investigation of crack propagation. *International Journal of Fracture*, *98*, 111-149.

Xu, S., Li, Q., Wu, Y., Dong, L., Lyu, Y., Reinhardt, H. W., Leung, C. K. Y., Ruiz, G., Kumar, S. & Hu., S. (2021). RILEM Standard: testing methods for determination of the double-K criterion for crack propagation in concrete using wedge-splitting tests and three-point bending beam tests, recommendation of RILEM TC265-TDK. *Materials and Structures*, *54(6)*, 220.

Xu, S., Reinhardt, W. H., Wu, Z. & Zhao., Y. (2003). Comparison between the double-K fracture model and the two parameter fracture model. *Otto-Graf-Journal, 14,* 131–157.

Yang, S., Tang, T., Zollinger, D. G. & Gurjar, A. (1997). Splitting tension tests to determine concrete fracture parameters by peak–load method. *Advanced Cement Based Materials*, *5*, 18–28.

Author(s) Information

Ragip Ince
Firat University
Engineering Faculty, Elazig, Türkiye
*Contact e-mail: *rince@firat.edu.tr*
ORCID iD: https://orcid.org/0000-0002-9837-8284

Erkin Eren
Firat University
Engineering Faculty, Elazig, Türkiye
ORCID iD: https://orcid.org/0000-0001-5282-398X

*Corresponding author(s) contact email

To cite this article:

Ince, R. & Eren, E. (2026). Determination of fracture parameters of lime-pumice composites using the double K fracture model. *The Eurasia Proceedings of Science, Technology, Engineering and Mathematics (EPSTEM), 42,* 1-10.

The Eurasia Proceedings of Science, Technology, Engineering and Mathematics (EPSTEM)
ISSN: 2602-3199

The Eurasia Proceedings of Science, Technology, Engineering and Mathematics (EPSTEM), 2026

Volume 42, Pages 11-18

ICBASET 2026: International Conference on Basic Sciences, Engineering and Technology

Evaluation of the Crack Resistance of Hot Mix Asphalt Mixtures Modified with Enprene 611 Elastomer

Esma Bakir
Malatya Turgut Ozal University

Erkut Yalcin
Fırat University

Abstract: In this study, the crack resistance of Hot Mix Asphalt (HMA) mixtures prepared using neat bitumen and bitumen modified with Enprene 611 elastomer was experimentally investigated through the Semi-Circular Bending (SCB) test. Asphalt mixtures were produced by incorporating 2%, 3%, and 4% Enprene 611 elastomer, by weight of the binder, into B70/100 penetration-grade bitumen. The compacted cylindrical specimens were cut into two equal halves, and artificial notches with depths of 10, 20, and 30 mm were introduced at the center of each semi-circular specimen to obtain SCB test samples. The SCB tests were conducted at 20°C and 40°C to evaluate the combined effects of temperature and notch depth on the fracture behavior of the asphalt mixtures. The experimental results demonstrated that the mixtures containing 4% Enprene 611 consistently exhibited the highest maximum fracture load (P_{max}) at all notch depths and test temperatures, significantly outperforming both the neat and the other modified mixtures. Furthermore, increasing the Enprene 611 content considerably enhanced the deformation resistance, cohesive bonding strength, and crack propagation resistance of the asphalt mixtures. Overall, the findings indicate that Enprene 611 is an effective polymer modifier for improving the fracture performance and mechanical durability of hot mix asphalt mixtures.

Keywords: Hot mix asphalt (HMA), Enprene 611 elastomer, Semi-circular bending (SCB), Crack resistance, Polymer-modified bitumen

Introduction

Road transportation is currently the most widely used mode of transportation worldwide. Among the various pavement systems, Hot Mix Asphalt (HMA) is the most preferred pavement type due to its cost-effectiveness, ease of construction, and satisfactory service performance. However, one of the most common forms of distress observed in HMA pavements is cracking, which significantly reduces pavement durability and service life. To minimize crack initiation and propagation, various modifier additives are incorporated into asphalt binders to enhance their adhesive and mechanical properties. These additives improve the rheological characteristics of bitumen, thereby extending the service life of flexible pavements.

The modification of neat bitumen using polymeric additives has become one of the most effective approaches for improving binder performance. Modified asphalt binders exhibit superior resistance to permanent deformation, fatigue damage, and thermal cracking compared with conventional binders. Consequently, Hot Mix Asphalt (HMA) technology utilizing polymer-modified binders has been widely adopted in pavement engineering applications (Zhao et al., 2025). In recent years, considerable attention has been devoted to the use of polymer- and elastomer-based modifiers for asphalt binder modification. These modifiers effectively improve rutting resistance at elevated temperatures while significantly reducing crack susceptibility caused by traffic loading and environmental conditions at intermediate and low temperatures.

- This is an Open Access article distributed under the terms of the Creative Commons Attribution-Noncommercial 4.0 Unported License, permitting all non-commercial use, distribution, and reproduction in any medium, provided the original work is properly cited.

- Selection and peer-review under responsibility of the Organizing Committee of the Conference

© 2026 Published by ISRES Publishing: www.isres.org

Among the available polymer modifiers, Enprene 611 elastomer has emerged as a promising additive for enhancing the engineering performance of asphalt binders and Hot Mix Asphalt mixtures. Recent studies have compared the performance of Enprene 611 with conventional modifiers such as Styrene–Butadiene–Styrene (SBS), Enprene 701, crumb rubber (CR), and various chemical additives, demonstrating its considerable potential for asphalt modification (Utku Tiryaki & Yalcin, 2025). Furthermore, Enprene 611 has been reported to significantly improve the high-temperature performance of asphalt binders by increasing their stiffness and resistance to permanent deformation (Seza Deveci & Yilmaz, 2025). To characterize the crack propagation behavior of asphalt mixtures under laboratory conditions, the Semi-Circular Bending (SCB) test has become one of the most widely accepted fracture testing methods because of its simplicity, repeatability, and ability to simulate crack initiation and propagation under controlled loading conditions.

Several laboratory test methods have been developed to evaluate the cracking resistance of asphalt mixtures, including the four-point bending test (Zhang et al., 2023), uniaxial fatigue push–pull test (Soltani & Anderson, 2005), Texas Overlay Test (Walubita et al., 2021), and indirect tensile fatigue test (Haggag et al., 2011). Depending on the loading protocol, these methods generally employ either monotonic or cyclic loading conditions. Among them, the SCB test has become one of the most frequently adopted techniques for evaluating the fracture behavior and cracking resistance of asphalt mixtures (Meng et al., 2023). Historically, asphalt fracture has been investigated through laboratory experiments, numerical simulations, and field observations. Over the past decades, laboratory investigations supported by analytical and numerical approaches have substantially improved the understanding of fracture mechanisms in asphalt mixtures (Saha & Biligiri, 2016). Although extensive research has been conducted on monotonic SCB testing, fatigue-based SCB investigations remain relatively limited and require further improvements regarding loading protocols and fracture characterization parameters (Meng et al., 2023). Recent studies have combined the SCB test with digital image correlation (DIC) to evaluate the low-temperature fracture and damage behavior of asphalt concrete. Such full-field deformation measurements allow damage to be monitored throughout the crack propagation process, providing a more comprehensive understanding of fracture evolution in asphalt mixtures (Zhu et al., 2025). In general, the cracking resistance of asphalt materials is primarily evaluated using two categories of testing methods: repeated-loading fatigue tests and monotonic fracture tests (Shi et al., 2025).

In the present study, the crack resistance of Hot Mix Asphalt mixtures produced with B70/100 penetration-grade bitumen modified by 2%, 3%, and 4% Enprene 611 elastomer was experimentally investigated. The crack propagation behavior of both neat and modified mixtures was comprehensively evaluated using the Semi-Circular Bending (SCB) test at 20°C and 40°C with notch depths of 10, 20, and 30 mm. The effects of polymer content, testing temperature, and notch geometry on the fracture performance of asphalt mixtures were systematically examined.

Materials and Methods

Materials

In this study, B70/100 penetration-grade neat bitumen, produced by the Batman TÜPRAŞ Refinery (Türkiye), was used as the asphalt binder. Considering the climatic and environmental conditions of Türkiye, B70/100 penetration-grade bitumen is one of the most commonly used binders in flexible pavement applications. The specific gravity of the neat bitumen used in this study was determined to be 1.033 g/cm³. The fundamental physical properties of the neat asphalt binder are summarized in Table 1 (Yalcin et al., 2026).

Table 1. Physical properties of the B70/100 penetration-grade neat bitumen

Properties	Unit	Standard	Results
Penetration	0.1mm	EN 1426	87.4
Softening point	°C	EN 1427	52.6
Flash point	°C	EN ISO 2719	230
Viscosity at 135°C /165°C	cP	ASTM D4402	562.5/162.5

Enprene 611 elastomer, supplied by Mpolimer Co., was used as the polymer modifier for bitumen modification. For the production of Hot Mix Asphalt (HMA) mixtures, limestone aggregate, which is characterized by its high abrasion resistance, was selected as the mineral aggregate.

Bitumen Modification

The modified asphalt binders were prepared by incorporating Enprene 611 elastomer into the B70/100 penetration-grade neat bitumen at concentrations of 2%, 3%, and 4% by weight of the binder. The modification procedure was carried out according to the following steps: Initially, the neat bitumen was heated in a laboratory oven at 180 ± 5°C for approximately 30 min until it reached a sufficiently fluid state. Subsequently, 800 g of the heated bitumen was transferred into a metallic mixing container and maintained at 180 ± 5°C until thermal equilibrium was achieved.

The predetermined amount of Enprene 611 elastomer was gradually added to the bitumen. The mixture was then blended using a high-speed mechanical mixer operating at 2700 rpm for 4 h to ensure the homogeneous dispersion of the polymer throughout the binder. At the end of the modification process, the polymer-modified asphalt binders were obtained and subsequently used for the preparation of the Hot Mix Asphalt (HMA) specimens.

Preparation of Hot Mix Asphalt (HMA) Specimens

The limestone aggregates used in the preparation of the asphalt mixtures were separated into individual size fractions according to the aggregate gradation specified for the Semi-Circular Bending (SCB) specimens. Each aggregate fraction was weighed using a precision balance to satisfy the target gradation limits presented in Table 2 (Yalcin et al., 2026).

Table 2. Aggregate gradation used in the hot mix asphalt (HMA) mixtures

Sieve Size (mm)	19	12.5	9.5	4.75	2.36	1.18	0.6	0.3	0.15	0.075
Passing (%)	100	95	88	65	35	23	14	10	8	6

Based on the preliminary mix design analyses, the optimum bitumen content (OBC) for the control mixture was determined to be 4.67%. Subsequently, 1975 g of the aggregate–bitumen mixture was thoroughly blended using a laboratory-scale Hot Mix Asphalt (HMA) mixer to ensure a homogeneous mixture. The prepared mixture was then placed into the mold of a Superpave Gyratory Compactor (SGC) and compacted to produce cylindrical HMA specimens. The specimen preparation procedure is illustrated in Figure 1 (Yalcin et al., 2026).

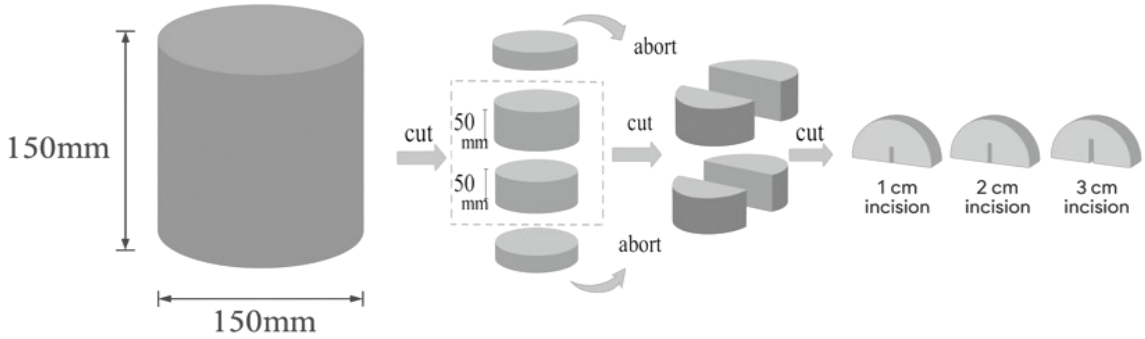

Figure 1. Schematic diagram of the preparation process of semi-circular bending specimen

Semi-Circular Bending (SCB) Test

The Semi-Circular Bending (SCB) test was employed to evaluate the cracking resistance of the asphalt mixtures, which represents one of the most critical distress mechanisms affecting flexible pavements throughout their service life. The compacted cylindrical HMA specimens with a diameter of 150 mm were cut into two equal halves to obtain semi-circular test specimens. Artificial notches with depths of 10, 20, and 30 mm were then introduced at the midpoint of the flat edge of each specimen to ensure controlled crack initiation during the SCB tests. The semi-circular specimens prepared using both neat and Enprene 611-modified bitumen were conditioned at 20°C and 40°C to investigate the influence of temperature on crack propagation behavior and specimen stiffness. The SCB tests were performed under three-point bending using a constant displacement rate of 50 mm/min under monotonic loading conditions. Throughout the tests, the applied load and the corresponding crack mouth opening displacement (CMOD), measured at the notch mouth, were continuously recorded using a computerized data acquisition system until complete failure of the specimens. The SCB test specimens and the experimental setup are shown in Figure 2.



Figure 2. Semi-circular bending (SCB) test specimens and experimental setup

Results and Discussion

The crack propagation behavior of the neat and Enprene 611-modified Hot Mix Asphalt (HMA) mixtures was evaluated under different testing temperatures (20°C and 40°C) and notch depths (10, 20, and 30 mm) using the load–Crack Mouth Opening Displacement (Load–CMOD) curves obtained from the Semi-Circular Bending (SCB) tests. The corresponding maximum fracture load (P_{max}) values obtained from the experiments are summarized in Table 3.

Table 3. Maximum fracture load values obtained from the SCB tests for neat and enprene 611-modified hot mix asphalt (HMA) mixtures

Test Temperature	Notch Depth(mm)	Neat	2%Enprene611 (kN)	3% Enprene 611 (kN)	4% Enprene 611 (kN)
20 °C	10	4.85	8.70	9.60	11.90
20 °C	20	3.70	7.50	8.30	9.20
20 °C	30	2.60	6.80	7.45	8.45
40 °C	10	2.70	6.30	7.50	8.35
40 °C	20	1.70	3.85	5.15	6.75
40 °C	30	0.80	3.35	4.15	5.50

The SCB test results obtained at 20°C clearly demonstrated that the incorporation of Enprene 611 elastomer significantly enhanced the load-carrying capacity and crack initiation resistance of the asphalt mixtures, regardless of notch depth. For the specimens with a 10 mm notch, the neat HMA mixture exhibited a maximum fracture load of 4.85 kN. Incorporating 2%, 3%, and 4% Enprene 611 increased the maximum fracture load to 8.70 kN, 9.60 kN, and 11.90 kN, respectively. Among all mixtures, the specimen containing 4% Enprene 611 exhibited the highest mechanical performance, corresponding to an approximately 145% increase in fracture load compared with the neat HMA mixture. As the notch depth increased from 10 mm to 20 mm and 30 mm, a gradual reduction in the maximum fracture load was observed for all mixtures owing to the decrease in the effective load-bearing cross-sectional area. Nevertheless, despite this geometric reduction in the net ligament area, the beneficial effect of polymer modification remained evident. Even for the specimens with a 30 mm notch, the mixture modified with 4% Enprene 611 exhibited a load-carrying capacity more than three times greater than that of the neat HMA specimen (2.60 kN), demonstrating the effectiveness of the elastomer in improving fracture resistance under severe crack conditions.

The influence of elevated temperature became more pronounced during the SCB tests conducted at 40°C. Owing to the viscoelastic nature of the asphalt binder, increasing the test temperature significantly reduced both the stiffness and maximum fracture load of all HMA mixtures compared with those tested at 20°C. The maximum fracture load of the neat HMA specimen with a 10 mm notch decreased from 4.85 kN to 2.70 kN. Furthermore, the neat specimen containing a 30 mm notch, which represented the most critical notch geometry, exhibited the lowest fracture load of only 0.80 kN, indicating that the asphalt mixture became considerably more susceptible to crack propagation under elevated-temperature conditions. In contrast, modification with Enprene 611 elastomer remarkably improved the high-temperature stability and cohesive strength of the asphalt matrix. Under the test condition of 40°C with a 10 mm notch, the specimen containing 4% Enprene 611 achieved a maximum fracture load of 8.35 kN, corresponding to an approximately 209% increase compared with the neat

HMA mixture. Even under the most severe testing condition (40°C and a 30 mm notch), the 4% Enprene 611-modified specimen sustained a fracture load of 5.50 kN, which was nearly seven times greater than that of the neat HMA specimen (0.80 kN). These findings suggest that the three-dimensional polymer network formed by Enprene 611 effectively enhanced the aggregate–binder interaction and delayed the transition of microcracks into macrocracks, thereby significantly improving the fracture resistance of the asphalt mixtures under elevated-temperature conditions.

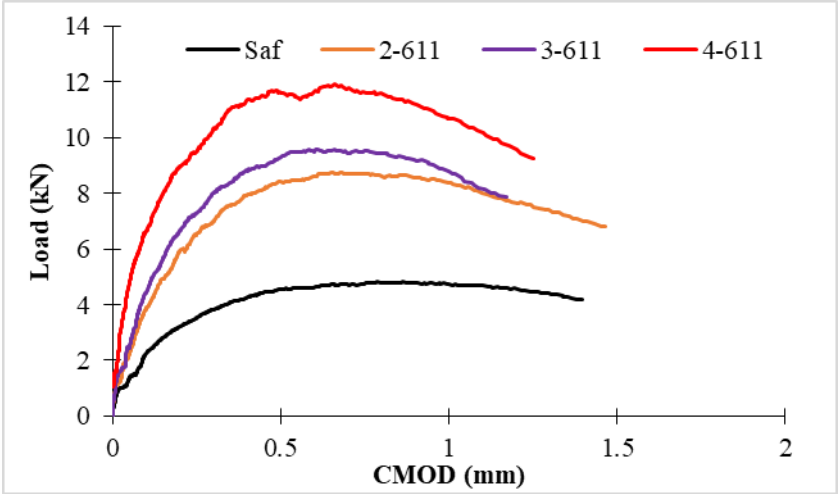

Load–CMOD Curve of the HMA Mixtures with a 10 mm Notch Depth

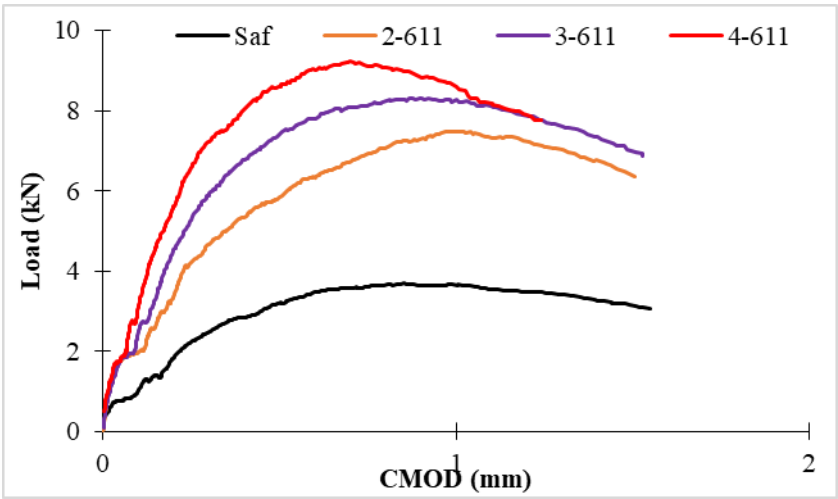

Load–CMOD Curve of the HMA Mixtures with a 20 mm Notch Depth

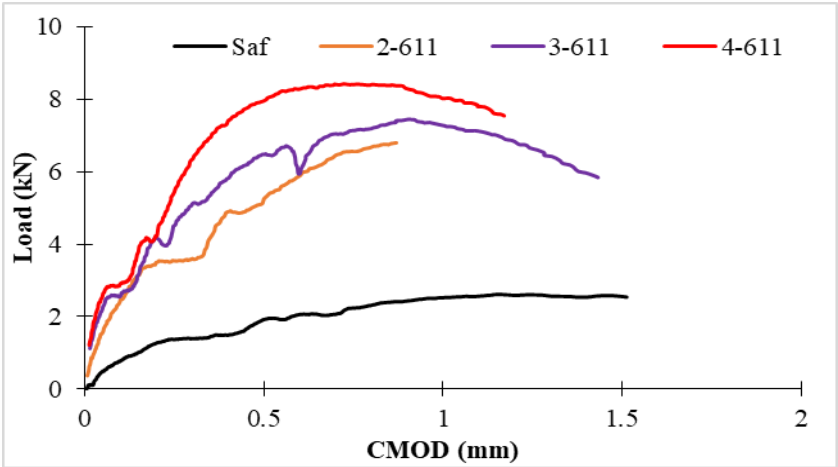

Load–CMOD Curve of the HMA Mixtures with a 30 mm Notch Depth

Figure 3. Load–CMOD Curves of HMA Mixtures with Different Notch Depths at 20°C

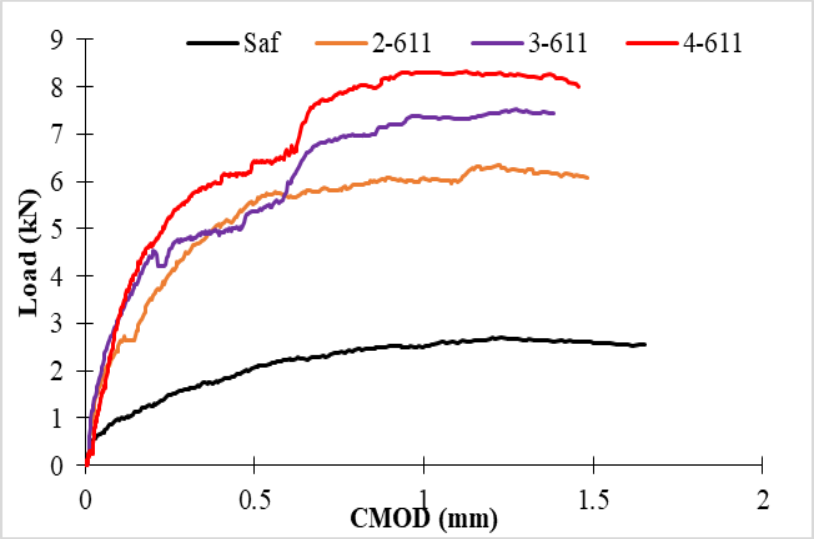

Load–CMOD Curve of the HMA Mixtures with a 10 mm Notch Depth

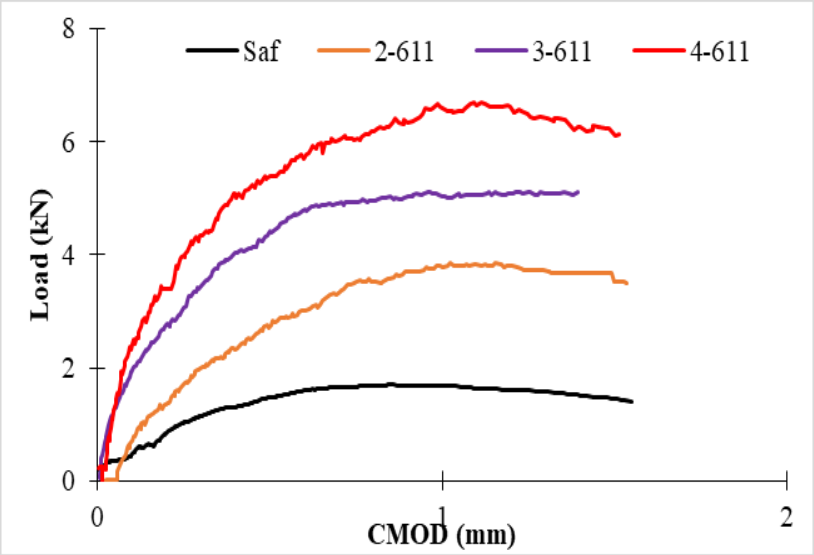

Load–CMOD Curve of the HMA Mixtures with a 20 mm Notch Depth

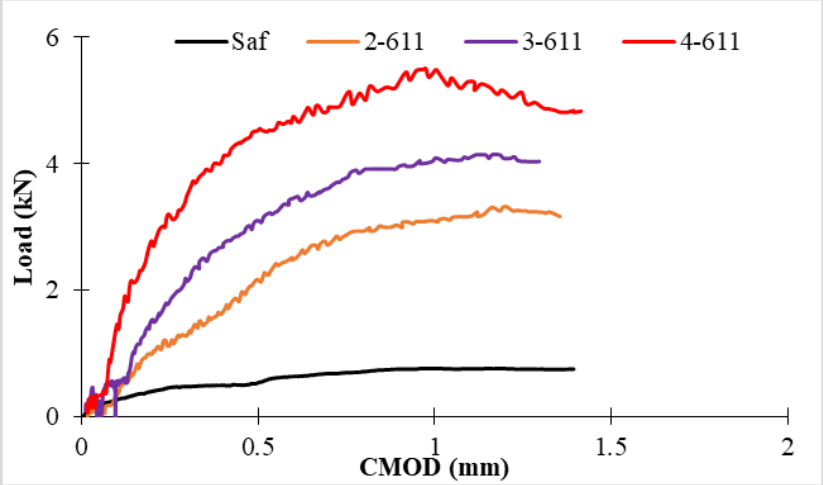

Load–CMOD Curve of the HMA Mixtures with a 30 mm Notch Depth

Figure 4. Load–CMOD Curves of HMA Mixtures with Different Notch Depths at 40°C

Conclusion

Based on the experimental findings obtained from the Semi-Circular Bending (SCB) tests, the following conclusions can be drawn:

Enprene 611 elastomer modification significantly improved the crack propagation resistance of the Hot Mix Asphalt (HMA) mixtures at both ambient (20°C) and elevated (40°C) temperatures across all notch geometries. The improvement became more pronounced with increasing polymer content. Among all experimental conditions, the HMA mixtures containing 4% Enprene 611 exhibited the highest crack resistance and load-carrying capacity, demonstrating the superior reinforcing effect of the elastomer within the investigated dosage range.

Increasing the notch depth from 10 mm to 30 mm reduced the maximum fracture load due to the decrease in the effective load-bearing cross-sectional area. Nevertheless, Enprene 611 modification effectively preserved the structural integrity of the asphalt matrix and mitigated brittle fracture, even under the most critical notch geometry.

Increasing the test temperature from 20°C to 40°C resulted in a noticeable reduction in fracture resistance owing to the thermal softening of the asphalt binder. However, the incorporation of Enprene 611 significantly enhanced the high-temperature stability of the asphalt mixtures by limiting viscous flow, thereby improving their resistance to permanent deformation and thermally induced cracking.

Overall, the findings of this study demonstrate that Enprene 611 is a promising polymer modifier for improving the fracture performance and long-term durability of Hot Mix Asphalt mixtures, providing valuable insights for the development of more durable and sustainable flexible pavement systems.

Scientific Ethics Declaration

* The authors declare that this study complies with scientific research and publication ethics. All scientific, ethical, and legal responsibilities related to the content of this article belong to the authors.

Conflict of Interest

* The authors declare that they have no conflicts of interest.

Funding

* This study was supported by the Fırat University Scientific Research Project Management Unit (FUBAP) under Project No. MF.26.83. The authors would like to acknowledge the financial support provided by the Scientific and Technological Research Council of Türkiye (TÜBİTAK) under Project No. 123M648, as well as the support received through the TÜBİTAK 2224-B Domestic Scientific Event Participation Support Program.

Acknowledgements or Notes

* This article was presented as an oral presentation at the International Conference on Basic Sciences, Engineering and Technology (www.icbaset.net) held in Istanbul/Türkiye on September 17-18, 2026.

References

Haggag, M., Mogawer, W., & Bonaquist, R. (2011). Evaluating the indirect tensile fatigue characteristics of asphalt mixtures. *Transportation Research Record: Journal of the Transportation Research Board, 2210*(1), 89–98.

Meng, Y., Kong, W., Gou, C., Deng, S., Hu, Y., Chen, J., & Fan, L. (2023). A review on evaluation of crack resistance of asphalt mixture by semi-circular bending test. *Journal of Road Engineering, 3*(1), 87–97.

Saha, G., & Biligiri, K. P. (2016). Fracture properties of asphalt mixtures using semi-circular bending test: A state-of-the-art review and future research. *Construction and Building Materials, 105*, 103–112.

Seza Deveci, I., & Yilmaz, M. (2025). Determination of physical properties of polymeric and different additives on bituminous binders. *The Eurasia Proceedings of Science, Technology, Engineering and Mathematics, 36*, 134–140.

Shi, C., Wang, T., Guo, P., Fan, Y., Wu, Y., & Yang, J. (2025). Investigation of cracking resistance of rubberized epoxy asphalt mixture using semi-circular bending (SCB) test. *Theoretical and Applied Fracture Mechanics, 139*, 105137.

Soltani, A., & Anderson, D. A. (2005). Uniaxial fatigue of asphalt mixes: A new approach (Report No. FHWA-PA-2003-019-97-04(20)). Pennsylvania Transportation Institute, The Pennsylvania State University.

Utku Tiryaki, S., & Yalcin, E. (2025). Evaluation of different additives on mechanical properties and performance of hot mix asphalt using Marshall stability and ITSM tests. *The Eurasia Proceedings of Science, Technology, Engineering and Mathematics, 36*, 125–133.

Walubita, L. F., Ho, C. H., Prakoso, A., & Scullion, T. (2021). The Texas Overlay Test (OT) for evaluating the cracking resistance of asphalt mixtures: A review and recommendations. *Construction and Building Materials, 270*, 121390.

Yalcin, B. F., Ince, R., & Yilmaz, M. (2026). Effect of temperature on the fracture characteristics of hot mix asphalt mixtures using the semi-circular bend (SCB) test. *Turkish Journal of Science and Technology, 21*(1), 253–269.

Zhao, K., Li, Y., He, F., Meng, Y., Hu, C., Ye, X., & Lin, P. (2025). A comprehensive study on the influence of Sasobit content on rheological properties and storage stability of CR/SBS composite-modified asphalt. *Construction and Building Materials, 463*, 140066.

Zhang, Y., Zhang, J., Ma, T., Qi, H., & Chen, C. (2023). Predicting asphalt mixture fatigue life via four-point bending tests based on viscoelastic continuum damage mechanics. Case Studies in Construction Materials, 19, e02671. https://doi.org/10.1016/j.cscm.2023.e02671

Zhu, S., Zhou, Z., Zhang, Z., Liu, Z., & Hou, X. (2025). Evaluation of low-temperature fracture and damage of asphalt concrete using SCB test combined with DIC. *Engineering Fracture Mechanics, 321*, 111135.

Author(s) Information

Esma Bakir
Malatya Turgut Ozal University, Civil Engineering Department, Engineering Faculty, Malatya, Türkiye
ORCID iD: https://orcid.org/0000-0002-4466-6862
*Contact e-mail: *esma.sarisin@ozal.edu.tr*

Erkut Yalcin
Firat University, Civil Engineering Department, Engineering Faculty, Elazig, Türkiye
ORCID iD: https://orcid.org/0000-0002-6389-4211

*Corresponding author(s) contact email

To cite this article:

Bakir, E. & Yalcin, E. (2026). Evaluation of the crack resistance of hot mix asphalt mixtures modified with enprene 611 elastomer**.** *The Eurasia Proceedings of Science, Technology, Engineering and Mathematics (EPSTEM), 42***,** 11–18.

The Eurasia Proceedings of Science, Technology, Engineering and Mathematics (EPSTEM)
ISSN: 2602-3199

The Eurasia Proceedings of Science, Technology, Engineering and Mathematics (EPSTEM), 2026

Volume 42, Pages 19-29

ICBASET 2026: International Conference on Basic Sciences, Engineering and Technology

The Role of Participatory Agricultural Extension in Mitigating the Adverse Effects of Climate Change on Agricultural Production

Bawer Taher Mohammad
University of Duhok

Hashim Saeed Murad
University of Duhok

Salah Jasim Amin
University of Kirkuk

Abstract: Climate changes pose significant challenges to agricultural production systems, necessitating the adoption of the effective extension approaches that enhance farmers` adaptive ability. This study evaluates the role of participatory agricultural extension in addressing the adverse impacts of climate change on agricultural production from farmers` perspective. Data were collected through a structured questionnaire and analyzed using descriptive and inferential statistical methods to examine the relationship between farmers' characteristics and their perception of participatory agricultural extension. Data were collected from simple random sample of 128 farmers (25% of the target population of 512 farmers) distributed across 12 villages in Sulaymaniyah Governorate. The findings revealed a limited implementation of participatory agricultural extension within agricultural extension centers in the centers in the study area, with 56.3% of respondents reporting low levels of participatory communication. Correlation analyses (Pearson and spearman) indicate significant negative relationships between participatory agricultural extension and farmers` age, education level, farm size, farm type, farming experience. Significant positive relationships were found with educational level, participation in training programs, and level of communication with information sources. In contrast, no significant relationship was found between farmers` attitudes toward climate change and their perceptions of participatory agricultural extension. Despite the weak implementation of participatory extension approaches, respondents demonstrated moderate to high adoption levels of climate-smart agricultural practices, accounting for 62.5% and 32.0% of the sample, respectively. Farmers identified three major constraints hindering the effective implementation of participatory agricultural extension. The predominance of conventional extension approaches among extension (92.29), prevailing social and cultural norms (92.45%). And insufficient governmental support for participatory extension programs (92.19%). The study highlights the urgent need to strengthen participatory agricultural extension systems through capacity building, modernization of extension methodologies, and increase institutional and financial support, enhancing participatory approaches can improve farmers resilience and adaptive capacity, thereby contributing to more sustainable agricultural systems under changing climatic conditions.

Keywords: Agricultural sustainability, Climate change mitigation, Farmers' perceptions, Participatory agricultural extension.

Introduction

Climate change and the need for environmental protection are global issues and call for an awareness response from all nations to be effectively mitigated ed (Houghton and WMO, 2002). The unpleasant reality of global warming and the human activities causing it are acknowledged by both the scientific and environmental sectors.

- This is an Open Access article distributed under the terms of the Creative Commons Attribution-Noncommercial 4.0 Unported License, permitting all non-commercial use, distribution, and reproduction in any medium, provided the original work is properly cited.

- Selection and peer-review under responsibility of the Organizing Committee of the Conference

© 2026 Published by ISRES Publishing: www.isres.org

The environment is being impacted by the quick rise in greenhouse gases more quickly than many living things can adjust, which is worrisome. All kinds of life face enormous hurdles in this ever-evolving and increasingly complicated environment (Hassan, 2024). Climate change is significantly impacting global agriculture, which is upsetting conventional agricultural practices and creating serious problems for food security.

Global food production systems are greatly influenced by the complex interactions between rising temperatures, changing patterns of precipitation, and an increase in the frequency of extreme weather events (Prajapati et al., 2024). North of Iraq is presently experiencing numerous issues related to climate change and agricultural deterioration, such as increasing temperatures, altered precipitation patterns, heightened drought conditions, escalating water shortages, and more frequent sand and dust storms. The absence of targeted data and analysis on the Kurdistan Region of Iraq has hindered comprehension of the unique challenges the region faces, given its different climate, terrain, and customs in comparison to central and southern Iraq (Iraq, 2022).

For the crucial development of rural areas through agricultural extension services in rural communities, some countries do not pay enough attention, which is significant, as agricultural extension workers can establish and formulate an active strategy and develop programs for transferring information (Hamasalih and Layeeq, 2023). The agriculture, biodiversity, natural resources, and practices that are harmful to human beings should be accepted as moral and human issues. It is necessary to make use of agricultural extension, which is a magic tool that helps bring a change in incorrect attitudes and notions. It has to be kept in mind that it should be used with perfectly correct and proper approaches, as helpful for farmers' problem-solving and participation (Özcatalbas *et al.,* 2017). The integration of different extension approaches, including both established and contemporary techniques, can improve the spread of innovation. Combining the traditional top-down approach with modern pluralistic and participatory approaches is likely to result in more favorable outcomes (Adefalu et al., 2023). Participatory approach in farming has proven to be transformative for agricultural practices in rural areas, significantly enhancing both productivity and sustainability. By actively participating in decision-making processes and leveraging local knowledge, this strategy has led to improved crop yields, helped with better water and soil management, and diversification of adopted cropping systems. However, it strengthened resilience to climate change impacts and restored degraded farmlands, boosting the long-term sustainability of agricultural practices (Sharma, 2017).

Participatory agricultural extension encompasses adaptation, mitigation, and various agricultural practices that enhance the system's ability to cope with different climate-related disruptions by minimizing damage and facilitating rapid recovery. In essence, it refers to the system's capacity to rebound. This approach fundamentally entails the careful and enhanced management of natural resources, such as land, water, soil, and genetic resources, through the implementation of optimal practices (Sulaiman, 2024). To facilitate the upscaling and integration of local knowledge systems in climate-smart agriculture (CSA), the political narratives surrounding CSA must ensure the representation of smallholder farmers in agricultural policy and decision-making processes, rather than allowing dominant development partners to dictate the discourse. Achieving the successful upscaling of the mitigation of climate change impacts requires a more equitable distribution of power and a commitment to social justice, thereby amplifying the voices of smallholder farmers. This process of inclusion should adopt a participatory, bottom-up approach within CSA initiatives. We propose that methods such as farmer-led knowledge creation and farmer school programs offer valuable production. Such a bottom-up model can help prevent development partners and national governments from imposing technocratic agendas, ensuring that the interests and insights of smallholder farmers remain central to the design of practices and technologies aimed at mitigating ing climate change (Ogunyiola et al., 2022; Mansour et al., 2026).

Future strategies should prioritize inclusive, decentralized, and community-driven methodologies to guarantee equitable access to programs designed for building climate resilience. Emphasizing farmer-led innovation, participatory approaches, and institutional reforms will be essential for fostering long-term sustainability. Enhancing the connections between research, extension services, and farmers, as well as integrating climate resilience into agricultural policies, can significantly improve food security, enhance rural livelihoods, and promote overall agricultural sustainability in the context of climate-related challenges (Priya et al., 2025).

To establish this approach, which integrates farmers into agricultural extension programs, the current research aimed to explore the significance of participatory agricultural extension in mitigating climate change impacts on agriculture, particularly through the lens of farmers in the Kurdistan Region of Iraq. By analyzing the relationship between various independent factors and farmers' assessments of the effectiveness of participatory extension methods, the researcher sought to identify key strategies and practices employed by farmers to adapt to climate challenges. Additionally, the research will reveal the primary challenges encountered in implementing the participatory agricultural extension approach, providing valuable insights into farmers' perspectives.

Ultimately, the findings will contribute to the development of more effective agricultural policies that prioritize farmers' needs and enhance resilience against climate impacts.
Therefore, this research attempts to answer the following questions:

1. How highly do farmers evaluate the role of participatory extension in mitigating the negative impacts of climate change on agriculture in general?
2. Do farmers' evaluations of the role of participatory extension vary according to their individual characteristics?
3. What are the strategies and practices employed by farmers to mitigate the negative impacts of climate change on agriculture in the Suleymani governorate, from the farmers' point of view?
4. What are the primary challenges faced in implementing the participatory agricultural extension approach from the farmers' point of view?

Objectives

1. Evaluating the role of participatory agricultural extension in mitigating the negative impacts of climate change on agriculture from the farmers' point of view.
2. Identifying the correlation between independent variables and the farmers' evaluation of the role of participatory agricultural extension in mitigating the climate change impacts on agriculture in the Soleymani governorate.
3. Identifying the strategies and practices employed by farmers to mitigate the negative impacts of climate change on agriculture in the Soleymani governorate, from the farmers' point of view.
4. Identifying the primary challenges faced in implementing the participatory agricultural extension approach from the farmers' point of view.

Research Hypotheses

To achieve the objective of the study, there is no significant relationship between the role of participatory agricultural extension approach in addressing the negative impacts of climate change on agriculture and each variable:

There is no statistically significant correlation between farmers' evaluation of the role of participatory agricultural extension in mitigating the negative effects of climate change on agriculture and some of their characteristics such as: age, educational level, farm size, type of farm, experience in agriculture, participation in training courses, attitudes toward climate change, and level of communication with information sources.

Materials & Methods

Methodology of Research

The study employed the descriptive research approach to evaluate the role of participatory agricultural extension, the strategies and practices employed by farmers, and primary challenges faced by implementing the role of participatory agricultural extension approach in Soleymani Governorate to mitigate the negative climate change impacts on agriculture product. It is considered an appropriate approach for evaluating the existing situation by collecting, analyzing, and interpreting data related to the characteristics, perceptions, and experiences of the selected population. This is also emphasized by previous studies, the situation in the study area is unstable, as suffering from climate change impacts on farmlands and water resources, which were conducted by all of (Grimes and Schulz (2002). Therefore, this approach was adopted in this research because it is suitable for the nature of the research topic and achieves its objectives scientifically and systematically.

Study Area

The study was conducted in the Governorate of Soleymani, located in the Kurdistan Region of Iraq. The area is famous for multiple agricultural practices, with a large number of farmers working in plant and animal production, and all those farmers are under the supervision of agricultural extension centers. For each of the mentioned sub-districts in Table 1, there is one directorate of the agricultural extension center, and the

agricultural extension agents have roles to support farmers in their diverse agricultural extension methods, including the participatory approach.

Population and Sample of Research

The research population included 512 farmers distributed across 12 villages in four sub-districts and two districts in Soleymani governorate. To achieve the research objectives, a simple random sample of 25% was selected, and thus the research sample size reached 128 farmers, as shown in Table 1.

Table 1. The population and sample of research.

No.	Governorate	Districts	Sub-districts	Villages	Population	Size of sample 25%
1.	Sulaymaniyah	Center	Tanjro	Qaraly	76	19
2.				Qaragul	24	6
3.			Bazyan	Arbati-kon	40	10
4.				Halla	36	9
5.				Lazyan	68	17
6.			Zerayan	Khaldan	64	16
7.				Deskera	32	8
8.		Bazyan		Kelakawy	44	11
9.			center	Alan	24	6
10.				Kani-Kewa	28	7
11.				Mahmod-Khane	36	9
12.				Kani-Meel	40	10
Total					512	128

Materials

The questionnaire was the primary data collection tool used by the researcher, as it facilitated obtaining accurate responses aligned with the research objectives through one-on-one personal interviews with farmers.

Data Collection

The role of participatory agricultural extension agents in facing the impacts of climate change on agriculture in the Soleymani governorate, comprises a set of questions to know the role of participatory agricultural extension approach in point of the farmers' view; it means the role of agricultural extension agents by using participatory agricultural extension approach in conducting and transferring the information to farmers about climate change impacts and the degree of their participation in agricultural extension activities such as "planning, program evaluation, field visits, training sessions, etc.". The 35 items were measured on a three-point Likert scale as follows: (Always = 3, Sometimes = 2, Never = 1). Correspondingly, the scores ranged theoretically from 35 to 105.

Personal characteristics include a set of questions to recognize the characteristics of farmers as follows: (age, educational background, area used for agricultural production in dunums, type of farmland possession, agriculture experience, participation in climate change sessions, farmers' trend towards climate change, and knowledge level of connecting to the information on climate change resources). Age, this variable was measured by the raw number of the respondent's age, considered from his/her birthday date to the time of data collection. Educational background, the level of education of the respondent was reached at the time of data collection, and it was measured by the following scales: illiterate = 1, read and write = 2, primary school = 3, intermediate school = 4, high school = 5, diploma = 6, bachelor = 7, and higher educational = 8., Area used for agricultural production in Dunums, this variable was measured by the raw number of donums that the farmer cultivated at the time of data collection.

Type of farmland possession, this variable refers to the type of production that farmers practice at the time of data collection, which is divided into three types: plant production, animal production, and mixed farm of plant and animal, and it was measured by the following scales: plant production = 1, animal production = 2, mixed farm = 3. Agriculture Experience: This variable refers to the number of years a farmer has spent in agricultural

practices, measured by the raw number of years spent in agriculture. Participation in climate change sessions: This variable refers to the farmer's participation in training sessions on the impacts of climate change on agriculture.

The following scales measured it: participated "Yes" = 2, not participated "No" = 1. Farmers' attitudes toward climate change, this variable was measured by using 12 statements, and 3 alternatives were used for each statement as scales (Agree, Average, and Disagree): Agree = 3, Average = 2, Disagree = 1. Knowledge level of connecting to the information on climate change resources, this variable was assessed using a set of 12 statements, each measured on a four-point Likert scale. The response options included: (Always, Sometimes, Rarely, and Never), corresponding to the numerical values of: Always = 4, Sometimes = 3, Rarely = 2, Never = 1.

The strategies and practices employed by farmers to mitigate the negative impacts of climate change on agriculture in the Soleymani governorate, Includes a set of strategies and practices that help farmers to face the current situation of climate conditions in the Kurdistan region, and then to identify the preferred degree of each one from the farmer's point of view; all strategies and practices were measured in four scales as follow, high = 4, medium = 3, low = 2, little = 1. Challenges faced in implementing the participatory agricultural extension approach from the farmers' point of view, comprise a set of challenges that are suggested to the farmers in the targeted area to know the extent of importance of challenges from the farmers' point of view; all items were measured on three scales to identify their importance to farmers as follows: big = 3, medium = 2, and few = 1.

Data Collection and Analysis

Data were collected during the period from 7 July 2025 to 25 September 2025, and were statistically analyzed using SPSS software, with the use of methods appropriate to the research objectives, which included frequencies, percentile weight, weighted mean, Pearson and Spearman correlation coefficients to study the relationship between the independent variables and the farmers' evaluation of the effectiveness of the role of participatory agricultural extension in combating the climate change impacts on agriculture in the Soleymani governorate

Reliability and Validity

Validity: This was achieved by presenting the questionnaire to several experts and specialists in agricultural extension. The necessary modifications were made to the items included in the form to make them more effective in achieving the desired objective.

Reliability: To examine the role of participatory agricultural extension in mitigating the negative impacts of climate change on agriculture, Cronbach's Alpha was used to assess the reliability of the measurement instrument based on the relationship between the items representing the independent and dependent variables. The analysis of the 35 – item scale produced a Cronbach's Alpha value of 0.73. This result indicates an acceptable to good level of internal consistency, suggesting that the items are sufficiently correlated and collectively measure the intended construct in a reliable manner.

Results and Discussion

1. Evaluate the role of participatory agricultural extension in mitigating the negative impacts of climate change on agriculture from the farmers' point of view

Table 2. Distribution of respondents by the role of participatory agricultural extension in mitigating the negative impacts of climate change on agriculture

Classes	Frequency	Percentage %	Mean	Std. Deviation
41 – 59 Low	72	56.3	57.111	18.2011
60 – 78 Medium	42	32.8	71.500	8.5290
79 – 97 High	14	10.9	87.142	4.5039
Total	128	100.0	65.117	17.7216

The results revealed that more than half of the respondents were within the low category with the ration 56.3%. In comparison, the high category only scored 10.9% of respondents, indicating a weak role of participatory agricultural extension in the study area.

2. To identify the correlation between independent variables and the farmers' evaluation of the role of participatory agricultural extension in mitigating the climate change impacts on agriculture in the Soleymani governorate.

Table 3. Distribution of respondents by personal and functional characteristics.

Variables	Classes	Frequency	Percent age (%)	Mean	Std. Deviation	Pearson/ Spearman (r/rs)	Sig.
Age	26 – 39 Low	23	18.0	33.782	3.716	r = -0.383**	Sig
	40 – 53 Medium	47	36.7	47.042	4.085		
	54 – 67 High	58	45.3	61.465	3.992		
	Total	128	100	51.195	11.182		
Educational Level	1 Illiterate	24	18.8			rs = 0.454**	Sig
	2 read and write	26	20.3				
	3 Primary school	31	24.2				
	4 Middle school	17	13.3				
	5 High school	7	5.5				
	6 Bachelor's Degree	11	8.6				
	7 Diploma	9	7.0				
	8 Higher certificates	3	2.3				
	Total	128	100				
Farm Size	6 – 70 Small	109	85.2	27.889	17.093	rs = -0.213*	Sig
	71 – 135 Medium	14	10.9	95.000	13.008		
	136 – 200 Large	5	3.9	184.000	23.021		
	Total	128	100	41.328	39.451		
Type of Farm	Plant production	93	72.7			rs = 0.212*	Sig
	Animal Production	18	14.1				
	Mixed farming	17	13.3				
	Total	128	100				
Experience in Agriculture	5 – 18 Low	35	27.3	11.000	3.903	r = -0.424**	Sig
	19 – 32 Medium	48	37.5	25.166	4.022		
	33 – 46 high	45	35.2	40.022	4.147		
	Total	128	100	26.515	12.153		
Participation in Training Courses	1 Participated	92	71.9			rs = 0.290**	Sig
	2 Not Participated	36	28.1				
	Total	128	100				
Attitudes Toward Climate Change	21 – 25 Low	25	19.5	23.280	1.242	r = 0.019	ns
	26 – 30 Medium	58	45.3	28.517	1.327		
	31 – 35 High	45	35.2	32.266	1.095		
	Total	128	100	28.8125	3.433		
Level of Communication with Information Sources	13 – 21 Low	64	50.0	17.578	1.933	r = 0.345**	Sig
	22 – 30 Medium	45	35.2	26.355	2.739		
	31 – 49 High	19	14.8	33.842	2.500		
	Total	128	100	23.078	6.459		

Age, respondents who are located in the high-age category (54 – 67 years) covered almost half of the population, with the ratio (45.3%), while the medium and young ages came lower with the ratios 36.7% and 18% consequently. The results indicate that agricultural activities in the study area are largely managed by individuals who are older rather than younger, and age was significantly and negatively correlated with the dependent variable ($r = -0.383$, $p < 0.01$), showing that higher age was associated with a lower extent of the outcome. *The level of education* among the respondents revealed that most farmers have a primary school certificate (24.2%), followed by the farmers who can only read and write (20.3%), and (18.8%) who are illiterate. Educational level indicated a significant positive relationship with the dependent variable ($rs = 0.454$, $P<0.01$), which means a better educational level tends to result in higher scores on the measured outcome.

Regarding *farm size*, the findings showed the limitation in the farm size, as most of the respondents with the ratio (85.2%) owned small farms ranging from 6 to 70 dunums, opposite the medium and large farms, where the ratio 10.9% and 3.9%, respectively. It also indicated that the standard deviation was equal to 39.45, which means the farm size relationship had a negative correlation with the dependent variable ($rs = -0.213$, at $p<0.05$), because the variable's lower outcome scores were associated with the larger farm holdings. Concerning *the type of farm***,** it showed that most of the respondents were practicing plant production, representing 72.7%, while animal production and mixed farming accounted for the ratios 14.1% and 13.3%, respectively. It indicated a positive and significant correlation with the dependent variable.

With respect to *agricultural experience*, the respondents possessed substantial agricultural experience, which was scored at ratios of about 37.5% medium levels and about 35.2% high levels of agricultural experience. As shown in the findings, the average experience was 26.52 years with SD = 12.15, which means that the newest in agriculture experience tended to higher scores on the outcome measure, as indicated by the relationship with a significant negative correlation with the dependent variable ($r = -0.424$, at $p<0.01$). For the *participants in training sessions* about climate change, the results showed that a high ratio of farmers participated, about 71.9%, which was positively and significantly associated with the dependent variable, with the correlation coefficient ratio $rs = 0.290$, at p-value 0.01, which means that the training helped to increase the measured outcome.

Concerning *attitudes toward climate change***,** the respondents reported that the highest ratio was in the moderate level of attitude toward climate change, about 45.3%, then the high and low ratios displayed about 35.2% and 19.5%, respectively. Since $r = 0.019$, at $p>0.05$, there was no significant relationship found between attitudes toward climate change and the dependent variable. Lastly, the low level was reported by half of the respondents (50%) for *communication with climate change information sources*, while medium and high levels reported lower scores (35.2% and 14.8%), respectively. The dependent variable had a positive and significant correlation with communication with climate change information sources ($r = 0.345$, $p<0.01$), indicating that more access to information sources improved the measured outcome.

Overall, significant relationships for the previous results, as follows: There were *positive relationships* for all (educational level, type of farm, participation in training sessions, and communication with climate change information sources); on the other hand, there were *negative significant relationships* for (age, farm size, and agricultural experience), and only attitudes toward climate change had *no significant relationship*.

3. To identify the strategies and practices employed by farmers to mitigate the negative impacts of climate change on agriculture in the Soleymani governorate, from the farmers' point of view.

Table 4. Distributing the respondents according to the strategies and practices preferability

Classes	Frequency	Percentage %	Mean	Std. Deviation
Low (21-26)	7	5.5	23.86	2.12
Medium (27-32)	41	32.0	30.22	1.37
High (33-38)	80	62.5	35.94	1.86
Total	128	100	33.45	3.91

The results revealed that the majority of respondents located at the high and medium level (62.5%), and (32%) of their preferability to use new strategies and practices in agriculture in facing the climate change impacts, while only (5.5%) reported in low level, it suggesting that the farmers are open to use new techniques in their farmlands and implement strategies to mitigate the climate change impacts on their agricultural product.

4. To identify the primary challenges faced in implementing the participatory agricultural extension approach from the farmers' point of view

Respondents reported high relative importance for all items using against climate change impacts on agriculture product, the top strategies and practices were recorded with using modern irrigation systems to reduce water consumption, and employing organic farming methods to improve soil health (94.92%, and 94,14), respectively, as the area exposed more to the draught and erosion in the farmlands, farmers suffer from water scarcity and unhealthy soil for the last two decades, this is also mentioned by the (Mohammed *et al.,* 2021) in their research at Soleymani governorate about irrigation water susceptibility indexing method, and water quality, then the last item scored with 73.24% for using biotechnology to improve crop resistance to diseases and pests, this was might back to unfamiliarity about this technique. The results indicated that the farmers had very high relative importance to all strategies and practices mentioned in Table 5, but the ability of application might be limited due to some challenges as described in Table 7, which were the most familiar challenges in the study area.

Table 5. Ranking the strategies and practices according to their mean and relative importance degrees.

Methods and Strategies	Frequency	Sum	Mean	Relative Importance	Ranking
Using modern irrigation systems to reduce water consumption	128	486.0	3.796	94.92	1
Employing organic farming methods to improve soil health	128	482.0	3.765	94.14	2
Using renewable resources such as solar energy	128	450.0	3.515	87.89	3
Using modern and advanced technologies to monitor climatic conditions	128	435.0	3.398	84.96	4
Training and educating farmers on sustainable farming techniques	128	425.0	3.320	83.01	5
Developing policies and legislation to support sustainable agriculture	128	423.0	3.304	82.62	6
Using crop varieties adapted to harsh climatic conditions	128	419.0	3.273	81.84	7
Using artificial intelligence to improve the efficiency of resource utilization	128	402.0	3.140	78.52	8
Raising awareness among individuals and communities about climate change and its negative impacts on agriculture.	128	384.0	3.000	75.00	9
Using biotechnology to improve crop resistance to diseases and pests	128	375.0	2.929	73.24	10

Table 6.Distribution of respondents to challenges of implementing the participatory agricultural extension.

Classes	Frequency	Percentage %	Mean	Std. Deviation
Low (16-22)	3	2.3	16.333	0.577
Moderate (23-29)	29	22.7	27.413	1.783
High (30-36)	96	75	33.260	2.187
Total	128	100	31.539	3.984

Table 7. Ranking the challenges according to their mean and relative importance.

Challenges	Frequency	Sum	Mean	Relative Importance	Ranking
Preference of agricultural extension agents for traditional extension methods	128	357.00	2.789	92.97	1
Prevailing traditional farming culture and customs	128	355.00	2.773	92.45	2
Limited government support for implementing extension programs	128	354.00	2.765	92.19	3
Lack of funding and financial support for the extension system to improve the participatory extension approach	128	341.00	2.664	88.80	4
Lack of training capacities within the extension system in the region	128	338.00	2.640	88.02	5
Shortage of specialized extension staff in agricultural extension agents	128	337.00	2.632	87.76	6
Lack of technical expertise among farmers regarding how to apply the participatory extension approach	128	332.00	2.593	86.46	7
Weak communication and coordination between farmers and agricultural extension agents in executing extension strategies	128	328.00	2.562	85.42	8
Weak policies and legislation supporting the participatory extension approach	128	325.00	2.539	84.64	9
Low interaction between farmers and extension agents in implementing participatory programs	128	325.00	2.539	84.63	10
Lack of technical expertise among agricultural extension agents on how to implement the participatory extension approach	128	323.00	2.523	84.11	11
Limited awareness among farmers about the participatory extension approach	128	318.00	2.484	82.81	12

For the challenges that were not helpful to practice the participatory agricultural extension, it revealed that the three quarters of respondents were scored at the highest level (75%), followed by the moderate level (22.7%), of the relative importance of the mentioned challenges in the table 7, only (2.3) reported at low level, suggesting a high importance of implementing the participatory agricultural extension approach in the studied area.

Concerning the most effective challenges faced by agricultural extension agents from the farmers' point of view, the top three challenges displayed by farmers were as follows: preference of agricultural extension agents for traditional extension methods, prevailing traditional farming culture, and customs. Limited government support for implementing extension programs (92.97%, 92.45%, and 92.19%), respectively. On the other hand, the lowest two challenges scored by farmers were low interaction between farmers and extension agents in implementing participatory programs, and limited awareness among farmers about the participatory extension approach, with the ratios 83.63% and 82.81%. The high ratios of mentioned challenges in the study area indicated that the application of the participatory agricultural extension approach is limited in reaching out to most of the farmers; it needs to reconsideration of agricultural extension strategies by diversifying the activities in their monthly and yearly planning.

Conclusion

The study findings displayed that the farmers in the target area cannot participate in agricultural extension service, especially due to the weak strategy to implement the participatory agricultural extension approach, which is considered a core subject to participate them in agricultural extension activities. These findings suggest that the participatory approach needs to be activated in agricultural extension centers, which are considered the main responsible. As well as the activation of the participatory agricultural extension approach needs government support from the Ministry of Agriculture to face the financial and technical challenges, and at the same time, agricultural extension agents need to reconsider their yearly or monthly strategies.

In general, to get rid of the current challenges in the study area and adaptation to the new strategies to help farmers mitigate the impacts of climate change on the agricultural products requires the diversification of activities in the agricultural extension programs and encouraging them by participating in all levels of agricultural extension programs, including "planning, evaluation, and implementation.

Recommendations

1. The agricultural extension centers need to redesign the agricultural extension programs in general.
2. Enhance the participatory agricultural extension approach by the agricultural extension agents to improve effectiveness and responsiveness to farmers' needs.
3. Equipping agricultural extension programs financially and technically to reactivate the participatory agricultural extension approach
4. Supporting agricultural extension centers with the necessary training materials and aids to activate the participatory agricultural extension approach.

Study Limitations

This study has several limitations that should be considered when interpreting the findings. First, the research was conducted in selected villages in Sulaymaniyah Governorate, Kurdistan Region of Iraq, which may limit the generalizability of the results to other geographical areas with different environmental, agricultural, and socio-economic conditions. Second, the study employed a cross-sectional descriptive correlational design, which is suitable for identifying associations among variables but does not permit causal inferences. Third, the findings were based on farmers' self-reported responses to a structured questionnaire and may therefore be subject to response bias, social desirability bias, and recall bias. Finally, the study focused primarily on farmers' demographic and farm-related characteristics and did not examine broader institutional and policy dimensions that may also influence the effectiveness of participatory agricultural extension.

Future Research Directions

Future research should extend this work by including farmers from different governorates and diverse agricultural production systems to improve the external validity and generalizability of the findings. Comparative studies across regions with varying climatic, institutional, and socio-economic conditions would provide a broader understanding of the effectiveness of participatory agricultural extension.

Longitudinal, quasi-experimental, or experimental research designs are recommended to evaluate the long-term effects of participatory agricultural extension on farmers' adaptive capacity, resilience, and adoption of climate-smart agricultural practices. Future studies should also investigate the influence of institutional and policy-related factors, including extension service capacity, extension agents' competencies, governmental support, financial resources, and digital agricultural advisory services. Furthermore, integrating quantitative and qualitative approaches would provide a more comprehensive understanding of farmers' participation, decision-making processes, and the practical challenges of implementing participatory agricultural extension under changing climate conditions.

Scientific Ethics Declaration

* The author declares that the scientific, ethical, and legal responsibility for this article belongs entirely to the author.

Conflict of Interest

* The author declares that there is no conflict of interest.

Funding

* This research received no specific grant from any funding agency in the public, commercial, or not-for-profit sectors.

Acknowledgements or Notes

* This article was presented as an oral presentation at the International Conference on Basic Sciences, Engineering and Technology (www.icbaset.net) held in Istanbul/Türkiye on September 17-18, 2026.

* The author would like to express sincere appreciation to all farmers who participated in this study and to the agricultural extension staff who facilitated the data collection process. Their valuable cooperation and support are gratefully acknowledged.

References:

Adefalu, L. L., Obafemi, B. O., Ayanda, V. O., Idris-Adeniyi, K., & Raza, H. A. (2023). Traditional and modern approaches in agricultural extension practice in Nigeria. *Journal of Social Sciences Review, 3*(1), 552–561.

Grimes, D. A., & Schulz, K. F. (2002). *Descriptive studies: What they can and cannot do. The Lancet, 359*(9301), 145–149. https://h1.nu/1yb7b

Hamasalih, C. M., & Layeeq, T. M. (2023). The importance of agricultural extension programs in technology transfer for rural farmers: A review. *Zagazig Journal of Agricultural Research, 50*(3), 387–394. https://h1.nu/1ybO0

Hassan, N. E. (2024). Global warming: Causes, impacts and urgent strategies for a sustainable future: A review. *GSC Advanced Research and Reviews, 20*(3), 073–087.

Houghton, D. D., & World Meteorological Organization. (2002). *Introduction to climate change: Lecture notes for meteorologists.* Geneva, Switzerland: Secretariat of the World Meteorological Organization. https://h1.nu/1sGlU

Iraq, I. O. M. (2022). *Migration, environment, and climate change in Iraq.* International Organization for Migration (IOM). Retrieved from https://h1.nu/1yb9F

Mansour, T. G. I., Abd El-Ghani, S. S., & Murad, H. S. (2026). Farmers' attitudes toward mechanisms and practices of climate change adaptation in Egypt and Iraq: A comparative field study. *Sustainability, 18*(5), 2502.

Mohammed, S. A., Nejad, R. A., & Hamamin, D. F. (2021). Irrigation water susceptibility indexing method, using pesticide DRASTIC and water quality index, for Basara Basin; Kurdistan region-Iraq. *Journal of Environmental Treatment Techniques, 9*(2), 435–445.

Ogunyiola, A., Gardezi, M., & Vij, S. (2022). Smallholder farmers' engagement with climate-smart agriculture in Africa: Role of local knowledge and upscaling. *Climate Policy, 22*(4), 411–426.

Özcatalbas, O., Imran, M., Gurkan, G., Durmuş, H., & Unlu, T. (2017, July). The role of agricultural extension and agricultural education for sustainability. In *ESEE 2017 Conference–Transformative Learning: New Directions in Agricultural Extension and Education* (pp. 4–7). Retrieved from https://h1.nu/1sGYx

Prajapati, H. A., Yada, K., Hanamasagar, Y., Kumar, M. B., Khan, T., Belagalla, N., & Malathi, G. (2024). Impact of climate change on global agriculture: Challenges and adaptation. *International Journal of Environment and Climate Change, 14*(4), 372–379.

Priya, N. K., Khatri, A., Kumar, A., Samota, S. D., Vishwakarma, S. K., Sukdeve, E. K., ... & Pathak, A. K. (2025). The important role of extension services in strengthening the capacity of farmers' resilience to climate change in India. *Journal of Experimental Agriculture International, 47*(3), 204–223.

Sharma, P. (2017, October). *Participatory approaches in farming: Enhancing farmer engagement and knowledge transfer in rural areas in Rajasthan.* ISSN: 2456-4184. Retrieved from https://www.ijnrd.org/papers/IJNRD1710009.pdf

Sulaiman, R. V. (2024). *Agricultural extension and advisory services in support of climate change adaptation and mitigation.* Retrieved from ttps://h1.nu/1yeKU

Author(s) Information

Bawer Taher Mohammad
University of Duhok
General Directorate of Agricultural Duhok, Iraq,
ORCID iD: https://orcid.org/0009-0002-5948-4284

Hashim Saeed Murad
University of Duhok
College of Agricultural Engineering Sciences, Duhok, Iraq
ORCID iD: https://orcid.org/0000-0002-8167-0123
*Contact e-mail: *hashim.saeed@uod.ac*

Salah Jasim Amin
University of Kirkuk
College of Agriculture Kirkuk, Iraq
ORCID iD: https://orcid.org/0009-0007-3700-0070
*Corresponding author(s) contact email

To cite this article:

Mohammad, B.T., Murad, H. S., & Amin, S. J. (2026). The role of participatory agricultural extension in mitigating the adverse effects of climate change on agricultural production. *The Eurasia Proceedings of Science, Technology, Engineering and Mathematics (EPSTEM), 42*, 19–29.

The Eurasia Proceedings of Science, Technology, Engineering and Mathematics (EPSTEM)
ISSN: 2602-3199

The Eurasia Proceedings of Science, Technology, Engineering and Mathematics (EPSTEM), 2026

Volume 42, Pages 30-38

ICBASET 2026: International Conference on Basic Sciences, Engineering and Technology

Performance Evaluation of Machine Learning Models for Gas Classification Under Sensor Drift on ESP32-S3

Gonca Uslu-Ozkucuk
OSTIM Technical University

Abstract: Machine learning has become an effective approach for electronic nose systems used in gas classification applications. However, most previous studies evaluate classification performance using randomly partitioned datasets, which often fail to represent the long-term sensor drift encountered in practical deployments. Furthermore, embedded implementation of different machine learning models on resource-constrained microcontrollers has received limited attention. In this study, the Gas Sensor Array Drift Dataset from the UCI Machine Learning Repository was used to investigate both classification performance and embedded deployment efficiency. Four supervised machine learning algorithms, namely Multi-Layer Perceptron (MLP), Support Vector Machine (SVM), Random Forest (RF), and Extreme Gradient Boosting (XGBoost), were evaluated under both random stratified and chronological batch-based data partitioning strategies. The chronological evaluation was designed to simulate realistic sensor drift conditions by separating the training and testing data according to acquisition time. Experimental results showed that all models achieved approximately 99% accuracy under random evaluation, whereas chronological testing produced substantially lower accuracies, highlighting the impact of sensor drift on real-world performance. Among the evaluated models, MLP achieved the highest chronological classification accuracy while demonstrating superior robustness against distribution shifts. To investigate practical applicability, all trained models were deployed on an ESP32-S3 microcontroller. Their average inference latency, flash memory usage, RAM consumption, and total firmware size were experimentally measured and compared. Among the evaluated models, the MLP achieved the highest chronological classification accuracy while also exhibiting the lowest inference latency and smallest firmware footprint on the ESP32-S3 platform.

Keywords: Electronic nose, TinyML, ESP32-S3, Gas classification, Sensor drift

Introduction

Electronic nose (e-nose) systems have become an important technology for gas identification and environmental monitoring in applications such as food quality assessment, industrial safety, environmental monitoring, and healthcare (Han et al., 2025; Ijaz et al., 2025; Illahi et al., 2021; Ivanov et al., 2025; Rabehi et al., 2024). These systems typically employ arrays of metal oxide semiconductor (MOS) gas sensors together with machine learning algorithms to recognize complex gas patterns (Ijaz et al., 2025; Vanaraj et al., 2025; Wijaya et al., 2022; Yi et al., 2021). Compared with conventional analytical instruments, electronic noses provide a low-cost, portable, and real-time solution for gas classification (Anwar et al., 2023; Baruah & Mazumder, 2025; Ivanov et al., 2025; Yang et al., 2023).

The performance of machine learning-based electronic nose systems, however, is strongly affected by sensor drift, which refers to the gradual change in sensor characteristics over time due to aging, contamination, and environmental conditions (Cinar et al., 2025; Dennler et al., 2022; Ziyatdinov et al., 2010). As sensor responses change, the statistical distribution of the collected data also changes, causing a significant degradation in classification accuracy when models are deployed in long-term applications (Cheng et al., 2020; R. Yi et al.,

- This is an Open Access article distributed under the terms of the Creative Commons Attribution-Noncommercial 4.0 Unported License, permitting all non-commercial use, distribution, and reproduction in any medium, provided the original work is properly cited.

- Selection and peer-review under responsibility of the Organizing Committee of the Conference

© 2026 Published by ISRES Publishing: www.isres.org

2021). Therefore, developing machine learning models that are robust to sensor drift has become an important research topic (Chang et al., 2023; Leon-Medina et al., 2020).

Previous studies have investigated various machine learning algorithms for gas classification using the Gas Sensor Array Drift Dataset, including Support Vector Machines (SVM), Random Forest (RF), Artificial Neural Networks (ANN), and Extreme Gradient Boosting (XGBoost) (Cinar et al., 2025; Dennler et al., 2022; Leon-Medina et al., 2020; R. Yi et al., 2021). Most of these studies have primarily focused on improving classification accuracy in an offline computing environment. In addition, many published results have relied on random train-test splitting strategies, where training and testing samples originate from the same data distribution (Dong et al., 2021; Gkogkidis et al., 2022; Shamim, 2022; Z. Yi et al., 2022). Although this approach often produces classification accuracies exceeding 99%, it does not accurately represent the performance of electronic nose systems operating under long-term sensor drift conditions (Dennler et al., 2022; Padilla et al., 2010).

Another limitation of the existing literature is that relatively few studies evaluate machine learning models on resource-constrained embedded platforms (Rahmawan et al., 2025; Shamim, 2022). TinyML has recently emerged as a promising approach for executing machine learning algorithms directly on low-power microcontrollers, enabling intelligent edge devices without continuous cloud connectivity (Farhat et al., 2025; Han et al., 2025). While TensorFlow Lite Micro has facilitated the deployment of neural network models on embedded systems, comparative studies involving both deep learning and classical machine learning models under identical embedded conditions remain limited (Farhat et al., 2025; Ivanov et al., 2025; Nivethika et al., 2026). Furthermore, most previous studies report only offline classification performance without experimentally evaluating memory usage and inference latency on actual hardware (Shamim, 2022).

To address these limitations, this study compares four supervised machine learning models—Multilayer Perceptron (MLP), Support Vector Machine (SVM), Random Forest (RF), and XGBoost—for gas classification under sensor drift conditions using the Gas Sensor Array Drift Dataset (Farbiz et al., 2025; Ivanov et al., 2025; Wang et al., 2023). Two evaluation protocols are considered: a conventional random stratified split and a chronological split that preserves the temporal order of measurements (Ansari et al., 2026; Kumar et al., 2026; Padilla et al., 2010; Yi et al., 2023). In addition to offline performance evaluation, all trained models are deployed on an ESP32-S3 DevKitC-1 N16R8 development board (Farhat et al., 2025; Nivethika et al., 2026; Rahmawan et al., 2025). The embedded implementations are experimentally compared in terms of classification consistency, firmware size, memory usage, and inference latency.

The main contributions of this study can be summarized as follows; the classification performance of four widely used machine learning models is systematically compared under both random and chronological evaluation protocols. The influence of sensor drift on model generalization is quantitatively analyzed using chronological validation. All trained models are successfully deployed on the ESP32-S3 platform, enabling a direct comparison of their embedded implementation characteristics. The proposed study jointly evaluates classification accuracy, memory footprint, and inference latency, providing practical guidance for selecting suitable machine learning models for TinyML-based electronic nose applications.

Overall, the proposed methodology provides a comprehensive evaluation framework that considers both classification performance under realistic sensor drift conditions and the computational constraints of embedded hardware, thereby contributing to the development of efficient intelligent gas sensing systems.

Method

This study used the Gas Sensor Array Drift Dataset from the UCI Machine Learning Repository to investigate the impact of sensor drift on gas classification performance (VERGARA, 2012). The dataset consists of 13,910 measurements belonging to six gas classes. Each sample contains 128 features, extracted from eight response characteristics of 16 metal oxide (MOS) gas sensors. The measurements are organized into 10 chronological batches, enabling the evaluation of long-term sensor drift effects (Vergara et al., 2012).

The dataset was processed in the Python environment by separating the feature vectors and class labels to construct the data matrix. Since the dataset contained no missing or erroneous records, no additional data cleaning procedures were required. Feature values were normalized using Min–Max scaling. The normalization parameters were calculated exclusively from the training data and subsequently applied to the validation and test sets to prevent data leakage.

Two evaluation protocols were employed. In the random stratified split, the dataset was divided into 70% training, 15% validation, and 15% testing while preserving the class distribution. In the chronological split, Batches 1–7 were used for training, Batch 8 for validation, and Batches 9–10 for testing. This protocol enabled the evaluation of model generalization under realistic sensor drift conditions. Figure 1 illustrates the overall experimental workflow adopted in this study.

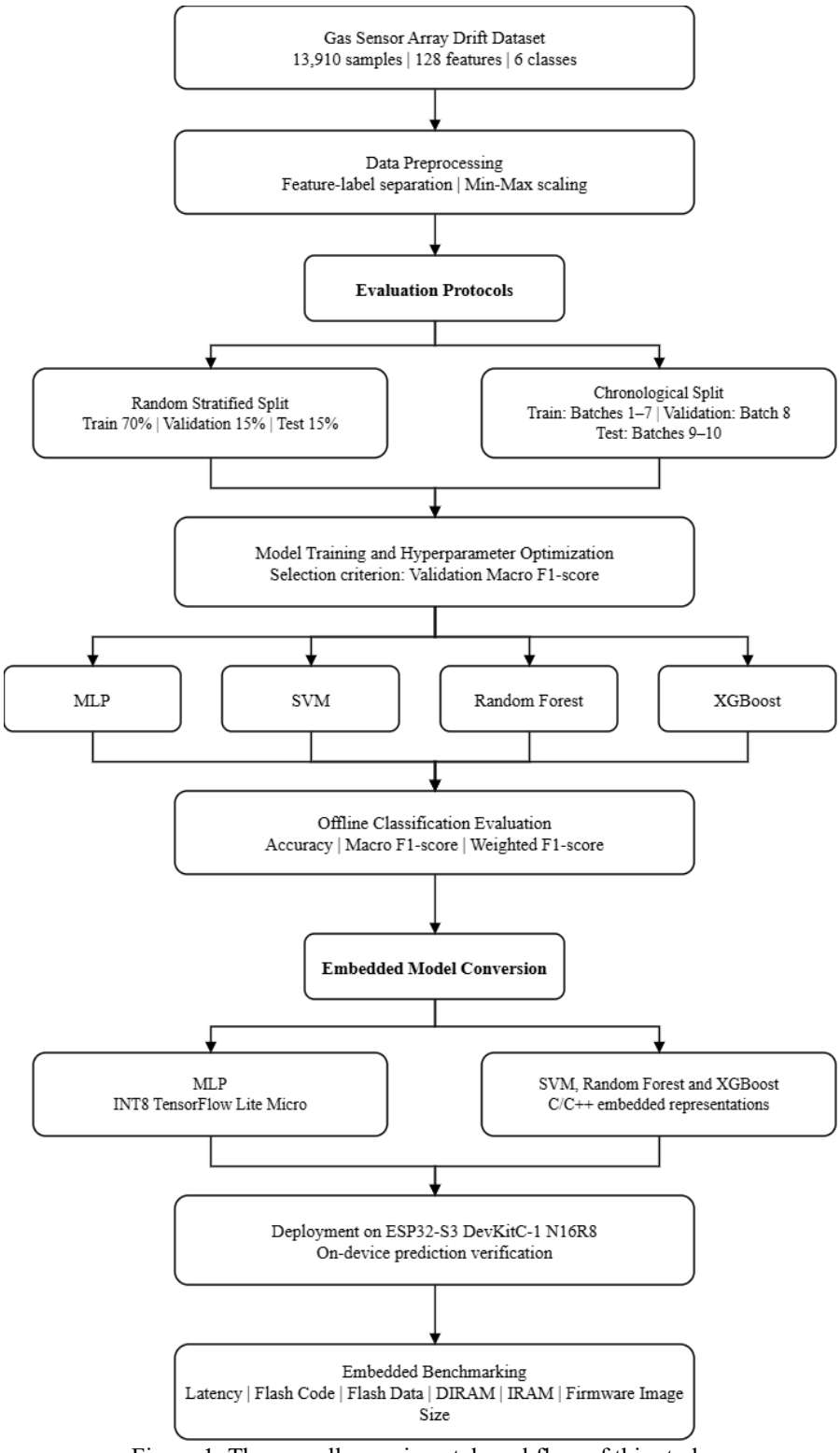

Figure 1. The overall experimental workflow of this study

Four supervised machine learning models were investigated: Multilayer Perceptron (MLP), Support Vector Machine (SVM), Random Forest (RF), and Extreme Gradient Boosting (XGBoost). The MLP model was

implemented using TensorFlow (Abadi et al., 2016), the SVM and Random Forest models were developed using Scikit-learn (Pedregosa FABIANPEDREGOSA et al., 2011), and the XGBoost model (Chen & Guestrin, 2016) was implemented using the XGBoost library. Hyperparameters were optimized using the training and validation datasets, and the final model configurations were selected according to the highest validation Macro F1-score.

All trained models were deployed on an ESP32-S3 DevKitC-1 N16R8 development board. The MLP model was converted to an INT8 TensorFlow Lite Micro model (David et al., 2021) using post-training quantization. The SVM, Random Forest, and XGBoost models were automatically converted into C/C++ header files and integrated into the ESP32-S3 firmware. The embedded applications were developed using the ESP-IDF framework, and all inference operations were executed locally on the microcontroller without cloud connectivity. Model performance was evaluated using Accuracy, Macro F1-score, and Weighted F1-score. For the embedded implementation, average inference latency, Flash Code, Flash Data, DIRAM, IRAM, and total firmware image size were measured to compare the computational efficiency and memory requirements of the deployed models.

Results and Discussion

A chronological data splitting approach was used to evaluate the performance of machine learning models under real-world operating conditions. In this method, Batches 1–7 were used for training, Batch 8 for validation, and Batches 9 and 10 for testing data. Thus, the temporal data distribution change caused by sensor drift was directly included in the evaluation process (Vergara et al., 2012).

Table 1. Chronological test performance on batches 9 and 10

Model	Accuracy (%)	Macro-F1 (%)	Weighted-F1 (%)	Batch 9 acc. (%)	Batch 10 acc. (%)	Prediction/sample (ms)
MLP	69.34	69.51	69.55	76.38	68.42	0.0349
SVM	63.88	65.22	65.20	75.96	62.31	0.0476
Random Forest	59.63	59.43	59.45	76.17	57.47	0.0148
XGBoost	58.18	58.36	58.36	71.49	56.44	0.0027

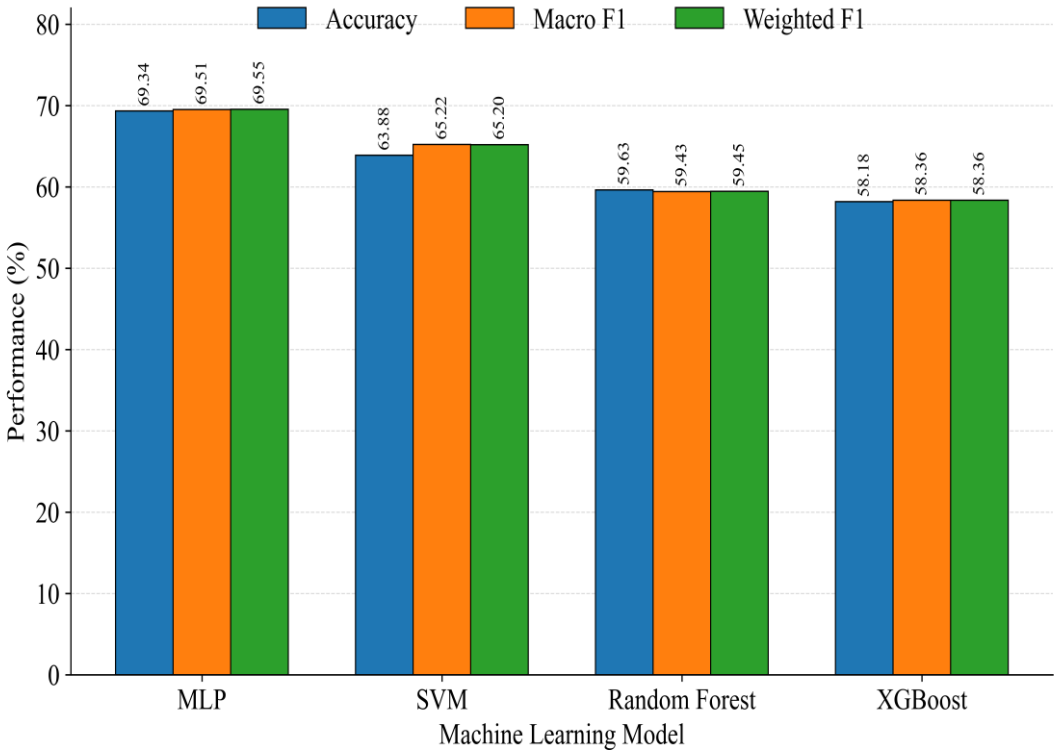

Figure 2. Accuracy comparison of models in chronological evaluation

Table 1 summarizes the numerical performance of the evaluated models, while Figure 2 provides a visual comparison of their classification accuracy. Among the four models, the MLP model achieved the highest

classification accuracy. With 69.34% accuracy, 69.51% Macro F1, and 69.55% Weighted F1, the MLP model outperformed the other models. The SVM model ranked second with 63.88% accuracy, while the Random Forest and XGBoost models achieved 59.63% and 58.18% accuracy, respectively. Furthermore, the MLP model maintained the highest accuracy values in both Batch 9 and Batch 10, demonstrating more stable performance against sensor drift.

These results show that the MLP model has a higher generalization ability than other methods against data distributions that change over time due to sensor drift. In particular, the fact that the accuracy and F1 scores are quite close to each other shows that the model exhibits a balanced classification performance not only in dominant classes but in all gas classes. In contrast, tree-based models, although they successfully learned the training data, struggled to adapt to temporal changes. The most commonly used evaluation method in machine learning studies is the random data splitting approach. However, in datasets with sensor drift, this approach does not fully reflect real-world performance because training and test samples do not come from the same distribution.

Table 2. Random stratified test performance

Model	Accuracy (%)	Macro-F1 (%)	Weighted-F1 (%)	Prediction/sample (ms)
Random Forest	99.47	99.44	99.47	0.0335
XGBoost	99.33	99.29	99.33	0.0022
MLP	99.23	99.18	99.23	0.0373
SVM	99.19	99.16	99.18	0.0773

Table 3. Comparison of random stratified and chronological evaluation protocols

Model	Random acc. (%)	Chronological acc. (%)	Accuracy gap (pp)	Random macro-F1 (%)	Chronological macro-F1 (%)	Macro-F1 gap (pp)
Random Forest	99.47	59.63	39.84	99.44	59.43	40.01
XGBoost	99.33	58.18	41.15	99.29	58.36	40.92
MLP	99.23	69.34	29.90	99.18	69.51	29.67
SVM	99.19	63.88	35.30	99.16	65.22	33.94

When Tables 2 and 3 are examined together, it is seen that while all models in the random data splitting approach achieve approximately 99% accuracy, the accuracy values drop to the 58–69% range under chronological evaluation. This demonstrates that random evaluation substantially overestimates the real-world performance of gas classification models in the presence of sensor drift. The accuracy loss in the MLP model is approximately 30 percentage points, while in the Random Forest and XGBoost models this loss reaches approximately 40 percentage points. The highest performance decrease was observed in the XGBoost model.

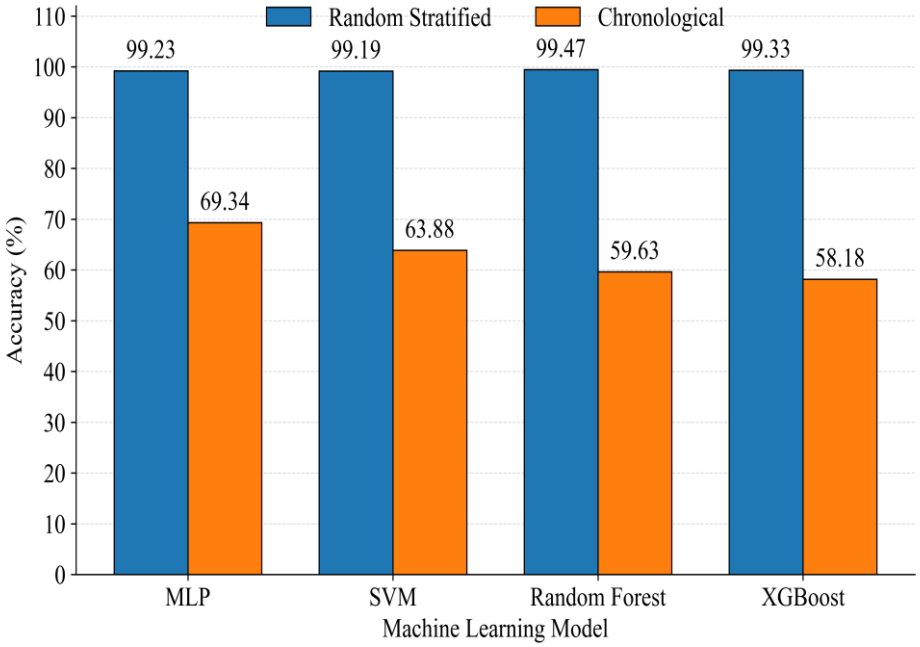

Figure 3. Comparison of random stratified and chronological classification accuracy.

In Figure 3 comparison of random stratified and chronological classification accuracy is showed. These results reveal that high accuracy values reported using only the random data splitting approach in datasets with sensor drift may overestimate performance under real operating conditions. Therefore, the chronological evaluation approach offers a more realistic method for assessing the generalization ability of models in long-term sensor applications such as electronic noses. In the second phase of the study, the four trained machine learning models were transferred to the ESP32-S3 DevKitC-1 N16R8 development board and run on real hardware. This allowed for the evaluation not only of offline classification success but also of the models' applicability on a microcontroller with limited resources.

Table 4. Comparison of memory usage and inference time of machine learning models on ESP32-S3

Model	Flash Code (B)	Flash Data (B)	DIRAM (B)	Firmware Size (B)	Avg. Latency (µs)
MLP (INT8)	98,156	65,404	49,990	222,530	401.64
Random Forest	902,680	38,180	45,126	999,814	5,117
XGBoost	62,780	370,484	45,126	492,218	12,600
SVM (RBF)	63,476	429,916	48,070	552,346	16,995

Table 4 shows the memory usage and inference time results obtained on the ESP32-S3. The MLP model was the fastest with an average inference time of 401.64 µs. The average inference times for the Random Forest, XGBoost, and SVM models were measured as 5117 µs, 12600 µs, and 16995 µs, respectively. Accordingly, the MLP model operates with approximately 13 times lower latency than Random Forest, 31 times lower latency than XGBoost, and 42 times lower latency than the SVM model. Furthermore, it was confirmed that the predictions obtained on the ESP32-S3 for all models were fully consistent with the results obtained in the Python environment.

Significant differences were also observed in terms of memory usage. The MLP model had the lowest memory requirement with a total firmware size of approximately 222.5 kB, while the Random Forest model reached the largest firmware size with approximately 999.8 kB. The firmware sizes of the XGBoost and SVM models were measured as approximately 492.2 kB and 552.3 kB, respectively. When the distribution of resource usage is examined, it is seen that Flash Code usage increased significantly in the Random Forest model due to the direct compilation of decision trees as program code. In contrast, Flash Data usage was higher in the SVM and XGBoost models because a large portion of the model parameters were stored in fixed data space. The MLP model, however, provided the most balanced resource usage in terms of both program code and data memory.

When these results are evaluated together, it is seen that the MLP model not only achieved the highest classification success under chronological evaluation, but also provided the lowest memory requirement and the shortest inference time on the embedded system. In contrast, while the Random Forest model offers relatively low latency, it suffers from a memory disadvantage due to its high firmware size. The SVM model achieved the second highest accuracy in chronological evaluation but had the longest inference time. The XGBoost model yielded moderate results in terms of both accuracy and hardware performance.

Overall, the proposed MLP-based TinyML implementation provides the best trade-off between classification performance, memory footprint, and inference latency, making it a promising solution for resource-constrained electronic nose and IoT applications. These findings demonstrate that deep learning-based models offer significant advantages in electronic nose applications with sensor drift, not only in terms of offline classification success but also in terms of real-time embedded systems applications (Fonollosa et al., 2015; Vergara et al., 2012).

Conclusion

In this study, the performance of four machine learning models (MLP, SVM, Random Forest, and XGBoost) was investigated for gas classification under sensor drift conditions using the Gas Sensor Array Drift Dataset. Unlike conventional studies that rely only on random data splitting, both random stratified and chronological evaluation protocols were employed to assess the effect of temporal distribution changes caused by sensor drift.

The experimental results demonstrated that random stratified evaluation produced classification accuracies of approximately 99% for all models, whereas chronological evaluation reduced the accuracy to 58–69%, revealing a substantial degradation in performance due to sensor drift. Among the evaluated models, the MLP achieved

the highest chronological performance with 69.34% Accuracy, 69.51% Macro F1-score, and 69.55% Weighted F1-score, indicating superior generalization capability under long-term sensor drift.

In addition to offline evaluation, all trained models were successfully deployed on an ESP32-S3 DevKitC-1 N16R8 development board, enabling a direct comparison of their embedded implementation characteristics. Experimental measurements showed that the MLP model required the smallest firmware size and achieved the shortest inference latency (401.64 µs), while maintaining complete agreement between Python and ESP32 predictions. In contrast, Random Forest exhibited the largest firmware footprint, whereas SVM and XGBoost required considerably longer inference times due to their computational complexity and memory organization.

Overall, the results demonstrate that the MLP model provides the most favorable balance between classification accuracy, memory consumption, and inference latency, making it the most suitable candidate for TinyML-based electronic nose applications on resource-constrained microcontrollers. The proposed evaluation methodology also highlights the importance of chronological validation for obtaining realistic performance estimates in sensor drift scenarios, where conventional random evaluation may significantly overestimate model performance.

Future work will focus on evaluating additional lightweight neural network architectures, investigating online adaptation techniques for long-term sensor drift compensation, and validating the proposed approach using real-time gas measurements acquired directly from an ESP32-based electronic nose prototype.

Recommendations

The proposed methodology can be extended by evaluating additional lightweight deep learning architectures specifically designed for TinyML applications. Future studies may also investigate online or continual learning techniques to compensate for long-term sensor drift without retraining the model offline. Furthermore, the proposed approach should be validated using real-time measurements collected from a physical electronic nose system instead of publicly available datasets. Finally, evaluating power consumption and energy efficiency on battery-powered embedded platforms would provide further insight into the practical applicability of the proposed system.

Scientific Ethics Declaration

* The author declares that the scientific ethical and legal responsibility of this article published in EPSTEM Journal belongs to the author.

Conflict of Interest

* The author declares that there is no conflict of interest.

Funding

* The author received no financial support for the research, authorship, and publication of this article.

Acknowledgements or Notes

* This article was presented as an oral presentation at the International Conference on Basic Sciences, Engineering and Technology (www.icbaset.net) held in Istanbul/Türkiye on September 17-18, 2026.

References

Abadi, M., Agarwal, A., Barham, P., Brevdo, E., Chen, Z., Citro, C., … Zheng, X. (2016). *TensorFlow: Large-scale machine learning on heterogeneous distributed systems*. Retrieved from http://arxiv.org/abs/1603.04467

Ansari, G., Singh, R., Kumar, S., & Kumar, R. (2026). Drift-resilient hybrid feature learning framework for accurate mixed industrial gas classification using chemical sensor arrays. *IEEE Sensors Journal, 26*(10), 15007–15019.

Anwar, H., Anwar, T., & Murtaza, S. (2023). Review on food quality assessment using machine learning and electronic nose system. *Biosensors and Bioelectronics: X, 14*, 100365.

Baruah, S., & Mazumder, D. H. (2025). A review on application of machine learning techniques coupled with E-nose in healthcare, agriculture, and allied domains. *IEEE Transactions on Instrumentation and Measurement, 74*.

Chang, I. S., Byun, S. W., Lim, T. B., & Park, G. M. (2023). A study of drift effect in a popular metal oxide sensor and gas recognition using public gas datasets. *IEEE Access, 11*, 26383–26392.

Chen, T., & Guestrin, C. (2016). XGBoost: A scalable tree boosting system. In *Proceedings of the ACM SIGKDD International Conference on Knowledge Discovery and Data Mining* (pp. 785–794).

Cheng, Y. C., Chou, T. I., Chiu, S. W., & Tang, K. T. (2020). A concentration-based drift calibration transfer learning method for gas sensor array data. *IEEE Sensors Letters, 4*(10).

Cinar, R. F., Yuksek, G., Lale, T., Ekinci, S., Izci, D., & Ma'arif, A. (2025). SHAP-based framework for temporal detection of sensor drift in gas sensor arrays. *Journal of Robotics and Control (JRC), 6*(5), 2592–2601.

David, R., Duke, J., Jain, A., Reddi, V. J., Jeffries, N., Li, J., … Warden, P. (2021). *TensorFlow Lite Micro: Embedded machine learning on TinyML systems*. Retrieved from http://arxiv.org/abs/2010.08678

Dennler, N., Rastogi, S., Fonollosa, J., van Schaik, A., & Schmuker, M. (2022). Drift in a popular metal oxide sensor dataset reveals limitations for gas classification benchmarks. *Sensors and Actuators B: Chemical, 361*.

Dong, X., Han, S., Wang, A., & Shang, K. (2021). Online inertial machine learning for sensor array long-term drift compensation. *Chemosensors, 9*(12).

Farbiz, F., Aggarwal, S., Maszczyk, T. K., Habibullah, M. S., & Hamadicharef, B. (2025). Reliability-improved machine learning model using knowledge-embedded learning approach for smart manufacturing. *Journal of Intelligent Manufacturing, 36*(7), 4941–4962.

Farhat, F., El Hamdi, R., & Dahman, H. (2025). Edge embedded deep learning intelligent electronic nose for real-time gas detection. In *2025 IEEE International Multi-Conference on Smart Systems and Green Process (IMC-SSGP 2025)*.

Fonollosa, J., Rodríguez-Luján, I., & Huerta, R. (2015). Chemical gas sensor array dataset. *Data in Brief, 3*, 85–89.

Gkogkidis, A., Tsoukas, V., Papafotikas, S., Boumpa, E., & Kakarountas, A. (2022). A TinyML-based system for gas leakage detection. In *2022 11th International Conference on Modern Circuits and Systems Technologies (MOCAST 2022)*.

Han, J., Li, H., Cheng, J., Ma, X., & Fu, Y. (2025). Advances in metal oxide semiconductor gas sensor arrays based on machine learning algorithms. *Journal of Materials Chemistry C, 13*(9), 4285–4303.

Ijaz, U., Ali, M., Ahmad, I., Hamza, S. A., & Kim, H. D. (2025). A comprehensive review of electronic nose systems: Design, sensors, and future directions. *Chemical Engineering Journal, 524*.

Illahi, A. A. C., Dadios, E. P., Bandala, A. A., & Vicerra, R. R. P. (2021). Electronic nose technology and application: A review. In *2021 IEEE 13th International Conference on Humanoid, Nanotechnology, Information Technology, Communication and Control, Environment, and Management (HNICEM 2021)* (pp. 1–5).

Ivanov, S., Wilk-Jakubowski, J. Ł., Ciopiński, L., Pawlik, Ł., Wilk-Jakubowski, G., & Mihalev, G. (2025). Modern trends in the application of electronic nose systems: A review. *Applied Sciences, 15*(19).

Kumar, G., Terauds, M., Ajayakumar Raji, A., Semenako, J., Smolaninovs, V., Sics, P. E., & Malayidinja Poikayil Thankappan, A. K. (2026). Design of a lightweight Edge-AI system for predictive maintenance on ESP32-S3. *Applied Sciences, 16*(11).

Leon-Medina, J. X., Pineda-Munoz, W. A., & Burgos, D. A. T. (2020). Joint distribution adaptation for drift correction in electronic nose type sensor arrays. *IEEE Access, 8*, 134413–134421.

Nivethika, G., Pragiyaa, V., Rohithaa, E., Padmaja, Y., & Mari Rajan, S. (2026). CookSafe AI: An Edge-AI framework for intelligent gas knob monitoring and autonomous safety actuation using ESP32 with TinyML. In *2026 International Conference on Data Science, Agents and Artificial Intelligence (ICDSAAI 2026)*.

Padilla, M., Perera, A., Montoliu, I., Chaudry, A., Persaud, K., & Marco, S. (2010). Drift compensation of gas sensor array data by orthogonal signal correction. *Chemometrics and Intelligent Laboratory Systems, 100*(1), 28–35.

Pedregosa, F., Varoquaux, G., Gramfort, A., Michel, V., Thirion, B., Grisel, O., … Duchesnay, E. (2011). Scikit-learn: Machine learning in Python. *Journal of Machine Learning Research, 12*, 2825–2830.

Rabehi, A., Helal, H., Zappa, D., & Comini, E. (2024). Advancements and prospects of electronic nose in various applications: A comprehensive review. *Applied Sciences, 14*(11).

Rahmawan, J., Yudhana, A., & Risky, J. M. (2025). Temporal gated neural model for odor classification in TinyML devices. In *ICoAIT 2025—1st International Conference on Artificial Intelligence Technology: Artificial Intelligence: Driving Prosperity and Sustainability in the Modern World* (pp. 149–154).

Shamim, M. Z. M. (2022). TinyML model for classifying hazardous volatile organic compounds using low-power embedded edge sensors: Perfecting Factory 5.0 using Edge AI. *IEEE Sensors Letters, 6*(9).

Vanaraj, R., I. P., B., Mayakrishnan, G., Kim, I. S., & Kim, S. C. (2025). A systematic review of the applications of electronic nose and electronic tongue in food quality assessment and safety. *Chemosensors, 13*(5), 1–23.

Vergara, A. (2012). *Gas sensor array drift dataset* [Data set]. UCI Machine Learning Repository.

Vergara, A., Vembu, S., Ayhan, T., Ryan, M. A., & Homer, M. L. (2012). Chemical gas sensor drift compensation using classifier ensembles. *Sensors and Actuators B: Chemical, 167*.

Wang, X., Zhou, Y., Zhao, Z., Feng, X., Wang, Z., & Jiao, M. (2023). Advanced algorithms for low dimensional metal oxides-based electronic nose application: A review. *Crystals, 13*(4).

Wijaya, D. R., Afianti, F., Arifianto, A., Rahmawati, D., & Kodogiannis, V. S. (2022). Ensemble machine learning approach for electronic nose signal processing. *Sensing and Bio-Sensing Research, 36*, 100495.

Yang, X., Li, M., Ji, X., Chang, J., Deng, Z., & Meng, G. (2023). Recognition algorithms in E-nose: A review. *IEEE Sensors Journal, 23*(18), 20460–20472.

Yi, D., Zhang, L., Wang, Z., Wang, L., Duan, S., & Yan, J. (2023). Robust domain correction latent subspace learning for gas sensor drift compensation. *IEEE Transactions on Systems, Man, and Cybernetics: Systems, 53*(12), 7668–7680.

Yi, R., Yan, J., Shi, D., Tian, Y., Chen, F., Wang, Z., & Duan, S. (2021). Improving the performance of drifted/shifted electronic nose systems by cross-domain transfer using common transfer samples. *Sensors and Actuators B: Chemical, 329*.

Yi, Z., Shang, W., Xu, T., Guo, S., & Wu, X. (2022). Local discriminant subspace learning for gas sensor drift problem. *IEEE Transactions on Systems, Man, and Cybernetics: Systems, 52*(1), 247–259.

Ziyatdinov, A., Marco, S., Chaudry, A., Persaud, K., Caminal, P., & Perera, A. (2010). Drift compensation of gas sensor array data by common principal component analysis. *Sensors and Actuators B: Chemical, 146*(2), 460–465.

Author(s) Information

Gonca Uslu- Ozkucuk
OSTIM Technical University
Department of Electricity and Energy
Ankara, Türkiye
ORCID iD: https://orcid.org/0000-0002-2523-2516
*Contact e-mail: *gonca.usluozkucuk@ostimteknik.edu.tr*

*Corresponding author(s) contact email

To cite this article:

Uslu-Ozkucuk, G. (2026). Performance evaluation of machine learning models for gas classification under sensor drift on ESP32-S3. *The Eurasia Proceedings of Science, Technology, Engineering and Mathematics (EPSTEM), 42,* 30-38.

The Eurasia Proceedings of Science, Technology, Engineering and Mathematics (EPSTEM)
ISSN: 2602-3199

The Eurasia Proceedings of Science, Technology, Engineering and Mathematics (EPSTEM), 2026

Volume 42, Pages 39-48

ICBASET 2026: International Conference on Basic Sciences, Engineering and Technology

Lengthwise Fracture Analysis of a Moving Thin-Walled Elliptical Cylinder

Victor Rizov
University of Architecture

Abstract: This paper is devoted to the problem of lengthwise fracture in moving thin-walled elliptical cylindrical shell structures with non-linear elastic behavior. Elliptical cylinders have continuous material inhomogeneity in height. The parameters of the non-linear constitutive law and the bulk density of the material of the cylinder wall change continuously in height. The lengthwise crack represents an elliptical surface whose location coincides with the middle surface of the cylinder. Two types of cylinder motion are considered (translational motion with constant upward acceleration and uniform rotation around the longitudinal axis). The cylinders are loaded with their own weight and with inertial forces from both types of motion. Strain energy release rate (SERR) solutions are obtained for both cylinder motions. In this regard, expressions for the complementary strain energy stored in both arms of the lengthwise crack and in the intact portion of the elliptical cylinder are obtained. A check was made with an existing approach in scientific literature.

Keywords: Elliptical cylinder, Motion, Lengthwise fracture

Introduction

Modern facilities, structures, mechanisms and machines include a variety of structural systems and components such as rods, plates, beams, thin-walled elements, shells, tanks, etc. with a variety of shapes, loads and support conditions (Kolev & Mladenov, 1992). The analysis of these structural systems and components requires solving a fairly wide range of diverse problems in the field of mechanics of rod systems, theory of elasticity and plasticity, theory of thin-walled systems, mechanics of continuous media, theory of shells and others (Malenov, 1993). Due to the complexity of the analyzed phenomena and processes in structural systems, it is very often necessary to introduce various simplifying hypotheses in practice.

In various fields of technology, thin-walled shell structures are increasingly used in our time. These structures are preferred primarily because of their low self-weight. The widespread use of these structures poses a number of specific tasks in the field of analysis of their behavior. In this regard, it can be noted that taking into account such factors as physical non-linearity, i.e. non-linear elastic or elastic-plastic behavior of various shell structural systems, material inhomogeneity, dynamic action of external load and others is of particular interest and introduces additional requirements for the analysis of shell structures (Mladenov et al., 2012; Obodovski & Hanin, 1971).

This paper deals with lengthwise fractured analysis of a moving thin walled continuously inhomogeneous shell. The latter is an elliptical cylinder with continuous material inhomogeneity along the length. The interest in the analysis of lengthwise cracks is due to the fact that very often continuously inhomogeneous materials, such as functionally graded ones, are produced by layering, which creates a risk of lengthwise fracture (Gandra et al., 2011; Gasik, 2010; Mahamood & Akinlabi, 2017; Rizov & Altenbach, 2019; El-Galy et al., 2019). The cylinder studied in this paper has non-linear elastic behavior. The SERR was obtained for two types of cylinder motion, namely translational motion with constant upward acceleration and uniform rotation around the longitudinal axis. The need for analysis of moving cylinders is due to their widespread use in various machines, mechanisms and vehicles. An existing approach to finding the SERR was used for verification.

- This is an Open Access article distributed under the terms of the Creative Commons Attribution-Noncommercial 4.0 Unported License, permitting all non-commercial use, distribution, and reproduction in any medium, provided the original work is properly cited.

- Selection and peer-review under responsibility of the Organizing Committee of the Conference

© 2026 Published by ISRES Publishing: www.isres.org

Analysis

The thin-walled elliptical cylinder in Fig. 1 has height, h, and wall thickness, b. The base of the cylinder is an ellipse with semi-major and semi-minor axes, r_1 and r_2, respectively (Fig. 2). There is a lengthwise crack in the cylinder with length, a, as shown in Fig. 1. The crack is an elliptical cylindrical surface coinciding with the middle surface of the thin-walled elliptical cylinder (Fig. 1). Therefore, the outer and inner arms of the crack are elliptical cylinders with wall thickness, $b/2$, and height, a.

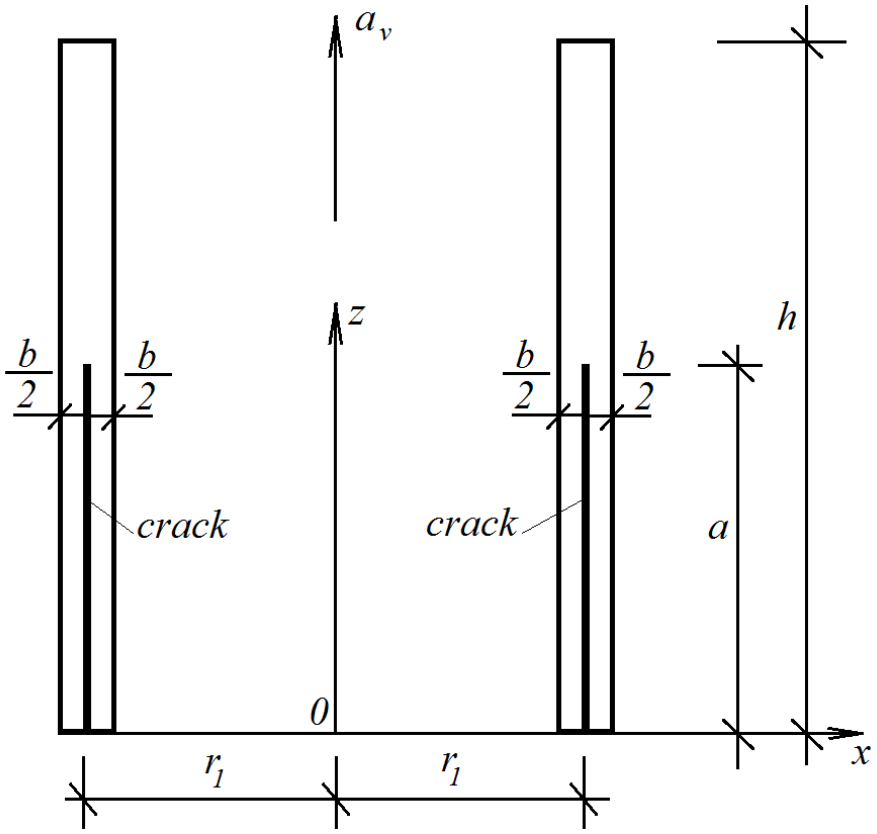

Figure 1. Thin-walled elliptical cylinder moving along the axis, z

First, we will analyze the case when the cylinder moves along the axis, z, with a constant acceleration, a_v, as shown in Fig. 1. The load acting on the thin-walled elliptical cylinder has two components, namely its own weight and the inertial load from the acceleration, a_v. Both components are directed vertically downward. We are looking for the meridional stress, σ_{ml}, in an arbitrary section in the outer arm of the crack at a distance, z, from the base of the thin-walled elliptical cylinder. For this purpose, we use the equilibrium condition

$$\sum F_{iz} = 0\,. \tag{1}$$

After substituting the force projections in (1) we obtain

$$\sigma_{ml}\frac{b}{2}c - z\gamma g\frac{b}{2}c - \gamma\frac{b}{2}zca_v = 0\,, \tag{2}$$

where γ is the bulk density of the cylinder material, g is the acceleration due to gravity, c is the perimeter of the ellipse. The third term on the left-hand side of equation (2) is the inertial load caused by the acceleration, a_v.

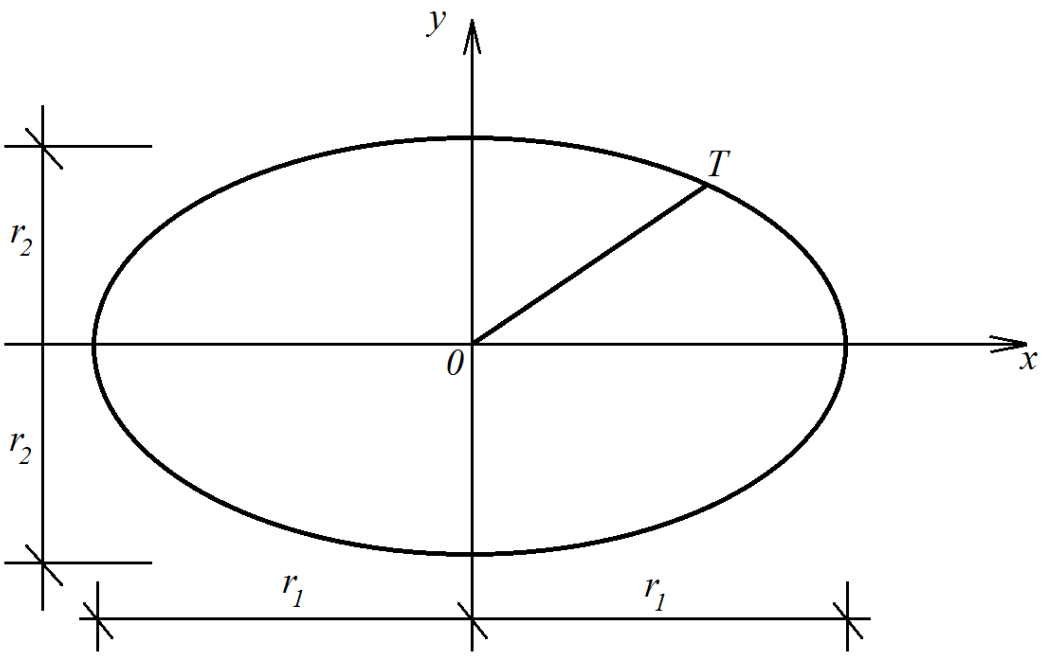

Figure 2. Schematic of the cross-section of the elliptical cylinder

The cylinder wall has a continuous material inhomogeneity in height. Therefore, the bulk density of the cylinder material varies continuously along the axis, z . To describe this variation, the following law is applied:

$$\gamma = \gamma_\alpha + \frac{\gamma_\beta - \gamma_\alpha}{h^\delta} z^\delta , \tag{3}$$

$$0 \le z \le h , \tag{4}$$

where γ_α and γ_β are the bulk densities at the lower and upper end of the cylinder, δ is a parameter. From equation (1) we obtain the following expression for the meridional stress in an arbitrary section in the outer arm of the crack

$$\sigma_{ml} = \gamma z\left(g + a_v\right), \tag{5}$$

where

$$0 \le z \le a . \tag{6}$$

The meridional stress, σ_{md} , in the inner arm of the crack is also found by formula (5).

It remains to determine the meridional stress, σ_m , in the intact portion, $z > a$, of the thin-walled elliptical cylinder. We formulate the condition for equilibrium along the axis, z

$$\sigma_m bc - z\gamma gbc - \gamma bzca_v = 0 , \tag{7}$$

from which we obtain

$$\sigma_m = \gamma z\left(g + a_v\right), \tag{8}$$

Where

$$a \le z \le h . \tag{9}$$

We will prove that the hoop stress, σ_{pl}, in the outer arm of the crack is zero. To do this, we write the Laplace equation for the outer arm

$$\frac{\sigma_{ml}}{\rho_m}+\frac{\sigma_{pl}}{\rho_p}=\frac{q}{\frac{b}{2}}, \tag{10}$$

where ρ_m and ρ_p are the radii of curvature of the elliptical cylinder. The equation of the base of the thin-walled elliptical cylinder is (Fig. 2)

$$\frac{x^2}{r_1^2}+\frac{y^2}{r_2^2}=1, \tag{11}$$

Where

$$-r_1 \le x \le r_1, \tag{12}$$

$$-r_2 \le y \le r_2. \tag{13}$$

Therefore, the radii of curvature of the elliptical cylinder are found by the formulas

$$\rho_m=\infty, \tag{14}$$

$$\rho_p=\frac{\left(1+\theta_\tau^2\right)^{\frac{3}{2}}}{\left|\theta_\zeta\right|}, \tag{15}$$

Where

$$\theta_\tau=-\frac{r_2 x}{r_1^2\sqrt{\theta_\kappa}}, \tag{16}$$

$$\theta_\zeta=-\frac{r_2}{r_1^2}\frac{r_1^2\theta_\kappa+x^2}{r_1^2\theta_\kappa^{\frac{3}{2}}}, \tag{17}$$

$$\theta_\kappa=1-\frac{x^2}{r_1^2}. \tag{18}$$

Furthermore,

$$q=0. \tag{19}$$

From equations (10) – (19) it follows that

$$\sigma_{pl}=0. \tag{20}$$

We are looking for the strains, ε_{ml}, in the outer arm of the crack. The thin-walled elliptical cylinder has non-linear elastic behavior. The relationship between stresses and strains obeys the following non-linear constitutive law (Lukash, 1997):

$$\sigma_{ml} = E\varepsilon_{ml} - B\varepsilon_{ml}^{s} - D\varepsilon_{ml}^{f}, \tag{21}$$

where E, B, D, s and f are material parameters. Since the wall of the cylinder has a continuous material inhomogeneity along the height, the parameters, E, B, D, s and f, vary along the axis, z, according to the laws

$$E = E_{\alpha} + \frac{E_{\beta} - E_{\alpha}}{h^{\lambda}} z^{\lambda}, \tag{22}$$

$$B = B_{\alpha} + \frac{B_{\beta} - B_{\alpha}}{h^{\mu}} z^{\mu}, \tag{23}$$

$$D = D_{\alpha} + \frac{D_{\beta} - D_{\alpha}}{h^{\eta}} z^{\eta}, \tag{24}$$

$$s = s_{\alpha} + \frac{s_{\beta} - s_{\alpha}}{h^{\nu}} z^{\nu}, \tag{25}$$

$$f = f_{\alpha} + \frac{f_{\beta} - f_{\alpha}}{h^{\psi}} z^{\psi}, \tag{26}$$

$$0 \le z \le h, \tag{27}$$

where E_{α}, B_{α}, D_{α}, s_{α} and f_{α} are the values of E, B, D, s and f at the lower end of the cylinder, E_{β}, B_{β}, D_{β}, s_{β} and f_{β} are the corresponding values at the upper end of the cylinder, λ, μ, η, ν and ψ are parameters.

The strain, ε_{ml}, is found from (21) for different values of z in the interval (27). Due to the specifics of the cylinder loading, the strains, ε_{md}, in the inner crack arm are equal to ε_{ml}. To find the strains, ε_{m}, in the intact section of the cylinder, we use relation (21). To do this, we replace σ_{ml} and ε_{ml} with σ_{m} and ε_{m} and then find ε_{m} for z varying in the interval (9).

We determine the SERR, G, by formula

$$G = \frac{dU^{*}}{dA}, \tag{28}$$

where

$$dA = cda. \tag{29}$$

The circumference of the ellipse is

$$c = \pi\left[3(r_1 + r_2) - \sqrt{(3r_1 + r_2)(r_1 + 3r_2)}\ \right]. \tag{30}$$

The complementary strain energy, U^*, involved in equation (29) is found as

$$U^* = 2U^*_{ml} + U^*_m, \tag{31}$$

where U^*_{ml} and U^*_m are the complementary strain energies in the outer crack arm and in the intact portion of the cylinder, respectively. The complementary strain energy in the outer arm is multiplied by two in (31) because the complementary strain energies in the two crack arms are equal. The complementary strain energy in the outer arm is

$$U^*_{ml} = \frac{b}{2} c \int_0^a u^*_{0ml} dz, \tag{32}$$

where u^*_{0ml} is the specific complementary strain energy. It is determined by the formula

$$u^*_{0ml} = \sigma_{ml}\varepsilon_{ml} - \int_0^{\varepsilon_{ml}} \sigma_{ml} d\varepsilon_{ml}. \tag{33}$$

We substitute (21) into (33) and obtain

$$u^*_{0ml} = \frac{E}{2}\varepsilon^2_{ml} - \frac{Bs}{s+1}\varepsilon^{s+1}_{ml} - \frac{Df}{f+1}\varepsilon^{f+1}_{ml}. \tag{34}$$

The complementary strain energy in the intact portion of the cylinder is

$$U^*_m = bc \int_a^h u^*_{0m} dz. \tag{35}$$

The specific complementary strain energy, u^*_{0m} is determined by replacing ε_{ml} with ε_m in (34). Then, the SERR is found by formula (28). To verify the thus obtained solution for the SERR, an existing approach is applied, according to which the SERR is found as (Rizov, 2017)

$$G = bcu^*_{0mlbh} - bcu^*_{0mfr}, \tag{36}$$

where u^*_{0mlbh} and u^*_{0mfr} are the specific complementary strain energies in the cylinder cross-sections behind and in ahead of the crack front. The use of (36) leads to results that match those obtained with (28).

The SERR is also derived for the case when the thin-walled elliptical cylinder performs a uniform rotation about the axis, z, with angular velocity, ω, as shown in Fig. 3. In this case, the cylinder has both meridional stress from its own weight and hoop stress from the inertial load generated by the normal acceleration due to uniform rotation around the axis, z.

First, the meridional stress, $\sigma_{ml\omega}$, in the outer arm of the crack is found. For this purpose,

$$a_v = 0 \tag{37}$$

is substituted into equation (5). The result is

$$\sigma_{ml\omega} = \gamma z g. \tag{38}$$

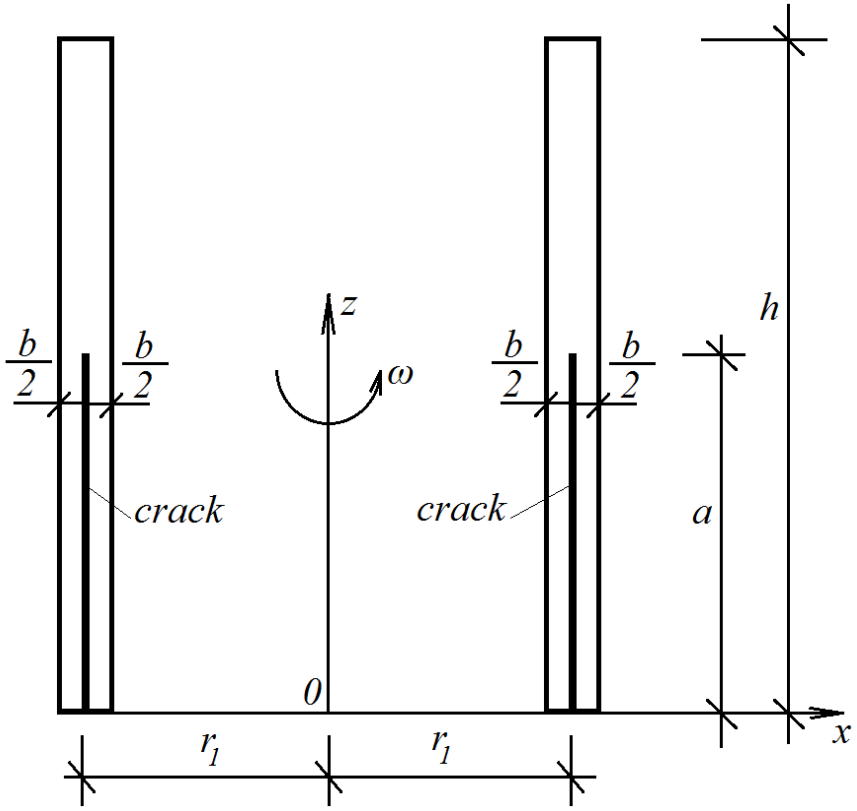

Figure 3. Thin-walled elliptical cylinder rotating around the axis, z

Then, the meridional stress, σ_{ml}, is found in the intact portion of the cylinder by substituting (37) in (8). This leads again to expression (38). However, in this case

$$a \le z \le h\,. \tag{39}$$

We seek the hoop stress, $\sigma_{pl\omega}$, in the outer arm of the crack. In this regard, we first find the inertial load component, q, generated by the normal acceleration, a_n.

$$q = \gamma \frac{b}{2} a_n \cos\theta_t\,, \tag{40}$$

where

$$a_n = \omega^2 OT\,, \tag{41}$$

$$\theta_t = -\frac{\pi}{2} + arctg\theta_\tau - arctg\left(\frac{r_2}{x}\sqrt{\theta_\kappa}\right). \tag{42}$$

The distance, OT, is shown in Fig. 2. It is found as

$$OT = \sqrt{x^2 + r_2^2\theta_\kappa}\,. \tag{43}$$

We write the Laplace equation for the outer crack arm

$$\frac{\sigma_{ml\omega}}{\rho_m}+\frac{\sigma_{pl\omega}}{\rho_p}=\frac{q}{\frac{b}{2}}. \tag{44}$$

From (44) we obtain

$$\sigma_{pl\omega}=\rho_p\frac{q}{\frac{b}{2}}. \tag{45}$$

The hoop stress, $\sigma_{pd\omega}$, in the inner arm of the crack is equal to $\sigma_{pl\omega}$, since the cylinder under consideration is thin-walled. The hoop stress, $\sigma_{p\omega}$, in the intact portion of the cylinder is found by replacing $b/2$ with b in formula (45).

We are looking for the meridional strain, $\varepsilon_{ml\omega}$, in the outer arm of the crack. We apply the relation (21). For this purpose, we replace σ_{ml} with $\sigma_{ml\omega}$ and then solve the equation thus obtained with respect to $\varepsilon_{ml\omega}$ using the MatLab. The strain along the meridian in the inner arm of the crack, $\varepsilon_{md\omega}$, is equal to $\varepsilon_{ml\omega}$.

To determine $\varepsilon_{m\omega}$ in the intact portion of the cylinder, we use (21) again. For this purpose, we replace σ_{ml} and ε_{ml} with $\sigma_{m\omega}$ and $\varepsilon_{m\omega}$ and then solve the equation with respect to $\varepsilon_{m\omega}$.

The hoop strain, $\varepsilon_{pl\omega}$, in the outer arm of the crack is determined from (21). To do this, we replace σ_{ml} and ε_{ml} with $\sigma_{pl\omega}$ and $\varepsilon_{pl\omega}$ and then solve the equation for $\varepsilon_{pl\omega}$. The hoop strain, $\varepsilon_{pd\omega}$, in the inner arm of the crack is equal to $\varepsilon_{pl\omega}$.

The hoop strain, $\varepsilon_{p\omega}$, in the intact portion of the cylinder is found by replacing σ_{ml} and ε_{ml} with $\sigma_{p\omega}$ and $\varepsilon_{p\omega}$ in (21) and then solve the equation in terms of $\varepsilon_{p\omega}$.

Finally, to find the SERR formula (28) is applied. For this purpose, both the meridional and hoop stresses in both arms of the crack and in the intact portion of the elliptical cylinder are taken into account when determining the complementary strain energy. To check the SERR, (36) is again applied.

Results and Discussion

The most important result of this paper is that the SERR solutions have been obtained for a lengthwise crack in a moving thin-walled continuously inhomogeneous elliptical cylinder with non-linear elastic behavior. The crack represents an elliptical surface coinciding with the middle surface of the cylinder. The cylinder itself is under the action of its own weight and the inertial load from the acceleration. In principle, the paper considers two types of mechanical motion of the thin-walled elliptical cylinder, namely:

1) translational motion in the vertical direction with constant acceleration;
2) uniform rotation around the axis, z.

The SERR solutions have been obtained for both types of motion. The solutions are presented in detail with all necessary explanations and diagrams of the cylinder. All necessary formulas are derived, which allows for direct application of the solutions in the analysis of moving elliptical cylinders with a lengthwise crack in them. As a result of continuous material inhomogeneity, the parameters of the non-linear constitutive law, as well as the bulk density of the material, change continuously along the height of the cylinder. The approach described in the

paper can also be applied when using other constitutive laws for non-linear elastic behavior of the cylinder and other laws for changing material parameters along the height.

Conclusion

It can be summarized that the analysis presented in this paper has the potential for practical application in the study of moving thin-walled elliptical cylinders with a lengthwise crack (two motions are considered, namely translational motion in the vertical direction and uniform rotation). The analysis is relatively general, because it takes into account the non-linear elastic behavior of the material from which the cylinder wall is made. In addition, the material is continuously inhomogeneous along the height of the cylinder. It is necessary to emphasize here that the obtained solutions of the SERR apply not only to cylinders in which the parameters of the non-linear constitutive law change continuously along the height, but also to cylinders in which the bulk density of the material is also a continuous function of the coordinate, z . The approach presented in the paper is also applicable to obtaining SERR in cylinders with linear-elastic behavior. For this purpose, Hooke's law should be applied instead of non-linear constitutive law. For example, this can be realized by setting $B=0$ and $D=0$ in law (21). Then, from the non-linear law (21), Hooke's law is obtained. This means that if we put $B=0$ and $D=0$ in the solution, we will obtain the SERR in a cylinder with linear-elastic behavior. The approach can also be applied to find the SERR in homogeneous cylinders. For this purpose, the resulting solution must assume equal values of the material parameters at both end of the cylinder (then the parameters, γ , E , B , D , s and f , will not change along the height (refer to formulas (3), (22) – (26))).

Recommendations

The analysis developed in this paper can be recommended as a means of studying the lengthwise fracture of moving thin-walled elliptical cylinders exhibiting non-linear elastic behavior.

Scientific Ethics Declaration

* The author declares that the scientific ethical and legal responsibility of this article published in EPSTEM Journal belongs to the author.

Conflict of Interest

* The author declares that there is no conflict of interest.

Acknowledgements or Notes

* This article was presented as an oral presentation at the International Conference on Basic Sciences, Engineering and Technology (www.icbaset.net) held in Istanbul/Türkiye on September 17-18, 2026.

References

El-Galy, I.M., Saleh, B.I., & Ahmed, M.H. (2019). Functionally graded materials classifications and development trends from industrial point of view. *SN Appl. Sci. 1*, 1378.

Gasik, M.M. (2010). Functionally graded materials: bulk processing techniques. *International Journal of Materials and Product Technology*, *39*, 20-29.

Gandra, J., Miranda, R., Vilaça, P., Velhinho, A., & Teixeira, J.P. (2011). Functionally graded materials produced by friction stir processing. *Journal of Materials Processing Technology, 211,* 1659-1668.

Kolev, P., & Mladenov, K. (1992). *Resistance of materials*. UP.

Lukash, P. (1997). *Fundamentals of non-linear structural mechanics*. Science.

Mahamood, R. C., & Akinlabi, E. T. (2017). *Functionally graded materials*. Springer.

Malenov, R. (1993). *Strength of materials*. UPH.

Mladenov, K., Klecherov, J., Lilkova-Markova, S., & Rizov, V. (2012). *Strength of materials*. ABC Tehnika.
Obodovski, B. A., & Hanin, C. E. (1971). *Strength of materials*. Harkov.
Rizov, V.I. (2017). Analysis of longitudinal cracked two-dimensional functionally graded beams exhibiting material non-linearity. *Frattura ed Integrità Strutturale*, *41*, 498-510.
Rizov, V.I., & Altenbach, H. (2019). On the analysis of lengthwise fracture of functionally graded round bars. *Structural Integrity and life*, *19*, 102–108.

Author(s) Information

Victor Rizov
University of Architecture, Civil Engineering and Geodesy
1 Chr. Smirnensky blvd., 1046 – Sofia, Bulgaria
ORCID iD: 0000-0002-0259-3984
Contact e-mail: *V_RIZOV_FHE@UACG.BG*

To cite this article:

Rizov, V. (2026). Lengthwise fracture analysis of a moving thin-walled elliptical cylinder. *The Eurasia Proceedings of Science, Technology, Engineering and Mathematics (EPSTEM), 42,* 39-48.

The Eurasia Proceedings of Science, Technology, Engineering and Mathematics (EPSTEM)
ISSN: 2602-3199

The Eurasia Proceedings of Science, Technology, Engineering and Mathematics (EPSTEM), 2026

Volume 42, Pages 49-58

ICBASET 2026: International Conference on Basic Sciences, Engineering and Technology

A Multiphysics Neural Network Framework for Microdamage Evolution with A Shadow Plasticity Observer

Utku Kaftancioglu
Atılım University

Cagatay Kasar
Sorbonne University

Abstract: Microdamage evolution in ductile solids is influenced by plastic deformation, stress redistribution and material degradation. A computational framework is presented in which gradient damage mechanics is combined with a neural constitutive predictor. Plastic history is retained through a mechanically inactive auxiliary observer, termed shadow plasticity here. Its state is supplied to a multilayer perceptron without inserting the plastic tensor into the actual elastic deformation. A local damage increment is proposed by the network and converted into a correction of damage resistance. The original constitutive corrector and finite element balance equations are retained. The framework is examined using a single edge notched specimen under nonlinear loading. Complete reference and control histories are compared with an independently verified neural interval covering the first 205 s of a 1000 s loading program. Damage initiation, spatial localization and force response are assessed on explicitly matched supports. Early neural damage error is substantially reduced relative to the original damage only model. The completed controls demonstrate recovery of the reference damage region and structural response. The strongest complete agreement is obtained after the base damage resistances are aligned. Later neural propagation remains unverified. The findings provide a basis for physically structured prediction of microdamage and demonstrate the importance of separating constitutive interaction from material calibration.

Keywords: Microdamage, Multiphysics modeling, Neural networks, Shadow plasticity, Finite element method

Introduction

Microdamage evolution in ductile solids is influenced by plastic deformation and stress redistribution. Its numerical representation requires the interaction between irreversible deformation and material degradation to be considered. Constitutive descriptions of these mechanisms and their application to ductile fracture were reviewed by Besson (2010). A simplified damage model can alter this interaction even when the same external loading is imposed. The resulting changes in damage initiation and localization must therefore be examined at both material and structural levels.

Spatial regularization has been introduced to address the localization sensitivity of continuum damage models. Gradient enhancement was demonstrated for quasi brittle materials by Peerlings et al. (1996). A broader framework for gradient elasticity, viscoplasticity and damage was presented by Forest (2009). An additional field associated with an internal variable was introduced through the micromorphic formulation. Coupled gradient plasticity and damage were subsequently treated at finite strains by Miehe et al. (2016). Their phase field framework provides relevant context for constitutive interaction. It is distinct from the multiplicative damage formulation considered here.

Neural networks have also been investigated for constitutive modeling. Mechanistic homogenization was incorporated into the deep material network of Liu et al. (2019). Thermodynamic laws were encoded in the neural

- This is an Open Access article distributed under the terms of the Creative Commons Attribution-Noncommercial 4.0 Unported License, permitting all non-commercial use, distribution, and reproduction in any medium, provided the original work is properly cited.

- Selection and peer-review under responsibility of the Organizing Committee of the Conference

© 2026 Published by ISRES Publishing: www.isres.org

architecture proposed by Masi et al. (2021). These developments support the retention of physical structure within a learned model. They do not imply that a small regression error alone establishes physical admissibility.

Material history must also be represented. Path dependent plasticity was learned through recurrent networks by Mozaffar et al. (2019). Constitutive models with evolving internal variables were embedded in a physically recurrent network by Maia et al. (2023). These approaches provide different representations of memory. In the present formulation, history is retained through persistent constitutive states supplied to a multilayer perceptron.

A mechanically inactive plasticity observer is introduced alongside the damage only mechanical branch. This auxiliary calculation is termed shadow plasticity here. Its plastic tensor and accumulated slip are retained as history descriptors. They are not inserted into the student's stress decomposition. A local damage increment is proposed by the neural network. The proposal is converted into a scalar correction of the complete raw damage resistance. The original constitutive corrector remains responsible for the actual damage update. The governing balance equations and resistance floor are retained.

The investigation is restricted to a fixed single edge notched specimen. The coupled reference, original damage only baseline, strength aligned control and analytical correction are included in the comparison with neural feedback. Damage initiation, spatial localization and force response are examined together. The strength aligned control separates the existing base resistance calibration difference from the influence of plastic kinematics.

Method

Constitutive Framework

Microdamage evolution was evaluated in a single edge notched specimen under plane strain. The displacement and gradient damage balance equations were solved with a four node user element in Abaqus. The nodal unknowns were two displacement components and the microdamage field χ_d. Spatial coupling remained governed by these equations. A mesh of 3184 physical elements was used. The prescribed displacement reached 0.3 mm over 1000 s. Fields were stored every 5 s. The geometry and loading are shown in Figure 1. The active source parameters are summarized in Table 1. Cubic elasticity was retained with the source crystal orientation. Twelve slip systems and the source damage normal $(0, 1, 0)$ were used.

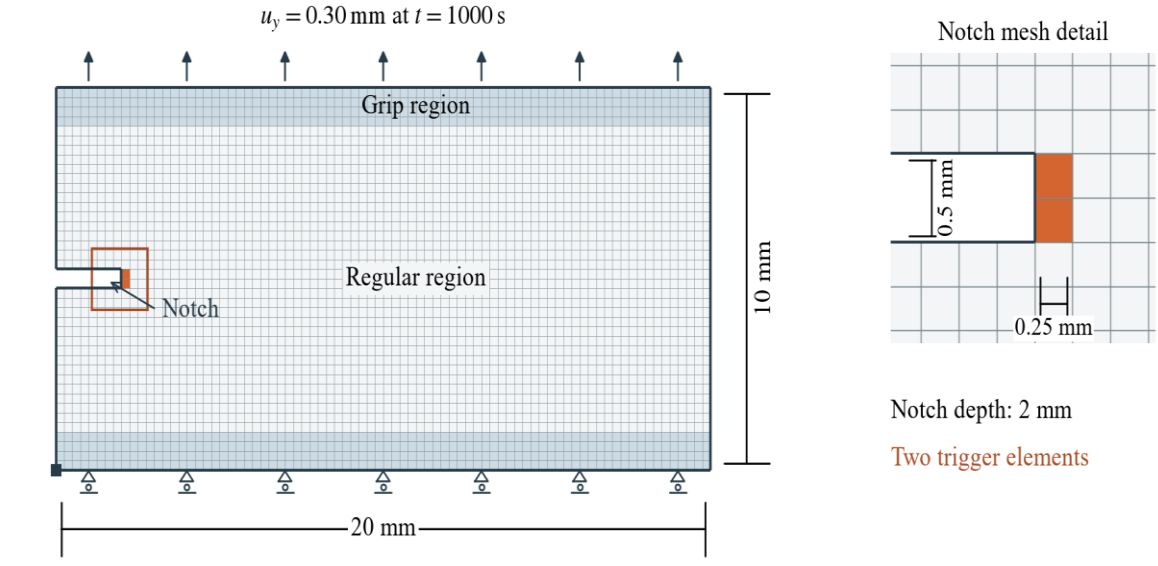

Bottom: $u_y = 0$; lower left node: $u_x = 0$. Plane strain; 3184 four node elements.

Figure 1. Specimen geometry and prescribed loading conditions

Numerical rate coefficients follow the source mm, N and s convention. No additional reference rate was introduced. Actual plasticity was suppressed in the student through $r_0 = 10^{13}$ MPa. This value was also used in the coupled and observer grip regions. The strength aligned control retained the student mechanics while its base resistances were matched to the reference.

Table 1. Material parameters retained from the source implementation

Parameter	Numerical value	Application
C_{11}, C_{12}, C_{44}	$205180, 144940, 92170$ MPa	Active cubic elasticity
H, x_H, T_{ult}	$-7500, 30000, 0.01$ MPa	Damage resistance and penalty
A	320	Gradient coefficient in the adopted unit convention
K_d, n_d	110,3	Damage rate
K_p, n_p, r_0	$551.3, 7.8, 122.5$	Coupled plasticity and observer
Student Y_0	$300, 120, 10^{13}$ MPa	Regular material, trigger and grip
Reference Y_0	$600,240, 10^{13}$ MPa	Coupled, strength aligned and scratch reference branches
θ	10 or 0	Coupled and scratch reference, or actual student branches

The coupled reference and damage only student were distinguished by their mechanical decompositions:

$$F = F_C^e F_C^p F_C^d \quad and \quad F = F_D^e F_D^d.$$

Plastic history was retained in an auxiliary observer with persistent state variables $\bar{F}^p$ and $\bar{\gamma}$. This auxiliary calculation is termed shadow plasticity here. The source plasticity update was evaluated using the current deformation and the student's previous damage state. The observer tensor was not inserted into the student's mechanical elastic gradient. Stress was calculated from $F_D^e = F(F_D^d)^{-1}$.

Model Variants and Resistance Correction

Strength Aligned Control

The strength aligned control was formed by changing only the base damage resistance in the original student. The regular and trigger values were increased from 300 and 120 MPa to 600 and 240 MPa. The grip value was unchanged. The damage only mechanical decomposition, suppressed plastic flow and original damage corrector were retained. Shadow plasticity was still calculated for observation, but its state was not used to correct resistance or actual stress. No neural predictor was used. This control was included to distinguish resistance calibration from the proposed plastic history correction.

Analytical Correction Control

In the analytical correction control, damage only mechanics and the original student base resistances were retained. The persistent shadow observer was advanced using the current deformation and previous student damage state. A separate local damage problem was then solved numerically using the updated observer plastic tensor, previous accumulated slip and reference resistance parameters. The proposed increment was converted into a scalar correction of the complete raw student resistance. The resistance floor was retained, and actual damage was computed by the original corrector. No network was used. Analytical therefore denotes a direct constitutive calculation, not a closed form solution.

Neural Correction Model

In the neural correction model, the active local proposal solve was replaced by a multilayer perceptron. Training targets were local damage increments generated on the analytical trajectory, not coupled finite element damage fields. Traction descriptors, student state and persistent shadow history were supplied as inputs. The proposal was limited by the source activation envelope and converted through the same inverse mapping into a raw resistance correction. The floor and original damage corrector were retained. Actual stress was still computed from the damage only branch with its original base resistances. No analytical proposal fallback or direct overwrite of actual damage was permitted.

A multilayer perceptron with two 64 neuron hidden layers and hyperbolic tangent activation was used. Ten mechanics derived inputs represented traction, damage, time increment, observer history and resistance. Positive source active proposals were fitted with Adam using a standardized logit target. Normalization statistics were

calculated from training data only. A bounded sigmoid output was used. Training and development validation were separated by time blocks. Trials and accepted records from each increment were kept in one partition.

The proposed increment δ_p was restricted by the original increment bound and a source activation envelope. The envelope causes the proposal to approach zero as the initial observer overstress approaches zero. The required resistance was then calculated as

$$Y_{\mathrm{req}} = t_D(\delta_p) - K_d \left(\frac{\delta_p}{\Delta t}\right)^{1/n_d}, a = Y_{\mathrm{req}} - Y_D^{\mathrm{raw}}(\delta_p).$$

Here t_D denotes the actual student damage traction. The source numerical rate coefficient $K_d = 110$ and exponent $n_d = 3$ were retained in the adopted mm, N and s convention. The scalar action a was held fixed during the original damage corrector. The complete raw resistance was corrected before its physical lower bound was applied. Infeasible inverse proposals were projected onto that bound. Inactive states were handled by the source activation rule. The analytical control solved the scratch damage problem directly. In the neural model, that active proposal solve was replaced by the network without an analytical fallback. Actual damage remained governed by the original corrector.

For the neural run, the complete element residual was differentiated numerically. Forward perturbations were applied to all twelve nodal unknowns. The corresponding displacement increments were perturbed consistently from identical incoming constitutive states. All blocks of the unsymmetric Jacobian were retained. The original controls used their existing approximate tangent.

Comparison Procedure

The coupled reference, original damage only model, strength aligned damage only control and analytical correction control were retained for comparison with the neural model. The regular and notch trigger reference resistances were twice the corresponding original damage only values. Grip resistance was unchanged. That calibration difference cannot be attributed to the plastic deformation decomposition.

Local damage and microdamage were compared over all elements and saved times. The complete control histories covered 0 to 1000 s. The independently verified neural fields covered 0 to 205 s. Field comparisons involving the neural model used the same 42 saved times for every model. The retained neural force history ended at 196.875 s. Force comparisons used exact common timestamps without interpolation. Damage regions were assessed at thresholds of 0.01, 0.05, 0.1 and 0.2. Region overlap, extent, area and first saved threshold crossings were evaluated alongside force and displacement. Shared edge connectivity was used to distinguish the damage region attached to the notch from remote activation. A threshold damage band was interpreted as an indication of fracture localization rather than a resolved traction free crack surface. The fixed specimen study was not an independent experimental or generalization test.

Results and Discussion

Early Neural Correction

The verified neural comparison covered 42 saved field times from 0 to 205 s. Every model was evaluated over the same 3184 elements. The mean field error in Table 2 is the average of the 42 spatial RMSE values. The neutral observer without resistance feedback reproduced the original damage only fields and force history exactly. It was therefore omitted from overlapping curves.

Table 2. Field agreement over the verified neural interval

Model	Mean RMSE of d	Mean RMSE of χ_d	Region RMSE of d	Force RMSE (N)
Original damage only	3.108×10^{-3}	2.826×10^{-3}	3.398×10^{-2}	2853.0
Strength aligned	2.162×10^{-5}	2.008×10^{-5}	4.599×10^{-4}	24.3
Analytical correction	2.068×10^{-5}	1.836×10^{-5}	5.190×10^{-4}	34.8
Neural correction	2.864×10^{-5}	2.436×10^{-5}	7.275×10^{-4}	33.2

The region errors in Table 2 were pooled over the same reference mask $d_C \geq 0.01$. There were 264 element and time pairs across 24 nonempty frames. Force errors used 49 identical native timestamps from 0 to 195 s. The available neural force record extended to 196.875 s, separately from its field record through 205 s. No force value was extrapolated to the field endpoint.

Mean damage error was reduced by 99.1% relative to the original damage only model. Both field errors were lower at 39 saved times and equal at the three remaining times. The damage region error was also substantially reduced. The improvement was therefore not explained solely by the large undamaged background. The analytical and strength aligned controls nevertheless retained lower mean field errors than the neural correction. Distinct superiority over these stronger controls was not established.

The force response is shown in Figure 2. Early neural feedback recovered the increasing reference response, whereas premature softening was obtained in the original damage only model. The complete control responses are shown separately in the lower panel. A neural curve is not extended into that later interval.

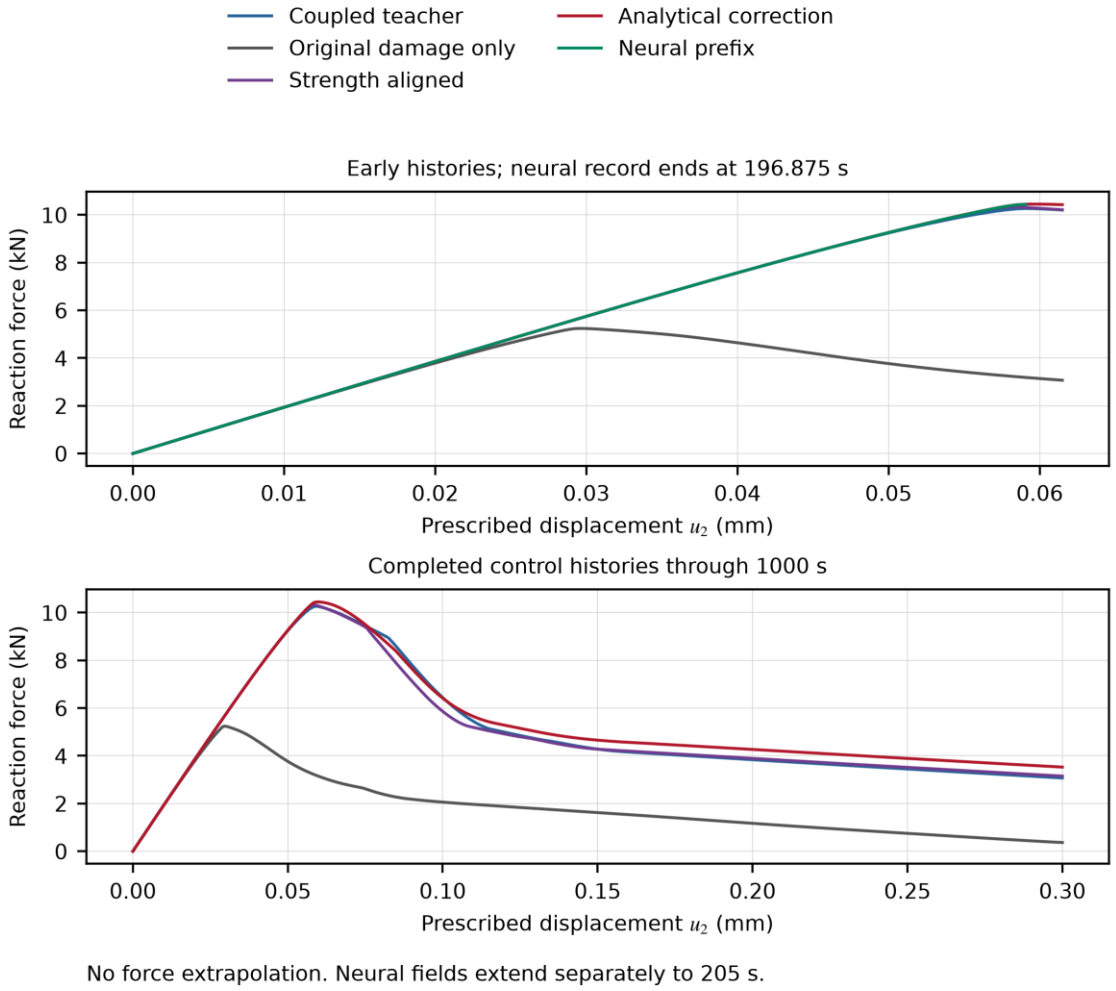

Figure 2. Force responses over separately verified loading intervals

Figure 3 shows the declared 90 and 195 s events. The excessive spread of early damage in the original model was suppressed by the corrected models. The figure uses one common scale from 0 to 0.09 across every model and all 42 early frames. Later control figures use a separate common scale from 0 to 0.4. The fields were not normalized independently. The reference regions at $d_C \geq 0.1$ and $d_C \geq 0.2$ were empty throughout the neural interval. These early results therefore establish damage initiation and localization agreement, not developed neural crack propagation.

At 195 s, the neural region with $d \geq 0.01$ contained 32 elements compared with 30 in the reference. Its intersection over union was 0.9375, compared with 0.0872 for the original model. Some overextension remained at the 205 s endpoint: 46 neural elements were active compared with 38 reference elements. The overlap decreased

to 0.8261 and the notch-connected extent exceeded the reference by 0.75 mm. The selected 195 s figure is therefore accompanied by the complete interval metrics rather than treated as a perfect endpoint prediction.

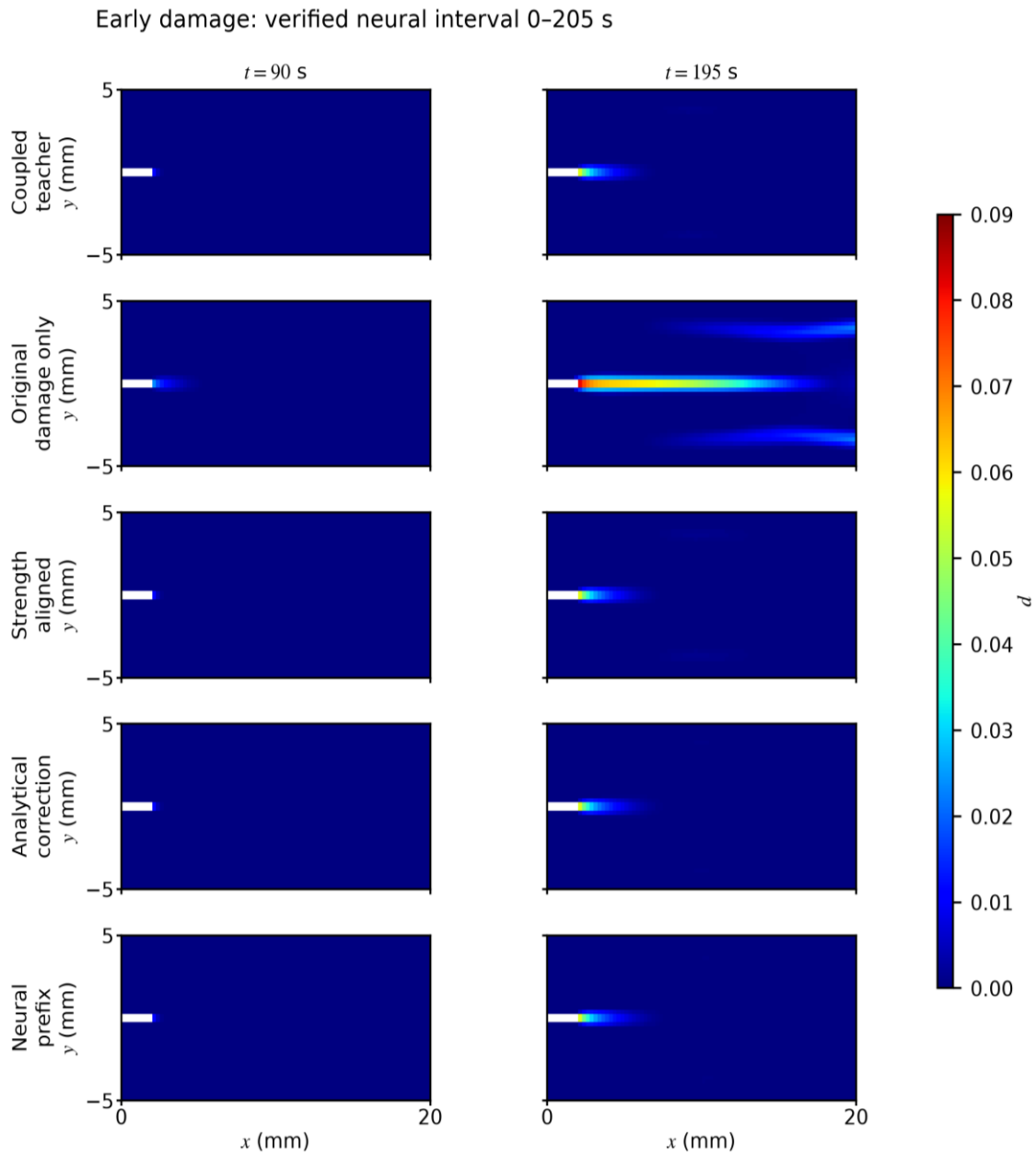

Figure 3. Early damage fields over matched neural increments

Complete Damage Localization in the Controls

The complete control comparison covered 201 saved times from 0 to 1000 s. The results in Table 3 are not directly comparable with the shorter averages in Table 2. The original damage only response was improved by both strength alignment and analytical correction. Both damage fields had lower error at 198 saved times and equal error at three times.

The strongest complete agreement was obtained with the strength aligned control. Its peak and terminal forces differed from the reference by 0.58% and 2.63%. The analytical correction also recovered the force level and damage band, but its terminal force remained 14.88% higher. Similar damage contours alone were therefore insufficient to establish identical structural response.

Table 3. Field and force agreement over complete histories

Model	Mean RMSE of d	Mean RMSE of χ_d	Peak force (kN)	Final force (kN)
Coupled reference	Reference	Reference	10.265	3.071
Original damage only	0.00925	0.00772	5.241	0.367
Strength aligned	0.00159	0.00141	10.324	3.151
Analytical correction	0.00341	0.00313	10.449	3.527

Native Abaqus damage contours are shown in Figure 4 for the coupled reference and analytical correction at 1000 s. The plotted variable UVARM6 is local damage d. The common rainbow scale and undeformed geometry were retained. Native within element extrapolation was used with averaging disabled. Small negative display extrema can arise from that extrapolation; they are not negative accepted local damage. Numerical errors were calculated from unextrapolated integration point means.

Figure 5 compares the completed controls at 300 and 1000 s. At 300 s, the reference region with $d \geq 0.1$ contained four elements and occupied 0.25 mm^2. At 1000 s, it contained 288 elements and occupied 18 mm^2. The same element sets were recovered by the strength aligned and analytical controls at both times. This is agreement in the threshold region, rather than equality of every damage amplitude.

Propagation was also assessed over the complete history. Shared edge connectivity was used to isolate the damage component attached to the notch. At $d \geq 0.1$, mean front position error was 1.44 mm for the original model, 0.54 mm after strength alignment and 0.64 mm with analytical correction. These values used 147, 147 and 146 times with defined paired fronts, respectively. Empty fronts were not assigned zero error. Remote activation occurred in the reference during part of the history. A global maximum damage coordinate was therefore not interpreted alone as the crack front. The advancing connected band provides an indication of fracture localization, not a resolved traction free surface.

Interpretation and scope

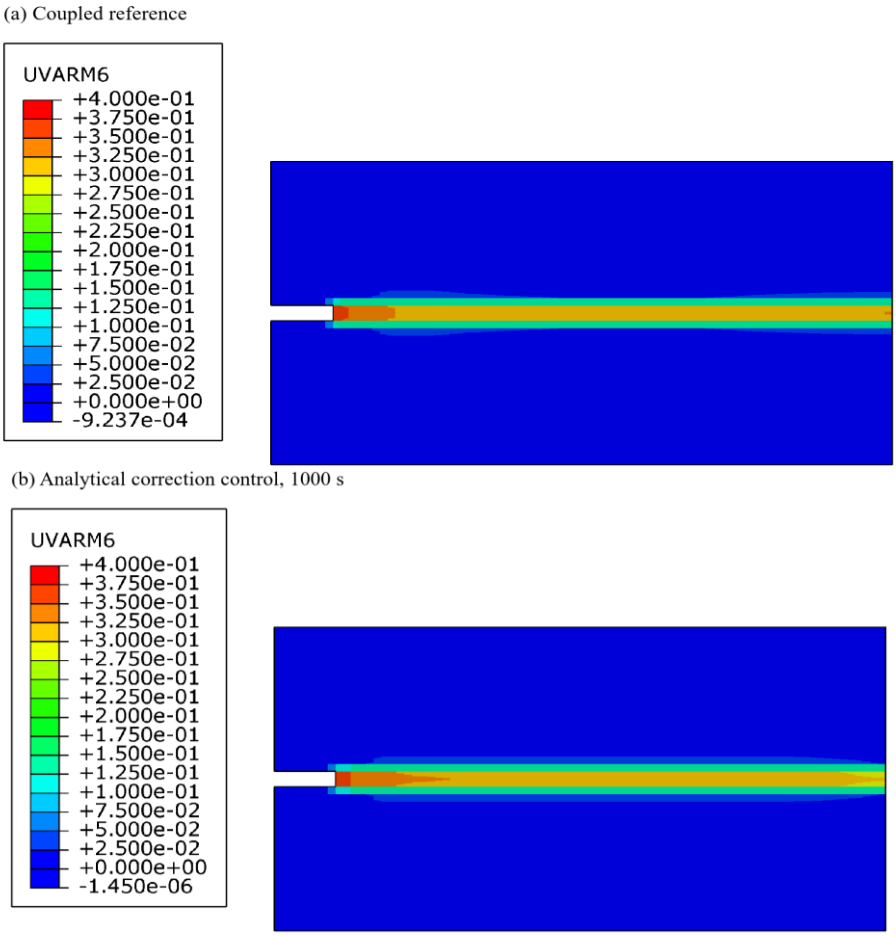

Figure 4. Native contours from the completed control simulations

The observer retained useful history but did not reproduce the coupled plastic state exactly. At 205 s, maximum element mean accumulated slip was 0.00122 in the neural observer and 0.00159 in the coupled reference. These values arose on different finite element trajectories. The comparison does not isolate observer error from the changed mechanical path.

The reported neural analysis terminated during a constitutive trial after the accepted 205 s state. That later trial was excluded. The retained interval passed finite output, irreversibility and corrector compatibility checks. One gate remained ambiguous at stored precision but compatible with the source rule. Full internal tensor histories were not independently exported. The early comparison is consequently a bounded result, not evidence of full neural completion or later propagation. Numerical safeguards in a subsequent implementation do not extend the scope of these reported data.

The positive finding is reliable early damage correction within the retained physical model, together with complete localization evidence from the controls. The base resistance difference was also shown to be important. The study does not establish an independent advantage of the observer or neural correction over appropriate strength alignment. Broader loading, mesh and experimental validation remain necessary.

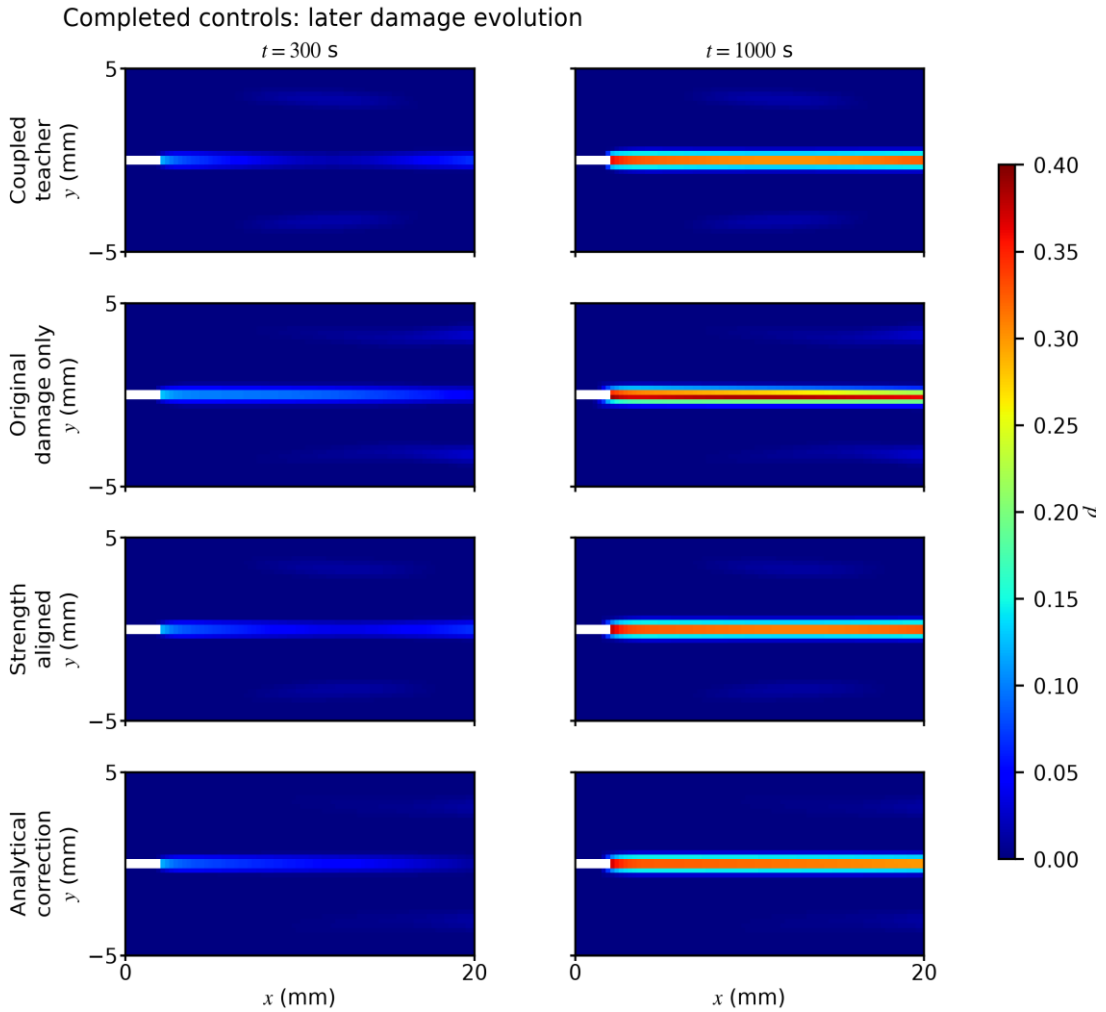

Figure 5. Damage propagation indicated by completed control histories

Conclusion

A neural increment proposal was embedded within the original constitutive damage corrector. Plastic history was retained by a mechanically inactive observer. Actual stress continued to be calculated from the damage only mechanical branch. The governing finite element equations were not replaced by a learned field map. Reliable damage localization and structural response were obtained in the completed control simulations. The reference threshold region was recovered at the declared later comparison times. The strength aligned damage only control

provided the closest complete agreement. The calibration difference must therefore be separated from any claimed benefit of plastic history or neural correction.

Early neural field agreement was substantially improved relative to the original damage only model. The neural findings are restricted to the independently verified early interval. Full neural completion and later crack propagation are not established by those results. The next requirement is a complete neural trajectory with the same field, connectivity and force checks. Additional loading paths and mesh resolution studies are required before broader predictive claims can be made

Scientific Ethics Declaration

* The authors declare that the scientific, ethical and legal responsibility of this article published in EPSTEM Journal belongs to the authors.

* This study was based on numerical simulations and did not involve human participants or animal experiments.

Conflict of Interest

* The authors declare that they have no conflicts of interest.

Funding

* No financial support was received for this study.

Acknowledgements or Notes

* This article was presented as an oral presentation at the International Conference on Basic Sciences, Engineering and Technology (www.icbaset.net) held in Istanbul/Türkiye on September 17-18, 2026.

* The authors thank the reviewers for their valuable feedback.

References

Besson, J. (2010). Continuum models of ductile fracture: A review. *International Journal of Damage Mechanics, 19*(1), 3–52. https://doi.org/10.1177/1056789509103482

Forest, S. (2009). Micromorphic approach for gradient elasticity, viscoplasticity, and damage. *Journal of Engineering Mechanics, 135*(3), 117–131. https://doi.org/10.1061/(ASCE)0733-9399(2009)135:3(117)

Liu, Z., Wu, C. T., & Koishi, M. (2019). A deep material network for multiscale topology learning and accelerated nonlinear modeling of heterogeneous materials. *Computer Methods in Applied Mechanics and Engineering, 345*, 1138–1168. https://doi.org/10.1016/j.cma.2018.09.020

Maia, M. A., Rocha, I. B. C. M., Kerfriden, P., & van der Meer, F. P. (2023). Physically recurrent neural networks for path-dependent heterogeneous materials: Embedding constitutive models in a data-driven surrogate. *Computer Methods in Applied Mechanics and Engineering, 407*, 115934. https://doi.org/10.1016/j.cma.2023.115934

Masi, F., Stefanou, I., Vannucci, P., & Maffi-Berthier, V. (2021). Thermodynamics-based artificial neural networks for constitutive modeling. *Journal of the Mechanics and Physics of Solids, 147*, 104277. https://doi.org/10.1016/j.jmps.2020.104277

Miehe, C., Aldakheel, F., & Raina, A. (2016). Phase field modeling of ductile fracture at finite strains: A variational gradient-extended plasticity-damage theory. *International Journal of Plasticity, 84*, 1–32. https://doi.org/10.1016/j.ijplas.2016.04.011

Mozaffar, M., Bostanabad, R., Chen, W., Ehmann, K., Cao, J., & Bessa, M. A. (2019). Deep learning predicts path-dependent plasticity. *Proceedings of the National Academy of Sciences, 116*(52), 26414–26420. https://doi.org/10.1073/pnas.1911815116

Peerlings, R. H. J., de Borst, R., Brekelmans, W. A. M., & de Vree, J. H. P. (1996). Gradient enhanced damage for quasi-brittle materials. *International Journal for Numerical Methods in Engineering, 39*(19), 3391–3403.

Author(s) Information

Utku Kaftancioglu
Atılım University, Graduate School of Natural and Applied Sciences, Ankara, Türkiye
ORCID iD: https://orcid.org/0009-0009-6387-1990
*Contact e-mail: *kaftancioglutku@gmail.com*

Cagatay Kasar
Sorbonne University, Institut Jean Le Rond d'Alembert, CNRS, 75005 Paris, France
ORCID iD: https://orcid.org/ 0009-0002-0642-9767

*Corresponding author(s) contact email

To cite this article:

Kaftancioglu, U., & Kasar, C. (2026). A multiphysics neural network framework for microdamage evolution with a shadow plasticity observer. *The Eurasia Proceedings of Science, Technology, Engineering and Mathematics (EPSTEM), 42,* 49-58.

The Eurasia Proceedings of Science, Technology, Engineering and Mathematics (EPSTEM)
ISSN: 2602-3199

The Eurasia Proceedings of Science, Technology, Engineering and Mathematics (EPSTEM), 2026

Volume 42, Pages 59-66

ICBASET 2026: International Conference on Basic Sciences, Engineering and Technology

Effect of Hollow Channel Cross-Section Shape on the Damage Mechanism of Reinforced Concrete Slabs Under Near-Field Blast Loading

Dursun Bakir
Bitlis Eren University

Abstract: Hollow-core reinforced concrete (RC) slabs are increasingly used for their reduced self-weight and integrated service voids, yet the influence of the internal channel cross-section shape on their behavior under near-field blast loading remains largely unexplored. Existing numerical studies on blast-loaded RC members focus almost exclusively on solid or circular-void cross-sections, leaving the systematic effect of void geometry unresolved. This study numerically investigates the contact detonation response of hollow-core RC slabs with three different channel cross-section shapes (square, circular, and hexagonal) using a coupled finite element method and smoothed particle hydrodynamics (FEM-SPH) approach in Abaqus/Explicit. The TNT charge is represented by the Jones-Wilkins-Lee (JWL) equation of state, concrete is modeled with the Concrete Damaged Plasticity (CDP) constitutive law, and an adaptive FEM-to-SPH conversion is employed in the contact region so that cratering and fragment ejection are captured without element-deletion artifacts. A parametric matrix of 48 models spanning three channel shapes, four lower-flange thicknesses (50-140 mm), and four charge masses (0.5-2.0 kg) was analyzed. The results show that the channel cross-section shape significantly governs blast resistance: the circular and hexagonal sections exhibit comparable performance and undergo approximately 20% lower mean bottom-flange displacement than the square section. The 90-degree corners of the square section promote premature crack initiation and concrete crushing through stress concentration. A critical lower-flange thickness is identified, beyond which the failure mode transitions from global flexural collapse to localized perforation. The predicted crater dimensions agree well with previously reported contact-explosion experiments.

Keywords: Hollow-core slab, Contact blast, FEM-SPH coupling, Channel geometry, Damage mechanism

Introduction

Protective reinforced concrete (RC) structures must resist blast loading, an extreme dynamic action characterized by a near-instantaneous rise of overpressure followed by rapid decay within a few milliseconds. Under such impulsive loading, concrete, being a brittle material, rapidly exceeds its elastic limit and may undergo severe local damage, spalling, and perforation. The conventional means of increasing blast resistance, namely adding mass and thickness, conflicts with the contemporary demand for lightweight and material-efficient construction. This tension has motivated the development of hollow-core RC slabs, in which periodic internal voids reduce self-weight while offering the potential to redistribute and attenuate blast-induced stresses (Savaş & Bakır, 2022; Bakır, 2026).

A substantial body of work has addressed the numerical simulation of blast-loaded RC members. Du et al. (2016) applied a coupled FEM-SPH method to model explosions inside pipes, capturing blast-wave propagation and dynamic fracture with a rate-dependent failure criterion. Karmakar and Shaw (2021) investigated the response of RC plates under blast loading using an FEM-SPH coupled framework, comparing several idealizations of the blast event and examining the effect of standoff distance and boundary conditions. Wang et al. (2023) employed an ALE-FEM-SPH coupling method to predict the spalling damage and fragment characteristics of RC slabs subjected to close-in detonation, validating fragment size and velocity distributions against experiments. Collectively, these studies established the FEM-SPH approach as an effective tool for blast problems that involve

- This is an Open Access article distributed under the terms of the Creative Commons Attribution-Noncommercial 4.0 Unported License, permitting all non-commercial use, distribution, and reproduction in any medium, provided the original work is properly cited.

- Selection and peer-review under responsibility of the Organizing Committee of the Conference

© 2026 Published by ISRES Publishing: www.isres.org

large deformation, discontinuity, and material fragmentation. However, they considered solid or single-void cross-sections; the systematic effect of the internal channel shape on the blast response of hollow-core slabs has not been addressed.

Although circular voids are the most common choice in hollow-core construction, the abrupt geometric transition at the tangent points of circular hollows can lead to irregular stress accumulation under highly dynamic loading, indicating that circular geometry is not necessarily optimal for blast resistance. Alternative void shapes such as square and hexagonal present different wall inclinations, corner angles, and load-transfer paths that may substantially alter the damage mechanism under contact blast. Square voids introduce sharp 90-degree corners at which stresses concentrate, whereas hexagonal voids form inclined web-walls that can redistribute load between adjacent cells through a Vierendeel-type framing action, in a manner analogous to the honeycomb cellular forms found in nature (Bakır, 2026). A direct, systematic comparison of these channel shapes under identical loading and boundary conditions is therefore required to guide the selection of void geometry for blast-resistant design.

The author's previous study (Bakır, 2026) focused on the parametric response and cross-validated surrogate modelling of hexagonal-hollow RC slabs subjected to standoff blast loading, using web thickness, charge mass, and hexagonal cell radius as the design variables. The present study addresses a distinct research question and uses a separate contact-detonation dataset: it systematically compares three channel cross-section shapes (square, circular, and hexagonal) while varying the lower-flange thickness and charge mass. Using a coupled FEM-SPH formulation in Abaqus/Explicit, a full-factorial parametric study of 48 models is carried out. The specific objectives are to quantify the influence of channel shape on peak deformation and energy dissipation, identify the failure-mode transition governed by lower-flange thickness, and characterize the crater morphology and damage mechanism associated with each void geometry. Thus, the present work extends the earlier geometry-specific standoff-blast study to a separate contact-blast regime and focuses on cross-sectional shape and local failure mechanisms rather than surrogate-model development.

Method

Coupled FEM-SPH Formulation

Contact and near-field detonation subject the concrete in the immediate vicinity of the charge to extreme distortion that a purely Lagrangian finite-element mesh cannot sustain without severe element tangling. To overcome this difficulty, an adaptive FEM-to-SPH conversion technique is employed. The slab is initially discretized entirely with Lagrangian finite elements. When a finite element in the contact region reaches a prescribed conversion criterion, here a maximum principal strain threshold, it is transformed into smoothed-particle-hydrodynamics (SPH) particles that inherit the mass, velocity, and momentum of the parent element. The deviatoric and volumetric stresses of the converted particles are reset, so that the particles carry only compressive pressure and thus represent the fragmented, cohesionless material realistically. The finite-element and particle domains are solved together, with forces transferred across the interface through hybrid elements, and because the kinetic energy of each converted element is preserved, the ejection velocity of the fragments is captured accurately. Cratering and material ejection are thereby reproduced without the mass and momentum inconsistency associated with pure element deletion.

In the present model the conversion is confined to the upper flange beneath the charge, the region that experiences direct contact loading and cratering, while the lower flange and the channel webs are retained as finite elements. This regional treatment reflects the physical observation that fragmentation is localized under the charge, keeps the particle count and computational cost manageable, and prevents spurious disintegration of the load-bearing lower flange, in agreement with the intact lower surfaces observed in contact-explosion experiments.

Explosive Model

The TNT charge is modeled with the Jones-Wilkins-Lee (JWL) equation of state, which describes the pressure p of the detonation products as a function of the relative volume V and the specific internal energy E, as given in Equation 1:

$$p = A\left(1 - \frac{\omega}{R_1 V}\right)e^{-R_1 V} + B\left(1 - \frac{\omega}{R_2 V}\right)e^{-R_2 V} + \frac{\omega E}{V} \quad (1)$$

where A, B, R_1, R_2, and ω are material constants determined from cylinder-expansion tests (Dobratz & Crawford, 1985). The JWL parameters adopted for TNT are listed in Table 1. The charge is placed in direct contact with the upper face of the slab above the central channel, and detonation is initiated at the charge center.

Table 1. JWL parameters for TNT

ρ (kg/m³)	D (m/s)	A (GPa)	B (GPa)	R_1 / R_2	ω / E_0 (GPa)
1630	6930	371.2	3.231	4.15 / 0.95	0.30 / 7.0

Concrete and Reinforcement Models

The concrete is represented by the Concrete Damaged Plasticity (CDP) model (Lee & Fenves, 1998), which combines isotropic tensile-cracking and compressive-crushing damage with multi-hardening plasticity and captures the degradation of elastic stiffness under load reversal. The strain-rate sensitivity of concrete and steel under blast loading is commonly represented through dynamic increase factors (Malvar & Crawford, 1998). A compressive strength of 30 MPa (grade C30) is adopted, with the plasticity-surface parameters summarized in Table 2. The tensile and compressive hardening behavior and the associated damage-evolution data are prescribed in tabular form, defined such that the plastic strain increases monotonically to ensure numerical consistency. The steel reinforcement consists of two orthogonal mats modeled with two-node truss elements (T3D2) and coupled to concrete through an embedded-region constraint, representing a perfect-bond idealization appropriate for the global flexural response of interest.

Table 2. Concrete damaged plasticity parameters

fc (MPa)	Dilation ψ	Eccentricity	f_{b0}/f_{c0}	Kc	Viscosity
30	36°	0.1	1.16	0.667	1×10^{-4}

Geometry, Boundary Conditions, and Mesh

The slab has overall plan dimensions of 1.0 × 2.0 m. A row of channels runs along the span, formed by a 50 mm upper flange, a channel of 150 mm height, and a lower flange whose thickness is varied parametrically. Three channel cross-section shapes (square, circular, and hexagonal) are considered(Figure 1), each generating a distinct wall geometry between adjacent voids while maintaining a comparable void size. The slab rests on a soil-type support, idealized by restraining the vertical displacement of the bottom surface while leaving the in-plane directions free, reproducing the support condition of the reference experimental configuration (Savaş & Bakır, 2022). The concrete domain is discretized with eight-node reduced-integration hexahedral elements (C3D8R) with enhanced hourglass and distortion control. The contact region beneath the charge uses a finer mesh (10 mm) to resolve the FEM-to-SPH conversion, whereas the remainder of the slab uses a coarser mesh (20 mm) and remains purely Lagrangian; the reinforcement is discretized with T3D2 truss elements embedded in the concrete host.

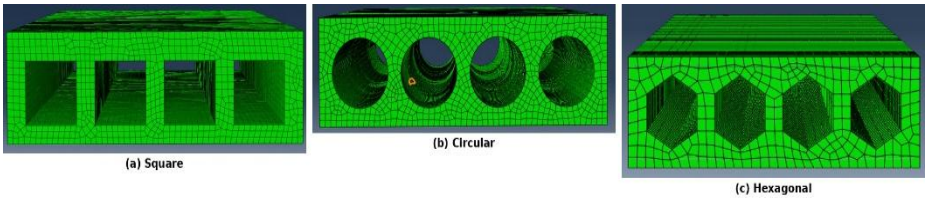

Figure 1. Finite-element models of the three channel shapes

Parametric Study

A full-factorial parametric matrix of 48 models was generated by combining three channel shapes, four lower-flange thicknesses, and four TNT charge masses, as summarized in Table 3. All other modeling choices (reinforcement layout, constitutive parameters, boundary conditions, and integration settings) were held constant,

so that the influence of the three design variables could be isolated. From each simulation the peak bottom-flange displacement, the crater depth, and the components of the energy balance were extracted

Table 3. Parametric design matrix

Variable	Levels	Count
Channel shape	Square, Circular, Hexagonal	3
Lower-flange thickness	50, 80, 110, 140 mm	4
TNT charge mass	0.5, 1.0, 1.5, 2.0 kg	4

Results and Discussion

Effect of Channel Cross-Section Shape

The channel cross-section shape has a pronounced effect on the blast resistance of the slab. Table 4 reports the mean peak bottom-flange displacement for each shape, averaged over all thickness and charge levels. The circular (84.2 mm) and hexagonal (87.0 mm) sections perform comparably and exhibit the smallest mean displacement, while the square channel undergoes the largest displacement (106.7 mm). The circular and hexagonal sections are therefore approximately 20% more effective than the square section in limiting the bottom-flange deflection.

This ranking is explained by the load-transfer geometry of each void. In the square channel, the flat soffit of the upper flange spans the full void width without inclined support, and the sharp 90-degree corners act as stress raisers that promote premature crack initiation and concrete crushing; the loaded flange therefore deflects most. By contrast, the circular section provides a smooth load-transfer path without sharp corners, while the inclined walls of the hexagonal section redistribute the load between adjacent cells. These geometric characteristics explain why the circular and hexagonal channels exhibit comparable responses and lower mean bottom-flange displacement than the square channel. The finite-element models of the three channel cross-section shapes are shown in Figure 1.

Table 4. Mean bottom displacement by shape

Channel shape	Mean displacement (mm)	Rel. to square
Circular	84.2	−21.1%
Hexagonal	87.0	−18.5%
Square	106.7	reference

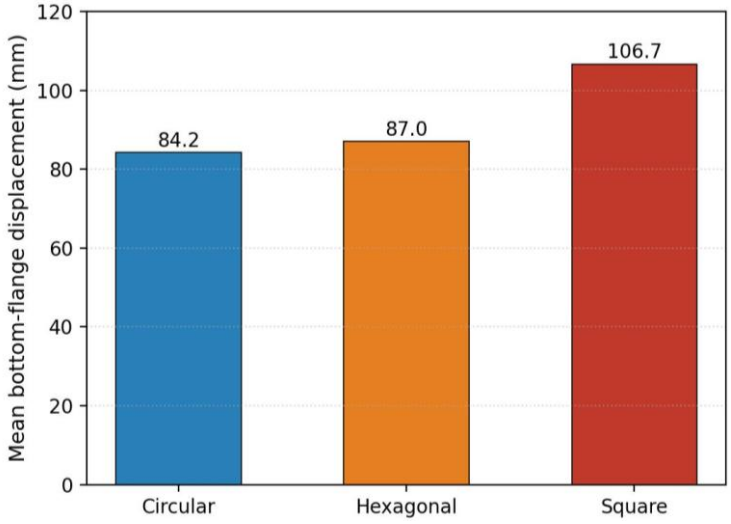

Figure 2. Mean bottom displacement by shape

Effect of Lower-Flange Thickness

The lower-flange thickness strongly governs deformation and the failure mode. Table 5 lists the peak bottom-flange displacement as a function of thickness for the three shapes at a fixed charge mass of 1.0 kg. For every shape, increasing the thickness from 50 to 140 mm reduces the displacement by a factor of four to five (for

example, from 136.4 to 28.1 mm in the square section). The reduction is steepest between 50 and 110 mm and diminishes beyond approximately 110 mm, indicating a region of diminishing returns and the existence of a critical lower-flange thickness above which further thickening yields little additional benefit. This trend is illustrated in Figure 3.

Two distinct failure regimes are observed. For thin lower flanges combined with large charges, the entire cross-section is driven downward and the slab fails by global flexural collapse, with the bottom flange displacing more than the crater depth on the loaded face. For thick lower flanges, the damage remains localized: the upper flange is perforated and a crater forms, but the lower flange and the reinforcement retain their integrity, corresponding to localized perforation. The transition between these regimes is controlled by the lower-flange thickness in combination with the charge mass.

Table 5. Bottom displacement (mm) vs thickness (M = 1.0 kg)

Shape	50 mm	80 mm	110 mm	140 mm
Square	136.4	93.0	54.6	28.1
Circular	109.5	49.1	30.6	20.6
Hexagonal	100.1	47.0	31.1	—

Dashes denote a small number of configurations that did not reach numerical completion under the initial-shock convergence limit.

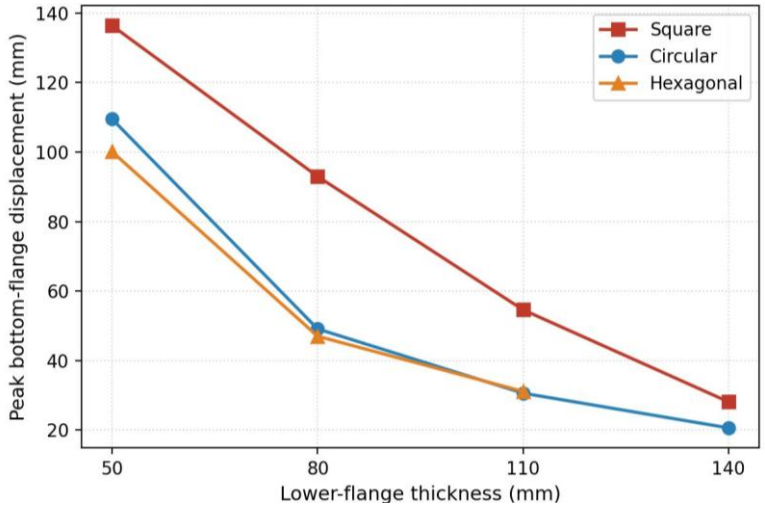

Figure 3. Displacement versus lower-flange thickness

Effect of Charge Mass and Energy Dissipation

Increasing the charge mass raises the deformation in a strongly nonlinear manner. For the square section with an 80 mm lower flange, the peak bottom-flange displacement increases from a negligible value at 0.5 kg to 93.0 mm at 1.0 kg, 165.6 mm at 1.5 kg, and 204.4 mm at 2.0 kg. At the lightest charge the upper flange is only locally damaged and the bottom flange is essentially undisturbed, whereas at the heaviest charge the section approaches global collapse. This confirms that, for a given geometry, the charge mass is the dominant driver of the overall response, and that the beneficial effect of the channel shape is most valuable in the intermediate range, where the response is sensitive to the load-transfer geometry.

The energy balance provides further insight. For the square section with an 80 mm lower flange under a 1.0 kg charge, the kinetic energy of the ejected material and detonation products dominates the balance (of the order of 3.6 MJ), while the energy dissipated by concrete damage and plasticity is much smaller (of the order of 0.18 MJ). The proportion of energy absorbed by the slab, rather than transmitted to the ejected fragments, is greatest for the geometries that distribute the load most effectively, consistent with the displacement ranking above.

Crater Morphology and Damage Mechanism

The adaptive FEM-to-SPH conversion reproduces the crater and fragment ejection on the loaded face while preserving the integrity of the lower flange. In all configurations the crater develops on the upper flange directly

beneath the charge, with the converted particles ejected away from the slab, while the lower flange and channel webs remain as finite elements and do not perforate, consistent with the intact lower surfaces reported in contact-explosion experiments. The square section shows the most extensive tensile-damage field around the crater, with damage bands emanating from the sharp corners, whereas the circular and hexagonal sections confine the damage to a smaller region, as compared in Figure 4. A cross-sectional view confirming the intact lower flange is shown in Figure 5. The predicted crater dimensions are in good agreement with the experimental crater measurements reported by Savaş and Bakır (2022) on hollow-core RC slabs subjected to contact charges, supporting the validity of the modeling approach.

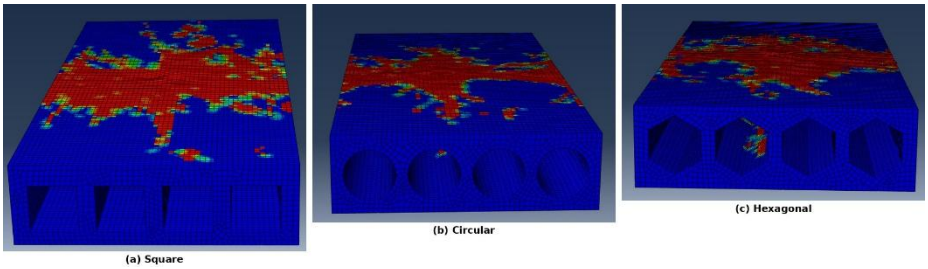

Figure 4. Tensile-damage distribution for the three shapes

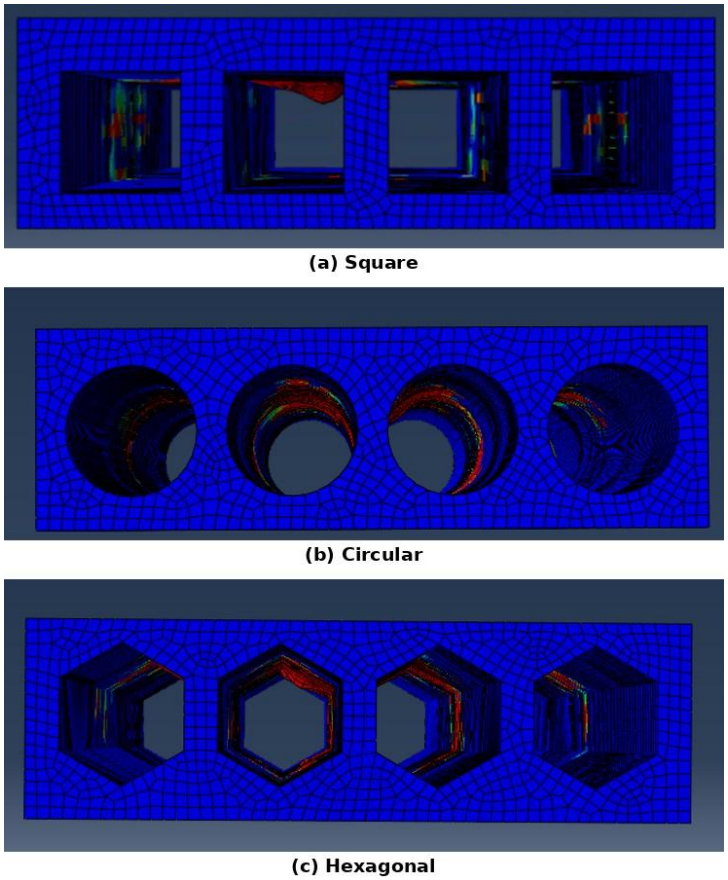

Figure 5. Cross-sections showing intact lower flange

Conclusion

This study numerically investigated the effect of the internal channel cross-section shape on the damage mechanism of hollow-core reinforced concrete slabs under near-field blast loading, using a coupled FEM-SPH approach in Abaqus/Explicit with a full-factorial parametric study of 48 models. Within the investigated contact-detonation dataset, the channel cross-section shape significantly influenced the blast response of the slab: the circular and hexagonal channels perform comparably and are the most effective in limiting the bottom-flange deflection, giving a mean displacement approximately 20% lower than the square channel. The comparable response of the circular and hexagonal sections independently corroborates the trend reported in the author's

earlier standoff-blast study (Bakır, 2026), although the present result is obtained from a separate loading regime and parametric matrix. Their favorable behavior relative to the square section is attributed to their curved and inclined walls, which distribute the applied load more uniformly, whereas the sharp 90-degree corners of the square section act as stress raisers that promote premature cracking and crushing.

The lower-flange thickness was found to strongly control both the magnitude of deformation and the failure mode. A critical thickness, of the order of 110 mm for the configurations studied, separates a global flexural-collapse regime from a localized-perforation regime, and thickening beyond this value yields diminishing returns. The adaptive FEM-to-SPH conversion reproduced the crater and fragment ejection on the loaded face without element-deletion artifacts and preserved the integrity of the lower flange, in agreement with experimental observations, and the predicted crater dimensions matched previously reported contact-explosion measurements. Overall, the results indicate that the internal void geometry is an effective design parameter for blast-resistant hollow-core slabs, and that the hexagonal geometry offers performance comparable to the conventional circular void while avoiding the stress concentrations of the square section.

Recommendations

Future work should extend the present study to additional charge standoffs to cover the full near-field to far-field range, incorporate bond-slip and strain-rate (dynamic increase factor) effects in the constitutive models for improved local accuracy, and examine the fragment size and velocity distributions in greater detail. A mesh-convergence study across the loading regimes and an experimental validation campaign specific to the non-circular channel shapes are also recommended to further establish the reliability of numerical predictions.

Scientific Ethics Declaration

* The author declares that the scientific, ethical, and legal responsibility for this article published in EPSTEM belongs to the author.

Conflict of Interest

* The author declares that there is no conflict of interest.

Funding

* The author would like to acknowledge the financial support provided by the Scientific and Technological Research Council of Türkiye (TÜBİTAK) through the 2224-B Domestic Scientific Event Participation Support Program.

Acknowledgements or Notes

* This article was presented as an oral presentation at the International Conference on Basic Sciences, Engineering and Technology (www.icbaset.net) held in Istanbul/Türkiye on September 17-18, 2026.

References

Bakır, D. (2026). A cross-validated data-driven surrogate model for the blast response of hexagonal-hollow reinforced concrete slabs. *Buildings, 16*(15), 3017.

Bakır, D., Savaş, S., & Üstündağ, H. (2024). Simulation of the behavior of reinforced concrete rectangular hollow sandwich plates under the effect of contact explosion through SPH method. *Revista de la Construcción, 23*, 554–567.

Dobratz, B. M., & Crawford, P. C. (1985). *LLNL explosives handbook: Properties of chemical explosives and explosive simulants* (UCRL-52997). Lawrence Livermore National Laboratory.

Du, Y., Zhang, F., Zhang, A., Ma, L., & Zheng, J. (2016). Consequences assessment of explosions in pipes using coupled FEM-SPH method. *Journal of Loss Prevention in the Process Industries, 43*, 549–558.

Karmakar, S., & Shaw, A. (2021). Response of R.C. plates under blast loading using FEM-SPH coupled method. *Engineering Failure Analysis, 125*, 105409.

Lee, J., & Fenves, G. L. (1998). Plastic-damage model for cyclic loading of concrete structures. *Journal of Engineering Mechanics, 124*(8), 892–900.

Malvar, L. J., & Crawford, J. E. (1998). Dynamic increase factors for concrete. In *Proceedings of the 28th DDESB Seminar*. Orlando, FL.

Savaş, S., & Bakır, D. (2022). An experimental study on the blast responses of hollow core concrete slabs to contact explosions. *Revista de la Construcción, 21*, 587–601.

U.S. Department of Defense. (2008). *Structures to resist the effects of accidental explosions* (UFC 3-340-02). Washington, DC: U.S. Department of Defense.

Wang, Z., Chen, W., Hao, H., Dong, Y., & Huang, Z. (2023). Numerical prediction of blast fragmentation of reinforced concrete slab using ALE-FEM-SPH coupling method. *Finite Elements in Analysis and Design, 220*, 103948.

Author(s) Information

Dursun Bakir
Bitlis Eren University,
Faculty of Engineering and Architecture,
Department of Civil Engineering, Bitlis, Türkiye
ORCID iD: https://orcid.org/0000-0001-6398-0497
*Contact e-mail: *dursunbakir23@gmail.com*

*Corresponding author(s) contact email.

To cite this article:

Bakir, D. (2026). Effect of hollow channel cross-section shape on the damage mechanism of reinforced concrete slabs under near-field blast loading. *The Eurasia Proceedings of Science, Technology, Engineering and Mathematics (EPSTEM), 42,* 59-66.

The Eurasia Proceedings of Science, Technology, Engineering and Mathematics (EPSTEM)
ISSN: 2602-3199

The Eurasia Proceedings of Science, Technology, Engineering and Mathematics (EPSTEM), 2026

Volume 42, Pages 67-75

ICBASET 2026: International Conference on Basic Sciences, Engineering and Technology

Response of Potato (Salanum Tuberosum L.) and Green Bean (Phaseolus Vulgaris L.) Crops to Mycorrhizal, NPK and Sheep Manure Fertilization in Soil

Mohammed Ayad Harbawi
University of Mosul

Fatih Abed Hasan
University of Mosul

Hesham Saadaldeen Younes
University of Mosul

Aziz, Rana Saadallah
University of Mosul

Abstract: A field experiment was conducted in the Al-Qubba region, north of Mosul, to evaluate the effects of mycorrhizal inoculation, NPK compound fertilization, and sheep manure on the growth parameters and yield components of potato and green bean. The study was carried out in a calcareous Silty Clay soil characterized by low organic matter content and a deficiency in plant-available nitrogen and phosphorus. The experiment followed a Randomized Complete Block Design (RCBD) with three replicates, comprising 18 experimental units resulting from the interaction of the studied factors. The results indicated that all treatments significantly enhanced the growth of both crops, leading to marked increases in growth indicators (plant height, shoot dry weight, and number of branches). Furthermore, there was a significant improvement in yield components: tuber weight, number of tubers, and yield per plant for the potato crop; and number of pods per plant, number of seeds per pod, and total yield for the green bean crop. Additionally, nitrogen and phosphorus concentrations in potato tubers and green bean pods were increased. The integrated treatment (Mycorrhiza + NPK) significantly outperformed all other treatments across all vegetative growth parameters, yield components, and nutrient concentrations (N and P) for both crops.

Keywords: Potato, Green bean, Fertilization

Introduction

Arbuscular mycorrhizal fungi (AMF) play a pivotal role in enhancing plant growth and productivity through a non-pathogenic symbiotic relationship established under natural conditions between the fungus and the host plant. Over 90% of vascular plants are capable of forming these symbiotic associations, which persist throughout the plant's life cycle (Sweeney et al., 2022). This symbiosis represents a key mechanism for improving plant health and yield by augmenting the uptake of essential nutrients, such as nitrogen (N), calcium (Ca), and magnesium (Mg), and particularly immobile soil elements like phosphorus (P). These fungi efficiently transport nutrients from soil zones beyond the reach of the root system; the mycorrhizal hyphae extend from the roots, effectively acting as an expanded root system that increases the reach, depth, and rate of water and nutrient absorption. Furthermore, fungal hyphae serve as a biological reservoir for nutrients, accumulating phosphorus within their structures and supplying it to the plant during periods of low soil P-availability (Smith et al., 2011; Ezawa & Saito, 2018). Mycorrhizae also play a crucial role in mitigating drought and salinity stress

- This is an Open Access article distributed under the terms of the Creative Commons Attribution-Noncommercial 4.0 Unported License, permitting all non-commercial use, distribution, and reproduction in any medium, provided the original work is properly cited.

- Selection and peer-review under responsibility of the Organizing Committee of the Conference

© 2026 Published by ISRES Publishing: www.isres.org

by enhancing water uptake, boosting antioxidant activities, and regulating phytohormones such as auxins and cytokinins (Kakouridis et al., 2022; Wang et al., 2023). Beyond abiotic stress, mycorrhizae bolster plant resistance against diseases and pests by stimulating the production of inhibitory compounds, including lignin and flavonoids, as well as phosphatase enzymes known for their antimicrobial and anti-insect activities (Weng et al., 2022; Li et al., 2024; Chen et al., 2024; Farhaoui et al., 2025). Additionally, mycorrhizae contribute to the improvement of soil physical properties by promoting the formation of stable soil aggregates and increasing soil organic matter content (Rillig & Mummey,2006; Fall et al., 2022; Wu et al., 2024)

Carrara et al. (2023) highlighted that soil inoculation with Arbuscular Mycorrhizal Fungi (AMF) resulted in an increase in tuber yield by up to 23% and a boost in antioxidant activity by as much as 120%. Furthermore, it led to a nine-fold increase in ergothioneine concentration and a 46% rise in soluble sugar levels. In a related context, Rodiño et al. (2025) indicated that AMF inoculation effectively enhances bean growth and improves grain quality. Their study suggests that the strategic integration of symbiotic mycorrhizae can mitigate pesticide dependence and foster the development of healthier, more sustainable food systems .

High crop productivity can be achieved through the balanced application of NPK fertilizers tailored to the specific requirements of the crop. This approach not only optimizes fertilizer costs but also mitigates adverse environmental impacts. Hochmuth and Hanlon (2014) reported that applying appropriate rates of NPK enhances the growth of potato crops and significantly increases both tuber number and total yield. Similarly, it has been observed that NPK fertilization in common beans (Phaseolus vulgaris) leads to marked increases in plant height and leaf number. Furthermore, it substantially improves yield components, including pod length, the number of pods per plant, and the number of seeds per pod .

Sheep manure is a nutrient-rich organic fertilizer renowned for its capacity to enhance the physical, chemical, and biological properties of soil. Its application reduces bulk density, increases water-holding capacity, promotes the stability of soil aggregates, and elevates soil organic matter content. Furthermore, it fosters microbial diversity and activity while supplying essential nutrients to the soil (Rayne & Aula, 2020; Elouear et al., 2016; Yu et al., 2024). Previous studies have demonstrated that fertilizing potatoes with sheep manure leads to significant increases in plant height, stem number, and chlorophyll content, as well as an improvement in tuber number and weight (El-Mesairy et al., 2022; Ierna & Distefano, 2024; Hou et al., 2024). Similarly, it has been found that sheep manure application enhances leaf area, leaf number, plant height, pod number and weight, and total yield in green beans (Bucagu et al., 2017; Sharifi et al., 2024).

The integration of chemical fertilizers with bio-fertilizers or organic amendments often yields greater benefits than their sole application. Alhrout et al. (2016) observed that the highest green bean yield was achieved by combining poultry manure with NPK fertilizer. Moreover, Tadang et al. (2025) reported that the maximum yield for beans resulted from the co-application of cattle manure and vermicompost alongside NPK. Similarly, the inoculation of potatoes with mycorrhizal fungi at a rate of 15 g plant^{-1}, in the presence of mineral fertilizer, played a vital role in increasing production (Carong & Rafiuddin, 2025).

Given the scarcity of research investigating the combined effects of bio-, mineral, and organic fertilizers on the growth and yield of potato and green bean, this study was conducted. The objective was to evaluate the impact of mycorrhizal inoculation, both in the presence and absence of NPK and sheep manure, on the growth parameters and yield components of these two crops. This research aims to contribute to ongoing efforts to enhance the productivity of these essential crops.

Method

A field experiment was conducted in the Al-Qubba region, Nineveh Governorate, during the 2018 growing season. The study was carried out on a Silty Clay soil;

Table 1. Illustrates the geographic coordinates of the experimental site and the taxonomic classification of the study soil

Location	Geographic Coordinates	Order	Suborder	Great Group
Al-Qubba	GPS °36.51′00″N, °43.25′00″E	Entisols	Fluvents	Typic Fluvents

Soil samples were collected from a depth of 0–30 cm from various locations across the experimental field. The collected samples were thoroughly mixed and homogenized, then passed through a 2-mm mesh sieve. From this mixture, a composite sample was obtained for the determination of key physical, chemical, and biological properties. Table (2) illustrates the physical and chemical characteristics of the study soil, which were analyzed following the methodologies described by Rikani et al. (2023).

Table 2. Some chemical and physical properties of Study Soil

Property	Unit	Value
pH	–	7.7
Electrical Conductivity (EC)	dS m^{-1}	0.75
Available Potassium (K)		160
Available Phosphorus (P)		9.2
Available Nitrogen (N)	mg kg^{-1}	15.8
Calcium Carbonate ($CaCO_3$)	g kg^{-1}	284
Organic Matter		11.2
Cation Exchange Capacity (CEC)	cmol(+) kg^{-1}	28.5
Field Capacity	g kg^{-1}	300
Bulk Density	Mg m^{-3}	1.34
Sand		95
Silt	g kg^{-1}	425
Clay		480
Soil Texture	–	Silty Clay

Experimental area was then divided into two separate fields, one for each crop. Each field was organized into three blocks, with each block consisting of six experimental units. Each unit contained three ridges, with a ridge length of 3 m and an inter-ridge spacing of 75 cm. The experiment included six treatments for each crop: a control treatment, mycorrhizal inoculation, NPK fertilization (18:18:18) following the recommended rates of 110 kg $dunam^{-1}$ for potato (Al-Nuaimi, 1999) and 100 kg $dunam^{-1}$ for green bean (Al-Abidi, 2010), a combination of Mycorrhiza + NPK, sheep manure application at a rate of 50 t ha^{-1}, and a combination of sheep manure + mycorrhizal inoculation

The mycorrhizal inoculum was harvested from a field previously cultivated with onion after the harvest stage. The infection of the plants with mycorrhizal fungi was verified via microscopic examination according to the method described by Phillips and Hayman (1970). Subsequently, fungal spores were isolated using the wet-sieving and decanting method as described by Gerdemann and Nicolson (1963). The spore density in the field soil was estimated at an average of 50 spores per 10 g of soil, which is consistent with the findings of Hammadi et al. (2017) regarding mycorrhizal spore isolation.

The two crops were planted on (/ /). Potato tubers (American 'Laberda' cultivar) were planted at a rate of one tuber per hill at a depth of 10–12 cm, with an intra-row spacing of 25 cm. Green bean seeds (cv. 'Izkyrda') were sown at a rate of 3 seeds per hill. Sufficient spacing was maintained between experimental units to prevent nutrient leaching and cross-contamination between treatments. Thirty days after planting, the potato and bean fields were inoculated with soil containing mycorrhizal inoculum, followed immediately by irrigation.

The experiment was concluded on (/ /). Plant samples were then ground and digested using concentrated sulfuric acid (H_2SO_4) and 30% hydrogen peroxide (H_2O_2). The concentrations of nitrogen (N) and phosphorus (P) in the acid extract were determined following the procedures of Tandon (1999). Finally, the total content of each element was calculated by multiplying the concentration by the dry weight (Jones, 2001).

Results and Discussion

Fertility Evaluation of the Study Soil

As indicated in Table (2), the available phosphorus (P) concentration in the study soil was 9.2 mg kg^{-1}, which falls below the critical threshold of 10–15 mg kg^{-1} proposed by Sandaña et al. (2018). This deficiency in available P may be attributed to the high calcium carbonate content (284 g kg^{-1}), elevated soil pH (7.7), and low organic matter content (11.2 g kg^{-1}) (Table 2). These conditions subject phosphorus to retention and precipitation reactions, thereby reducing its bioavailability. The dissociation of calcium carbonate into Ca^{2+} and CO_3^{2-} raises the soil solution pH, facilitating the reaction of dissolved calcium ions with

monocalcium phosphate to form dicalcium or tricalcium phosphate precipitates of lower solubility. Over time, these compounds transform into insoluble octacalcium phosphate. Furthermore, the high clay content in the study soil (480 g kg^{-1}) increases the specific surface area, enhancing the contact between dissolved phosphorus and clay minerals, which leads to greater P-fixation and reduced availability (Xiong et al., 2022).

Similarly, Table (2) shows a low concentration of available nitrogen (N) in the research soil (15.8 mg kg^{-1}), which is below the critical level of 20 mg kg^{-1} suggested by Al-Mosuli et al. (2019). The low N-availability is likely due to the low soil organic matter content (11.2 g kg^{-1}), nitrate leaching, and reduced microbial activity resulting from high temperatures, drought, lack of vegetative cover, and poor residue management (Hudhaifa, 2025). Moreover, the high calcium carbonate levels and alkaline pH promote nitrogen loss through ammonia volatilization (Li et al., 2022; Ahmad et al., 2023). Consequently, the study soil requires an effective fertilization program to enhance nutrient availability, ensure optimal plant growth, and maximize yield. Overall, these findings align with previous studies emphasizing that calcareous soils necessitate precise fertilization management (Khan et al., 2018; Ali et al., 2020).

Mycorrhizal Colonization Percentage of Potato and Green Bean Plants

As presented in Table (3), the average mycorrhizal colonization rate of the roots reached 30% for both potato and green bean crops one month after planting. The table also indicates that the colonization percentages after two months were 40% and 60% for the two crops, respectively. This variation in colonization rates is consistent with the findings reported by Al-Kartani et al. (2013).

Table 3. Mycorrhizal root colonization percentage in potato and green bean plants

Plant type	Mycorrhizal colonization percentage	
Potato	After a month	After two months
Beans	30	40
	30	60

The Effect of Mycorrhizal Inoculation, NPK Fertilizer, and Sheep Manure on Some Growth Parameters and Yield Components of Potato and Bean Crops

Results presented in Table (4) indicate that all fertilization treatments and their interactions led to significant improvements in growth, resulting in increased values of growth parameters for both potato and green bean crops. The highest growth values for both crops were recorded in the Mycorrhiza + NPK treatment. The interaction between mycorrhizal inoculation and NPK mineral fertilization led to a significant increase in plant height, shoot dry weight, and the number of branches per plant, with increase percentages of 46.60%, 71.89%, and 116.98%, respectively, for the potato crop. For green beans, the increase rates for the same three parameters were 58.06%, 12.96%, and 36.92%, respectively, compared to the control treatment, which recorded the lowest values for all indicators in both crops. Furthermore, Table (5) demonstrates that the applied fertilization treatments had a distinct impact on yield components, causing significant increases in these traits. The highest yield component values for both crops were observed in the Mycorrhiza + NPK treatment. Soil inoculation with mycorrhiza combined with NPK mineral fertilization resulted in a significant increase in the number and weight of potato tubers and total yield, with increase percentages of 114.50%, 117.46%, and 344.11%, respectively, compared to the control. In green beans, the increase rates for the number of pods per plant, number of seeds per pod, and yield per plant were 77.41%, 39.63%, and 100%, respectively, compared to the control.

The observed increases in growth parameters and yield components under mycorrhizal inoculation and NPK fertilization may be attributed to the vital role of mycorrhizal fungi in enhancing plant growth. These fungi coat the roots with hyphae that functions as an extended root system, thereby increasing root expansion and penetration. This enhances the volume and rate of water and nutrient absorption. Additionally, mycorrhizae possess the ability to regulate growth hormones, particularly auxins and cytokinins. Moreover, the increase in organic matter in mycorrhiza-inoculated soil improves the physical, chemical, and biological properties of the soil, which is positively reflected in growth and yield components.

The improvement in plant growth and yield components can also be attributed to the role of NPK compound fertilizer in providing essential elements (N, P, and K). These elements influence cell division and elongation; Nitrogen (N) is fundamental in the synthesis of chlorophyll, proteins, enzymes, and nucleic acids (Ye et al., 2022). Phosphorus (P) is essential for the formation of energy compounds (ATP) and the synthesis of

Tryptophan, a precursor for the auxin Indole-acetic acid (IAA), as well as its role in DNA and RNA structures (Khan et al., 2023). Potassium (K) acts as a cofactor in cell growth and division, plays a key role in regulating cellular osmotic pressure, and contributes to stomatal opening and closing (Xu et al., 2020).

The increase in growth and yield for both potato and bean crops may further be attributed to the enhancement of physical, fertile, and biological soil properties resulting from the addition of sheep manure. This organic amendment is rich in nutrients and crucial for boosting microbial activity and soil organic content (Du et al., 2020). These findings are in agreement with Al-Tawarah et al. (2025) and Oladele et al. (2024), who reported improvements in potato and bean growth following mycorrhizal inoculation and sheep manure fertilization.

Table 4. The effect of mycorrhizal inoculation, NPK fertilizer, and sheep manure on some growth parameters of potato and bean crops

Treatment	Potato			Green beans		
	Tuber Weight (gm tuber-1)	Tuber Number (Tuber plant-1)	Yield (g plant-1)	Number of pods (pod plant-1)	Number of seeds (Seed pod- 1)	Yield (g plant-1)
Control	f38.60	e6.30	f243.18	e8.90	d13.32	f200
Mycorrhiza	e69.10	d6.50	e656.45	d10.20	c14.33	e220
NPK	c77.20	b11.00	c849.20	b11.63	b15.21	c250
Mycorrhiza+ NPK	a82.80	a13.70	a1080	a15.79	a18.60	a400
Sheep manure	b80.01	c8.11	d753.33	c10.89	f9.14	d230
Sheep manure + Mycorrhiza	d76.40	b10.93	b883.12	10.87c	13.79e	210f

The Effect of Mycorrhizal Inoculation, NPK Fertilizer, and Sheep Manure on Nitrogen and Phosphorus Concentrations (%) in Potato Tubers and Bean Pods

Figures (1) and (2) illustrate that all applied fertilization treatments and their interactions led to an increase in nitrogen (N) and phosphorus (P) concentrations in both potato tubers and bean pods. As shown in Figure (1), the interaction treatments (Mycorrhiza + NPK and Mycorrhiza + Sheep Manure) outperformed all other treatments regarding N and P concentrations in potato tubers. The nitrogen concentration reached 2.10%, representing an increase of 35.48% compared to the control treatment, which recorded the lowest value (1.55%). Furthermore, the figure indicates that the highest phosphorus concentration in tubers was 0.39% under mycorrhizal inoculation, an increase of 77.27% over the control, which registered the lowest P concentration at 0.22%.

Figure (2) shows that the highest concentrations of N and P in bean pods were observed in the Mycorrhiza + NPK treatment, reaching 3.21% and 0.41%, respectively. These values represent increase percentages of 73.51% and 70.83%, respectively, compared to the control for each element.

Table 5. The Effect of mycorrhizal inoculation, NPK fertilizer, and sheep manure on some yield components of potato and bean crop

Treatment	Potato			Green beans		
	Plant Height (cm)	Dry weight. (gm)	Nu.branches Plant-1	Plant Height (cm)	Dry weight (gm)	Nu.branches Plant-1
Control	f58.40	f39.10	f6.30	c54.30	f12.40	g6.50
Mycorrhiza	d62.10	d53.11	e9.00	a75.40	d13.60	c8.21
NPK	b69.50	c58.63	b12.00	b64.50	b14.20	d7.75
Mycorrhiza+ NPK	a85.62	a67.21	a13.67	a85.83	a15.62	a8.90
Sheep manure	e60.31	e43.33	d10.31	c56.12	e12.81	f6.97
Sheep manure +Myc.	c70.12	b60.42	c10.92	b67.45	13.78c	7.53e

The low concentrations of N and P in potato tubers and bean pods in the unfertilized (control) soil may be attributed to the low availability of these elements in the soil (Table 2), as N and P are subject to various loss processes that reduce their bioavailability. Conversely, the increased concentration of these elements in tubers and pods upon mycorrhizal inoculation can be attributed to the role of these fungi in enhancing nutrient uptake. Mycorrhizae support root absorption through an extensive network of fungal hyphae. Additionally, sheep manure plays a vital role in supplying the plant with N and P, while simultaneously improving the physical and biological soil properties that facilitate nutrient absorption. These findings are consistent with those of Nielsen et al. (1998), Ingraffia et al. (2019), Yang et al. (2020), and Karavidas et al. (2022), who observed significant

increases in N and P concentrations in plants following mycorrhizal inoculation and fertilization with sheep manure.

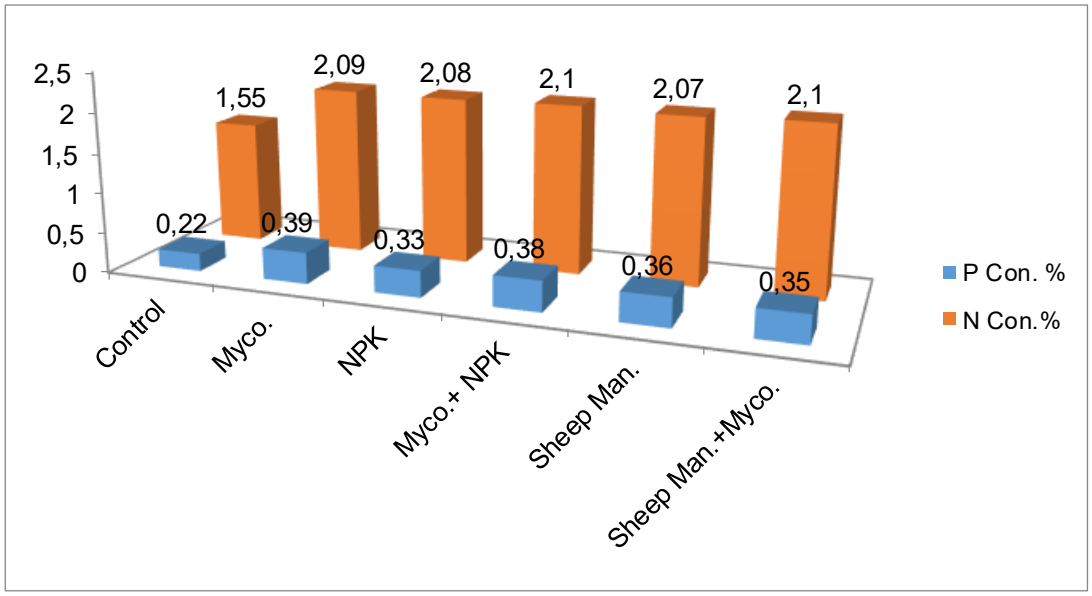

Figure 1. The effect of mycorrhizal inoculation, NPK fertilizer, and sheep manure on nitrogen and phosphorus concentrations (%) in potato tubers

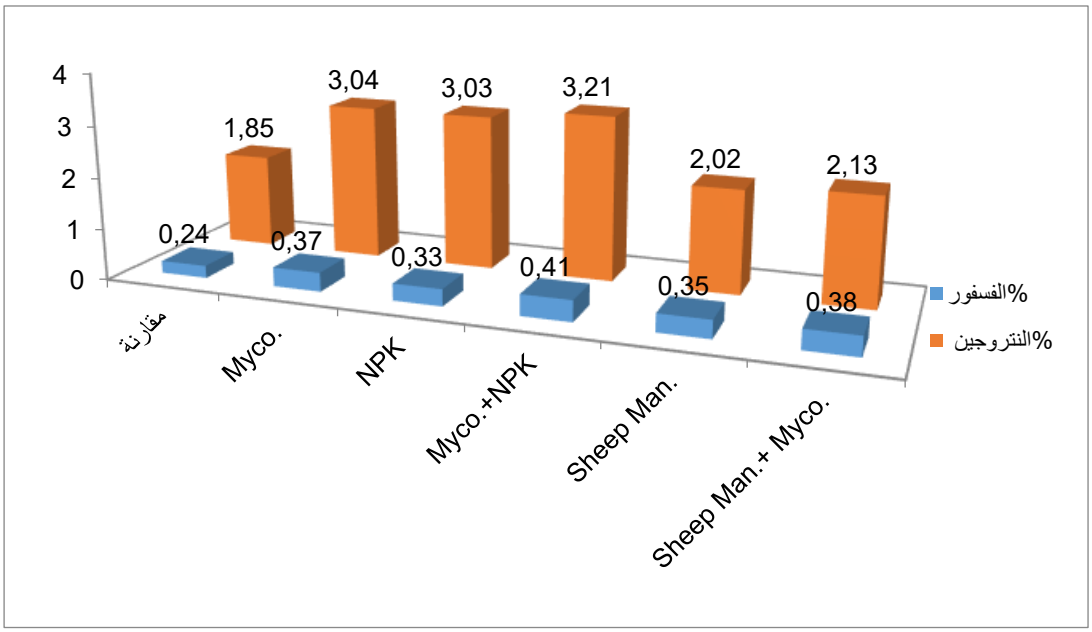

Figure 2. The effect of mycorrhizal inoculation, NPK fertilizer, and sheep manure on nitrogen and phosphorus concentrations (%) in green bean pods

Conclusions

Based on the aforementioned results, it can be concluded that the soil in this study suffers from a significant deficiency in available nitrogen (N) and phosphorus (P). Soil inoculation with mycorrhizal fungi, combined with the application of NPK mineral fertilizer and sheep manure (organic amendment), substantially improved vegetative growth and enhanced the total yield of both potato and green bean crops. Furthermore, these treatments led to a marked increase in N and P concentrations within the plant tissues. Among all evaluated treatments, the Mycorrhiza + NPK interaction consistently demonstrated superior performance, achieving the highest values across all growth parameters, yield components, and nutrient concentrations for both crops.

Scientific Ethics Declaration

* The authors declare that the scientific, ethical, and legal responsibility for this article published in EPSTEM Journal belongs to the authors.

Conflict of Interest

* The authors declare that they have no conflicts of interest

Funding

* No financial support was received for this study.

Acknowledgements or Notes

* This article was presented as an oral presentation at the International Conference on Basic Sciences, Engineering and Technology (www.icbaset.net) held in Istanbul/Türkiye on September 17-18, 2026.

References

Ahmad Al-Badrani, W. A., Hassan, F. A., & Harbawi, M. A. (2023). Effect of agricultural sulfur and poultry manure on ammonia volatilization from urea fertilizer in two different soil textures. *International Journal of Agricultural & Statistical Sciences, 19*, 1153–1159.

Al-Badrani, A. A., & Al-Khafagi, Q. D. E. (2025). Description of magnesium adsorption under the influence of different temperatures in calcareous soils with varied agricultural uses. *Mesopotamia Journal of Agriculture, 53*(3).

Alhrout, H. H., Aldalin, H. K. H., Haddad, M. A., Bani-Hani, N. M., & Al-Dalein, S. Y. (2016). The impact of organic and inorganic fertilizer on yield and yield components of common bean (*Phaseolus vulgaris*). *Advances in Environmental Biology, 10*(9), 8–14. Retrieved from http://www.aensi.org/aeb.html

Ali, S., Rizwan, M., Qayyum, M. F., Ok, Y. S., Ibrahim, M., Riaz, M., Arif, M. S., Hafeez, F., & Al-Wabel, M. I. (2020). Biochar soil amendment on alleviation of drought and salt stress in plants: A critical review. *Environmental Science and Pollution Research, 27*(6), 1–18.

Al-Tawarah, B., Alasasfa, M. A., & Mahadeen, A. Y. (2024). Efficacy of compost and vermicompost on growth, yield and nutrient content of common beans crop (*Phaseolus vulgaris* L.). *Journal of Ecological Engineering, 25*(2), 215–226.

Arf, M. V., Buzetti, S., Arf, O., Kappes, C., Ferreira, J. P., de Castilho Gitti, D., & Yamamoto, C. J. T. (2011). Nitrogen sources and application times on winter common bean under no-till system. *Pesquisa Agropecuária Tropical, 41*(3).

Bucagu, C., Ufitinema, B., Umutoniwabo, D., Niyitanga, F., & Karangwa, A. (2017). Effect of sheep manure and phosphorus fertiliser on productivity of snap bean (*Phaseolus vulgaris* L.) in Northern Rwanda. *Journal of Agriculture and Ecology Research International, 12*(1), 1–9.

Carong, N. F. R., & Rafiuddin, M. K. (2025). Arbuscular mycorrhiza fungi and mineral fertilizer effects on growth and production traits of the potato (*Solanum tuberosum* L.). *SABRAO Journal of Breeding & Genetics, 57*(2).

Carrara, J. E., Reddivari, L., Lehotay, S. J., Zinati, G., & Heller, W. P. (2023). Arbuscular mycorrhizal fungi increase the yield and nutritional quality of yellow and purple fleshed potatoes (*Solanum tuberosum*). *American Journal of Potato Research, 100*(3), 210–220.

Chen, L., Zhang, X., Li, Q., Yang, X., Huang, Y., Zhang, B., ... Li, X. (2024). Phosphatases: Decoding the role of mycorrhizal fungi in plant disease resistance. *International Journal of Molecular Sciences, 25*(17), 9491.

Du, Y., Cui, B., Wang, Z., Sun, J., & Niu, W. (2020). Effects of manure fertilizer on crop yield and soil properties in China: A meta-analysis. *Catena, 193*, 104617.

El-Mesairy, M., Ramadan, M., Ramadan, E., & Shalaby, O. A. (2022). Effect of sheep manure and sulfur on growth and yield of potato under saline conditions. *Future Journal of Horticulture, 4*(1), 36–46.

Elouear, Z., Bouhamed, F., Boujelben, N., & Bouzid, J. (2016). Application of sheep manure and potassium fertilizer to contaminated soil and its effect on zinc, cadmium and lead accumulation by alfalfa plants. *Sustainable Environment Research, 26*(3), 131–135.

Ezawa, T., & Saito, K. (2018). How do arbuscular mycorrhizal fungi handle phosphate? New insight into fine-tuning of phosphate metabolism. *New Phytologist, 220*(4), 1116–1121.

Fall, A. F., Nakabonge, G., Ssekandi, J., Founoune-Mboup, H., Apori, S. O., Ndiaye, A., ... Ngom, K. (2022). Roles of arbuscular mycorrhizal fungi on soil fertility: Contribution in the improvement of physical, chemical, and biological properties of the soil. *Frontiers in Fungal Biology, 3*, 723892.

Farhaoui, A., Taoussi, M., Laasli, S. E., Legrifi, I., El Mazouni, N., Meddich, A., ... Lahlali, R. (2025). Arbuscular mycorrhizal fungi and their role in plant disease control: A state-of-the-art. *The Microbe*, 100438.

Harbawi, M. A., Khaleel Al-Barhawee, N. I., & Al-Wazzan, F. A. (2025, April). Molecular and biochemical characterization of rhizobacterial isolates from agricultural soils and estimation of indole-3-acetic acid production. *IOP Conference Series: Earth and Environmental Science, 1487*(1), 012210.

Hassan, F. A., Aziz, R. S., & Harbawi, M. A. (2026). Effect of nitrogen fertilizer type and application method on ammonia volatilization from a calcareous soil in Nineveh Governorate, Iraq. *International Journal of Design & Nature and Ecodynamics, 21*(4), 1195–1201.

Hochmuth, G., & Hanlon, E. (2014). *A summary of N, P, and K research with potato in Florida* (CV233). Gainesville, FL: University of Florida Institute of Food and Agricultural Sciences.

Hou, J., Xing, C., Zhang, J., Wang, Z., Liu, M., Duan, Y., & Zhao, H. (2024). Increase in potato yield by the combined application of biochar and organic fertilizer: Key role of rhizosphere microbial diversity. *Frontiers in Plant Science, 15*, 1389864.

Hudhaifa, A. H. (2025). Effect of biochar of temperature and time differences on some chemical properties and available nutrients in Mosul city soil. *NTU Journal of Agriculture and Veterinary Science, 5*(1).

Ibrahim, K., Wang, Q., Wang, L., Zhang, W., Peng, C., & Zhang, S. (2021). Determining the optimum level of soil Olsen phosphorus and phosphorus fertilizer application for high phosphorus-use efficiency in *Zea mays* L. in black soil. *Sustainability, 13*(11), 5983.

Ierna, A., & Distefano, M. (2024). Crop nutrition and soil fertility management in organic potato production systems. *Horticulturae, 10*(8), 886.

Ingraffia, R., Amato, G., Frenda, A. S., & Giambalvo, D. (2019). Impacts of arbuscular mycorrhizal fungi on nutrient uptake, N2 fixation, N transfer, and growth in a wheat/faba bean intercropping system. *PLOS ONE, 14*(3), e0213672.

Kakouridis, A., Hagen, J. A., Kan, M. P., Mambelli, S., Feldman, L. J., Herman, D. J., ... Firestone, M. K. (2022). Routes to roots: Direct evidence of water transport by arbuscular mycorrhizal fungi to host plants. *New Phytologist, 236*(1), 210–221.

Karavidas, I., Ntatsi, G., Marka, S., Ntanasi, T., Consentino, B. B., Sabatino, L., ... Savvas, D. (2022). Fresh pod yield, physical and nutritional quality attributes of common bean as influenced by conventional or organic farming practices. *Plants, 12*(1), 32.

Khan, A., Ullah, S., Khan, M. Z., & Ahmad, W. (2018). Role of iron in plant growth and metabolism. *International Journal of Agricultural and Biological Engineering, 21*(3), 56–62.

Khan, F., Siddique, A. B., Shabala, S., Zhou, M., & Zhao, C. (2023). Phosphorus plays key roles in regulating plants' physiological responses to abiotic stresses. *Plants, 12*(15), 2861.

Li, N., Chen, W., Wang, B., Zhang, C., Wang, Y., Li, R., ... He, J. (2024). Arbuscular mycorrhizal fungi improve the disease resistance of *Lycium barbarum* to root rot by activating phenylpropane metabolism. *Frontiers in Plant Science, 15*, 1459651.

Li, T., Wang, Z., Wang, C., Huang, J., Feng, Y., Shen, W., ... Yang, L. (2022). Ammonia volatilization mitigation in crop farming: A review of fertilizer amendment technologies and mechanisms. *Chemosphere, 303*, 134944.

Nielsen, K. L., Bouma, T. J., Lynch, J. P., & Eissenstat, D. M. (1998). Effects of phosphorus availability and vesicular–arbuscular mycorrhizas on the carbon budget of common bean (*Phaseolus vulgaris*). *The New Phytologist, 139*(4), 647–656.

Oladele, S., Gould, I., & Varga, S. (2025). Is arbuscular mycorrhizal fungal addition beneficial to potato systems? A meta-analysis. *Mycorrhiza, 35*(1), 5.

Rayne, N., & Aula, L. (2020). Livestock manure and the impacts on soil health: A review. *Soil Systems, 4*(4), 64.

Rillig, M. C., & Mummey, D. L. (2006). Mycorrhizas and soil structure. *New Phytologist, 171*(1), 41–53.

Rodiño, A. P., Aguín, O., Tejada-Hinojoza, J. L., & De Ron, A. M. (2025). Arbuscular mycorrhizal fungi in common bean roots: Agricultural impact and environmental influence. *Agriculture, 15*(13), 1452.

Sandaña, P., Orena, S., Rojas, J. S., Kalazich, J., & Uribe, M. (2018). Critical value of soil Olsen-P for potato production systems in volcanic soils of Chile. *Journal of Soil Science and Plant Nutrition, 18*(4), 965–976.

Sharifi, M. A., Nowrozi, A., Rostazada, M. D., & Ali, J. (2024). Effect of different doses of animal manure on growth and yield of common bean. *Engineering and Technology Quarterly Reviews, 7*(2). Retrieved from https://www.asianinstituteofresearch.org

Smith, S. E., Jakobsen, I., Grønlund, M., & Smith, F. A. (2011). Roles of arbuscular mycorrhizas in plant phosphorus nutrition: Interactions between pathways of phosphorus uptake in arbuscular mycorrhizal roots have important implications for understanding and manipulating plant phosphorus acquisition. *Plant Physiology, 156*(3), 1050–1057.

Sweeney, C. J., Bottoms, M., Ellis, S., Ernst, G., Kimmel, S., Loutseti, S., ... Marx, M. T. (2022). Arbuscular mycorrhizal fungi and the need for a meaningful regulatory plant protection product testing strategy. *Environmental Toxicology and Chemistry, 41*(8), 1808–1823.

Tadang, M., Lipi, R., Kasinam, D., Dirchi, G., & Mercy, C. (2025). Effect of organic and inorganic fertilizers on growth and yield of French bean (*Phaseolus vulgaris* L.). *Ecology, Environment & Conservation, 31*.

Wang, G., Jin, Z., George, T. S., Feng, G., & Zhang, L. (2023). Arbuscular mycorrhizal fungi enhance plant phosphorus uptake through stimulating hyphosphere soil microbiome functional profiles for phosphorus turnover. *New Phytologist, 238*(6), 2578–2593.

Wang, Y., Zhang, R., Li, S., Guo, X., Li, Q., Hui, X., ... Wang, H. (2024). An evaluation of potato fertilization and the potential of farmers to reduce the amount of fertilizer used based on yield and nutrient requirements. *Agronomy, 14*(3), 612.

Weng, W., Yan, J., Zhou, M., Yao, X., Gao, A., Ma, C., ... Ruan, J. (2022). Roles of arbuscular mycorrhizal fungi as a biocontrol agent in the control of plant diseases. *Microorganisms, 10*(7), 1266.

Wu, S., Fu, W., Rillig, M. C., Chen, B., Zhu, Y. G., & Huang, L. (2024). Soil organic matter dynamics mediated by arbuscular mycorrhizal fungi—An updated conceptual framework. *New Phytologist, 242*(4), 1417–1425.

Xiong, J., Liu, Z., Yan, Y., Xu, J., Liu, D., Tan, W., & Feng, X. (2022). Role of clay minerals in controlling phosphorus availability in a subtropical Alfisol. *Geoderma, 409*, 115592.

Xu, X., Du, X., Wang, F., Sha, J., Chen, Q., Tian, G., ... Jiang, Y. (2020). Effects of potassium levels on plant growth, accumulation and distribution of carbon, and nitrate metabolism in apple dwarf rootstock seedlings. *Frontiers in Plant Science, 11*, 904.

Yang, Q., Ravnskov, S., & Neumann Andersen, M. (2020). Nutrient uptake and growth of potato: Arbuscular mycorrhiza symbiosis interacts with quality and quantity of amended biochars. *Journal of Plant Nutrition and Soil Science, 183*(2), 220–232.

Ye, J. Y., Tian, W. H., & Jin, C. W. (2022). Nitrogen in plants: From nutrition to the modulation of abiotic stress adaptation. *Stress Biology, 2*(1), 4.

Yu, Z., Yao, X., Yang, M., Hu, S., An, X., & Li, C. (2024). Co-application of sheep manure and commercial organic fertilizer enhances plant productivity and soil quality in alpine mining areas. *Frontiers in Microbiology, 15*, 1488121.

Author(s) Information

Mohammed Ayad Harbawi
University of Mosul
Mosul, Iraq
ORCID iD: https://orcid.org/0009-0008-9885-5176
Contact e-mail: *Harbawee79@uomosul.edu.iq*

Fatih Abed Hasan
University of Mosul
Mosul, Iraq
ORCID iD: https://orcid.org/0009-0009-6822-184X

Hesham Saadaldeen Younes
University of Mosul
Mosul, Iraq
ORCID iD: https://orcid.org/0009-0002-9031-198X

Aziz, Rana Saadallah
University of Mosul
Mosul, Iraq
ORCID iD: https://orcid.org/0009-0007-6918-2817

*Corresponding author(s) contact email.

To cite this article:

Harbawi, M. A., Hasan, F. A., Younes, H. S., & Saadallah, A. Z. (2026). Response of potato *(*Solanum tuberosum L.) and green bean *(*Phaseolus vulgaris L.) crops to mycorrhizal, NPK and sheep manure fertilization in soil. *The Eurasia Proceedings of Science, Technology, Engineering and Mathematics (EPSTEM), 42*, 67–75.

The Eurasia Proceedings of Science, Technology, Engineering and Mathematics (EPSTEM)
ISSN: 2602-3199

The Eurasia Proceedings of Science, Technology, Engineering and Mathematics (EPSTEM), 2026

Volume 42, Pages 76-84

ICBASET 2026: International Conference on Basic Sciences, Engineering and Technology

Assessment of *Thymus numidicus* and *Lavandula stoechas* Essential Oils Effects on Deltamethrin-Induced Toxicity in Female Rabbits

Farida Fernane
Mouloud Mammer's University

Nacira Daoudi-Zerrouki
Mouloud Mammer's University

Ouardia Chaouchii
Mouloud Mammer's University

Hakima Aitissad
Mouloud Mammer's University

Abstract: *Thymus numidicus* and *Lavandula stoechas* are aromatic and medicinal plants belonging to the Lamiaceae family. They are widespread in Algeria and used in traditional medicine and in the culinary arts. Deltamethrin is a chemical compound belonging to the pyrethroid family. It is mainly used as an insecticide and repellent for insects or snakes due to its neurotoxic properties. This study aims to evaluate the protective effects of *Thymus numidicus* (TNEO) and *Lavandula stoechas* (LSEO) essential oils against deltamethrin-induced toxicity in female rabbits. The chemical composition and biological activities of these two essential oils were assessed beforehand. The GC/MS analysis revealed that both essential oils are rich in monoterpene hydrocarbons and oxygenated monoterpenes. In TNEO, the major compounds identified were thymol and carvacrol, whereas in LSEO, fenchone and camphor. The antibacterial activity results showed that TNEO exhibited strong inhibitory effects against Gram-positive bacteria, while its activity was lower against Gram-negative strains. On the other hand, LSEO demonstrated moderate antibacterial activity against both Gram+ and Gram- bacteria. The administration of deltamethrin at 1.28mg/kg/day for 14 days induced significant hematological, biochemical, and histopathological damage in both the liver and kidneys of female rabbits. The combination of *Thymus numidicus* and *Lavandula stoechas* essential oils exhibited a remarkable protective effect against the biochemical and histopathological alterations caused by deltamethrin exposure.

Keywords: *Thymus numidicus*, *Lavandula stoechas*, Essential oils, Deltamethrin, Toxicity

Introduction

Over recent decades, essential oils (EOs) have attracted growing interest as promising agents for protecting against oxidative damage (Gupta et al. 2023). Essential oils have long been recognized for their medicinal value; they are a rich source of bioactive compounds with a wide range of therapeutic, industrial and environmental applications. They are increasingly regarded as valuable alternatives for mitigating the harmful effects of toxic agents, as well as for the prevention and treatment of various diseases (Borromeo et al., 2024; Küçükler et al., 2021; Domingues et al., 2021). Among these, the essential oils of *Thymus numidicus* (TN) and *Lavandula stoechas* are important in both traditional medicine and culinary practices (Messara et al., 2018; Boukhatem et al., 2021; Yildizhan et al., 2023). These two species of the Lamiaceae family are distinguished by their remarkable pharmaceutical properties, and their antioxidant, anti-inflammatory, and antibacterial activities (Messara et al., 2018; Kaki et al., 2021; Rasheed et al., 2023).

- This is an Open Access article distributed under the terms of the Creative Commons Attribution-Noncommercial 4.0 Unported License, permitting all non-commercial use, distribution, and reproduction in any medium, provided the original work is properly cited.

- Selection and peer-review under responsibility of the Organizing Committee of the Conference

© 2026 Published by ISRES Publishing: www.isres.org

Pesticides are chemical substances used to control pests such as insects, pathogens, and weeds (Alokail et al., 2024; Yadav & Devi, 2017). Their widespread use poses a major threat to both public health and the environment due to their accumulated toxic effects (Makhlouf et al., 2025). According to WHO data prolonged exposure to pesticides is associated with adverse health effects, including endocrine disruption, neurological disorders, and an increased risk of cancer (Alokail et al., 2024; Bellala et al., 2022; Chargui et al., 2012). Depending on their chemical properties, pesticides may accumulate in the food chain and in various biological fluids such as blood, urine, and cerebrospinal fluid (Benedetti et al., 2018; Carvalho et al. 2017; and Mohammed et al., 2022). Among the organs most affected by pesticide toxicity, the liver and kidneys play a central role. The liver is the organ responsible for metabolism and detoxification, ensuring the biotransformation of endogenous and exogenous compounds (Mohammed et al., 2022). The kidneys, for their part, are essential for the elimination of metabolic waste and the maintenance of homeostasis (Sharma et al., 2014; Saoudi et al., 2017; Küçükler et al., 2021).

Deltamethrin is a synthetic pyrethroid insecticide widely used for controlling pests in agriculture and public health programs (Basak et al., 2021; Bellala et al., 2022; Ilyas et al., 2023; Kangyuan Qu et al., 2024; Sharma et al., 2014). Its popularity is due to its effectiveness, low mammalian toxicity, and rapid degradation in the environment (WHO, 2011). However, the use of deltamethrin has raised concerns over its potential toxicity towards non-target organisms, including humans, pets, and wildlife.

Therefore, understanding the toxicity of deltamethrin is critical for its safe use and protecting the environment and human health. The WHO has set a maximum residue limit (MRL) of 5 mg/kg, but exposure to this concentration has been linked to histological alterations in the gastric mucosa (Halima et al., 2023). As a lipophilic molecule, it accumulates in fat-rich tissues such as eggs, muscles, and adipose tissues, as well as in aquatic ecosystems and agricultural soils, sometimes exceeding regulatory limits (Yadav et al., 2023)

The main objective of this study is to evaluate the therapeutic potential of *Thymus numidicus* and *Lavandula stoechas* essential oils by evaluating their protective effect against deltamethrin-induced toxicity in female rabbits.

Method

Extraction and GC-MS Analysis of Essential Oils

Samples of the aerial parts of the *Thymus numidicus* (TN) and *Lavandula stoechas* (LS) harvested were dried in the open air and protected from light for two weeks. After drying, the essential oils were extracted by hydrodistillation using a Clevenger-type apparatus. The chemical composition of the essential oils (TNEO and LSEO) was carried out by gas chromatography–mass spectrometry (GC-MS) using a Shimadzu gas chromatograph coupled with a selective mass detector. The system was equipped with an auto-sampler injector and an HP-5 fused silica capillary column (30 m × 0.25 mm, 0.25 µm film thickness). Helium was used as the carrier gas at a flow rate of 0.5 mL/min. The ionization voltage of the mass spectrometer was set to 70 eV.

In Vivo Toxicity Study

The study involved forty healthy nulliparous female rabbits. The rabbits were 4 months old and had an average body weight of 2600 ± 200 g. The rabbits were ear-tagged and divided into eight groups of six females each. The animals were kept in individual cages and all the necessary procedures were carried out in accordance with the standard laboratory conditions. These conditions included a 12-hour light/dark cycle, a temperature of 25 ± 3°C and adequate ventilation. The rabbits were given a standard commercial pellet diet and had free access to drinking water ad libitum. The study was conducted over 28 days, divided into two distinct periods: the acclimatization and the treatment period (OCDE, 2008).

The rabbits underwent a 14-day acclimatization period to adapt to the experimental conditions. After this period, the animals were randomly divided into different groups and received repeated doses of deltamethrin and/or essential oils by oral gavage once daily for 14 consecutive days. The control group received corn oil under the same conditions (Table 1). This was done in accordance with European Directive 2010/63/EU on the protection of animals used for scientific purposes.

Several studies (Rohan Yadav et al., 2023; Mohammed et al., 2022; Yousef et al., 2006) have used a deltamethrin dose of 1.28 mg/kg, corresponding to 1/100 of the median lethal dose (128 mg/kg).Based on these data, we selected the same dose (1.28 mg/kg) for our experiments. The essential oil dose was set at 0.5 mg/kg, based on previous work (Bokreta et al., 2021).

Table 1. The allocation of experimental groups

Groups	Treatment
Group S	Group received corn oil
Group P	Deltamethrin (DM) treated group received 1.28 mg/kg/d BW
Group TNEO	*Thymus numidicus* essential oil (TNEO) treated group received 0.5mg/kg/d BW
Group P+TNEO	(Deltamethrin + TNEO) treated group received 1.28 mg/kg/d BW of Deltamethrin followed by 0.5 mg/kg/d BW after 1 h of DM administration
Group LSEO	*Lavandula stoechas* essential oil (LSEO) treated group received 0.5mg/kg/d BW
Group P+LSEO	Deltamethrin+ LSEO treated group received 1.28 mg/kg/d BW of Deltamethrin followed by 0.5 mg/kg/d BW of LSEO after 1 h of DM administration
Group X	Group received 0.5mg/kg/d BW of LSEO and 0.5mg/kg/d BW of TNEO
Group P+X	Group received 1.28 mg/kg/d BW of Deltamethrin followed by 0.5mg/kg/d BW of LSEO and 0.5mg/kg/d BW of TNEO after 1 hour of DM administration

d BW : per day and body weight

After dissection, the hides were removed immediately and organs (Kidneys and liver) were removed, weighed and measured to prevent any tissue degradation, then preserved in dry tubes filled with 10% formaldehyde (formalin) solution until uses. The coverslips were mounted onto the slides using a mounting machine after the slides had been stained and dried. The histological slides were observed and photographed using an optical microscope ″micros Austria″ which was equipped with a digital camera. Image acquisition was performed using ImageView (version x64, 4.10.17614.20200822) software, which allowed for precise and detailed capture of histological structures. Data were statistically analyzed to establish the dose–response relationship and to assess the significance of the observed alterations.

Results and Discussion

Chemical Composition of Essential Oils

Essential oils of *Thymus numidicus* (TNEO) and *Lavandula stoechas* (LSEO) are both rich in monoterpenes and oxygenated monoterpenes (Tables 2 and 3, respectively). For TNEO, 16 major compounds are identified with thymol is the most predominant compound (32.71%), followed by carvacrol (10.3%), γ-terpinene (9.0%), and p-cymene (8.0%). For LSEO, 13 major compounds are mentioned (Table 3). The results indicate a predominance of camphor (25.32%), followed by fenchone (19.16%) and eucalyptol (5.99%).

Table 2. Chemical composition of *Thymus numidicus* EO (TNEO)

Retention time (min)	Compounds	%
9.1	α-thujene	1.0
9.4	α-Pinene	4.3
10.8	1-Octen-3-ol	1.1
11.1	β-Myrcene	2.5
11.9	*α-Terpinene*	2.9
12.1	p-Cymene	8.0
12.2	Limonene	1.8
13.1	γ-Terpinene	9.0
13.3	Cis-Sabinene hydrate	1.0
14.1	Linalool	1.7
17.4	Thymol methyl ether	1.2
18.9	**Thymol**	**32.7**
19.1	**Carvacrol**	**10.3**
21.6	Caryophyllene	4.0
23.1	β-Bisabolene	4.4
23.5	δ-Cadinene	1.1

Table 3. Chemical composition of *Lavandula stoechas* EO (LSEO)

Retention time (min)	Compounds	%
9.4	α-Pinene	1.4
9.9	Camphene	2.9
12.2	D-Limonene	1.0
12.3	Eucalyptol	6.0
14.0	**Fenchone**	**19.2**
15.6	**Camphor**	**25.3**
15.9	Borneol	1.7
16.3	p-Cymen-7-ol	3.9
16.9	Eucarvone	1.8
18.7	Borneyl acetate	3.4
19.5	Myrtenyl acetate	2.0
24.9	Viridiflorol	1.8
25.1	Cubebol	1.2

In Vivo Toxicity Study

Animal's Behavior

During the acclimation period, the female rabbits remained calm, with no notable behavioral changes observed across all groups, indicating good adaptation to the experimental conditions. However, during the treatment period, rabbits in the DLM-treated groups showed significant behavioral disturbances starting from the first hour of administration. These included tremors, agitation, unusual hyperactivity, tachycardia, and stereotyped behaviors such as excessive grooming and repetitive circular movements upon being returned to their cages. These alterations were particularly noticeable during the first two days of treatment and appeared to subside approximately one hour after gavage. These manifestations may be attributed to esophageal irritation caused by pesticide. In contrast, no behavioral changes were observed in the control group (S) or in the group treated with essential oils (TNEO and LSEO).

Histomorphological on Kidneys

The control group showed normal morphological features, with no signs of hemorrhage or pyknosis (Figure 1A). In the renal cortex, the Malpighian corpuscles appeared well-organized, with rounded glomeruli and a clearly defined Bowman's space, capillary and mesangial cells are clearly visible. No structural alterations were observed in the glomeruli, proximal convoluted tubules, or distal convoluted tubules, indicating that the renal structure remained intact and unaffected under the experimental conditions.

The group of female rabbits treated with Deltamethrin (DLM) at a dose of 1.28 mg/kg/day showed significant destruction of renal structures, observable at both low and high magnifications (Figure 1B). In the group of female rabbits treated separately with TNEO (Figure 1C) and LSEO (Figure 1E), the glomeruli and renal tubules appear overall well-preserved. However, vascular dilation and possible red blood cell accumulation suggest a slight vascular disturbance, which may indicate mild toxicity. Notably, the toxic effects appear to be more pronounced in the LSEO-treated group, as evidenced by more visible vascular alterations and congestion (Figure 1E). Figure 1F showed that the DLM+LSEO-treated group had no major alterations in renal structure, no cellular disorganization or destruction, and numerous well-rounded glomeruli surrounded by renal tubules. However, the group treated with the mixture of the two essential oils (TNEO + LSEO) showed mild vascular congestion and preserved renal architecture, with intact glomeruli and no signs of inflammatory infiltration (Figure 1G). This suggests that the simultaneous combination of these two essential oils induces a protective effect against renal toxicity induced by DLM (Figure 1H).

Histomorphological on Liver

Histological observation of the liver sections shows that the control group (Figures 2A) exhibits well-preserved hepatic architecture, characterized by hepatocytes arranged in radial cords around the central vein. The hepatic lobules are well-defined, composed of hepatocytes with a regular shape, organized in plates and radially arranged around a central vein, known as the centrilobular vein. The hepatic sinusoids are well-defined, with no

signs of congestion, inflammation, or necrosis. The absence of structural abnormalities suggests a normal physiological state of the hepatic tissue.

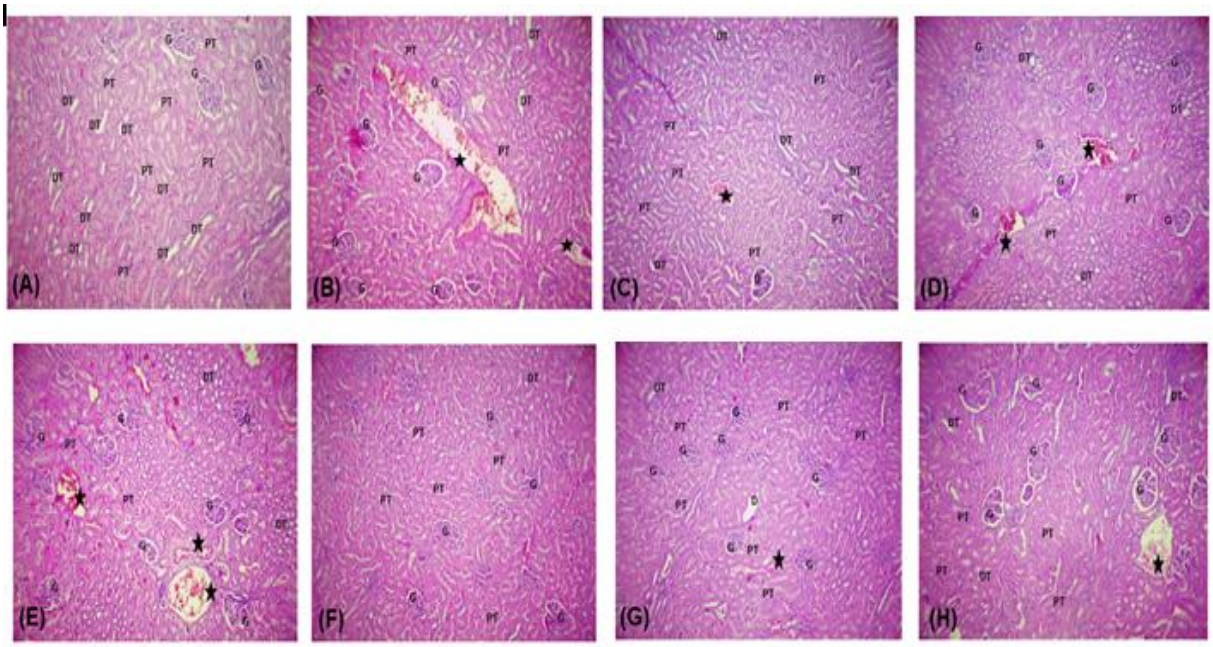

Figure 1. Histological sections of kidney tissue from female rabbits (H&E staining, ×100 magnification). Comparison between the control group (A), the DLM-treated group (B), the TNEO treated group (C), the DLM+TNEO-treated group (D), the LSEO treated group (E), the DLM+LSEO – treated group (F), TNEO+LSEO treated group (G) and DLM + TNEO + LSEO treated group (H)
(G: Glomeruli; DT: Distal Tube; PT: Proximal Tube; and ★ hemorrhages

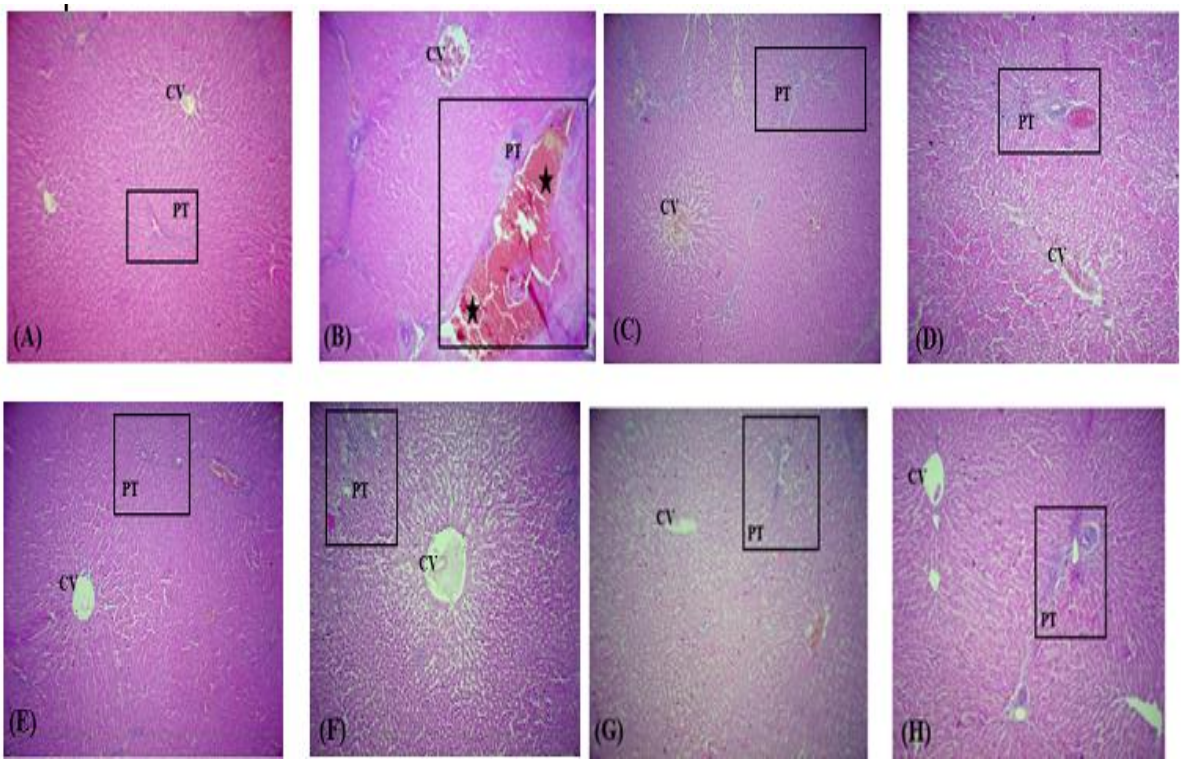

Figure 2.Histological sections of liver tissue from female rabbits (H&E staining, ×100 magnification). Comparison between the control group (A), the DLM-treated group (B), the TNEO treated group (C), the DLM+TNEO-treated group (D), the LSEO treated group (E), the DLM+LSEO – treated group (F), TNEO+LSEO treated group (G) and (DLM + TNEO + LSEO) treated group (H)
(CV: Central Vein; PT: Portal Triad; and ★ hemorrhages)

The group of female rabbits treated with Deltamethrin (DLM) at a dose of 1.28 mg/kg/day exhibits hepatic lesions characterized by significant histopathological alterations (Figure 2B). Necrosis, hemorrhages, and dilation of the sinusoids and portal spaces are observed. Additionally, inflammation with cellular infiltration is evident, indicating severe hepatic damage (Figure2B). The liver of the TNEO-treated group exhibits visible sinusoidal dilation and vascular congestion (Figure 2C). Small scattered hemorrhagic areas are also observed, along with mild inflammatory infiltrates. However, the overall hepatic architecture remains preserved, suggesting moderate toxicity (Figure 2C). The group treated with DLM+TNEO (Figure 2D), exhibits significant dilation of the portal spaces and enlarged sinusoids, which may indicate blood congestion or hepatic distress. A slight perivascular edema is also observed, suggesting a moderate inflammatory reaction.

Although hepatocytes are generally preserved, signs of cellular stress are evident (Figure 2D).The liver of the LSEO- treated group exhibits modifications in the portal spaces, characterized by dilation and a clearer appearance around the vessels, suggesting the presence of edema (Figure 2E). A mild inflammatory infiltrate is visible in the portal space, marked by dark cells around the vessel, indicating a moderate inflammatory response. Hepatocytes are generally preserved, but a slight dilation of the sinusoids is observed, potentially indicating moderate congestion, which may suggest hepatic distress or moderate toxicity (Figure 2E). The liver of DLM+LSEO treated group exhibits hypertrophy of the portal space accompanied by perivascular inflammation (Figure 2F). An inflammatory infiltrate, in the form of small dark cells surrounding the vessel, is observed, indicating an inflammatory reaction (Figure 2F). Vascular congestion is also noted, with an accumulation of red blood cells in the vessels, suggesting an alteration in hepatic blood circulation. Furthermore, the clear zone around the vessel may reflect an inflammatory response and could be an early sign of hepatic fibrosis (Figure 2F). The liver of the group treated with both essential oils (TNE + LSEO) exhibits generally preserved hepatocytes, although the sinusoids appear slightly more visible (Figure 2G). No inflammatory infiltrate is observed, but moderate signs of hepatic distress are present (Figure 2G). The group of female rabbits treated with DLM and both essential oil (TNEO and LSEO), exhibits dilation of the portal spaces, with a clear halo around the vessels, suggesting the presence of marked perivascular edema (Figure 2H). An inflammatory infiltrate is also observed, along with slight modifications in the sinusoids. Additionally, possible hepatocyte alterations are noted, indicating signs of intermediate hepatic distress (Figure 2H).

Conclusion

The present study clearly demonstrates that administration of DLM at 1.28 mg/kg/day for 14 days, acting on the nervous system induced significant histopathological damage in both the liver and kidneys. Our findings are consistent with those reported by Saoudi et al., (2017), who observed marked renal histopathological alterations in rats treated with an intraperitoneally injection of deltamethrin at a dose of 7.2 mg/kg body weight, including tubular epithelial cell necrosis and vacuolation.

In the kidneys, DLM caused glomerular alterations suggestive of atrophy and inflammation, tubular dilatation, and cellular damage (pyknosis), consistent with previous reports of DLM-induced nephrotoxicity. Saoudi et al. (2017) observed tubular necrosis and vacuolation in rats, while Jiang et al. (2024) linked DLM to renal fibrosis via the TGF- β/Smad2/3 pathway and noted inflammatory infiltration. The observed glomerular proliferation and capillary compression in our study might reflect an acute inflammatory response or early glomerulonephritis (Ahmadvand et al., 2016; Yildizhan et al., 2023).

The liver, as the primary site of detoxification, is particularly vulnerable to damage from xenobiotics like DLM. Similarly, the liver exhibited severe lesions following DLM exposure, including hepatocyte necrosis, hemorrhage, sinusoidal dilation, and inflammation. These findings align with the known hepatotoxicity of DLM, attributed mainly to its metabolism in the liver leading to the generation of reactive oxygen species (ROS) and subsequent oxidative damage (Abdel-Daim et al., 2015; Küçükler et al., 2021).

The administration of essential oil alone induced mild histological changes, primarily vascular congestion in both organs and slight inflammation in the liver. This suggests that the dose used (0.5 mg/kg/day) might have slight pro-inflammatory or vasoactive effects, or it could reflect a physiological response. However, the overall architecture remained preserved, indicating low intrinsic toxicity at this dose under the current experimental conditions. The hemorrhages observed in the liver of the TN-treated group may be due to thymol metabolism (Liu et al., 2022). Although the use of EO rich in monoterpenes is generally considered safe, an overdose can be harmful to humans (Wojtunik-Kulesza, 2022).

Scientific Ethics Declaration

* The authors declare that the scientific ethical and legal responsibility of this article published in EPSTEM Journal belongs to the authors.

* The animal experiments in this study were conducted in accordance with European Directive 2010/63/EU on the protection of animals used for scientific purposes. All experimental procedures were approved by the Ethics Committee of Mouloud Mammeri University in Tizi-Ouzou, (Approval Number: UMMTO/2022/Ani024).

Conflict of Interest

* The authors declare that they have no conflicts of interest

Funding

* This research did not receive any specific grant from funding agencies in the public, commercial, or not-for-profit sectors.

Acknowledgements or Notes

* This article was presented as an oral presentation at the International Conference on Basic Sciences, Engineering and Technology (www.icbaset.net) held in Istanbul/Türkiye on September 17-18, 2026.

References

Abdel-Daim, M. M., & El-Ghoneimy, A. (2015). Synergistic protective effects of ceftriaxone and ascorbic acid against subacute deltamethrin-induced nephrotoxicity in rats. *Renal Failure, 37*(2), 297–304.

Ahmadvand, H., Ghabaee, D. N. Z., Malekshah, A. K., & Navazesh, A. (2016). Virgin olive oil ameliorates deltamethrin-induced nephrotoxicity in mice: A biochemical and immunohistochemical assessment. *Toxicology Reports, 3*, 584–590.

Alokail, M. S., Elhalwagy, M. E. A., Abd-Alrahman, S. H., Alnaami, A. M., Hussain, S. D., Amer, O. E., Sabico, S., & Al-Daghri, N. M. (2024). Pesticide residues and associated health effects in marketed fruits in Saudi Arabia. *Arabian Journal of Chemistry, 17*(11), 105993.

Basak, M., Choudhury, R. A., Goswami, P., Dey, B. K., & Laskar, M. A. (2021). A review on non-target toxicity of deltamethrin and piperonyl butoxide: Synergist. *Journal of Pharmaceutical Research International, 33*(51B), 85–89.

Bellala, H., Mahmoud, F. M., Ziane, A. H., & Batam, A. (2022). Chronic toxicity of six pesticides mixture traces on biochemical, hematological, and histological parameters of liver and kidney in female Wistar rats. *Nutrition & Santé, 11*(02), 119-129.

Benedetti, D., Lopes Alderete, B., de Souza, C. T., Ferraz Dias, J., Niekraszewicz, L., Cappetta, M., Martínez-López, W., & Da Silva, J. (2018). DNA damage and epigenetic alteration in soybean farmers exposed to complex mixture of pesticides. *Mutagenesis, 33*(1), 87–95.

Bokreta, S., Hassina, K.-O., Amine, F. M., Makhlouf, C., & Nacira, D.-Z. (2021). Protective effects of *Thymus vulgaris* essential oil against Voliam Targo® induced kidney and brain toxicity in male rabbits. *Egyptian Academic Journal of Biological Sciences, D. Histology & Histochemistry, 13*(1), 79–95.

Borromeo, I., De Luca, A., Domenici, F., Giordani, C., Rossi, L., & Forni, C. (2024). Antioxidant properties of *Lippia alba* essential oil: A potential treatment for oxidative stress-related conditions in plants and cancer cells. *International Journal of Molecular Sciences, 25*(15), Article 15.

Boukhatem, M. N., Chader, H., Houche, A., Oudjida, F., Benkebaili, F., & Hakim, Y. (2021). Topical emulsion containing *Lavandula stoechas* essential oil as a therapeutic agent for cutaneous wound healing. *J, 4*(3), 288–307.

Calfee, R. C., & Valencia, R. R. (1991). *APA guide to preparing manuscripts for journal publication*. Washington, DC: American Psychological Association.

Carvalho, F. P. (2017). Pesticides, environment, and food safety. *Food and Energy Security, 6*(2), 48–60.

Chargui, I., Grissa, I., Bensassi, F., Hrira, M. Y., Haouem, S., Haouas, Z., & Bencheikh, H. (2012). Oxidative stress, biochemical and histopathological alterations in the liver and kidney of female rats exposed to low doses of deltamethrin (DM): A molecular assessment. *Biomedical and Environmental Sciences, 25*(6), 672–683.

Domingues, J. L., Delgado, F. M. G., Gonçalves, J. C., & Pintado, C. S. (2021). Essential oils of *Lavandula stoechas* subsp. *luisieri* as antifungal agent against fungi from strawberry tree fruit. *Journal of Pharmacy and Pharmacology, 9*(3). Retrieved from https://repositorio.ipcb.pt/handle/10400.11/7881

Gupta, V. K., Park, U., Kim, E., Kim, S., Siddiqi, N. J., Huh, Y. S., & Sharma, B. (2023). Antioxidative effect of *Aloe vera* against malathion induced neurotoxic response in Wistar rats. *Arabian Journal of Chemistry, 16*(10), 105169.

Halima, A., Akbar, W., Ali, H., Junaid, & Imtiaz, H. (2023). Residual level of deltamethrin induced gastritis and preventive role of curcumin on stomach mucosa. *Journal of Ayub Medical College Abbottabad, 35*(4), 534–537.

Ilyas, W. M., Chavan, G., & Gadkari, C. (2023). Deltamethrin poisoning mimicking organophosphate poisoning: A case report. *Cureus*.

Kaki, F. A., Benkiniouar, R., Touil, A., Demirtas, I., Merzoug, A., & Khattabi, L. (2021). *Thymus numidicus*: Phenolic constituents, antibacterial, and antioxidant activities of butanolic extract. *Environmental and Experimental Biology, 19*(2), 67–72.

Qu, K., Shi, M., Chen, L., Liu, Y., Yao, X., Li, X., Tan, B., & Xie, S. (2024). Residual levels of dietary deltamethrin interfere with growth and intestinal health in *Litopenaeus vannamei*. *Ecotoxicology and Environmental Safety, 288*, 117376.

Küçükler, S., Kandemir, F. M., Özdemir, S., Çomaklı, S., & Caglayan, C. (2021). Protective effects of rutin against deltamethrin-induced hepatotoxicity and nephrotoxicity in rats via regulation of oxidative stress, inflammation, and apoptosis. *Environmental Science and Pollution Research, 28*(44), 62975–62990.

Liu, Y., Yan, H., Yu, B., He, J., Mao, X., Yu, J., Zheng, P., Huang, Z., Luo, Y., & Luo, J. (2022). Protective effects of natural antioxidants on inflammatory bowel disease: Thymol and its pharmacological properties. *Antioxidants, 11*(10), 1947.

Makhlouf, C., Khaldoun, H., Béchohra, L., Djennane, N., Settar, A., Tarzaali, D., Oularbi, Y., Krabi, S., Bokreta, S., & Zerrouki Daoudi, N. (2025). Ampligo® 150 ZC affect the expression of sex hormone receptors and cell proliferation marker in female rabbit ovary: Protective effects of thyme essential oil and vitamin C. *Reproductive Toxicology, 132*, 108833.

Messara, Y., Fernane, F., & Meddour, R. (2018). Chemical composition, antibacterial, and antifungal activities of the essential oil of *Thymus numidicus* Poiret from Algeria. *Phytothérapie, 16*(3), 163–168.

Mohammed, N., Hassan, H., Ali, A., Khaled, F., & Mohamed, S. (2022). Histopathological alterations in liver of male rabbits exposed to deltamethrin and the ameliorative effect of folic acid. *Alq J Med App Sci, 5*(2), 454–460.

Rasheed, H. M., Farooq, U., Bashir, K., Wahid, F., Khan, T., Khusro, A., Gajdács, M., Alghamdi, S., Alsaiari, A. A., & Almehmadi, M. (2023). Isolation of oleanolic acid from *Lavandula stoechas* and its potent anticancer properties against MCF-7 cancer cells via induced apoptosis. *Journal of King Saud University-Science, 35*(2), 102454.

Yadav, R., Shinde, N. G., Patil, K. T., Kote, A., & Kadam, P. (2023). Deltamethrin toxicity: Impacts on non-target organisms and the environment. *Environment and Ecology, 41*(3D), 2039–2043.

Saoudi, M., Badraoui, R., Bouhajja, H., Ncir, M., Rahmouni, F., Grati, M., Jamoussi, K., & El Feki, A. (2017). Deltamethrin induced oxidative stress in kidney and brain of rats: Protective effect of *Artemisia campestris* essential oil. *Biomedicine & Pharmacotherapy, 94*, 955–963.

Sharma, P., Singh, R., & Jan, M. (2014). Dose-dependent effect of deltamethrin in testis, liver, and kidney of Wistar rats. *Toxicology International, 21*(2), 131.

Tewari, A., Banga, H., & Gill, J. P. (2018). Sublethal chronic effects of oral dietary exposure to deltamethrin in Swiss albino mice. *Toxicology and Industrial Health, 34*, 423–432.

Wojtunik-Kulesza, K. A. (2022). Toxicity of selected monoterpenes and essential oils rich in these compounds. *Molecules, 27*(5), Article 5.

World Health Organization. (2011). *Deltamethrin in drinking-water: Background document for development of WHO guidelines for drinking-water quality* (pp. 179–249). Geneva, Switzerland: World Health Organization.

Yadav, I. C., & Devi, N. L. (2017). Pesticides classification and its impact on human and environment. *Environmental Science and Engineering, 6*(7), 140–158.

Yildizhan, E., Ülger, B. V., Akkuş, M., Katanalp, Ö. F., Özkorkmaz, E. G., & Yıldızhan, İ. (2023). Rosmarinic acid ameliorates deltamethrin induced hepatotoxicity and nephrotoxicity. *Medical Records, 5*(2), 400–405.

Yousef, M. I., Awad, T. I., & Mohamed, E. H. (2006). Deltamethrin-induced oxidative damage and biochemical alterations in rat and its attenuation by vitamin E. *Toxicology, 227*(3), 240–247.

Author(s) Information

Farida Fernane
Mouloud Mammer's University, Natural Resources Laboratory, BP17 – 15000 – Tizi Ouzou, Algeria
ORCID iD: https://orcid.org/ 0000-0001-7828-884X
*Contact e-mail: *farida.fernane@ummto.dz*

Nacira Daoudi - Zerrouki
Mouloud Mammer's University, Natural Resources Laboratory, BP17 – 15000 – Tizi Ouzou, Algeria
ORCID iD: https://orcid.org/ 0009-0000-0915-2594

Ouardia Chaouchi
Mouloud Mammer's University, Natural Resources Laboratory, BP17 – 15000 – Tizi Ouzou , Algeria
ORCID iD: https://orcid.org/0009-0008-3453-4982

Hakima Aitissad
Mouloud Mammer's University, Natural Resources Laboratory, BP17 – 15000 – Tizi Ouzou, Algeria
ORCID iD: https://orcid.org/0009-0007-3140-7638

*Corresponding author(s) contact email

To cite this article:

Fernane, F., Daoudi-Zerrouki, N., Chaouchi, O., & Aitissad, H. (2026). Assessment of *Thymus numidicus* and *Lavandula stoechas* essential oils effects on deltamethrin-induced toxicity in female rabbits. *The Eurasia Proceedings of Science, Technology, Engineering and Mathematics (EPSTEM), 42*, 76–84.

The Eurasia Proceedings of Science, Technology, Engineering and Mathematics (EPSTEM)
ISSN: 2602-3199

The Eurasia Proceedings of Science, Technology, Engineering and Mathematics (EPSTEM), 2026

Volume 42, Pages 85-96

ICBASET 2026: International Conference on Basic Sciences, Engineering and Technology

Pedogenic Development and Mineralogical Characteristics of Sedimentary Soil Pedons

Radhwan A. Alkiki
University of Mosul

Khalid Anwar Khalid
University of Mosul

Abd Al-Kader A. Alhadede
University of Mosul

Abstract: The study focus on determining the pedogenic development, mineralogical and micromorphological characteristics of sedimentary soils in northern Iraq. Four soil pedons had been selected around Mosul Dam Lake in northern Nineveh province, to represent these soils. The main objective of this study was to determining some of the mineralogical and development characteristics of sedimentary soils in these sites. The process involved a morphological description of soil pedons in the sites, laboratory analyses to determine the physical and chemical properties of soil samples, XRD analysis of clay minerals, and thin section analysis for soil micromorphology. The results indicated That the soil textures were clay, silty clay and clay loam, with the variations in physical and chemical and morphological characteristics of studied sites. whereas, thin section analysis revealed carbonate and gypsum nodules, clay masses, and dissolution voids, indicating transmission and accumulation processes. XRD analysis identified a mixed mineral assemblage consisting of chlorite, illite, palygorskite, montmorillonite, and gypsum. The occurrence of palygorskite under alkaline and moisture-deficient conditions reflects pedogenic processes typical of semi-arid environments (Azimi et al, 2025). Therefore, these findings provide new insights into soil genesis and mineral transformation in northern Iraq and contribute to the sustainable management and conservation soil resources in semi arid zones.

Keywords: Sediment soils, XRD analysis, Micromorphological characteristics

Introduction

The sediment soils of northern Iraq have unique properties influenced by semi-arid climatic conditions, it were formed as a result of fluvial and wind deposition of clastic materials originating from the surrounding mountain ranges, particularly in the Tigris basin and foothill areas (Aziz et al., 2009; Sissakian et al., 2025). Most of these sediments are composed of limestone, marl, and gypsum (Khalaf et al, 2024; AlQaisi et al., 2026). These soils play a fundamental role in agricultural productivity, environmental sustainability, and land use development (Sardoo et al., 2023; Al baghdady & Alabadi, 2021; Al-Badrani & Al-Khafagi, 2025; Altaee et al., 2025). The geological and climatic diversity of the region has contributed to make a significant spatial variability in their physical, chemical, mineralogical, and morphological characteristics, including differences in texture, fertility, and clay mineral composition (Husein et al., 2017; Kaletova et al., 2022). Soil formation and pedogenic development in semi-arid regions is often influenced by interaction between parent material mineralogy and the prevailing moisture regime. Despite of some studies being conducted on these soils, detailed investigations into the micromorphological fabric and clay mineral stability are limited (Horváth et al., 2016). The development of sediment soils in semi-arid regions is governed by numerous environmental conditions, including climate defined by annual rainfall, temperature average, wind intensity and direction (Nortcliff, 2009; Verheye, 2009).

- This is an Open Access article distributed under the terms of the Creative Commons Attribution-Noncommercial 4.0 Unported License, permitting all non-commercial use, distribution, and reproduction in any medium, provided the original work is properly cited.

- Selection and peer-review under responsibility of the Organizing Committee of the Conference

© 2026 Published by ISRES Publishing: www.isres.org

Topography also plays a significant role, along with human activities such as tillage systems and irrigation methods, as well as the impact of soil parent material (Blume et al., 2002; Azimi et al., 2025). In general, soil development is a result of soil forming factors and processes over time, which include the weathering of geological materials and their transformation under new conditions into new products that are similar to or different from the parent material, and the degree of soil development depends on the intensity of influencing factors and the type of parent materials, (Nesbitt & Young, 1996; Silva et al., 2025). However, the processes of soil formation and development are numerous and complex, no one process can be given priority over another, and these processes proceed in a specific direction and under specific conditions, and the final result is the formation and development of the soil (Bockheim et al., 2014). The development of soil profiles includes the weathering of clay minerals and their transformation it from primary to secondary minerals, interspersed with processes of transport and deposition of mineral components between the horizons of soil profiles (Al-Khalaf & Al-Saad, 2017; Khalid, 2019). Clay minerals are the most active component of soil minerals, such as Mica, Chlorite, Illite, Montmorillonite, Kaolinite, Palygorskite, Gypsum, Vermiculite and others, making their chemical, physical, and micromorphological properties a significant factor of many soil characteristics (Usul & Dengiz, 2010; Heeshan et al., 2022; Alhadede et al., 2025). X-ray diffraction is the most common and accurate method for characterizing the mineral composition of clay particles and detecting clay minerals in soil, both quantitatively and qualitatively (Zhou et al., 2018). XRD is available technology to identify and measure all minerals present in clay-rich rocks such as mudstone, shale, and marls (Srodoi et al, 2001; Remigio et al., 2022). The study of soil micromorphological characteristics is an essential tool for understanding the degree of change that occurs within soil pedons as a result of pedogenic processes, soil development, human activities, and the influence of soil organisms (Ismaeal, 2022). Micromorphological investigations provide valuable information on soil genesis, mineral composition, and the mechanisms involved in soil formation and evolution (Jahan & Manafi, 2018). These characteristics are commonly examined using thin-pedon techniques under optical or electron microscopes, allowing detailed observation of soil constituents and their spatial relationships in three dimensions. Such analyses contribute significantly to the assessment of biogenic features and the interpretation of soil-forming environments and processes (Dincă et al., 2022). Therefore, this study aimed to: [1] identify the different properties of sedimentary soils in selected areas of northern Iraq. [2] Assessing the pedogenic development of soil pedons. [3] determine the micromorphological and mineralogical characteristics of soil pedons.

Materials and Methods

The Studied Sites Description

This study was conducted on the sedimentary soils surrounding Mosul Dam lake, which is located to north of Nineveh province, Iraq. The study area are located within semi-arid zones, and these soils were classified into Aridisols and Inceptisols orders according to USDA (Soil Survey Staff, 2006). Four soil pedons were chosen and randomly distributed around the lake (Figure 1), to represent all directions (north, west, south and east). Soils of the study area are characterized with difference of parent material, as gypsum, limestone and marls constitute the majority of it (Issa et al., 2014). Land in the study area is flat to a slight slope, the vegetation consists of wheat, barley, and vegetable crops.

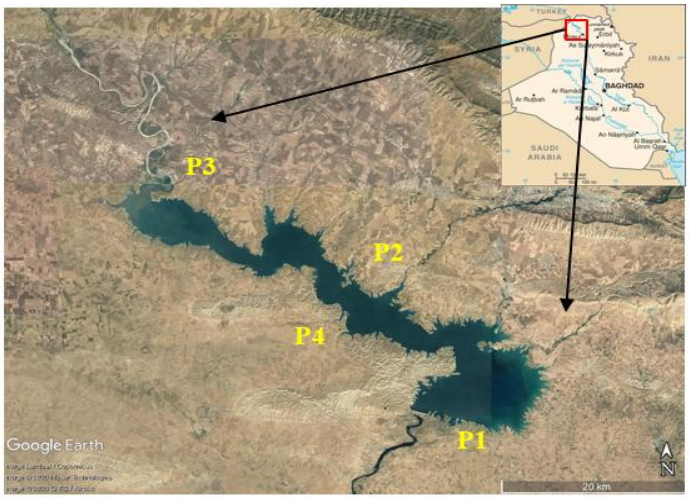

Figure 1. The map of study sites

Table 1 shows the informations (the coordinates, the elevation and the vegetation) of soil pedons, the symbols P1, P2, P3 and P4 were assigned to represent first, second, third and fourth soil pedons respectively. The climate of the study area is characterized by variations in average temperatures throughout the year. In Summer, the temperatures ranged between (30-45) ℃, while in winter, the temperatures ranged between (0-12) ℃. This climate is generally considered the Mediterranean. The average annual rainfall is between (150-400) mm, and the periods of rainfall are concentrated during winter and spring seasons.

Table 1. The information of soil pedons

Pedon	Coordinates N.	E.	Elevation (m)	Vegetation
P1	36.609779°	42.903001°	327	wheat
P2	36.691454°	42.938047°	332	vegetable crops
P3	36.764594°	42.755139°	330	vegetable crops
P4	36.717219°	42.734122°	329	barley

Field Work and Morphological Description

Four soil pedons (P1, P2, P3 and P4) were excavated, and the soil profiles that direct sunlight were characterized into horizons, and described morphologically according to USDA (Table 2). Undisturbed soil samples were collected from subsurface horizons (B horizons) for thin pedons preparation and micromorphological analysis. In addition, soil samples were collected from all horizons (12 soil samples), then the samples were placed in labeled plastic containers and subsequently transported to the laboratory for analyses.

Table 2. Morphological properties for soil pedons

Pedon	Horizon	Depth (cm)	Soil color				Structure	Consistency	Boundary
			dry		wet				
	A_p	0-20	10YR 5/3	b	10YR 3/3	db	Bfsa	SFpl	c
P1	B	20-47	10YR 5/4	yb	10YR 4/4	dyb	Bmsa	SFpl	c-w
	C_k	47-100	10YR 7/4	ypab	10YR 4/4	dyb	Bma	SFspl	w
	A_p	0-8	10YR 5/3	b	10YR 4/3	b	Bfsa	SFpl	c-w
P2	B	8-38	10YR 5/4	yb	10YR 3/3	db	Bma	SFpl	c-w
	C	38-95	10YR 5/6	yb	10YR 4/6	dyb	Bma	Shp	w
	A	0-12	10YR 6/4	lyb	10YR 4/4	dyb	gfm	Shpl	w
P3	B	12-57	10YR 5/4	yb	10YR 3/3	db	Bma	SFpl	c-w
	C_k	57-100	10YR 5/3	b	10YR 3/3	db	Bma	SFpl	w
	A_p	0-15	10YR 6/4	lyb	10YR 4/4	dyb	Bfm	FSpl	w
P4	B	15-48	10YR 5/3	b	10YR 3/3	db	prma	Shpl	w
	C	48-95	10YR 5/3	b	10YR 3/3	db	Bma	SFpl	w

Notes: l=light, y=yellowish, b=brown, d= dark, pa=pale;: B=blocky, f=fine, sa=subangular, m=moderate, a=angular, pr=prismatic, g=granular : S=Slightly, h=hard, F=friable, pl=plasticity, s=sticky,: c=clear, w=wavy.

Laboratory Work

Disturbed and undisturbed soil samples were prepared for the physical and chemical laboratory analyses, that following: particle size distribution, bulk density, soil pH, soil EC, O.M., CEC, $CaCO_3$, and $CaSO_4.2H_2O$, analytical procedures were carried out according to (Rowell, 1994).

Preparation of Soil Thin Pedons

Thin pedons thick (30 μm) were prepared from undisturbed soil samples collected from B horizon of each soil pedon. Micromorphological observations were conducted using a polarized transmitted light microscope (Leitz Laborlux S model) at 40× magnification. Soil constituents and micromorphological features, including voids, mineral crystals, and soil aggregates, were characterized according to the methods described by FitzPatrick (1981).

Soil Mineralogical Analyses (XRD)

The clay particles present in the soil samples of B horizon for all soil pedons were separated from other soil components (sand and silt) in the laboratory by precipitation according to Stokes' law, the carbonates, soluble salts, organic matter, and iron oxides have been removed (Moore & Reynolds, 1997). Approximately (30) mg of clay sample was placed on a (2.6 × 2.3) cm glass slide, then these samples were analyzed using the X-ray diffraction instrument (XRD-6000, Shimadzu, Japan). Clay samples that loaded on the glass slides have been subjected to the following treatments prior to XRD analysis (Al-Rawas et al., 1998):

- Mg-saturated, air-dried.
- Mg-saturated, ethylene glycol.
- K-saturated, air-dried.
- K-saturated, heated at 350 C°.
- K-saturated, heated at 550 C°.

Results and Discussion

Physical and Chemical Characteristics for Soil Pedons

Table (3) shows some physical and chemical characteristics of soil pedons in the studied sites, it is note that there variations within horizons and soil pedons. The particle size distribution results showed that the soil texture were clay (C), clay loam (CL), and silty clay (SC), sand particles content ranged between (185-242) g kg^{-1} in horizon C of P3 and the surface horizon A of P2 respectively, silt particles ranged between (295-411) g kg^{-1} in horizon C of P2, and horizon A of pedon P3 respectively, whereas the clay particles ranged between (375-500) g kg^{-1} in horizon A of P3 and horizon C of P2. These variations may be attributed to parent materials nature, intensity of weathering processes, and soil forming and development processes in the studied sites (Kabi & Jena, 2025).

Table 3. Physical and chemical characteristics for soil pedons

Pedon	Horizon	Depth (cm)	particles size distribution g.kg^{-1}			Texture	Bulk density *M*g.m^{-3}	pH	EC ds.m^{-1}	g.kg^{-1}			CEC cmol.kg^{-1} soil
			sand	silt	clay					O.M.	$CaCO_3$	$CaSO_4$	
	A_p	0-20	196	400	404	SC	1.47	7.70	1.18	18.00	203	13.63	25.22
P1	B	20-47	193	389	418	C	1.52	7.90	0.70	16.12	191	13.50	21.39
	C_k	47-100	214	375	411	C	1.41	7.70	0.47	10.14	235	16.81	20.00
	A_p	0-8	242	378	380	CL	1.45	7.80	0.85	19.50	186	12.15	26.50
P2	B	8-38	191	390	419	C	1.56	7.60	0.62	14.33	200	11.85	23.68
	C	38-95	205	295	500	C	1.60	7.80	0.49	10.52	228	15.47	20.62
	A	0-12	214	411	375	CL	1.44	7.90	1.21	17.40	184	14.63	23.41
P3	B	12-57	194	386	420	C	1.53	7.70	0.71	13.82	219	11.77	18.37
	C_k	57-100	185	393	422	C	1.59	7.50	0.50	8.65	227	12.74	17.54
	A_p	0-15	192	403	405	SC	1.46	7.90	1.00	20.13	193	10.42	24.71
P4	B	15-48	206	410	384	CL	1.50	7.70	0.62	12.50	197	10.66	22.45
	C	48-95	200	338	462	C	1.57	7.60	0.70	9.12	228	13.80	20.36

Notes: SC= Silty Clay, C= Clay, CL= Clay Loam.

Bulk density values ranged between (1.41-1.60) $Mg.m^{-3}$ in horizon C of P1 and horizon C of pedon P2 respectively. Generally, bulk density tended to increase with depth, which can be attributed to lower organic matter content, increasing clay content, and reduced biological activity in subsurface horizons, while the lower bulk density values in surface horizons are associated with organic matter accumulation and better soil aggregates. Such conditions enhance soil porosity, water infiltration, and root penetration. Soil pH values ranged between (7.50-7.90), indicating that all studied soils were neutral to slightly alkaline, that is due to the high $CaCO_3$ content in the studied soils. Soil EC values at generally, were relatively low of all sites, the values ranged between (0.47-1.21) $dS.m^{-1}$ in horizon C of P2 and the horizon A of P1 respectively. Soil O.M. content showed considerable variation among the horizons, ranging from (8.65) g kg^{-1} in horizon C of P3 to (20.13) g kg^{-1} in horizon A of P4. In general, organic matter content was highest in the surface horizons and decreased progressively with depth. This distribution pattern reflects the accumulation of plant residues and greater biological activity in soil surface, differences along pedons may also be related to variations in vegetation cover and environmental conditions. $CaCO_3$ content of studied soils ranged between (184-235) g kg^{-1}, with the lowest value recorded in horizon A of P3, while the highest value was recorded in horizon C of P1. Moreover, soils of these areas are characterized by an abundance of lime as a natural result of the parent material, climate and environmental conditions of these soils containing calcite minerals, which is the main component of limestone. It was noted that $CaCO_3$ increased with depth in the most of soil pedons (Li et al., 2021). Similarly, CaSO4.2H2O content showed a slight increase with depth of soil pedons, it was ranged between (10.42-16.81) g kg^{-1}. in horizon A of P4 and the horizon C of P1 respectively. In general, the distribution of gypsum is also influenced by the mineralogical composition of parent material and environmental conditions. While CEC values ranged between (17.54-26.50) $cmol.kg^{-1}$ soil, in horizon C of P3 and horizon A of P2. These values have been associated with the clay and organic matter content along the horizons of soil pedons in studied sites. In addition, CEC has a clear influence in determining soil fertility and the content of nutrients necessary for plants.

Thin Sections of Soil Pedons

The results of micromorphological analyses (using a transmitted polarized light microscope) of undisturbed soil samples, obtained from subsurface horizon (B horizon) of all studied pedons, showed variation in the nature of micromorphological characteristics, including nodules, voids, and aggregate shapes. These features indicate the activity of some pedogenic processes responsible for soil formation in the study area, especially the processes of loss and gain of some soil components. Figure (2) indicates that the soil in this site is composed of sedimentary rocks of calcareous and gypsum origin, as evidenced by the presence of carbonates remnants and gypsum minerals, this results was consistent with the chemical and morphological properties of this soil pedon.

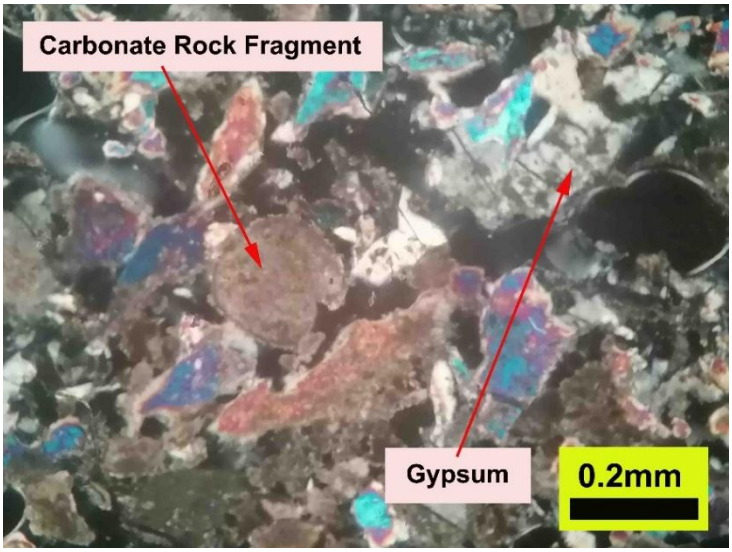

Figure 2. Thin section for soil P1

A figure also shows voids or cavities measuring (0.3 mm), which indicate the dissolution of minerals by rainwater or by plant roots growing in the soil. The presence of carbonate and gypsum minerals in the soil affects some of its chemical properties, such as its pH level and some of its fertility characteristics, in addition to physical properties such as permeability, structure, and aggregation. Figure (3) shows the presence of silicate clay minerals, specifically feldspars, which are aluminum silicates containing calcium and sodium between their

layers. It also shows the presence of clay masses, indicating the accumulation of clay minerals within the soil body, this result was consistent with the results of (Alhashyme & Khaled, 2025). Furthermore, the figure clearly shows the presence of carbonates and the distinctive forms of gypsum minerals (CaSO4.2H2O) in this horizon, and the predominant type of structure in the soil sample is crumb and granular.

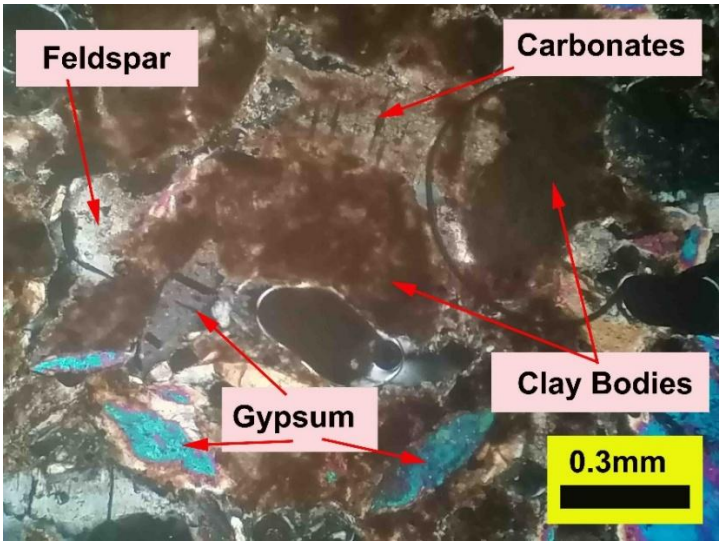

Figure 3. Thin section for soil P2

These results reflect the pedogenic processes under which this soil has been formed. The results of the analyses in Figure (4) showed the presence of quartz, indicating the presence of silica at this site, in addition to clay minerals inherited from the original sedimentary material. Quartz is characterized by its hardness and relatively high resistance to chemical weathering processes, and this mineral influences the physical properties of the soil. The soil at this site also exhibits vugs with difference sizes, which further indicate the dissolution and leaching of some soil components to deeper horizons by water.

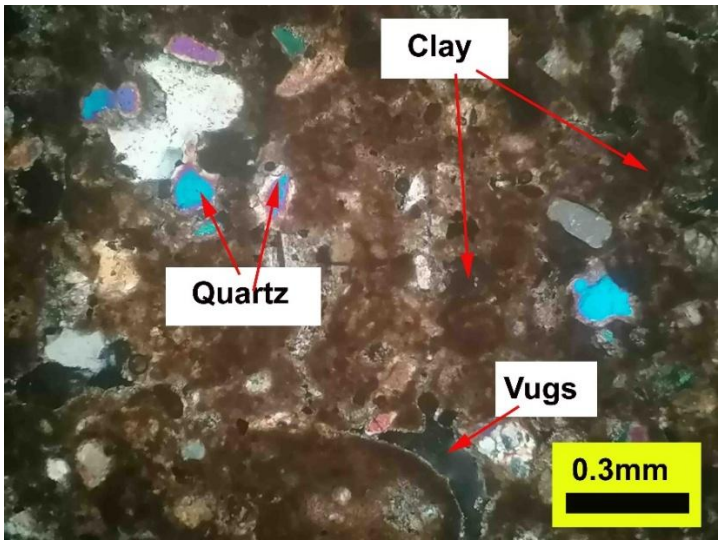

Figure 4. Thin section for soil P3

Figure (5) shows the carbonate and gypsum groups, in addition to clay and various voids. These results reflect the state of the interconnected influence of the main soil components, especially the lime and gypsum content in this horizon, and the influence of the environmental factors surrounding those soils, in addition to the basic role in the activity of some pedogenic processes responsible for the formation of those soils. These processes indicate the occurrence of a movement of transport and deposition of mineral and organic materials (Soil plasma) with a size of soil colloids (less than 2 microns) within the soil, with the availability of the transporting agent represented by water (Owliaie & Abtahi, 2006).

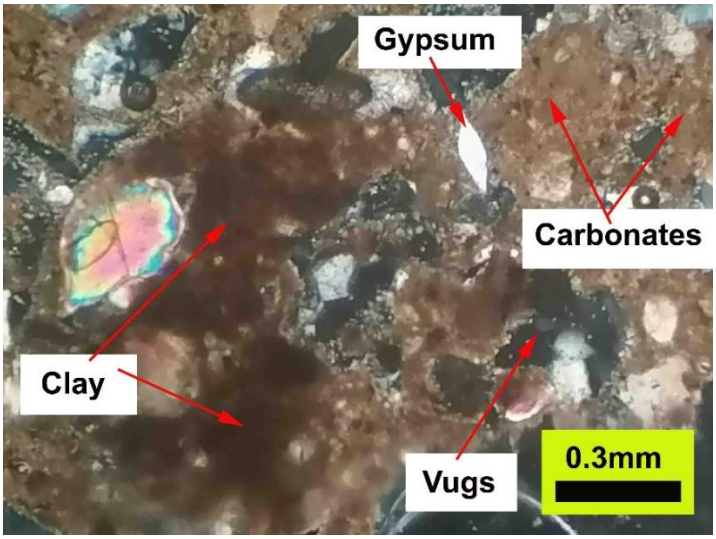

Figure 5. Thin section for soil P4

XRD Analyses for Soil Pedons

Figures (6-9) showed the XRD curves of clay samples taken from B horizon for each soil pedon, which were treated according to the treatments mentioned previously for Mg and K. The XRD analysis revealed the presence of a group of minerals represented by chlorite, illite, palygorskite, montmorillonite and gypsumt, this mixture of minerals is specifically a characteristic feature of soils in semi-arid climates. Figure (6) showed the presence of chlorite at the (14.7 A°) inversion, which remained stable upon heating up to 550 C°, (10.4 A°) peak and partial collapse upon heating of the K-saturated layer indicate the presence of palygorskite with thin montmorillonite layers. Illite appeared at diffraction (10 A°) in (Mg-air dry) treatment.

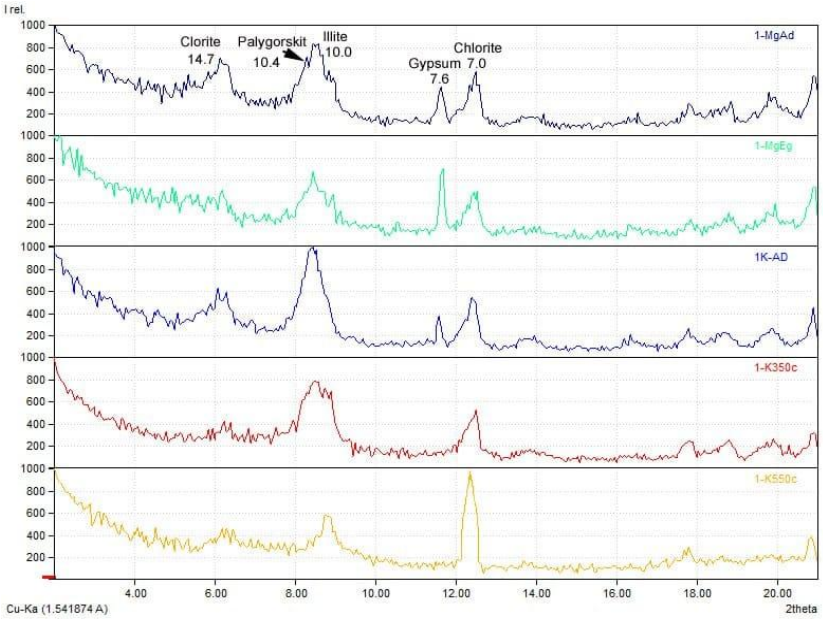

Figure 6. XRD analysis for soil P1

Gypsum (7.6 A°) is present alongside the palygorskite, indicating its concentration by evaporation under alkaline conditions rich in Mg and silicon (Khormali et al, 2003; Al-Mallah et al, 2016). This composition is consistent with soil formation models in the semi-arid regions of northern Iraq, where palygorskite forms spontaneously in gypsum-rich subsurface layers under conditions of soil moisture deficiency. Figure (7) showed the XRD analysis of soil pedon (P2) clay sample, that the montmorillonite appeared with chlorite at diffraction (14.7A°) in the (Mg-ad) treatment, then it expanded at diffraction (17.7A°) in the (mg-Eg) treatment. The palygorskite (10.4 A°) reflection coincides with the gypsum (7.64 A°) reflection, while chlorite is clearly visible at (7.0 A°) and (14 A°).

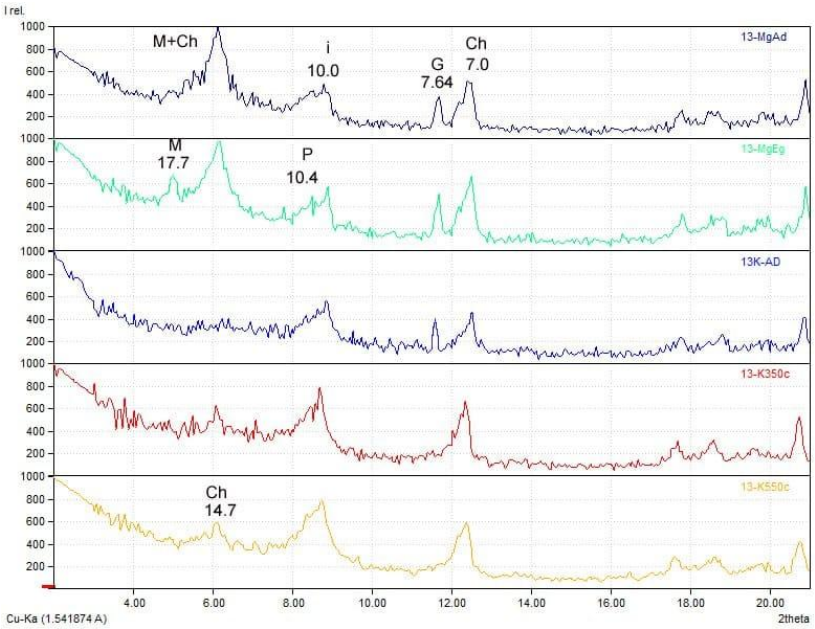

Figure 7. XRD analysis for soil P2

Gradual heating with K to 550 C° leads to the decomposition of montmorillonite, while palygorskite and chlorite remain stable, indicating the presence of a mixed assemblage of montmorillonite, palygorskite, chlorite, and gypsum, a characteristic feature of soil formation in semi-arid and low-moisture regions. In Figure (8), the peak of 17.7A° after treatment with Mg-eg confirms the presence of montmorillonite, while palygorskite persists within the 10.4 A° inversion and gypsum within the 7.64 A° inversion. Chlorite is identified by the stable peaks of (14.7A° and 7.0 A°) up to 550 C°. K-saturation and gradual heating to 550 C° lead to the decomposition of montmorillonite, but do not affect palygorskite and chlorite, indicating the presence of a mixture of soil minerals (montmorillonite-palygorskite-chlorite-gypsum) that formed under alkaline conditions with the influence of seasonal wetting and drying cycles (Song et al., 2020). Figure (9) showed appeared of a peak with (17.7 A°), unequivocally indicating montmorillonite with (Mg-eg). The 10.4 A° and 7.66 A° reflections correspond to palygorskite and gypsum, respectively. Chlorite is identified in 14.7 A° and 7.0 A°, which persists after K-550 C°. The thermal stability of chlorite and palygorskite contrasts with the complete collapse of montmorillonite (Emadi et al., 2008).

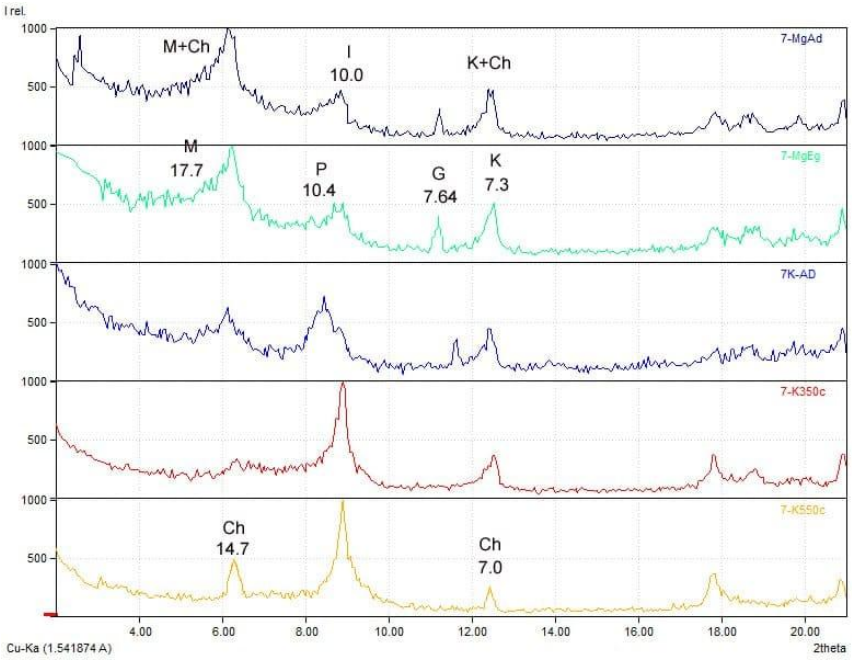

Figure 8. XRD analysis for soil P3

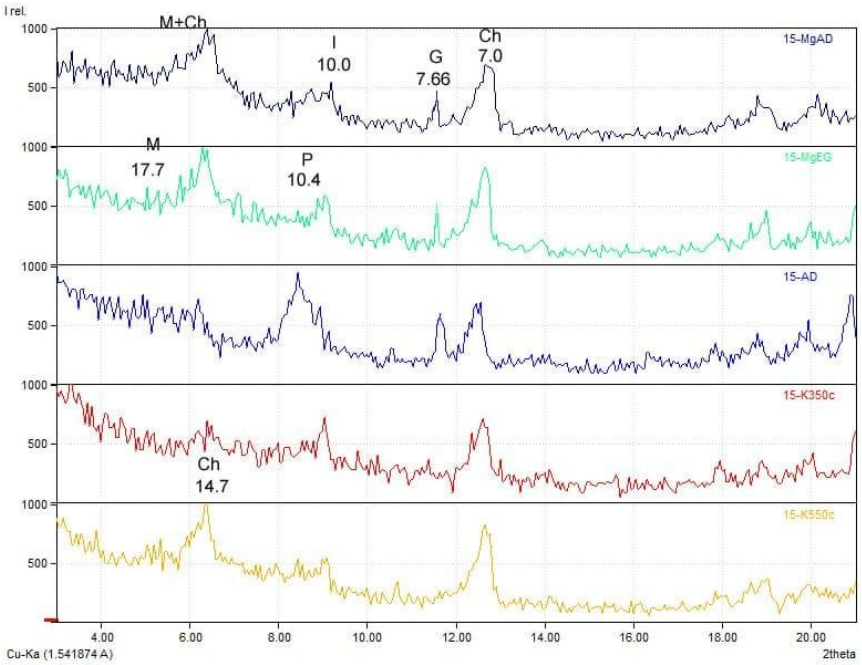

Figure 9. XRD analysis for soil P4

Conclusioun

This study provided an important assessment of the developmental degree, micromorphological and mineralogical characteristics of Sedimentary soils of the sites surrounding Mosul Dam lake in northern Nineveh, that classified into Aridisols and Inceptisols orders according to USDA. The study included thin sections and XRD anlyses, soil morphological data, and laboratory physical and chemical analyses for 12 soil samples, involved excavating 4 soil pedons, and providing scientific explanations of the processes controlling soil formation and development under semi arid conditions.

The studied soils exhibited variations in physical, chemical, and morphological properties due to differences in the nature of parent materials (calcareous and gypsum), and the impact of soil formation processes. The results indicated that soils texture were clay, silty clay, and clay loam, with variations in CEC, O.M., CaCO3, and gypsum content. Thin section analyses using a polarizing microscope of subsurface horizon soil samples revealed the presence of carbonate and gypsum nodules, clay aggregates, and voids resulting from dissolution of the gypsum and carbonates. These formations are influenced by Translocation and deposition processes, and redistribution of the soil components within pedon horizons. These characteristics explain the chemical weathering impact on the secondary minerals' formation, and the clay accumulation indicates movement of the clay particles through soil horizons under the seasonal rainfall impact, living organisms and the human activities through tillage processes and movement of the agricultural machinery. XRD analyses for clay samples identified assemblage of minerals Represented by chlorite, illite, montmorillonite, palygorskite, and gypsum. with stability of chlorite and palygorskite after thermal tretment, along with the inhibition of expansion and collapse of montmorillonite. The inclusion of palygorskite and chlorite reflects the geochemical conditions and low moisture, characteristics of semi arid environments.

In general, the studied soils represent weak developed soils, resulting in the influence of parent material, climate, and inveromental conditions. These findings contribute to a better understanding of agricultural lands in these sites, and provide a scientific basis for soil agricultural management, and the sustainable use of soil resources in the semi arid regions. Furthermore, this study offers valuable insights regarding micromorphological and mineralogical characteristics, and sedimentary soils development, and can form a reference framework for future educational studies in similar areas.

Scientific Ethics Declaration

* The authors declare that the scientific ethical and legal responsibility of this article published in EPSTEM journal belongs to the authors

Conflict of Interest

* The authors declare that they have no conflicts of interest.

Funding

* No funding is available for this study.

Acknowledgements

* This article was presented as an oral presentation at the International Conference on Basic Sciences, Engineering and Technology (www.icbaset.net) held in Istanbul/Türkiye on September 17-18, 2026.

* The authors would like to express their gratitude to the university of Mosul and the dean of Agriculture and Forestry college at university of Mosul.

References

Al Baghdady, S. N. Sh., & Alabadi, L. A. S. (2021). Grain size analysis of sand fractions and the sedimentary environment of selected soil samples from southern and northern Iraq. *Malaysian Journal of Chemistry, 23*(4), 77–88.

Al-Badrani, A., & Al-Khafagi, Q. (2025). Description of magnesium adsorption under the influence of different temperatures in calcareous soils with varied agricultural uses. *Mesopotamia Journal of Agriculture, 53*(3), 109–122.

Alhadede, A. A.-K. A., Alhadidi, K. E. N., & Essa Al-Khafagia, Q. D. (2025). Effect of ionic strength on dissolution and precipitation of carbonate minerals and the nature of ionic species from some calcareous soil. *Journal of Global Innovations in Agricultural Sciences, 13*(2), 699–705.

Alhashyme, G. A., & Khaled, K. A. (2025). Assessing soil weathering and micromorphological characteristics under different land use practices in northern Iraq. *International Journal of Design & Nature and Ecodynamics, 20*(10), 2471–2478.

Al-Khalf, N. A., & Al-Saad, H. A. (2017). Mineralogy and geochemistry of recent sediments in Basrah, southern Iraq. *Iraqi Geological Journal, 52*(1).

Al-Mallah, I., Al-Suhail, Q., & Albadran, A. (2016). Mineralogical and geochemical analysis of the sediments surrounding the Main Drain area, middle of Iraq. *Iraqi Journal of Science, 57*(3B), 2025–2042. Retrieved from https://ijs.uobaghdad.edu.iq/index.php/eijs/article/view/6910

AlQaisi, S. M., Al-Wazzan, F. A., & Albayati, H. (2026). Synergistic effects of nano-NPK and organic fertilization on potato yield and soil nutrient availability under drip irrigation. *International Journal of Design & Nature and Ecodynamics, 21*(2), 417–424.

Al-Rawas, A., Sutherland, H., Hago, A. W., Basma, A., & Al-Shihi, B. (1998). Quantitative analysis of clay minerals using X-ray diffraction technique. Part 1. *Sultan Qaboos University Journal for Science, 3*(1), 31–39.

Altaee, M. A., Alhadede, A. A.-K. A., & Al-Badrani, W. A. A. (2025). Evaluation of Mosul inflow's wastewater quality for irrigation. *Mesopotamia Journal of Agriculture, 53*(1), 29–45.

Azimi, M., Alkhaled, K., Mirdeilami, S. Z., & Vahid, H. (2025). Eco-hydrological impacts and socio-economic drivers of rangeland degradation due to overgrazing in semi-arid and arid regions: A review. *Mesopotamia Journal of Agriculture, 53*(3), 63–86.

Aziz, S. N., Muhaimeed, A. S., & Amin, I. M. (2009). Climatic conditions effects on formation and development status of some soils in northern part of Iraq/Kurdistan region. *Journal of Kirkuk University, Scientific Studies, 4*(1).

Blume, H. P., Beyer, L., Kalk, E., & Kuhn, D. (2002). Weathering and soil formation. In *Geoecology of Antarctic ice-free coastal landscapes* (Vol. 154, pp. 115–138). Berlin, Germany: Springer.

Bockheim, J. G., Gennadiyev, A. N., Hartemink, A. E., & Brevik, E. C. (2014). Soil-forming factors and soil taxonomy. *Geoderma, 226*, 231–237.

Dincă, L. C., Grenni, P., Onet, C., & Onet, A. (2022). Fertilization and soil microbial community: A review. *Applied Sciences, 12*(3), 1198.

Emadi, M., Baghernejad, M., Memarian, H., Saffari, M., & Fathi, H. (2008). Genesis and clay mineralogical investigation of highly calcareous soils in semi-arid regions of southern Iran. *Journal of Applied Sciences, 8*(2), 288–294.

FitzPatrick, E. A. (1981). The micromorphology of soils, a manual for the preparation and description thin pedons of soils. *Soil Science, 132*(5), 380.

Heeshan, A. M., Ismaeal, A. S., & Rashid, A. A. (2022). Genesis and the degree of development of the clay and calcareous horizons of some soils in northern Iraq. *International Journal of Agricultural and Statistical Sciences, 18*(1), 1617–1627. Retrieved from https://connectjournals.com/03899.2022.18.1617

Horváth, A., Szita, R., Bidló, A., et al. (2016). Changes in soil and sediment properties due the impact of the urban environment. *Environmental Earth Sciences, 75*, 1211.

Husein, H. H. M., Nammora, T., Zaghtiti, I., Al-Khateeb, A., & Zenyah, E. (2017). Soil catena properties of Daher Al-Jabal in South Syria. *International Journal of Environment, 6*(1), 87–107.

Ismaeal, A. S. (2022). Diagnostics and characterization of micromorphological features of some soil series in Baiji City, central Iraq. *Tikrit Journal for Agricultural Sciences, 22*(2), 132–147.

Issa, I. E., Al-Ansari, N., & Knutsson, S. (2014). Mosul Dam reservoir sedimentation characteristics, Iraq. *Journal of Environmental Hydrology, 22*.

Jahan, T., & Manafi, S. (2018). Evolution micromorphology of argillic horizons in some arid soils in the west of Urmia Lake in Western Azerbaijan Province, Iran. *Agronomy Journal, 40*(1).

Kabi, A., & Jena, S. (2025). Soil forming factors and soil profile development. In *Principles and applications of soil science* (1st ed., Chapter 3). Varanasi, India: Department of Soil Science and Agricultural Chemistry. Retrieved from https://agrirootpublicationhouse.com/ISBN:978-81-995733-9-0

Kaletova, T., Arifjanov, A., Samiev, L., & Babajanov, F. (2022). Importance of river sediments in soil fertility. *Journal of Water and Land Development, 52*, 21–26.

Khalaf, A. A., Obiad, M. M., & Hayyood, E. M. (2024). Evaluating and maps of chemical weathering indices for gypsiferous soils using geospatial techniques. *IOP Conference Series: Earth and Environmental Science, 1371*.

Khalid, K. A. (2019). Using unsupervised classification to determined land cover northren of Ninvah provianec by using remote sensing techniques. *Journal of Physics: Conference Series, 1294*, 092037.

Khormali, F., Abtahi, A., Mahmoodi, S., & Stoops, G. (2003). Argillic horizon development in calcareous soils of arid and semiarid regions of southern Iran. *Catena, 53*(3), 273–301.

Li, J., Du, J., Zhong, S., Ci, E., & Wei, C. (2021). Changes in the profile properties and chemical weathering characteristics of cultivated soils affected by anthropic activities. *Scientific Reports, 11*, 20822.

Moore, D. M., & Reynolds, R. C. (1997). *X-ray diffraction and the identification and analysis of clay minerals* (2nd ed.). Oxford, England: Oxford University Press.

Nesbitt, H. W., & Young, G. M. (1996). Petrogenesis of sediments in the absence of chemical weathering: Effects of abrasion and sorting on bulk composition and mineralogy. *Sedimentology, 43*, 341–358.

Nortcliff, S. (2009). Soils of cold and temperate regions. In *Land use, land cover and soil sciences* (Vol. 7). Reading, England: Department of Soil Science, University of Reading.

Owliaie, H. R., & Abtahi, A. (2006). Pedogenesis and clay mineralogical investigation of soils formed on gypsiferous and calcareous materials on a transect, southwestern Iran. *Geoderma, 134*(1–2), 62–81.

Remigio, G. D., Rocchi, I., & Zania, V. (2022). *XRD quantification of clay minerals: Impact of sample preparation and quantitative interpretation methods choice*. Australian Geomechanics Society.

Rowell, D. L. (1994). *Soil science: Methods and applications* (1st ed.). London, England: Longman Scientific and Technical.

Sardoo, E. S., Farpoor, M. H., Mahmoodabadi, M., & Jafari, A. (2023). Evaluation of selected soil development indices in soils derived from sedimentary and igneous rocks, northern Kerman. *Iranian Journal of Soil and Water Research, 54*(1), 85–103.

Silva, L. F., Nascimento, P. C., Zinn, Y. L., & Inda, A. V. (2025). Pedogenesis and the study of lithological discontinuity in a Planosol in Southern Brazil. *Revista Brasileira de Ciência do Solo, 49*, e0240221.

Sissakian, V. K., Othman, A. A., Obaid, A. K., & Abdulhaq, H. A. (2025). Soil types and erosion in Iraq: A critical discussion. *Iraqi Bulletin of Geology and Mining, 21*(1), 343–364. Retrieved from https://orcid.org/0000-0002-9840-5422

Soil Survey Staff. (2006). *Keys to soil taxonomy* (10th ed.). Washington, DC: United States Department of Agriculture, Natural Resources Conservation Service.

Song, Y., Zong, X., Qian, L., Liu, H., Dong, J., Chang, H., & Zhang, M. (2020). Mineralogical record for stepwise hydroclimatic changes in Lake Qinghai sediments since the last glacial period. *Minerals, 10*(11), 963.

Srodoi, N., Drits, V. A., McCarty, D. K., Hsieh, J. C., & Eberl, D. (2001). Quantitative X-ray diffraction analysis of clay-bearing rocks from random preparations. *Clays and Clay Minerals, 49*(6), 514–528.

Usul, M., & Dengiz, O. (2010). Pedological development on four different parent materials. *Anadolu Tarım Bilimleri Dergisi, 25*(3), 204–211.

Verheye, W. (2009). *Soils of arid and semi-arid areas*. Ghent, Belgium: National Science Foundation Flanders and Geography Department, University of Gent.

Zhou, X., Liu, D., Bu, H., Deng, L., Liu, H., Yuan, P., Du, P., & Song, H. (2018). XRD-based quantitative analysis of clay minerals using reference intensity ratios, mineral intensity factors, Rietveld, and full pattern summation methods: A critical review. *Solid Earth Sciences, 3*(1), 16–29.

Author(s) Information

Radhwan A. Alkiki
University of Mosul, College of Agriculture and Forestry, Department of Soil Science and Water Resources, Mosul 41002, Iraq
ORCID iD: https://orcid.org/0009-0004-5334-1746
*Contact e-mail:*Radhwan.23agp45@student.uomosul.edu.iq*

Khalid Anwar Khalid
University of Mosul, College of Agriculture and Forestry, Department of Soil Science and Water Resources, Mosul 41002, Iraq
ORCID iD: https://orcid.org/0000-0003-2198-0100

Abd Al-Kader A. Alhadede
University of Mosul, College of Agriculture and Forestry, Department of Soil Science and Water Resources, Mosul 41002, Iraq
ORCID iD: https://orcid.org/0000-0002-3518-9179

*Corresponding author(s) contact email

To cite this article:

Alkiki, R.A., Khalid, K.A. & Alhadede, A.A.A. (2026). Pedogenic development and mineralogical characteristics of sedimentary soil pedons. *The Eurasia Proceedings of Science, Technology, Engineering and Mathematics (EPSTEM), 42,* 85-96.

The Eurasia Proceedings of Science, Technology, Engineering and Mathematics (EPSTEM)
ISSN: 2602-3199

The Eurasia Proceedings of Science, Technology, Engineering and Mathematics (EPSTEM), 2026

Volume 42, Pages 97-127

ICBASET 2026: International Conference on Basic Sciences, Engineering and Technology

Digital Transformation, Cocoa Downstreaming and Export Competitiveness

Dwi Putri Jeng Ivo Nurun Nisa
Gadjah Mada University

Jamhari Jamhari
Gadjah Mada University

Dwidjono Hadi Darwanto
Gadjah Mada University

Arini Wahyu Utami
Gadjah Mada University

Abstract: The global cocoa industry is changing dramatically, with the supply chain facing disruptions, climate change challenges, sustainability demands, and an increasing demand for technology-enabled processing and value-added products. Indonesia must improve its cocoa export competitiveness by shifting away from raw commodity exports to higher-value processed products. The current study analyzes comparative advantage, export market dynamics, and downstreaming of Indonesian cocoa exports, focusing on cocoa beans (HS 1801) and cocoa butter, fat and oil (HS 1804) in selected European markets. The research adopts a quantitative descriptive approach using international trade data from the United Nations Commodity Trade Statistics Database (UN Comtrade) and the International Trade Center (ITC) Trade Map. To measure the comparative advantage of cocoa beans and cocoa butter, Revealed Symmetric Comparative Advantage (RSCA) is used, and Export Product Dynamics (EPD) is used to measure their market position in the Netherlands, Belgium, France, and Germany. A Downstreaming Index measures the proportion of cocoa butter exports to total cocoa bean and cocoa butter exports. Results suggest that cocoa butter has a stronger comparative advantage than cocoa beans in some European markets, while EPD shows different market positions across destination countries. The Downstreaming Index indicates a transition from raw cocoa beans to cocoa butter. Processing enabled by technology, digital traceability, quality management, and supply-chain integration may enhance downstream competitiveness and help to comply with sustainability-oriented market demands, the findings suggest. The study emphasizes the importance of the integration of cocoa downstreaming, technological upgrading and sustainable value chain development to improve Indonesia's position in the global cocoa trade and sustainable international markets.

Keywords: Digital transformation, Cocoa downstreaming, Cocoa industry

Introduction

Cocoa is a strategic plantation commodity in world agricultural trade, and it plays an important role in value addition, export revenue, and food industry development. However, the global cocoa industry is currently undergoing increasingly complex structural changes, driven by climate change, supply chain disruptions, price volatility, sustainability demands, and growing international market requirements. Such conditions stimulate cocoa-producing countries to focus not only on increasing the production of raw materials but also on improving supply chain efficiency, product quality, added value, and the ability to meet sustainability standards. Recent trends in the global cocoa market have highlighted the significance of supply chain resilience. The International

- This is an Open Access article distributed under the terms of the Creative Commons Attribution-Noncommercial 4.0 Unported License, permitting all non-commercial use, distribution, and reproduction in any medium, provided the original work is properly cited.

- Selection and peer-review under responsibility of the Organizing Committee of the Conference

© 2026 Published by ISRES Publishing: www.isres.org

Cocoa Organization (ICCO) said global cocoa production was well below demand in the 2023/2024 season while cocoa prices were at very high levels on the back of supply constraints and erratic weather conditions. These conditions create opportunities for producing countries, such as Indonesia, to improve their position in the global cocoa value chain via productivity improvements, processing, product diversification, and the ability to improve export competitiveness.

Conversely, the cocoa trade is increasingly fueled by demand for sustainability and more transparency in the supply chain. One of the most important and, at the same time, hardest markets is the European market, which places increasing importance on traceability, product origin, and compliance with ecological standards. With the entry into force of Regulation (EU) 2023, the EU Deforestation Regulation (EUDR) has increased the need for commodity exporters, such as cocoa producers, to provide traceability information to ensure that products placed on the market are deforestation-free and meet legality requirements. As a consequence, the competitiveness of cocoa in the European market is not only related to the price and volume of exports but also to the ability of the business actors to establish a transparent and well-documented supply chain that meets the criteria of sustainability. These changes make technology increasingly important in the development of the cocoa industry. Post-harvest processing technology, fermentation, quality control, digital traceability systems, supply chain management, and market information exchange can support efficiency improvements while also producing higher value-added products. In the context of international trade, technological transformation allows producing countries to shift from raw material suppliers to higher-value processing activities. Therefore, cocoa's competitiveness in a sustainable economy must be understood as a combination of the ability to produce competitive products, carry out value-added processing, meet quality standards, and respond to market demands that are increasingly technology- and sustainability-based.

Indonesia is one of the world’s biggest cocoa producers and holds a strategic position in the global cocoa trade. However, the Indonesian cocoa sector has traditionally exported raw cocoa beans that have a relatively lower economic value compared to processed cocoa products. The Indonesian government has acknowledged this limitation and has ramped up downstream industrialization policies to enhance domestic value addition and to reduce reliance on raw commodity exports. Simultaneously, national cocoa development programs have focused on the rehabilitation and replanting of plantations, as many cocoa plantations are run by smallholder farmers with aging trees and decreasing yields. Better planting material, improved cultivation technology, and modern processing systems can be used to support sustainable production and industrial development (Ministry of Agriculture of Indonesia, 2024).

In response to these conditions, the Indonesian government has promoted cocoa downstreaming policies to boost domestic processing and reduce dependence on raw-material exports. These policies have changed the structure of Indonesia's cocoa exports. Zikria et al. (2019) found that after the policy change in 2010, Indonesia's cocoa bean exports decreased, while processed cocoa exports increased and showed greater expansion potential than cocoa beans. This indicates that downstream processing can be an important instrument for increasing domestic value addition. However, an increase in the share of processed products does not automatically mean Indonesia has gained strong and sustainable competitiveness in every target market. In other words, structural downstreaming needs to be distinguished from the success of downstreaming in creating sustainable export competitiveness. Recent studies show that sustainable cocoa production systems combining technological innovation and agroforestry practices have the potential to improve ecological and environmental performance and market competitiveness (Schroth et al., 2024; FAO, 2023).

Based on this gap, this research analyses the competitiveness and dynamics of Indonesian cocoa exports by comparing two product groups, namely cocoa beans (HS 1801) as the upstream product and cocoa butter, fat, and oil (HS 1804) as the processed product. The analysis covered four European markets: the Netherlands, Belgium, France, and Germany. Revealed Symmetric Comparative Advantage (RSCA) identifies comparative advantages more symmetrically, while Export Product Dynamics (EPD) identifies product positions based on market share developments and demand dynamics. The Downstreaming Index complements both approaches by illustrating changes in the export structure from cocoa beans to processed products. This approach allows the research to answer not only whether Indonesian cocoa has a comparative advantage but also whether that advantage persists in developing markets and whether changes in export structure indicate a greater orientation toward downstreaming. The analytical framework aligns with the research design in the article, which specifically compares HS 1801 and HS 1804 using RSCA, EPD, and the Downstreaming Index. Thus, the contribution of this research lies in the integration of comparative advantage, market dynamics, and downstream structure within a single framework for analysing Indonesian cocoa exports. Unlike previous studies that primarily assessed competitiveness or the impact of downstream policies separately, this research compares the performance of upstream and downstream products while considering the characteristics of the European target market. The

subsequent analysis results are interpreted in the context of technological transformation, value addition, traceability, and sustainability demands. With this approach, the research is expected to provide a more comprehensive understanding of whether Indonesia's shift from exporting raw materials to processed products has resulted in a tangible and sustainable export upgrading.

Based on this background, this research aims to (1) analyze the comparative advantages of Indonesian cocoa bean and cocoa butter exports in the European market, (2) identify the dynamics and positions of both products in the Dutch, Belgian, French, and German markets, and (3) measure the development of downstream orientation through the Downstreaming Index. The research results are expected to inform downstream policy development, strengthen processing technology, improve quality and traceability, and support strategies to enhance the competitiveness of Indonesian cocoa in international trade, which is increasingly oriented toward sustainability.

Method

Research Design

This study employed a quantitative descriptive approach to analyze the competitiveness and market dynamics of Indonesian cocoa exports in the context of global economic transformation and technology-driven downstream industrialization. The analysis focused on cocoa beans and processed cocoa products exported by Indonesia to the international market. Secondary data were obtained from the United Nations Commodity Trade Statistics Database (UN Comtrade) and the International Trade Centre (ITC Trade Map), which provide comprehensive international trade statistics. The study utilized annual export data covering the period 2014–2024 for cocoa products classified under the Harmonized System (HS).

Research Framework

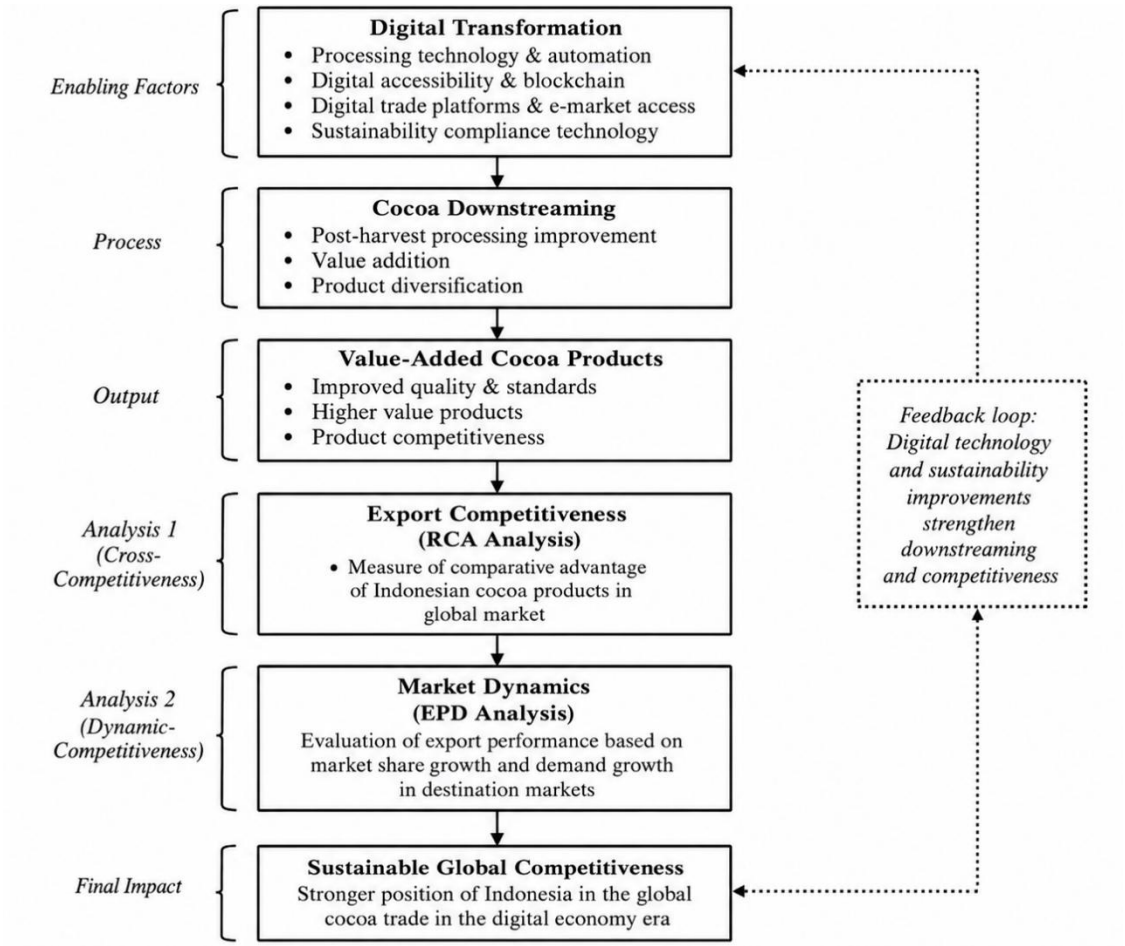

Figure 1. Research framework

This study adopts a quantitative descriptive approach to examine Indonesia's cocoa export competitiveness within the context of digital transformation, cocoa downstreaming, and sustainable agro-industrial development. The study is based on the premise that technological advancements in post-harvest processing, digital trade systems, supply chain management, and sustainability compliance contribute to the creation of higher-value cocoa products, which in turn affect export competitiveness and market dynamics.

The analytical framework assumes that digital and processing technologies do not directly determine export performance; rather, they facilitate downstream industrialization, increase value addition, improve product quality, strengthen traceability systems, and enhance access to international markets. These improvements are expected to be reflected in higher comparative advantage and stronger market positioning of processed cocoa products compared to raw cocoa beans.

Data Source

This study uses secondary data obtained from the United Nations Commodity Trade Statistics Database (UN Comtrade) and the International Trade Center (ITC) Trade Map. The analysis focuses on Indonesia's cocoa exports to selected European markets, namely the Netherlands, Belgium, France, and Germany, classified according to the Harmonized System (HS). The study specifically examines cocoa beans (HS 1801) as the primary raw cocoa product and cocoa butter, fat and oil (HS 1804) as the processed cocoa product. Export value data are collected for each product and destination market over the 2014–2024 observation period. The data are used to assess comparative advantage, export market dynamics, and the structural shift from raw cocoa beans toward processed cocoa through the Revealed Symmetric Comparative Advantage (RSCA), Export Product Dynamics (EPD), and Downstreaming Index approaches. The 2014–2024 period captures changes in Indonesia's cocoa export structure during the development of downstream industrialization and the growing adoption of digital trade and supply chain systems. Data from UN Comtrade provide the primary basis for international trade values, while ITC Trade Map is used as a complementary source for cross-checking and validating export statistics.

Data Analysis

To evaluate export competitiveness, the study applied the Revealed Comparative Advantage (RCA) index developed by Balassa (1965). RCA measures the comparative advantage of a country's export commodity relative to global trade performance. An RCA value greater than one indicates that the commodity possesses a comparative advantage and is internationally competitive.

$$RCA_{ij} = \left(X_{ij}/X_i\right) \Big/ \left(X_{wj}/X_w\right)$$

where X_{ij} represents Indonesia's export value of cocoa product j , X_{it} is Indonesia's total export value, W_j denotes world exports of cocoa product j , and W_t represents total world exports**.**

In this study, RCA is employed not only to evaluate competitiveness but also to identify whether downstream cocoa products demonstrate stronger comparative advantages than raw cocoa beans. Higher RCA values for processed products are interpreted as evidence of successful value addition supported by technological upgrading and industrial processing capabilities. However, the RCA index has several weaknesses, including: the values are not symmetrical; the comparisons between countries or between commodities are not proportional/unbalanced. In addressing the issue, the symmetric comparison index has been used. The RSCA index is formulated as follows :

$$\mathrm{RSCA}_{ij} = \frac{\mathrm{RCA}_{ij} - 1}{\mathrm{RCA}_{ij} + 1}$$

Explanation: RCA_{ij}= RCA Index for country i, commodity j. Interpretation of RSCA Value: RSCA > 0, The country has a comparative advantage in that commodity; RSCA < 0, The country does not have a comparative advantage; RSCA = 0, Neutral (threshold point of advantage).

To complement the competitiveness analysis, Export Product Dynamics (EPD) was employed to examine the dynamics of Indonesia's cocoa export position in the global market. EPD evaluates export performance based on growth in export market share and product demand in destination markets. The results are classified into four

categories: *Rising Star*, *Falling Star*, *Lost Opportunity*, and *Retreat*. This method enables the identification of market opportunities and the strategic positioning of cocoa products in international trade. EPD evaluates export performance using two dimensions: Growth of Indonesia's export market share. Growth of product demand in destination markets. Based on these dimensions, products are classified into four categories:

Y-Axis: Growth of Market Share

$$\frac{\sum_{t=1}^{t}\left(\left(\frac{X_{ij}}{W_{ij}}\right)_t \times 100\% - \left(\frac{X_{ij}}{W_{ij}}\right)_{t-1} \times 100\%\right)}{T}$$

Explanation: X_{ij} = total export value of Indonesia to the European Union market; W_{ij} = total world export value to the European Union market.

X-Axis: Growth of Export Share

$$\frac{\sum_{t=1}^{t}\left(\left(\frac{X_{aj}}{W_{aj}}\right)_t \times 100\% - \left(\frac{X_{aj}}{W_{aj}}\right)_{t-1} \times 100\%\right)}{T}$$

Explanation: X_{aj} = the export value of cocoa commodities (beans/processed) from Indonesia to the European Union market; W_{aj} = the export value of cocoa commodities (beans/processed) from the world to the European Union market. Based on these dimensions, products are classified into four categories:

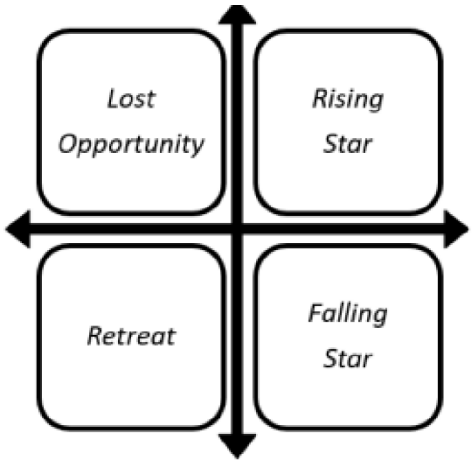

Figure 2. Export product dynamics (EPD) matrix

Within this study, the EPD classification is interpreted within the framework of digital transformation and cocoa downstreaming. Products classified as Rising Star indicate that Indonesia has successfully increased its market share in expanding markets through value-added processing, technological innovation, and improved product quality. Falling Star products suggest that Indonesian cocoa products remain competitive despite declining market demand, reflecting the industry's ability to maintain market presence through efficiency and technological adaptation. Lost Opportunity products indicate that the industry has not fully captured growing market potential, highlighting the need for further technological upgrading, innovation, and market responsiveness. Meanwhile, products categorized as Retreat reflect declining competitiveness in shrinking markets, underscoring the need to strengthen downstream industrialization, digital integration, and sustainable production systems to improve future export performance.

Interpretation of Digital Transformation and Downstreaming Effects

The combined application of RCA and EPD provides a comprehensive assessment of both static competitiveness and dynamic market performance. Furthermore, the results were interpreted within the broader framework of cocoa downstreaming, technological transformation, and sustainable agro-industrial development to evaluate how value-added processing contributes to Indonesia's export competitiveness in the global sustainable economy. The results of RCA and EPD are subsequently interpreted within the framework of digital economic transformation

and sustainable cocoa industrialization. Rather than measuring technology directly, this study uses competitiveness and market dynamics as outcome indicators of structural changes associated with technology adoption.

A higher competitiveness level of processed cocoa products relative to cocoa beans is interpreted as evidence that technological upgrading in processing activities, quality management, traceability systems, and supply chain efficiency contributes to strengthening Indonesia's position in global cocoa markets. Furthermore, the EPD results are used to identify whether downstream products benefit from evolving market preferences associated with sustainability standards, digital traceability requirements, and environmentally friendly production systems. The X-Model Potential Export Products method is a method that combines the results of the Vollrath Index with the Export Product Dynamic (EPD) results to generate a grouping of potential export products to specific countries. Here is the clustering of the X-Model Potential Export Product.

Table 1. Combination of RSCA and EPD matrix

RSCA	*Export Product Dynamic* (EPD)	X-Model
RSCA > 0	Rising Star	Optimistic Market Development
	Lost opportunity	Development of Potential Markets
	Falling star	Development of Potential Markets
	Retreat	Development of Less Potential Markets
RSCA < 0	Rising Star	Development of Potential Markets
	Lost opportunity	Development of Less Potential Markets
	Falling star	Development of Less Potential Markets
	Retreat	Development of Non-Potential Markets

Source : Nurhayati *et al*. (2019)

Downstreaming Index

This study proposes a Downstreaming Index (DI) to quantify the downstreaming level of Indonesia's cocoa exports by calculating the ratio of processed cocoa butter exports to total cocoa beans and cocoa butter exports. The index captures the structural shift from upstream raw cocoa beans (HS 1801) toward a higher value-added processed cocoa product, namely cocoa butter, fat, and oil (HS 1804). The Downstreaming Index is calculated using the following formula:

$$DI_{ct} = \frac{X_{1804,ct}}{X_{1801,ct} + X_{1804,ct}}$$

where denotes the Downstreaming Index of Indonesia's cocoa exports to the destination country in year ; denotes the export value of cocoa butter, fat, and oil (HS 1804) from Indonesia to the destination country in year ; and denotes the export value of cocoa beans (HS 1801) from Indonesia to the destination country in year . Export values are expressed in US dollars and sourced primarily from UN Comtrade, with the ITC Trade Map used for complementary data validation.

The index ranges from 0 to 1 and can also be expressed as a percentage. A higher DI indicates that a larger proportion of Indonesia's combined exports of cocoa beans and cocoa butter consists of the processed product (HS 1804), indicating a stronger downstream orientation in the destination market. Conversely, a lower DI indicates that exports are relatively more concentrated in cocoa beans (HS 1801), reflecting a stronger upstream orientation.

For example, a DI value of 0.75 indicates that 75% of Indonesia's combined exports of cocoa beans and cocoa butter to a particular destination in a given year consist of cocoa butter. The index is calculated for each destination market—Netherlands, Belgium, France, and Germany—and for each year during the 2014–2024 observation period. The resulting index is subsequently used to describe changes in Indonesia's cocoa export structure and to complement the analysis of comparative advantage and export market dynamics.

Results and Discussion

Comparative Advantage of Indonesian Cocoa Products

The RSCA analysis highlights the difference in competitiveness between cocoa beans (HS 1801) and processed cocoa products. The results indicate that in the case of processed cocoa products, positive RSCA values are consistently greater than the raw cocoa bean which indicates a greater comparative advantage in international markets. The research results showed that the competitiveness of Indonesia is more to the in value-added value-added cocoa products, not primary commodity. This study is to analyze the comparative advantage of Indonesian cocoa products in the international market with Revealed Symmetric Comparative Advantage (RSCA) index.

Compared to the conventional Revealed Comparative Advantage (RCA) index, RSCA symmetrically scales the RCA values in the range of [−1, +1]. This avoids asymmetry, and provides a better comparison of commodities against each other, and over time. Positive values of the RSCA suggest a comparative advantage while negative values of the RSCA suggest a comparative disadvantage. These results provide some empirical evidence on structural transformation of cocoa sector in Indonesia. One example of how downstream industrialization policies are being applied to increase the domestic value added and improve export competitiveness is the shift from exporting raw cocoa beans to processed cocoa products. Industrial upgrading can help countries to move up the global value chains by moving from exporting primary commodities to higher value-added processing activities (Gereffi & Fernandez-Stark, 2016).

The competitive advantage of processed cocoa products is closely linked to technological upgrading in the cocoa value chain. The competitiveness of processed cocoa products is closely linked to the technological upgrading of the cocoa value chain. Technological upgrading in the cocoa value chain is an important factor in the competitive advantage of processed cocoa products. Modern processing technologies, quality assurance systems, digital traceability and innovations in the supply chain allow companies to produce products that satisfy the increasingly demanding requirements of the international market. As global buyers seek greater transparency, sustainability and quality of products, these technologies have become important. The RSCA analysis has been applied to cocoa beans (HS 1801) and several processed cocoa products in an effort to identify the structural shifts of the export competitiveness of Indonesia during the period of observation. The analysis compares the comparative advantages of raw and processed cocoa products to provide insights on the effectiveness of cocoa downstreaming strategies and how far value-added activities could help to strengthen Indonesia's position in the global markets. The results of RSCA are shown in Figure 3.

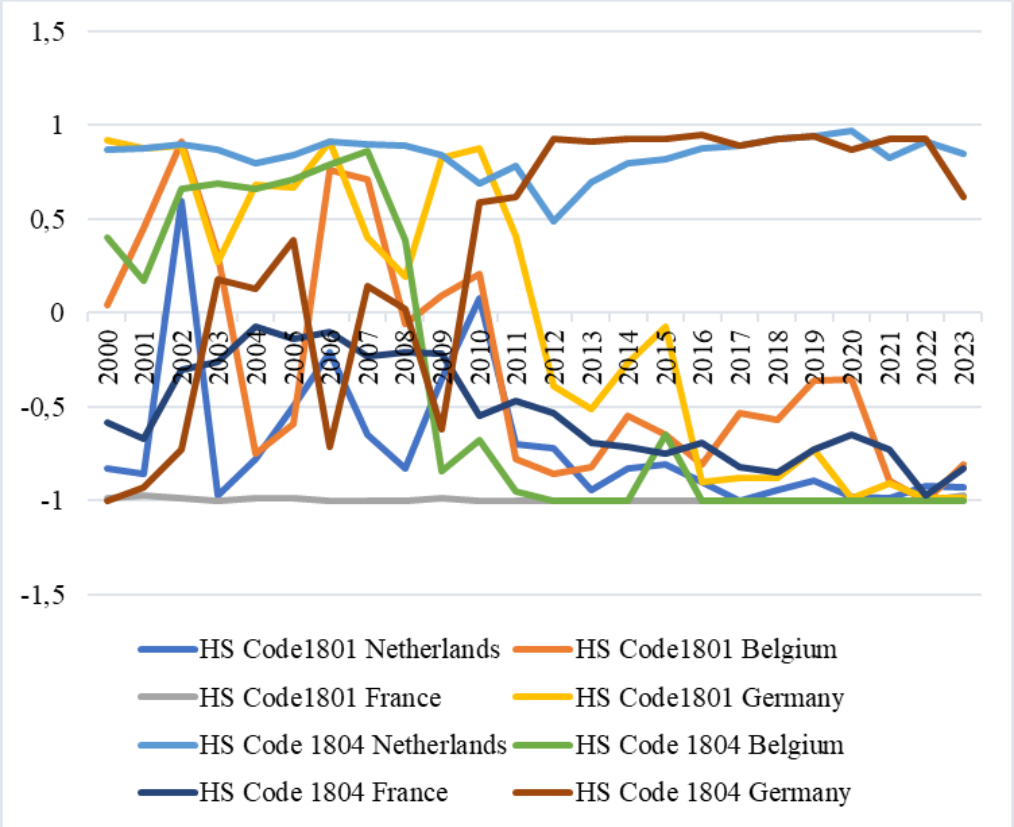

Figure 3. Graph of RSCA main destination countries for Indonesian cocoa

The RSCA analysis shows that in most of the destination markets in Europe, cocoa butter (HS 1804) has a higher comparative advantage than cocoa beans (HS 1801). The continued positive values of the RSCA of cocoa butter showed that Indonesia has built a more competitive position in processed cocoa products compared to raw cocoa exports. The finding suggests that downstream processing activities and value-added production are at the heart of the export competitiveness of the country.

The shift from cocoa bean exports to cocoa butter exports is one example of a more general transformation in global agricultural value chains. According to Amfo et al. (2023) the competitiveness of the agricultural commodity markets is increasingly determined by a country's ability to develop value-added products rather than the export of primary commodities. Usually, agricultural products are more profitable and less sensitive to fluctuations in world commodity prices.

The higher comparative advantage of cocoa butter also points to the successful implementation of the downstream industrialization strategy in Indonesia. Indonesia can increase its share of value creation in the cocoa value chain by increasing domestic processing capacity. Similar findings were reported by Effendy et al. (2019) that agro-industrial upgrading significantly contributes to export competitiveness by increasing product diversification, industrial productivity, and market adaptability.

Cocoa butter performance has improved through improved processing technologies, quality management systems, and industrial innovations. Making cocoa butter is more difficult than producing raw cocoa beans. It requires extraction technologies. It needs to be quality-standardized. High industrial processing efficiency. One of the most important determinants of the competitiveness of agro-processing industries is technological upgradation. It helps companies to be more efficient, lower the cost of production, and comply with international quality standards (Ndlovu & Thamaga-Chitja, 2023).

Cocoa butter's competitiveness is closely related to the digital transformation of agricultural value chains. Overseas buyers are increasingly driving demand for digital traceability, transparency in supply chains and verification systems for sustainability. Digital technologies enable the tracking, certification and dissemination of information along the supply chain, and improve market access and consumer confidence. Digitalization is becoming increasingly important for the improvement of transparency and competitiveness of global agri-food systems, especially in export-oriented sectors (Kamilaris et al., 2021).

Furthermore, the declining comparative advantage of cocoa beans in European markets may reflect a changing pattern of demand in the world cocoa market. Chocolate manufacturers are using semi-processed or processed cocoa inputs and this is reducing transaction cost and improving the efficiency of production. Similar trends have also been reported by Voora et al. (2023) who indicate that value capture in the current cocoa markets is increasingly concentrated in downstream segments where processing, branding, quality differentiation and sustainability certification are located. The decline of comparative advantage of cocoa beans in some European markets may be another indication of changing structures of demand in the world cocoa industry. "We are seeing more and more chocolate makers going into semi-processed, processed cocoa inputs. These commodities cut down the transaction price and efficiency in the production. Voora et al. (2023) further note these trends, citing the current cocoa markets are characterized by an increasing concentration of value capture in the downstream segments, where processing, branding, quality differentiation and sustainability certification take place.

These results are especially relevant for the implementation of sustainability-oriented regulations such as the EU Deforestation Regulation (EUDR). Exporting countries need to demonstrate traceability, transparency and sustainable sourcing practices to be able to comply with EUDR. Historically, these requirements have favored countries with more advanced technology capabilities and more integrated supply chain systems. Sustainability requirements are increasingly becoming a major competitive advantage in global agricultural value chains, especially for commodities going to European markets (Tröster and Staritz 2023).

Overall, the results of RSCA show a gradual shift of comparative advantage in Indonesia from exports of raw cocoa to exports of processed cocoa products. The empirically higher RSCA values of cocoa butter from the global cocoa market demonstrate that competitiveness is increasingly determined by downstream industrialization, technological upgrading, digital transformation, and sustainability compliance.

This finding is consistent with the study by Neilson, Wright, and Aklimawati (2020) who argue that the creation of value in agricultural commodity chains depends more and more on the integration of technology, quality standards and market governance mechanisms. Moreover, Aung and Chang (2014) illustrate that traceability

systems and technology innovations play a significant part in increasing competitiveness by increasing product quality, food safety and market access.

Higher RSCA values of processed cocoa products further support recent evidence that downstream processing creates more economic benefits than raw commodity exports. Fold and Neilson (2016) argue that by participating in higher stages of agricultural value chains, producing countries can capture more value and reduce their vulnerability to fluctuations in global commodity prices. Thus, the comparative advantage of Indonesian processed cocoa products could be interpreted as the outcome of successful downstream industrialization, supported by technological development and value-added production.

Export Product Dynamics (EPD) of Indonesian Cocoa Exports in the European Market

The Export Product Dynamics (EPD) analysis was conducted to assess the dynamic position of Indonesian cocoa exports to four major European destination markets, namely the Netherlands, Belgium, France and Germany in the period 2000-2023. EPD is a popular tool for evaluating export performance by combining two dimensions of market attractiveness and business strength. The resulting matrix classifies export performance in four categories: Rising Star, Falling Star, Lost Opportunity and Retreat. The best position is Rising Star, which means that a country's export market share is increasing in a growing market. The EPD matrix indicates that the Netherlands and France belong to the Rising Star quadrant, while Belgium and Germany are in the Falling Star quadrant.

The Netherlands is in the Rising Star quadrant." Indonesia has managed to win its share of the export market in an expanding market. This is evidence that the Netherlands is one of the biggest cocoa trading and processing centers in Europe. The country has a large cocoa processing industry and is one of the main entry points for cocoa into the European Union through the Port of Rotterdam. The increasing share of Indonesian cocoa products in the Dutch market shows that Indonesian cocoa products are still competitive and relevant in the European value chains. Fold and Neilson (2016) obtained similar results, and stressed the importance of integration into global value chains for the competitiveness of agricultural commodity exports. Moreover, competitiveness on international cocoa markets is increasingly determined not only by production capacity but also by the ability to meet the quality standards, traceability requirements and sustainability criteria imposed by European buyers (Voora et al., 2019).

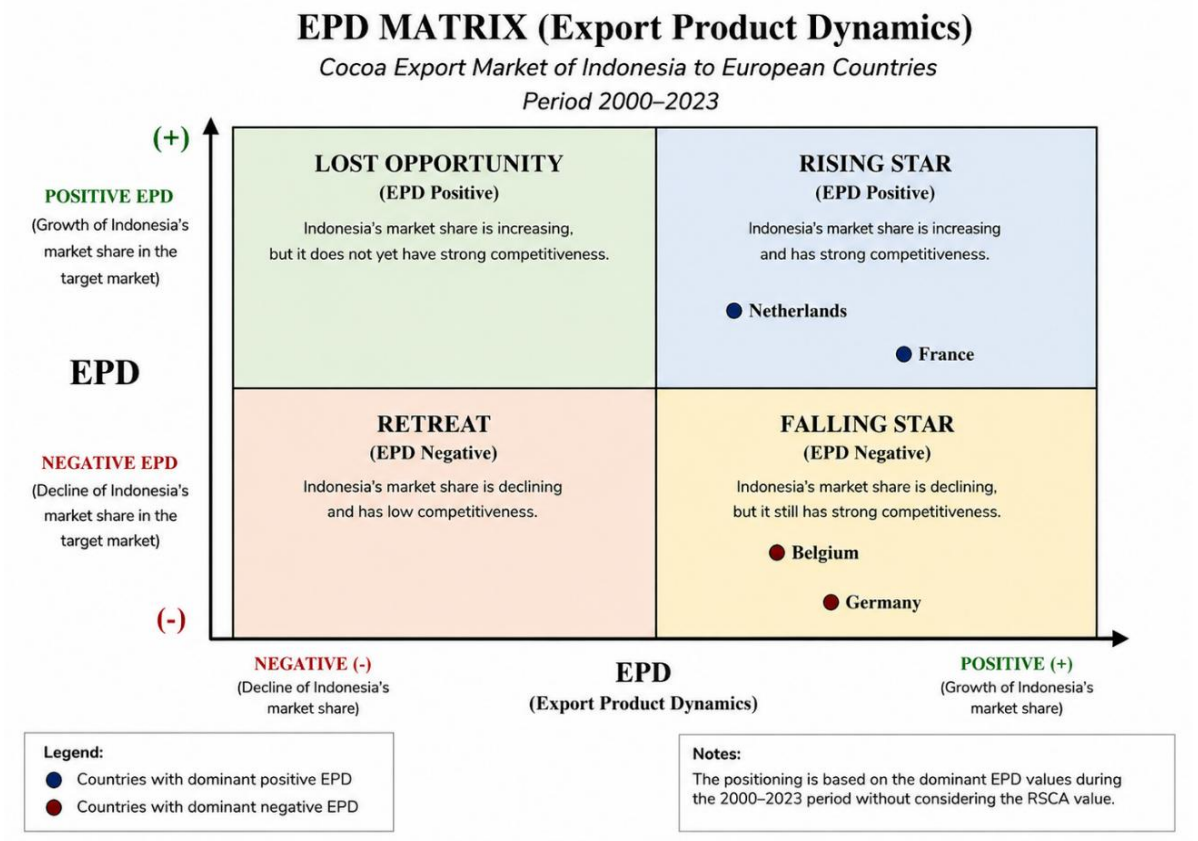

Figure 4. EPD matrix for HS code 1801

France also displays a similar pattern and is also considered a Rising Star market. The dominance of this category proves that Indonesian cocoa exports have been able to take an increasing share of the market with rising demand. This is especially important as France is a high-value consumer market with increasing demand for premium chocolate and sustainably sourced cocoa products. The positive performance in France can be explained by better product quality, a greater involvement in downstream processing of cocoa and a growing adaptation to changing consumer preferences. "European cocoa markets are increasingly driven by sustainability, product differentiation and traceability requirements, which create opportunities for exporters able to provide higher value-added products (Lambin et al., 2023)." The rising star position of France has seen Indonesian cocoa exporters relatively successful in responding to these market transformations.

By contrast, Belgium is mostly categorized as a Falling Star market. This position suggests that the Indonesian cocoa market position is still relatively strong, but its market share growth has slowed relative to overall market developments. Belgium is one of the world's leading countries in cocoa processing and chocolate manufacturing, making it a highly competitive destination market. A Falling Star position could imply Indonesian cocoa is facing increasing competition from big producers like Ivory Coast, Ghana and Ecuador, which together make up the global cocoa exports. West African countries still dominate the world's supply of cocoa beans, which means that there is fierce competition for supplies in the main European processing markets (International Cocoa Organization (ICCO, 2024). Therefore, to increase the export figures in Belgium more differentiated strategies are needed, particularly through sustainability certification, quality improvement and the export of processed cocoa.

Belgium, however, is mainly classified as a Falling Star market. The position shows the position of Indonesian cocoa market is still strong enough, but the growth of the market share is slowing down along with the development of the whole market. Belgium is one of the world's leading countries in processing cocoa and manufacturing chocolate, which makes it a very competitive destination market. The position of a Falling Star may mean Indonesian cocoa is having a hard time with the increasing competition from the big producers like Ivory Coast, Ghana, and Ecuador, which are the world's cocoa exporters. West African countries continue to dominate the global supply of cocoa beans, so there is a fierce competition for supplies in the major European processing markets (International Cocoa Organization (ICCO, 2024). Therefore, more differentiated strategies are needed to increase export figures in Belgium, especially through sustainability certification, quality improvement, and export of processed cocoa.

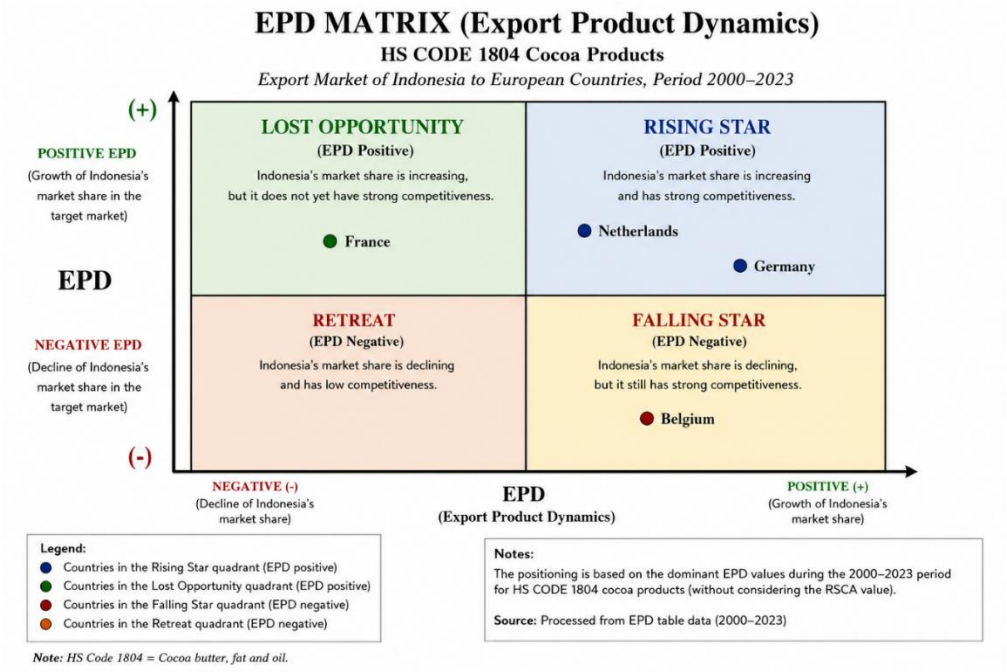

Figure 5. EPD matrix for HS code 1804

Overall, EPD results show that the competitiveness of Indonesian cocoa exports in the European destination markets is uneven. The Rising Star positions in the Netherlands and France are opportunities for market expansion, while the Falling Star positions in Belgium and Germany indicate the need for strategic measures to preserve the export performance. These results are consistent with the proposition that the long-term competitiveness of the

global cocoa market increasingly depends on moving beyond raw commodity exports to higher value-added processed products, sustainability certification, and integration into global value chains (Kaplinsky & Morris, 2016; Voora et al., 2019). From a policy standpoint, the emphasis for Indonesia should be on market consolidation strategies in the Netherlands and France by enhancing trade partnerships, broadening downstream cocoa exports, and guaranteeing compliance with European sustainability standards. At the same time, efforts to restore market dynamism in Belgium and Germany should focus on more product differentiation, promotion of certified sustainable cocoa and productivity improvements along the entire domestic cocoa value chain. Such measures are expected to build up Indonesia's resilience and competitiveness in the increasingly demanding European cocoa market.

The Export Product Dynamics (EPD) analysis of Indonesian cocoa butter (HS Code 1804) reveals heterogeneous market dynamics for the main European destination countries in the period 2000-2023. The Netherlands and Germany are in the Rising Star quadrant according to the prevalent EPD classifications, Belgium is in the Falling Star quadrant, and France is in the Lost Opportunity quadrant. These results show that the performance of Indonesian cocoa butter exports differs significantly between European markets, reflecting differences in market attractiveness, competitive positions, and the ability of Indonesian exporters to respond to changing market demands.

Indonesia's position in the Rising Star quadrant indicates that Indonesian cocoa butter exports have been successful in gaining market share in a fast-growing market. This finding is in line with the strategic position of the Netherlands as the largest European importer and processor of cocoa. The Dutch cocoa industry is an important gateway for cocoa products into the EU, due to sophisticated logistics infrastructure, significant processing capacity, and a high degree of integration in global value chains. Thus, the Rising Star position indicates that Indonesian cocoa butter has been able to improve its competitiveness and at the same time, it has also benefited from the expanding market demand. This supports the argument of Fold and Neilson (2016) that participation in global value chains is a key determinant of export competitiveness in agricultural commodity markets. In addition, the Netherlands has emerged as a center for value-added processing of cocoa, providing opportunities for exporters who can provide semi-processed cocoa products such as cocoa butter, instead of raw cocoa beans (Voora et al., 2019).

A similar story is apparent in Germany, another Rising Star market. Germany is one of the largest consumers and processors of cocoa products in Europe and has a well-developed confectionery and chocolate manufacturing industry. The Rising Star position shows that Indonesia has not only maintained but gained market share in a market with positive growth. This shows that German processors have accepted Indonesian cocoa butter which could be due to improvements in the quality of the product, continuity of supply and growth of the domestic cocoa-processing industry in Indonesia. Demand for processed cocoa products in Europe has continued to grow, particularly among manufacturers seeking to source reliable cocoa ingredients to produce high-value chocolate (International Cocoa Organization, ICCO, 2024). Positive performance in Germany therefore reflects the growing importance of Indonesia's downstream cocoa sector in international markets.

In contrast, Belgium is positioned in the Falling Star quadrant, indicating that although Indonesian cocoa butter continues to maintain a presence in the market, its market share growth has not kept pace with overall market developments. Belgium is globally recognized as one of the leading chocolate-producing countries and hosts numerous multinational chocolate manufacturers. The Falling Star classification suggests that Indonesian cocoa butter faces increasing competitive pressure from major cocoa-processing countries and suppliers, particularly those with stronger integration into European supply chains. Previous studies have demonstrated that competitiveness in processed cocoa markets is increasingly influenced by factors beyond price competitiveness, including product quality, sustainability certification, traceability, and compliance with environmental standards (Lambin et al., 2018; Araujo et al., 2023). Therefore, maintaining and expanding Indonesia's position in Belgium will require stronger efforts to enhance value-added production and compliance with sustainability requirements.

Meanwhile, France is in the Lost Opportunity quadrant, which indicates that although the market is growing positively, Indonesia has not been able to fully capitalize on the increasing demand. The finding points to a latent export potential in the French market. Lost Opportunity conditions are usually identified when market demand rises but exporters are unable to increase their market share because of limited competitiveness, lack of market penetration or poor adaptation to consumer preference. "France is one of the largest premium chocolate markets in Europe where consumers increasingly seek sustainability, product origin, quality assurance and ethical sourcing practices. Fountain and Huetz-Adams (2020) find that European consumers are increasingly sensitive to sustainability-related attributes in cocoa and chocolate products with challenges and opportunities for exporting countries. Thus, the Lost Opportunity position of France implies that Indonesia has not fully exploited the market

developments, given the favorable demand conditions.Meanwhile, France is in the Lost Opportunity quadrant, which indicates that although the market is growing positively, Indonesia has not been able to fully capitalize on the increasing demand. The finding points to a latent export potential in the French market. Lost Opportunity conditions are usually identified when market demand rises but exporters are unable to increase their market share because of limited competitiveness, lack of market penetration or poor adaptation to consumer preference. "France is one of the largest premium chocolate markets in Europe where consumers increasingly seek sustainability, product origin, quality assurance and ethical sourcing practices. Fountain and Huetz-Adams (2020) find that European consumers are increasingly sensitive to sustainability-related attributes in cocoa and chocolate products, with challenges and opportunities for exporting countries. Thus, the Lost Opportunity position of France implies that Indonesia has not fully exploited the market developments, given the favorable demand conditions. More broadly, the EPD results indicate that downstream industrialization is becoming more important for increasing Indonesia's export competitiveness. As a semi-processed product, cocoa butter has a much higher value-added content and is more integrated in global manufacturing networks than raw cocoa beans. The rise of the Netherlands and Germany as Rising Star markets shows that Indonesia's cocoa-processing policies have had positive effects, by increasing its share in the higher stages of the cocoa value chain.

Finally, the EPD analysis shows that Indonesian cocoa butter exports have developed better market dynamics than traditional raw cocoa exports in some European markets. The Rising Star statuses for the Netherlands and Germany indicate good opportunities for further growth. Conversely, the Falling Star and Lost Opportunity positions of Belgium and France point to potential areas for strategic intervention. In an effort to maintain its competitiveness over the long term, Indonesia needs to keep strengthening its cocoa processing industry, improve the quality of its products, broaden the scope of sustainability certification schemes and enhance compliance with new European regulations such as the European Union Deforestation Regulation (EUDR). These measures are expected to improve market penetration and strengthen Indonesia's position in the global cocoa value chain.

Cocoa Downstreaming and Export Structure

To study the degree of the shift in the direction of Indonesia from exporting primary cocoa commodities to higher-value processed cocoa products, the downstreaming structure of Indonesian cocoa exports is evaluated. In this study, the relative contribution of cocoa butter, fat and oil (HS 1804) to the total exports of cocoa beans (HS 1801) and cocoa butter is measured using the Downstreaming Index (DI) . A higher DI implies a larger share of processed cocoa products in the export structure, suggesting a higher level of downstream processing, whereas a lower DI implies a greater dependence on raw cocoa bean exports. It provides an important insight into the upgrading of Indonesia's exports by complementing the analysis of comparative advantage and the dynamics of export markets. The change in the Downstreaming Index in the selected European markets is shown in Figure 6.

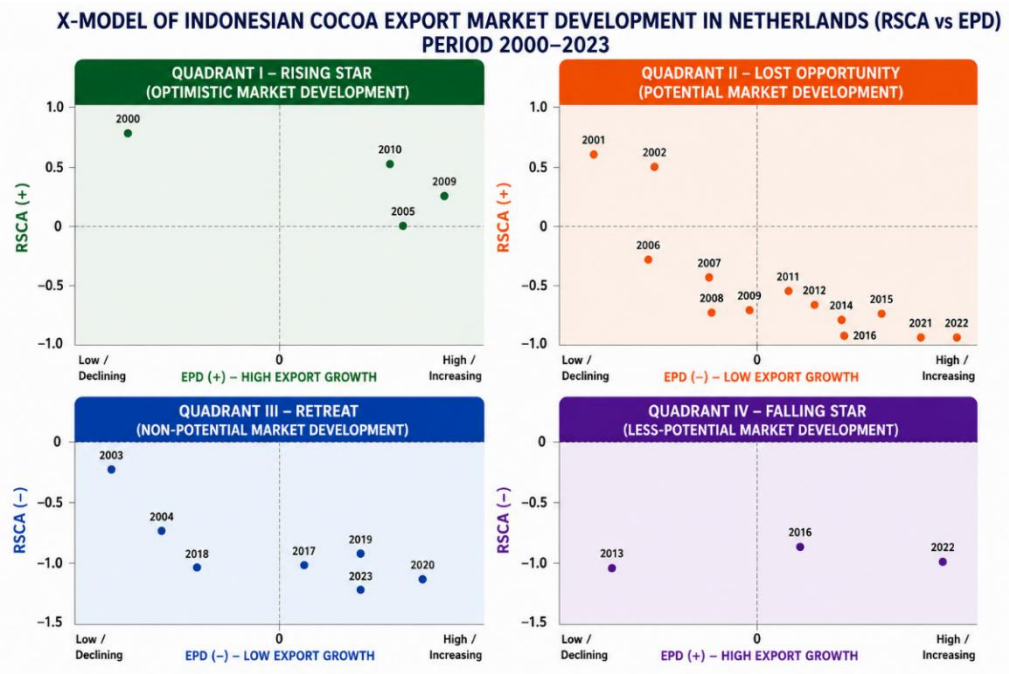

(a)

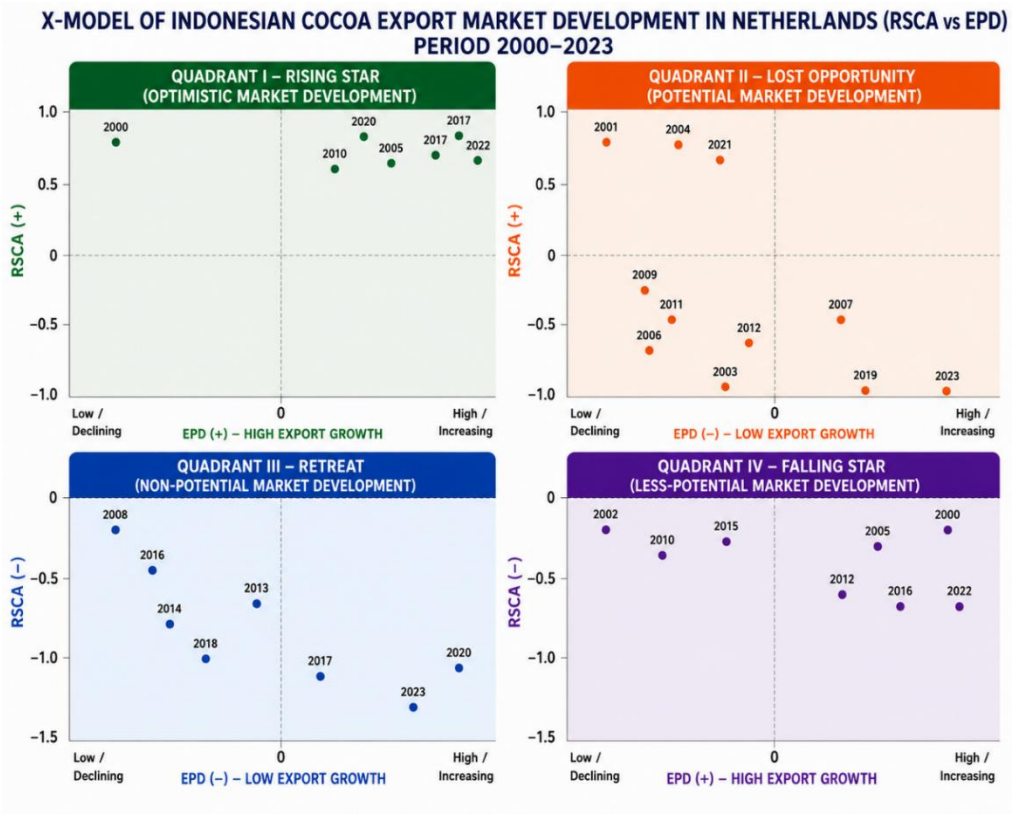

(b)

Figure 6. X-model of Indonesian cocoa export market development in the Netherlands, 2000–2023

Figure 6(a) shows the dynamic position of Indonesian cocoa exports in the Netherlands during 2000–2023 based on the interaction of Revealed Symmetric Comparative Advantage (RSCA) and Export Product Dynamics (EPD). The position map shows substantial changes in the competitiveness of Indonesia during the observation period. Indonesian cocoa has been moving in all four categories of the EPD, namely Rising Star, Lost Opportunity, Falling Star and Retreat. The result suggests that Indonesia's competitiveness in the Dutch cocoa market has been dynamic rather than persistent. This is in agreement with the proposition that export competitiveness must be assessed not only through the lens of comparative advantage, but also in terms of the ability of a product to maintain or improve its position in a dynamic international market. Fahmid et al. (2022) also show that for Indonesian cocoa, the comparative advantage and market position could be significantly different across destination markets. Thus, the competitiveness of Indonesia's cocoa is very market-specific.

The Rising Star quadrant is the most favorable competitive position because it has positive RSCA and positive EPD. This means that Indonesia has a comparative advantage and the related export market is growing. Indonesian cocoa was the Rising Star in 2002, 2004, 2005 and 2010 in the Netherlands. Among the observations, 2002 has a relatively high positive RSCA, indicating a stronger comparative advantage, while the observations for 2004 and 2005 remain positive but at a more moderate level. The 2010 observation is close to the RSCA threshold, indicating that the good position was quite fragile by then. These periods show that there were times when Indonesia was able to combine export specialization with positive market dynamics. Such a position is strategically important as it provides the opportunity to convert the existing comparative advantage into sustainable export growth through technological upgrading, quality improvement and value addition. Here, Gehl Sampath and Vallejo (2018) argue that participation in global value chains is not a sufficient condition for technological upgrading; instead, technological and innovation capabilities must be developed to be able to convert trade participation into higher-value export activities.

But the good Rising Star job didn't go all the way. For the years 2001, 2008, 2011, 2015, 2021 and 2022, observations are in the Lost Opportunity quadrant with positive EPD but negative RSCA. The Dutch market was doing well in terms of export. But Indonesia was at comparative disadvantage. These observations are especially significant as the RSCA values of the observations in 2015, 2021 and 2022 are well below zero, indicating the widening gap between market growth and Indonesia's comparative advantage. Therefore, Indonesia is in a situation where market opportunities exist but have not been translated into competitive gains enough. This is important because an increase in export growth in a destination market does not necessarily imply an increase in

competitiveness. Fahmid et al. (2022) also found that the relative competitive advantage of Indonesian cocoa is relatively low compared to other cocoa-producing countries, but there is still potential to develop the market in several destination countries. "This shows the need to upgrade product quality and downstream processing and not just rely on the existing export capacity."

2006, 2009, 2012, 2014, 2016 and 2017 with a positive EPD but a negative RSCA fall into the Falling Star quadrant. The position shows that Indonesian cocoa had relatively favorable market dynamics but no corresponding comparative advantage. Several Falling Star observations suggest that Indonesia experienced periods of market expansion, but these opportunities were not paralleled by a sufficient strengthening of export specialization. Economically, it might be a transient market opportunity rather than a structurally competitive advantage. In this sense, the results are in line with the findings of Yemima and Novianti (2020), who found that processed Indonesian cocoa can have a comparative advantage and at the same time can have an EPD position in the less advantageous categories, which shows that comparative advantage and market dynamics do not necessarily go in the same direction. That is to say, to be able to form a sustainable competitive position, market expansion must be accompanied by improvements in productivity, product quality, processing capacity and market access.

The Retreat quadrant is the weakest position compared to the standard, as both RSCA and EPD are negative. This third quadrant includes Indonesian cocoa in the years of 2003, 2007, 2013, 2018, 2019, 2020 and 2023. The clustering of observations in this quadrant toward the latter part of the study period is of particular importance. The observations show that in 2018, 2019, 2020 and 2023 Indonesia has a comparative advantage in the Netherlands, but also an unfavorable market dynamic. In particular, 2023 is the lowest RSCA position in the figure, which shows that Indonesia's relative advantage had substantially deteriorated at the end of the period of observation. This pattern suggests that the competitive position of Indonesia was not automatically maintained and that the structural characteristics of the cocoa export sector may have constrained the ability to maintain market competitiveness.

The decline in the latter period is linked to the structural problems of the Indonesian cocoa industry, particularly the challenges related to productivity, quality and limited value capture from downstream activities. In addition to improvements in the quality of cocoa beans, including fermentation, also required to improve the competitiveness of cocoa in Indonesia is the strengthening of downstream processing industries (Fahmid et al., 2022). Their findings indicate that there are still opportunities for market development, but Indonesia's comparative competitiveness in cocoa beans and processed cocoa lags well behind several rival producers. Thus, the Retreat-positions observed in the Netherlands should not be interpreted as a temporary decrease of exports, but as a sign of the need for a structural upgrading of the Indonesian cocoa value chain.

The overall distribution of observations reveals a clear shift from relatively favorable competitive positions in the earlier period toward less favorable positions in the later period. The period 2002–2010 includes several Rising Star observations, whereas after 2010 the observations increasingly appear in Lost Opportunity, Falling Star, and Retreat categories. In particular, the period from 2018 to 2023 is marked by negative RSCA positions, where 2018, 2019, 2020, and 2023 are classified as Retreat, and 2021–2022 as Lost Opportunity. This pattern indicates that the challenge for Indonesia in the Dutch market is not only the absence of market demand, as several years still show positive EPD, but also the difficulty of translating the opportunities in the market into sustained comparative advantage.

This finding provides an important basis to understand the role of cocoa downstreaming in strengthening Indonesia's export competitiveness. Downstream processing of cocoa beans into processed products may improve the value captured in the domestic cocoa value chain but does not necessarily lead to upgrading. Van Huellen and Abubakar (2021) demonstrate that cocoa processing offers opportunities for functional upgrading in the Ghanaian cocoa sector, although these may be limited by the structure and concentration of global value chains. To summarize, processing capacity needs to be complemented with stronger technological capabilities, market access, and control over higher-value functions to increase the value added from cocoa exports.

The structure of the world cocoa trade is a good example of downstreaming. It is estimated that seven transnational traders' control 62% of global cocoa export volumes, revealing a highly concentrated global cocoa trade system and uneven traceability and sustainability commitments across the supply chain (Parra-Paitan et al., 2023). This concentration may limit the ability of producing countries to capture more value and may increase the importance of technological, institutional, and traceability capabilities to access higher value international markets. The Netherlands' fall in position on the map therefore indicates that Indonesia has to shift from a comparative

advantage based mainly on the availability of raw materials to value-added processing, quality upgrading, digital traceability, and supply-chain integration.

Overall, the Netherlands position map shows that Indonesian cocoa competitiveness is dynamic, market-specific, and not automatically maintained by comparative advantage. The presence of Rising Star positions in several past years indicates that Indonesia has the potential to achieve a favorable mix of comparative advantage and market growth. But the later move into Lost Opportunity, Falling Star, and especially Retreat indicates that these advantages have not consistently translated into continued market competitiveness. Thus, the results support the strategic importance of downstreaming as one of the strategies to improve Indonesia's cocoa export. Indonesia needs to move beyond just increasing the volume of cocoa exports and instead process more cocoa and move into higher-value cocoa products while also improving quality, traceability and sustainability performance. This direction is consistent with the direction taken by Fahmid et al. (2022) who acknowledge downstream processing and industrial development as important parts in strengthening Indonesian cocoa competitiveness in international markets.

Figure 6(b) presents the dynamic export position of Indonesian cocoa butter, fat and oil (HS 1804) in the Netherlands from 2000 to 2023 as a function of the interaction between Revealed Symmetric Comparative Advantage (RSCA) and Export Product Dynamics (EPD). The position map shows that the competitive position of Indonesian cocoa butter changed significantly over the period of observation, with observations falling into the Rising Star, Lost Opportunity, Falling Star and Retreat categories. The distribution shows that the Dutch market has not been a uniformly good competitive environment for Indonesian cocoa butter, despite the potential of the product as a higher-value derivative of cocoa beans. This result is in line with the general evidence that Indonesia's processed cocoa products have better export potential after the downstream processing policy of the country, but competitiveness depends on market conditions and product differentiation (Zikria et al., 2019).

The most favorable export position is the Rising Star quadrant, which has positive RSCA and positive EPD. In the Netherlands this number shows observations for 2000, 2006, 2007, 2009 and 2010 related to this quadrant. The periods indicate that Indonesian cocoa butter enjoyed comparative advantage and favorable export-market dynamics at the same time. The relatively high RSCA positions during 2006 and 2007, imply especially strong comparative advantage during these periods. However, the observations for 2009 and 2010 are positive, but are closer to the RSCA threshold.

The presence of several Rising Star observations is important because cocoa butter is a processed cocoa derivative, not a primary commodity. Thus, a favorable position for HS 1804 means that Indonesia has at times been able to turn its capacity to process cocoa into an internationally competitive export product. This interpretation is also supported by Zikria et al. (2019) who found that the export potential of Indonesia's processed cocoa products is higher than that of cocoa beans after the 2010 policy shift toward downstream processing. Their results also suggest that the policy reduced the share of expenditure on cocoa beans and increased the share of processed cocoa in world demand, indicating a structural shift toward higher value cocoa products.

This finding is also in accordance with the evidence from the Indonesian cocoa agro-industry that HS 1804 has continued to maintain comparative advantage in the international markets. One of the Indonesian cocoa products having a comparative advantage is cocoa butter, as stated by Dianawati et al. (2023). The product is at the commercial maturity stage, which means that the product has shifted from an emerging export activity to a more mature position in international trade.

The Lost Opportunity quadrant is a situation where EPD is positive, and RSCA is negative. In the figure, observations belonging to this quadrant are 2001, 2004, 2008 and 2012. This position suggests that the Dutch market had relatively good growth dynamics, but that Indonesia did not have a positive comparative advantage in cocoa butter at the same time. This implication is important in our interpretation of the export performance of Indonesia. A growing market does not necessarily mean that you are more competitive. Indonesia may have been exposed to increasing demand for cocoa butter but may have had limitations in capturing that demand versus competing suppliers. This can happen when exports are not growing fast enough to increase the relative specialization of the product, or when competitors are expanding faster.

This is especially important for processed cocoa. Competitiveness is not only determined by the availability of cocoa beans, but also by the efficiency of processing, quality of the product, its consistency, and the ability to meet the requirements of the buyer. Dianawati et al. (2023) mentioned that Indonesian cocoa products faced challenges in terms of quality, food safety, environmental standards, market access, and supply-chain efficiency.

The availability of downstream processing capacity does not guarantee sustained competitiveness in international markets.

The Falling Star quadrant combines negative RSCA with positive EPD and suggests that the product is experiencing relatively favorable market dynamics despite Indonesia's weak comparative advantage. The observations associated with this position in the figure are 2002, 2005, 2013, 2014, 2015, 2016, 2017, 2018, 2019, 2020, 2021, 2022 and 2023. Interestingly, most observations are concentrated in this category, especially in the later years. It means that although Indonesian cocoa butter was still available in the Dutch market, the market dynamics were not always in a coupling with the positive comparative advantage. This can be read as a market opportunity that has not yet been fully converted into structural competitiveness.

This pattern also points to the need to decouple the issue of the presence of exports from the issue of export competitiveness. Indonesian cocoa butter is not competitive with other exporting countries but can be a major processed export commodity. Recent evidence shows this with Indonesian cocoa derivative products such as cocoa butter and cocoa powder being very competitive in the major destination markets. But the level of competitiveness varies quite a lot across countries and products. RCA value for Indonesian cocoa butter is high in some major destination markets, indicating strong competitive potential of the product. The market performance is destination-dependent. The worst position is the Retreat quadrant where both RSCA and EPD are negative. In the figure some observations in this category are shown, especially in the second half of the observation period. This pattern is indicative of periods of weak relative specialization and adverse market dynamics of Indonesian cocoa butter in the Netherlands.

In particular, the increasing number of observations in the lower right part of the map is noteworthy. The observations show that Indonesian cocoa butter had to deal with both decreasing comparative advantage and negative market development. This pattern is more worrying than a temporary Falling Star position because it indicates that Indonesia was not only weak relative to competing exporters but also was operating in an unfavorable market environment.

The result indicates that downstreaming should be combined with a continuous process of upgrading technology and organization from a value chain perspective. Cocoa beans are processed into cocoa butter which is exported at a higher value. But for the cocoa processing industry to be competitive, it needs to improve the entire value chain. According to Dianawati et al., the Indonesian cocoa agro-industry can enhance its competitiveness through a good supply chain, market access, regulatory support, and stakeholder coordination. The position map shows that there is a potential for Indonesian cocoa butter to be competitive in the Netherlands, but this potential did not bring about a consistently good market position over the entire period 2000–2023. The presence of Rising Star observations indicates that Indonesia has the right combination of comparative advantage and positive growth in the market. The high number of observations for both Falling Star and Retreat in the later period suggests that HS 1804 was struggling more to compete.

This finding is very important especially for the downstream strategy of Indonesian cocoa. The evidence from Zikria et al. (2019) suggests that processed cocoa has more potential for export expansion than cocoa beans, which supports the strategic rationale for moving toward downstream products. However, the current EPD-RSCA results indicate that downstreaming per se may not be sufficient to ensure sustainable export competitiveness. The processed product must also have a comparative advantage, and respond to the specific growth dynamics of the destination market.

Therefore, the Netherlands is a market for Indonesian cocoa butter which has proven to have competitive potential, but this must be kept up with ongoing upgrades. Better processing technology, consistent product quality, supply chain efficiency and compliance with international technical and environmental requirements could help turn periods of market opportunity into more enduring Rising Star positions. This interpretation is in line with the global value-chain view of Indonesian cocoa, where competitiveness is not only determined by the processing activities, but also by the capability of domestic firms to effectively integrate into international production networks and meet the growing demands of the market (Dianawati et al., 2023).

Figure 7(a) shows the dynamic export position of Indonesian cocoa beans (HS 1801) in the Belgian market in 2000–2023 based on the interaction of Revealed Symmetric Comparative Advantage (RSCA) and Export Product Dynamics (EPD). The position map shows large swings in Indonesia's competitive position with the observations scattered across the Rising Star, Lost Opportunity and Retreat positions. Generally, the figure shows that Indonesia possessed relatively strong comparative advantage at different times in the early 2000s, but this advantage declined significantly in the subsequent years. The pattern is consistent with evidence that Indonesian cocoa has

enjoyed comparative advantage in European markets in the past, but that this has tended to diminish over time. For instance, Anggoro and Widyastutik (2016) found that the RCA value of Indonesian cocoa exports to European destinations was generally above one, but showed a downward trend, indicating that the existence of comparative advantage did not necessarily guaranty its persistence.

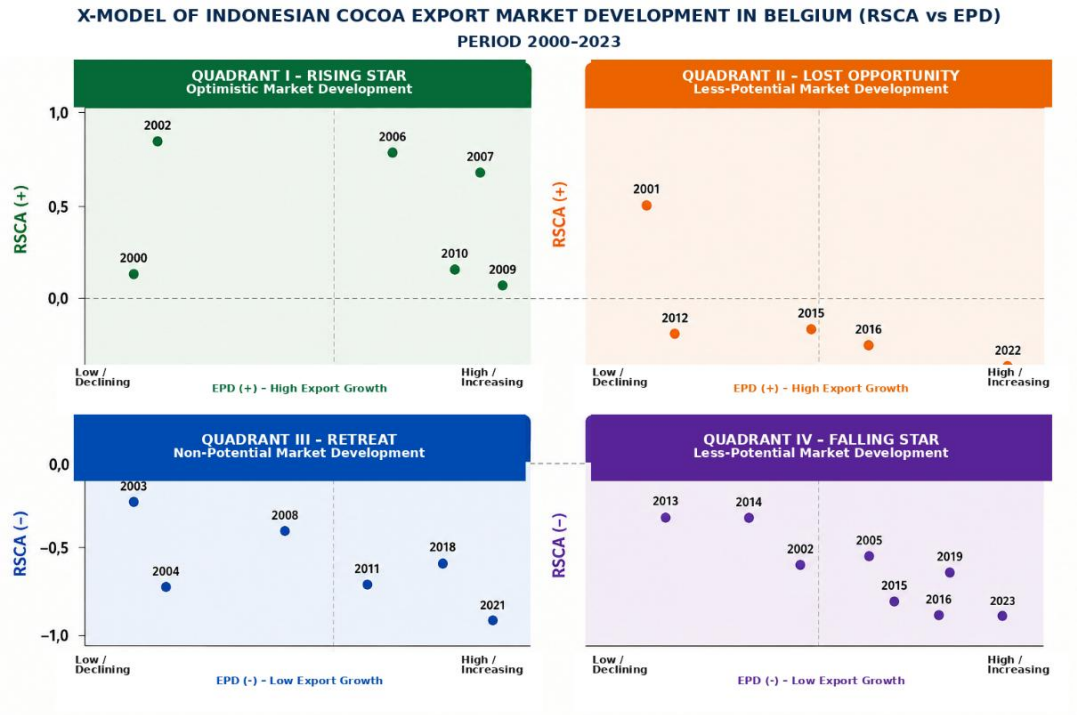

(a)

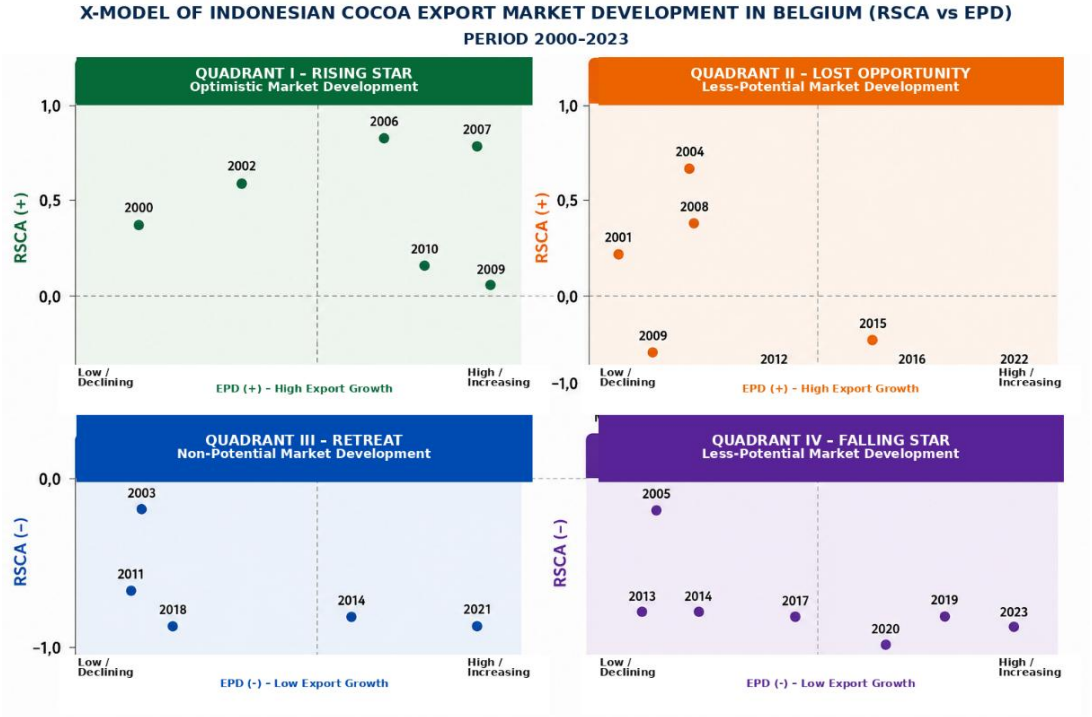

(b)

Figure 7. X-model of Indonesian cocoa export market development in Belgium, 2000–2023

The Rising Star quadrant is the best position to be in, with positive RSCA and positive EPD. This number places 2000, 2002, 2006, 2007, 2009 and 2010 in this quadrant in the Belgian market. Among these observations, 2002, 2006, and 2007 exhibit relatively high positive RSCA values, indicating a particularly strong comparative advantage in Indonesian cocoa beans. The observations for 2009 and 2010 remain positive but are considerably

closer to the zero line, suggesting that the strength of comparative advantage was already weakening toward the end of this favorable period. Thus, the early part of the observation period represents a period in which Indonesia was relatively successful in combining specialization in cocoa beans with favorable market development.

The Rising Star position is particularly important considering that Belgium is a major European hub for cocoa processing and chocolate production. Note that Belgium was a large exporter of chocolate and a large importer of cocoa beans at the same time. Cocoa beans are an important raw material to European processing industries. Their analysis also indicated that the relative competitiveness of Indonesia for cocoa beans was weaker than that of major producing countries, but there were opportunities in European markets. Hence, the Rising Star observations of Indonesia in Belgium point to periods in which its cocoa beans could tap on the demand created by Belgium's processing-oriented cocoa market.

2001, 2012, 2015, 2016 and 2022 form the Lost Opportunity quadrant. This position has a positive EPD but a negative RSCA. Thus, the Belgian market was still offering relatively attractive growth opportunities but Indonesia did not have a corresponding comparative advantage. The observations from 2015, 2016 and 2022 are of special interest because they combine relatively strong positive EPD with clearly negative RSCA. This implies that the problem was not so much the absence of market opportunities, but rather the inability of Indonesia's cocoa beans to translate those opportunities into a sufficiently strong relative competitive position.

This distinction is important because market growth and comparative advantage are not equivalent concepts. A product may be traded in a growing market while simultaneously losing relative competitiveness against competing suppliers. The Indonesian cocoa sector has faced precisely this type of challenge. Anggoro and Widyastutik (2016) found that Indonesian cocoa exports to Europe were affected by economic conditions, exchange rates, tariffs, and non-tariff barriers, while Indonesian cocoa competitiveness in European destinations tended to decline. Such restrictions may account for an inability to convert favorable market dynamics into improved comparative advantage.

The Retreat quadrant, where RSCA and EPD are negative, is the least desirable position. In this quadrant, we find 2003, 2004, 2008, 2011, 2018, and 2021 (see Figure). The results point to a low comparative advantage and discouraging market dynamics for Indonesian cocoa beans in Belgium. The subsequent observations, especially those from 2018 and 2021, are relevant because they suggest that the loss of competitiveness was not limited to the first part of the period but continued in the more recent years.

The Retreat position points to a problem of structural competitiveness and not just to a dip in export performance. Indonesia's cocoa sector has experienced problems related to productivity, quality and the structure of its export composition. A change in government policy on downstream processing has reduced incentives to export cocoa beans and has encouraged domestic processing. While this policy can increase value addition in the domestic front, it can simultaneously reduce the relative competitiveness and export presence of raw cocoa beans. Research on Indonesian cocoa competitiveness also shows that the downstreaming policy has been associated with a decrease in cocoa-bean exports and an increase in processed cocoa exports.

This point is particularly important for interpreting the negative RSCA values after 2010. RSCA for HS 1801 is declining, but that doesn't automatically mean that Indonesia's cocoa sector as a whole has failed. However, some of the decline might be a structural shift from exporting cocoa beans to processed cocoa products. This interpretation is supported by the German market evidence, where Indonesian cocoa beans had a weaker comparative advantage after the implementation of the export-duty policy, while processed cocoa products became more prominent. Thus, the declining competitiveness of HS 1801 may be partly due to downstreaming rather than only a decline in production capability.

However, the EPD results reveal that this structural transition constitutes a competitiveness challenge on markets where raw cocoa beans are still strongly demanded. The cluster of later observations in negative-RSCA positions suggests that Indonesia must ensure that adequate gains in higher-value processed products offset the decline in raw-bean exports. Thus, the loss of competitiveness in HS 1801 is economically significant only if it is not compensated by gains in competitiveness in HS 1804 and other processed cocoa products.

Figure 7(b) shows the dynamic export position of Indonesian cocoa butter, fat and oil (HS 1804) in the Belgian market from 2000 to 2023, considering the intersection of Revealed Symmetric Comparative Advantage (RSCA) and Export Product Dynamics (EPD). The distribution of observations in the position map shows that Indonesia's position in terms of competitiveness in cocoa butter has changed significantly over time. The earlier period shows a number of observations in the Rising Star quadrant, suggesting the simultaneous presence of competitive

advantage and a favorable market dynamic. However, the increasing number of observations with negative RSCA in the latter period indicates that Indonesia has had difficulties to maintain its relative competitive position in the Belgian market. This pattern suggests that the emergence of processed cocoa exports should not be seen only in terms of processing capacity, but also in relation to the organization and governance of the wider cocoa value chain.

The Rising Star observations, particularly those located in the upper-right area of the figure, indicate periods when Indonesian cocoa butter achieved both comparative advantage and favorable market dynamics. This is an important result because HS 1804 represents a processed cocoa product and therefore reflects a higher degree of value addition than cocoa beans. The existence of Rising Star positions demonstrates that Indonesia has been able to compete in a processed cocoa segment rather than relying exclusively on exports of primary cocoa commodities. Nevertheless, the subsequent movement away from this quadrant indicates that the competitive advantage was not automatically sustained.

One reason is that competitiveness of processed cocoa is dependent on coordination across the different stages of the value chain. Making cocoa butter is a combination of a good supply of quality cocoa beans, good processing, quality control, logistics and stable relationships with the buyers." Awafo and Owusu (2022) in their study on the cocoa value chain, reveal that processing is one of the links in a broader chain of production, post-harvest handling, certification, marketing and industrial activities and significant resources are needed in all these areas. They find that "positive changes in one part of the cocoa chain are not able to offset inefficiencies elsewhere in the system.

The Lost Opportunity observations are especially relevant because they indicate that there were periods of favorable market development in Indonesia which were not translated into corresponding comparative advantage. This pattern suggests that there were opportunities for the expansion of cocoa butter exports in the Belgian market but Indonesian exporters were not always able to take advantage of such opportunities in relation to competing suppliers. This means that market attractiveness is not enough to generate sustained competitiveness. Product quality, supply reliability, buyer relationships and ability to meet destination-market requirements can determine if an expanding market translates into greater export specialization.

This interpretation is consistent with Codjoe et al. (2023), who show that cocoa value chains are characterized by differences in bargaining power between upstream and downstream actors. Their study finds that direct connections with external buyers are not sufficient by themselves to create bargaining power; strong internal governance, cooperative leadership, and sustained engagement with buyers are also required. For Indonesian cocoa butter, this suggests that improving export competitiveness requires stronger organizational and commercial linkages rather than relying exclusively on domestic processing capacity.

Also important are those observations that are in the negative-RSCA region later period. The positions suggest that Indonesia's relative specialization in cocoa butter exports decreased over time. This should not be taken as evidence that downstream processing was unsuccessful. Instead, it suggests a distinction between structural downstreaming and long-term downstream competitiveness. Indonesia may be processing more cocoa beans and exporting more cocoa butter, while losing relative competitiveness in a specific destination market. As such, an increase in processed exports should not automatically be seen as a sign of successful export upgrading.

Another explanation for this pattern is the governance of European-linked cocoa value chains. Ingram et al. (2018) argue that cocoa value chains linked to European markets are increasingly governed by mechanisms that consider ecosystem services, such as certification, market-based mechanisms, multi-actor platforms and public regulation. These mechanisms mean that exporters competing in European markets increasingly work within a system where environmental and sustainability attributes may shape relationships among producers, processors, traders and buyers. Therefore, Indonesian cocoa butter must compete not only on price and processing ability but also on the broader sustainability attributes of its supply chain.

This is especially the case for the interpretation of the weaker positions at the end of the observation period. Sustainability is changing the way European cocoa is governed, from cocoa bean processing to the origin and conditions of cocoa cultivation. For example Busquet et al (2021) show that social issues in cocoa production are not just at farm level but are embedded within the wider global value chain. They emphasize the multi-dimensionality of cocoa value chains and the need to take into consideration relationships between upstream producers and downstream market actors.

The Retreat-type observations, characterized by negative RSCA and negative EPD, therefore are the most difficult periods for Indonesian cocoa butter in Belgium. These observations indicate that Indonesia suffered from a weak

comparative advantage and unfavorable market dynamics. From an export strategy perspective, such a position implies that simply holding on to market presence may not be enough. Indonesian exporters should work on product differentiation, processing efficiency, quality consistency, and supply chain coordination to prevent temporary market weaknesses from becoming permanent competitive disadvantages.

The combination of Rising Star and negative-RSCA positions also indicates that market and time specificity is the competitiveness of Indonesian cocoa butter. Indonesia has proven that it can compete in the Belgian market, but it has not been able to sustain this advantage. This underscores the necessity of a dynamic assessment of competitiveness rather than a static comparative-advantage measure. Therefore, EPD component is very important in this study because it shows that Indonesia's comparative advantage is accompanied by good market growth.

The results can be better understood from the perspective of downstream cocoa processing in the Indonesian strategy. Cocoa butter is worth more than cocoa beans. Selling only processed exports will not magically make you more competitive internationally. Providing value through integration of upstream supply, organisational governance, buyer relationships and sustainability requirements. Organisational governance and direct engagement with buyers are also important in strengthening the bargaining power of cocoa value chain actors as pointed out by Codjoe et al. (2023). More and more, Europe needs governance mechanisms for sustainable commodity chains (Ingram et al., 2018).

Therefore, the Belgium–HS 1804 results suggest that Indonesian downstreaming should evolve from processing-oriented downstreaming toward value-chain-oriented upgrading. Processing cocoa beans into cocoa butter is an important step, but sustaining competitiveness requires improvements in the entire chain, including raw-material quality, processing efficiency, market coordination, certification, traceability, and relationships with international buyers. The sustainability dimension is particularly relevant because European-linked cocoa chains increasingly incorporate governance mechanisms that extend beyond the conventional price and volume dimensions of international trade.
To summarize, the figure indicates that the competitive potential of Indonesian cocoa butter in Belgium has been proven, but has not been consistently maintained over the 2000-2023 period. Early Rising Star observations are linked to successful specialization and market expansion periods, while negative-RSCA later positions are linked to mounting competitive pressure. The finding suggests that Indonesia's downstreaming strategy has created an important platform of value addition, but that more needs to be done to translate processing capacity into sustained competitiveness in destination markets.

The result also provides an important basis for interpreting the Downstreaming Index (DI). If the DI increases over time while the RSCA–EPD position of HS 1804 weakens, this would indicate that Indonesia has achieved structural downstreaming without fully achieving sustained market competitiveness. Conversely, if a higher DI is accompanied by persistent positive RSCA and favorable EPD positions, the evidence would be stronger that downstreaming has contributed to genuine export upgrading. Thus, the DI and RSCA–EPD results should be interpreted jointly rather than independently.

Figure 8(a) shows the dynamic export position of Indonesian cocoa beans (HS 1801) in the French market (2000–2023) based on the interplay of Revealed Symmetric Comparative Advantage (RSCA) and Export Product Dynamics (EPD). The position map shows a relatively weak and unstable competitive position, compared to the more favorable positions found in some of the periods in other European markets. There are a few observations in the Rising Star quadrant, but the concentration is higher in the negative-RSCA region. This pattern shows that Indonesian cocoa beans have quite a challenge to maintain comparative advantage in France, especially in the latter period of observation. This is in line with evidence that there are structural constraints in Indonesia's cocoa sector on productivity, output prices, input costs and production efficiency that impact its sustainability of competitiveness in international markets (Fahmid et al., 2018). The most favorable position is the Rising Star, which combines positive RSCA with positive EPD. In the French market, there are few observations in this quadrant, especially in 2001 and 2005. The low number of observations for Rising Star indicates that Indonesia was only able to combine comparative advantage and strong market growth in France at the same time on rare occasions.

The early Rising Star positions show that Indonesia was able to compete in the French cocoa-bean market under specific market conditions. But the lack of persistence for this position suggests that the advantage is not structurally strong. The interpretation is in line with the findings of Fahmid et al. (2018) that Indonesian cocoa farming has a competitive advantage at the farm level, but it has weaknesses in comparative efficiency, productivity, output prices, and input costs. They see improvements in productivity and price as important requirements to strengthen the competitiveness of Indonesian cocoa.

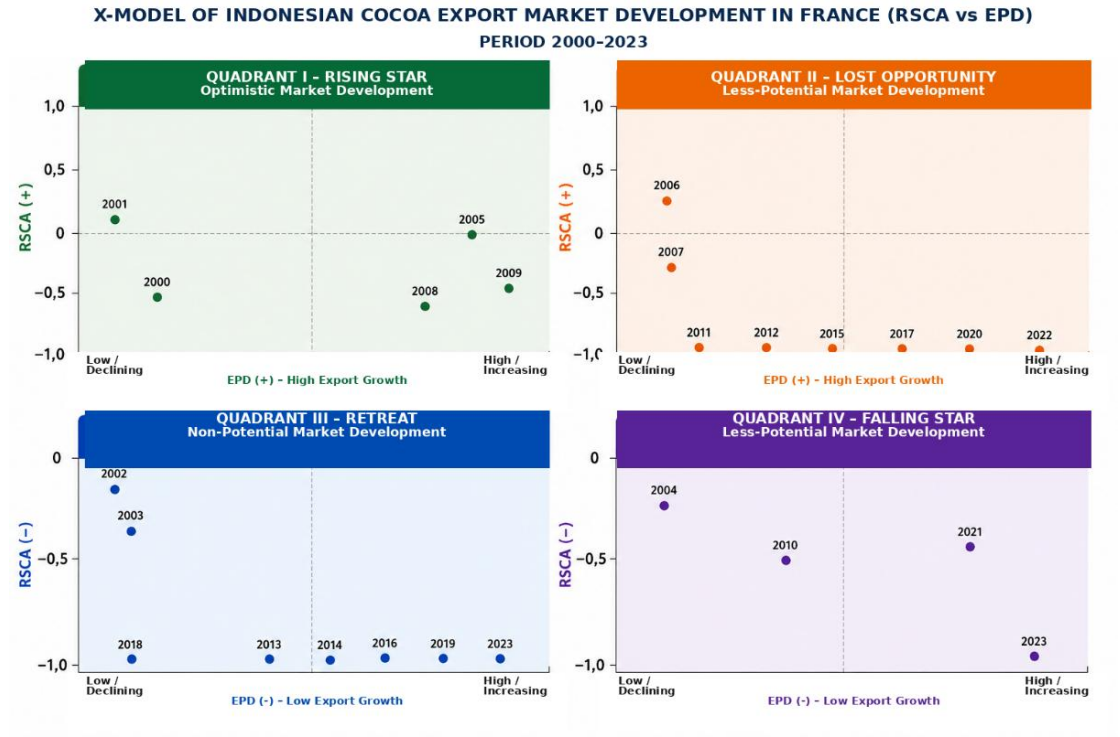

(a)

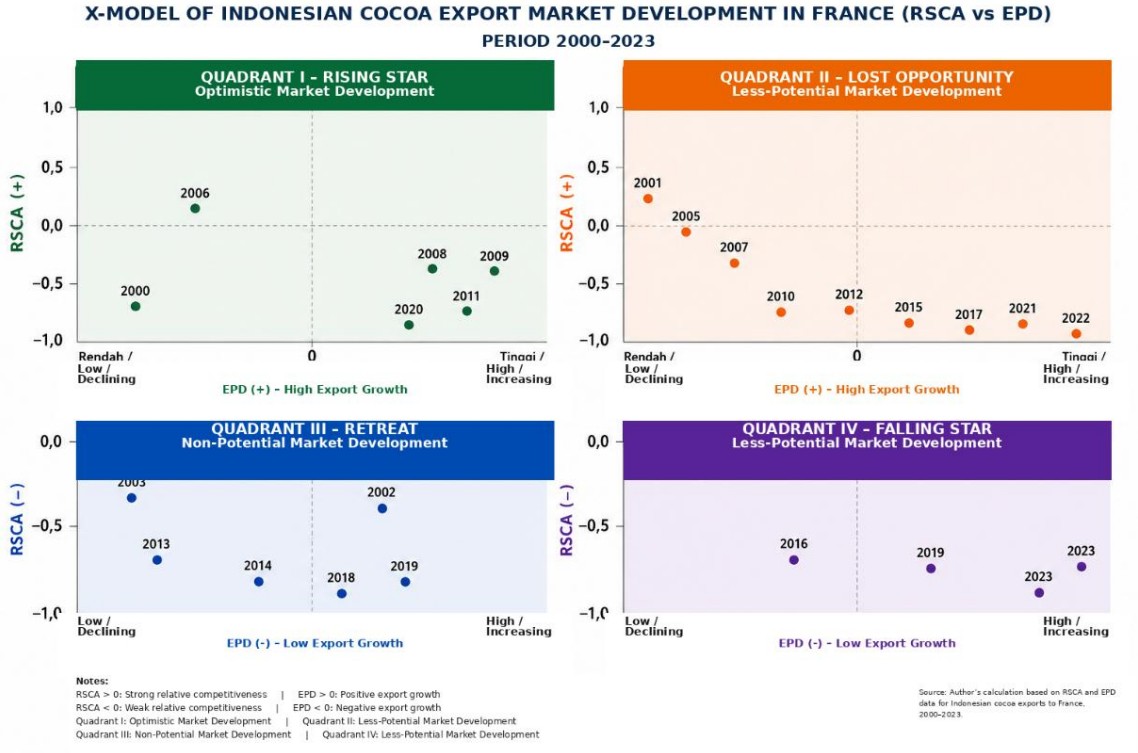

(b)

Figure 8. X-model of Indonesian cocoa export market development in France, 2000–2023

The result suggests that the early favorable market positions of Indonesia in France must be viewed as episodic competitiveness, not sustained competitive advantage. That is, the Indonesian cocoa sector managed to benefit in some years from market conditions that proved to be advantageous but not to establish a persistent position in the French market. There are a large number of observations in the Lost Opportunity quadrant, with positive EPD and negative RSCA. The figure in this region has observations like 2006, 2007, 2011, 2012, 2015, 2016 and 2022. This condition indicates that the French market had good development, but Indonesia was not in a more advantageous position in cocoa beans during the same period. This is an important finding as it shows that the

weakness of Indonesian cocoa in France cannot be simply explained by the lack of market opportunities. “There were still growth periods in the market, but Indonesia was not competitive enough to take advantage of it. The difference between EPD and RSCA implies that market attractiveness and export competitiveness were not in line.

An alternative is the integration of Indonesian cocoa into international price and market mechanisms. Izaati et al. (2020) demonstrated that the prices of Indonesian cocoa-beans were integrated with some international markets in the long run, but there was limited price transmission with some importing markets. Such differences in price transmission may cause difficulties for Indonesian cocoa exporters to fully transmit international market conditions into domestic export prices and incentives.

This provides a useful interpretation of the observations of Lost Opportunity. Even if the French demand conditions had been favorable, Indonesian exporters might not have been able to respond competitively to them due to differences in price transmission, production costs, exchange rate conditions, or supply-side constraints. The Retreat quadrant is in the most negative position as both RSCA and EPD are negative. There are relatively many observations in this region in the figure, such as 2002, 2003, 2013, 2014, 2018, 2019, 2023, etc. The concentration of observations in the lower region of the map is especially striking because it shows that the negative comparative advantage was not a short-term phenomeon.

The latter findings are especially disturbing. A number of points for the post-2010 period are close to the lower edge of the RSCA axis, which means a significant drop in Indonesia’s relative specialization in cocoa beans. The position of 2023 is still very negative, which means that Indonesia had not regained its comparative advantage in the French cocoa-bean market at the end of the observation period. The persistence of negative positions is in line with the broader structural problems of Indonesian cocoa production. Fahmid et al. (2018) found that cocoa productivity in Indonesia was relatively low and the costs of production, particularly those related to labor and land, represented important components of the production structure. They analyzed that to increase the competitiveness of Indonesian cocoa, productivity improvement, better output prices and more efficient input management are needed.

Thus, the Retreat positions in France can be interpreted as evidence that the competitiveness problem extends beyond export-market conditions. Indonesia's ability to compete in the French market is also linked to the underlying efficiency and productivity of its domestic cocoa production system. The lower-right observations in the figure, including points around 2004, 2010, 2021, and 2023, require particular attention. Based on the mathematical definition of the RSCA–EPD framework, observations with negative RSCA and negative EPD correspond to the Retreat position, rather than Falling Star. A Falling Star position should have positive RSCA and negative EPD.

This distinction matters because the lower-right observations indicate that Indonesian cocoa beans experienced both weak comparative advantage and unfavorable market dynamics. Therefore, they represent periods in which Indonesia was not only relatively less specialized but was also operating in a less favorable market environment. The increasing appearance of such negative positions toward the end of the period reinforces the conclusion that the French market has become increasingly challenging for Indonesian cocoa beans. This pattern contrasts with the earlier Rising Star observations and suggests a gradual deterioration in the competitive position of the raw cocoa-bean export segment.

Overall, the France–HS 1801 position map shows a predominantly weak and unstable competitive trajectory for Indonesian cocoa beans during 2000–2023. Unlike a market characterized by persistent Rising Star positions, France shows only limited periods in which Indonesia simultaneously achieved comparative advantage and favorable market development. A much larger proportion of observations is associated with negative RSCA, particularly after 2010. These results confirm recent evidence in terms of cocoa competitiveness in Indonesia. The EPD and other indicators of competitiveness of Indonesia’s cocoa export performance are influenced by productivity, price, exchange rates, destination-country GDP, and comparative competitiveness (Setiawan et al., 2025). They demonstrate that the impact of such factors may be different in the short and long run, as cocoa markets are subject to volatility and structural constraints. The French case thus points to a problem which is not only one of market access. Instead, Indonesia needs to improve the basic competitiveness of its cocoa supply, including productivity, quality, pricing and responsiveness to the demand of destination markets. The interpretation is particularly important, as France is a major European market for the consumption and processing of chocolate. Thus for Indonesian cocoa to continue to have access to this market, it must be able to compete not only in terms of availability, but also in terms of quality and consistency.

Figure 8(b) shows the dynamic export position of Indonesian cocoa butter, fat, and oil (HS 1804) in the French market during 2000-2023 from RSCA and EPD. Figure shows that the competitive position of Indonesian cocoa butter is relatively unstable with few observations located in the favorable Rising Star area, and most observations are located in the negative RSCA positions. Early observations (notably 2006) suggest a relatively good combination of comparative advantage and market development while several later observations are placed well below the RSCA threshold. This pattern shows that Indonesia has been able to compete in the French processed-cocoa market, but this has not been sustained consistently. The evidence also shows that cocoa butter is one of the stronger products of cocoa derivatives in Indonesia, but its competitiveness varies in the market (Nurwansyah et al., 2023).

The distribution of observations in the Lost Opportunity and Retreat areas is of particular interest. Negative RSCA over several years such as 2001, 2005, 2007, 2010, 2012, 2015, 2017, 2021 and 2022 suggest that market opportunities in France were not always translated into comparative advantage despite relatively favorable EPD positions. Data for 2013, 2014, 2018, 2019 and 2023 point, in parallel, to a less favorable position when the negative comparative advantage is combined with unfavorable market dynamics. This divergence between comparative advantage and market development is in line with the research on Indonesian processed cocoa, which suggests that products of processed cocoa can maintain comparative advantage and at the same time have less favorable EPD positions. This implies that structural competitiveness does not necessarily translate into market growth (Yemima & Novianti, 2020).

The downward trend of HS 1804 in the second period also indicates that downstream processing alone cannot guarantee sustained competitiveness. The competitiveness of cocoa butter still depends on the availability and quality of cocoa beans as processing inputs and the efficiency of the downstream industry. Research on the export of Indonesian cocoa butter shows that upstream factors, namely the supply of cocoa beans, are important for the development of cocoa butter exports. The competitiveness downstream cannot be separated from the performance of the upstream cocoa sector (Hermawan, 2019). This is especially true in France, where cocoa is a major industrial input: France imported some 439 000 tons of cocoa per year on average between 2012 and 2021, of which some 15 percent of its cocoa imports was cocoa butter.

Overall, the results from France-HS 1804 suggest that Indonesian cocoa butter has export potential but has not been a consistently strong competitive position in 2000–2023. The limited observations on the Rising Star suggest that Indonesia has the potential to achieve favorable competitiveness under certain market conditions, but the dominance of negative RSCA positions in later years indicates the need for stronger product quality, processing efficiency, supply-chain integration and market adaptation. This result strengthens the argument for examining the Downstreaming Index: a rising proportion of cocoa butter exports would indicate structural downstreaming, but its combination with weak RSCA–EPD performance would suggest that downstreaming has not yet been fully translated into durable competitiveness in the French market.

The dynamic export position of Indonesian cocoa beans (HS 1801) in the German market in 2000-2023 based on the interaction between RSCA and EPD is presented in Figure 9(a). The results show a relatively strong competitive position in the early period, where 2000, 2009, 2010 and 2006 are located in the Rising Star quadrant. Positive RSCA values during 2000, 2009 and 2010, in particular, indicate that Indonesian cocoa beans had comparative advantage, while enjoying favorable market dynamics. But later the situation tilted toward negative RSCA which means that the initial competitive advantage was not sustained through the observation period.

In the Lost Opportunity quadrant there are several observations, such as 2001, 2002, 2004, 2007 and 2015, that indicate a period when the German market was relatively favorable in terms of dynamics, while Indonesia's comparative advantage was already declining. It implies that Indonesia did not fully exploit market opportunities although Germany is a major European destination for cocoa products. Recent research that specifically examines the German market finds that Indonesian cocoa competitiveness is affected by international cocoa prices and export-duty policy, while processed cocoa products have shown significant competitive potential in the market (Udayana & Setiawina, 2023). However, the Retreat positions show times with weak comparative advantage and unfavorable market development at the same time, especially during the 2011–2016. The clustering of negative RSCA values in the later period shows that raw cocoa bean competitiveness in Germany became more and more vulnerable. This pattern can be partly linked to the structural change of Indonesia from raw-bean exports into processed cocoa after the implementation of the downstreaming-oriented export policies. Indonesia's exports of cocoa beans declined after the 2010 policy change, but its processed cocoa exports increased, suggesting a structural shift to higher-value products (Zikria et al., 2019). On the supply side, productivity, output prices, and input cost are also important determinants of Indonesian cocoa competitiveness, which are still important determinants of the sector's international competitiveness (Fahmid et al., 2018).

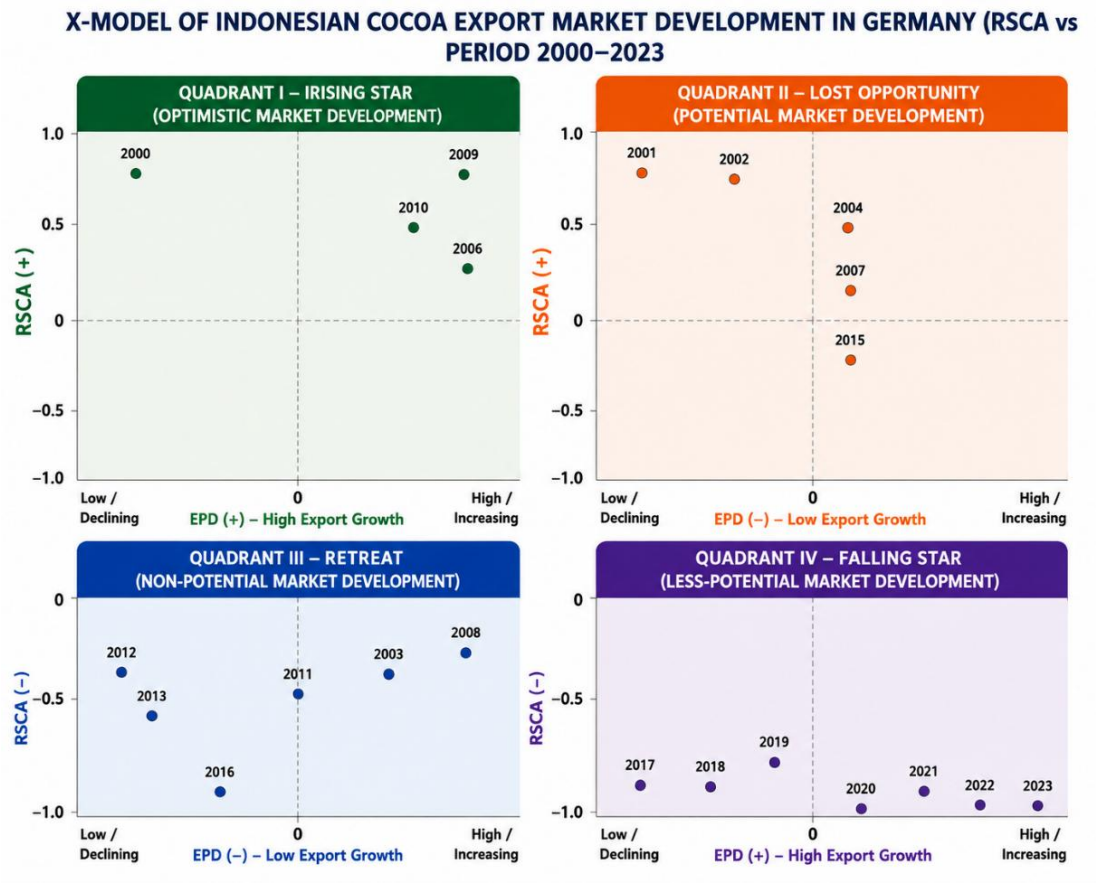

Figure 9 (a).

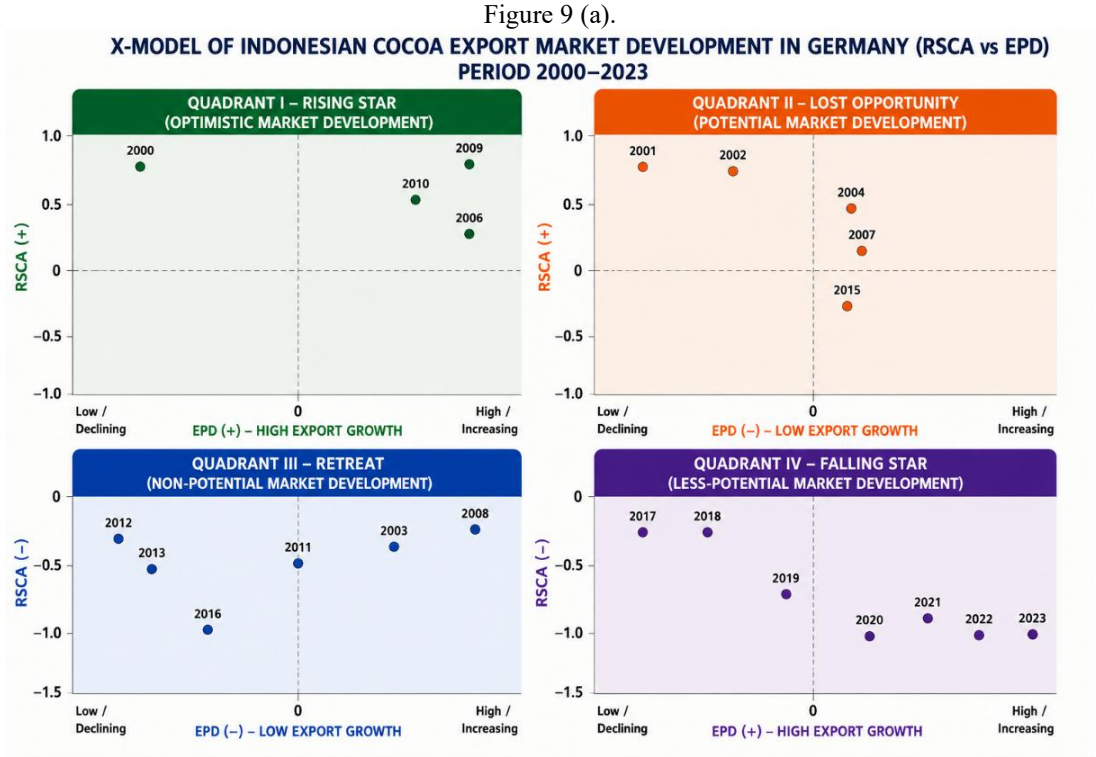

(b)

Figure 9 (b) X-model of Indonesian cocoa export market development based on RSCA and EPD in Germany, 2000–2023

Overall, the Germany–HS 1801 results indicate that Indonesia's cocoa beans have experienced a transition from relatively favorable competitiveness toward a weaker and more unstable market position. The persistence of negative RSCA in the later period suggests that maintaining competitiveness through raw-bean exports alone may

be increasingly difficult. This provides an important rationale for examining HS 1804 and the Downstreaming Index: if processed cocoa demonstrates stronger competitiveness than HS 1801, the decline in raw-bean competitiveness can be interpreted as part of Indonesia's export upgrading process rather than simply a deterioration of the cocoa sector. However, the transition needs to be supported by improvements in productivity and the quality of domestic cocoa supply.

Figure 9(b) depicts the dynamic export position of Indonesian cocoa butter (HS 1804) in the German market in 2000–2023. The result showed that Indonesian cocoa butter had strong competitive position in the early period with 2000, 2006, 2009 and 2010 located in Rising Star quadrant. These observations suggest that Indonesia managed to combine a positive comparative advantage with a favorable market development. However, the later clustering of observations in negative-RSCA positions indicates that this advantage became less stable over time.

The positions of Lost Opportunity observed in 2001, 2002, 2004, 2007 and 2015 suggest that favorable market dynamics were not always matched with comparative advantage. But, the lower-quadrant observations after 2010 show a more persistent weakening of Indonesia's relative position. This pattern is interesting because after the abolishment of export duties, Tupamahu and Apituley (2022) found that cocoa butter was still one of the Indonesian cocoa products with high comparative advantage, though the competitiveness of cocoa beans and some other derivatives declined. Thus the weaker RSCA–EPD position found specifically for Germany may reflect destination-market differences rather than a general loss of competitiveness in Indonesian cocoa butter.

The negative positions indicate that competitive advantage does not always result in good market dynamics. Syarif et al. (2022) stated that Indonesian processed cocoa has a comparative advantage and competitive advantage, but the position in the market is very different between the destination countries. Moreover, the quality of cocoa beans, especially low fermentation, was identified as one of the important barriers to the competitiveness of processed cocoa in Indonesia. This explains a likely reason for the change in the position of HS 1804 in Germany. Downstream processing can add value but export performance is still dependent on stable quality of raw materials and the ability to meet destination market requirements. Map Position Germany HS 1804 shows that Indonesian cocoa butter has large competitive potential but has not been able to maintain a sustainable market position in the period 2000-2023. The early Rising Star periods show Indonesia's success in competing in this processed segment, and the later negative-RSCA positions indicate rising competitive pressure. Therefore, Indonesia's downstreaming strategy must be supported by increasing the quality of raw materials, processing efficiency, product differentiation and market adaptation to specific destinations. The result also confirms the importance of the comparison between HS 1804 and HS 1801: if cocoa butter still remains more competitive than cocoa beans, the change toward processed exports can be considered as a feature of export upgrading, although the competitiveness of HS 1804 remains market-specific.

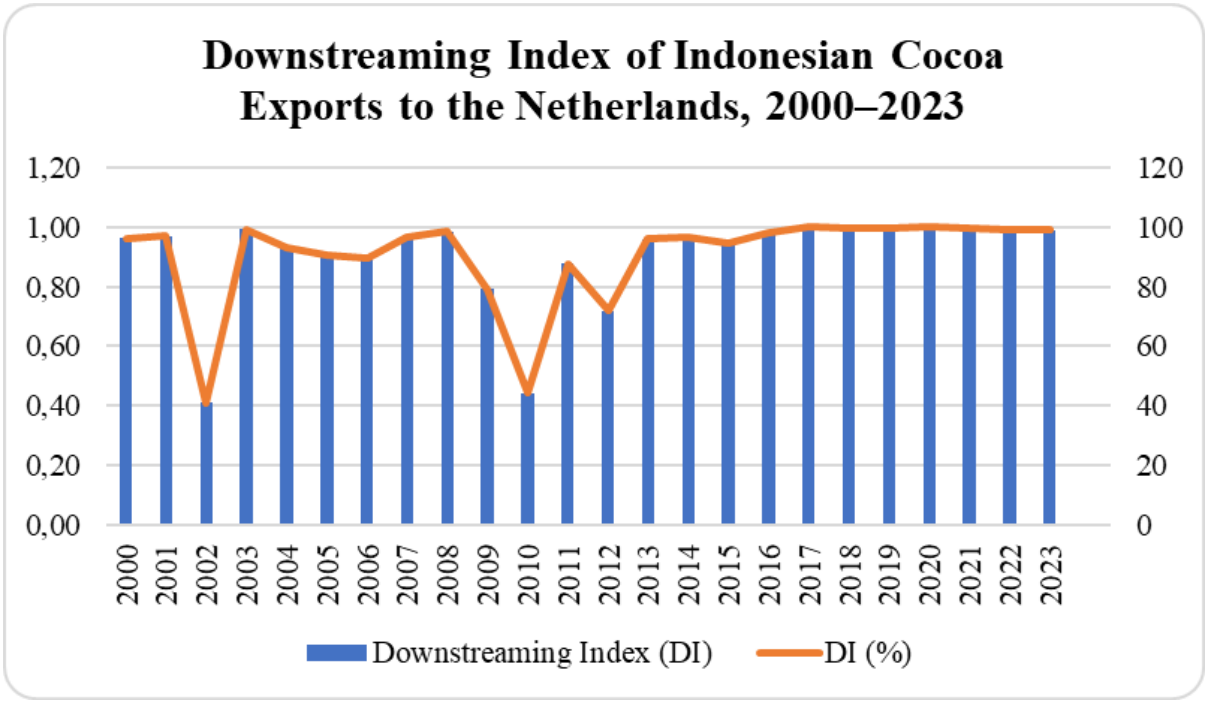

Figure 10. Downstreaming index of Indonesian cocoa exports to the Netherlands, 2000-2023

In analyzing export competitiveness, it is not only about Indonesia's ability to maintain its position in the international market, but also about the extent to which the export structure has shifted to higher value-added products. An important indicator of successful downstreaming is an increasing share of processed cocoa products in the cocoa sector. This can reduce dependence on cocoa bean exports and increase the economic value generated from exported cocoa. Therefore, the development of Indonesia's cocoa export orientation toward processed and higher value-added products, especially in the Netherlands market is reflected in the Downstreaming Index (DI). The higher the DI, the higher the orientation to processed cocoa products and the higher the value addition in the export structure.

Figure 10 shows the development of the Downstreaming Index (DI) of Indonesian cocoa exports to the Netherlands in 2000–2023. In general, the DI stayed quite high during the whole observation period, but there were some remarkable fluctuations in the early and mid-part. The DI is relatively high at the beginning of the period, at around 0.95 in 2000–2001 and declines sharply to around 0.40 in 2002. The index then rebounded sharply in 2003, reaching close to 1.00, and remained relatively stable around 0.90–1.00 in the years that followed.

Between 2009 and 2012, there was another significant fluctuation period. The DI declined from around 0.98 in 2008 to around 0.77 in 2009 and a low of around 0.43 in 2010. The index then recovered in 2011 before falling back to around 0.71 in 2012. These fluctuations suggest that the downstream orientation of Indonesian cocoa exports to the Netherlands did not develop in a fully linear way. Changes in the DI may reflect changes in the composition of exported cocoa products, in particular the relative contribution of primary cocoa products and processed cocoa products.

From 2013 onward, the DI rebounded substantially and remained high, mostly between 0.95 and 1.00. Most importantly, the index stayed very close to 1.00 between 2017 and 2023, suggesting a high degree of stability. The pattern suggests a strong and continued downstream orientation of Indonesia's cocoa exports to the Netherlands. The DI, which is increasingly stable and high, shows that Indonesian cocoa exports are increasingly characterized by processed or value-added cocoa products, rather than being dominated by primary cocoa commodities exclusively.

Overall, the DI trend during 2000–2023 indicates that, despite several periods of decline, the long-term direction points toward stronger downstreaming of Indonesian cocoa exports. The sustained DI values close to 1.00 during 2017–2023 are particularly important, as they suggest that Indonesia has strengthened its orientation toward exporting cocoa products with higher levels of processing and value addition to the Netherlands. This finding complements the export competitiveness analysis by demonstrating that Indonesia's competitiveness is not only associated with its ability to maintain market performance, but also with its capacity to transform the export structure toward higher value-added cocoa products.

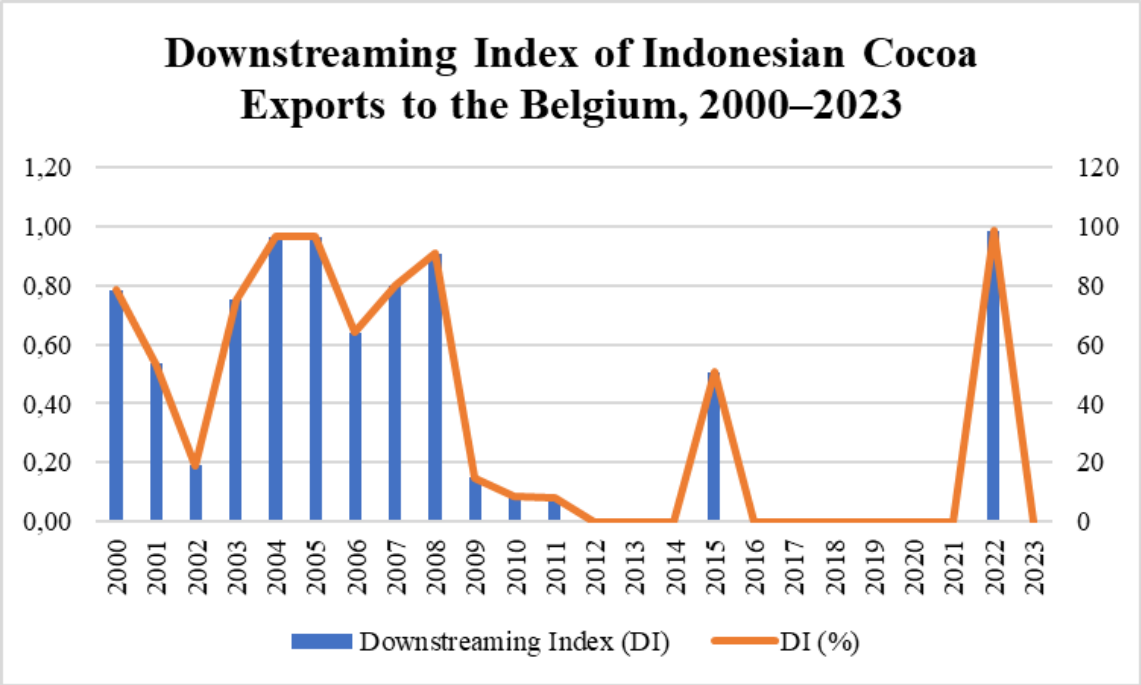

Figure 11. Downstreaming index of Indonesian cocoa exports to the Belgium, 2000-2023

The pattern of the Downstreaming Index (DI) of Indonesian cocoa exports to Belgium for the period 2000-2023 is very fluctuating compared to the Netherlands. The DI was quite high in the first period (around 0.80 in 2000) and then fell to around 0.20 in 2002. Then the index rose to about 0.95 in 2003-2005, indicating a greater orientation toward downstream or value-added cocoa products. But the DI fell again to around 0.65 in 2006, and then rose to 0.80-0.90 in 2007-2008. A big drop then, after 2008. The DI fell to a very low 0.15 in 2009 and remained at a very low level in 2010-2011. The DI was close to zero in the period 2012-2014, which implies that the downstreaming orientation measured by the index was very weak in this period. The DI temporarily recovered to around 0.50 in 2015, but this recovery was not sustained, and the index returned to almost zero in the period 2016-2021. In 2022, the DI rose significantly, but this was a transient effect. It leaped to near 1.00, the strongest downstream position seen in the period. But the spike was short-lived, and by 2023 the index was back to about nothing. The downstreaming pattern is rather stable and high in the Netherlands, but volatile and discontinuous in Belgium. The results of the study show that for a long time the structure of Indonesia's cocoa exports to Belgium has not been strongly downstream oriented. There are several periods with high DI values, especially 2003-2005, 2007-2008 and 2022. But these gains were short-lived with large declines thereafter. The long periods of very low or zero DI indicate that the downstream performance of Indonesian cocoa exports to Belgium is still erratic. This finding suggests that the Belgian market may need to improve its diversification of value-added products, stable supply of processed cocoa products and market penetration strategies to be able to successfully sustain the downstreaming gains over time.

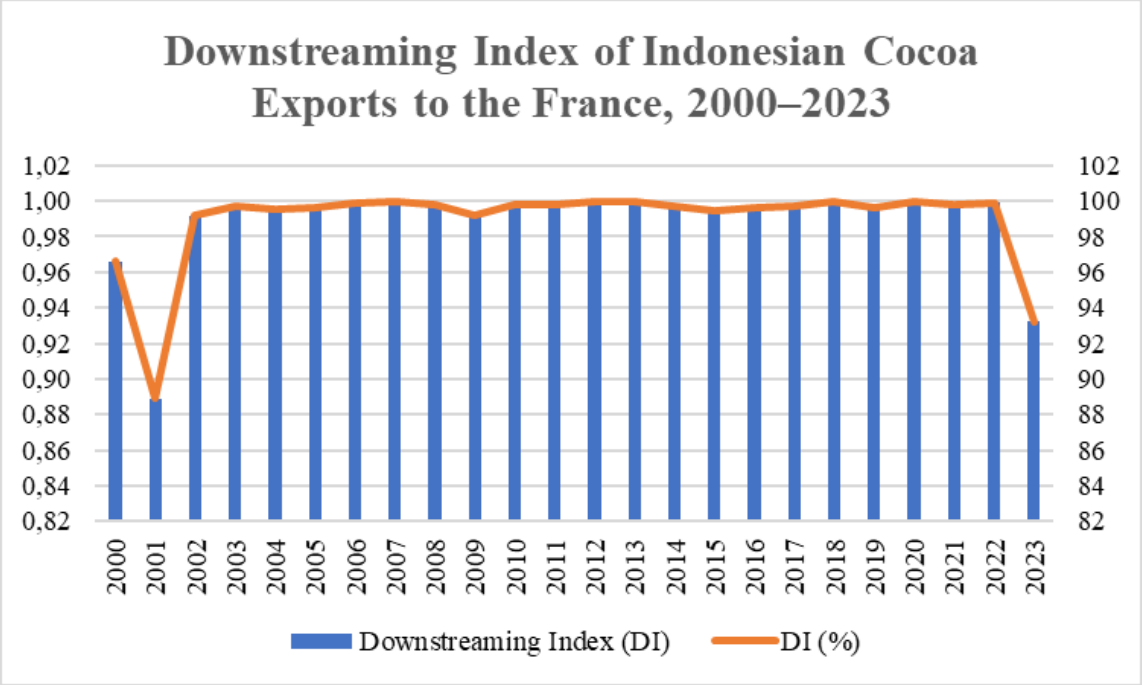

Figure 12. Downstreaming index of Indonesian cocoa exports to the France, 2000-2023

The Downstreaming Index (DI) of Indonesian cocoa exports to France in the period 2000-2023 is very high and stable and has a downstream orientation compared to Belgium. The DI was already very high in 2000 at about .97 and declined to about .2001: 89. There was a small dip (DI around 0.99) before a sharp rebound in 2002. The index from 2002 to 2022 was around 1.00, which means that the tendency of Indonesian cocoa exports toward downstream or added-value products in the French market is quite stable. During this period, there are some minor fluctuations, notably in 2009, 2015-2016, and 2018. These are, however, very small changes and do not alter the overall pattern. The overall DI was 0.98-1.00, which indicates that the composition of Indonesian cocoa exports to France tended to be relatively stable and biased toward processed or value-added cocoa products. The most significant change occurred in 2023, when DI fell to about 0.93. The index was still very high, but down from near-maximum levels seen earlier. Of all the markets studied so far, the French market shows the most marked and regular downstreaming pattern. For the last twenty years, the DI values of Indonesia have been stable at around 1.00 which indicates the success of Indonesia in maintaining a highly downstream-oriented structure of cocoa exports in France. The stability indicates that the French market is a quite well established destination of value added cocoa products from Indonesia. However, the French market should give a more solid basis for the Indonesian strategy in terms of the exports of value added products and development of downstream industries. In 2023 there has been a fall which must be watched to see if it is a transitory variation or the beginning of a structural change in the composition of exports.



Figure 13. Downstreaming index of Indonesian cocoa exports to the Germany, 2000-2023

The Downstreaming Index (DI) of Indonesian cocoa exports to Germany over the period 2000–2023 clearly shows a shift from a very volatile downstreaming pattern in the early period to a consistently high and stable level after 2012. The DI was close to zero during 2000–2002, showing that Indonesia's cocoa exports to Germany were very little downstream oriented. The index rose substantially in 2003 to approximately 0.55, but declined to approximately 0.40 in 2004 and rose again to approximately 0.50 in 2005. 2006-2011 saw continued considerable volatility. The DI dropped to near zero in 2006, bounced back to around 0.40-0.45 during 2007-2008 and then dropped again to near zero in 2009. The index recovered gradually in 2010–2011 and then increased sharply to about 0.95 in 2012. The sharp structural change indicates a significant turning point in the downstreaming performance of Indonesian cocoa exports to Germany. Between 2012 and 2023, the DI was consistently high, often between 0.95 and 1.00 with very small fluctuations. In particular, from 2016 the index was almost constantly around or very close to 1.00. This shows that the orientation of Indonesian cocoa exports to Germany strongly to processed and value-added cocoa products . The downstream structure is maintained for a long time. In general, the data suggest a strong structural shift in the German market toward downstream orientation in Indonesian cocoa exports. This period after 2012 is characterized by a persistent DI close to 1.00 unlike the highly volatile pattern during 2000-2011. Thus, Indonesia has shifted its positioning in Germany from primarily a supplier of primary cocoa commodities to a provider of value-added cocoa products. The continued high DI also suggests that the downstreaming process in the German market is relatively well established and can be an important foundation for improving Indonesia's export competitiveness through higher value cocoa products.

Conclusion

The study found that there has been a structural shift in the Indonesia cocoa export competitiveness from the export of raw cocoa beans to the export of higher value added processed cocoa products. The analysis of the RSCA shows that processed cocoa products, in particular cocoa butter (HS 1804), have continued to have stronger comparative advantages than cocoa beans (HS 1801) in the main European markets. The results underscore the increasing importance of downstream industrialization, technology upgrades, and value-added processing as drivers of Indonesia's competitiveness in the global cocoa trade.

The analysis of EPD shows that the dynamics of Indonesian cocoa exports are different among destination markets. Cocoa bean markets in the Netherlands and France are Rising Star markets, while Belgium and Germany are Falling Star markets. Meanwhile, the Netherlands and Germany are identified as the Rising Star markets for cocoa butter products, Belgium as a Falling Star, and France as a Lost Opportunity. The results show that processed cocoa products tend to perform better in the market and have more favorable growth dynamics than raw cocoa exports.

The results also show the growing importance of sustainability standards, digital traceability systems and supply chain efficiency for export competitiveness. Demand for environmentally sustainable production systems, transparent supply chains and technology-based monitoring mechanisms is being driven by the adoption of international regulations such as the European Union Deforestation Regulation (EUDR). This implies that competitiveness in the global cocoa industry is no longer solely a matter of volume of production but increasingly of technological capacities, efficiency of processing, compliance with sustainability standards and participation in higher stages of global value chains.

Overall, this study confirms that cocoa downstreaming and digital transformation contribute positively to strengthening Indonesia's position in the global sustainable economy. The transition toward processed cocoa exports provides greater opportunities for value creation, market expansion, and long-term competitiveness in international markets.

Recommendations

The government and industry players need to keep speeding up policies on cocoa downstream industrialization by expanding the capacity of domestic processing and encouraging increased production of value-added cocoa products to bolster Indonesia's position in the global cocoa market. The switch from exporting raw cocoa beans to exporting processed cocoa products is more powerful in building up comparative advantages and in generating better market dynamics, especially in the major European markets. Therefore, strengthening the downstream sector is important to increase export value, improve industrial competitiveness, and reduce reliance on primary commodity exports. In addition, technological innovation and digital transformation should be a top priority for the cocoa industry in Indonesia. Advanced processing techniques, digital traceability systems, quality assurance systems, and integrated supply chain management are increasingly important in meeting the requirements of international markets. These technological improvements may enhance the production efficiency, product consistency, and transparency of the cocoa value chain, and thereby increase the competitiveness of Indonesian cocoa products in global markets. Indonesia needs to develop governance of sustainability and compliance with environmental regulations across the cocoa sector, especially with the enforcement of international regulations such as the European Union Deforestation Regulation (EUDR). The promotion of sustainable cocoa farming, agroforestry systems, and environmentally friendly production practices is necessary to maintain long-term market access and improve the reputation of Indonesian cocoa products in sustainability-oriented markets. At the same time, the expansion of sustainability certification and traceability systems will serve to improve consumer confidence and bolster Indonesia's competitive position in European markets. Export promotion strategies should also aim to retain and increase market share in countries classified as Rising Star markets, such as the Netherlands and Germany, while at the same time enhancing competitiveness in Belgium and France through deeper market penetration, product differentiation and sustainability-oriented branding strategies. It is important to foster collaboration between government institutions, exporters, processing industries, and smallholder farmers to ensure consistency in the quality of products and continuous supply of products in international markets. Last but not least, with the majority of Indonesia's cocoa plantations being run by smallholder farmers, policies aimed at improving productivity should continue to be a national priority. To support sustainable cocoa production and strengthen the durability of Indonesia's cocoa sector in the era of digital economic transformation and sustainable global trade, it is important to implement programs related to plantation rehabilitation, replanting using superior planting materials, farmer capacity building, and access to modern cultivation technologies.

Scientific Ethics Declaration

* The authors declare that the scientific ethical and legal responsibility of this article published in EPSTEM Journal belongs to the authors.

Conflict of Interest

* The authors declare that they have no conflicts of interest

Funding

* This research received financial support from the Indonesia Endowment Fund for Education (LPDP), Ministry of Finance of the Republic of Indonesia. The authors declare that there are no competing financial or non-financial interests that could have influenced the results and interpretation of this study. Ethical approval was not required because this research was conducted exclusively using publicly available secondary data obtained from international trade databases.

Acknowledgements or Notes

* This article was presented as an oral presentation at the International Conference on Basic Sciences, Engineering and Technology (www.icbaset.net) held in Istanbul/Türkiye on September 17-18, 2026.

* The authors would like to express their sincere gratitude to the Indonesia Endowment Fund for Education (LPDP), Ministry of Finance of the Republic of Indonesia, for the financial support provided for this research. The authors also extend their appreciation to the Department of Agricultural Socio-Economics, Faculty of Agriculture, Universitas Gadjah Mada, for academic support and valuable research guidance throughout the study process. In addition, the authors are grateful to all parties who contributed directly or indirectly to the completion of this research and manuscript preparation.

References

Adewopo, J. B., Nwafor, C. U., van der Fels-Klerx, H. J., & Oude Lansink, A. (2023). Sustainability challenges and opportunities in cocoa value chains: A systematic review. *Journal of Cleaner Production, 398*, 136529.

Amfo, B., Aidoo, R., Mensah, J. O., & Maanikuu, P. M. I. (2023). Linkage between working conditions and wellbeing: Insight from migrant and native farmhands on Ghana's cocoa farms. *Heliyon, 9*(2), e13383.

Aung, M. M., & Chang, Y. S. (2014). Traceability in a food supply chain: Safety and quality perspectives. *Food Control, 39*, 172–184.

Effendy, Pratama, M. F., Rauf, R. A., Antara, M., Basir-Cyio, M., Mahfudz, & Muhardi. (2019). Factors influencing the efficiency of cocoa farms: A study to increase income in rural Indonesia. *PLoS ONE, 14*(4), e0214569.

European Commission. (2023). *Regulation (EU) 2023/1115 on deforestation-free products (EUDR).* Retrieved from https://environment.ec.europa.eu/topics/forests/deforestation/regulation-deforestation-free-products_en

Fahmid, I. M., Wahyudi, Salman, D., Kariyasa, I. K., Fahmid, M. M., Agustian, A., Perdana, R. P., Rachman, B., Darwis, V., & Mardianto, S. (2022). "Downstreaming" policy supporting the competitiveness of Indonesian cocoa in the global market. *Frontiers in Sustainable Food Systems, 6*, 821330.

Food and Agriculture Organization of the United Nations. (2023). *Sustainable cocoa ınitiative*. Retrieved from https://www.fao.org/investment-centre/about-us/how-we-work/investmentplanningpolicy/sustainable-cocoa-initiative/en

Fold, N., & Neilson, J. (2016). Global value chains and global production networks in the changing international political economy: An introduction. In N. Fold & J. Neilson (Eds.), *Value chains and global capitalism: A multidisciplinary perspective* (pp. 1–19). London, England: Routledge.

Gehl Sampath, P., & Vallejo, B. (2018). Trade, global value chains and upgrading: What, when and how? *The European Journal of Development Research, 30*, 481–504.

Gereffi, G., & Fernandez-Stark, K. (2016). *Global value chain analysis: A primer* (2nd ed.). Durham, NC: Duke University, Center on Globalization, Governance & Competitiveness.

Hermawan, R. (2019). Analisis pengaruh kebijakan bea keluar biji kakao, impor biji kakao, ekspor biji kakao dan harga cocoa butter terhadap ekspor cocoa butter. *Indonesian Treasury Review, 4*(3).

Huetz-Adams, F., & Fountain, A. C. (2020). *Cocoa Barometer 2020*. Cocoa Barometer Consortium. Retrieved from https://www.voicenetwork.eu/cocoa-barometer-2020

Humphrey, J., & Schmitz, H. (2002). How does insertion in global value chains affect upgrading in industrial clusters? *Regional Studies, 36*(9), 1017–1027.

International Cocoa Organization. (2024). *Quarterly bulletin of cocoa statistics* (Vol. 50). International Cocoa Organization. Retrieved from https://www.icco.org/icco-documentation/icco-publications/icco-publications/

Kamilaris, A., Cole, I. R., & Prenafeta-Boldú, F. X. (2021). Blockchain in agriculture. In C. M. Galanakis (Ed.), *Food technology disruptions* (pp. 247–284). Elsevier.

Kaplinsky, R., & Morris, M. (2016). *A handbook for value chain research*. International Development Research Centre.

Lambin, E. F., et al. (2023). Large gaps in voluntary sustainability commitments covering the global cocoa trade. *Global Environmental Change, 81*, 102696.

Ministry of Agriculture of the Republic of Indonesia. (2024). *Agricultural statistics 2024 (Statistik Pertanian 2024)*. Jakarta, Indonesia: Center for Agricultural Data and Information Systems (PUSDATIN), Ministry of Agriculture.

Ndlovu, P., & Thamaga-Chitja, J. M. (2023). Inclusive and sustainable agricultural value chains in developing countries: A review of challenges and opportunities. *Sustainability, 15*(8), 6502.

Neilson, J., Wright, J., & Aklimawati, L. (2018). Geographical indications and value capture in the Indonesian coffee sector. *Journal of Rural Studies, 59*, 35–48.

Nurhayati, N., Setyabudi, F. M. C. S., Marseno, D. W., & Supriyanto, S. (2019). The effects of roasting time of unfermented cocoa liquor using the oil bath methods on physicochemical properties and volatile compound profiles. *AgriTECH, 39*(1), 36–47.

Nurwansyah, A., Nuraini, C., & Apriyani, D. (2023). Daya saing ekspor lemak kakao Indonesia di pasar internasional. *Forum Agribisnis, 14*(1), 50–58.

Parra-Paitan, C., zu Ermgassen, E. K. H. J., Meyfroidt, P., & Verburg, P. H. (2023). Large gaps in voluntary sustainability commitments covering the global cocoa trade. *Global Environmental Change, 81*, 102696.

Schroth, G., Figueiredo, M. G., Rocha-Santos, L., Mariano-Neto, E., & colleagues. (2024). *Management practices can improve yields of carbon-rich cocoa agroforests in Brazil*. Research Square.

Tröster, B., & Staritz, C. (2023). Price-setting power in global value chains: The cases of price stabilisation in the cocoa sectors in Côte d'Ivoire and Ghana. *The European Journal of Development Research, 35*(4), 840–868.

Udayana, H. P., & Setiawina, N. D. (2023). Comparative analysis and factors affecting the competitiveness of Indonesian cocoa commodities in the German market. *Jurnal Manajemen, 14*(2).

Van Huellen, S., & Abubakar, F. M. (2021). Potential for upgrading in financialised agri-food chains: The case of Ghanaian cocoa. *The European Journal of Development Research, 33*(2), 227–252.

Voora, V., Bermúdez, S., & Larrea, C. (2023). *Global market report: Cocoa prices and sustainability*. International Institute for Sustainable Development.

World Bank. (2024). *Commodity markets outlook: October 2024*. Washington, DC: World Bank Group.

Yemima, R., & Novianti, T. (2020). Competitiveness and determinant of Indonesian processed cocoa demand in the AANZFTA framework. *Jurnal Ilmu Ekonomi Terapan, 5*(1).

Zikria, V., Takahashi, K., & Maeda, K. (2019). International competitiveness of Indonesia's cocoa sector: From the viewpoint of product differentiation. *Journal of the Faculty of Agriculture, Kyushu University, 64*(2), 407–413.

Author(s) Information

Dwi Putri Jeng Ivo Nurun Nisa
Gadjah Mada University, Faculty of Agriculture, Department of Agricultural Socio-Economics, Flora Street, Bulaksumur, 55281, Yogyakarta, Indonesia.
ORCID iD: https://orcid.org/0000-0003-0872-7928

Jamhari Jamhari
Gadjah Mada University, Faculty of Agriculture, Department of Agricultural Socio-Economics, Flora Street, Bu-laksumur, 55281, Yogyakarta, Indonesia
ORCID iD: https://orcid.org/0000-0002-5982-8983
*Contact e-mail: *jamhari@ugm.ac.id*

Dwidjono Hadi Darwanto
Gadjah Mada University, Faculty of Agriculture, Department of Agricultural Socio-Economics, Flora Street, Bulaksumur, 55281, Yogyakarta, Indonesia
ORCID iD: https://orcid.org/0000-0002-9954-7086

Arini Wahyu Utami
Gadjah Mada University, Faculty of Agriculture, Department of Agricultural Socio-Economics, Flora Street, Bulaksumur, 55281, Yogyakarta, Indonesia
ORCID iD: https://orcid.org/0000-0001-6379-8492

*Corresponding author(s) contact email

To cite this article:

Nisa, D.P.J.I.N., Jamhari, J., Darwanto, D.H & Utami, A.W. (2026). Digital transformation, cocoa downstreaming and export competitiveness. *The Eurasia Proceedings of Science, Technology, Engineering and Mathematics (EPSTEM), 42,* 97-127.

The Eurasia Proceedings of Science, Technology, Engineering and Mathematics (EPSTEM)
ISSN: 2602-3199

The Eurasia Proceedings of Science, Technology, Engineering and Mathematics (EPSTEM), 2026

Volume 42, Pages 128-135

ICBASET 2026: International Conference on Basic Sciences, Engineering and Technology

Low-Temperature Fatigue Performance of Polymer-Modified Asphalt Mixtures Evaluated by Cyclic SCB Testing

Abdullah Demirbag
Firat University

Erkut Yalcin
Firat University

Abstract: Fatigue cracking is one of the most critical deterioration mechanisms affecting the service life of asphalt pavements. This study investigates the fatigue crack propagation behavior of asphalt mixtures modified with styrene-butadiene-styrene (SBS), Enprene 611, Enprene 701, and crumb rubber (CR) under low-temperature conditions. Semi-Circular Bending (SCB) specimens with notch depths of 10, 20, and 30 mm were subjected to cyclic loading at −20°C. Static SCB tests were first conducted to determine the reference load levels, and the resulting values were used to establish the loading protocol for the cyclic experiments. The deformation–load cycle relationships obtained from the cyclic SCB tests were analyzed to evaluate fatigue resistance and crack propagation characteristics. The results showed that all modifiers improved fatigue performance compared with the virgin and control mixtures by reducing deformation accumulation and delaying crack growth. Among the additives, Enprene 611 exhibited the highest fatigue resistance, particularly at a dosage of 4%, providing the greatest number of load cycles and the lowest deformation growth rate. SBS also significantly enhanced fatigue performance, while Enprene 701 and CR provided moderate improvements. Increasing notch depth accelerated crack propagation and reduced fatigue life for all mixtures. Based on the overall performance, the mixtures were ranked as Enprene 611 > SBS ≈ Enprene 701 > CR > Control > Virgin mixture. The findings indicate that polymer modification, particularly with Enprene 611, is an effective approach for improving the low-temperature fatigue crack resistance of asphalt mixtures and extending pavement service life.

Keywords: Asphalt mixture, Fatigue cracking, Cyclic SCB test, Fracture mechanics, Polymer modification

Introduction

Fatigue cracking is one of the major distress mechanisms in asphalt pavements, together with rutting and low-temperature cracking. It develops when pavement structures lose their ability to resist repeated traffic loading, eventually leading to functional failure and the need for rehabilitation or replacement (Roberts, 1996). Fatigue damage generally consists of two stages: crack initiation and crack propagation. Two main approaches are commonly used to evaluate this phenomenon: the phenomenological approach and fracture mechanics. In the phenomenological approach, smooth specimens are tested under controlled stress or strain conditions, and fatigue life is defined as the number of load cycles required for crack initiation and subsequent growth until failure. Fracture mechanics, however, assumes that materials contain inherent defects prior to loading. Accordingly, fatigue life is described as the number of cycles required for an existing flaw to propagate to a critical size. Crack growth behavior is commonly characterized using the Paris law equation (Paris, 1963; Huang, 2013).

The selection of an appropriate testing method is critical for accurately assessing fatigue performance. Although the Semi-Circular Bending (SCB) test effectively distinguishes asphalt mixtures based on fracture resistance, the

- This is an Open Access article distributed under the terms of the Creative Commons Attribution-Noncommercial 4.0 Unported License, permitting all non-commercial use, distribution, and reproduction in any medium, provided the original work is properly cited.

- Selection and peer-review under responsibility of the Organizing Committee of the Conference

© 2026 Published by ISRES Publishing: www.isres.org

fracture energy parameter (Jc) alone may not fully represent fatigue behavior. Repeated loading tests provide a more realistic simulation of damage accumulation in pavement structures; therefore, cyclic SCB testing combined with Paris law analysis has become a widely adopted approach for evaluating fatigue crack growth (Huang, 2013; Paris, 1963; Cheng, 2022; Walubita, 2012). However, determination of Paris law parameters requires accurate crack length measurements, which cannot be directly obtained using conventional devices such as strain gauges, extensometers, or LVDTs. To address this limitation, Digital Image Correlation (DIC) has emerged as a non-contact optical technique capable of monitoring surface deformations and crack development during testing (Chu, 1985). Previous studies have successfully applied DIC to investigate crack propagation in asphalt mixtures, demonstrating its effectiveness in fracture characterization (Birgisson, 2009; Chehab, 2007; Al-Qadi, 2022; Xing, 2017).

The integration of cyclic SCB testing and fracture mechanics has attracted considerable attention in recent years. Hofman et al. monitored crack growth during cyclic SCB tests using digital image analysis and mortar displacement methods (Hofman, 2003). Similarly, Paris law has been applied together with cyclic SCB testing to characterize crack propagation by relating strain energy release rates obtained from load–displacement hysteresis loops to fatigue crack growth behavior (Mull, 2005). Saha et al. developed a fatigue prediction model based on crack mouth opening displacement (CMOD) measurements obtained from cyclic SCB experiments (Saha, 2017). Zhang et al. employed DIC to establish a relationship between crack length and CMOD, enabling crack length estimation throughout fatigue testing (Zhang, 2018). Teixeira et al. demonstrated that cyclic SCB testing provides fatigue results comparable to indirect tensile fatigue tests while offering improved repeatability and shorter testing durations (Teixeira, 2023). Huang et al. combined SCB fatigue testing with finite element analysis and reported that binder modifiers significantly influenced fracture resistance, while the obtained Paris law parameters were consistent with previous studies (Huang, 2013). Ma et al. proposed an optimized cyclic SCB procedure and showed that Paris law coefficients were less sensitive to notch depth and loading frequency than fatigue life measurements (Ma, 2024). Furthermore, Saha and Biligiri related modulus degradation to fracture characteristics obtained from dynamic SCB tests and developed a nomograph to predict stiffness reduction as crack growth progressed (Saha, 2018). The novelty of this study lies in the comparative evaluation of SBS, Enprene 611, Enprene 701, and crumb rubber-modified asphalt mixtures using cyclic SCB tests under low-temperature conditions. By investigating fatigue crack propagation behavior at different notch depths, the study provides insight into the effectiveness of these modifiers in improving the low-temperature fatigue resistance of asphalt mixtures.

Method and Testing

In this study, B70/100 penetration-grade bitumen supplied by Batman Refinery was used as the base binder. The density of the reference binder was measured as 1.033 g/cm³, and its basic properties are presented in Table 1. Four modifiers were used to modify the base binder: SBS, Enprene 701, Enprene 611, and crumb rubber (CR). CR was obtained from waste vehicle tires and sieved through a No. 40 sieve before use. The remaining modifiers were supplied by their respective manufacturers. The technical properties of SBS, Enprene 701, and Enprene 611 are summarized in Table 2 based on the manufacturers' data sheets.

Table 1. Physical properties of the base binder

Properties	Unit	Standard	Results
Penetration	0.1mm	EN 1426	87.4
Softening point	°C	EN 1427	52.6
Flash point	°C	EN ISO 2719	230
Viscosity at 135°C /165°C	cP	ASTM D4402	562.5/162.5

Table 2. Properties of the polymer modifiers used in the study

Properties	SBS	701	611
Molecular structure	Linear	Linear	Radial
Styrene/butadiene ratio	31/69	33/67	31/69
Density (g/cm^3)	0.94	0.93	0.94
Oil content	None	None	None
Viscosity (5%, cps)	-	14	24
Tensile strength (kgw/cm^2)	324	220	200
Hardness	70	80	83
Ash content	-	0.2	0.2
Elongation at break (%)	880	600	700

Preparation of Modified Bitumen and Asphalt Mixtures

Modified binders were produced by incorporating SBS, 611, 701, CR, into the base bitumen. The base binder was first heated to 180 ± 5°C and then blended with the selected modifiers at dosages of 2%, 3%, and 4% for SBS, Enprene 611, and Enprene 701, and 4%, 6%, and 8% for CR, by mass of the base binder (Yalcin, 2022; Sayedzada, 2024).

In the figures, C denotes the asphalt mixture prepared with the untreated base binder. MC denotes the control mixture prepared with the base binder subjected to the same heating and mixing procedure used for modification (180 ± 5°C, 2700 rpm, 4 h), without adding any modifier. This control was included to distinguish the effects of modifier addition from those of the heating and mixing procedure. The notation used for modified mixtures consists of two parts. The first number indicates the additive dosage by weight of binder (e.g., 2, 3, and 4 correspond to 2%, 3%, and 4%, respectively), whereas the second part identifies the type of modifier used. For example, 2-611, 3-611, and 4-611 represent asphalt mixtures modified with 2%, 3%, and 4% Enprene 611, respectively. This naming convention is adopted throughout the study to facilitate comparison of the effects of additive type and dosage on the fatigue and fracture performance of asphalt mixtures.

Asphalt mixtures were prepared using the aggregate gradation shown in Table 3. Specimens were compacted with a gyratory compactor under a pressure of 600 ± 18 kPa, an internal angle of 1.25 ± 0.02°, and 100 gyrations to achieve approximately 4% air voids. The control mixture was mixed and compacted at 171 °C and 158 °C, respectively. Volumetric properties of the reference mixture included 3.78% air voids (Va), 74.3% voids filled with asphalt (VFA), 14.7% voids in mineral aggregate (VMA), and a bulk specific gravity (Gmb) of 2.292.

For cyclic SCB testing, 150-mm-diameter gyratory-compacted specimens were cut into semicircular specimens. Notches with depths of 10, 20, and 30 mm were introduced at the midpoint of the straight edge. These three notch depths were used to investigate the influence of initial notch depth on the cyclic response of the mixtures.

Table 3. Aggregate gradation used in asphalt mix

Sieve Size (mm)	19	12.5	9.5	4.75	2.36	1.18	0.6	0.3	0.15	0.075
Passing (%)	100	95	88	65	35	23	14	10	8	6

SCB Experiment

To determine the loading levels applied in the cyclic SCB tests, the maximum load values obtained from the static SCB experiments were first considered. These values provided the reference stress levels representing the load-carrying capacity of the mixtures under monotonic loading for each temperature and initial notch depth. At −20°C, the average maximum loads were measured as 13,420 N, 8,221 N, and 5,901 N for notch depths of 10 mm, 20 mm, and 30 mm, respectively.

At −20°C, the average maximum load decreased from 13,420 N at a notch depth of 10 mm to 8,221 N at 20 mm and 5,901 N at 30 mm. This corresponds to an approximately 56% reduction between the 10 and 30 mm notch depths, demonstrating the influence of initial notch depth on the load-carrying capacity of the specimens.

As the notch depth increased from 10 mm to 30 mm, the maximum load capacity decreased substantially, confirming the significant effect of specimen geometry on fracture behavior. These findings demonstrate that the fracture behavior of asphalt mixtures is highly sensitive to both temperature and specimen geometry. The average maximum load values obtained from the static SCB tests were subsequently used to establish the loading protocol for the cyclic SCB experiments. In this way, loading levels appropriate to the static strength of the material were selected for each testing condition, ensuring a consistent and reliable evaluation of fatigue crack propagation behavior.

Results and Discussion

Figure 1 presents the deformation–load cycle curves obtained at −20°C with a 10 mm notch depth. The results clearly show that all modified mixtures outperformed the virgin and control mixtures by increasing fatigue life and reducing deformation accumulation. While the virgin and control mixtures failed after approximately 2,200–2,700 cycles, most modified mixtures survived between 6,000 and 14,000 cycles. All curves exhibited three typical stages: initial deformation settlement, a stable deformation accumulation phase, and a rapid

increase in deformation before failure. The modified mixtures displayed a considerably longer stable region, indicating slower damage development.

Among the additives, Enprene 611 provided the best performance. The 4% Enprene 611 mixture achieved the highest fatigue life, reaching approximately 13,500–14,000 cycles while maintaining low deformation levels. The 3% and 2% Enprene 611 mixtures also showed substantial improvements compared with the virgin mixture. SBS-modified mixtures exhibited similar behavior, with the 4% SBS mixture reaching approximately 11,500–12,000 cycles. Increasing SBS content consistently improved fatigue performance, although Enprene 611 produced slightly better results at comparable dosages.

Enprene 701 also improved fatigue resistance, but its performance remained below that of Enprene 611 and SBS. The 4% Enprene 701 mixture reached approximately 8,500–9,000 cycles, whereas lower dosages exhibited shorter fatigue lives. CR-modified mixtures showed higher initial deformation but relatively stable behavior during later loading stages. The 8% CR mixture achieved the best result within the CR group, reaching approximately 6,000–6,200 cycles. These findings suggest that CR primarily enhances ductility and deformation tolerance, whereas Enprene 611 and SBS are more effective in improving overall fatigue resistance.

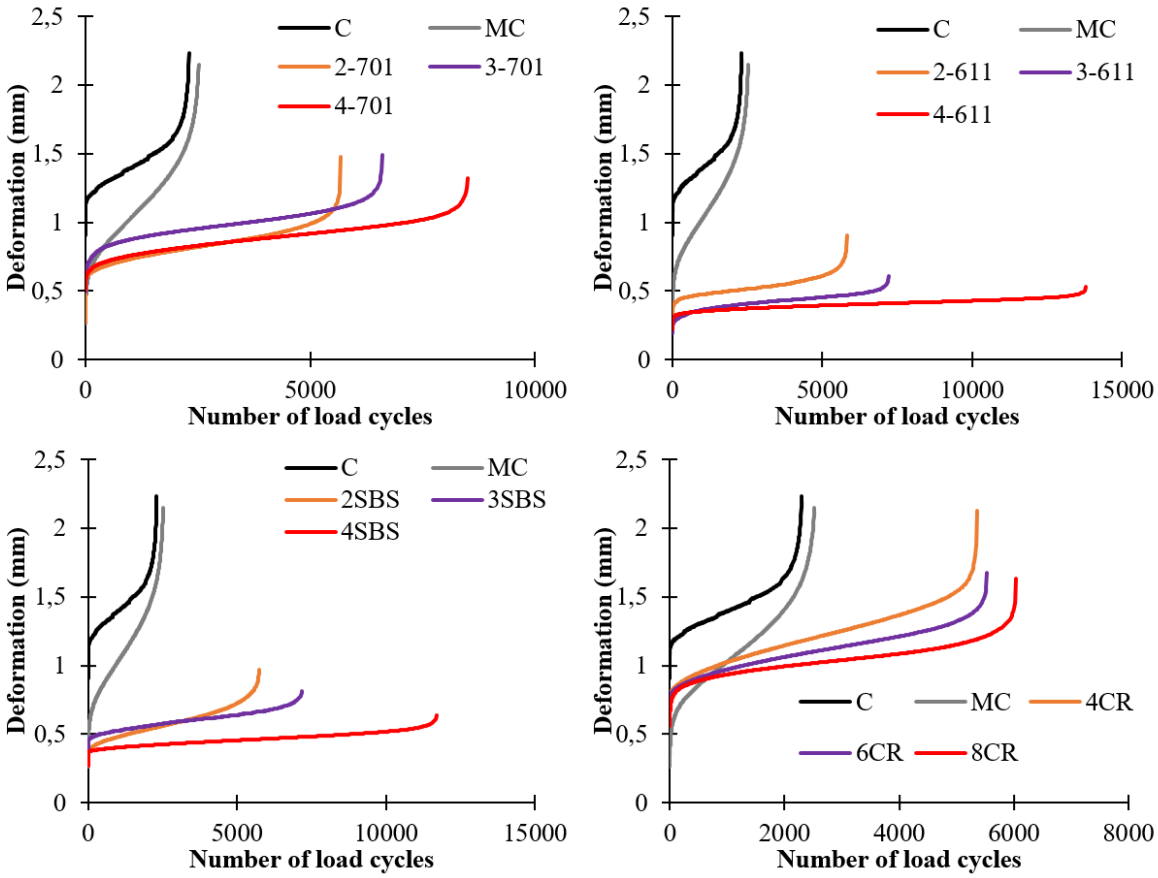

Figure 1. Deformation-load cycle count curves at -20°C and 10 mm notch

As shown in Figure 2, the virgin and control mixtures exhibited a rapid increase in deformation and reached failure at relatively low numbers of load cycles under the conditions of −20°C and a 20 mm notch depth. In contrast, the modified mixtures accumulated deformation more gradually, resulting in an improvement in fatigue life. Among the additives, Enprene 611 demonstrated the best performance, with deformation curves becoming flatter as the additive content increased, indicating delayed crack propagation. The 4% Enprene 611 mixture achieved the highest number of load cycles and the lowest rate of deformation growth. SBS-modified mixtures exhibited stable behavior and high fatigue resistance with moderate deformation accumulation, while Enprene 701 provided similar but slightly lower performance. Although CR-modified mixtures showed greater ductility and higher initial deformation levels, their fatigue performance remained lower than that of the other modifiers due to a faster increase in deformation during later loading stages. Overall, all additives improved fracture resistance and delayed crack propagation at low temperatures, with the performance ranking determined as: Enprene 611 > SBS ≈ Enprene 701 > CR > Control > Virgin mixture.

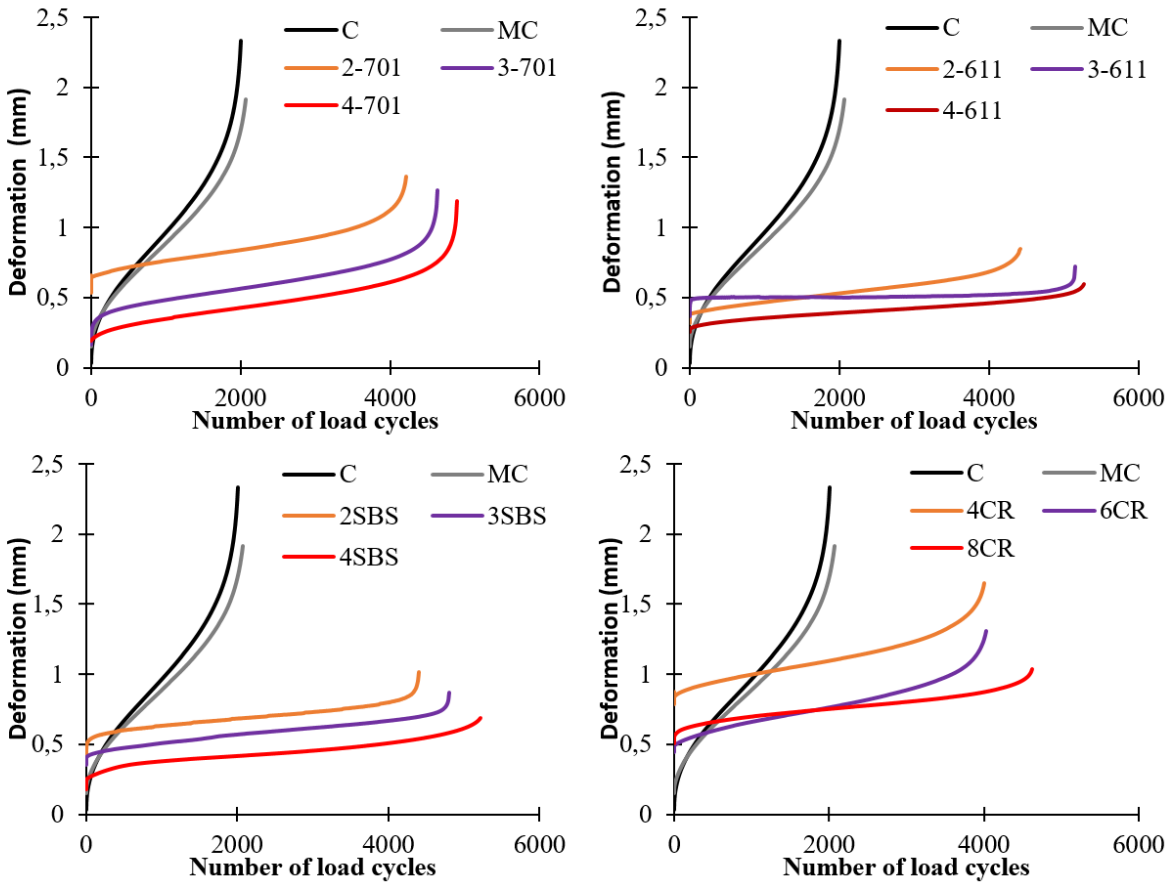

Figure 2. Deformation-load cycle count curves at -20°C and a 20 mm notch

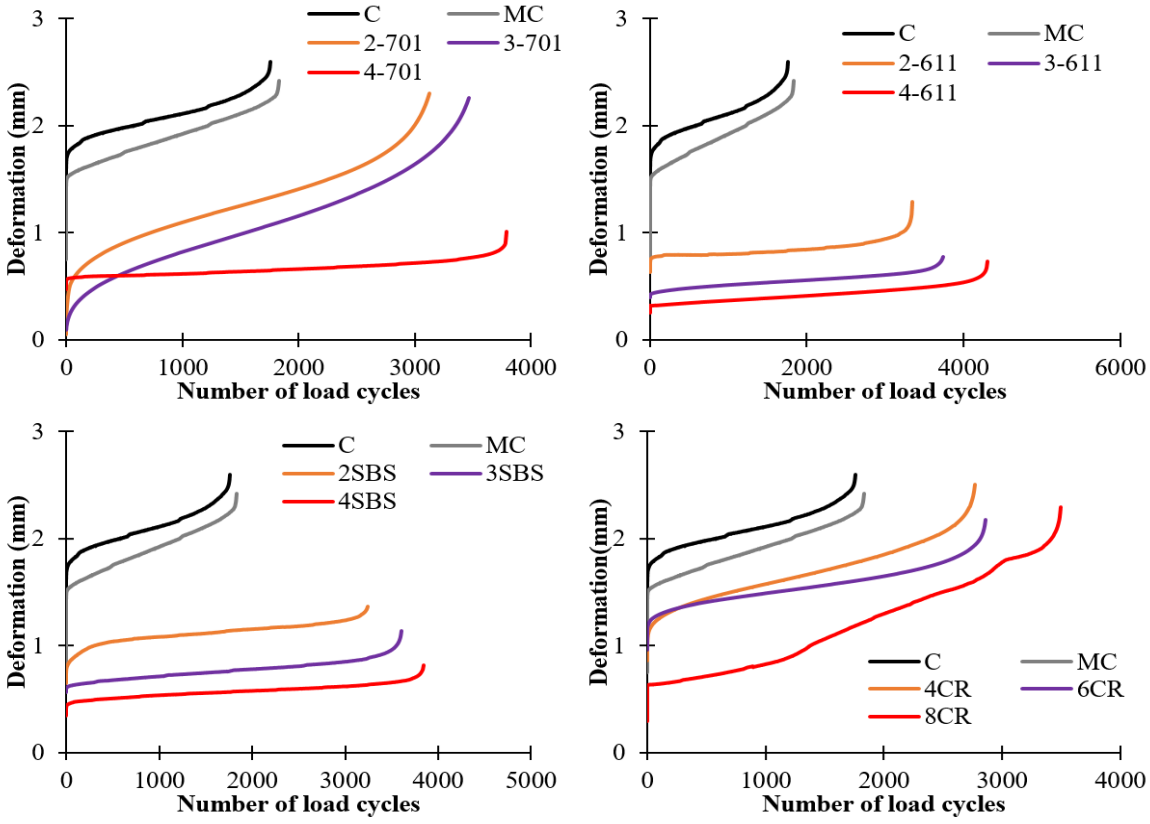

Figure 3. Deformation-load cycle count curves at -20°C and a 30 mm notch

As illustrated in Figure 3, the virgin and control mixtures exhibited a rapid increase in deformation and failed at relatively low numbers of load cycles under dynamic loading at −20°C with a 30 mm notch depth. The effect of notch depth became more pronounced, accelerating crack propagation and reducing fatigue life. In contrast, all modified mixtures reduced deformation accumulation and achieved higher load cycle numbers, indicating improved resistance to crack growth.

Among the modifiers, Enprene 611 provided the best overall performance. As the additive content increased, the deformation curves became noticeably flatter, demonstrating slower crack propagation and enhanced fatigue resistance. The 4% Enprene 611 mixture exhibited the lowest deformation growth rate and the highest fatigue life. SBS-modified mixtures also showed stable and balanced deformation behavior, with performance improving as the SBS content increased, although their effectiveness remained slightly lower than that of Enprene 611. Enprene 701 exhibited a similar trend to SBS but generally showed higher deformation levels and lower fatigue resistance. CR-modified mixtures displayed greater initial ductility and higher initial deformation; however, deformation accumulated more rapidly at higher load cycles, resulting in lower fatigue performance compared with the other modifiers.

Overall, although increasing the notch depth to 30 mm accelerated crack propagation, all modifiers substantially mitigated this adverse effect. The performance ranking was determined as: Enprene 611 > SBS ≈ Enprene 701 > CR > Control > Virgin mixture.

Conclusion

The fatigue crack propagation behavior of asphalt mixtures modified with SBS, Enprene 611, Enprene 701, and crumb rubber (CR) was evaluated using cyclic SCB tests conducted at −20°C under different notch depths. The results demonstrated that all modifiers improved fatigue performance compared with the virgin and control mixtures by reducing deformation accumulation and delaying crack propagation. Increasing notch depth accelerated crack growth and reduced fatigue life, highlighting the significant influence of specimen geometry on fracture behavior. Among the additives, Enprene 611 exhibited the best overall performance, with the 4% Enprene 611 mixture providing the highest fatigue life and the lowest deformation growth rate under all test conditions. SBS also significantly enhanced fatigue resistance, although its performance remained slightly lower than that of Enprene 611. Enprene 701 improved fatigue behavior compared with the virgin mixture but was less effective than Enprene 611 and SBS. CR-modified mixtures exhibited greater ductility and improved fatigue resistance; however, their higher deformation levels resulted in lower overall performance than the polymer-modified mixtures. Based on all test results, the overall performance ranking was determined as Enprene 611 > SBS ≈ Enprene 701 > CR > Control > Virgin mixture. Under the investigated laboratory conditions, the mixture containing 4% Enprene 611 exhibited the most favorable cyclic SCB response at −20°C among the mixtures tested.

Recommendations

The laboratory results identify Enprene 611 as a promising modifier for improving the cyclic SCB response of asphalt mixtures at −20°C. Future studies should investigate the long-term aging performance of Enprene-modified mixtures and evaluate their behavior under different temperatures, loading frequencies, and environmental conditions. In addition, field-scale validation studies are recommended to confirm the laboratory findings and assess the practical applicability of these modifiers in pavement construction. Further research incorporating Digital Image Correlation (DIC) and fracture mechanics parameters is also suggested to provide a more comprehensive understanding of crack initiation and propagation mechanisms in modified asphalt mixtures.

Scientific Ethics Declaration

* The authors declare that this study complies with scientific research and publication ethics. All scientific, ethical, and legal responsibilities related to the content of this article belong to the authors.

Conflict of Interest

* The authors declare that they have no conflicts of interest.

Funding

* This study was supported by the Fırat University Scientific Research Project Management Unit (FUBAP) under Project No. MF.26.83. The authors would like to acknowledge the financial support provided by the Scientific and Technological Research Council of Türkiye (TÜBİTAK) under Project No. 123M648, as well as the support received through the TÜBİTAK 2224-B Domestic Scientific Event Participation Support Program.

Acknowledgements or Notes

* This article was presented as an oral presentation at the International Conference on Basic Sciences, Engineering and Technology (www.icbaset.net) held in Istanbul/Türkiye on September 17-18, 2026.

References

Al-Qadi, I. L., Said, I. M., Ali, U. M., & Kaddo, J. R. (2022). Cracking prediction of asphalt concrete using fracture and strength tests. *International Journal of Pavement Engineering, 23*(10), 3333–3345.

Birgisson, B., Montepara, A., Romeo, E., Roncella, R., Roque, R., & Tebaldi, G. (2009). An optical strain measurement system for asphalt mixtures. *Materials and Structures, 42*(4), 427–441.

Chehab, G. R., Seo, Y., & Kim, Y. R. (2007). Viscoelastoplastic damage characterization of asphalt–aggregate mixtures using digital image correlation. *International Journal of Geomechanics, 7*(2), 111–118.

Cheng, L., Zhang, L., Liu, X., Yuan, F., Ma, Y., & Sun, Y. (2022). Evaluation of the fatigue properties for the long-term service asphalt pavement using the semi-circular bending tests and stereo digital image correlation technique. *Construction and Building Materials, 317*, 126119.

Chu, T. C., Ranson, W. F., & Sutton, M. A. (1985). Applications of digital-image-correlation techniques to experimental mechanics. *Experimental Mechanics, 25*(3), 232–244.

Hofman, R., Oosterbaan, B., Erken, S. M. J. G., & van de Kuilen, J. (2003). Semi-circular bend test to assess the resistance against crack growth. In *Proceedings of the Sixth International RILEM Symposium* (pp. 257–263). Zurich, Switzerland.

Huang, B., Shu, X., & Zuo, G. (2013). Using notched semi-circular bending fatigue test to characterize fracture resistance of asphalt mixtures. *Engineering Fracture Mechanics, 109*, 78–88.

Ma, Y., Mohammad, L. N., Liu, J., Asghar, M., Elnaml, I., Cooper, S. B., et al. (2024). Development of a cyclic semi-circular bending test protocol to characterize fatigue cracking of asphalt mixture at intermediate temperature. *Construction and Building Materials, 443*, 137669.

Mull, M. A., Othman, A., & Mohammad, L. (2005). Fatigue crack propagation analysis of chemically modified crumb rubber–asphalt mixtures. *Journal of Elastomers and Plastics, 37*(1), 73–87.

Paris, P., & Erdogan, F. (1963). A critical analysis of crack propagation laws. *Journal of Basic Engineering, 85*(4), 528–533.

Roberts, F. L., Kandhal, P. S., Brown, E. R., Lee, D. Y., & Kennedy, T. W. (1996). *Hot mix asphalt materials, mixture design and construction* (2nd ed.). NAPA Education Foundation.

Saha, G., & Biligiri, K. P. (2017). Stato-dynamic response analyses through semi-circular bending test: Fatigue life prediction of asphalt mixtures. *Construction and Building Materials, 150*, 664–672.

Saha, G., & Biligiri, K. P. (2018). Modulus prediction of asphalt mixtures using dynamic semicircular bending test: Estimation algorithm and nomograph development. *International Journal of Fatigue, 109*, 137–144.

Sayedzada, S. E., Ozdemir, A. M., Yalcin, E., & Yilmaz, M. (2024). Investigation of mechanical properties of hot mix asphalts with modified binders with SBS, 611 and 701 polymers. *Polymer Bulletin, 81*, 3695–3724.

Teixeira, J. E. S. L., Amaecing Junior, C. M., Rezende, L. R., Castelo Branco, V. T. F., & Kim, Y. R. (2023). Evaluation of asphalt concrete's fatigue behavior using cyclic semi-circular bending test. *Construction and Building Materials, 400*, 132772.

Walubita, L. F., Simate, G. S., Ofori-Abebresse, E., Martin, A. E., Lytton, R. L., & Sanabria, L. E. (2012). Mathematical formulation of HMA crack initiation and crack propagation models based on continuum fracture-mechanics and work-potential theory. *International Journal of Fatigue, 40*, 112–119.

Xing, C., Tan, Y., Liu, X., Anupam, K., & Scarpas, T. (2017). Research on local deformation property of asphalt mixture using digital image correlation. *Construction and Building Materials, 140*, 416–423.

Yalcin, E., & Demirbag, A. (2022). Effects of modified binders obtained from different polymers on conventional and rheological properties. *Construction and Building Materials, 357*, 129366.

Zhang, J., Sakhaeifar, M., Little, D. N., Bhasin, A., & Kim, Y. R. (2018). Characterization of crack growth rate of sulfur-extended asphalt mixtures using cyclic semicircular bending test. *Journal of Materials in Civil Engineering, 30*(11).

Author(s) Information

Abdullah Demirbag
Firat University, Engineering Faculty,Civil Engineering Department, Elazig, Türkiye
ORCID iD: https://orcid.org/0000-0002-0979-5730

Erkut Yalcin
Firat University, Engineering Faculty,Civil Engineering Department, Elazig, Türkiye
ORCID iD: https://orcid.org/0000-0002-6389-4211
*Contact e-mail: *erkutyalcin@firat.edu.tr*

*Corresponding author(s) contact email

To cite this article:

Demirbag A. & Yalcin, E. (2026). Low-temperature fatigue performance of polymer-modified asphalt mixtures evaluated by cyclic SCB testing. *The Eurasia Proceedings of Science, Technology, Engineering and Mathematics (EPSTEM), 42,* 128-135.

The Eurasia Proceedings of Science, Technology, Engineering and Mathematics (EPSTEM)
ISSN: 2602-3199

The Eurasia Proceedings of Science, Technology, Engineering and Mathematics (EPSTEM), 2026

Volume 42, Pages 136-151

ICBASET 2026: International Conference on Basic Sciences, Engineering and Technology

Why Two's Complement Became the Standard: A Comparative Analysis of Unsigned, Sign-Magnitude, One's Complement, and Two's Complement Representations

Bojken Shehu
Polytechnic University of Tirana

Abstract: Binary number representation is a fundamental concept in computer architecture that directly influences arithmetic operations, data representation, processor design, and hardware implementation. Although several methods have been developed for representing signed integers, modern computer systems predominantly employ Two's Complement representation. This paper presents a comparative analysis of four binary number representation methods: Unsigned, Sign-Magnitude, One's Complement, and Two's Complement. The analysis examines their numerical ranges, number of distinct representable values, zero representation, binary encoding, bit-width expansion procedures, sign extension techniques, overflow and underflow behavior, and suitability for hardware arithmetic. A unified comparative framework, supported by mathematical formulas, illustrative examples, conversion cases, and comparative tables, is used to systematically examine the similarities, differences, and architectural trade-offs among the four representations. The results show that the four representations differ in how numerical values are encoded and how numerical meaning is preserved during bit-width expansion. Unsigned representation relies on zero padding, while Sign-Magnitude preserves the sign bit and inserts additional zeros between the sign bit and the magnitude bits. In contrast, One's Complement and Two's Complement employ classical sign extension by replicating the most significant bit. The comparison further demonstrates that Sign-Magnitude and One's Complement suffer from duplicate zero representations and additional arithmetic complexity. Two's Complement, however, provides a unique representation of zero, fully utilizes all available binary combinations, supports efficient sign extension, and enables addition and subtraction using simplified arithmetic circuitry. The analysis also highlights numerical limitations and overflow characteristics associated with fixed-width representations. These technical advantages explain why Two's Complement has become the standard representation for signed integers in modern computer systems. The proposed framework provides a structured reference for understanding design trade-offs and practical implications in computer architecture and digital systems.

Keywords: Binary number representation, Unsigned representation, Sign-magnitude, One’s complement, Two’s complement

Introduction

Binary number representation is a fundamental concept in digital computer systems and computer architecture. Since digital hardware operates using only two voltage levels, all numerical values must be represented in binary form. The choice of a binary number representation directly influences arithmetic operations, processor design, memory organization, compiler implementation, instruction execution, and the overall efficiency of computer systems. Consequently, understanding how computers represent both positive and negative integers is essential in computer architecture and digital systems (Stallings, 2022; Patterson & Hennessy, 2020; Mano & Ciletti, 2018). Representing unsigned integers in binary is straightforward because every bit contributes directly to the numerical value. However, representing signed integers introduces additional challenges, as the system must distinguish between positive and negative values while maintaining efficient arithmetic operations. Throughout the history of

- This is an Open Access article distributed under the terms of the Creative Commons Attribution-Noncommercial 4.0 Unported License, permitting all non-commercial use, distribution, and reproduction in any medium, provided the original work is properly cited.

- Selection and peer-review under responsibility of the Organizing Committee of the Conference

© 2026 Published by ISRES Publishing: www.isres.org

computer architecture, several techniques have been developed to address this problem, including Sign-Magnitude, One's Complement, and Two's Complement representations. Although these methods represent signed integers using the same fixed bit width, they differ significantly in terms of numerical range, zero representation, arithmetic complexity, bit-width expansion, sign extension, and hardware implementation (Stallings, 2022; Mano & Ciletti, 2018; Parhami, 2010).

Today, virtually all modern computer systems use Two's Complement for signed integer representation (Patterson & Hennessy, 2020; Intel Corporation, n.d.; RISC-V International, n.d.). This widespread adoption is primarily motivated by its ability to eliminate duplicate zero representations, fully utilize all available binary combinations, simplify arithmetic circuits, and support efficient sign extension (Stallings, 2022; Parhami, 2010; Bastien, 2018). Despite the widespread use of Two's Complement in modern computer systems, a unified comparison of the four principal binary number representation methods is rarely presented within a single analytical framework. Existing literature in computer architecture, digital design, and computer arithmetic commonly discusses these representation methods in separate contexts, which can make their relationships, implementation differences, and practical implications less apparent when considered as a unified system. This paper addresses this gap by providing a structured comparative analysis that examines all four representation methods using identical evaluation criteria.

This paper presents a comprehensive comparative analysis of four binary number representation methods: Unsigned, Sign-Magnitude, One's Complement, and Two's Complement. The comparison is performed using a unified framework that examines their numerical ranges, maximum number of representable values, zero representation, bit-width expansion mechanisms, sign extension techniques, and suitability for hardware arithmetic. To improve clarity, the paper also provides comparative tables and illustrative examples that highlight the similarities and differences among the four representations.

The main contributions of this paper are as follows:

- A unified comparative framework for analyzing Unsigned, Sign-Magnitude, One's Complement, and Two's Complement representations.
- A systematic comparison of numerical range, zero representation, bit-width expansion, sign extension, and hardware arithmetic characteristics.
- Comparative tables and illustrative binary examples that highlight the similarities and differences among the four representations.
- A technical explanation of why Two's Complement has become the standard representation for signed integers in modern computer systems.

To guide the analysis, the following research questions are addressed:

RQ1: What are the fundamental differences among Unsigned, Sign-Magnitude, One's Complement, and Two's Complement representations?
RQ2: How do these representations differ in terms of numerical range, zero representation, bit-width expansion, sign extension, and hardware arithmetic?
RQ3: Why has Two's Complement become the standard representation for signed integers in modern computer systems?

The contribution of this study is not the introduction of a new binary representation method, but the systematic comparison of the four principal representations using a unified set of technical criteria, including numerical range, zero representation, bit-width expansion, sign extension, overflow behavior, and hardware arithmetic. The remainder of this paper is organized as follows. Section II introduces the fundamental concepts of binary number representation and discusses the four representation methods. Section III presents a comparative analysis supported by comparative tables and illustrative examples. Section IV discusses the findings of the comparative analysis and explains why Two's Complement has become the standard representation for signed integers in modern computer systems. Finally, Section V concludes the paper by summarizing the main findings and outlining directions for future work.

Binary Number Representation Fundamentals

Binary numbers can be represented using different encoding methods depending on whether only non-negative integers or both positive and negative integers need to be represented. Each representation has distinct

characteristics regarding numerical range, zero representation, arithmetic operations, and bit-width expansion. Figure 1 provides an overview of the four binary number representation methods analyzed in this paper and illustrates their fundamental relationships (Stallings, 2022; Patterson & Hennessy, 2020; Mano & Ciletti, 2018; Tanenbaum & Austin, 2013).

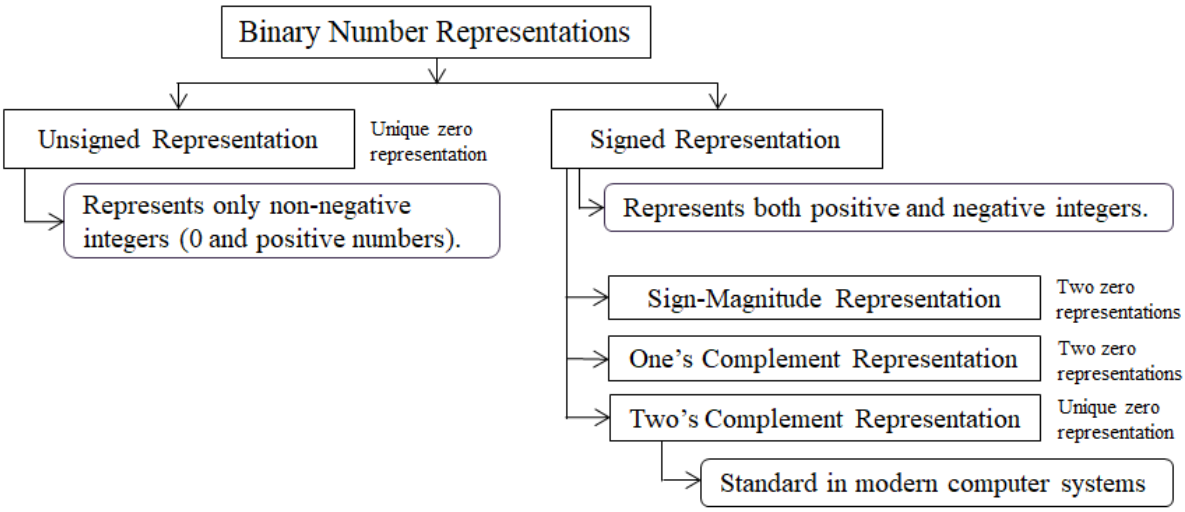

Figure 1. Classification of binary number representations methods

As illustrated in Figure 1, binary number representations can be broadly classified into unsigned and signed representations. Unsigned representation is suitable only for non-negative integers, whereas signed representations support both positive and negative values. Among the signed methods, Sign-Magnitude and One's Complement provide two representations of zero, while Two's Complement has a unique representation of zero and is therefore adopted as the standard representation in modern computer systems (Stallings, 2022; Patterson & Hennessy, 2020; Parhami, 2010; Intel Corporation, n.d.; RISC-V International, n.d.). The following subsections examine each representation in detail, including its numerical range, binary encoding, bit-width expansion, and main advantages and disadvantages.

Unsigned Representation

The Unsigned Representation is the simplest method for representing binary integers. In this representation, all bits are used to represent the magnitude of the number, and no bit is reserved to indicate the sign. Consequently, only non-negative integers (zero and positive values) can be represented (Stallings, 2022; Mano & Ciletti, 2018). The numerical range of an *n*-bit unsigned representation is :

$$0 \leq x \leq 2^n - 1 ,$$

providing a total of 2^n distinct numerical values. Since no sign bit exists, there is only one representation of zero, and all possible binary combinations correspond to unique decimal values. Consequently, any arithmetic result greater than $2^n - 1$ cannot be represented within the given bit width, resulting in positive overflow. Similarly, a negative result falls outside the representable range of the unsigned representation. Table 1 summarizes the numerical range for both the 3-bit example and the general *n*-bit case.

Table 1. Numerical range of unsigned representation

Representation	Minimum Value	Maximum Value
Unsigned (3-bit)	0	7
n-bit	0	$2^n - 1$

Table 2 presents the complete 3-bit unsigned representation, illustrating all eight binary combinations and their corresponding decimal values from 0 to 7. Because every bit contributes directly to the numerical value, the Unsigned representation provides the largest range of non-negative integers among the four methods for the same bit width (Mano & Ciletti, 2018).

Table 2. Three-bit unsigned representation

Binary (3 Bits)	Decimal Value (Unsigned)
000	0
001	1
010	2
011	3
100	4
101	5
110	6
111	7

When the bit width is increased, unsigned numbers are expanded by inserting leading zeros to the left of the most significant bit. Unlike signed representations, unsigned numbers do not require sign extension because no sign bit exists. Examples of bit-width expansion are presented in Table 3 (Stallings, 2022; Hamacher et al., 2012).

Table 3. Examples of bit-width expansion in unsigned representation

Number	Original Unsigned Representation	Extended 8-Bit Unsigned Representation
$1_{(10)}$	$0001_{(2)}$ (n = 4 bits)	$00000001_{(2)}$
$3_{(10)}$	$00011_{(2)}$ (n = 5 bits)	$00000011_{(2)}$
$5_{(10)}$	$0000101_{(2)}$ (n = 7 bits)	$00000101_{(2)}$
$0_{(10)}$	$00_{(2)}$ (n = 2 bits)	$00000000_{(2)}$

Finally, the principal advantages and disadvantages of the unsigned representation are summarized in Table 4 (Patterson & Hennessy, 2020; Stallings, 2022).

Table 4. Advantages and disadvantages of unsigned representation

Aspect	Description
Advantages	Utilizes all 2^n available binary combinations to represent distinct numerical values. Provides a unique representation of zero, eliminating ambiguity. Simple and intuitive representation, making binary-to-decimal conversion straightforward. Enables efficient arithmetic operations for non-negative integers. Requires no sign bit, allowing the maximum possible positive range for a given bit-width.
Disadvantages	Cannot represent negative numbers. Unsuitable for applications requiring signed arithmetic. Arithmetic underflow may occur when subtracting a larger value from a smaller one. Additional mechanisms are required when both signed and unsigned values must be processed together.

Sign-Magnitude Representation

Sign-Magnitude Representation is one of the earliest methods developed for representing signed integers in binary form. In this representation, the most significant bit (MSB) is reserved as the sign bit, while the remaining n−1 bits represent the magnitude (absolute value) of the number. A sign bit of 0 indicates a positive number, whereas a sign bit of 1 indicates a negative number (Mano & Ciletti, 2018; Stallings, 2022).

The numerical range of an *n*-bit Sign-Magnitude representation is :

$$-(2^{n-1}-1) \leq x \leq +(2^{n-1}-1),$$

providing a total of $2^n - 1$ distinct numerical values because zero has two separate representations (+0 and −0). Therefore, arithmetic results exceeding $+(2^{n-1}-1)$ or falling below $-(2^{n-1}-1)$ cannot be represented within the given bit width, resulting in a range overflow condition. Table 5 summarizes the numerical range for both the 3-bit example and the general *n*-bit case (Mano & Ciletti, 2018; Stallings, 2022).

Table 5. Numerical range of sign-magnitude representation

Representation	Minimum Value	Maximum Value
Sign-Magnitude (3-bit)	-3	+3
n-bit	$-(2^{n-1}-1)$	$+(2^{n-1}-1)$

Table 6 presents the complete 3-bit Sign-Magnitude representation, illustrating the binary encoding of all representable values from -3 to +3. Unlike the Unsigned representation, Sign-Magnitude supports both positive and negative integers by reserving the most significant bit as the sign bit (Mano & Ciletti, 2018).

Table 6. Three-bit sign-magnitude representation

Binary number(3 Bits)	Decimal Value (Sign-Magnitude)
000	+0
001	+1
010	+2
011	+3
100	-0
101	-1
110	-2
111	-3

When the bit width is increased, the sign bit remains unchanged, while additional bits are inserted between the sign bit and the magnitude bits. This differs from One's Complement and Two's Complement representations, which use classical sign extension by replicating the sign bit. Examples of bit-width expansion are presented in Table 7 (Hamacher et al., 2012; Stallings, 2022).

Table 7. Examples of bit-width expansion in sign-magnitude representation

Number	Original Sign Magnitude Representation	Extended 8-Bit Sign-Magnitude Representation
$-5_{(10)}$	$1101_{(2)}$ (n=4 bit)	$10000101_{(2)}$
$-8_{(10)}$	$11000_{(2)}$ (n=5 bit)	$10001000_{(2)}$
$-37_{(10)}$	$1100101_{(2)}$ (n=7 bit)	$10100101_{(2)}$
$-0_{(10)}$	$10_{(2)}$ (n=2 bit)	$10000000_{(2)}$
$+0_{(10)}$	$00_{(2)}$ (n=2 bit)	$00000000_{(2)}$
$+42_{(10)}$	$0101010_{(2)}$ (n= 7 bit)	$00101010_{(2)}$

Finally, the main advantages and disadvantages of the Sign-Magnitude representation are summarized in Table 8 (Parhami, 2010; Stallings, 2022).

Table 8. Advantages and disadvantages of sign-magnitude representation

Aspect	Description
Advantages	Represents both positive and negative numbers using an intuitive sign-and-magnitude format.
	Easy to understand because the sign and magnitude are stored separately, resembling the decimal representation of signed numbers.
	Positive and negative numbers have the same magnitude representation, differing only in the sign bit.
Disadvantages	Has two representations of zero (+0 and -0), leading to ambiguity.
	Equality checking requires special handling because both +0 and -0 must be recognized as zero.
	Addition and subtraction require separate processing depending on the signs of the operands, increasing arithmetic complexity.
	Requires more complex hardware implementation than Two's Complement representation.
	Rarely used for signed integer representation in modern computer systems.

One's Complement Representation

One's Complement Representation is a signed binary representation in which positive numbers are represented using standard binary notation, while negative numbers are obtained by inverting every bit of the corresponding positive number. In other words, every bit is inverted: each 0 becomes 1, and each 1 becomes 0 (Parhami, 2010; Stallings, 2022).

The numerical range of an n-bit One's Complement representation is:

$$-(2^{n-1}-1) \leq x \leq +(2^{n-1}-1),$$

providing a total of $2^n - 1$ distinct numerical values. Similar to Sign-Magnitude representation, One's Complement contains two representations of zero: +0, represented by all zeros, and −0, represented by all ones. Therefore, arithmetic results exceeding $+(2^{n-1} - 1)$ or falling below $-(2^{n-1} - 1)$cannot be represented within the given bit width. Table 9 summarizes the numerical range for both the 3-bit example and the general n-bit case (Parhami, 2010; Stallings, 2022).

Table 9. Numerical range of one's complement representation

Representation	Minimum Value	Maximum Value
One's Complement (3-bit)	-3	+3
n-bit	$-(2^{n-1} - 1)$	$+(2^{n-1} - 1)$

Table 10 presents the complete 3-bit One's Complement representation, illustrating the binary encoding of all representable values. Unlike Sign-Magnitude representation, negative numbers are generated by complementing every bit of the corresponding positive value rather than storing the sign separately (Parhami, 2010).

Table 10. Three-bit one's complement representation

Binary Number (3 Bits)	Decimal Value (One's Complement)
000	0
001	1
010	2
011	3
100	-3
101	-2
110	-1
111	-0

When the bit width is increased, One's Complement uses classical sign extension by replicating the most significant bit (MSB). If the MSB is 0, additional leading zeros are inserted; if the MSB is 1, additional leading ones are inserted. This process preserves the numerical value of the represented integer. Examples of bit-width expansion are presented in Table 11 (Hamacher et al., 2012; Parhami, 2010).

Table 11. Examples of sign extension in one's complement representation

Number	One's Complement Representation	8-Bit Representation after Sign Extension
$-5_{(10)}$	$1010_{(2)}$ (n = 4 bits)	$11111010_{(2)}$
$-8_{(10)}$	$10111_{(2)}$ (n = 5 bits)	$11110111_{(2)}$
$-37_{(10)}$	$1011010_{(2)}$ (n = 7 bits)	$11011010_{(2)}$
$-0_{(10)}$	$11_{(2)}$ (n = 2 bits)	$11111111_{(2)}$
$+0_{(10)}$	$00_{(2)}$ (n = 2 bits)	$00000000_{(2)}$
$+42_{(10)}$	$0101010_{(2)}$ (n = 7bits)	$00101010_{(2)}$

Finally, the principal advantages and disadvantages of the One's Complement representation are summarized in Table 12 (Parhami, 2010; Patterson & Hennessy, 2020).

Table 12. Advantages and disadvantages of one's complement representation

Aspect	Description
Advantages	Negative numbers can be generated by inverting all bits of the corresponding positive number. Sign extension is performed by replicating the most significant bit (MSB).
Disadvantages	Two representations of zero (+0 and -0) complicate comparisons and equality checking. Addition requires an end-around carry, increasing arithmetic and hardware complexity. Less efficient hardware implementation than Two's Complement representation.

Two's Complement Representation

Two's Complement Representation is the most widely used method for representing signed integers in modern computer systems. Positive numbers are represented using standard binary notation, whereas negative numbers are obtained by taking the One's Complement of the corresponding positive value and adding 1 to the resulting bit pattern (Parhami, 2010; Patterson & Hennessy, 2020; Stallings, 2022).

The numerical range of an *n*-bit Two's Complement representation is:

$$-2^{n-1} \leq x \leq +(2^{n-1}-1),$$

providing a total of 2^n distinct numerical values. Unlike Sign-Magnitude and One's Complement representations, Two's Complement has only one representation of zero, eliminating the ambiguity associated with positive and negative zero. Therefore, arithmetic results greater than $+(2^{n-1}-1)$ or less than -2^{n-1} cannot be represented within the given bit width. Table 13 summarizes the numerical range for both the 3-bit example and the general n-bit case (Parhami, 2010; Stallings, 2022).

Table 13. Numerical range of two's complement representation

Representation	Minimum Value	Maximum Value
Two's Complement (3-bit)	-4	+3
n-bit	-2^{n-1}	$+(2^{n-1}-1)$

Table 14 presents the complete 3-bit Two's Complement representation, illustrating the binary encoding of all representable values. The minimum value is represented by 100, while the maximum value is 011, resulting in an asymmetric numerical range with one additional negative value (Parhami, 2010).

Table 14. Three-bit two's complement representation

Binary Number (3 Bits)	Decimal Value (Two's Complement)
000	0
001	1
010	2
011	3
100	-4
101	-3
110	-2
111	-1

When the bit width is increased, Two's Complement uses classical sign extension by replicating the most significant bit (MSB). If the MSB is 0, leading zeros are inserted; if the MSB is 1, leading ones are inserted. This operation preserves the numerical value of both positive and negative integers. Examples of bit-width expansion are presented in Table 15 (Hamacher et al., 2012; Parhami, 2010).

Table 15. Examples of sign extension in two's complement representation

Number	Two's Complement Representation	8-Bit Representation after Sign Extension
$-5_{(10)}$	$1011_{(2)}$ (n = 4 bits)	$11111011_{(2)}$
$-8_{(10)}$	$11000_{(2)}$ (n = 5 bits)	$11111000_{(2)}$
$-37_{(10)}$	$1011011_{(2)}$ (n = 7 bits)	$11011011_{(2)}$
$0_{(10)}$	$00_{(2)}$ (n = 2 bits)	$00000000_{(2)}$
$+42_{(10)}$	$0101010_{(2)}$ (n = 7 bits)	$00101010_{(2)}$

Table 16. Advantages and disadvantages of two's complement representation

Aspect	Description
Advantages	Provides a unique representation of zero. Simplifies arithmetic operations by eliminating the end-around carry required in One's Complement representation. The standard binary adder can be used for both addition and subtraction. Simple and efficient sign extension by replicating the most significant bit (MSB). Supports efficient hardware implementation, making it the standard representation for signed integers in modern computer systems.
Disadvantages	Negating the minimum representable value results in overflow. Less intuitive for beginners than Sign-Magnitude because the stored bit pattern does not directly represent the numerical magnitude. The asymmetric numerical range provides one additional negative value (e.g., -128 to +127 in 8-bit representation). Requires understanding of complement-based representation rather than direct sign-and-magnitude notation.

Finally, the principal advantages and disadvantages of the Two's Complement representation are summarized in Table 16. The combination of a unique zero representation, efficient hardware arithmetic, and straightforward sign extension has made Two's Complement the standard representation for signed integers in virtually all modern processors (Intel Corporation, n.d.; Patterson & Hennessy, 2020; RISC-V International, n.d.; ARM Ltd., n.d.).

Comparative Analysis

This section presents a comparative analysis of the four binary number representation methods discussed in the previous section. The comparison focuses on their numerical ranges, binary encoding, bit-width expansion mechanisms, conversion processes, and overall characteristics. Through a series of comparative tables, the similarities and differences among Unsigned, Sign-Magnitude, One's Complement, and Two's Complement representations are systematically analyzed.

Comparison of Numerical Ranges, Overflow, and Underflow

The numerical range is one of the most important characteristics of a binary number representation method, as it determines the minimum and maximum values that can be represented using a fixed number of bits. Although all four representations use the same bit width, they differ in the allocation of binary patterns, resulting in different numerical ranges and numbers of representable values. These numerical limits also determine the boundaries at which overflow or underflow may occur during arithmetic operations. When an arithmetic result exceeds the maximum or falls below the minimum value representable within a fixed bit width, the result cannot be represented correctly. Therefore, comparing numerical ranges also provides a basis for analyzing the overflow and underflow behavior of the four representation methods. Table 17 summarizes the numerical range formulas for Unsigned, Sign-Magnitude, One's Complement, and Two's Complement representations for an arbitrary n-bit word.

Table 17. Numerical range formulas for different number representation methods

Representation	Minimum Value	Maximum Value	Range
Unsigned	0	$2^n - 1$	0 to $2^n - 1$
Sign-Magnitude	$-(2^{n-1} - 1)$	$+(2^{n-1} - 1)$	$-(2^{n-1} - 1)$ to $+(2^{n-1} - 1)$
One's Complement	$-(2^{n-1} - 1)$	$+(2^{n-1} - 1)$	$-(2^{n-1} - 1)$ to $+(2^{n-1} - 1)$
Two's Complement	-2^{n-1}	$+(2^{n-1} - 1)$	-2^{n-1} to $+(2^{n-1} - 1)$

As shown in Table 17, the Unsigned representation allocates all available bit patterns to non-negative integers, resulting in a range from 0 to $2^n - 1$. In contrast, Sign-Magnitude and One's Complement reserve one bit for the sign, reducing the number of distinct representable values because both methods include separate representations for +0 and −0. Consequently, their numerical range extends from $-(2^{n-1} - 1)$ to $+(2^{n-1} - 1)$. Two's Complement differs by eliminating the duplicate representation of zero, thereby utilizing all 2^n binary combinations and extending the minimum value to -2^{n-1}, while the maximum value remains $+(2^{n-1} - 1)$.

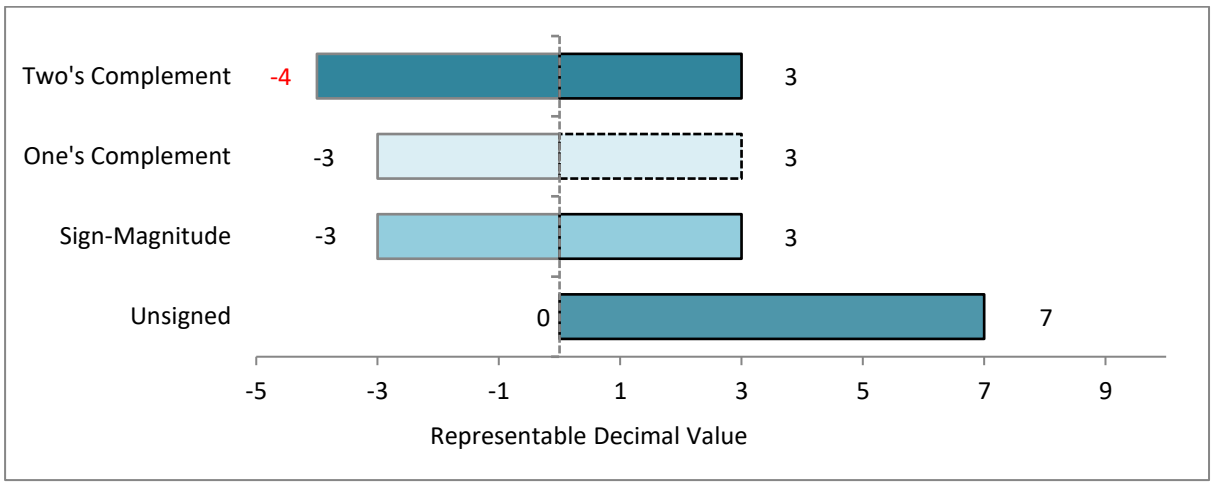

Figure 2. Numerical range comparison of 3-bit binary number representations

The differences in numerical ranges can also be visualized using a 3-bit representation. Figure 2 provides a graphical comparison of the representable decimal values for Unsigned, Sign-Magnitude, One's Complement, and Two's Complement representations. As illustrated in Figure 2, Unsigned representation provides the widest positive range, from 0 to 7, while Sign-Magnitude and One's Complement represent values from −3 to +3. Two's Complement provides an asymmetric range from −4 to +3, thereby representing one additional negative value compared with the other signed representations. The figure also demonstrates visually how the available numerical range depends on the representation method even when the same 3-bit word length is used.

The numerical limits identified in Table 17 and illustrated in Figure 2 also determine the overflow and underflow boundaries of each representation. When the result of an arithmetic operation exceeds the maximum or minimum value representable within a fixed bit width, the result can no longer be represented correctly. Although all representation methods are affected by fixed-width limitations, their overflow and underflow boundaries differ according to their respective numerical ranges. Table 18 summarizes the representable ranges and the corresponding positive and negative overflow boundaries for the four binary number representation methods.

Table 18. Representable numerical ranges and overflow boundaries for fixed-width binary representations

Representation	Representable Range	Positive Overflow	Negative Overflow / Underflow
Unsigned	0 to $2^n - 1$	Result > $2^n - 1$	N/A
Sign-Magnitude	$-(2^{n-1} - 1)$ to $+(2^{n-1} - 1)$	Result > $+(2^{n-1} - 1)$	Result < $-(2^{n-1} - 1)$
One's Complement	$-(2^{n-1} - 1)$ to $+(2^{n-1} - 1)$	Result > $+(2^{n-1} - 1)$	Result < $-(2^{n-1} - 1)$
Two's Complement	-2^{n-1} to $+(2^{n-1} - 1)$	Result > $+(2^{n-1} - 1)$	Result < -2^{n-1}

As shown in Table 18, the overflow boundaries are directly determined by the numerical range available in each representation. Unsigned representation provides the largest positive range, but it cannot represent negative values. Sign-Magnitude and One's Complement have identical numerical ranges, resulting in the same positive and negative boundaries. Two's Complement provides an asymmetric range, extending one value further in the negative direction than in the positive direction. Consequently, its minimum representable value is-2^{n-1}, while its maximum value is$+(2^{n-1} - 1)$. These differences in numerical boundaries are important when evaluating the behavior of fixed-width arithmetic operations.

The practical implications of these numerical boundaries can be illustrated using specific boundary values and arithmetic operations in a 3-bit representation. Because each representation assigns different numerical meanings to the available binary combinations, the same binary pattern may represent different values depending on the encoding scheme. Table 19 presents boundary cases and arithmetic operations that reach or exceed the representable limits of the four representation methods.

Table 19. Boundary values and arithmetic overflow conditions in 3-bit binary representations

Case	Result	Unsigned	Sign-Magnitude	One's Complement	Two's Complement
Boundary value	+4	100,Representable	Not representable-Overflow	Not representable-Overflow	Not representable-Overflow
Boundary value	-4	N/A	Not representable-Underflow	Not representable-Underflow	100,Representable
Arithmetic operation	3+1=4	Representable	Overflow	Overflow	Overflow
Arithmetic operation	-3+(-1)=-4	N/A	Underflow	Underflow	Representable

As shown in Table 19, the representability of boundary values and the occurrence of overflow or underflow depend directly on the selected representation method. In particular, +4 is representable in 3-bit Unsigned representation but exceeds the positive range of the three signed representations, whereas −4 is representable only in 3-bit Two's Complement among the signed methods considered. The arithmetic examples further demonstrate how these boundaries are encountered during addition. These cases illustrate the direct relationship between numerical range, binary encoding, and fixed-width arithmetic behavior.

Comparison of Binary Representations

To illustrate these theoretical ranges, Table 20 presents the complete set of 3-bit binary combinations interpreted according to the four representation methods. This comparison demonstrates how the same binary pattern can represent different decimal values depending on the selected representation.

Table 20. Comparison of three-bit unsigned and signed number representations

Binary Number	Unsigned	Sign-Magnitude	One's Complement	Two's Complement
000	0	+0	0	0
001	1	+1	1	1
010	2	+2	2	2
011	3	+3	3	3
100	4	-0	-3	-4
101	5	-1	-2	-3
110	6	-2	-1	-2
111	7	-3	-0	-1

Table 20 highlights the fundamental differences in the interpretation of binary numbers across the four representation methods. The binary patterns with the most significant bit equal to 0 (000, 001, 010, and 011) represent the same positive decimal values in all four representations. However, significant differences arise when the most significant bit is 1. In the Unsigned representation, these binary patterns are interpreted as ordinary positive binary numbers because no sign bit exists. In contrast, the same binary patterns are interpreted as signed values in Sign-Magnitude, One's Complement, and Two's Complement representations. As a result, each binary pattern corresponds to three different negative decimal values depending on the selected representation method. Furthermore, Sign-Magnitude and One's Complement provide two representations of zero, whereas Two's Complement eliminates the duplicate zero and introduces one additional negative value (−4 in the 3-bit case). This comparison demonstrates that the decimal value of a binary number depends not only on its bit pattern but also on the representation method used for its interpretation.

While the previous subsection demonstrated how the same binary pattern may correspond to different decimal values depending on the selected representation method, this subsection examines the reverse process. Specifically, it compares how identical decimal values are encoded into binary using Unsigned, Sign-Magnitude, One's Complement, and Two's Complement representations. Table 21 summarizes the binary representations of decimal values using the four encoding methods.

Table 21. Binary representations of decimal values using unsigned, sign-magnitude, one's complement, and two's complement (3 bits)

Decimal	Unsigned	Sign-Magnitude	One's Complement	Two's Complement
3	011	011	011	011
2	010	010	010	010
1	001	001	001	001
0	000	000	000	000
-0	x	100	111	x
-1	x	101	110	111
-2	x	110	101	110
-3	x	111	100	101
-4	x	x	x	100

Table 21 shows that all positive decimal values within the common representable range have identical binary representations in the four methods. Differences arise only when negative numbers are encoded. Since the Unsigned representation supports only non-negative integers, negative decimal values cannot be represented. In contrast, the three signed representations use different encoding techniques to represent the same negative decimal values. Sign-Magnitude represents negative numbers by setting the most significant bit to 1 while preserving the magnitude. One's Complement obtains the negative representation by inverting every bit of the corresponding positive number. Two's Complement generates the negative representation by adding 1 to the One's Complement representation.

Furthermore, Table 21 clearly demonstrates that the same negative decimal value is represented by different binary patterns in the three signed representation methods. For example, the decimal value −2 is represented as 110 in Sign-Magnitude, 101 in One's Complement, and 110 in Two's Complement, while the decimal value −3 is represented as 111, 100, and 101, respectively. These differences highlight that the binary encoding of signed integers depends entirely on the selected representation method.

The comparison also illustrates the fundamental distinction between the three signed representations. Sign-Magnitude stores the sign and magnitude separately, One's Complement represents negative values through bit inversion, whereas Two's Complement represents negative values by combining bit inversion with the addition of one. These differences form the basis for the distinct arithmetic properties discussed in the following subsections.

Comparison of Bit-Width Expansion

Increasing the bit width while preserving the numerical value is an essential operation in digital systems, particularly during data type conversions and arithmetic operations. Although all binary number representation methods support bit-width expansion, the expansion procedure differs according to the encoding scheme used for representing signed and unsigned integers.

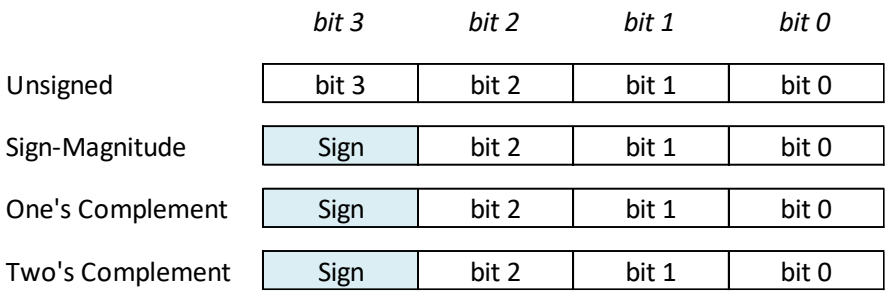

Figure 3. 4-bit layout of each representation (shaded box = sign bit)

Figure 3 illustrates the structural organization of a 4-bit word for each representation method and highlights the position of the sign bit in the three signed representations. Table 22 compares the expansion of 4-bit binary numbers to 6-bit binary numbers using the four representation methods (Hamacher et al., 2012; Parhami, 2010).

Table 22. Expansion of 4-bit binary numbers to 6 bits for different number representations

Representation	Original (4 Bits, MSB = 1)	Expanded (6 Bits)	Original (4 Bits, MSB = 0)	Expanded (6 Bits)
Unsigned	$1011_2 = 11$	$001011_2 = 11$	$0101_2 = 5$	$000101_2 = 5$
Sign-Magnitude	$1011_2 = -3$	$100011_2 = -3$	$0101_2 = +5$	$000101_2 = +5$
One's Complement	$1011_2 = -4$	$111011_2 = -4$	$0101_2 = +5$	$000101_2 = +5$
Two's Complement	$1011_2 = -5$	$111011_2 = -5$	$0101_2 = +5$	$000101_2 = +5$

Table 22 demonstrates that the Unsigned representation increases the bit width by inserting leading zeros before the original binary number. Since unsigned numbers do not contain a sign bit, this operation preserves the numerical value without requiring any additional processing. For the Sign-Magnitude representation, the expansion procedure differs because the most significant bit is reserved for the sign. Instead of inserting leading zeros before the entire binary number, the sign bit remains unchanged**,** while zeros are inserted between the sign bit and the magnitude bits. Consequently, the sign and the numerical magnitude are both preserved after the expansion. In contrast, One's Complement and Two's Complement employ classical sign extension. During this process, the most significant bit (MSB) is replicated into the newly added higher-order bits. Therefore, if the MSB is 0, leading zeros are inserted, whereas if the MSB is 1, leading ones are inserted. This procedure guarantees that both positive and negative values retain their original numerical meaning after increasing the bit width.

The comparison clearly demonstrates that, although all four representations preserve the numerical value after bit-width expansion, they employ different mechanisms to achieve this objective. Unsigned representation relies on zero padding, Sign-Magnitude preserves the sign while inserting additional bits between the sign bit and the magnitude bits, whereas One's Complement and Two's Complement employ classical sign extension by replicating the most significant bit. This distinction is particularly important in computer architecture because sign extension is extensively used by modern processors during data type conversions between different word sizes (Hamacher et al., 2012; Parhami, 2010; Intel Corporation, n.d.; RISC-V International, n.d.)

Illustrative Binary Representation Examples

To further demonstrate the differences among the four binary number representation methods, this subsection presents a set of illustrative conversion examples. Unlike the previous comparisons, which were limited to 3-bit

representations, the following examples use binary numbers with different bit widths. These examples provide a practical demonstration of how decimal values are encoded into binary and how binary patterns are interpreted as decimal values under different representation methods.

Table 23 presents the conversion of decimal numbers into binary using Unsigned, Sign-Magnitude, One's Complement, and Two's Complement representations. The examples demonstrate that positive decimal values generally produce identical binary representations in all four methods, whereas negative values require different encoding techniques depending on the selected representation. As expected, negative decimal values cannot be represented using the Unsigned representation.

Table 23. Conversion of decimal numbers to binary using different binary representation methods

Decimal	Unsigned	Sign-Magnitude	One's Complement	Two's Complement
$10_{(10)}$	$1010_{(2)}$	$01010_{(2)}$	$01010_{(2)}$	$01010_{(2)}$
$-10_{(10)}$	X	$11010_{(2)}$	$10101_{(2)}$	$10110_{(2)}$
$-25_{(10)}$	X	$111001_{(2)}$	$100110_{(2)}$	$100111_{(2)}$
$25_{(10)}$	$11001_{(2)}$	$011001_{(2)}$	$011001_{(2)}$	$011001_{(2)}$

Table 24 illustrates the reverse conversion process by interpreting the same binary value according to each representation method. The examples clearly show that identical binary patterns may correspond to different decimal values depending on the representation used. This observation reinforces one of the central findings of this study: a binary pattern has no intrinsic numerical meaning unless the corresponding representation method is specified.

Table 24. Conversion of binary numbers to decimal by interpreting the same binary value using different binary representation methods

Binary	Unsigned	Sign-Magnitude	One's Complement	Two's Complement
$1101_{(2)}$	$13_{(10)}$	$-5_{(10)}$	$-2_{(10)}$	$-3_{(10)}$
$10001_{(2)}$	$17_{(10)}$	$-1_{(10)}$	$-14_{(10)}$	$-15_{(10)}$
$1111_{(2)}$	$15_{(10)}$	$-7_{(10)}$	$-0_{(10)}$	$-1_{(10)}$
$101011_{(2)}$	$43_{(10)}$	$-11_{(10)}$	$-20_{(10)}$	$-21_{(10)}$

Taken together, Tables 23 and 24 provide complementary examples of binary encoding and interpretation. While Table 23 focuses on converting decimal values into binary representations, Table 24 demonstrates how the same binary pattern may produce different decimal values when interpreted using different representation methods. These examples reinforce the theoretical comparisons presented in the previous subsections and facilitate a deeper understanding of binary number representations.

Comparative Advantages and Disadvantages

Table 25. Comparative advantages and disadvantages of binary number representation methods

Representation	Advantages	Disadvantages
Unsigned	• Utilizes all 2^n binary combinations. • Single zero representation. • Simple encoding and decoding. • Efficient for non-negative values.	• Cannot represent negative values. • Unsuitable for signed arithmetic.
Sign-Magnitude	• Simple representation of sign and magnitude. • Easy to determine the sign of a number.	• Two zero representations. • More complex arithmetic operations. • Does not use classical sign extension; the sign bit must be preserved separately during bit-width expansion.
One's Complement	• Simple generation of negative values by bit inversion. • Supports sign extension.	• Two zero representations. • End-around carry required during addition. • More complex hardware implementation.
Two's Complement	• Single zero representation. • Uses all 2^n binary combinations. • Supports classical sign extension. • Efficient hardware arithmetic. • Standard representation in modern systems.	• Asymmetric numerical range. • Slightly less intuitive for beginners.

Each binary number representation method offers specific advantages and limitations that influence its suitability for different applications. While some methods simplify the representation of signed numbers, others improve arithmetic efficiency or maximize the number of representable values. Table 25 provides a comparative summary of the principal advantages and disadvantages of Unsigned, Sign-Magnitude, One's Complement, and Two's Complement representations.

As shown in Table 25, each representation method involves a different set of design trade-offs. Unsigned representation is simple and efficiently utilizes all available binary combinations but cannot represent negative values. Sign-Magnitude provides an intuitive separation between the sign and magnitude; however, it introduces two representations of zero and complicates arithmetic operations. One's Complement simplifies the generation of negative numbers through bit inversion and supports classical sign extension, but it also suffers from duplicate zero representations and requires an end-around carry during addition. In contrast, Two's Complement combines a unique representation of zero, full utilization of the available binary combinations, efficient hardware arithmetic, and classical sign extension, making it the preferred representation for signed integers in modern computer systems (ARM Ltd., n.d.; Intel Corporation, n.d.; Parhami, 2010; Patterson & Hennessy, 2020; RISC-V International, n.d.).

Summary Comparison

The previous subsections examined the four binary number representation methods from different perspectives, including numerical range, binary encoding, bit-width expansion, conversion examples, and their respective advantages and disadvantages. To consolidate these findings, Table 26 summarizes the principal characteristics of Unsigned, Sign-Magnitude, One's Complement, and Two's Complement representations. The comparison focuses on the maximum number of representable values, zero representation, support for classical sign extension, and suitability for efficient hardware arithmetic.

Table 26. Summary comparison of unsigned, sign-magnitude, one’s complement, and two’s complement representations

Representation	Maximum Number of Representable Values	Zero Representation	Classical Sign Extension	Efficient Hardware Arithmetic
Unsigned	2^n	Single Zero	N/A	√
Sign-Magnitude	$2^n - 1$	Positive and Negative Zero	x	x
One’s Complement	$2^n - 1$	Positive and Negative Zero	√	x
Two’s Complement	2^n	Single Zero	√	√

As summarized in Table 26, each representation method has distinct characteristics and design trade-offs. Unsigned representation efficiently utilizes all available binary combinations but is limited to non-negative integers**.** Sign-Magnitude and One's Complement extend the representation to signed integers; however, both introduce two representations of zero, reducing the number of distinct representable values and increasing arithmetic complexity. In contrast, Two's Complement combines a unique representation of zero, full utilization of the available binary combinations, support for classical sign extension, and efficient hardware arithmetic. These characteristics explain why Two's Complement has become the standard representation for signed integers in modern computer systems (ARM Ltd., n.d.; Intel Corporation, n.d.; Parhami, 2010; Patterson & Hennessy, 2020; RISC-V International, n.d.).

The comparative analysis presented in this section demonstrates that, although all four representation methods encode binary integers, they differ significantly in their design, implementation, and practical applications. The unified comparison highlights the strengths and limitations of each method and provides a structured foundation for understanding their use in computer systems. These observations naturally lead to the discussion in the following section, which examines the reasons behind the widespread adoption of Two's Complement in modern computer architectures.

Discussion

The comparative analysis presented in the previous section demonstrates that binary number representation methods differ not only in their numerical ranges but also in their encoding mechanisms, bit-width expansion procedures, arithmetic properties, and hardware implementation. Although all four representations encode binary

integers, each method was developed to address specific limitations of its predecessors. The findings of this study provide clear answers to the research questions introduced in Section I (Parhami, 2010; Stallings, 2022).

Regarding RQ1**,** the analysis shows that the four representation methods differ fundamentally in the way they encode signed integers. Unsigned representation is limited to non-negative values because all available bits are allocated to representing numerical magnitude. In contrast, Sign-Magnitude**,** One's Complement**,** and Two's Complement extend binary representation to include negative values using different encoding strategies. Sign-Magnitude stores the sign and magnitude separately, One's Complement generates negative numbers through bit inversion, whereas Two's Complement combines bit inversion with the addition of one (Parhami, 2010; Stallings, 2022).

Regarding RQ2, the comparison demonstrates that these representations exhibit different characteristics in terms of numerical range, zero representation, bit-width expansion, and arithmetic implementation. Unsigned representation provides the largest range of non-negative integers by utilizing all available binary combinations. Sign-Magnitude and One's Complement, however, sacrifice one distinct representable value because both contain two representations of zero. Furthermore, the analysis highlights different approaches to bit-width expansion. Unsigned representation performs zero padding, Sign-Magnitude preserves the sign while inserting additional bits between the sign bit and the magnitude bits, whereas One's Complement and Two's Complement employ classical sign extension by replicating the most significant bit. These differences have a direct impact on arithmetic operations and processor implementation (Hamacher et al., 2012; Parhami, 2010; Stallings, 2022).

Regarding RQ3**,** the results clearly explain why Two's Complement has become the standard representation for signed integers in modern computer systems. Unlike Sign-Magnitude and One's Complement, Two's Complement eliminates the duplicate representation of zero and fully utilizes all available binary combinations (Parhami, 2010). Furthermore, Two's Complement allows addition and subtraction to be implemented using a common binary adder, with subtraction performed by complementing the subtrahend and adding one. Classical sign extension simplifies data type conversion between different word sizes, making Two's Complement particularly suitable for modern processor architectures (ARM Ltd., n.d.; Intel Corporation, n.d.; Parhami, 2010; Patterson & Hennessy, 2020; RISC-V International, n.d.).

Overall, the comparative analysis confirms that the adoption of Two's Complement is not arbitrary but is the result of several technical advantages. While the other representation methods remain valuable for understanding the historical development of signed binary arithmetic and the fundamental concepts of computer architecture, Two's Complement offers the best balance between representational efficiency, arithmetic simplicity, and hardware implementation. These characteristics explain why Two's Complement has remained the dominant representation for signed integers in virtually all modern computer systems (ARM Ltd., n.d.; Intel Corporation, n.d.; Parhami, 2010; Patterson & Hennessy, 2020; RISC-V International, n.d.).

Conclusion

This paper presented a comprehensive comparative analysis of four binary number representation methods: Unsigned, Sign-Magnitude, One's Complement, and Two's Complement. The comparison examined their numerical ranges, binary encoding mechanisms, bit-width expansion techniques, zero representation, sign extension, and suitability for hardware arithmetic. A unified comparative framework supported by formulas, illustrative examples, and comparative tables was developed to highlight the similarities and differences among these representation methods.

The analysis demonstrated that each representation method has distinct characteristics, advantages, and limitations. Unsigned representation efficiently utilizes all available binary combinations for non-negative integers, whereas Sign-Magnitude and One's Complement extend the representation to signed numbers but introduce additional complexity due to the existence of two representations of zero. In contrast, Two's Complement combines a unique zero representation, full utilization of the available binary combinations, classical sign extension, and efficient hardware arithmetic, making it the most practical and widely adopted representation for signed integers in modern computer systems.

The comparative framework presented in this paper provides a structured reference for understanding binary number representations and their practical implications in computer architecture and digital systems. By evaluating the four representation methods using consistent technical criteria, the analysis clarifies the design

trade-offs associated with numerical range, zero representation, bit-width expansion, overflow behavior, and arithmetic implementation.

Future work may extend this analysis by examining the implications of these representations for subtraction, multiplication, and division, as well as their hardware complexity and implementation in contemporary processor architectures. Further studies may also investigate how knowledge of binary number representations can be applied in computer architecture education.

Recommendations

Based on the comparative analysis presented in this study, several recommendations can be formulated regarding the selection and interpretation of binary number representation methods.

First, Two's Complement should be preferred for signed integer representation in modern digital systems because it provides a unique representation of zero, utilizes all available binary combinations, supports straightforward sign extension, and enables efficient implementation of arithmetic operations.

Second, the representation method should always be explicitly specified when binary patterns are interpreted or communicated. The same binary pattern may correspond to substantially different numerical values depending on whether Unsigned, Sign-Magnitude, One's Complement, or Two's Complement representation is assumed.

Third, particular attention should be given to the numerical boundaries of fixed-width representations when designing or analyzing arithmetic operations. Overflow conditions should be considered whenever an arithmetic result exceeds the maximum representable value, while negative boundary violations should be evaluated against the minimum representable value of the selected representation.

Finally, the comparative framework presented in this study can be extended in future work to examine additional aspects of computer arithmetic, including subtraction, multiplication, and division, hardware implementation complexity, and the behavior of fixed-width arithmetic in contemporary processor architectures.

Scientific Ethics Declaration

* The author declares that the scientific ethical and legal responsibility of this article published in EPSTEM Journal belongs to the author.

Conflict of Interest

* The author declares that there is no conflict of interest.

Funding

* There is no funding available for this study.

Acknowledgements or Notes

* This article was presented as an oral presentation at the International Conference on Basic Sciences, Engineering and Technology (www.icbaset.net) held in Istanbul/Türkiye on September 17-18, 2026.

References

ARM Ltd. (n.d.). *Arm® architecture reference manual.* https://support.arm.com/documentation/ddi0487/mc/
Bastien, J. F. (2018). *Signed integers are two's complement* (P0907R4). ISO/IEC JTC1/SC22/WG21.

Hamacher, C., Vranesic, Z., Manjikian, N., & Zaky, S. (2012*). Computer organization and embedded systems* (6th ed.). McGraw-Hill.

Intel Corporation. (n.d.). *Intel® 64 and IA-32 architectures software developer's manual.* https://www.intel.com/content/www/us/en/developer/articles/technical/intel-sdm.html

Mano, M. M., & Ciletti, M. D. (2018). *Digital design* (6th ed.). Pearson.

Parhami, B. (2010). *Computer arithmetic: Algorithms and hardware designs* (2nd ed.). Oxford University Press.

Patterson, D. A., & Hennessy, J. L. (2020). *Computer organization and design RISC-V edition* (2nd ed.) Morgan Kaufmann.

RISC-V International. (n.d.). *The RISC-V instruction set manual: Volume I, unprivileged ISA*. https://docs.riscv.org/reference/isa/v20260120/unpriv/unpriv-index.html

Stallings, W. (2022). *Computer organization and architecture: Designing for performance* (11th ed.). Pearson.

Tanenbaum, A. S., & Austin, T. (2013). *Structured computer organization* (6th ed.). Pearson.

Author(s) Information

Bojken Shehu
Polytechnic University of Tirana
"Mother Tereza" Square. Tirana, 1001, Albania
ORCID iD: https://orcid.org/0009-0003-2109-00666
*Contact e-mail: *bshehu@fti.edu.al*

*Corresponding author(s) contact email

To cite this article:

Shehu, B. (2026). Why two's complement became the standard: A comparative analysis of unsigned, sign-magnitude, one's complement, and two's complement representations. *The Eurasia Proceedings of Science, Technology, Engineering and Mathematics (EPSTEM), 42,* 136-151.

The Eurasia Proceedings of Science, Technology, Engineering and Mathematics (EPSTEM)
ISSN: 2602-3199

The Eurasia Proceedings of Science, Technology, Engineering and Mathematics (EPSTEM), 2026

Volume 42, Pages 152-161

ICBASET 2026: International Conference on Basic Sciences, Engineering and Technology

GCD Matrices Associated with Nathanson's Totient Function

Yahia Awad
Lebanese International University

Haissam Chehade
Lebanese International University

Wiam Zeid
Lebanese International University

Abstract: Let $\Phi(n)$ denote Nathanson's Euler-type function for subsets of $\{1,2,\dots,n\}$, defined as the number of nonempty subsets A satisfying $\gcd(\gcd A, n) = 1$. We introduce the second Möbius transform $\Psi = \mu * \Phi$, derive explicit formulas for Ψ, prove $\Psi(n) > 0$ for every positive integer n, and obtain lower bounds and asymptotic estimates. We then study the Nathanson GCD matrix $G_{\Phi}(S) = \left[\Phi\left(\gcd(x_i, x_j)\right)\right]_{i,j=1}^{r}$ associated with a finite set S of distinct positive integers. Using divisor-incidence factorization, we prove positive definiteness for arbitrary finite sets, derive exact determinant formulas, and obtain an explicit inverse formula on factor-closed sets.

Keywords: Nathanson's totient function; GCD matrix; Möbius inversion; Dirichlet convolution; Positive definite matrix; Factor-closed set; Mersenne numbers.

Introduction

Arithmetic functions and structured matrices provide a natural meeting point between number theory and linear algebra. One of the classical examples is the GCD matrix the GCD matrix whose (i,j)-entry is $\gcd(x_i, x_j)$, defined on a finite set $S = \{x_1, \dots, x_r\}$ of distinct positive integers. The subject originates with Smith's classical arithmetical determinant (Smith, 1875–1876) and was developed systematically in the modern literature by Beslin and Ligh (1989). Subsequent work extended these ideas to matrices generated by general arithmetic functions and to the broader theory of meet and join matrices; see Korkee and Haukkanen (2003) and Ovall (2004). Divisor-incidence factorizations are particularly effective for studying determinants, inverses, nonsingularity, and positive definiteness of matrices whose entries have the form $f(\gcd(x_i, x_j))$.

Another direction in arithmetic combinatorics concerns analogues of Euler's totient function obtained by counting relatively prime subsets. Nathanson (2007) introduced a phi function for subsets of $\{1,2,\dots,n\}$; in the notation adopted here, $\Phi(n)$ counts the nonempty subsets $A \subseteq \{1,\dots,n\}$ for which $\gcd(\gcd(A), n) = 1$. Nathanson obtained exact formulas for this function, while Nathanson and Orosz (2007) developed related asymptotic estimates. A fundamental identity is $\Sigma\, \Phi(d) = 2^n - 1$, where the sum is over all divisors d of n. Thus Φ is naturally connected with the Mersenne sequence $M(n) = 2^n - 1$. In the language of Dirichlet convolution, the preceding identity is $M = 1 * \Phi$, and Möbius inversion gives $\Phi = \mu * M$. Standard background on arithmetic functions, Möbius inversion, and Dirichlet convolution may be found in Apostol (1976) and McCarthy (1986). This convolutional relation is the starting point of the present investigation.

- This is an Open Access article distributed under the terms of the Creative Commons Attribution-Noncommercial 4.0 Unported License, permitting all non-commercial use, distribution, and reproduction in any medium, provided the original work is properly cited.

- Selection and peer-review under responsibility of the Organizing Committee of the Conference

© 2026 Published by ISRES Publishing: www.isres.org

Mersenne-type arithmetic matrices have also been studied recently. Awad, Mghames, and Amin (2024) investigated Mersenne power GCD matrices and obtained structural results for associated determinants and inverses. Zeid, Chehade, and Awad (2025) subsequently considered Mersenne GCED matrices in the setting of exponential divisors. These works motivate a closer examination of arithmetic functions arising from the Mersenne sequence through Möbius transformation.

Motivated by $M = 1 * \Phi$, we apply Möbius inversion to Nathanson's function once more and introduce the second Möbius transform $\Psi(n) = (\mu * \Phi)(n)$. Equivalently, $\Phi(n) = \Sigma\, \Psi(d)$, where d runs through the divisors of n. Since $\Phi = \mu * M$, we also have $\Psi = (\mu * \mu) * M$. Thus M, Φ, and Ψ form a natural convolutional hierarchy, with each successive step obtained by a Möbius transform.

The first objective of this paper is to investigate the arithmetic structure of Ψ. We determine the prime-power values of $h = \mu * \mu$, derive an explicit divisor representation for $\Psi(n)$, and prove the fundamental positivity property $\Psi(n) > 0$ for every $n \geq 1$. We further obtain explicit formulas for primes, prime powers, semiprimes, and squarefree integers, together with lower bounds involving the prime divisors of n and an asymptotic estimate $\Psi(n) \sim 2^{\mathrm{n}}$.

The second objective is to use this positivity to study the matrix $G_{\Phi(S)}$, whose (i,j)-entry is $\Phi(gcd(x_{\mathrm{i}}, x_{\mathrm{j}}))$, which we call the Nathanson GCD matrix associated with S. General matrices of the form $[f(gcd(x_{\mathrm{i}}, x_{\mathrm{j}}))]$ belong to the established theory of GCD and meet matrices (Beslin & Ligh, 1989; Korkee & Haukkanen, 2003; Ovall, 2004). Accordingly, the general incidence-matrix machinery used here is classical; the arithmetic contribution specific to the present setting is the analysis and positivity of $\Psi = \mu * \Phi$, which makes that machinery effective for Nathanson's subset totient.

Using $\Phi(n) = \Sigma\, \Psi(d)$, where d runs through the divisors of n, we obtain a divisor-incidence factorization $G_{\Phi(S)} = E_{\mathrm{s}}\, D\Psi\, E_{\mathrm{s}}{}^{\mathrm{T}}$. Since $\Psi(d) > 0$, this representation implies that $G_{\Phi(S)}$ is positive definite for every finite set of distinct positive integers. For factor-closed sets it yields the product determinant $\det G_{\Phi(S)} = \prod_{x \in S} \Psi(x)$ and an explicit inverse formula; for arbitrary finite sets, Cauchy–Binet gives an exact determinant expansion.

The principal contributions are therefore the introduction and arithmetic analysis of the second Möbius transform $\Psi = \mu * \Phi$; the proof of its strict positivity; explicit formulas and asymptotic estimates; and the resulting positive-definiteness, determinant, and inverse results for Nathanson GCD matrices. This provides a direct link among relatively prime subset enumeration, Mersenne-type arithmetic functions, and structured GCD matrices.

The remainder of the paper is organized as follows. Section 2 recalls basic identities for Nathanson's totient function. Sections 3–5 develop the second Möbius transform, its positivity, explicit formulas, and bounds. Sections 6–8 study the associated GCD matrices, determinants, and inverses. Section 9 contains worked examples, followed by the Mersenne connection, conclusions, recommendations for future research, declarations, and references.

Basic Identities for Nathanson's Totient Function

Proposition 2.1. For every positive integer n,

$$\sum_{d|n} \Phi(d) = 2^n - 1.$$

Proof. Take any nonempty subset $A \subseteq \{1, \ldots, n\}$ and define

$$g = \gcd(\gcd A, n).$$

Then $g \mid n$. Dividing every element of A by g produces a nonempty subset of $\{1, \ldots, n/g\}$ whose common gcd is relatively prime to n/g. Conversely, multiplying such a subset by g recovers A. Thus the nonempty subsets are partitioned by the value of g, and the class corresponding to g contains $\Phi(n/g)$ subsets. Hence

$$2^n - 1 = \sum_{g|n} \Phi(n/g) = \sum_{d|n} \Phi(d).$$

This proves the result.

Corollary 2.2. By Möbius inversion,

$$\Phi(n) = \sum_{d|n} \mu(d)\left(2^{n/d} - 1\right).$$

For $n > 1$, since $\sum_{d|n} \mu(d) = 0$,

$$\Phi(n) = \sum_{d|n} \mu(d) 2^{n/d}.$$

Proposition 2.3. If p is prime and $a \geq 1$, then

$$\Phi(p^a) = 2^{p^a} - 2^{p^{a-1}}.$$

Proof. Among the divisors of p^a, the Möbius function is nonzero only at 1 and p. Substitution into Corollary 2.2 gives the formula.

For distinct primes p, q,

$$\Phi(pq) = 2^{pq} - 2^p - 2^q + 2.$$

3. The Second Möbius Transform

Define

$$\Psi(n) = (\mu * \Phi)(n) = \sum_{d|n} \mu(d)\Phi(n/d).$$

By Möbius inversion,

$$\Phi(n) = \sum_{d|n} \Psi(d).$$

Let $M(n) = 2^n - 1$. Since $\Phi = \mu * M$,

$$\Psi = (\mu * \mu) * M.$$

Put $h = \mu * \mu$.

Lemma 3.1. The function h is multiplicative and, for every prime p,

$$h(p^a) = \begin{cases} 1, & a = 0, \\ -2, & a = 1, \\ 1, & a = 2, \\ 0, & a \geq 3. \end{cases}$$

Proof. Dirichlet convolution preserves multiplicativity. Moreover,

$$h(p^a) = \sum_{j=0}^{a} \mu(p^j)\mu(p^{a-j}),$$

and $\mu(p^j) = 0$ for $j \geq 2$. The stated values follow.

Proposition 3.2. For every $n \geq 1$,

$$\Psi(n) = \sum_{d|n} h\,(d)2^{n/d} - \mu(n).$$

Proof. Since $\Psi = h * M$,

$$\Psi(n) = \sum_{d|n} h\,(d)\big(2^{n/d} - 1\big).$$

Also,

$$\sum_{d|n} h\,(d) = (h * \mathbf{1})(n) = (\mu * \mu * \mathbf{1})(n) = \mu(n).$$

Substitution gives the result.

4. Positivity of Ψ

Lemma 4.1. For every $n \geq 1$,

$$\Phi(n) \geq 2^{n-1}.$$

Proof. Every subset of $\{1, \dots, n\}$ containing 1 has gcd 1 and is counted by $\Phi(n)$. Exactly 2^{n-1} subsets contain 1.

Theorem 4.2. For every positive integer n,

$$1 \leq \Psi(n) \leq \Phi(n).$$

In particular, $\Psi(n) > 0$.

Proof. We argue by induction. For $n = 1$, $\Psi(1) = \Phi(1) = 1$. Assume the assertion for every proper divisor $d < n$. From $\Phi(n) = \sum_{d|n} \Psi\,(d)$,

$$\Psi(n) = \Phi(n) - \sum_{\substack{d|n \\ d<n}} \Psi\,(d).$$

Using the induction hypothesis $\Psi(d) \leq \Phi(d)$,

$$\Psi(n) \geq \Phi(n) - \sum_{\substack{d|n \\ d<n}} \Phi\,(d).$$

By Proposition 2.1,

$$\Psi(n) \geq 2\Phi(n) - 2^n + 1.$$

Lemma 4.1 gives $2\Phi(n) \geq 2^n$, hence $\Psi(n) \geq 1$. Since every proper-divisor term $\Psi(d)$ is positive, the defining identity also gives $\Psi(n) \leq \Phi(n)$.

Corollary 4.3. For $n \geq 3$,

$$\Psi(n) \geq 2^{n-2} + 1.$$

Proof. Besides all subsets containing 1, every subset containing both 2 and 3 but not 1 has gcd 1. There are 2^{n-3} such subsets. Hence

$$\Phi(n) \geq 2^{n-1} + 2^{n-3}.$$

Substituting into $\Psi(n) \geq 2\Phi(n) - 2^n + 1$ gives the result.

5. Explicit Formulas and Prime-Divisor Bounds

Proposition 5.1. If p is prime, then

$$\Psi(p) = 2^p - 3.$$

Proof. $\Psi(p) = \Phi(p) - \Phi(1) = (2^p - 2) - 1$.

Proposition 5.2. If $a \geq 2$, then

$$\Psi(p^a) = 2^{p^a} - 2 \cdot 2^{p^{a-1}} + 2^{p^{a-2}}.$$

Proof. By Lemma 3.1, only $1, p, p^2$ contribute, and $\mu(p^a) = 0$ for $a \geq 2$.

Proposition 5.3. For distinct primes $p < q$,

$$\Psi(pq) = 2^{pq} - 2^{q+1} - 2^{p+1} + 7.$$

Proof. The relevant divisors are $1, p, q, pq$, with h-values $1, -2, -2, 4$, and $\mu(pq) = 1$. Thus

$$\Psi(pq) = 2^{pq} - 2 \cdot 2^q - 2 \cdot 2^p + 4 \cdot 2 - 1,$$

which simplifies to the stated formula.

Proposition 5.4. If n is squarefree, then

$$\Psi(n) = \sum_{d|n} (-2)^{\omega(d)}\, 2^{n/d} - \mu(n).$$

Proof. For square free d, multiplicativity and Lemma 3.1 give $h(d) = (-2)^{\omega(d)}$. Substitute into Proposition 3.2.

Theorem 5.5. For $n > 1$,

$$\Psi(n) \geq 2^n - 2 \sum_{\substack{p|n \\ p \text{ prime}}} 2^{n/p} + 2\omega(n) - 1.$$

Proof. A subset is excluded from $\Phi(n)$ only if all its elements are divisible by at least one prime $p \mid n$. For fixed p, there are $2^{n/p} - 1$ nonempty subsets consisting entirely of multiples of p. By the union bound,

$$(2^n - 1) - \Phi(n) \leq \sum_{\substack{p|n \\ p \text{ prime}}} \left(2^{n/p} - 1\right).$$

Therefore

$$\Phi(n) \geq 2^n - 1 + \omega(n) - \sum_{\substack{p|n \\ p \text{ prime}}} 2^{n/p}.$$

Combining this with $\Psi(n) \geq 2\Phi(n) - 2^n + 1$ proves the result.

Corollary 5.6. If $p = P^-(n)$ is the smallest prime divisor of n, then

$$\Psi(n) \geq 2^n - 2\omega(n)2^{n/p} + 2\omega(n) - 1.$$

Proof. For every prime $q \mid n$, $q \geq p$, hence $2^{n/q} \leq 2^{n/p}$. Apply Theorem 5.5.

Corollary 5.7. As $n \to \infty$,

$$\Psi(n) \sim 2^n.$$

Indeed,

$$\frac{\Psi(n)}{2^n} = 1 + O\big(\omega(n)2^{-n/2}\big).$$

6. Nathanson GCD Matrices

Let $S = \{x_1, \dots, x_r\}$ be a finite set of distinct positive integers and define

$$G_\Phi(S) = \left[\Phi\left(\gcd(x_i, x_j)\right)\right]_{i,j=1}^{r}.$$

Let $D(S)$ be the set of all positive divisors of elements of S. Define the divisor-incidence matrix E by

$$E_{i,d} = \begin{cases} 1, & d \mid x_i, \\ 0, & d \nmid x_i, \end{cases}$$

and let

$$D_\Psi = \operatorname{diag}\big(\Psi(d) : d \in D(S)\big).$$

Theorem 6.1.

$$G_\Phi(S) = E D_\Psi E^T.$$

Proof. The (i, j) entry of the right-hand side is

$$\sum_{\substack{d \mid x_i \\ d \mid x_j}} \Psi(d) = \sum_{d \mid \gcd(x_i, x_j)} \Psi(d) = \Phi\left(\gcd(x_i, x_j)\right),$$

which is the (i, j) entry of $G_\Phi(S)$.

Lemma 6.2. The divisor-incidence matrix E has full row rank.

Proof. Order $x_1 < \cdots < x_r$ and select the r columns indexed by $x_1, \dots, x_r$. The resulting square matrix has entry 1 when $x_j \mid x_i$. If $j > i$, then $x_j > x_i$, so $x_j \nmid x_i$. Hence this submatrix is lower triangular with diagonal entries 1, and its determinant is 1.

Theorem 6.3. For every finite set S of distinct positive integers, $G_\Phi(S)$ is positive definite.

Proof. Let $z \neq 0$. By Theorem 6.1,

$$z^T G_\Phi(S) z = (E^T z)^T D_\Psi (E^T z).$$

Lemma 6.2 implies $E^T z \neq 0$. By Theorem 4.2, every diagonal entry $\Psi(d)$ is positive, so D_Ψ is positive definite. Therefore, the displayed quadratic form is strictly positive

Consequently every eigenvalue and every principal minor of $G_\Phi(S)$ is positive, and

$$\det G_\Phi(S) > 0.$$

7. Determinant Formulas

Theorem 7.1. If S is factor closed, then

$$\det G_{\Phi}(S) = \prod_{x \in S} \Psi(x).$$

Proof. For a factor-closed set, $D(S) = S$. After increasing ordering, E is lower triangular with diagonal entries 1, so $\det E = 1$. Taking determinants in $G_{\Phi}(S) = E D_{\Psi} E^{T}$ gives

$$\det G_{\Phi}(S) = (\det E)^2 \det D_{\Psi} = \prod_{x \in S} \Psi(x).$$

□

Corollary 7.2. For $S = \{1,2,\dots,n\}$,

$$\det\left[\Phi\left(\gcd(i,j)\right)\right]_{i,j=1}^{n} = \prod_{k=1}^{n} \Psi(k).$$

Theorem 7.3. For arbitrary S with $|S| = r$,

$$\det G_{\Phi}(S) = \sum_{\substack{K \subseteq D(S) \\ |K| = r}} (\det E[:, K])^2 \prod_{d \in K} \Psi(d).$$

Proof. Write

$$G_{\Phi}(S) = \left(E D_{\Psi}^{1/2}\right)\left(E D_{\Psi}^{1/2}\right)^{T}.$$

Applying the Cauchy-Binet formula to this Gram product gives the stated expansion.

8. Inverse on Factor-Closed Sets

Theorem 8.1. If S is factor closed, then

$$(G_{\Phi}(S)^{-1})_{ij} = \sum_{\substack{x_k \in S \\ x_i | x_k,\, x_j | x_k}} \frac{\mu(x_k/x_i)\mu\left(x_k/x_j\right)}{\Psi(x_k)}.$$

Proof. Möbius inversion gives

$$(E^{-1})_{ij} = \begin{cases} \mu\left(x_i/x_j\right), & x_j \mid x_i, \\ 0, & x_j \nmid x_i. \end{cases}$$

Since

$$G_{\Phi}(S)^{-1} = E^{-T} D_{\Psi}^{-1} E^{-1},$$

taking the (i,j) entry gives the claimed formula.

9. Worked Examples

Example 9.1. Arithmetic Values of Ψ

$$\Psi(4) = 2^4 - 2 \cdot 2^2 + 2 = 10,$$
$$\Psi(6) = 2^6 - 2^4 - 2^3 + 7 = 47,$$
$$\Psi(8) = 2^8 - 2^5 + 2^2 = 228,$$

$$\Psi(9) = 2^9 - 2^4 + 2 = 498,$$
$$\Psi(10) = 2^{10} - 2^6 - 2^3 + 7 = 959.$$

Example 9.2. A Factor-Closed Set

Let $S = \{1,2,3,6\}$. Then

$$G_\Phi(S) = \begin{pmatrix} 1 & 1 & 1 & 1 \\ 1 & 2 & 1 & 2 \\ 1 & 1 & 6 & 6 \\ 1 & 2 & 6 & 54 \end{pmatrix}.$$

Moreover,

$$\Psi(1) = 1, \qquad \Psi(2) = 1, \qquad \Psi(3) = 5, \qquad \Psi(6) = 47.$$

Therefore

$$\det G_\Phi(\{1,2,3,6\}) = 1 \cdot 1 \cdot 5 \cdot 47 = 235.$$

Example 9.3. Another Factor-Closed Set

For $S = \{1,2,3,4\}$,

$$\det G_\Phi(S) = \Psi(1)\Psi(2)\Psi(3)\Psi(4) = 1 \cdot 1 \cdot 5 \cdot 10 = 50.$$

Example 9.4. A Non-Factor-Closed Set

Take $S = \{2,3,6\}$. Then

$$G_\Phi(S) = \begin{pmatrix} 2 & 1 & 2 \\ 1 & 6 & 6 \\ 2 & 6 & 54 \end{pmatrix},$$

and a direct calculation gives

$$\det G_\Phi(\{2,3,6\}) = 470 > 0.$$

Thus, factor closure is unnecessary for positive definiteness; it is needed only for the simple product determinant formula.

10. Mersenne Connection

Since $M(n) = 2^n - 1$ and $M = \mathbf{1} * \Phi$,

$$M\left(\gcd(x_i, x_j)\right) = \sum_{d \mid \gcd(x_i, x_j)} \Phi(d).$$

Hence

$$\left[M\left(\gcd(x_i, x_j)\right)\right] = E\ \mathrm{diag}\big(\Phi(d)\big)E^T.$$

For factor-closed S,

$$\det\left[M\left(\gcd(x_i, x_j)\right)\right] = \prod_{x \in S} \Phi(x).$$

Thus, the arithmetic chain

$$M \to \Phi \to \Psi$$

links Mersenne GCD matrices with the Nathanson GCD matrices studied here.

Conclusion

The second Möbius transform $\Psi = \mu * \Phi$ is the arithmetic object controlling GCD matrices generated by Nathanson's totient function. Its positivity yields positive definiteness for arbitrary finite sets, while factor-closed sets admit exact determinant and inverse formulas. Natural further questions concern divisibility and p-adic properties of Ψ and the separate study of the LCM kernel $\Phi\left(\mathrm{lcm}(x_i, x_j)\right)$.

Recommendations and Future Research

The results obtained in this study suggest several directions for further investigation. In particular, the arithmetic properties of the second Möbius transform $\Psi = \mu * \Phi$ deserve deeper study, including its divisibility properties, congruence behavior, p-adic valuations, and possible characterizations of its extremal values. It would also be interesting to investigate spectral properties, eigenvalue bounds, and condition numbers of Nathanson GCD matrices.

A natural continuation is the study of the corresponding LCM matrices $[\Phi(lcm(x_i, x_j))]$, where questions concerning nonsingularity, inertia, and determinant structure are expected to differ substantially from the GCD case. Another direction is to examine analogous constructions arising from other subset-counting arithmetic functions and their successive Möbius transforms.

Finally, the connection M → Φ → Ψ between Mersenne numbers, Nathanson's totient function, and its second Möbius transform suggests that further arithmetic-matrix constructions based on this convolution hierarchy may provide new families of structured GCD and LCM matrices.

Scientific Ethics Declarations

* The authors declare that the scientific ethical and legal responsibility of this article published in EPSTEM Journal belongs to the authors.

Conflict of Interest

* The authors declare that there is no conflict of interest regarding the publication of this article.

Funding

* This research received no specific grant from any funding agency in the public, commercial, or not-for-profit sectors.

Data Availability Statement

* No datasets were generated or analyzed during the current study. All results presented in this article are theoretical.

Acknowledgements or Notes

* This article was presented as an oral presentation at the International Conference on Basic Sciences, Engineering and Technology (www.icbaset.net) held in Istanbul/Türkiye on September 17-18, 2026.

* The authors gratefully acknowledges the anonymous referees for their careful reading, valuable comments, and constructive suggestions that helped improve the quality and clarity of the manuscript.

AMS Subject Classification

* 2020 Mathematics Subject Classification: 11C20, 11A25, 15B36, 11A05.

References

Apostol, T. M. (1976). *Introduction to analytic number theory*. New York, NY: Springer-Verlag.

Awad, Y., Mghames, R., & Amin, K. (2024). On Mersenne power GCD matrices. *The Eurasia Proceedings of Science, Technology, Engineering & Mathematics, 28*, 224–233.

Beslin, S., & Ligh, S. (1989). Greatest common divisor matrices. *Linear Algebra and Its Applications, 118*, 69–76.

Korkee, I., & Haukkanen, P. (2003). On meet and join matrices associated with incidence functions. *Linear Algebra and Its Applications, 372*, 127–153.

McCarthy, P. J. (1986). *Introduction to arithmetical functions*. New York, NY: Springer-Verlag.

Nathanson, M. B. (2007). Affine invariants, relatively prime sets, and a phi function for subsets of {1, 2, ..., n}. *Integers, 7*, Article A01.

Nathanson, M. B., & Orosz, B. (2007). Asymptotic estimates for phi functions for subsets of {m+1, m+2, ..., n}. *Integers, 7*, Article A54.

Ovall, J. S. (2004). An analysis of GCD and LCM matrices via the LDL^T-factorization. *Electronic Journal of Linear Algebra, 11*, 51–58.

Smith, H. J. S. (1875–1876). On the value of a certain arithmetical determinant. *Proceedings of the London Mathematical Society, 7*, 208–212.

Zeid, W., Chehade, H., & Awad, Y. (2025). On mersenne GCED matrices. *The Eurasia Proceedings of Science, Technology, Engineering & Mathematics, 34*, 58–65.

Author(s) Information

Yahia Awad
Lebanese International University (LIU)
Department of Mathematics and Physics
AlKhyara, West Bekaa, Lebanon.
ORCID iD: https://orcid.org/0000-0001-9878-2482
*Contact e-mail: *yehya.awad@liu.edu.lb*

Haissam Chehade
Lebanese International University (LIU)
Department of Mathematics and Physics
Saida, Lebanon.
ORCID iD: https://orcid.org/0000-0002-0639-0236

Wiam Zeid
Lebanese International University (LIU)
Department of Mathematics and Physics
Saida, Lebanon.
ORCID iD: https://orcid.org/0000-0003-1003-8515

To cite this article:

Awad, Y., Chehade, H. & Zeid, W. (2026). GCD matrices associated with Nathanson's totient function. *The Eurasia Proceedings of Science, Technology, Engineering and Mathematics (EPSTEM), 42,* 152-161.

The Eurasia Proceedings of Science, Technology, Engineering and Mathematics (EPSTEM)
ISSN: 2602-3199

The Eurasia Proceedings of Science, Technology, Engineering and Mathematics (EPSTEM), 2026

Volume 42, Pages 162-175

ICBASET 2026: International Conference on Basic Sciences, Engineering and Technology

DBSCAN-Based Spatial Hotspot Detection of Motorcycle and Three-Wheeled Vehicle Crashes

Ghaidaa A. Majeed
Mustansiriyah University

Abeer K. Jameel
Mustansiriyah University

Abstract: Because of the lack of physical protection and the often-complex interaction between motorcycles and 3-wheelers and the other components of urban transportation systems, motorcycles and 3-wheelers are among the most vulnerable road users. Therefore, it is important to determine spatial crash hotspots to enable evidence-based road safety management and targeted interventions. The purpose of this study is to detect crash hotspot areas of motorcycles and three-wheel vehicles for the Rusafa district in Baghdad using the density-based spatial clustering of applications with noise (DBSCAN) algorithm and the Haversine distance measure. There were 802 crash records that were georeferenced and analyzed to identify areas that have been more prone to crashes. We used a Ball Tree nearest-neighbor search algorithm to implement DBSCAN and preprocessed the geographic coordinates before we applied DBSCAN, converting them to radians. We did a sensitivity analysis and selected the optimal clustering parameters (eps = 0.5 km, min_samples = 5). Three spatial indicators (Zone_Label, Zone_Count, Hotspot_Flag) were then calculated to describe the identified hotspot regions. The framework recommended 37 spatial clusters, with 656 (81.8%) of these crashes being identified as a hotspot and 146 crashes (18.2%) as spatial noise. The greatest number of crashes recorded occurred in the largest hotspot (Zone 8) with 116 crashes, or 14.46% of all crashes recorded. Results also indicate that the most common crash locations are not necessarily the most severe, suggesting that, in addition to severity, crash frequency should be taken into account when assessing road safety. The framework proposed here may assist transportation agencies in determining persistent crash locations, prioritizing engineering and enforcement measures, and combining with machine learning methods to forecast crash severity.

Keywords: DBSCAN, Spatial hotspot detection, Haversine distance, GIS, Road safety

Introduction

Motorcycles and three-wheelers are indispensable elements of urban transport networks, especially in developing countries, where they offer low-cost, flexible, and efficient transportation. They are maneuverable and can be used for both passenger and commercial traffic in busy streets. Unlike enclosed vehicles, however, these modes provide little physical protection to riders and passengers and put them at significant risk of serious injury or death in the event of a traffic accident. Motorcycle and three-wheeled vehicle crashes have thus emerged as a significant public health and transportation safety problem, particularly in rapidly urbanizing cities with mixed traffic, high traffic volumes, and complex roadway environments (WHO, 2023).

Traffic accidents do not happen uniformly throughout the urban road network. Rather, they usually focus in one or more geographic areas where roadway geometry, traffic exposure, land use, operational characteristics, and human behavior combine to raise the risk of crashes. These high-risk locations, also known as crash hotspots, are key to evidence-based road safety management. Hotspot identification helps the transportation agency prioritize engineering improvements, optimize enforcement efforts, allocate limited safety resources more

- This is an Open Access article distributed under the terms of the Creative Commons Attribution-Noncommercial 4.0 Unported License, permitting all non-commercial use, distribution, and reproduction in any medium, provided the original work is properly cited.

- Selection and peer-review under responsibility of the Organizing Committee of the Conference

© 2026 Published by ISRES Publishing: www.isres.org

effectively, and target limited education resources to reduce the number and severity of crashes (National Research Council, 2010; Shokat & Jameel, 2025).

The typical approaches to identifying hot spots are based on crash frequency rankings, administrative boundaries, roadway segments, or statistical aggregation techniques. While these methods offer valuable insights, crash patterns seldom align with administrative or roadway boundaries, making them less useful for capturing localized spatial patterns. In addition, standard clustering algorithms may fail to capture crash patterns around complex intersections, commercial areas, or urban activity centers, where crash clusters may form in irregular shapes (Li & Wang, 2022; Jameel & Jameel).

New developments in Geographic Information Systems (GIS), spatial data analytics, and machine learning have enabled more sophisticated strategies for crash hotspot detection. The growing popularity of this type of clustering algorithm is due to its ability to detect spatial clusters in the data that are not created by aggregating data in arbitrary spatial units. The Density-Based Spatial Clustering of Applications with Noise (DBSCAN) algorithm has proven to be one of the most popular methods for traffic safety analysis. One advantage of DBSCAN over standard clustering methods is that it automatically determines the number of clusters (no prior knowledge of it), automatically finds clusters of any shape (no requirement for them to be convex), and classifies isolated data points as noise. The advantages of DBSCAN render it particularly suitable for traffic crash analysis, as crash locations often are not arranged in a compact geometric pattern, but in an irregular road corridor (Ali & Alhusaynat, 2026; Mandala et al., 2026).

Choosing a distance measure is also crucial if geographic coordinates are used to analyze relationships. Latitude and longitude are not Cartesian coordinates, but rather angular measurements on the surface of the Earth. For that reason, spherical distance measures must be used in place of Euclidean distance measures. The Haversine distance is a perfect choice because it provides the shortest distance between two points on Earth's surface while accounting for its curvature. The Haversine metric is combined with DBSCAN to enhance the reliability of hotspot detection by augmenting the neighborhood relationships between crash locations with a geographical sense (Sharmila & Sabarish, 2021; Pusuluri, & Dangeti, 2024).

Although density-based clustering has been increasingly applied in transportation safety studies, several challenges remain. The performance of DBSCAN is strongly affected by both the neighborhood radius (eps) and the minimum number of samples (min_samples) required to form a cluster. These parameters required to form a cluster strongly affect DBSCAN's performance. Furthermore, most previous studies have examined all traffic crashes, with relatively few specifically examining motorcycles and three-wheeled vehicle crashes using coordinate-level spatial analysis. Further, there is little research that investigates the sensitivity of DBSCAN parameters or that converts clustering results into more practical hotspot indicators to inform further crash severity modeling and transportation planning (Lai et al., 2019; Zhang et al., 2024).

With urbanization and rising traffic volumes, Iraq's capital, Baghdad, has seen an increase in the number of motorcycles and 3-wheelers. The city is home to several signalized intersections, commercial corridors, mixed land-use zones, and freewheeling road networks in district Rusafa, one of the city's busiest urban areas, which contributes to high crash rates. While enhancing road safety in this context is important, there is a lack of in-depth coordinate-based hotspot analyses of vulnerable road users.

In view of this, the aim of this study is to use the DBSCAN algorithm, with Haversine distance as the metric, to detect crash hotspots for motorcycles and three-wheeled vehicles in the city of Rusafa in Baghdad. A set of 802 georeferenced crash records was analyzed to identify dense crash clusters and isolated crash locations, and to assess the impact of varying neighborhood radii through a sensitivity analysis. To quantify the detected clusters and support integration with crash severity prediction and transportation safety assessment models in the future, three spatial indicators were developed: Zone_Label, Zone_Count, and Hotspot_Flag.

This study helps in the following four ways:

- It introduces a hotspot detection system based on a coordinate-based approach and specifically tailored to motorcycle and three-wheeled vehicle crashes, based on the DBSCAN cluster algorithm and Haversine distance measure.
- It tests the sensitivity of DBSCAN neighborhood parameters to determine the balance between the accuracy of the hotspot detection and spatial resolution.
- It develops spatial hotspot indicators that can be integrated into future machine learning and crash severity prediction models.

- It offers a first-hand account of how transportation planners and road safety agencies can identify high-risk areas in urban settings in Baghdad and prioritize interventions that will enhance safety.

The results provide valuable insights into the evolving field of GIS-based traffic safety analysis and highlight the potential of density-based spatial clustering for data-driven decision-making on enhancing road safety for vulnerable road users in urban areas.

Methods

Research Framework

The methodology used in this study was density-based spatial clustering (DBSCAN), which was used to detect crash hotspots for motorcycles and 3-wheelers in Baghdad. The proposed framework is a sequential six-step process of crash data collection and preprocessing, Geographic coordinate preparation, Spatial distance computation (with the Haversine metric), Hotspot detection (with the DBSCAN algorithm), Sensitivity analysis for parameter selection, spatial visualization, and descriptive analysis of the identified hotspots. The overall research framework is presented in Figure 1.

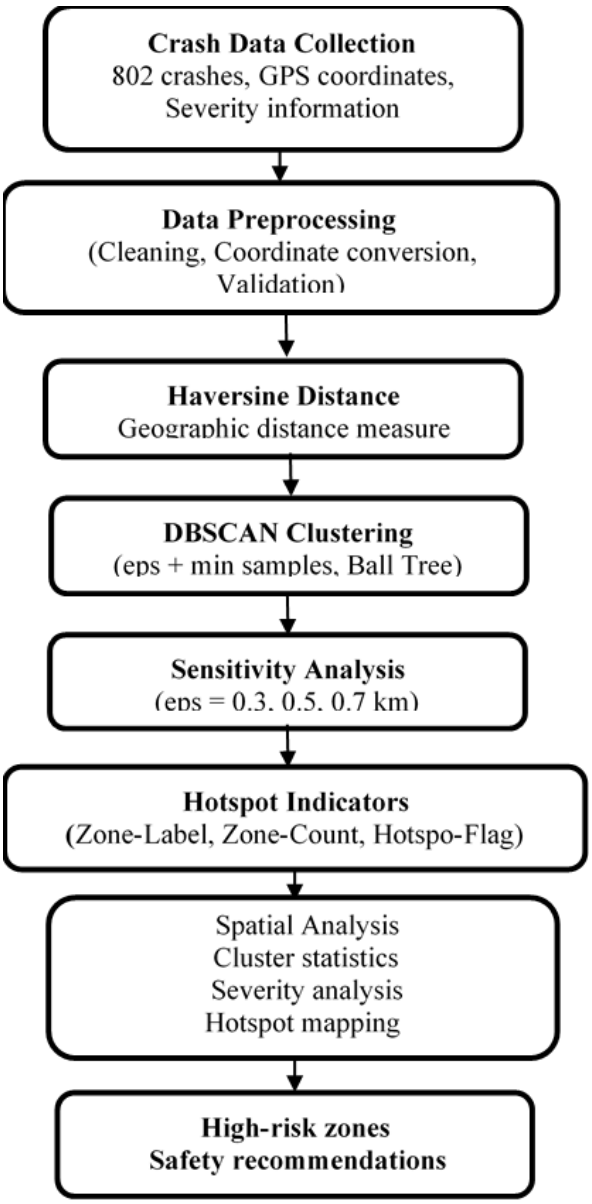

Figure 1. Proposed research framework for DBSCAN-based spatial hotspot detection of motorcycle and three-wheeled vehicle crashes.

Study Area and Crash Database

The study was conducted in Baghdad, Rusafa, one of the most densely populated urban areas with a dense network of transportation corridors, including arterial roads, signalized intersections, commercial corridors, residential neighborhoods, and mixed land-use developments. The district has a high number of motorcyclists and high traffic demand, which makes it ideal for studying spatial patterns of crash concentrations.

The 802 motorcycle and three-wheeled vehicle crashes in the crash database were officially recorded traffic crashes with geographic information. Geographic coordinates (latitude and longitude) were included with the severity information, which was classified into 3 levels for each crash record: Fatal crashes, Injury crashes, and Property damage only (PDO) crashes. Crash severity was used to describe the characteristics of the detected hotspot zones but did not affect the clustering process, whereas geographic variables were used as the main variables for detecting hotspot zones.

Data Preparation

All crash data were first extensively processed to enhance data quality and facilitate accurate spatial analysis prior to clustering. The preprocessing consisted of the following steps:

- Geographic information system (GIS) data; and
- Removing duplicated observations;
- Correcting incomplete or incorrect geographic coordinates;
- Converting Degrees–Minutes–Seconds (DMS) to decimal degrees;
- Converting degrees to radians for Haversine distance calculation.

Angles recorded in DMS were converted into decimal degrees (Eleiche, 2010):

$$DD = D + M/60 + S/3600 \quad (1)$$

where:

DD is the coordinate in decimal degrees, D = degree, M = minute, S = second.

Since Scikit-learn uses angular coordinates to implement the haversine metric, all latitudes and longitudes were converted from decimal degrees to radians prior to clustering.

Geographic Distance Measurement

Geographic coordinates are used to determine points on the Earth's surface, which is curved, unlike planar coordinate systems (Mahmoud & Akkari, 2016). As such, the Euclidean distance is not suitable for measuring the real distance between crash sites. Therefore, this study used the Haversine distance: the shortest great-circle distance between two points (A and B) on the Earth's surface. The Haversine metric ensures neighborhood relationships reflect real geographic distances, rather than planar approximations.
The Haversine distance is the distance between two points on the globe.

$$d = 2R \arcsin\left(\sqrt{sin^2\left(\frac{\Delta\emptyset}{2}\right) + \cos\emptyset_1 \cos\emptyset_2 sin^2\left(\frac{\Delta\lambda}{2}\right)}\right) \quad (2)$$

Where R is the Earth's radius (6371.0088 km), d is the geographic distance between two crash locations, $\emptyset_1$ and are the latitudes of the two points in radians, $\Delta\emptyset$ is the difference between the two latitudes, and $\Delta\lambda$ is the difference between the two longitudes.

DBSCAN Spatial Clustering

The Density-Based Spatial Clustering of Applications with Noise (DBSCAN) algorithm was employed with the Python library Scikit-learn to identify crash hotspots. DBSCAN is different from partition-based clustering methods like K-means in that it doesn't rely on a fixed number of clusters. Unlike partition-based clustering

algorithms like K-means, DBSCAN doesn't assume a fixed number of clusters (Zhang et al., 2018; Saputra & Sihabudin, 2023; Kamh et al., 2024). The characteristics of DBSCAN are particularly interesting for traffic crash analysis because hotspot areas often exhibit irregular spatial patterns along road corridors, at intersections, and in urban activity centers.

DBSCAN divides observations into 3 categories:

- Core points are those that have a minimum of min-samples crashes within a search radius.
- Border points that are in the neighborhood of a core point but have fewer observations in the neighborhood.
- Noise points are those that don't meet the density requirement and aren't clustered together.

There are two parameters that control the algorithm:

- eps: radius of the maximum neighborhood; The term “eps” refers to the maximum distance between points in the clusters in DBSCAN. eps must be in radians and not kilometers when using Haversine as the distance metric (Mahmoud & Akkari, 2016; Prasetya et al., 2020; Sharmila & Sabarish, 2021).
- min_samples: minimum number of crashes in neighbors to form a dense area.

Based on preliminary experiments and sensitivity analysis, the following values were selected: eps = 0.5 km and min_samples = 5. The neighborhood radius was converted to radians for calculation by scikit-learn, which uses radians to compute the Haversine distance. In neighborhood search, a Ball Tree nearest-neighbor search structure was used to speed up the computation.

Sensitivity Analysis

The neighborhood radius parameter is sensitive to DBSCAN's performance; hence, a sensitivity analysis was conducted to determine the value of EPS. The term “eps” refers to the maximum distance between points in the clusters in DBSCAN. eps must be in radians and not kilometers when using Haversine as the distance metric (Mahmoud & Akkari, 2016; Prasetya et al., 2020; Sharmila & Sabarish, 2021).

The following performance indicators were used to assess each radius:

- The number of clusters identified;
- Clustered crash records;
- Noise observations;
- Percent of crashes that are clustered;
- Spatial coverage;
- Maintaining local spatial resolution.

The chosen parameter should be maximized to detect hotspots and prevent over-segmentation or merging of hotspot areas.

Spatial Hotspot Indicators

Three spatial indicators were derived for each crash record after the clustering process.

- Zone_Label: The identifier of the DBSCAN cluster to which a crash was linked was used as the identifier for that crash. Noise observations received Zone_Label = −1

Zone labels are simply categories and do not specify the intensity of the hotspot.

- Zone_Count: It is the total number of crashes in each cluster zone. This variable represents the magnitude of hotspots and can be used to compare hotspot regions.
- Hotspot_Flag: A binary variable was created to differentiate between clustered crashes and isolated crashes:

$$\text{Hotspot_Flag} = \begin{cases} 1, & \textit{cluster member} \\ 0, & \textit{noise point} \end{cases} \tag{3}$$

This indicator aids in future statistical analyses and may be included in future crash prediction or machine learning models.

Descriptive Spatial Analysis

Characteristics of the identified clusters were quantified with descriptive statistics.
The analysis included: The sum of the number of clusters; The ratio of hotspot to noise proportions;
The number of crashes for each hotspot; largest hotspot; Average hotspot size; and
Distribution of crash severity by hotspot areas.
The average cluster size was computed as:

$$\text{Mean Cluster Size} = \frac{Nc}{K} \tag{4}$$

Where Nc is the total number of clustered crash points, and K is the total number of detected clusters. Noise points were excluded from the calculation of mean cluster size.

Spatial visualization was performed using Python GIS libraries, with OpenStreetMap as the base map. The visualization consisted of: a crash severity map; a hotspot map and a non-hotspot map; the spatial distribution of clusters from the DBSCAN algorithm; hotspot frequency distribution, the composition of crash severity by hotspot; and a detailed visualization of the largest hotspot. These visualizations enable intuitive interpretation of spatial clustering results and help transportation agencies determine locations for priority safety interventions.

Results and Discussion

Sensitivity Analysis of DBSCAN Parameters

The density-based clustering algorithm also relies heavily on the choice of neighborhood radius (eps), as it affects hotspot identification results. Three neighborhood radii (0.3, 0.5, and 0.7 km) were studied for each neighborhood size of 5 crash points to assess the robustness of the clustering results. The clustering performance for the three values that were considered is summarized in Table 1.

Table 1. Sensitivity analysis of the DBSCAN neighborhood parameter eps for hotspot detection

eps (km)	eps (radians)	Hot spot points	Total Points	Percentage (%)	Note
0.3	0.00004708	452	802	57 %	Smaller radius; detects fewer hotspot points
0.5	0.00007846	656	802	82 %	Balanced value; selected for final modeling
0.7	0.00010985	760	802	95 %	Larger radius; broader coverage, lower spatial resolution

As predicted, the neighborhood radius showed a progressive increase in the number of crash records included in the clusters and a progressive decrease in the number of observations deemed spatial noise. If the radius was reduced to 0.3km, only 452 crashes (57%) were assigned to hotspot clusters, suggesting that only a small number of crashes were classified as highly concentrated. This setup provided good local spatial resolution but caused several meaningful hotspot areas to be spread apart and many local crashes to be treated as single observations.

The values of the radius 1.0 km and 1.5 km, however, resulted in a high proportion of “clustered” crashes (96% and 95%) and a marked reduction in noise points. This larger neighborhood, however, geographically grouped clusters of crashes together into larger areas, making it difficult for the algorithm to detect and separate individual hazardous areas. The usefulness of hotspot analysis for engineering interventions might be reduced if too many clusters are merged, as different roadway environments would end up being represented as a single hotspot.

The intermediate radius of 0.5 km, yielded a balanced solution, with 656 crashes (81.8%) being clustered together, and with good spatial separation between the adjacent hotspots. This parameter was selected for further analysis due to the good hotspot coverage and spatial resolution. The results validate the impact of neighborhood definition in the sensitivity of DBSCAN and highlight the importance of parameter tuning before interpreting the spatial hotspot patterns.

Statistical Summary of the Derived Spatial Variables

The identified crash hotspots are summarized in Table 2.

Table 2. Summary statistics of the derived spatial variables

Spatial Indicators	Value
Total Crash Records	802
Number of DBSCAN-clustered	37
Clustered Crash Points	656
Noise Points	146
Cluster Crashes%	81.8%
Noise Points%	18.2%
Large Cluster	Zone 8
Crashes in Large Cluster	116
Large Cluster%	14.46%
Mean Cluster Size*	17.73

Using the same parameters, DBSCAN resulted in 37 spatial clusters and 146 noise observations, which accounted for 81.8% and 18.2% of the total number of crash records, respectively. The hotspot clusters had an average of 17.7 crashes, with some having more and others having fewer. There were 116 crashes in the largest hotspot (Zone 8), which made up 14.46% of all motorcycle/3-wheeled vehicle crashes.

The clustered crashes indicate that the locations of motorcycle crashes are not random in the transportation network but are concentrated at certain locations. Clustering suggests that the variables related to roadway, traffic exposure, and land use near the roadway are significant factors in the occurrence of a crash. Spatial heterogeneity is further suggested by the distribution of crashes with a relatively low number of crashes occurring at a disproportionately high share of locations.

Spatial Distribution of Crash Frequencies

The distribution of the crash frequencies along the detected DBSCAN clusters is shown in Figure 2.

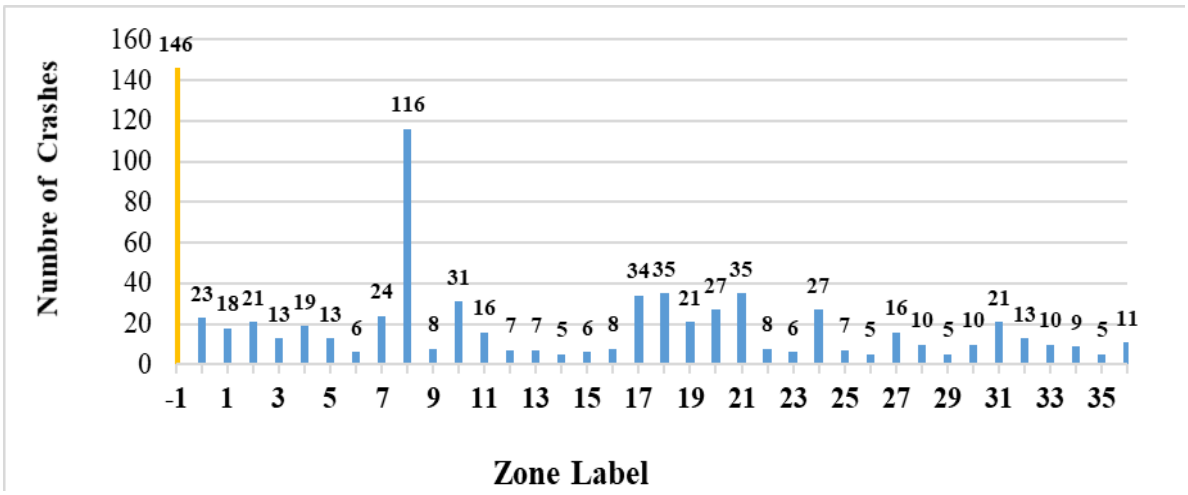

Figure 2. Distribution of crashes across the identified spatial zones

These results show significant variability in hotspot sizes. The highest crash frequency was in Zone 8, followed by Zones 18, 21, 17, and 10. However, a few clusters had fewer than 10 crashes, and 146 observations fell outside the identified hotspots. The dominance of Zone 8 implies that the area is not only subject to isolated crashes, but also to a persistent occurrence. These concentrations tend to occur where there are high traffic demand areas, traffic conflict areas, high pedestrian volumes, and intricate intersection geometries. The small groups also show that the risk of a crash is not concentrated in a single hazardous corridor but is spread across a variety of smaller regions. This spatial heterogeneity aligns with urban transportation systems that exhibit significantly different roadway functions, land uses, and traffic operations over relatively short distances. Therefore, hotspot identification data are more useful than crash frequencies, as they can be used to direct safety interventions to specific locations.

Hotspot Classification

The DBSCAN classification identified the crash locations as hotspot or non-hotspot areas. Figure 2 presents the proportion of crash records assigned to each category. About 82% of the crashes occurred in hotspot areas, and 18% occurred in isolated areas. There is evidence of a high level of geographic dependence in motorcycle crashes because of the high percentage of clustered crashes. Non-hotspot locations, however, should not be taken as a given to be safe locations. Instead, these observations are of crashes that did not meet the density threshold criteria. Even if no specific hotspots are identified, individual severe crashes can occur outside of these areas, as many factors contribute to their severity. To further examine the geographic distribution of hotspot locations, the DBSCAN results were visualized using spatial mapping techniques. Figure 3 illustrates the locations of hotspot and non-hotspot crashes within the study area.

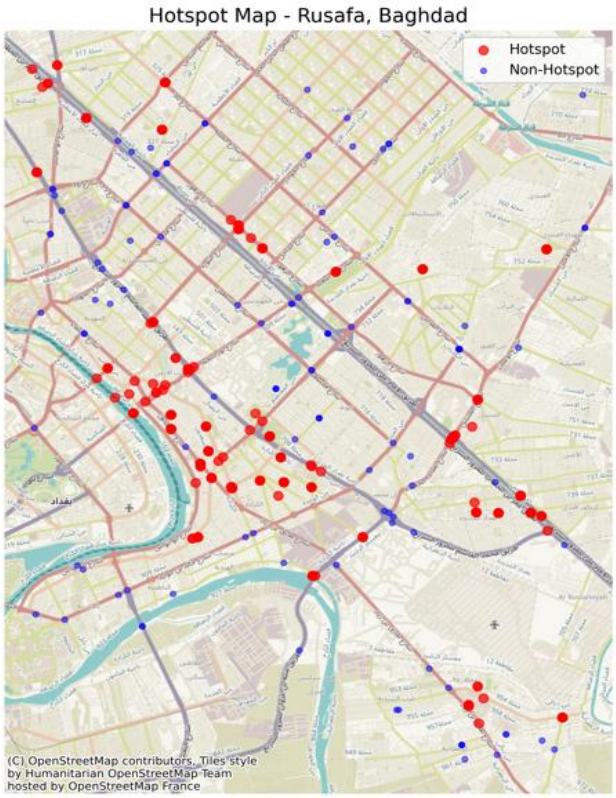

Figure 3. Hotspot and non-hotspot crash locations in Rusafa, Baghdad

The hotspot locations (red points) in Figure 3 are clearly concentrated in urban corridors and intersections in Rusafa, Baghdad with non-hotspot locations (blue points) being more spatially dispersed. The distribution indicates that there is a strong relationship between the distribution pattern of motorcycle and three-wheeled vehicle accidents and traffic interaction and urban activity. Identified hotspot areas are useful to transportation planners and decision makers as they will be able to prioritize safety interventions in areas where crashes are concentrated over a period of time.

Distribution of Crash Severity Inside and Outside Hotspots

The distribution of fatal, injury, and PDO crashes was analyzed between hotspot and non-hotspot areas to investigate the relationship between the severity of the crashes and the presence of the hotspots. The distribution of crash severities by hotspot and non-hotspot locations is presented in Figure 4. In absolute numbers, hotspot areas showed more fatal, injury, and PDO crashes than non-hotspot areas. This observation is not surprising, as most reported crash data comes from hotspot areas.

The findings indicate that hotspots have higher crash rates across all severity levels. This analysis, however, is descriptive and based on crash frequencies rather than severity proportions. Thus, hotspot designation should not be assumed to be associated with more severe crashes. Instead, the location of hotspots mainly corresponds to higher absolute crash frequencies. Further zone-wise analyses are needed to pinpoint zones with a disproportionately high incidence of severe crash outcomes.

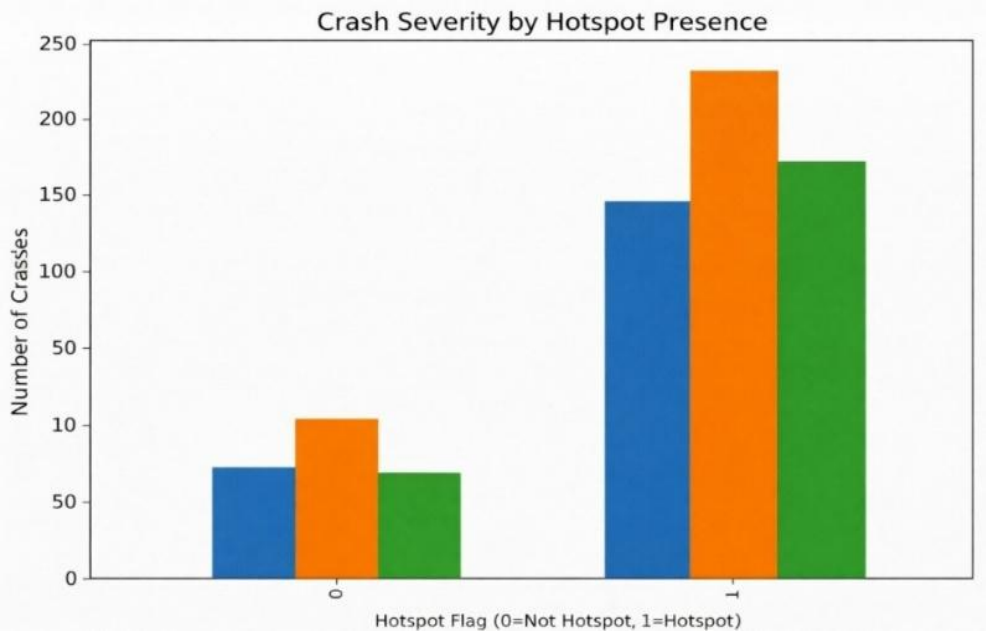

Figure 4. Distribution of crash severity according to hotspot presence.

Spatial Distribution of Crash Severity

The distribution of severity of the crashes in the identified DBSCAN zones is shown in Figure 5. Zone 8 experienced the most crashes (116), and therefore has the greatest concentration of crashes in the study area. Relatively high crash frequencies were also found in other zones (Zones 17, 18, and 21).

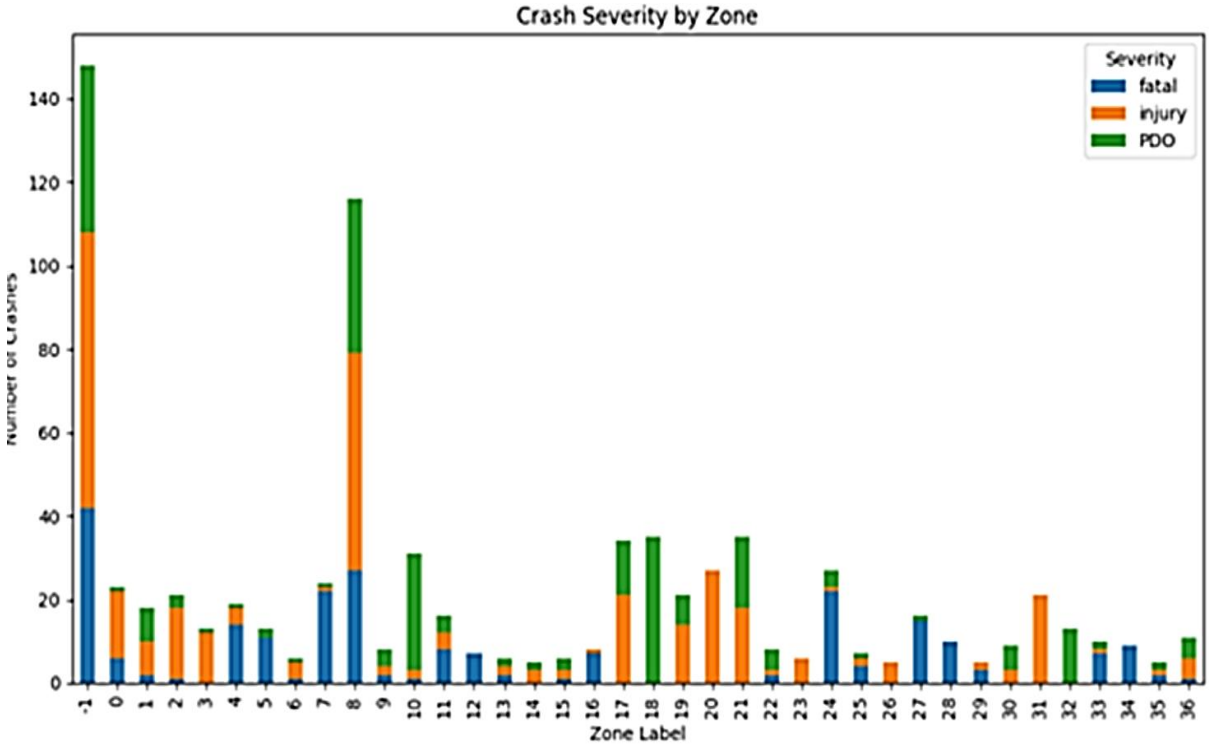

Figure 5. Distribution of crash severity across the identified DBSCAN zones.

The spatial distribution of fatal crashes was different, however. There were a few zones with relatively high numbers of fatal crashes and relatively low overall crash counts compared to Zone 8, including Zones 24, 27, and 28. This finding suggests that there is no correlation between the severity of crashes and their frequency. The findings show that frequency and severity of crashes are two complementary aspects of road safety. Although DBSCAN clustering works well to find clusters of crashes, further analyses based on the severity of

crashes are necessary to find areas with disproportionately severe crash outcomes. Therefore, both indicators should be taken into account if prioritizing road safety interventions in urban areas.

Spatial Distribution of Motorcycle Crashes in Baghdad

The overall spatiotemporal distribution of the severity of crashes and hotspot classification in Baghdad is shown in Figure 6. The severity map presents the geographic distribution of fatal, injury, and PDO crashes, and the hotspot map differentiates between crashes of multiple clusters and non-crashed locations. The maps depict a similar pattern of high rates of crashes in the middle, high-traffic-volume portions of the study area. The hotspot map also reflects that a significant percentage of crashes did occur in spatially clustered locations, while crashes at non-hotspot points were more spread out.

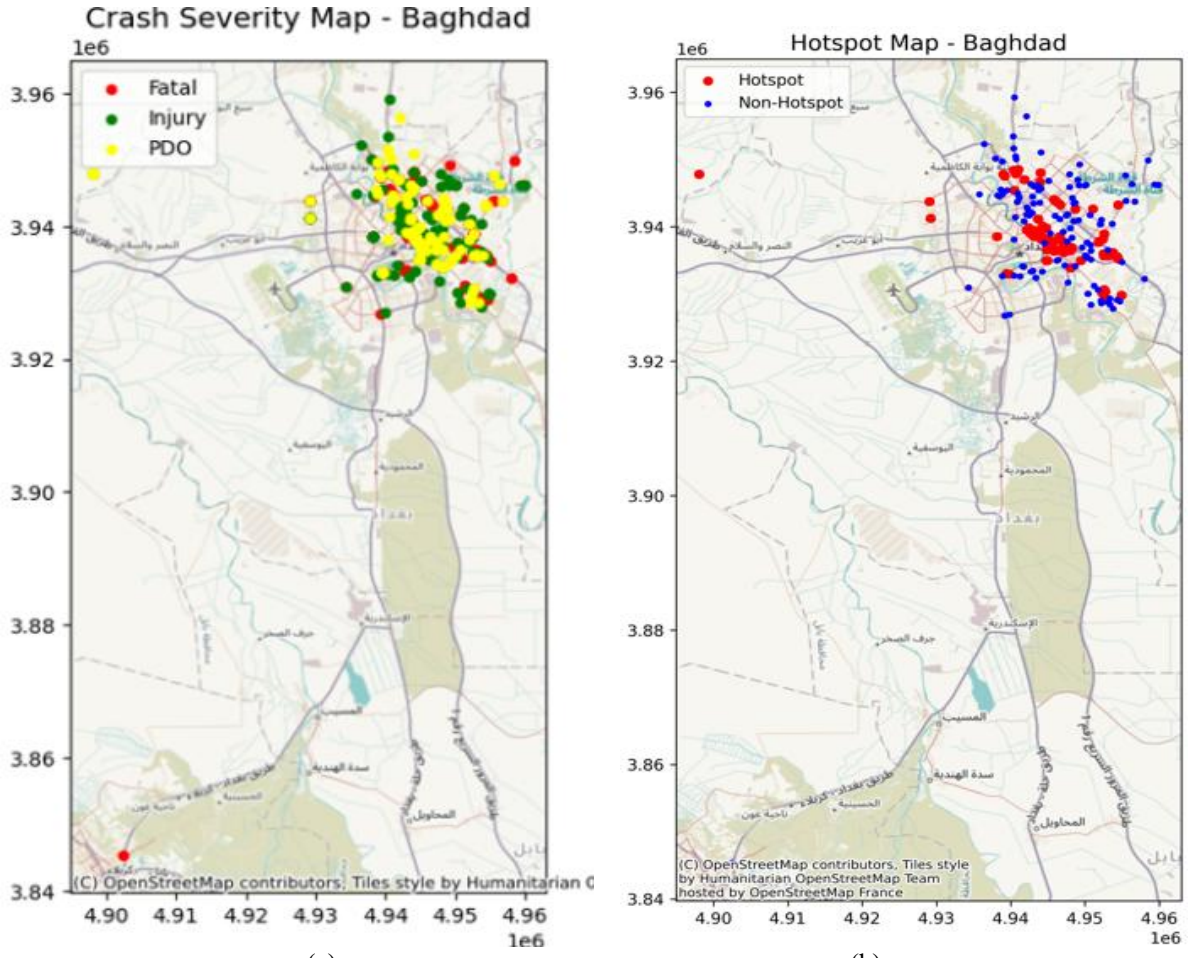

(a) (b)

Figure 6. Spatial distribution of crash severity and hotspot classification in Baghdad: (a) crash severity map and (b) hotspot map.

Spatial Distribution of DBSCAN Clusters

Figure 7 shows the spatial distribution of the DBSCAN clusters found in the study area. There were 37 clusters detected with heterogeneous spatial patterns throughout Rusafa. There were relatively few crashes in several of the clusters but the highest number of crash events occurred in Zone 8. The detailed visualization of Zone 8 shows the concentration of crashes around major intersections and in urban corridors, and the algorithm's ability to detect concentrated areas of crashes within the urban road network.

Results indicate that the majority of the crashes occurred in a small area, including around major intersections and traffic corridors. The spatial distribution of crashes in the area of Zone 8 (Rusafa-Baghdad) shows some major urban features like Al-Firdaws Square, Al-Saadoon Street, Kahramana Square, and Al-Nidhal Street. The location of crashes is slightly jittered to bring out clear visualizations.

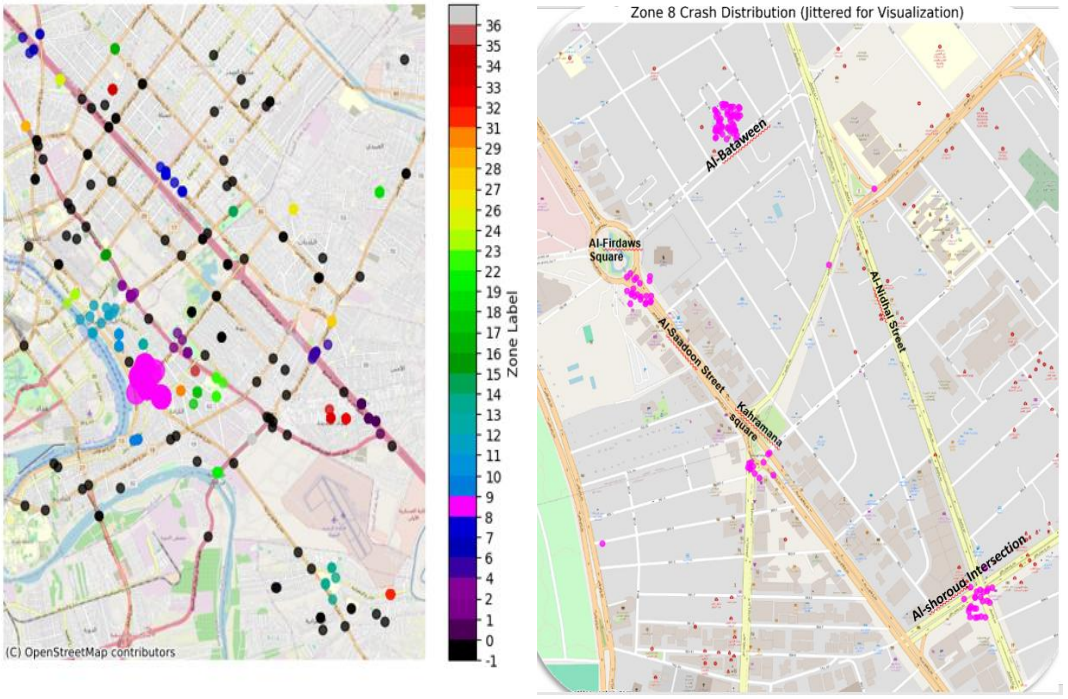

(a) (b)

Figure 7. DBSCAN clustering results: (a) spatial distribution of all detected clusters in Rusafa, Baghdad, and (b) detailed visualization of Zone 8, the largest identified crash cluster.

Discussion

This study introduced a spatial hotspot detection methodology that could be implemented in GIS to identify spatial clusters of motorcycle and three-wheeled motorcycle crashes in the Rusafa district of Baghdad, using the DBSCAN (density-based spatial clustering of application with noise) clustering algorithm and the Haversine distance metric. The proposed framework effectively identified repeat crash locations by analyzing 802 geo-referenced crash records and separating isolated locations that were not deemed crash hotspots based on the density requirement. The sensitivity analysis showed that the clustering performance was strongly influenced by the neighborhood radius, and that eps = 0.5 km was the optimal compromise between the number of hotspots covered and the spatial resolution. With these optimal parameters, 37 spatial clusters were found; 81.8% of these crashes were in hotspot areas, and 18.2% were classified as spatial noise. In this largest hotspot (Zone 8) there were 116 crashes (14.46% of all crashes recorded).

The results demonstrate that motorcycle and 3-wheeled vehicle crashes are not randomly distributed over the road network, but clustered in a few urban areas. Furthermore, the analysis will show that hotspot frequency and severity of crashes are complementary and not interchangeable measures. The highest number of crashes was found in the largest hotspot, but some smaller hotspots had relatively high percentages of fatal crashes, suggesting that hotspots with the highest number of crashes are not hotspots with the highest percentage of fatal crashes. The overall conclusion is that both frequency- and severity-based analyses are important for setting road safety priorities.

In terms of method, the study shows the effectiveness of using the Haversine distance metric with DBSCAN for the geographic analysis of crash data. The proposed spatial indicators, Zone_Label, Zone_Count, and Hotspot_Flag, are additional explanatory variables that can be added to future statistical and machine learning models for crash severity prediction, transportation risk assessment and intelligent transportation systems. Beyond visualization, these indicators bring spatial information to hotspot detection to enhance the value of the information to predictive safety analysis.

At a practical level, the identified hotspot locations could be used by transportation planners and road safety authorities to gain insight into what aspects of the roadway and traffic network require improvement, traffic management, enforcement and public education. Interventions can be targeted to persistent hotspots to increase the safety of vulnerable road users and maximize the use of limited transportation safety resources.

While all of these contributions have been made, there are a few things that need to be recognized. All crash locations are analyzed without accounting for traffic exposure, roadway geometry, traffic control characteristics, weather, land-use attributes or temporal variations. These factors should be integrated into spatiotemporal and machine learning models in future studies to gain a fuller understanding of motorcycle crash risk. Furthermore, comparing Hotspot Detection Method with other methods, like Kernel Density Estimation (KDE), Getis–Ord Gi*, Local Moran's I, OPTICS, and HDBSCAN, would better support the robustness and generalizability of the Hotspot Detection Method.

In general, the proposed framework shows that density-based spatial clustering is an effective and practical method for detecting hotspot areas of motorcycle and three-wheeled vehicle crashes in urban areas. The methodology helps the transportation safety analyst conduct a safety analysis based on GIS and it also serves as a basis for data-driven decision making to increase road safety for vulnerable road users.

Conclusion

This research aimed to develop a spatial hotspot detection methodology to identify areas of motorcycle and three-wheel vehicle (TWV) crash concentration in the Rusafa district of Baghdad city, utilizing the DBSCAN clustering algorithm, the Haversine distance measure, and GIS. The proposed framework identified persistent crash hotspots and excluded crash locations that were not dense enough to warrant inclusion in the persistent hotspot list by analyzing 802 geo-referenced crash records. The sensitivity analysis showed that the clustering results were highly sensitive to the neighborhood radius; eps = 0.5 km was found to be the most suitable value to balance hotspot coverage and spatial resolution. With these optimal parameters, 37 spatial clusters were identified, with 81.8% of crashes falling into hotspot areas and 18.2% considered spatial noise. A total of 116 crashes occurred in the largest hotspot (Zone 8), accounting for 14.46% of all reported crashes.

The results show that the crashes involving motorcycles and three-wheel vehicles are not randomly distributed on the road network but are clustered in relatively small numbers of locations within the city. Furthermore, this analysis shows that hotspot frequency and crash severity must be regarded as complementary, not synonymous. The highest frequency of crashes was in the largest hot spot; however, several smaller hot spots had relatively high percentages of fatal crashes, meaning that areas with the highest crash rates are not necessarily the highest risk of injury. This discovery is significant in terms of the need to combine frequency and severity-based analysis for setting road safety priorities.

From the methodological point of view, the study shows the effectiveness of this methodology for analyzing geographic crash data based on a hybrid approach of DBSCAN and Haversine distance. The proposed spatial indicators: Zone_Label, Zone_Count, and Hotspot_Flag, are additional explanatory variables that can be utilized by future statistical and machine learning models to predict crash severity, transportation risk assessments, and intelligent transportation systems. The indicators are useful beyond visualization to provide spatial information as a tool to predictive safety analytics.

As a practical example, the identified hotspot locations can serve as evidence for transportation planners and road safety authorities to prioritize engineering improvements, traffic management, enforcement, and public awareness programs. Strategic deployment of interventions at hotspot locations can enhance the safety of vulnerable road users and maximize the use of limited transportation safety resources.

Several limitations should, however, be noted in the face of these contributions. This analysis only examined the spatial distribution of crash locations, and the other data elements such as traffic exposure, roadway geometry, traffic control characteristics, weather, land use, and temporal changes were not included. These factors should be incorporated into spatiotemporal and machine learning models in future studies to gain a more comprehensive understanding of motorcycle crash risk. Furthermore, comparative assessments with other hotspot detection methods (e.g., Kernel Density Estimation (KDE), Getis–Ord Gi*, Local Moran's I, OPTICS, and HDBSCAN) would help to support the robustness and generalizability of hotspot identification techniques.

In general, the proposed framework is an effective and practical method for identifying persistent crash hot spots involving motorcycles or three-wheeled vehicles in urban areas. The methodology is part of GIS transportation safety analysis and serves as a foundation for data-driven decision-making for improving road safety for vulnerable road users.

Scientific Ethics Declaration

* The authors declare that the scientific, ethical, and legal responsibility for this article published in EPSTEM Journal belongs to the authors.

Conflict of Interest

* The authors declare that they have no conflicts of interest

Funding

* Authors have not received financial support.

Acknowledgments or Notes

* This article was presented as an oral presentation at the International Conference on Basic Sciences, Engineering and Technology (www.icbaset.net) held in Istanbul/Türkiye on September 17-18, 2026.

* The authors would like to thank Mustansiriyah University, Baghdad, Iraq, and the College of Engineering, Highway and Transportation Department, for their support in the present work. This research did not receive any specific grant from funding agencies in the public, commercial, or not-for-profit sectors. This study has not been supported financially by any public or private funding agencies.

References

Ali, W., & Alhusaynat, A. D. (2026). An intelligent model for traffic accident hotspot detection. *Journal of Education for Pure Science, 16*(1).

Eleiche, M. (2010, June). A minutes-based metric system for geographic coordinates in mobile GIS. In *2010 18th International Conference on Geoinformatics* (pp. 1–5). IEEE.

Jameel, A. H., & Jameel, A. (2024). Risk assessment of the Latifiya expressway segment using a proactive approach. *Journal of Engineering and Sustainable Development, 28*(5), 601–610.

Kamh, H., Alyami, S. H., Khattak, A., Alyami, M., & Almujibah, H. (2024). Exploring road traffic accident hotspots using clustering algorithms and GIS-based spatial analysis. *IEEE Access, 13,* 60944-60954.

Lai, W., Zhou, M., Hu, F., Bian, K., & Song, Q. (2019). A new DBSCAN parameters determination method based on improved MVO. *IEEE Access, 7*, 104085–104095.

Li, J., & Wang, X. (2022). Hotspot identification on urban arterials at the meso level. *Accident Analysis & Prevention, 169*, 106632.

Mahmoud, H., & Akkari, N. (2016, March). Shortest path calculation: A comparative study for location-based recommender system. In *2016 World Symposium on Computer Applications & Research (WSCAR)* (pp. 1–5). IEEE.

Mandala, S. K., Gurrapu, N., Praneeth, K. S., Vikas, M., Sanskar, K., & Rohith, T. (2026, March). Accident hotspot detection and spatial analysis. In *2026 IEEE International Conference on Interdisciplinary Approaches in Technology and Management for Social Innovation (IATMSI)* (Vol. 4, pp. 1–6). IEEE.

National Research Council U.S. (2010). *Transportation research board, task force on development of the highway safety manual, & transportation officials, joint task force on the highway safety manual*. . Highway Safety Manual (Vol. 1). Washington, DC: AASHTO.

Pusuluri, V. L., & Dangeti, M. R. (2024). Applications of QGIS and machine learning for road crash spot identification. *Earth Science Informatics, 17*(3), 2331–2346.

Saputra, R., & Sihabudin, A. (2023). Hotspot identification through pick-up and drop-off analysis of ride-hailing transport service. *International Journal of Advanced Computer Science and Applications, 14*(11).

Sharmila, S., & Sabarish, B. A. (2021, February). Analysis of distance measures in spatial trajectory data clustering. In *IOP Conference Series: Materials Science and Engineering* (Vol. 1085, No. 1, p. 012021). IOP Publishing. Retrieved from https://iopscience.iop.org/article/10.1088/1757-899X/1085/1/012021/meta

Shokat, D. M., & Jameel, A. K. (2025, September). Detecting high-risk road segments using kriging and inverse distance weighted methods. In *Proceedings of the Institution of Civil Engineers–Transport* (Vol. 178, No. 6, pp. 430–442). Emerald Publishing Limited.

World Health Organization. (2023). *Global status report on road safety 2023*. Geneva, Switzerland: World Health Organization. Retrieved from https://www.who.int/teams/social-determinants-of-health/safety-and-mobility/road-safety/global-status-report-on-road-safety-2023

Zhang, J., Li, Z., Pu, Z., & Xu, C. (2018). Comparing prediction performance for crash injury severity among various machine learning and statistical methods. *IEEE Access, 6*, 60079–60087.

Zhang, L., Wan, W., Lv, B., Li, Q., Sun, K., & Wan, Q. (2024, October). Identification of urban traffic accident hotspots using Getis-Ord Gi and DBSCAN algorithms. In *2024 3rd International Conference on Cloud Computing, Big Data Application and Software Engineering (CBASE)* (pp. 93–99). IEEE.

Author(s) Information

Ghaidaa A. Majeed
Mustansiriyah University, College of Engineering, Highway and Transportation Engineering Department, Baghdad, Iraq
ORCID iD: https://orcid.org/0009-0004-3014-9102

Abeer K. Jameel
Mustansiriyah University, College of Engineering, Highway and Transportation Engineering Department, Baghdad, Iraq
ORCID iD: https://orcid.org/0000-0001-9999-9974
*Contact e-mail:*abeer_khudhur@uomustansiriyah.edu.iq*

*Corresponding author(s) contact email

To cite this article:

Majeed, G. A., & Jameel, A. K. (2026). DBSCAN-based spatial hotspot detection of motorcycle and three-wheeled vehicle crashes. *The Eurasia Proceedings of Science, Technology, Engineering and Mathematics (EPSTEM), 42*, 162–175.

The Eurasia Proceedings of Science, Technology, Engineering and Mathematics (EPSTEM)
ISSN: 2602-3199

The Eurasia Proceedings of Science, Technology, Engineering and Mathematics (EPSTEM), 2026

Volume 42, Pages 176-183

ICBASET 2026: International Conference on Basic Sciences, Engineering and Technology

BIM Technologies at Structural Design

Ahmet Cagatay Tahaoglu
Istanbul Technical University

Yasin Fahjan
Istanbul Technical University

Abstract: Building Information Modeling (BIM), also referred to as the digital twin of a building, is a widely used methodology for digitalizing building properties and parameters throughout the entire building lifecycle, from the planning stage to demolition. This process enables effective management of information, thereby increasing profitability and productivity while saving time. Compared with conventional design approaches, BIM coordination during the preliminary design stage has been shown to provide significant savings during construction and throughout the subsequent stages of a project. Recent BIM software has increasingly incorporated algorithm-assisted design tools to automate repetitive tasks. These tools perform a series of analyses based on constraints defined by the user and subsequently identify the most suitable solution. In addition, BIM models can be connected to external software through Application Programming Interfaces (APIs). Data transfer to SAP2000 can be achieved through the use of genetic algorithms within Grasshopper and Dynamo. Structural design under seismic loading requires considerable experience and time. Reinforced concrete shear walls are commonly used in buildings because of their substantial stiffness against lateral forces. The aim of this study is to obtain an optimum shear wall layout by utilizing Building Information Modeling (BIM) technologies. The optimization of the shear wall arrangement is formulated as a topology optimization problem that aims to minimize cost, provide accurate analytical results, and reduce the time required from the engineer. In a typical project, the arrangement of shear walls is generally determined during the preliminary design stage through a coordination process involving architectural, mechanical, and electrical (MEP) disciplines. The main workflow of this study consists of identifying potential shear wall locations from architectural models and subsequently performing a series of structural analyses using different wall layout alternatives. Genetic algorithms and finite element software APIs are employed iteratively until an optimum solution is achieved. Dynamo visual programming software and the Python programming language are used to create BIM and structural models, establish connections between BIM models and structural analysis software, retrieve structural analysis results, and execute the optimization algorithm.

Keywords: Shear wall optimization, Computational design, Earthquake and structural engineering

Introduction

This study presents an innovative method that integrates Building Information Modeling (BIM) technologies and the Genetic Algorithm (GA) to automatically determine the optimal reinforced concrete shear wall layout (topology optimization) under seismic loads. Main purpose of the study is to automatically determine the lowest-cost shear wall layout (minimizing concrete volume) that fully complies with structural design code regulations without disrupting the coordination of architectural, mechanical, and electrical (MEP) disciplines or aesthetic decisions during the conceptual design phase and to save design time for engineers (Carlos, 2018). In design, significant amount of time is often spent during the conceptual design phase (Nouredine, 2022). A key aspect of structural design work is the placement of load-bearing elements without conflicting with voids, service channels, or architectural spaces. When all the mentioned concerns are considered together, it becomes

- This is an Open Access article distributed under the terms of the Creative Commons Attribution-Noncommercial 4.0 Unported License, permitting all non-commercial use, distribution, and reproduction in any medium, provided the original work is properly cited.

- Selection and peer-review under responsibility of the Organizing Committee of the Conference

© 2026 Published by ISRES Publishing: www.isres.org

necessary to generate analysis models through programming and intervention within Building Information Modeling (BIM) software and to identify the optimal configuration for these models via a series of analyses. (Aydoğdu, 2021)

Method

The study focused on mid-rise structures and linear modal analysis scenarios. Three actual construction projects were selected based on engineering experience. These examples exhibit diverse characteristics, such as floor plans featuring non-orthogonal or angled layouts. Furthermore, the structural systems vary, encompassing both flat-slab systems and beam-column-wall frame systems (Yu, 2017). As a starting point, architectural plans were converted into BIM objects. Subsequently, a structural model was created using Dynamo; grid lines, columns, walls, beams, and floor elements were derived from the architectural model (Korus, 2021). Wall elements were segmented at 1-meter intervals to allow for adjustments to the wall layout length, and each segment was tagged as a shear wall component. Preliminary design thicknesses were assigned to the shear walls and columns. The structural BIM model was then exported to ETABS software. Definitions from the Turkish Earthquake Code were used to establish various story height categories and seismic load levels; specifically, four seismic levels and eight height categories were considered. In total, thirty-two analyses were conducted for each building type. After defining the height and seismic parameters in ETABS, a genetic algorithm was executed via the API to determine the optimal shear wall layout. Dynamo features a built-in genetic algorithm function known as Generative Design (GD) (Alanani, 2024). It was determined that the GA (Genetic Algorithm) employs a genetic algorithm approach to achieve the optimal result (Wenjie, 2021). The genetic algorithm draws inspiration from the biological principle of "survival of the fittest." It is a practical, widely used method for addressing engineering problems (Bekdaş, 2016). The algorithm operates by conducting trials with random parameters for each population. Once results are obtained, favorable alternatives are filtered; the selected "offspring" then undergo mutation and crossover—mimicking biological processes—to generate new alternatives. Through successive iterations of this evolutionary process, the optimal result is identified. Moreover, custom code was developed to define Revit objects and transfer them to ETABS. Each shear wall segment was then tagged with a binary value (1 or 0) to define the configuration: a "1" indicated an existing shear wall, while a "0" signified a wall to be removed during the trial. Multiple configurations—represented by binary strings—were randomly generated and sent to ETABS, with the results of these sequential runs forming the population. custom algorithm coded by the designer. The advantages of using a custom program include reduced data storage requirements, increased speed, and optimization tailored specifically to the target problem. The program executed sequential analyses using a population of two hundred samples at each step. Following the selection of the best results from a given step via "elitist selection," a new population was generated using variations derived from the most promising samples of the previous generation. Additionally, adaptive mutation and crossover rates were defined. Since each successive step brought the process closer to the final result, the expected duration for any given analysis was six to eight hours. The final step automatically yielded the optimal layout.

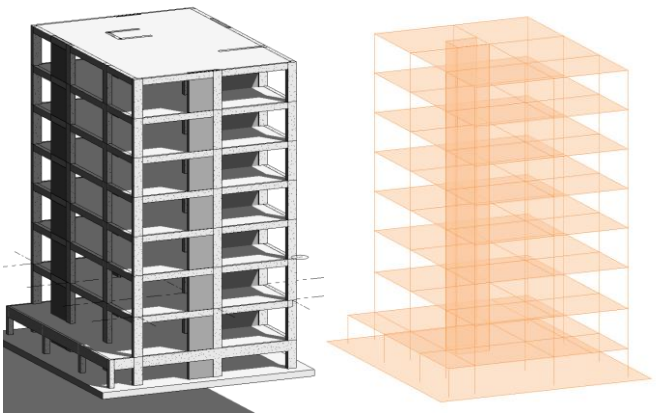

Figure 1. (a) Solid BIM View (b) Analytical Model Representation

Formulation of Problem

The design philosophy was outlined in the previous section. The process described in the previous section is practically applied as follows: Design workflow is summarized at Figure 2. 3D model, initially created as a BIM

model, is parameterized within the Dynamo environment. This parametric model is then transferred to ETABS via the API. The structural design software verifies compliance with code requirements; these constraints are illustrated in Figure 2. Subsequently, trials involving the placement of shear walls are conducted, and for each iteration, it is checked whether the design remains within the specified constraints (Gradisar, 2024). The program computes the total shear wall area, at each calculation step. The objective is to determine the minimum required area; however, if a given trial violates the constraints shown in Figure 3, the calculated shear wall area is multiplied by a fictitious coefficient to ensure that such alternatives are disregarded.

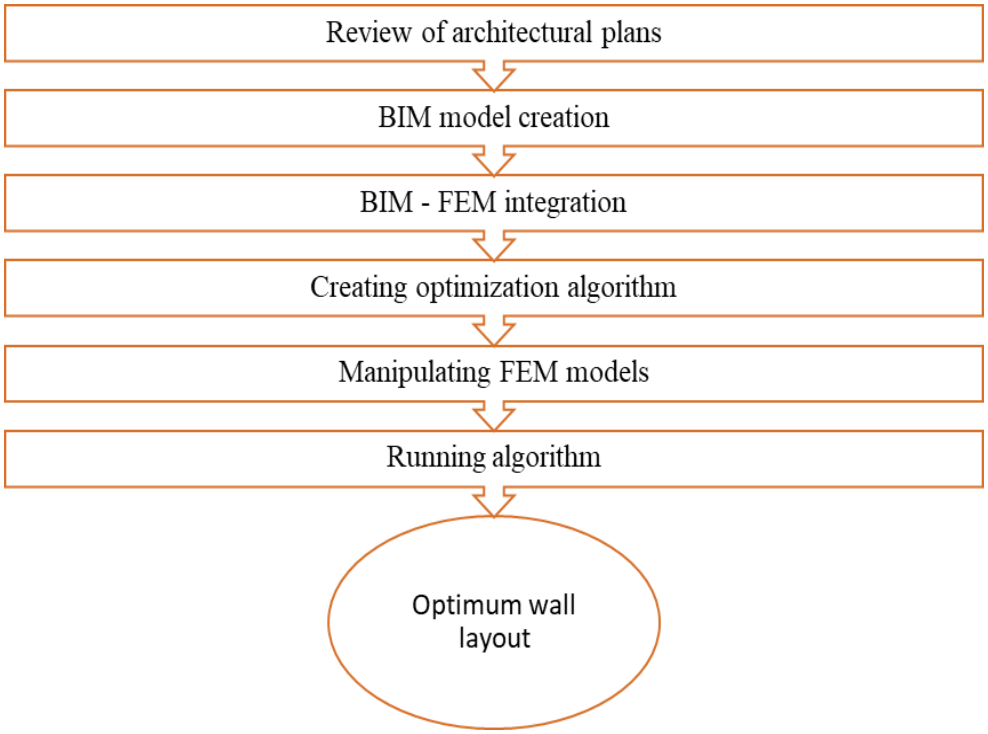

Figure 2. Topology optimization flowchart

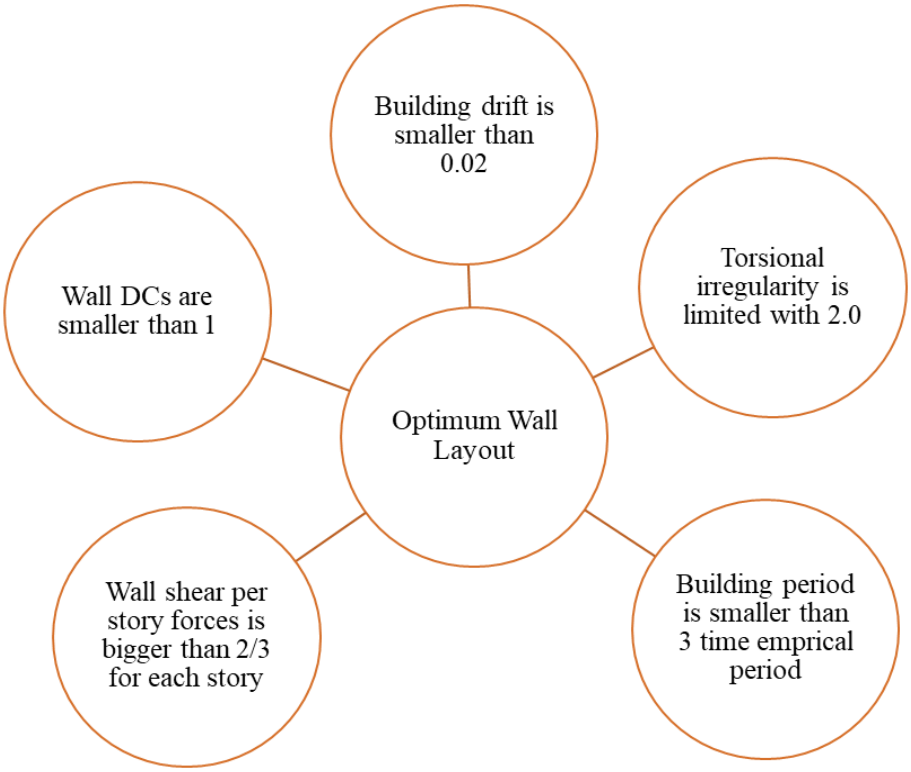

Figure 3. Optimum design constraints

Case Buildings

Three different building types exhibiting distinct behavioral characteristics are shown in Figure 4. The first is an example featuring flat-slab construction where shear walls carry the entire lateral load and are concentrated near the center of the structure. The second is an angular structure susceptible to torsional irregularities. The third utilizes a combination of moment-resisting frames and shear walls, though the shear walls are not arranged in a regular grid pattern.

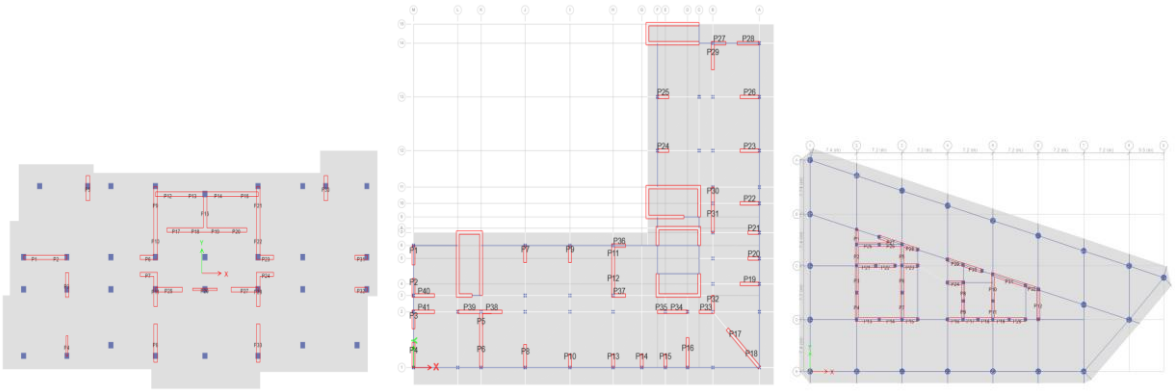

Figure 4. Case buildings

Sample Algorithmic Design Results

The analysis results for the sample building height are presented in Figure 4. As can be seen, as seismicity increases, the frequency of shear walls increases, and they are positioned towards the building's exterior axes.

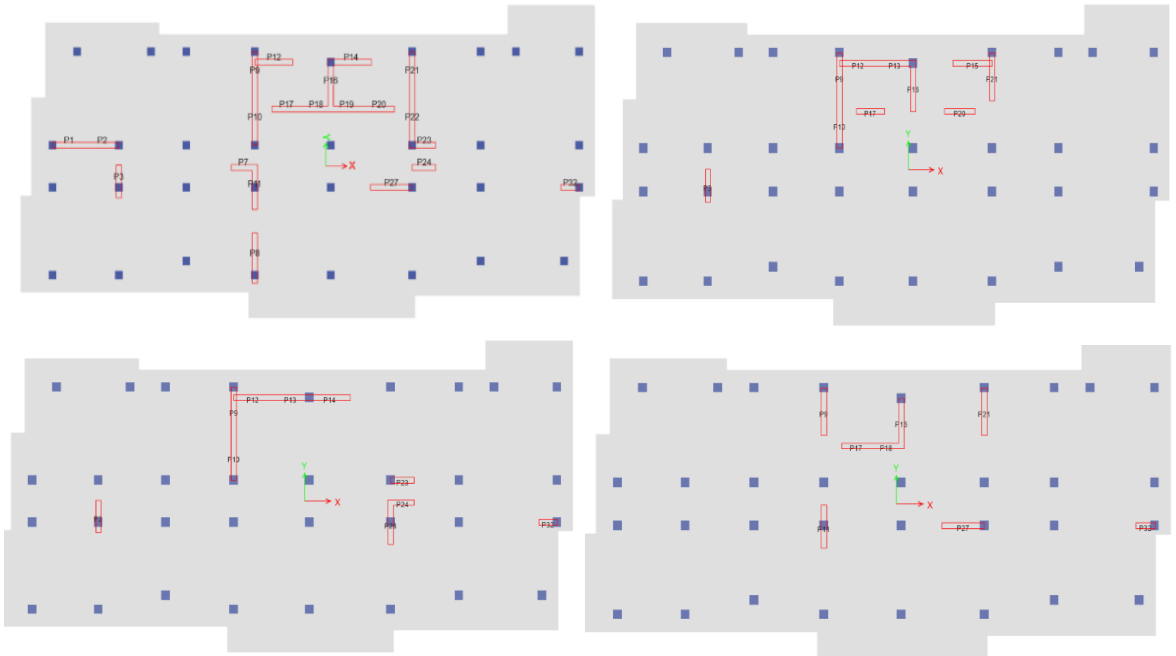

Figure 4. Optimum wall layout for a) Seismic class 1, b) Seismic class 2, c) Seismic class 3, d) Seismic class 4

Similarly, the algorithm was run for the other two building types using comparable building heights, and the results are presented in the subsequent figures. Each analysis result was recorded, and the correlations between them were examined. The study demonstrated a linear relationship across all building samples. As the study was limited to various iterations of three primary sample types, it established a general correlation. With an increased sample size, it would be possible to create a database of the existing building stock and use the information derived from the developed method to formulate design guidelines for new buildings.

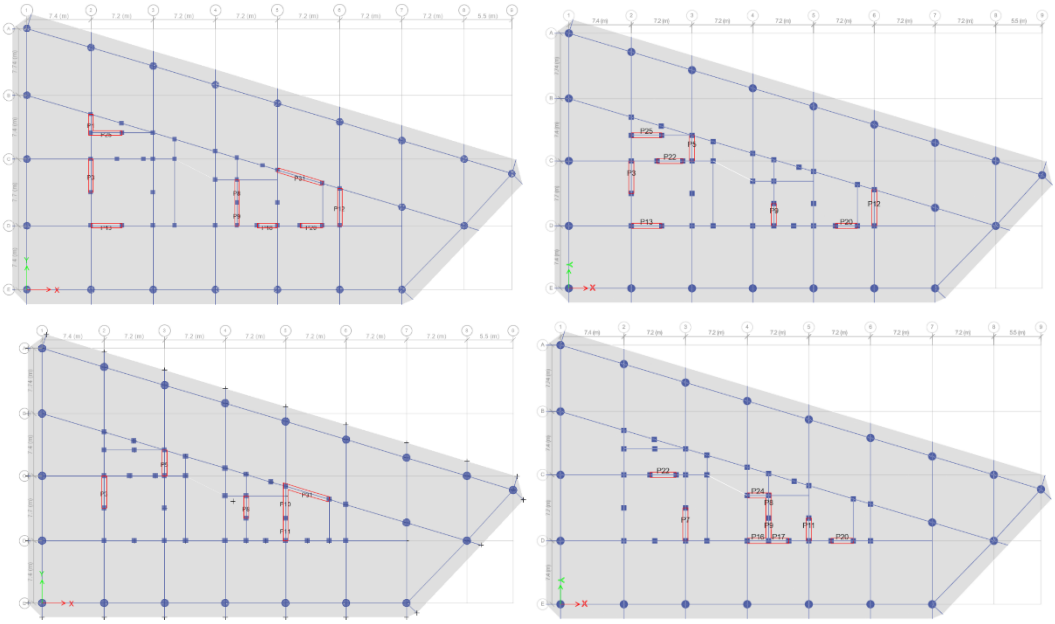

Figure 5. Optimum wall layout for a) Seismic class 1, b) Seismic class 2, c) Seismic class 3, d) Seismic class 4

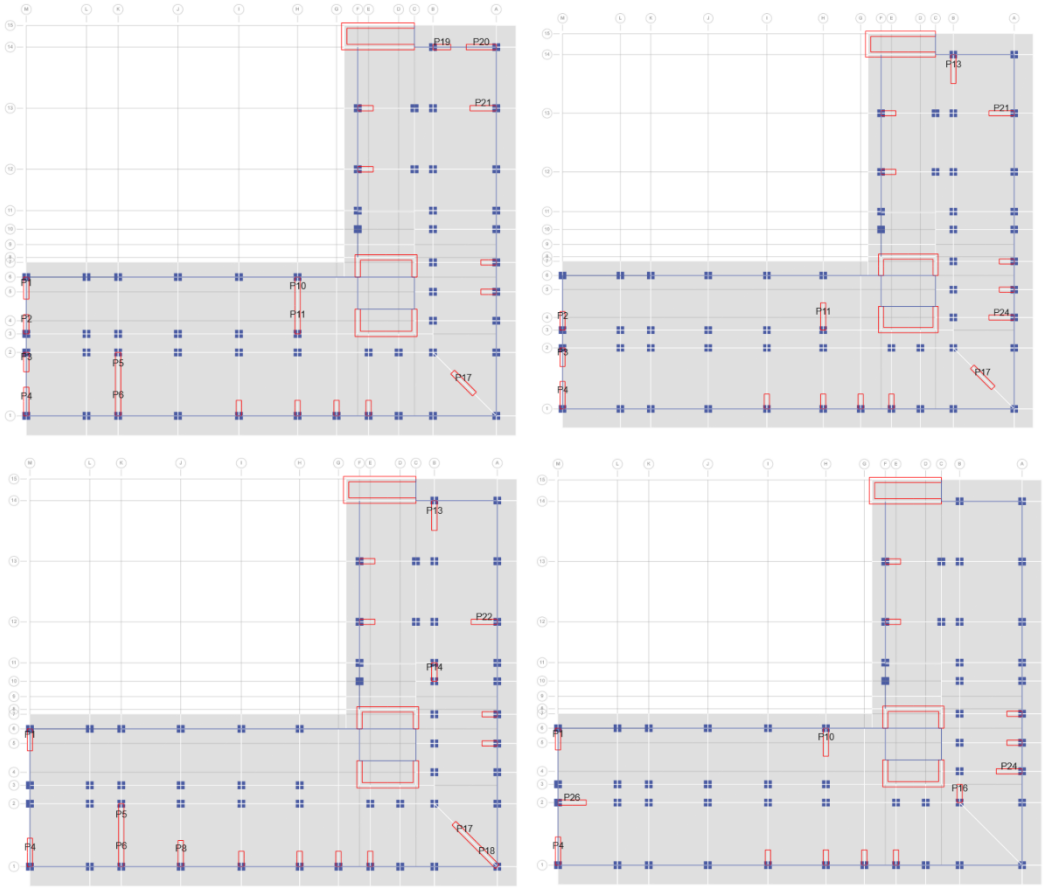

Figure 6. Optimum wall layout for a) Seismic class 1, b) Seismic class 2, c) Seismic class 3, d) Seismic class 4

Results and Discussion

Similar behavioral patterns were observed in the analyzed samples. It was found that the ratio calculated by dividing the required shear wall area (determined by analysis) by the product of the floor area and the short-period spectral acceleration coefficient (Sds) increases as the number of stories increases, exhibiting a trend

close to linear behavior, as shown in Figure 7. When the calculation result is normalized to remove the influence of Sds and the number of stories, a trend approaching horizontal behavior is expected. These relationships are illustrated in Figure 8.

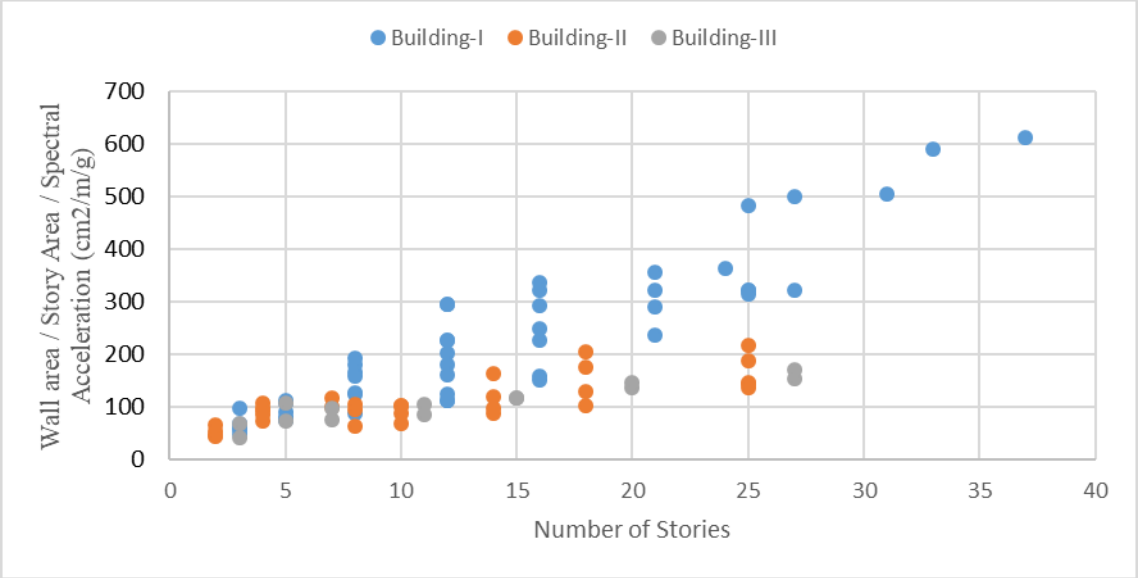

Figure 7. Optimum wall area per (single story area x spectral acceleration)

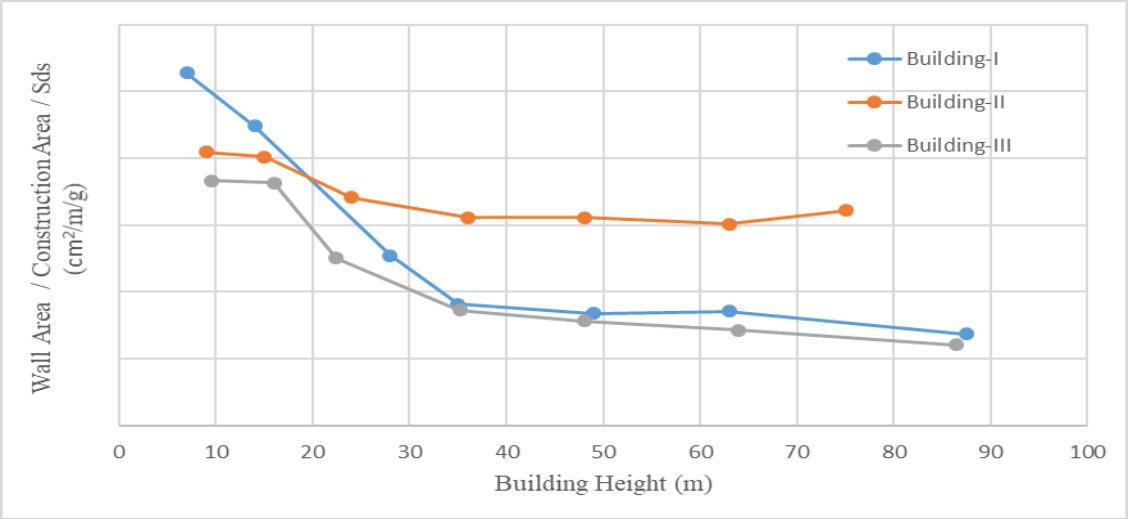

Figure 8. Optimum wall area per (construction area x spectral acceleration)

The observed relationship indicates that the demand for shear walls is higher in low-rise structures lacking shear wall-frame interaction; conversely, as the number of stories increases, the frame engages, thereby minimizing the load on the shear walls (Hu, 2025). In Example I, since a system featuring entirely flat slab was designed, this interaction did not occur, resulting in a strictly linear relationship. Consequently, when creating an idealized model, distinct equations should be employed for shear wall-frame structures versus systems with flat slabs where seismic loads are ensured exclusively by the shear walls. The first scenario can be idealized using a curve that begins with a large shear wall area, shows a relative decrease in this area as the number of stories rises, and levels off to a constant value once the building height exceeds 35–40 meters. The second scenario, however, can be idealized simply as a horizontal line. The idealization of the trendline can be expressed with a two-segment curve equation by establishing a building height of 35 meters as the threshold.

Ideal bilinear curve, including the consideration of building irregularities can be expressed as follows:

$Aw = C \times (-0.00005 \times Hn + 0.0036) \times (Apj \times N \times Sds)$ For $Hn \leq 35$ m:

$Aw = C \times (0.0018) \times (Apj \times N \times Sds)$ For $Hn > 35$ m:

Where :

Apj : Floor plan area
Aw : Required shear wall area
Hn : :Building height
N : :Number of stories
Sds : Short period spectral acceleration coefficient

C = C1 x C2 x C3 x C4 x C5 x C6

Where :

C1 : Frame components. 0.9 if a system detailed with high-ductility frames exists in addition to shear walls (excluding ribbed or waffle slab systems); 1.0 if seismic loads are resisted solely by shear walls.
C2 : Mass distribution. 1.1 if the structure exhibits regular behavior due to efficient distribution of architectural functions or a live load participation ratio of 0.6 or 0.8; 1.0 otherwise.
C3 : Stiffness distribution between adjacent stories. 1.15 for configurations involving soft story irregularity; 1.0 for other types.
C4 : Shear wall arrangement. 1.15 if at least one rigid core (such as an elevator or stairwell) is located on an exposed outer axis; 1.0 otherwise.
C5 : Plan orthogonality. 1.2 for asymmetric or L-, C-, or T-shaped buildings; 1.0 otherwise.
C6 : Plan dimensions. 1.1 if the ratio of the long side to the short side of the plan is 3 or greater; 1.0 otherwise.

Conclusion

This study demonstrates how structural design can be manipulated using BIM technologies, specifically through examples of parametric and computational design. The main objective of the study is to use a visual programming language to iteratively analyze various shear wall layout configurations and verify their compliance with code requirements. An optimal layout was achieved by applying a genetic algorithm to three sample structures in accordance with the Turkish Earthquake Code. Required shear wall areas derived from these examples were multiplied for various building heights and seismic hazard levels. Based on the resulting analysis data, the required shear wall areas were plotted against building characteristics. In addition to calculating the required area, the specific layout of shear wall elements was determined for each analysis set; it was observed that as seismic hazard levels increased, the walls tended to shift toward the building's outer axes, whereas layouts showed more randomness at lower seismic hazard levels.

Recommendations

The study is based on algorithmic design which requires computational time and effort. AI and machine learning studies can be developed in order to automate the algorithmic process. Accuracy of study can be ensured with increasing the number of observed real projects. Projects can be coordinated with municipalities or construction ministries of each country that is compatible with design code that is studied. Observed buildings will create a data pool for AI training; mapping of layout will be the guide for new designs and automation of shear wall layout can be done without executing any calculation effort. Moreover, optimum layouts can be verified by executing time history analysis and nonlinear behavior can be observed.

Scientific Ethics Declaration

* The authors declare that the scientific ethical and legal responsibility of this article published in EPSTEM Journal belongs to the authors.

Conflict of Interest

* The authors declare that they have no conflicts of interest

Funding

* No funding has been received during the study.

Acknowledgements or Notes

* This article was presented as an oral presentation at the International Conference on Basic Sciences, Engineering and Technology (www.icbaset.net) held in Istanbul/Türkiye on September 17-18, 2026.

* The authors thank to APCB Engineering and Nodus Engineering for valuable moral support.

References

Alanani, M., Brown, T., & Elshaer, A. (2024). Multiobjective structural layout optimization of tall buildings subjected to dynamic wind loads. *Journal of Structural Engineering, 150*(7).

Aydogdu, I., Ormecioglu, T. O., Tunca, O., & Carbas, S. (2022). Design of large-scale real-size steel structures using various modified grasshopper optimization algorithms. *Neural Computing and Applications, 34*(16), 13825–13848.

Bourahla, N., Tafraout, S., Bourahla, Y., Sereir-El-Hirtsi, A., & Skoudarli, A. (2022). GA based design automation and optimization of earthquake resisting CFS structures in a BIM environment. *Structures, 43*, 1334–1341.

Gomes, C., Parente, M., Azenha, M., & Lino, J. C. (2018). An integrated framework for multi-criteria optimization of thin concrete shells at early design stages. *Advanced Engineering Informatics, 38*, 330–342.

Hu, J., Zhou, X., Liu, J., Shan, W., Qi, H., Chen, W., & Zhang, Y. (2025). Intelligent design of shear wall structures based on BIM and multi-objective genetic algorithm. *Journal of Building Engineering, 104*, 112284.

Korus, K., Salamak, M., & Jasiński, M. (2021). Optimization of geometric parameters of arch bridges using visual programming FEM components and genetic algorithm. *Engineering Structures, 241*, 112465.

Liao, W., Lu, X., Huang, Y., Zheng, Z., & Lin, Y. (2021). Automated structural design of shear wall residential buildings using generative adversarial networks. *Automation in Construction, 132*, 103931.

Gradišar, L., Dolenc, M., & Klinc, R. (2024). Towards machine learned generative design. *Automation in Construction, 159*, 105284.

Yang, X.-S., Bekdaş, G., & Nigdeli, S. M. (Eds.). (2016). *Metaheuristics and optimization in civil engineering*. Cham, Switzerland: Springer.

Zhang, Y., & Mueller, C. T. (2017). Shear wall layout optimization for conceptual design of tall buildings. *Engineering Structures, 140*, 225–240.

Author(s) Information

Ahmet Cagatay Tahaoglu
Istanbul Technical University
34467 Maslak - Sarıyer / İstanbul, Turkiye
ORCID iD: https://orcid.org/0009-0005-5451-7974
*Contact e- mail:*tahaoglua@itu.edu.tr*

Yasin Fahjan
Istanbul Technical University
34467 Maslak - Sarıyer / İstanbul, Türkiye
ORCID iD: https://orcid.org/0000-0003-1254-4526

*Corresponding author(s) contact email

To cite this article:

Tahaoglu, A.C. & Fahjan, Y. (2026). BIM technologies at structural design. *The Eurasia Proceedings of Science, Technology, Engineering and Mathematics (EPSTEM), 42,* 176-183.

The Eurasia Proceedings of Science, Technology, Engineering and Mathematics (EPSTEM)
ISSN: 2602-3199

The Eurasia Proceedings of Science, Technology, Engineering and Mathematics (EPSTEM), 2026

Volume 42, Pages 184-190

ICBASET 2026: International Conference on Basic Sciences, Engineering and Technology

Machine Learning-Based Pollution Risk Classification in Industrial Wastewater Treatment

Mustafa Ozan Ozkok
Sakarya University

Abstract: Industrial wastewater contains various pollutants that can impact water quality and the environment. It is important to identify pollution risk conditions in order to monitor wastewater treatment processes effectively. This study compares four machine learning algorithms — Random Forest, Support Vector Machine (SVM), XGBoost and LightGBM — for classifying pollution risk. The Melbourne Eastern Industrial Wastewater Plant dataset was used for this study, containing 600 observations and 14 physicochemical and operational variables. The dataset includes two predefined classes: 'Normal' and 'High Risk'. The models were evaluated using stratified five-fold cross-validation. Accuracy, precision, recall, F1-score and ROC-AUC were used to compare their performance. XGBoost achieved the highest mean accuracy of 93.5%, precision of 90.32%, recall of 91.43%, F1 score of 90.72% and ROC-AUC of 0.9803. LightGBM achieved an accuracy of 93%, followed by random forest with 91.67% and SVM with 90.33%. SHAP analysis was used to examine the contribution of input variables to XGBoost predictions. According to the mean absolute SHAP values, COD and BOD5 were the most influential variables. The results showed that the models could distinguish between the predefined pollution risk categories. However, the risk classes were derived from a composite pollution index, and further validation using independent datasets is needed.

Keywords: Industrial wastewater, Pollution risk classification, Machine learning, XGBoost, SHAP

Introduction

Industrial wastewater is an important source of water pollution due to the different pollutants it may contain. Organic compounds, heavy metals, suspended solids, and nitrogen compounds can affect water quality and aquatic ecosystems when wastewater is discharged without proper treatment (Breida et al., 2019; Zhang & Ren, 2019). For this reason, wastewater treatment and pollution control are important for reducing the environmental effects of industrial activities. Different approaches have been developed to manage industrial pollution and improve wastewater treatment processes (Singh & Mishra, 2023; Kato & Kansha, 2024).

Several physicochemical and operational parameters are used to evaluate the conditions of wastewater treatment. These include Chemical Oxygen Demand (COD), Biochemical Oxygen Demand (BOD_5), ammonia nitrogen (NH_3-N), pH, temperature and suspended solids, which provide information about the characteristics of the wastewater. Energy consumption, production load and system load are also related to the operation of treatment facilities. Changes in these parameters may indicate changes in wastewater quality or treatment conditions. Trubetskaya et al. (2021) presented a methodology for assessing and monitoring risks in the industrial wastewater sector. In a subsequent study, Trubetskaya et al. (2025) examined tools used to assess risks associated with wastewater and water technologies.

Wastewater quality is commonly monitored through laboratory measurements and the analysis of individual parameters. These measurements are necessary for evaluating treatment conditions, but examining several variables together can provide additional information. Machine learning methods can be used to analyze such data

- This is an Open Access article distributed under the terms of the Creative Commons Attribution-Noncommercial 4.0 Unported License, permitting all non-commercial use, distribution, and reproduction in any medium, provided the original work is properly cited.

- Selection and peer-review under responsibility of the Organizing Committee of the Conference

© 2026 Published by ISRES Publishing: www.isres.org

and identify relationships between variables. Their use in wastewater treatment has been investigated for different purposes, including water quality prediction and process monitoring. Zamfir et al. (2025) reviewed machine learning models applied to wastewater treatment optimization and discussed their applications in monitoring and operational management.

Machine learning has been used in previous studies to address various wastewater-related issues. For example, Hammond et al. (2021) investigated the use of machine learning to detect untreated sewage discharges into watercourses. Elsayed et al. (2022), meanwhile, compared 23 machine learning classification algorithms for mitigating the risk of wastewater treatment. They found that an ensemble bagged trees algorithm achieved the highest classification accuracy. Nguyen et al. (2024) used boosting algorithms to predict the toxicity of industrial wastewater effluent and examine possible control strategies. Shu et al. (2025) applied machine learning to trace the sources of wastewater using fluorescence information, achieving an identification accuracy of 94.25%. While these studies addressed different issues, they demonstrate the application of machine learning in wastewater monitoring, risk classification, toxicity prediction and source identification.

There are several machine learning algorithms available for classification tasks. Random Forest, for example, combines the predictions of multiple decision trees (Breiman, 2001). A Support Vector Machine (SVM) determines a decision boundary between classes and can handle non-linear classification problems through kernel functions (Boser et al., 1992). XGBoost and LightGBM use gradient boosting to build decision trees sequentially (Chen & Guestrin, 2016; Ke et al., 2017). The performance of these algorithms can be compared using the same dataset and evaluation procedure. However, classification metrics alone do not explain which variables influence model predictions. SHapley Additive exPlanations (SHAP), introduced by Lundberg and Lee (2017), can be used to analyse the impact of individual input variables on model predictions.

This study compared Random Forest, SVM, XGBoost and LightGBM for the classification of pollution risk in industrial wastewater treatment. The Melbourne Eastern Industrial Wastewater Plant dataset, containing 600 observations and 14 physicochemical and operational variables, was used for this comparison. The target variable includes two predefined classes, Normal and High Risk, obtained from a composite pollution risk index. The models were evaluated using stratified five-fold cross-validation. Accuracy, Precision, Recall, F1-score, and ROC-AUC were calculated to compare their performance. SHAP analysis was also performed for the XGBoost model to examine the contribution of the input variables. The study focuses on comparing the four algorithms and identifying the parameters associated with the predefined pollution risk categories.

Method

Four machine learning algorithms — Random Forest, Support Vector Machine (SVM), XGBoost and LightGBM — were used to classify pollution risk conditions in industrial wastewater treatment. The dataset was prepared and preprocessed prior to model training. All four models were evaluated using the same dataset and cross-validation procedure. Their classification performance was then compared using different evaluation metrics. SHAP analysis was also applied to the XGBoost model to examine the contribution of the input variables to its predictions.

Dataset

For the classification experiments, data from the Melbourne Eastern Industrial Wastewater Plant were used (Melbourne Eastern Industrial Wastewater Plant, Kaggle). The dataset is available on Kaggle and includes 600 records. Each record contains 14 measurements related to wastewater quality and plant operation. These measurements are heavy metals, COD, BOD5, suspended solids, NH3-N, pH, temperature, conductivity, flow velocity, energy consumption, production load, effluent flow, daily output, and system load.

The 'Pollution_Risk' column was used as the target variable. Of the 600 records, 390 were classified as 'Normal' and 210 as 'High Risk'. In the original dataset, 'Normal' was coded as 1 and 'High Risk' as 0, and these labels were determined using a pollution index based on COD, BOD5, NH_3-N, energy consumption and suspended solids. The 65th percentile of the index was used as the threshold. Records exceeding this threshold were assigned to the 'High Risk' class, while the others were assigned to the 'Normal' class.

Data Preprocessing

The dataset contained no missing values. For the classification task, the original class labels were changed to 1 for High Risk and 0 for Normal. All 14 numerical features were used in the experiments. Feature standardization was performed only for SVM using StandardScaler. In each fold, the scaling parameters were obtained from the training set and then applied to the test set. This ensured that the test data did not influence the preprocessing stage.

Machine Learning Models

In this study, three tree-based machine learning algorithms and SVM were used to classify pollution risk conditions in industrial wastewater treatment. The models were evaluated using the same input variables and cross-validation procedure to compare their classification performance. Random Forest combines the predictions of multiple decision trees (Breiman, 2001). In this study, the model was trained with 300 trees. For SVM, the radial basis function (RBF) kernel was selected, and the regularization parameter was set to 1.0. The algorithm uses the maximum margin principle to separate observations belonging to different classes (Boser et al., 1992).

Two gradient boosting algorithms, XGBoost and LightGBM, were also included in the experiments. XGBoost constructs decision trees sequentially, with each new tree contributing to the correction of previous prediction errors (Chen & Guestrin, 2016). A total of 300 estimators were used, together with a maximum tree depth of 4 and a learning rate of 0.05. LightGBM was included as another tree-based boosting method with an emphasis on computational efficiency (Ke et al., 2017). Its configuration consisted of 300 estimators, a learning rate of 0.05, and 15 leaves. All experiments used a random seed of 42.

Experimental Setup and Performance Evaluation

The models were evaluated using stratified five-fold cross-validation. The 600 observations were divided into five folds with similar class distributions. Four folds were used to train the models, and the remaining fold was used for testing. The training and testing folds were changed in each iteration. After five iterations, every observation had been used once for testing. Model performance was evaluated using accuracy, precision, recall, F1-score and ROC-AUC. Precision, recall and F1 score were calculated by considering high risk as the positive class. The mean and standard deviation of the five folds were calculated for each performance metric. Additionally, out-of-fold predictions were combined to construct confusion matrices and ROC curves.

SHAP Analysis

SHAP (SHapley Additive exPlanations) was used to examine how the input variables affected the predictions of XGBoost. Following the five-fold cross-validation experiments, XGBoost was trained again on all 600 observations. SHAP values were then calculated for the input variables, and their mean absolute values were used to compare feature importance. This analysis focused on the physicochemical and operational variables associated with the predicted pollution risk classes.

Results and Discussion

The classification performances of Random Forest, SVM, XGBoost, and LightGBM were evaluated using stratified five-fold cross-validation. Accuracy, Precision, Recall, F1-score, and ROC-AUC were used to compare the models. The mean and standard deviation values obtained from the five folds are presented in Table 1.

Table 1. Classification performance of machine learning models (mean ± standard deviation)

Model	Accuracy	Precision	Recall	F1-score	ROC-AUC
Random Forest	0.9167 ± 0.0156	0.8957 ± 0.0456	0.8667 ± 0.0643	0.8786 ± 0.0258	0.9692 ± 0.0146
SVM	0.9033 ± 0.0095	0.8604 ± 0.0337	0.8667 ± 0.0361	0.8625 ± 0.0129	0.9702 ± 0.0033
XGBoost	0.9350 ± 0.0137	0.9032 ± 0.0287	0.9143 ± 0.0598	0.9072 ± 0.0232	0.9803 ± 0.0047
LightGBM	0.9300 ± 0.0095	0.9025 ± 0.0344	0.9000 ± 0.0543	0.8996 ± 0.0170	0.9783 ± 0.0068

As shown in Table 1, all four models achieved high classification performance. XGBoost obtained the highest mean Accuracy of 0.9350, followed by LightGBM with 0.9300, Random Forest with 0.9167, and SVM with

0.9033. XGBoost also achieved the highest Precision (0.9032), Recall (0.9143), F1-score (0.9072), and ROC-AUC (0.9803). These results indicate that XGBoost provided the highest overall classification performance among the evaluated models.

The performance of LightGBM was close to that of XGBoost, with a difference of 0.0050 in mean Accuracy. LightGBM also achieved an F1-score of 0.8996. Although Random Forest had a higher Accuracy than SVM, SVM achieved a slightly higher ROC-AUC. This difference was also observed in the comparison of the evaluation metrics. Recall was evaluated by considering High Risk as the positive class. LightGBM achieved a mean Recall of 0.9000, while Random Forest and SVM both obtained 0.8667. Compared with these models, XGBoost achieved a higher Recall and identified a larger proportion of high-risk observations. The mean ROC-AUC values were 0.9783 for LightGBM, 0.9702 for SVM, and 0.9692 for Random Forest. All four models achieved ROC-AUC values above 0.96. The ROC curves of the models are presented in Figure 1.

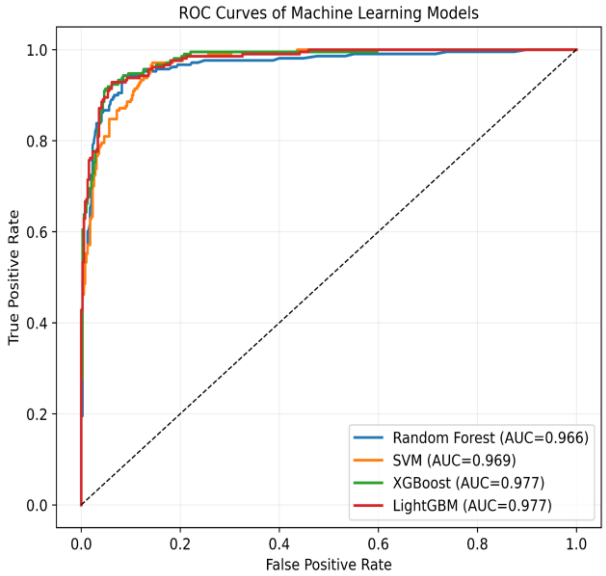

Figure 1. ROC curves of the four machine learning models based on combined out-of-fold predictions.

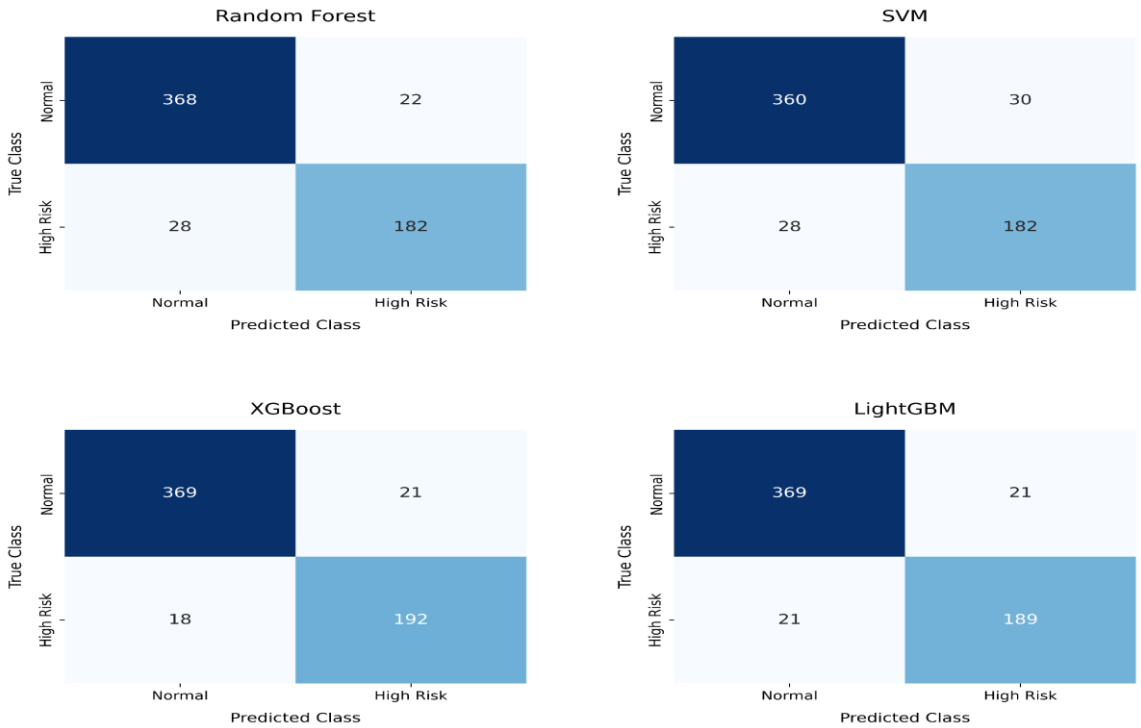

Figure 2. Confusion matrices of the four machine learning models.

The pollution risk labels were generated using a composite index based on selected wastewater parameters. Since COD and BOD5 were included in this index, their contribution to the classification results was expected. Therefore, the model performances represent the classification of the risk levels defined in the dataset and do not directly indicate their ability to detect actual pollution events.

Figure 2 shows the confusion matrices obtained from the combined out-of-fold predictions. XGBoost correctly classified 369 Normal and 192 High Risk observations, while 18 High Risk observations were incorrectly assigned to the Normal class. LightGBM correctly classified 189 High Risk observations, compared with 182 for both Random Forest and SVM. XGBoost had the lowest number of missed High Risk observations among the four models.

The SHAP results for XGBoost are given in Figure 3. Among the 14 input variables, COD had the largest mean absolute SHAP value (4.3872). BOD5 followed with a value of 1.4431. Suspended solids, ammonia nitrogen, and conductivity had much lower values of 0.3019, 0.2725, and 0.2238, respectively. The difference was particularly large between BOD5 and the remaining variables. COD and BOD5 were also among the five variables used to calculate the pollution risk index. Their high importance in the XGBoost model should therefore be considered together with the way the risk classes were defined.

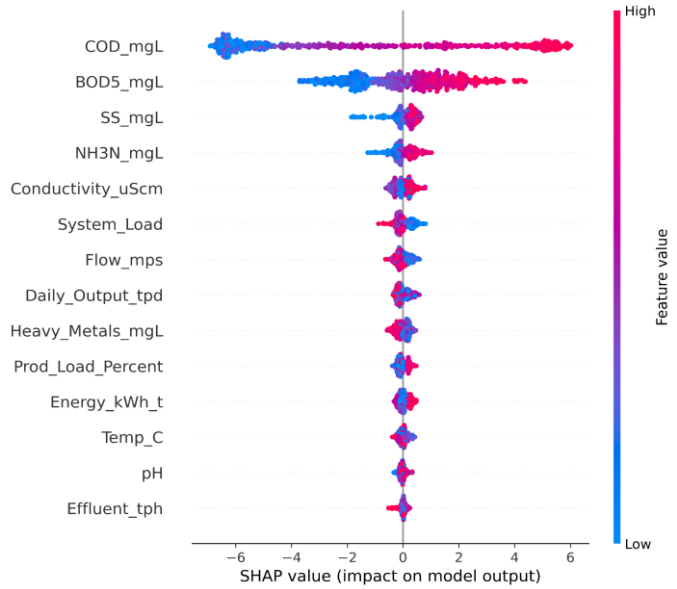

Figure 3. SHAP summary plot showing the contribution of input variables to XGBoost predictions.

Conclusion

This study investigated the classification of pollution risk conditions in industrial wastewater treatment using four machine learning algorithms: Random Forest, SVM, XGBoost and LightGBM. The Melbourne Eastern Industrial Wastewater Plant dataset was used, containing 600 observations and 14 input variables. Model performance was evaluated using stratified five-fold cross-validation based on accuracy, precision, recall, F1-score and ROC-AUC.

The results of the experiments showed that all four models achieved high classification performance. XGBoost performed the best overall, achieving an accuracy of 93.5%, precision of 90.32%, recall of 91.43%, an F1 score of 90.72% and a ROC-AUC of 0.9803. LightGBM achieved comparable results with an accuracy of 93%, followed by random forest and SVM with 91.67% and 90.33%, respectively. XGBoost correctly classified 192 out of 210 high-risk observations. SHAP analysis showed that COD and BOD5 had the greatest influence on XGBoost predictions. Both variables were also used to calculate the composite index from which the pollution risk labels were generated. Therefore, their importance in the model predictions should be interpreted in relation to the labeling method.

The four models were able to classify the predefined pollution risk categories with high accuracy. However, the dataset did not contain independently observed pollution events, so the reported results are limited to the risk categories defined by the composite index. Further studies could use larger wastewater datasets and independent

test data to examine how well these models perform on new observations. Different feature selection methods could also be evaluated to determine their effects on classification performance.

Recommendations

Future studies should investigate larger and independent wastewater datasets to evaluate the generalization performance of machine learning models. Different feature selection and hyperparameter optimization methods could be applied to improve classification performance. In addition, the integration of machine learning models into wastewater monitoring systems could be investigated to support early pollution risk detection.

Scientific Ethics Declaration

* The author declares that the scientific ethical and legal responsibility of this article published in EPSTEM Journal belongs to the author.

Conflict of Interest

* The author declares that there is no conflict of interest.

Funding

* This study was supported by COST Action CA23104 – Mainstreaming Water Reuse into the Circular Economy Paradigm (Water4Reuse).

Acknowledgements or Notes

* This article was presented as an oral presentation at the International Conference on Basic Sciences, Engineering and Technology (www.icbaset.net) held in Istanbul/Türkiye on September 17-18, 2026.

References

Boser, B. E., Guyon, I. M., & Vapnik, V. N. (1992). A training algorithm for optimal margin classifiers. In *Proceedings of the Fifth Annual Workshop on Computational Learning Theory* (pp. 144–152). Association for Computing Machinery.

Breida, M., Younssi, S. A., Ouammou, M., Bouhria, M., & Hafsi, M. (2019). Pollution of water sources from agricultural and industrial effluents: Special attention to NO3−, Cr(VI), and Cu(II). In *Water chemistry*. IntechOpen.

Breiman, L. (2001). Random forests. *Machine Learning, 45*(1), 5–32.

Chen, T., & Guestrin, C. (2016). XGBoost: A scalable tree boosting system. In *Proceedings of the 22nd ACM SIGKDD International Conference on Knowledge Discovery and Data Mining* (pp. 785–794). Association for Computing Machinery.

Elsayed, A., Siam, A., & El-Dakhakhni, W. (2022). Machine learning classification algorithms for inadequate wastewater treatment risk mitigation. *Process Safety and Environmental Protection, 159*, 1224–1235.

Hammond, P., Suttie, M., Lewis, V. T., Smith, A. P., & Singer, A. C. (2021). Detection of untreated sewage discharges to watercourses using machine leaning. *npj Clean Water, 4*(1), 18.

Kato, S., & Kansha, Y. (2024). Comprehensive review of industrial wastewater treatment techniques. *Environmental Science and Pollution Research, 31*(39), 51064–51097.

Ke, G., Meng, Q., Finley, T., Wang, T., Chen, W., Ma, W., Ye, Q., & Liu, T.-Y. (2017). LightGBM: A highly efficient gradient boosting decision tree. In *Advances in Neural Information Processing Systems* (Vol. 30, pp. 3146–3154).

Lundberg, S. M., & Lee, S.-I. (2017). A unified approach to interpreting model predictions. In *Advances in Neural Information Processing Systems* (Vol. 30, pp. 4765–4774).

Melbourne Eastern Industrial Wastewater Plant. (n.d.). *Melbourne Eastern Industrial Wastewater Plant* [Data set]. Kaggle. Retrieved August 15, 2026.

Nguyen, D. V., Park, J., Lee, H., Han, T., & Wu, D. (2024). Assessing industrial wastewater effluent toxicity using boosting algorithms in machine learning: A case study on ecotoxicity prediction and control strategy development. *Environmental Pollution, 341*, 123017.

Shu, Y., Kong, F., He, Y., Chen, L., Liu, H., Zan, F., Lu, X., Wu, T., Si, D., Mao, J., & Wu, X. (2025). Machine learning-assisted source tracing in domestic-industrial wastewater: A fluorescence information-based approach. *Water Research, 268*, 122618.

Singh, G., & Mishra, S. (2023). Industrial pollution management approach. In *Heavy metal toxicity: Environmental concerns, remediation and opportunities* (pp. 363–388). Springer Nature Singapore.

Trubetskaya, A., Horan, W., Conheady, P., Stockil, K., Merritt, S., & Moore, S. (2021). A methodology for assessing and monitoring risk in the industrial wastewater sector. *Water Resources and Industry, 25*, 100146.

Trubetskaya, A., Hennessy, A., Ryan, I., Stockil, K., & Gaskin, C. (2025). Industrial assessment tools of risks associated with wastewater and water technologies. *ACS ES&T Water, 5*(10), 6131–6151.

Zamfir, F. S., Carbureanu, M., & Mihalache, S. F. (2025). Application of machine learning models in optimizing wastewater treatment processes: A review. *Applied Sciences, 15*(15), 8360.

Zhang, X., & Ren, H. (Eds.). (2019). *High-risk pollutants in wastewater*. Elsevier.

Author(s) Information

Mustafa Ozan Ozkok
Sakarya University
Sakarya, Turkiye
ORCID iD: https://orcid.org/0000-0001-8109-3197
*Contact e-mail: mustafaozanozkok@gmail.com

*Corresponding author(s) contact email

To cite this article:

Ozkok, M.O. (2026). Machine learning-based pollution risk classification in industrial wastewater treatment. *The Eurasia Proceedings of Science, Technology, Engineering and Mathematics (EPSTEM), 42,* 184–190.

The Eurasia Proceedings of Science, Technology, Engineering and Mathematics (EPSTEM)
ISSN: 2602-3199

The Eurasia Proceedings of Science, Technology, Engineering and Mathematics (EPSTEM), 2026

Volume 42, Pages 191-210

ICBASET 2026: International Conference on Basic Sciences, Engineering and Technology

Integrating Mean Weight Diameter and Environmental Sensitivity Index for Modeling Soil Erosion Risk and Land Degradation in Soils under Different Agricultural Land Uses

Tayseer Thaker Mohammed
University of Mosul

Khaled Anwar Khaled
University of Mosul

Abstract: The study area is located between latitudes (36°42′24.52″ N – 36°24′38.40″ N) and longitudes (43°38′14.98″ E – 43°22′14.58″ E), covering an area 1245 km². The elevation ranges from 283 to 1015 m above sea level. The climate classified as a transitional zone between semi-arid and Mediterranean climates. Twenty-five sites were selected within the study area. Approximately 2 kg of soil was collected per site, with samples carefully selected to ensure homogeneity. The samples were then transported to the laboratory, air-dried, gently crushed using a wooden hammer, and sieved through a 2 mm mesh sieve. Subsequently, they were stored in plastic containers for further physical and chemical analyses. Laboratory analyses included the determination of soil organic matter, calcium carbonate ($CaCO_3$) content, and particle size distribution, and Environmental Sensitivity Index equations were applied.The results indicated that the dominant soil textures in the study area ranged from clay to clay loam.. This variability is primarily attributed to differences in soil organic matter content and calcium carbonate levels, which reached maximum values of 2.28% and 37.2%, respectively. Furthermore, the results revealed relatively uniform sorting values across most sites, indicating a generally homogeneous particle size distribution, except for site, which exhibited a high sorting value of 2.420, reflecting poorer sediment uniformity. The study demonstrates that both water and wind erosion processes in the region are controlled by a complex interaction of natural and anthropogenic factors acting simultaneously, which significantly influence soil stability and susceptibility to detachment and transport.

Keywords: Erosion, USLE, SEI, Sorting, Land use.

Introduction

Water erosion has been the subject of numerous studies that have looked at it from a variety of angles, including how to measure it, what causes it, and how it affects the ecosystem. Kefi and Yoshino (2010) pointed out the significance of studying water erosion both inside and outside of watersheds, stressing that, especially when using contemporary spatial analysis techniques, looking into the environmental factors influencing this process helps manage watersheds and lessen soil degradation. According to Ganasri and Ramesh (2016); Adeyeri et al. (2024); Kafroshy and Alkhaled (2025), soil loss rates are directly correlated with the energy of raindrops falling and the intensity of precipitation for short periods of time, making rainfall intensity the most important climatic factor in promoting water erosion.

In a study conducted in Iraq's Abu Ghraibat Basin, Maaroof et al. (2025) demonstrated that soil erosion is highly related to land use and prevailing climate conditions Alhashyme & Khaled (2025). The study showed that sites with limited plant cover and those heavily exploited for agriculture have the highest rates of erosion. Dutucu et al. (2025) also stated that changes in land use play a critical role in influencing the future direction of soil

- This is an Open Access article distributed under the terms of the Creative Commons Attribution-Noncommercial 4.0 Unported License, permitting all non-commercial use, distribution, and reproduction in any medium, provided the original work is properly cited.

- Selection and peer-review under responsibility of the Organizing Committee of the Conference

© 2026 Published by ISRES Publishing: www.isres.org

erosion. Quinton and Fiener (2024), in a study analyzing the causes of erosion in agricultural lands on a global scale, demonstrated that human activities, especially agriculture and the conversion of forests to farmland, are the main reason for the acceleration of soil erosion compared to natural rates. Yanqing et al. (2025) also stated that human activities represent the most influential factor in increasing soil erosion compared to natural factors.

The Modified Global Soil Loss Equation (RUSLE) is one of the most well-known and often utilised formulas in the world. Its usefulness in semi-arid situations was proved by Akbari et al. (2022), who showed its potential for identifying geographical heterogeneity in loss rates. Wischmeier and Smith (1978) developed an equation to estimate the average annual soil loss caused by water erosion, which later became known as the Universal Soil Loss Equation (USLE).

$$A = R \times K \times LS \times C \times P \quad (1)$$

Where: A: Annual soil loss rate (tons/hectare/year)., R: Rainfall-runoff Erosivity, reflecting the ability of rainfall to break down and transport soil., K: Soil Erodibility, expressing the soil's susceptibility to breakdown and transport., LS: Topography, representing the effect of slope length and steepness on accelerating surface runoff., C: Vegetation cover and soil management, reflecting the role of vegetation cover in protecting the soil from rainfall., P: Supporting practices, encompassing the impact of agricultural methods and measures that reduce surface runoff.

According to Akpa et al. (2024), the RUSLE model's effectiveness in estimating soil loss under various climatic circumstances was examined in a reevaluation of the model's dependability in semi-arid regions. Ho et al. (2026) showed that the RUSLE model is a useful tool for estimating sedimentation volume and erosion risk when combined with remote sensing and geographic information systems (GIS). Lukić et al. (2022) noted the application of the MEDALUS model in Southeast Europe, which revealed a clear variation in land sensitivity to environmental degradation (Azimi et al 2025). Similarly, Gül and Esen (2024) demonstrated that the Environmental Sensitivity Index (ESAI) used in semi-arid forest systems revealed high levels of desertification susceptibility. Alhamdany and Alnaser (2024) also showed that the application of the MEDALUS model indicated that most of the studied sites fell within the critical categories for desertification, with some areas falling within the fragile categories. Abbood et al. (2025) reported that the application of the MEDALUS model and its modified version in southern Iraq demonstrated high efficiency in assessing desertification risks using several environmental scenarios. This study relied on integrating 19 environmental criteria within a spatial analysis using GIS.

Wu et al. (2019) showed that changes in soil erosion sensitivity are directly reflected in long-term variations in (Normalized Difference Vegetation Index) NDVI maps. These results demonstrate that, especially in arid and semi-arid areas, plant loss is both an environmental indicator and a direct predictor of the beginning or escalation of erosion processes. In a study carried out in Iran's semi-arid Saravan region, Ebrahimi et al. (2024) discovered that spectral indices exhibited a correlation with field measurements ranging from 0.52 to 0.88, showing their great potential to explain erosion and deterioration. Meanwhile, Mahgoub et al. (2024) found that spectral indices are substantially connected with the C factor, and that increasing vegetation cover (higher NDVI) reduces erosion rates significantly. The study also found that these indices can be utilised as a quantitative alternative to assessing vegetation cover in erosion models.

As a result, monitoring soil erosion in northern Iraq using RS and GIS techniques is an important scientific step toward identifying geographical variations in soil loss rates and developing practical strategies to reduce their consequences. This helps to achieve sustainable agricultural development and conserve natural resources for future generations. The study aims to:

Implement long-term methods to decrease soil erosion and track how land usage affects its rate of progression and Identify the spatial factors affecting soil erosion intensity and estimate the areas of soil exposed to erosion in the study region by applying the modified global soil loss equation and using remote sensing and GIS techniques.

Materials and Methods

Description of the Study Area

The study area, which spans many administrative units and villages with a variety of geomorphological features and land uses, is located in the northeastern part of the Nineveh Governorate. The study sites were chosen to reflect the region's prevailing environmental conditions and geographic differences in soil attributes. The region is located between latitudes (36˚42¯24.52ᵎ N - 36˚24¯38.40ᵎ N) and longitudes (43˚38¯14.98ᵎ E - 43˚22¯14.58ᵎ E). With an area of 1274.737 km² and elevations ranging from 283 to 1015 m above sea level, the topography is remarkably diverse as showed in (Figure 1).

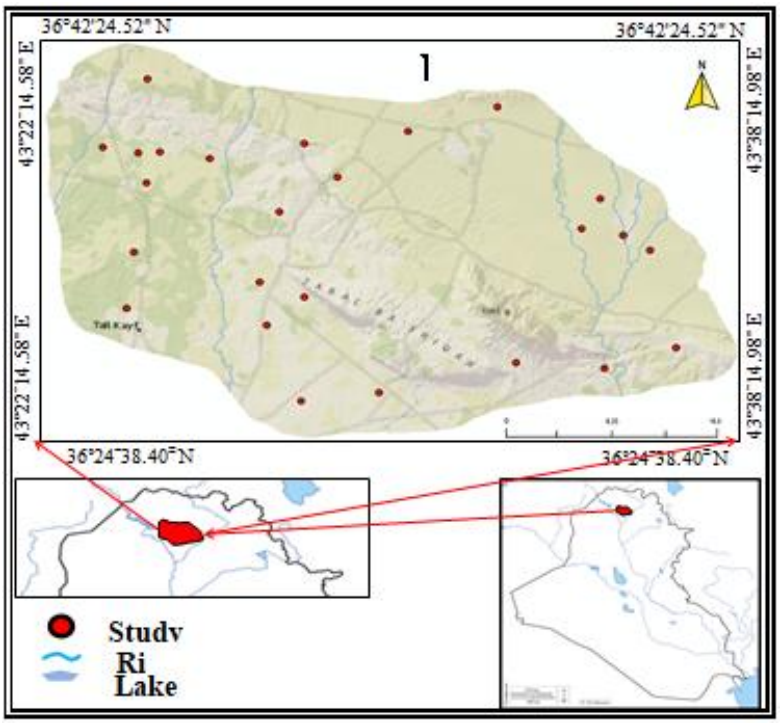

Figure 1. The study area

Climatic Characteristics of the Study Area

The climate of northern Mosul is classified as a transitional climate between semi-arid and Mediterranean, and it lies within the continental climate zone of northern Iraq. It is characterized by significant temperature variations and distinct seasons between summer and winter. Summers are hot and dry, with temperatures soaring during June, July, and August, sometimes exceeding 40°C. Winters are relatively cold, with seasonal rainfall concentrated between November and April. Average annual rainfall ranges from 300 to 450 mm, depending on topography and elevation.

Table 1. The climatic data rates for the weather station in Nineveh.

Date	Temperature rate AT Avg C°	Relative humidity RH Avg %	Total solar radiation SLR Total Mj/m2	Wind speed rate WS Avg m/s	Max. wind speed WS Max m/s	Wind direction WD m/s	Evaporation rate ET mm
2015	22.30	42.26	16.37	2.83	6.62	196.83	2.83
2016	22.35	41.62	17.55	2.84	6.59	201.62	2.84
2017	22.43	42.14	15.76	3.02	6.80	193.65	3.02
2018	22.68	45.56	16.94	3.40	7.26	201.85	3.40
2019	22.34	47.04	16.92	2.95	8.23	189.76	2.95
2020	22.39	43.96	17.81	5.27	7.48	192.02	5.27
2021	23.39	43.10	16.63	2.51	7.14	209.59	5.74
2022	22.80	44.89	14.99	2.55	6.54	206.69	5.76
2023	16.79	57.65	13.87	2.17	7.48	178.58	3.87
2024	20.69	48.85	15.85	2.51	3.29	246.72	3.78
2025	22.23	48.46	16.67	2.08	5.92	183.85	4.83

Table (1) shows the climatic data averages for the Nineveh and surrounding areas meteorological station for the years (2015-2025), showing the maximum and minimum temperatures. The highest temperature reached approximately (31.49) in 2021, and the lowest was (12.47) in 2023. The total solar radiation reached its peak at (17.81) in 2020, and the average wind speed ranged between (17.81-5.27) m/s. The amount of evapotranspiration ranged between (2.83 - 5.76) mm. This pattern is prevalent in northern Iraq, with a clear influence of topographical elements on the higher rainfall levels in Duhok compared to Mosul.

Field Work

According to Renard et al. (1997), each of the chosen sites was represented by 16 composite soil samples at a depth of (0–15) cm using the grid method, representing an area with dimensions of 100 x 100 m. As indicated in Table (2), the samples were taken from 25 locations in the northern Nineveh Governorate with varying soil grades and land uses. A GPS (Global Positioning System) was used to pinpoint their whereabouts.

Table 2. Study area and their coordinates, and nature of land use..

No	Location	Coordinates		Soil Depth سم	Gravel ratio in 1 m	Tobography	Land use
		N	E				
1	En bakri	36.683438°	43.122926°	24	4	Undulated	Wheat
2	Shekan	36.646563°	43.346618°	30	1	Undulated	Wheat
3	Baryma	36.529393°	43.221895°	25	0	Level land	Potato
4	Bashiqa	36.446593°	43.325450°	25	1	Level land	Olive
5	Kelkji	36.574458°	43.495979°	80	2	L. Sloping	Wheat
6	Batnaya	36.55100°	43.114618°	35	7	Undulated	Wheat
7	Khorsibat	36.497122°	43.229075°	25	1	Level land	Wheat
8	Telyara	36.439353°	43.259807°	35	1	L. Sloping	Wheat
9	Fadlya	36.519004°	43.260068°	30	0	Level land	Olive
10	Khoshaba	36.623483°	43.177410°	25	9	Level land	Wheat
11	Telkef	36.507921°	43.109344°	30	0	Level land	Wheat
12	Jarghan	36.635931°	43.257653°	25	1	Undulated	Wheat
13	Sharqia	36.630771°	43.085575°	40	1	Undulated	Wheat
14	Dermati	36.471340°	43.441744°	20	11	Foot hell	Wheat
15	Mamrshan	36.666621°	43.422397°	25	1	Undulated	Wheat
16	Malon	36.583636°	43.237575°	30	5	Undulated	Barley
17	Telsqef	36.604098°	43.123645°	35	0	Level land	Wheat
18	Zenawa	36.597454°	43.511759°	80	2	Level land	Corn
19	Karmlk	36.569789°	43.531336°	70	0	Level land	Wheat
20	Doghat	36.628127°	43.134835°	30	2	Level land	Wheat
21	Mandan	36.468158°	43.517746°	50	1	Flood Plain	Wheat
22	Nveria	36.626703°	43.115903°	80	3	Undulated	Wheat
23	Bardarsh	36.484073°	43.578345°	30	3	Level land	Wheat
24	Narqizlia	36.611118°	43.286892°	30	1	Undulated	Wheat
25	Ismawa	36.558255°	43.554962°	50	4	Level land	Wheat

Laboratory Analyses: Physical Properties

1- Particle Size distribution of soil : Soil texture was estimated using the hydrometer method with chalcone as a dispersing agent for soil particles. The hydrometer reading was taken with the temperature of the suspension in order to adjust the hydrometer reading and determine the soil texture based on the texture triangle and according to the method described by Gee and Bauder, (1986).

2- Bulk Density: Estimated using the paraffin wax encapsulation method. Particle Density: Estimated for soil samples using a pycnometer. according to Black (1965).

3 - Soil porosity was calculated using the following mathematical relationship, as reported in (klute, 1986):

$$\% \text{ Porosity} = 1 - (\text{ Bulk Density} / \text{Partial Density}) * 100 \quad (2)$$

Chemical Properties

1- The pH: Soil reaction of the saturated in soil extract using a pH meter as described in Richards, (1954). EC is measured in the soil extract according to Page et al., (1982).
2- Calcium carbonate CaCO3: Estimated by gravimetric method using 1 N hydrochloric acid as described in Hesse, (1971).
3- Organic Matter: It is estimated by oxidizing organic carbon with potassium dichromate solution $K_2Cr_2O_7$, and then tidylating with ammoniacal ferrous sulfate solution, as stated in the method mentioned by Page et al. (1982).

Soil Erodibility Index

This is accomplished using the equation below, and the CORINE (Coordination of Information on the Environment) model is employed based on the ranges of the variables (texture type, depth, gravel coverage) Table (3) European Environment Agency. (1997). with the assistance of Arc Map software

$$SEI = Soil\ Texture\ Map * Soil\ Depth\ Map * Gravel\ Surface\ cover\ Map \quad (3)$$

Table 3. The classification of soil texture, depth, surface gravel cover, and soil erosion factor according to the CORINE model

Soil Erodibility Class	Class	Surface Gravel Cover (%)	Class	Soil Depth (cm)	Class	Soil Texture	Class
Non-erodible	0	–	0	–	0	Rock Outcrops	0
Low	1	>10	1	>75	1	Low erodibility (Clay, Sandy Clay, Silty Clay)	1
Moderate	2	<10	2	25–75	2	Moderate erodibility (Sandy Clay Loam, Clay Loam, Silty Clay Loam, Sandy Loam, Loamy Sand)	2
High	3	–	–	<25	3	High erodibility (Loam, Silt Loam, Silt, Sandy Loam, Sand)	3

Structural Stability Index

The physical degradation (SSI) of the studied soils are estimated based on Tesfahunegn and Gebru (2020).

$$SSI = OM * 100 / Clay\ \% + Silt\ \% \quad (4)$$

Using the Modified Global Soil Loss Equation (RUSLE) to Predict Soil Loss Amounts

To estimate A (Annual Soil Loss) we should find the Characters listed below:

First: R *: Erosivity Factor,* The Fournier Index is used according to the formula below

$$FI = \sum_{i=1}^{12} \left(\frac{pi^2}{p}\right) \quad (5)$$

Where is: Pi is Monthly rainfall (mm), P is Total annual rainfall (mm), It is based on private data from the Ministry of Agriculture/Agricultural Meteorology Centre, the website of the UK's Natural Environment Research Council (NERC) and the US Department of Energy, and is then processed in the Arc Map software.

Second: K *: Erodibility Factor*, It is estimated according to Foster et al. (1981), as this factor combines the relationship between soil texture and organic matter content, which are critical elements in influencing soil susceptibility to erosion, in addition to soil structure and permeability.

$$K= [2.1 * 10\text{-}4 * (12 - OM)\ M1.14 + 3.25\ (SC - 2) + 2.5\ (PC - 3)]/100 \quad (5)$$

$$M = [(100 - \% \text{ Clay}) \times (\% \text{ VFS} + \text{Silt})] \quad (6)$$

Where: OM is % organic matter content., SC ; Soil structure classification as in Table (4), PC = Soil permeability class as in Table (5)

Table 4. Soil Structure ranges in calculating the K factor according to Foster et al. (1981)

Structure Code	Soil Structure Class	Description
1	Very Fine Granular	Very small soil aggregates (<1 mm), commonly found in organic matter-rich surface soils.
2	Fine Granular	Granular aggregates (1–2 mm) with good permeability and relatively high resistance to erosion.
3	Medium or Coarse Granular	Granular aggregates (>2 mm), common in many agricultural soils.
4	Blocky, Platy, Prismatic or Massive	Includes blocky, angular blocky, platy, prismatic, columnar, or structureless soils, generally more susceptible to erosion.

Table 5. Soil permeability ranges in calculating the K factor according to Wischmeier & Smith (1978)

Permeability Class	Permeability Description	Approximate Permeability Rate (cm h^{-1})
1	Very Rapid	>15
2	Rapid to Moderate	5–15
3	Moderate	1.5–5
4	Slow to Moderate	0.5–1.5
5	Slow	0.13–0.5
6	Very Slow	<0.13

Third: (LS), *Topographic Factor,* It relies on the effect of slopes on erosion rates, and DEM digital elevation data can be used to obtain some of the equation's data with high accuracy within GIS software. Then, the Wischmeier and Smith (1978) equation is used to calculate the values for each location as follows:

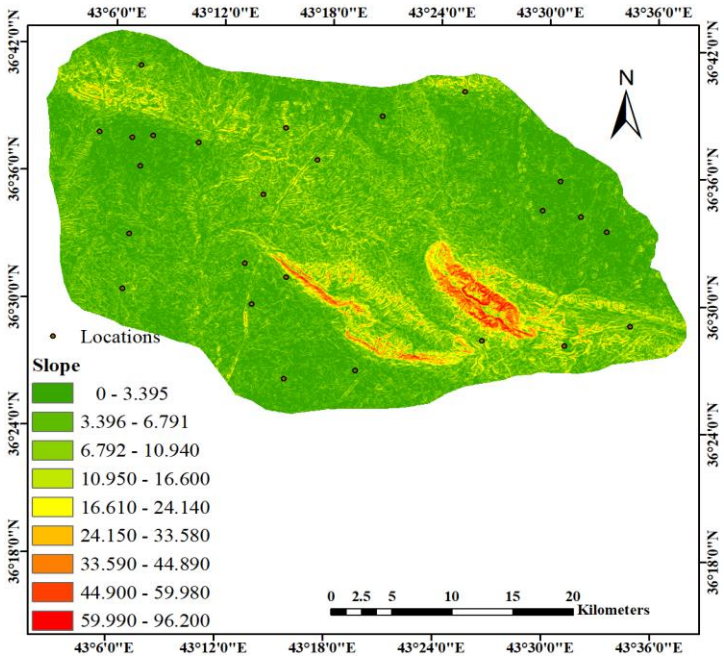

Figure 2. Spatial distribution of slope degree used in calculating the LS

$$LS = \text{Pow}\,[(\text{Flow Accumulation}) * \text{Cell Size}/22.1]m\ \text{Pow}[\text{Sin}(\text{Slop}) * 0.01745/0.089665]m \quad (7)$$

The flow direction is obtained first using the Spatial Analyst Hydrology Flow of Direction steps, which are applied to the DEM map. Then the direction of water exit (Outlet) towards the lowest height is determined. Then the slope is estimated from the Flow Accumulation, according to Figure (2) below, to be applied later in Equation (7) for the LS factor, as reported in Moore and Burch (1986). Where: L = length of slope (m), S = degree of Slop (%) m = 0.6, 1.3, a coefficient defined in terms of the degree of Slop.

Forth: C-Factor, Cropping Management, The C factor is used to determine the effects of both land cover and land management related to different types of vegetation on soil erosion. In this study, we used the Natural Vegetation Differences Index (NDVI) to calculate the C factor. The index is first calculated from the ArcMap program, and then the equation below is applied as reported in Kouli et al. (2009***).***

$$\text{NDVI}=[NIR\text{-}R/\ NIR+R] \tag{7}$$

Where *NIR*= near-infrared band , *R*= Red band. Then, the value of the factor (C) is calculated from the following relationship in terms of NDVI, as reported in Woldemariam et al. (2018):

$$C = 1\text{- NDVI} / 2 \tag{8}$$

Fifth: Soil practical Factor , The P factor refers to the extent to which land use management practices such as terraces, contour lines, and tillage affect erosion rates. These practices reduce soil erosion by affecting surface runoff velocity. The values of the soil conservation factor range between (0 and 1). When the value is close to (0), it indicates that the conservation measures are good, while it indicates very poor conservation measures when the values are close to (1) (Ganasri and Ramesh, 2016). Its value in this study was considered to be equal to (1) because no soil conservation measures were followed in the study area. Finally, the map of soil loss quantities (A) is prepared using the modified global equation model for soil loss RUSLE from the product of the maps of (Rainfall factor R, Soil erosion factor K, Topography factor LS, Vegetation cover factor C).

Results and Discussion

Physical Characteristics of Soil Samples

The particle size distribution, shown in Table (6), demonstrated a clear variance among the study areas, as evidenced by the differences in prevailing soil textures. The clay content varied from 22.6% to 65.8%, with the Kelkji site having the greatest at 65.8% and the Mandan sample had the lowest at 22.6%. The silt content ranged between 11.2% and 52.8%, with the Karmlk site having the highest percentage and Kelkji having the lowest. In contrast, the sand content varied from 20.0% to 50.8%, with the Telsqef site having the highest proportion and the Telkef site having the lowest. According to the texture triangle, clayey and clay loam textures were found to be the most common at the study sites, with loam, silty, and sandy clay loam textures appearing in numerous additional areas. This variation is the result of changes in the nature of the parent material and the depositional circumstances. Soil bulk density varied significantly, ranging from 0.78 to 2.02 Mg m^{-3}. This variation is due to changes in soil texture, structure, and organic matter content. Moisture content varied from 4.07% to 23.65%, indicating differences in soil water retention ability based on fine particle percentage, porosity, and surrounding environmental variables. Porosity values varied significantly between the study locations, ranging from 23.5% to 70.3%. The Doghat site had the highest porosity value (70.3%), followed by the Bardarsh site (65.5%), and the Dermati site had the lowest value (23.5%), followed by the Mlon site (25.9%). This variation reflects changes in the physical qualities of the soils under study, particularly bulk density and texture.

Chemical Characteristics of Soil Samples

The soil pH measurement results indicated low variance between study locations, with values ranging between (7.5-8.0), indicating that the region's soils generally tend towards a neutral reaction, tending towards alkalinity. The electrical conductivity (EC) data show that the study sites had salinity values ranging from 0.42 to 1.10 dSm^{-1}, indicating that the soils in the region are non-saline to mildly saline. This variance is due to the influence of current environmental circumstances, the composition of the parent material, and the amount of soluble salt accumulating in the soil.

Organic matter contents were consistent throughout research sites, ranging from 13.11 to 22.78 g kg^{-1}. Most semi-arid soils show a decline in organic matter content, indicating deterioration. A lack of organic matter causes poor soil structure and lower stability of soil aggregates, as well as decreased cation exchange capacity and water and nutrient retention, making the soil more susceptible to water erosion. Furthermore, a decrease in organic matter reduces soil resistance to rainwater runoff and increases the likelihood of crust formation and surface runoff, which accelerates land degradation. These findings are consistent with those of FAO and ITPS (2020), which indicated that declining organic matter is a key indicator of soil degradation and deteriorating agricultural land quality.

Calcium carbonate values ranged from 136 to 372 g kg^{-1}, reflecting variations in the nature of the parent material, environmental conditions, and the degree of calcareous precipitation within the soil profile. The highest calcium carbonate value was recorded in the soils of the Jarghan, followed by the Mandan site at 364 g kg^{-1}. It has been observed that the high calcium carbonate content in some locations is related to the nature of the predominant calcareous parent material in the area, as well as the influence of arid and semi-arid climatic conditions that limit leaching processes and promote the precipitation and accumulation of calcareous compounds in the soil. Furthermore, low rainfall and high evaporation rates cause calcium to remain precipitated in the soil profile rather than being transferred to lower depths.

Conversely, the low calcium carbonate content in some locations may be due to variations in the nature of the deposits or to the soil being subjected to relative leaching processes that have reduced the accumulation of calcareous compounds compared to other locations. Variations in soil texture and drainage may also play a role in the different distribution of carbonates within the soil.High levels of calcium carbonate lead to increased soil alkalinity and reduced decomposition and accumulation of organic matter. Conversely, some sites with relatively low $CaCO_3$ levels have shown a significant increase in organic matter, indicating a relative improvement in environmental conditions conducive to its accumulation.

Table 6. Physical and chemical properties of the study area

No	Location	Particle Disterbution		Size	Texture	Bulk Density	Particle Density	Porosity	pH	EC	O.M	$CaCO_3$
		Sand	Silt	Clay		$Mg.m^{-3}$		%		dSm^{-1}		gkg^{-1}
1	En bakri	21.0	23.2	55.8	C	1.53	2.65	42.4	7.5	0.63	21.42	300
2	Shekan	27.0	25.2	47.8	C	1.23	2.65	53.5	7.7	0.62	22.08	316
3	Baryma	23.0	29.2	47.8	C	1.21	2.65	54.3	7.6	0.79	22.53	324
4	Bashiqa	27.0	39.2	33.8	CL	1.62	2.65	38.8	7.6	0.71	19.36	320
5	Kelkji	23.0	11.2	65.8	C	1.23	2.65	53.7	7.8	0.91	15.52	164
6	Batnaya	30.8	36.2	33.0	CL	1.36	2.65	48.6	7.6	0.54	19.73	352
7	Khorsibat	27.8	47.0	25.2	L	1.74	2.65	34.2	7.6	0.44	14.14	340
8	Telyara	31.8	43.0	25.2	L	1.64	2.65	38.3	8.0	0.86	22.60	328
9	Fadlya	28.8	35.8	35.4	CL	1.62	2.65	38.9	7.7	1.09	20.81	356
10	Khoshaba	30.0	32.8	37.2	CL	1.47	2.65	44.4	8.0	0.62	13.11	180
11	Telkef	20.0	48.6	31.4	SiCL	1.84	2.65	30.4	7.9	1.10	21.18	328
12	Jarghan	36.0	32.0	32.0	CL	1.94	2.65	26.7	8.0	0.9	21.08	372
13	Sharqia	38.8	29.2	32.0	CL	1.73	2.65	34.6	7.7	0.91	20.71	336
14	Dermati	32.8	33.2	34.0	CL	2.03	2.65	23.5	7.5	0.81	16.21	228
15	Mamrshan	22.2	43.0	34.8	CL	1.44	2.65	45.8	7.7	0.82	16.18	292
16	Malon	41.6	33.2	25.2	L	1.96	2.65	25.9	7.8	1.01	13.80	212
17	Telsqef	50.8	20.0	29.2	SCL	1.80	2.65	31.9	7.6	0.76	20.36	260
18	Zenawa	36.6	35.4	28.0	CL	1.94	2.65	26.7	7.6	0.80	18.56	140
19	Karmlk	22.0	52.8	25.2	SiL	1.24	2.65	53.3	7.6	0.65	19.95	192
20	Doghat	44.0	30.2	25.8	L	0.79	2.65	70.3	7.8	0.62	21.4	136
21	Mandan	33.0	44.4	22.6	L	1.42	2.65	46.3	7.7	0.42	15.52	364
22	Nveria	39.4	29.6	31.0	CL	1.64	2.65	38.2	7.8	0.60	18.50	240
23	Bardarsh	41.4	32.2	26.4	L	0.92	2.65	65.5	7.7	0.52	20.36	164
24	Narqizlia	45.4	28.2	26.4	L	1.37	2.65	48.2	7.6	0.73	22.78	204
25	Ismawa	38.8	36.0	25.2	L	1.11	2.65	58.1	7.6	0.81	21.40	224

Soil Erodibility Index (SEI)

In order to create a spatial distribution map of the soil erosion index, as illustrated in Figures (3, 4, 5, 6), the results of equation (3) and table (3), which shows the percentage of gravel distribution for each location and soil depth in the Materials and Methods table (2) of Work section, were transformed into a map using the (IDW) Inverse Distance Weighting algorithm to determine the spatial distribution of each factor within the equation. According to Table (7) and Figure (3), clay soil type (C), which is the least erodible, was localised in small, dispersed patches and covered an area of 107.205 km^2, or just 8.4% of the region's total area. Its high clay particle content, which improves soil structure stability and grain cohesion, is responsible for its low Erodibility. With an area of 868.455 km^2, or 68.1% of the total area, the second, intermediate soil type (CL, SiCL, SCL) was the most common and was categorized as having moderate Erodibility. This broad distribution suggests that the majority of the soil in the research area has a moderate resistance to erosion, where grain separation under the effect of erosion agents is balanced with water retention qualities.

Table 7. Percentage and area of Texture classes in the study area

Class	Texture Class	Area (km²)	Percentage (%)	Erodibility Classification
1	C	107.205	8.4	Low Erodibility
2	CL, SiCL, SCL	868.455	68.1	Moderate Erodibility
3	L, SiL	299.077	23.5	High Erodibility
Total		1274.737	100	

The third group (L, SiL) is very erodible and accounts for around 299,077 km², or 23.5% of the total area. This category was mostly concentrated in the east and southwest. Its high erosion susceptibility is related to the presence of silt and fine sand, as well as the low clay concentration, which causes the grains to separate and transport by rainwater or wind.

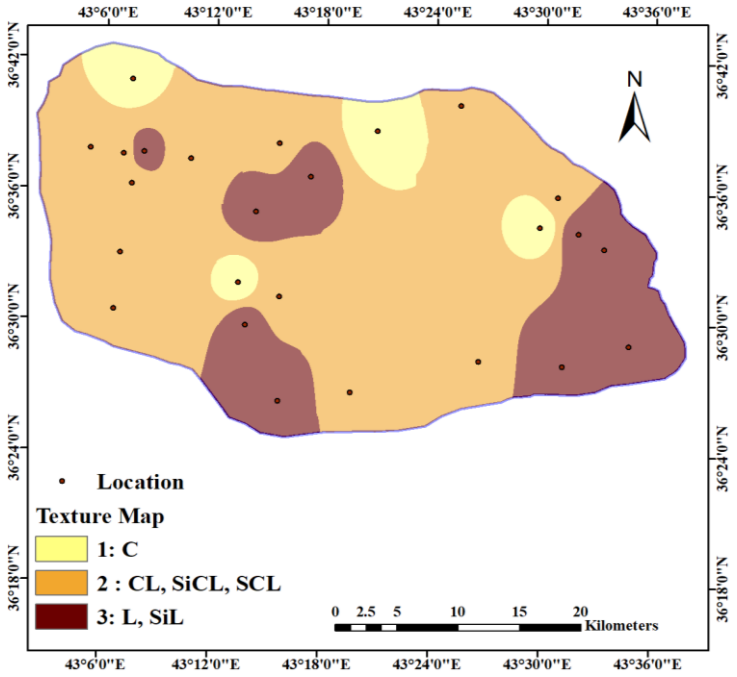

Figure 3. The spatial distribution of texture in the study area.

Soil Depth

Figure (4) shows that soils with a depth of (>75 cm), classified as having low erosion susceptibility, occupied an area of (93,444) km², equivalent to only (7.3%) of the total area (Table 8). These soils were found in limited and scattered areas, particularly in the northeastern parts and some northwestern locations. Their low erosion susceptibility is attributed to the large thickness of the soil profile, which provides a higher capacity for rainwater absorption and reduces surface runoff, in addition to increasing the soil volume available for root anchorage and improving stability. Medium-depth soils (25–75 cm) were the most widespread, covering an area of (675,808) km², representing (53.0%) of the region's area, and were classified as having medium erosion susceptibility. This widespread nature indicates that the majority of the region's land has a medium-thickness soil profile that provides moderate resistance to erosion processes. However, this resistance may decrease in areas with steep slopes or sparse vegetation cover.

Table 8. Percentage and area of Depth classes in the study area

Class	Texture Class	Area (km²)	Percentage (%)	Erodibility Classification
1	75 >	93.444	7.3	Low Erodibility
2	2575 –	675.808	53.0	Moderate Erodibility
3	25 <	505.485	39.7	High Erodibility
Total		1274.737	100	

Gravel Cover

Figure (5) and Table (9) show that areas with high stone cover (>10%) covered an area of 599,745 km² (47.0%), concentrated in the eastern and northwestern parts, providing better protection for the soil from erosion. In contrast, areas with low stone cover (<10%) covered an area of 674,992 km² (53.0%), spread across most of the central, southern, and western parts, increasing soil vulnerability to erosion due to reduced natural protection. Overall, the results indicate that more than half of the study area has limited stone cover, increasing its sensitivity to erosion according to the CORINE classification.

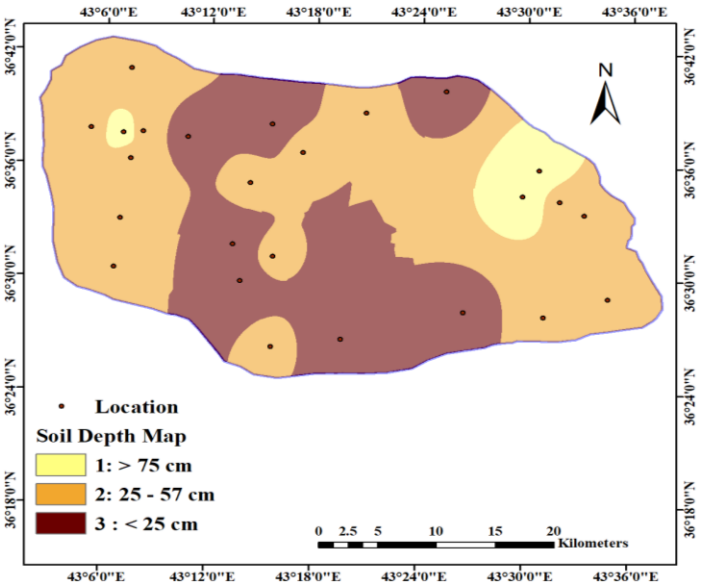

Figure 4. The spatial distribution of Depth in the study area.

Table 9. Percentage and area of Cover classes in the study area

Class	Texture Class	Area (km²)	Percentage (%)	Erodibility Classification
1	10 >	599.745	47.0	Complete Soil Protection
2	10 <	674.992	53.0	Low Soil Protection
Total		1274.737	100	

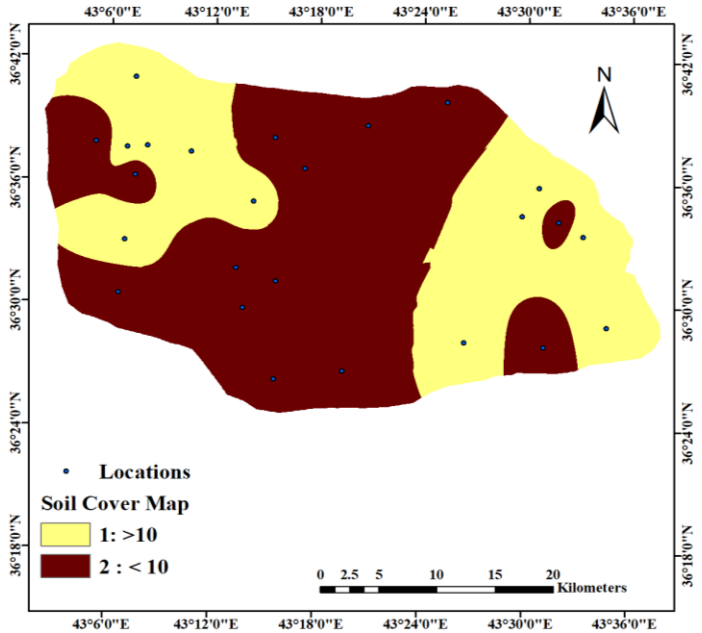

Figure 5 The spatial distribution of Gravel Cover in the study area.

The SEI values were ultimately obtained by multiplying the three maps together. As shown in Table 10 , the third, highly eroded soil class (>6) was dominant, covering an area of 1013.409 km², representing 79.5% of the total study area, as illustrated in Figure 6. This class was prevalent in most of the central, southern, and western

parts of the area. In contrast, the intermediate class (3–6) covered approximately 224.136 km² (17.6%), concentrated in the northeastern and northwestern parts. The sparse class (0–3) was limited to 37.192 km² (2.9%) and appeared in limited and scattered areas, specifically in the locations of Ain Bakri, Nafiriya, Zinawa, and Kelkji. These results indicate that the majority of the study area has a high susceptibility to erosion due to the influence of the soil's natural properties, making it more sensitive to soil loss according to the CORINE methodology.

Table 10. Percentage and area of SEI in the study area

Class	Texture Class	Area (km²)	Percentage (%)	Erodibility Classification
1	0 - 3	37.192	2.9	Low Erodibility
2	3 - 6	224.136	17.6	Moderate Erodibility
3	> 6	1013.409	79.5	High Erodibility
Total		1274.737	100	

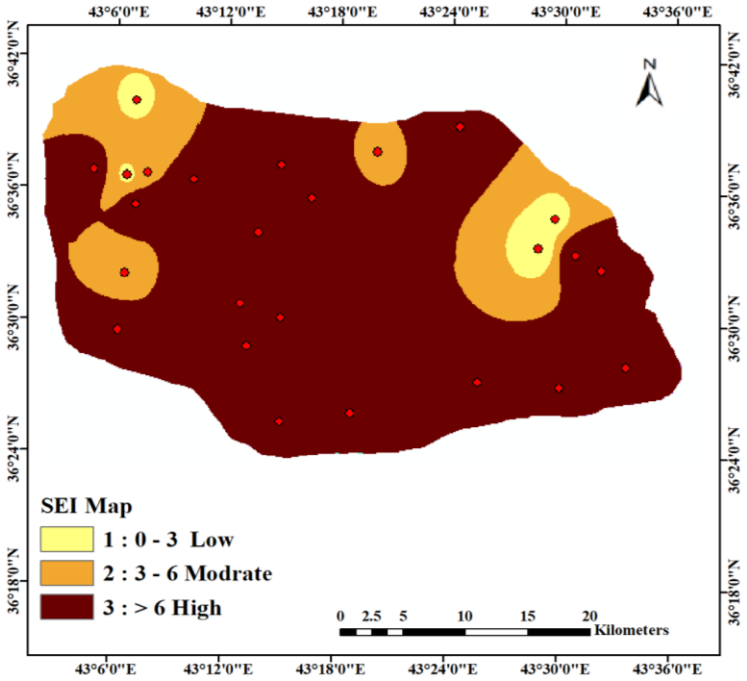

Figure 6. The spatial distribution of SEI in the study area.

Annual Soil Loss

Erosivity Factor

According to the Fournier index, the factor (R), representing the rate of soil loss due to the impact of raindrops, was calculated by determining the amount of rainfall in the study area based on the established monthly rainfall data, However, the calculation of equation (5) relied on the sum of the squares of the rainy months divided by the total annual rainfall. Figure (7) shows the spatial distribution and variation of rainfall rates during the rainy year in the study area, based on the rainfall data collected in (NCF) format and then transferred to ArcMap software for data processing within the ArcToolbox. The rainfall ranged from (181) mm/year in the southern and southeastern parts to (237) mm/year in the northwestern parts of the study area, with the highest rates recorded in the En bakri area.

The rainfall factor (R-factor) map in figure (8) clearly indicates an increase from south to north. Because of the greater intensity and influence of rainfall in those areas, the R-factor values steadily rise towards the northern portions of the research area. Low values in MJ.mm.ha^{-1}.h^{-1} (54.4–64.4)The southern and southeastern regions had the highest concentrations of •yr^{-1}, whilst the majority of the center region had medium values (64.41–74.4). The highest values were found in the northern and northwest strip. This gradient is due to increased rainfall with higher topographic elevations in the northern half of the research area, which results in higher kinetic energy of raindrops and enhanced surface runoff capacity for separating and moving soil particles. These findings also show that the northern regions are more vulnerable to water erosion than the southern regions, particularly when

a high R factor coincides with low vegetation cover or weak soil resistance to erosion, necessitating the implementation of soil and water conservation measures in these areas in order to reduce soil loss and maintain productivity.

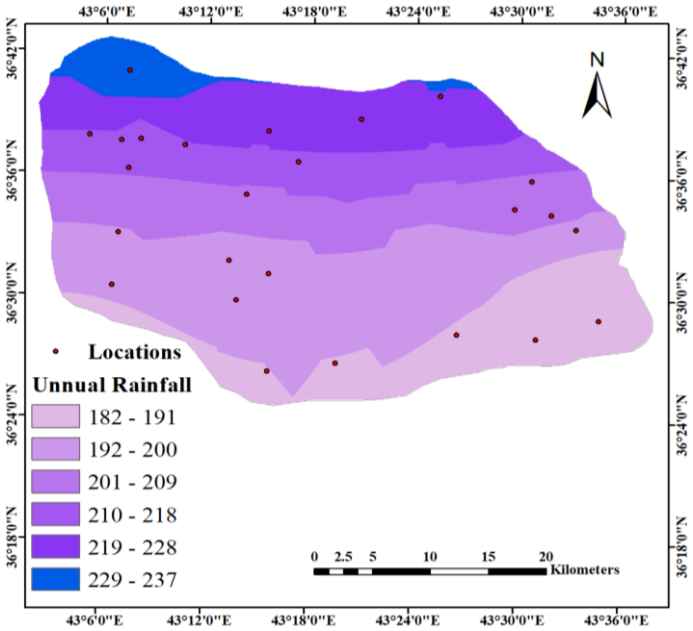

Figure 7. Annual rainfall rates distribution for the period (2015-2025)

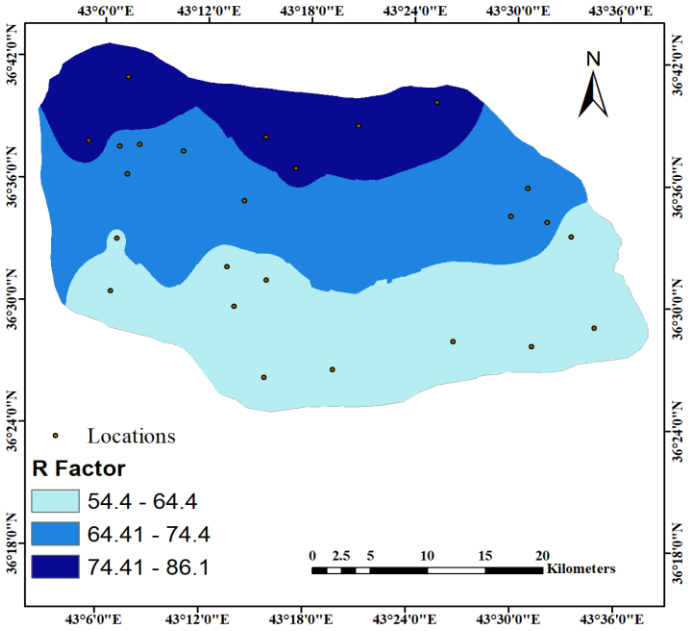

Figure 8. Spatial distribution of Erosivity Factor (R)

Table (11) shows the results of the rainfall erosion potential. The first class occupied the largest area, at (502.334) km² (39.41%), followed by the third class at (30.78%), and then the second class at (29.81%). These results indicate that the study area has a rainfall erosion potential ranging from moderate to high, due to variations in rainfall intensity and spatial distribution. These results are consistent with the CORINE concept, which considers climate, particularly rainfall energy, as a major determinant of environmental sensitivity to erosion. They also align with the R factor in the RUSLE model, which expresses the Erosivity potential of rainfall. Higher R values lead to increased energy of raindrops and surface runoff, thus increasing the likelihood of soil particle separation and transport, especially in areas with steep slopes or limited vegetation cover. Therefore, areas in the highest class require greater attention when developing soil management and conservation measures to reduce the risks of water erosion. These results are consistent with the findings of Samara and Khalid (2021).

Table 11. Erosivity factor classes in the study area

Class	Texture Class	Area (km²)	Percentage (%)
1	64.4 - 54.4	502.334	39.41
2	74.4 - 64.41	380.098	29.81
3	86.1 - 74.41	392.304	30.78
Total		1274.737	100

Erodibility Factor

The calculation of the K factor was based on the components (M, OM, SC, PC) according to Equation (5) , and their values are shown in Table (2) and (3). The results in Table (12) show that the study area is predominantly characterized by high soil erosion susceptibility. The high Erodibility soils occupied the largest area, covering (554.828) km², or (43.53%) of the total area. This was followed by the moderate Erodibility soils, covering (375.464) km² (29.45%), and then the low Erodibility soils, covering (344.445) km² (27.02%). Figure (9) illustrates that soils with high Erodibility are mainly found in the southern and southeastern parts and some central areas, while soils with lower Erodibility are concentrated in the northern and northeastern parts. These results are consistent with what Esfandiar et al. (2018) stated, as he explained that high K-factor values reflect increased soil susceptibility to separation and transport by rainwater due to weak structural stability and low soil resistance to erosion.

These results indicate how soil characteristics, including texture, organic matter content, structure, and permeability, affect the K factor. Soils with little organic matter content and weak structure are more susceptible to erosion, whereas more cohesive and structurally robust soils are less affected. These findings are in line with the RUSLE model idea, which was introduced by Renard et al. (1997) as a measure of the inherent sensitivity of soil to erosion and precipitation transport. Additionally, they are consistent with the CORINE approach, which highlights the importance of soil qualities in determining environmental sensitivity to water erosion.

Table 12. Erosivity factor classes in the study area

Class	Texture Class	Area (km²)	Percentage (%)	Erodibility Classification
1	0.25 - 0.04	344.445	27.02	Low Erodibility
2	0.30 - 0.21	375.464	29.45	Moderate Erodibility
3	0.41 - 0.31	554.828	43.53	High Erodibility
Total		1274.737	100	

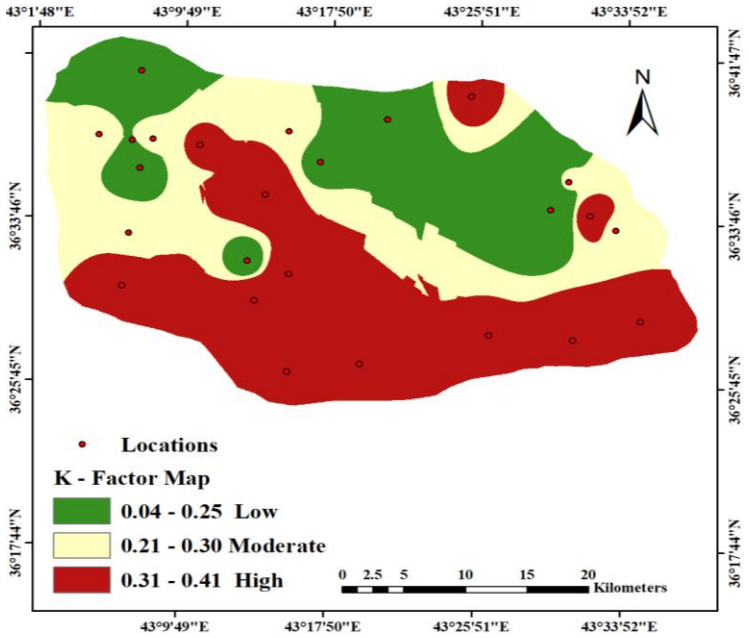

Figure 9. Spatial distribution of Erodibility Factor (K)

Topographic Factor LS- Factor

The results for LS- Factor, which cover an area of 1088,958 km², or 85.43% of the study's entire area, indicate the dominance of the second class with a moderate influence, as shown in Table 13 and Figure 10. The high-impact class, on the other hand, was restricted to a 56,864 km² (4.46%) area. This indicates that the majority of the region has limited slope lengths and fairly steep slopes, which means that topography has a moderate effect on water erosion. There are few places with steeper slopes where the high impact is focused. These results are in line with those of Moore and Burch (1986) and Panda et al. (2005), who showed that the LS factor rises with slope length and steepness, increasing surface runoff energy and soil erosion risk. On the other hand, topography that contributes less to erosion processes is reflected in low and medium values.

Table 12. Topographic factor classes in the study area

Class	Texture Class	Area (km²)	Percentage (%)	Erodibility Classification
1	1.44 - 0.19	128.810	10.11	Low Topographic Effect
2	2.70 - 1.45	1.088.958	85.43	Moderate Topographic Effect
3	3.95 - 2.71	56.864	4.46	High Topographic Effect
Total		1274.737	100	

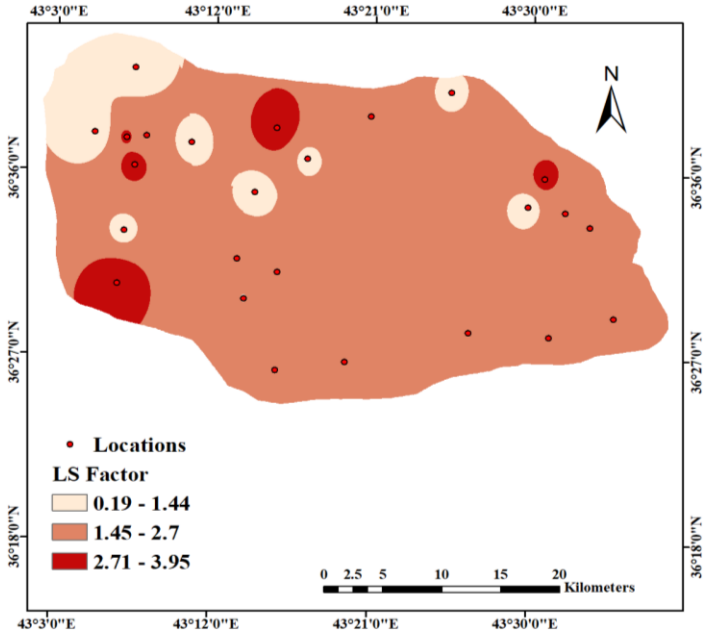

Figure 10. Spatial distribution of Topographic Factor (LS)

Cropping Management C factor

The spatial distribution of the C Factor values, which varied from (-0.30 to 0.65), is shown in Figure (11) and clearly shows the variation in vegetation density within the study area. While values between 0.31 and 0.50 dominated most of the region, indicating a degree of moderately dense vegetation, negative values were found in a small number of locations that represented watercourses or non-vegetated surfaces. Additionally, scattered areas which indicate areas with dense, highly active vegetation—recorded values higher than 0.50. These results are in line with those of Xue and Su (2017), who explained that low NDVI values indicate little to no vegetation cover, which increases the soil surface's susceptibility to runoff and erosion, while high values reflect increased biomass and photosynthetic activity of plants.

Based on the values of the Vegetation Differences Index, the vegetation cover factor was calculated according to Equation (17) in the Materials and Methods section. Figure (12) and the results in Table (13) for the C-factor show that the Very High Soil Protection and High Soil Protection varieties were the most widespread, covering an area of 349.052 km² (27.38%) and 352.735 km² (27.67%) respectively, totaling 55.05% of the study area. This indicates that the vegetation cover provides a high level of protection in more than half of the area. In contrast, the Very Low Soil Protection variety occupied only 111.002 km² (8.71%), representing areas with limited vegetation cover and therefore the most vulnerable to water erosion. These results are consistent with what Xiong et al. (2023) showed, as they explained that low C factor values reflect increased effectiveness of vegetation cover in protecting the soil, while high C factor values are associated with low efficiency of vegetation cover and a high risk of water erosion.

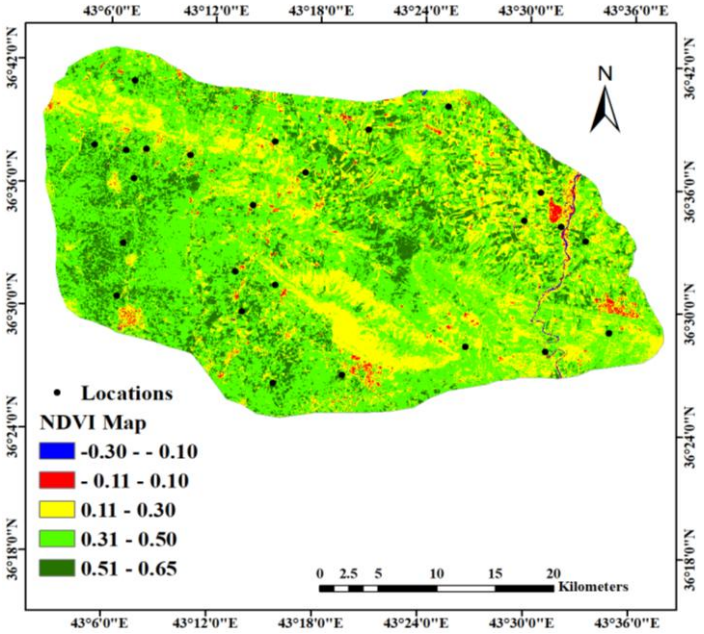

Figure 11. Spatial distribution of NDVI of the study area

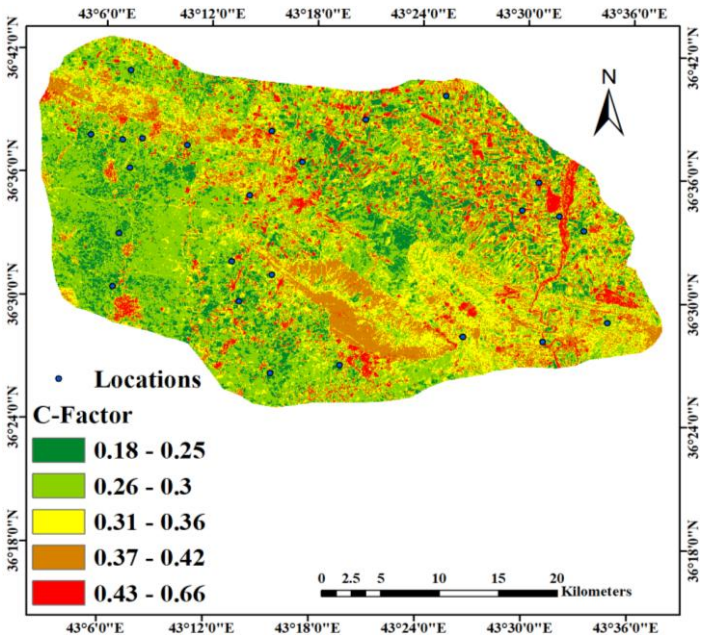

Figure 12. Spatial distribution of Cropping Management Factor (C)

Table 13. Cropping management factor classes in the study area

Class	Texture Class	Area (km²)	Percentage (%)	Erodibility Classification
1	0.25 - 0.18	349.052	27.38	Very High Soil Protection
2	0.30 - 0.26	352.735	27.67	High Soil Protection
3	0.36 - 0.31	252.609	19.82	Moderate Soil Protection
4	0.42 - 0.37	209.339	16.42	Low Soil Protection
5	0.66 - 0.43	111.002	8.71	Very Low Soil Protection
Total		1274.737	100	

Soil Management and Practice Factor (P-Factor)

The Soil Conservation Factor (P) represents the impact of agricultural and management practices used by most farmers to reduce water erosion, such as contour plowing on sloping areas, strip farming, and terracing, to decrease runoff velocity and increase water infiltration into the soil, thus reducing soil loss. Accurate data for

the study area indicating the widespread application of organized soil conservation practices were not available; therefore, a value of P = 1 was adopted, representing the baseline condition where no supportive erosion control measures are in place. This aligns with the RUSLE model methodology, which states that P equals 1 in the absence of soil conservation practices, while its value decreases as the effectiveness of these practices in reducing runoff and soil loss increases, as reported by Renard et al. (1997).

After completing the calculation of all the indicators, the annual soil loss rate (the global equation for soil loss) was calculated. We were able to estimate and calculate it through the ArcMap program by multiplying the four indicators as maps to obtain a map of its own. Its results were close to the computational data for each point after converting it to point values representing the locations of the (25) study area according to Table (14).

Table 13. Values used to calculate the annual soil loss rate for the study area

No.	Location	Rainfall (mm)	R Factor	SC	PC	Texture Factor (m)	K Factor	LS Factor	C Factor	A (t ha^{-1} yr^{-1})
1	En bakri	232	86.1	3	3	1865.24	0.14	0.57	0.26	1.79
2	Shekan	223	79.4	2	2	2568.24	0.13	1.82	0.45	8.45
3	Baryma	198	62.7	3	2	2829.24	0.18	2.42	0.23	6.28
4	Bashiqa	191	58.4	4	3	3985.24	0.33	1.66	0.37	11.84
5	Kelkji	204	66.7	2	2	1101.24	0.04	0.93	0.3	0.74
6	Batnaya	200	63.9	3	2	3899.4	0.27	1.12	0.24	4.64
7	Khorsibat	195	61.0	3	3	5161.2	0.41	1.43	0.4	14.31
8	Telyara	191	58.3	2	2	5086.4	0.32	1.76	0.28	9.19
9	Fadlya	197	62.5	4	3	3992.28	0.33	1.69	0.32	11.15
10	Khoshaba	214	73.7	3	3	3755.44	0.3	1.07	0.27	6.39
11	Telkef	192	59.1	3	2	4500.16	0.31	3.95	0.25	18.09
12	Jarghan	221	78.1	3	3	3808.0	0.28	3.88	0.43	36.48
13	Sharqia	218	76.1	3	3	3617.6	0.27	0.19	0.24	0.94
14	Dermati	190	58.0	3	3	3841.2	0.3	2.19	0.25	9.53
15	Mamrshan	227	82.5	3	3	4042.4	0.31	1.36	0.28	9.74
16	Malon	208	69.5	3	3	4577.76	0.36	0.93	0.29	6.75
17	Telsqef	211	71.1	3	2	3044.4	0.2	3.27	0.24	11.16
18	Zenawa	208	69.4	2	2	4132.8	0.26	3.11	0.35	19.64
19	Karmlk	202	65.2	2	2	5295.84	0.34	1.85	0.24	9.84
20	Doghat	215	74.3	3	2	3947.44	0.27	1.42	0.27	7.69
21	Mandan	186	55.2	2	2	5139.36	0.35	2.01	0.28	10.87
22	Nveria	215	74.1	3	2	3560.4	0.25	2.87	0.33	17.55
23	Bardarsh	184	54.4	3	3	3989.12	0.3	2.17	0.22	7.79
24	Narqizlia	217	75.6	2	2	3768.32	0.22	1.24	0.26	5.36
25	Ismawa	198	62.6	2	2	4338.4	0.27	2.46	0.3	12.47

Table (14) and Figure (13) show the results of the annual soil loss rate, The medium risk class for erosion was the most common, with an area of 642,254 km^2, representing 50.38% of the total area. The low risk class covered 610,854 km^2 (47.92%), whereas the high risk class only covered to 21,629 km^2 (1.70%). These results show that most of the study area experiences low to medium soil loss rates, which reflects the positive impact of plant cover and the region's moderate topography. High loss rates were concentrated in a few places with increased slope and low vegetation cover, particularly at Jarghan, Zenawa, and Telkef. These results are consistent with those of Kumar et al. (2022), who found that spatial variability in the annual soil loss rate in the RUSLE model is caused by the interaction of rainfall, soil erosion ability, topography, and vegetation cover, and that areas with higher vegetation cover also moderate slopes typically have low to moderate loss rates. They also agree with the results of Sidharthan et al. (2024), who found that including RUSLE elements into a GIS environment gives an accurate and reliable spatial representation of erosion-risk areas and is helpful in the identification of priority locations for soil conservation measures.

Table 14. Classification of Annual soil loss, areas, and percentage within the study area.

Class	Texture Class	Area (km^2)	Percentage (%)	Erodibility Classification
1	10.0 - 0.601	610.854	47.92	Low Erosion Risk
2	20.0 - 10.1	642.254	50.38	Moderate Erosion Risk
3	38.6 - 20.1	21.629	1.70	High Erosion Risk
Total		1274.737	100	

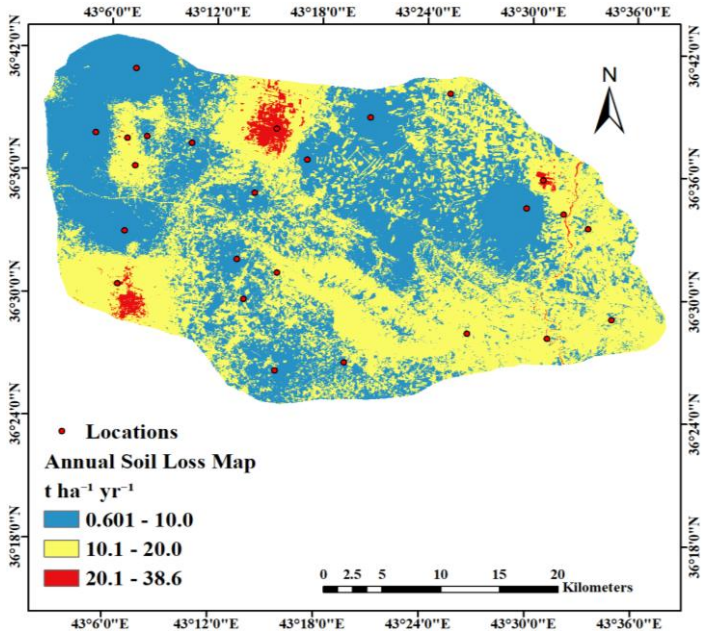

Figure 13. Spatial distribution of annual soil loss in the study area

Conclusion

The results of the RUSLE model showed that the topographic factor (LS) was one of the most influential factors in the distribution of water erosion, as the medium topographic influence category occupied about 85.43% of the study area, while high LS values were associated with increased soil loss rates in steep areas. Also The results of the Normalised Difference Vegetation Index (NDVI) and the C-factor showed that increasing the density of vegetation cover effectively contributed to reducing the impact of raindrops and the speed of surface runoff, as the very high and high protection categories constituted more than half of the area, resulting in a reduction in erosion rates in most parts of the study area.

The combination of remote sensing techniques and geographic information systems with the RUSLE model has proven extremely effective in characterising the spatial variability of erosion factors and producing accurate maps of the annual rate of soil loss, providing a solid scientific foundation for sustainable planning and land management in northern Nineveh Governorate.

Recommendations

The study recommends conducting long-term time-based monitoring of water erosion rates using multi-time satellite data and modern digital models, with the aim of tracking spatial and temporal changes in soil loss, and assessing the impact of climate change and land-use change on the future development of erosion.

The study recommends expanding the use of artificial intelligence and machine learning technologies, as well as remote sensing and geographic information systems, to improve the accuracy of water erosion modelling and predicting areas most vulnerable to future degradation, thereby contributing to decision-making and sustainable land resource management.

Scientific Ethics Declaration

* The authors declare that the scientific ethical and legal responsibility of this article published in EPSTEM Journal belongs to the authors.

* The authors declare that this study complies with scientific research ethics and that all data were collected, analyzed, and reported honestly and transparently.

Conflict of Interest

* The author declares that there is no conflict of interest.

Funding

* This research received no external funding

Acknowledgements or Notes

* This article was presented as oral presentation at the International Conference on Basic Sciences, Engineering and Technology (www.icbaset.net) held in Istanbul/Türkiye on September 17-18, 2026.

* The author would like to thank the Iraqi Meteorological Organization and Seismology, the Directorate of Agriculture of Nineveh Governorate, and the Department of Soil Sciences and Water Resources for their support and assistance.

References

Abbood, R. A., Jafarzadeh, A. A., Hamad, A. I., & Oustan, S. (2025). Using the environmental sensitivity scenarios of desertification in arid and semi-arid regions (A case study of the Al-Nasr area in Dhi Qar, Iraq). *Iraqi Journal of Agricultural Sciences, 56*(4), 1410–1422.

Adeyeri, O. E., Folorunsho, A. H., Adeliyi, T. E., Ayegbusi, K. I., Akinsanola, A. A., Ndehedehe, C. E., Ahmed, N., & Babalola, T. E. (2024). Climate change is intensifying rainfall erosivity and soil erosion in West Africa. *Science of the Total Environment, 955*, 177174.

Akbari, M., Neamatollahi, E., Alizadeh Noughani, M., & Memarian, H. (2022). Spatial distribution of soil erosion risk and its economic impacts using an integrated CORINE-GIS approach. *Environmental Earth Sciences, 81*(10), 287.

Akpa, E. A., Obalum, S. E., & Igwe, C. A. (2024). Revisiting the questioned reliability of the revised universal soil loss equation (RUSLE) for soil erosion prediction in the tropics. *Soil Science Annual, 75*(2), 189538.

Alhamdany, S. A., & Alnaser, Y. H. (2024). Assessing environmental sensitivity areas (ESA) using MEDALUS model in Telkaif District of Northern Iraq. *Asian Journal of Soil Science and Plant Nutrition, 10*(3), 384–393.

Alhashyme, G. A., & Khaled, K. A. (2025). Assessing soil weathering and micromorphological characteristics under different land use practices in northern Iraq. *International Journal of Design & Nature and Ecodynamics, 20*(10), 2471–2478.

Azimi, M., Alkhaled, K. A., Mirdielamy, S. Z., & Vahid, H. (2025). Eco-hydrological impacts and socio-economic drivers of rangeland degradation due to overgrazing in semi-arid and arid regions: A review. *Mesopotamia Journal of Agriculture, 53*(3), 63–86.

Black, C. A. (1965). *Method of soil analysis, Part 2: Chemical and microbiological properties*. Madison, WI: American Society of Agronomy.

Dutucu, A. A., Koç, D. E., & Ustaoğlu, B. (2025). Projected soil erosion risk under shared socioeconomic pathways: A case study with RUSLE modelling in Sakarya, Türkiye. *Land, 14*(11), 2153.

Ebrahimi, A., Zolfaghari, F., Ghodsi, M., & Narmashiri, F. (2024). Assessing the accuracy of spectral indices obtained from Sentinel images using field research to estimate land degradation. *PLoS ONE, 19*(7), e0305758.

Esfandiar, S., Mahdi, M., Vahid, M., & Farshad, M. H. (2018). An improved RUSLE/SDR model for the evaluation of soil erosion. *Environmental Earth Sciences, 77*, Article 454.

European Commission. (1992). *CORINE soil erosion risk and important land resources in the southern regions of the European Community*. https://www.eea.europa.eu/en/analysis/publications/cor0-soil

FAO, & Intergovernmental Technical Panel on Soils (ITPS). (2020). *State of knowledge of soil biodiversity: Status, challenges and potentialities*. Food and Agriculture Organization of the United Nations. Retrieved from https://www.fao.org/documents/card/en/c/cb1928en

Foster, G. R., McCool, D. K., Renard, K. G., & Moldenhauer, W. C. (1981). Conversion of the Universal Soil Loss Equation to SI metric units. *Journal of Soil and Water Conservation, 36*, 355–359.

Ganasri, B. P., & Ramesh, H. (2016). Assessment of soil erosion by RUSLE model using remote sensing and GIS: A case study of Nethravathi Basin. *Geoscience Frontiers, 7*(6), 953–961.

Gee, G. W., & Bauder, J. W. (1986). Practical size analysis. In A. Klute (Ed.), *Methods of soil analysis, Part 1: Physical and mineralogical methods* (2nd ed., pp. 383–409).

Gül, E., & Esen, S. (2024). High desertification susceptibility in forest ecosystems revealed by the Environmental Sensitivity Area Index (ESAI). *Sustainability, 16*(23), 10409.

Hesse, P. R. (1971). *Text book of soil chemical analysis*. New York, NY: Chemical Publishing Co. Inc.

Ho, C. C., Kassa, D. A., Wasie, Y. Y., et al. (2026). GIS-based RUSLE modeling for soil erosion risk assessment, sediment yield estimation, and area prioritization in the Hamassa Watershed, Ethiopia. *Natural Hazards, 122*, 149.

Kafroshy, K. H., & Alkhaled, K. A. (2025). Assessing agricultural land degradation near oil refineries using geospatial techniques south Erbil-Iraq. *IOP Conference Series: Earth and Environmental Science, 1549*, 012014.

Klute, A. (1986). *Methods of soil analysis. Part 1: Physical and mineralogical methods* (2nd ed., Agronomy Monograph No. 9). Madison, WI: ASA-SSSA.

Kouli, M., Soupios, P., & Vallianatos, F. (2009). Soil erosion prediction using the Revised Universal Soil Loss Equation (RUSLE) in a GIS framework, Chania, Northwestern Crete, Greece. *Environmental Geology, 57*, 483–497.

Kumar, M., Sahu, A. P., Sahoo, N., Dash, S. S., Raul, S. K., & Panigrahi, B. (2022). Global-scale application of the RUSLE model: A comprehensive review. *Hydrological Sciences Journal, 67*(5), 806–830.

Lukić, S., Baumgertel, A., Obradović, S., Kadović, R., Beloica, J., Pantić, D., Miljković, P., & Belanović Simić, S. (2022). Assessment of land sensitivity to degradation using MEDALUS model: A case study of Grdelica Gorge and Vranjska Valley (Southeastern Serbia). *iForest – Biogeosciences and Forestry, 15*(3), 163–170.

Maaroof, B. F., Kareem, H. H., Al-Zubaydi, J. H., Al-Husseini, A. A., Al-Quraishi, A. M. F., Al-Tamimi, W. H., & Al-Maliki, M. A. (2025). Estimating soil erosion utilizing geospatial method and revised universal soil loss equation (RUSLE) of Abu Ghraibat Watershed, Eastern Misan Governorate, Iraq. *Scientific Reports, 15*, 44422.

Mahgoub, M., Elalfy, E., Soussa, H., & Abdelmonem, Y. (2024). Relation between the soil erosion cover management factor and vegetation index in semi-arid basins. *Environmental Earth Sciences, 83*(10), 337.

Moore, I. D., & Burch, G. J. (1986). Physical basis of the length-slope factor in the Universal Soil Loss Equation. *Soil Science Society of America Journal, 50*, 1294–1298.

Page, A. L. (Ed.). (1982). *Methods of soil analysis. Part 2: Chemical and microbiological properties* (2nd ed.). Madison, WI: American Society of Agronomy.

Panda, S. S., Andrianasolo, H., & Steele, D. D. (2005). Application of geotechnology to watershed soil conservation planning at the field scale. *Journal of Environmental Hydrology, 13*(16), 1–22.

Quinton, J. N., & Fiener, P. (2024). Soil erosion on arable land: An unresolved global environmental threat. *Progress in Physical Geography: Earth and Environment, 48*(1), 136–161.

Renard, K. G., Foster, G. R., Weesies, G. A., McCool, D. K., & Yoder, D. C. (1997). *Predicting soil erosion by water: A guide to conservation planning with the Revised Universal Soil Loss Equation (RUSLE)* (Agriculture Handbook No. 703). U.S. Department of Agriculture.

Richards, L. A. (1954). *Diagnosis and improvement of saline and alkaline soils* (USDA Agriculture Handbook No. 60). U.S. Department of Agriculture.

Samara, S. Y., & Khalid, F. H. (2021). Validity of some international rainfall erosivity models for Mosul climatic condition at Northern Iraq. *NTU Journal of Agriculture and Veterinary Science, 1*(1), 43–47.

Sidharthan, J., Udayar Pillai, S., Subbaiyan, M., Govindraj, S., & Kantamaneni, K. (2024). Harmonizing models and measurements: Assessing soil erosion through RUSLE model. *Environmental Science and Pollution Research*.

Wischmeier, W. H., & Smith, D. D. (1978). *Predicting rainfall erosion losses: A guide to conservation planning* (Agriculture Handbook No. 537). U.S. Department of Agriculture.

Wischmeier, W. H., & Smith, D. D. (1978). *Predicting rainfall erosion losses: A guide to conservation planning* (Agriculture Handbook No. 537). U.S. Department of Agriculture.

Wischmeier, W. H., & Smith, D. D. (1978). *Predicting rainfall erosion losses: A guide to conservation planning* (USDA Agriculture Handbook No. 537). Washington, DC: USDA.

Woldemariam, G. T., Iguala, A. D., Tekalign, S., & Reddy, R. (2018). Land use land cover change and its environmental impact in Ethiopia: A case study of the Kilte Awulaelo watershed. *Environmental Systems Research, 7*, Article 17.

Wu, X., Wang, S., Fu, B., Feng, X., & Chen, Y. (2019). Socio-ecological changes on the Loess Plateau of China after Grain to Green Program. *Science of the Total Environment, 678*, 565–573.

Xiong, M., Leng, G., & Tang, Q. (2023). Global analysis of the cover-management factor for soil erosion modeling. *Remote Sensing, 15*(11), 2868.

Xue, J., & Su, B. (2017). Significant remote sensing vegetation indices: A review of developments and applications. *Journal of Sensors, 2017*, 1–17.

Yanqing, L., Xiaohuan, Y., & Hongyan, C. (2025). Depicting, spatializing, and decoupling the impact of human activities on soil erosion in the hilly red soil region of southern China from the perspective of soil erosion influence factors. *Journal of Environmental Management, 376*, 124371.

Author(s) Information

Tayseer Thaker Mohammed
University of Mosul
Mosul, Iraq
ORCID iD: https://orcid.org/0009-0004-4446-4947

Khaled Anwar Khaled
University of Mosul
Mosul, Iraq
ORCID iD https://orcid.org/0000-0003-2198-0100
*Contact e-mail:*khalid.anwar31@uomosul.edu.iq*

*Corresponding author(s) contact email

To cite this article:

Mohammed, T.T., & Khaled, K.A. (2026). Integrating mean weight diameter and environmental sensitivity index for modeling soil erosion risk and land degradation in soils under different agricultural land uses. *The Eurasia Proceedings of Science, Technology, Engineering and Mathematics (EPSTEM), 42,* 191-210.

The Eurasia Proceedings of Science, Technology, Engineering and Mathematics (EPSTEM)
ISSN: 2602-3199

The Eurasia Proceedings of Science, Technology, Engineering and Mathematics (EPSTEM), 2026

Volume 42, Pages 211-222

ICBASET 2026: International Conference on Basic Sciences, Engineering and Technology

Efficiency of Nano and Mineral Iron in Sustaining Faba Bean (*Vicia Faba* L.) Productivity Within Different Soil Orders

Maryam Abdulkader Albadranie
University of Mosul

Rana Saadallah Aziz
University of Mosul

Abstract: The decline in agricultural production rates necessitates the advancement of this sector by enhancing production efficiency through various modern technologies. Among these technologies in the field of fertilizers and fertilization is nanofertilizer technology. To achieve this goal, a biological experiment was conducted in the greenhouse of the Department of Soil Sciences and Water Resources, College of Agriculture and Forestry, University of Mosul, during the winter season of 2024/2025. The study aimed to evaluate the response of Broad Bean (Vicia faba L., Mornash cultivar) to the interaction between nano and mineral iron in two different soil orders within Nineveh Governorate.The experiment was implemented according to a Completely Randomized Design (CRD) as a factorial experiment with three replicates and three factors, first (S) Two types of soil with different textures., Second (M) Mineral fertilization, Tharid (N) Nano-fertilization. The total number of experimental units was 54 (2 soil types × 3 soil application levels × 3 foliar application levels × 3 replicates). Significant differences between treatments were evaluated using the Least Significant Difference (LSD) test at a significance level of 0.05. Key Results,Foliar Application: The foliar application of iron (both nano and mineral) had a clear impact on the growth of the broad bean plant. It resulted in a significant increase in growth indicators compared to the control treatment, including: plant height (cm), number of branches (branch plant^{-1}), leaf area (cm^2 plant^{-1}), chlorophyll concentration (SPAD), and shoot dry weight (g plant^{-1}). Yield Components, Significant increases were observed in yield components, including seed dry weight, seed fresh weight (g plant^{-1}), and biological yield (g plant^{-1}). Optimal Concentrations, Foliar applications of 100 mg Fe L^{-1} and 1.5 g L^{-1} outperformed other treatments, recording the highest values across all growth and yield indicators. Soil Application, Soil application at rates of 15 kg Fe ha^{-1} and 4 kg Fe ha^{-1} excelled over other concentrations in all studied growth and yield traits. Interaction Effects, The results of the dual interaction between soil and foliar application methods showed that the fertilizer combination of 100 mg Fe L^{-1} (foliar) + 4 kg Fe ha^{-1} (soil) (N2 + M3) significantly outperformed all other interactions in growth indicators and yield components.

Keywords: Faba bean, Nano-fertilizer, Mineral iron, Soil orders, Crop productivity

Introduction

Broad bean (*Vicia faba* L.) is considered one of the most significant pulse crops globally, valued for its high nutritional content of plant proteins, amino acids, minerals, and vitamins. Beyond its direct use as human food and animal feed, it holds strategic importance in sustainable agriculture due to its capacity for atmospheric nitrogen fixation and its role in improving the physical and chemical properties of soil (Abd El-Hady et al., 2023). However, the productivity of broad beans in calcareous soils—which are prevalent in many regions, including Iraq is adversely affected by the low bioavailability of micronutrients, particularly iron (Fe). This occurs due to high pH levels and the presence of calcium carbonates, which lead to the fixation of the element

- This is an Open Access article distributed under the terms of the Creative Commons Attribution-Noncommercial 4.0 Unported License, permitting all non-commercial use, distribution, and reproduction in any medium, provided the original work is properly cited.

- Selection and peer-review under responsibility of the Organizing Committee of the Conference

© 2026 Published by ISRES Publishing: www.isres.org

and the inhibition of its uptake. Consequently, this results in iron-deficiency chlorosis, stunted growth, and degraded yield (Jassim et al., 2023).

Iron (Fe) is a vital micronutrient required by plants in small quantities, yet it performs essential functions in growth and development. It is a structural component of numerous enzymes and proteins responsible for redox reactions, such as cytochromes and ferredoxin. Furthermore, it contributes indirectly to chlorophyll synthesis and the activation of photosynthesis, while playing a crucial role in cellular respiration and energy production. Additionally, iron is a key factor in root nodule formation and the stimulation of *Rhizobium* bacteria activity, which fixes atmospheric nitrogen in legumes, thereby enhancing biological nutrition efficiency and increasing soil fertility (Khan et al., 2022).

Traditionally, mineral fertilization has been employed to address iron deficiency. Soil application of compounds such as ferrous sulfate ($FeSO_4.7H_2O$) aims to increase available iron concentrations in the soil and improve root uptake. However, the efficacy of this method is often compromised in calcareous soils due to nutrient fixation. Consequently, foliar application has been adopted as a complementary technique, where iron is sprayed directly onto the leaves. This method accelerates absorption, improves chlorophyll content, and exerts a rapid positive effect on vegetative growth (Shirsat et al., 2024).

With recent advancements in nanotechnology, nano-fertilization has emerged as an innovative strategy to enhance fertilizer use efficiency (FUE). Iron nanoparticles (Fe-NPs) are characterized by their small particle size and large surface area, which increase their solubility and bioavailability to the plant. Soil application of nano-iron contributes to improving the availability of the element and its subsequent uptake by roots. Meanwhile, foliar application has demonstrated exceptional effectiveness in boosting vegetative growth, increasing chlorophyll concentrations, and improving photosynthetic efficiency in leguminous plants, including broad beans (Mohamed et al., 2023; Al-Khafaji et al., 2024).

Accordingly, studying the impact of mineral and nano-iron fertilization—via both soil and foliar applications—on broad bean crops under calcareous soil conditions is a fundamental scientific step toward developing advanced fertilization programs. Such programs aim to enhance production efficiency and achieve agricultural sustainability. The primary objectives of this study are:

1. To evaluate the impact of mineral and nano-iron, along with their application methods, on certain growth parameters and yield components of the broad bean plant.
2. To determine the optimal levels of nano and mineral iron fertilizers, as well as the best interaction between application methods, to achieve the maximum yield for the broad bean crop.

Method

Soil Sampling Sites and Preparation

Two distinct locations with varying chemical and physical properties were selected within Nineveh Governorate to collect soil samples for cultivating the faba bean (*Vicia faba* L.) plant.

Site 1: Al-Rashidiya

Located in the Al-Rashidiya fields on the left bank of the Tigris River. It is situated at Longitude 43.1167° E and Latitude 36.4333° N in the northern suburbs of Mosul, approximately 10 km from the city center. According to the soil taxonomy, the soil at this site belongs to the Inceptisols order (specifically the suborder Uceptisols).

Site 2: Filfil

Located in the Filfil sub-district fields, approximately 60 to 70 km from Mosul city center on the left bank of the Tigris River. It is situated at Longitude 43.0343° E and Latitude 36.5467° N. The soil at this site belongs to the Aridisols order.

The selection of these two sites was based on the clear variation in their soil orders and properties, as illustrated in the figure below.



Figure 1. Geographical locations of the two study sites (Source: Google Maps).

Soil Sampling and Preparation

Materials and Methods

Surface soil samples were collected from a depth of 0–30 cm on November 10, 2025. Samples from each site were thoroughly mixed separately to obtain a composite representative sample for the field soil. The samples were then air-dried, crushed, and passed through a 4 mm sieve for use in pot experiments. Each pot (experimental unit) was filled with 8 kg of air-dried soil. For physical and chemical characterization, a sub-sample from each site was ground and passed through a 2 mm sieve, then stored in airtight plastic containers.

Soil Physical Analysis

Particle Size Distribution (Soil Texture): Soil texture was determined using the hydrometer method. A known weight of soil was treated with calgon (sodium hexametaphosphate). Readings were taken at 40 seconds and 2 hours, adjusted for temperature as described by Gee and Bauder (1986). The texture class was identified using the USDA Soil Texture Triangle.
Field Capacity (Moisture Content): Moisture content was determined gravimetrically. Samples were saturated with water and placed in funnels with filter paper for 24 hours. The remaining moisture content was measured after oven-drying the samples at 105°C for 24 hours, following Klute (1986) and USDA (2006).
Bulk Density: Bulk density was measured in situ using the core sampler method as outlined by Black (1965).

Soil Chemical Analysis

1. *Soil pH:* Determined in a 1:1 (soil:water) extract using a digital pH meter according to Rowell (1996).
2. *Electrical Conductivity (EC):* Measured in a 1:1 soil extract at 25°C using an EC-meter as described by Rowell (1996).
3. *Calcium Carbonate ($CaCO_3$):* Determined chemically by adding excess 1.0 N HCl to the soil and back-titrating the unreacted acid with 1.0 N NaOH in the presence of phenolphthalein indicator (FAO, 1973).
4. *Organic Matter (O.M.):* Determined by the Walkley-Black wet oxidation method. Organic carbon was oxidized using concentrated H2SO4 (95%) and 1.0 M potassium dichromate K2Cr2O7then titrated against 0.5 N ferrous ammonium sulfate using diphenylamine as an indicator.
5. *Cation Exchange Capacity (CEC):* Determined by saturating the soil with 1.0 N sodium acetate (1N) pH=8.2 to replace exchangeable cations with sodium. Sodium was then extracted using 1.0 N ammonium acetate and measured using a flame photometer.
6. *Available Nitrogen (N):* Extracted using 2.0 N KCl (1:20 ratio). Nitrogen in the filtrate was determined via the Micro-Kjeldahl distillation method, with ammonia captured in boric acid containing a mixed indicator (Black, 1965).

7. *Available Phosphorus (P):* Determined using the Modified Olsen Method (1982). Phosphorus was extracted with 0.5 M NaHCO3 (pH 8.5) at a 1:20 ratio and measured colorimetrically using a spectrophotometer at a wavelength of 882 nm.
8. *Available Potassium (K):* Extracted with 1.0 N neutral ammonium acetate =pH 7.0) at a 1:10 ratio and measured using a flame photometer.
9. *Available Iron (Fe, mg/kg):* Extracted using a DTPA solution (1:2 ratio). 10 g of soil was shaken with 20 ml of DTPA (pH = 7.3) for two hours. The iron concentration was measured using an Atomic Absorption Spectrophotometer.

Seeds Used in the Experiment

Broad bean (*Vicia faba* L.) seeds of the Mornache cultivar were used. This variety is produced by the Moroccan company Agrosem. The germination rate was tested and confirmed at 90%.

Biological Experiment

Experimental Design

To accurately determine plant response to applied fertilizers, a factorial experiment was conducted following a Completely Randomized Design (C.R.D.). The study took place in the greenhouse of the Department of Soil Sciences and Water Resources, College of Agriculture and Forestry, University of Mosul, during the 2024–2025 growing season. The experiment investigated three factors with three replicates:

Factor 1: Two Soil Locations (Varying in Texture, Calcium Carbonate, and Iron Content)

- S1: Filfil region, Nineveh Governorate.
- S2: Al-Rashidiya region, Nineveh Governorate.

Factor 2: Mineral Iron Fertilizer

Using ferrous sulfate ($FeSO_4.7H_2O$) containing 19% Fe, applied based on fertilizer recommendations:

- M1: Control (No application).
- M2: Soil application (15 kg Fe ha^{-1}).
- M3: Foliar application (100 mlg Fe L^{-1}).

Factor 3: Nano-Iron Fertilizer

An Iranian-origin nano-fertilizer (manufactured by Al-Khadra Company) containing 6% Fe, applied as follows:

- N1: Control (No application).
- N2: Soil application (4 kg Fe ha^{-1}).
- N3**:** Foliar application (1.5 mlg L^{-1}).

Total Experimental Units

The experiment comprised 54 units (2 Soil Locations × 3 Mineral Levels × 3 Nano Levels × 3 Replicates). Each location included 27 experimental units.

Studied Traits

I. Vegetative Growth Traits

1. *Plant Height (cm):* Measured from the soil surface to the plant apex using a metallic measuring tape.
2. *Number of Branches (branch plant^{-1}):* Total count of primary branches per plant.
3. *Chlorophyll Content (SPAD):* Measured using a portable hand-held Chlorophyll Meter (Model SPAD-502, Minolta, Japan) following the methods of Sotiropoulos and Mouhtaridou (2005) and Cerovic et al. (2012).
4. *Leaf Area (cm^2):* Calculated for a single leaf by measuring the length and maximum width using a ruler, then applying the equation by Wali (2018):

LA = 0.04 + 0.45(L \times W)

Where:

- *LA:* Leaf Area.
- *L:* Leaf Length.
- *W:* Leaf Width.

II. Maturity and Yield Traits

5. *Shoot Dry Weight (g plant^{-1}):* Plants were placed in perforated paper bags and dried in an electric oven at 60–65°C for 48–72 hours until a constant weight was achieved (Al-Sahaf, 1989).
6. *Biological Yield (g plant^{-1}):* Calculated as the total weight of pods plus the total weight of the vegetative shoot system.
7. *Seed Fresh Weight (g plant-1):* Measured immediately after harvesting seeds from the pods.
8. *Seed Dry Weight (g plant^{-1}):* Seeds were extracted from pods and dried in an oven at 60–65°C for 48–72 hours until weight stabilization (Al-Sahaf, 1989).

Results and Discussion

Plant Height (cm)

Table (1) illustrates the impact of nano and mineral iron fertilization, soil texture, and application methods on plant height (cm). The data indicates that both nano and mineral iron fertilization—applied via soil and foliar methodshad a statistically significant effect on plant height.Nano-Fertilization EffectsRegarding nano-iron treatments, the highest plant height was recorded under the N3 treatment (foliar application), reaching 100.17 cm. This treatment significantly outperformed the control, achieving a growth increase of 7.58%. In contrast, the soil application of nano-fertilizer (N2) resulted in a more modest increase of 2.80% compared to the non-fertilized control.Mineral Fertilization Effects For mineral iron fertilization, the foliar application (M_3) yielded the most substantial results, with a significant increase of 19.31%. Soil application of mineral iron (M_2) followed with an increase of 9.09%. Environmental and Interaction Factors A significant difference was observed between the two study locations: Al-Rashidiya (S_2) and Filfil (S_1). Site S_2 exhibited superior growth, surpassing S1 by 1.08%. The triple interaction—encompassing application method, fertilizer type (nano vs. mineral), and soil texture—showed that the highest overall plant height was recorded at site S2 under the $M_3N_3S_2$ treatment, reaching 113 cm (a 34.52% increase over the control).

Table 1. Effect of nano-iron and mineral iron fertilization and soil texture on plant height (cm).

Effect S	Effect M	N3	N2	N1		
		92.33	89.67	87.00	M1	S1
95.82		97.67	96. 00	94.00	M2	
	88.00	109.00	98.67	98. 00	M3	
	96.00	89.00	86.00	84. 00	M1	
96.85	105.00	100.00	96.67	91.67	M2	S2
		113.00	107.33	104. 00	M3	
LSD N= 0.6629 M= 0.6629 S= 0.5412 MNS= 1.6237		100.17	95.72	93.11	Effect N	

At site S1, the peak height was 109 cm under the M3N3S1 treatment, representing a significant increase of 25.28% compared to the control.Scientific DiscussionThe positive response of the plants to both soil and foliar fertilization, as evidenced by increased plant height, can likely be attributed to the enhanced bioavailability of iron (Fe) in the soil and its efficient uptake by the root system. This availability stimulates vital biological processes and metabolic activities, which are directly reflected in improved growth parameters, specifically plant height (Al-Ansi & Al-Maghrabi, 2025).

Number of Branches (branch plant^{-1})

Table (2) illustrates the impact of nano and mineral iron fertilization, along with soil texture, on the number of branches (branch plant^{-1}). The data reveals that both nano and mineral iron fertilization, via soil and foliar applications, significantly influenced plant growth parameters.Effects of Nano-Iron FertilizationRegarding nano-fertilization, foliar application (N_3) resulted in the highest number of branches, reaching 9 branches plant^{-1}. This represents a statistically significant increase of 40% over control. Meanwhile, soil application (N_2) achieved a 20% increase compared to the non-fertilized treatment.Effects of Mineral Iron Fertilization Mineral iron fertilization showed even more pronounced effects. The foliar application (M3) recorded a substantial significant increase of 166%, while the soil application (M2) resulted in a 100% increase.Site Variations and InteractionsStatistical analysis showed a significant difference between the two study sites, with the first site (S1) outperforming the second by 6.66% Regarding the triple interaction (application method × fertilizer type × soil texture):In the first site (S1), the M3N3S1 treatment yielded the highest number of tillers, with a 200% increase compared to the control. In the second site (S2), the M3N3S2 treatment achieved the maximum response, with a significant increase of 350% over the non-fertilized treatment. Scientific DiscussionThe increase in the number of branches and tillers can be attributed to the development of a dense root system resulting from soil fertilization. This robust root architecture enables the plant to absorb higher quantities of water and essential nutrients, thereby enhancing overall vegetative growth. Furthermore, the effectiveness of foliar nano-fertilization is due to the unique properties of nanoparticles, specifically their small particle size. This allows for efficient penetration of the leaf surface and rapid integration into the plant's internal tissues, where they participate in vital biological processes that stimulate branching. These findings are consistent with the results reported by Rabih et al. (2023).

Table 2. Effect of nano and mineral iron fertilization and soil texture on the number of branches (branch plant^{-1}).

Effect S	Effect M	N3	N2	N1		
		6	4	3	M1	S1
6.4		8	7	5	M2	
	3	9	8	8	M3	
	6	5	3	2	M1	
6	8	7	6	6	M2	S2
		9	8.	8	M3	
LSD M= 0.6707 N= 0.6707 S= 0.5477 MNS=1.643		7	6	5	Effect N	

Chlorophyll Concentration (SPAD)

Table (3) illustrates the impact of nano and mineral iron fertilization, alongside soil texture, on chlorophyll concentration (SPAD). The results indicated that both fertilization types, applied via soil and foliar methods, significantly influenced chlorophyll levels. Nano-Iron Fertilization Effects Regarding nano-fertilization, the foliar application (N3) yielded the highest chlorophyll concentration, reaching 52.221 SPAD, which represents a significant increase of 17.48% over the control. In comparison, the soil application (N2) showed an increase of 8.11% relative to non-fertilized treatment. Mineral Iron Fertilization EffectsMineral iron fertilization also showed substantial improvements. The foliar application (M3) achieved a significant increase of 61.75%, while the soil application resulted in a 33.33% increase. A significant geographical variation was observed, as the second site (S2) outperformed the first by 1.08%. Interaction Effects. The triple interaction (application method × fertilizer type × soil texture) revealed that:At the second site (S2), the M3N3S2 treatment achieved the peak chlorophyll concentration of 64 SPAD, a 95.89% increase over the control. At the first site (S1), the M3N3S1 treatment reached 63.33 SPAD, representing a significant increase of 82.66% compared to the control.

Table 3. Effect of nano and mineral iron fertilization and soil texture on chlorophyll concentration (SPAD).

Effect S	Effect M	N3	N2	N1		
		39	37	34.67	M1	S1
47.1852		50	47.67	43	M2	
	36.6	63.33	57	53	M3	
	48.8	40.67	35.67	32.67	M1	
49.2963	59.2	56.33	50.67	45.67	M2	S2
		64	60.33	57. 67	M3	
LSD M= 0.8996 N= 0.8996 S= 0.7345 MNS=2.2036		52.221	48.056	44. 45	Effect N	

Scientific Discussion The increase in chlorophyll concentration across fertilized treatments (both nano and mineral, soil and foliar) can be attributed to the enhanced activity of enzymes responsible for chlorophyll biosynthesis as a result of increased internal iron (Fe) concentrations. Iron plays a critical role in the photoperiod of the photosynthetic process, acting as a structural component of various enzymes and co-enzymes. These findings are consistent with the results reported by Abdul-Jabbar (2017).

Leaf Area (cm²)

Table (4) presents the impact of nano and mineral iron fertilization, along with soil texture, on leaf area (cm²). The results indicate that both nano and mineral iron treatments, applied through soil and foliar methods, significantly influenced the leaf area. Effects of Nano-Iron Fertilization Regarding nano-fertilization, the foliar application (N3) recorded the highest leaf area at 10.5488 cm², representing a significant increase of 21.46% over the control. Meanwhile, the soil application (N2) achieved a 9.53% increase compared to the non-fertilized treatment.Effects of Mineral Iron FertilizationMineral iron fertilization also showed substantial improvements. The foliar application (M3) achieved a significant increase of 79.02%, while the soil application resulted in a 38.12% increase. Additionally, a significant difference was observed between the two sites, with the second site (S2) outperforming the first site (S1) by a margin of 9.57%. Interaction Effects The triple interaction (application method × fertilizer type × soil texture) revealed that: In the second site (S2), the highest leaf area reached 14.2045 cm² under the M3N3S2 treatment, with a remarkable increase of 147.9% compared to the control.In the first site (S1), the maximum value was 12.0700 cm² under the M3N3S1 treatment, showing a significant increase of 84.65% over the non-fertilized treatment. Scientific Discussion The enhancement in leaf area following the application of nano and mineral fertilizers (via both soil and foliar routes) can be attributed to the high efficiency and rapid penetration of nanoparticles into plant tissues. This rapid integration into vital biological processes subsequently improves overall plant growth and expands the photosynthetic surface area. These findings are in alignment with the results reported by Rafiq and Al-Jubour (2020).

Table 4. Effect of nano and mineral iron fertilization and soil texture on leaf area (cm²).

Effect S		Effect M	N3	N2	N1		
			7.7185	7.0540	6.5365	M1	S1
	9.14417	6.8910	10.1845	8.8420	7.9915	M2	
		9.5180	12.0700	11.2615	10.6390	M3	
		12.3368	7.8025	6.5065	5.7280	M1	
	10.01967		11.3125	9.9775	8.8000	M2	S2
			14.2045	13.4335	12.4120	M3	
LSD N= 0.2327	M= 0.2327	S= 0.19 MNS= 0.5701	10.5488	9.5125	8.6845	Effect N	

Shoot Dry Weight (g plant^{-1})

Table (5) presents the impact of nano and mineral iron fertilization, along with soil texture, on the shoot dry weight (g plant^{-1}). The data indicates that both fertilization types, applied via soil and foliar methods, significantly influenced the dry matter accumulation of the shoots Effects of Nano-Iron Fertilization For the nano-iron treatments, the foliar application (N3) yielded the highest value of 22.83 g plant^{-1}, representing a statistically significant increase of 17.49% over the control. Meanwhile, the soil application (N2) resulted in a 9.41% increase compared to the non-fertilized treatment. Effects of Mineral Iron Fertilization Mineral iron fertilization also showed substantial improvements. The foliar application (M3) achieved a significant increase of 48.53%, while the soil application resulted in a 25.5% increase. A significant difference was observed between the study locations, with the first site (S1) outperforming the second site (S2) by 9.12%.Interaction Effects Regarding the triple interaction (application method × fertilizer type × soil texture): In the first site (S1), the highest shoot dry weight was recorded under the M3N3S1 treatment, with an increase of 86.30% compared to the control. In the second site (S2), the M3N3S2 treatment showed a significant increase of 71.02% over the non-fertilized treatment. Scientific Discussion The increase in shoot dry weight in the fertilized treatments can be attributed to the enhanced uptake of iron (Fe) following soil application, as well as the high efficiency of both nano and mineral fertilizers in translocating across plant cell membranes. This leads to stimulated vegetative growth due to the vital role of these elements in cell division, photosynthesis, and the enhancement of enzymatic activity and biochemical reactions. Furthermore, nanoparticles play a protective role by reducing the formation and activity of reactive oxygen species (ROS) and preventing oxidative stress, which delays senescence and

promotes sustained vegetative growth. These findings are in agreement with (Mohammed, 2022), who highlighted the role of nano and mineral fertilizers in increasing the dry matter of plant shoots.

Table 5. Effect of nano and mineral iron fertilization and soil texture on shoot dry weight (g plant^{-1}).

Effect S	Effect M	N3	N2	N1		
		19.30	16.80	14.60	M1	S1
22.073		24.10	23.23	22.30	M2	
	16.983	`27.20	26.23	24.90	M3	
	21.316	18.83	16.70	15.67	M1	
20.277	25.226	20.77	19.67	17.83	M2	S2
		26.80	24.93	21.30	M3	
LSD N= 0.289 M= 0.289 S= 0.2359 MNS= 0.7078		22.83	21.26	19.43	Effect N	

Seed Fresh Weight (g plant^{-1})

Table (6) presents the impact of nano and mineral iron fertilization, along with soil texture, on the seed fresh weight (g plant^{-1}). The results demonstrate that both nano and mineral iron fertilization—via soil and foliar applications—significantly influenced the seed fresh weight. Effects of Nano-Iron Fertilization Regarding nano-fertilization, the foliar application (N3) yielded the highest value of 81.92 g plant^{-1}, representing a statistically significant increase of 52.63% over the control. Meanwhile, the soil application (N2) achieved a 36.63% increase compared to the non-fertilized treatment. Effects of Mineral Iron Fertilization Mineral iron fertilization also showed substantial improvements. The foliar application (M3) recorded a significant increase of 50.34%, while the soil application resulted in a 23.26% increase. A significant difference was observed between locations, with the second site (S2) outperforming the first site (S1) by 3.39%.Interaction Effects The triple interaction (application method × fertilizer type × soil texture) revealed that: At the second site (S2), the maximum total seed fresh weight was recorded under the M3N3S2 treatment, with an increase of 104.3% compared to the control.At the first site (S1), the M3N3S1 treatment showed a significant increase of 76.63% over the non-fertilized treatment. Scientific Discussion The enhancement in seed fresh weight is attributed to the fact that nano and mineral fertilizers improve the utilization of Photosynthetically Active Radiation (PAR). This enhances the availability of photosynthetates required for the initiation and development of tiller primordia. This, in turn, positively reflects on the total seed fresh weight per cultivated area due to the increased bioavailability of iron (Fe) concentrations. These results align with the findings of Al-Saidan (2019). Furthermore, the absorption of nutrients through the stomata during foliar application led to accelerated plant growth and development, as noted by Sajadinia et al. (2021).

Table 6. Effect of nano and mineral iron fertilization and soil texture on seed fresh weight (g plant^{-1}).

Effect S	Effect M	N3	N2	N1		
		65.96	61. 66	55. 67	M1	S1
72.55		76.96	70.70	66. 33	M2	
	59.45	98.33	84.53	72.83	M3	
	72.51	61. 66	58.10	53. 67	M1	
75.01	89.38	78.97	74.46	67. 67	M2	S2
		109. 67	90.53	80.40	M3	
LSD N= 0.6119 M= 0.6119 S= 0.4996 MNS= 1.4988		81.92	73.33	66.10	Effect N	

Seed Dry Weight (g plant^{-1})

Table (7) illustrates the impact of nano and mineral iron fertilization, along with soil texture, on seed dry weight (g plant^{-1}). The data indicates that both fertilization types, applied via soil and foliar methods, significantly influenced the dry matter accumulation in seeds. Effects of Nano-Iron Fertilization Regarding nano-fertilization, the foliar application (N3) recorded the highest value of 23.32 g plant^{-1}, representing a statistically significant increase of 21.9% over the control. In contrast, the soil application (N2) achieved an increase of 8.89% compared to the non-fertilized treatment. Effects of Mineral Iron Fertilization Mineral iron fertilization also showed substantial improvements. The foliar application (M3) achieved a significant increase of 61.92%, while the soil application resulted in a 16.89% increase. A significant difference was observed between the study locations, with Site S2 outperforming Site S1 by a margin of 3.91%. Interaction Effects The triple interaction

(application method × fertilizer type × soil texture) revealed that: At Site S2, the highest seed dry weight was recorded under the M3N3S2 treatment, with a 97.89% increase over the control. At Site S1, the M3N3S1 treatment reached its peak with a significant increase of 90.39% compared to the non-fertilized treatment. Scientific Discussion The enhancement in seed dry weight is attributed to the role of nano and mineral fertilizers in improving the utilization of Photosynthetically Active Radiation (PAR). This facilitates the availability of essential compounds that support the initiation of tiller primordia, which positively reflects on the total seed dry weight per unit area due to the increased bioavailability of iron (Fe). These findings are consistent with the results reported by Al-Jubouri et al. (2017, 2019). Furthermore, the efficient nutrient uptake through the stomata during foliar application led to enhanced plant growth and developmental stages, as noted by Sajadinia et al. (2021).

Table 7. Effect of nano and mineral iron fertilization and soil texture on seed dry weight (g plant^{-1}).

Effect S	Effect M	N3	N2	N1		
20.69	16.81	18.53	15.73	14. 67	M1	S1
		22.43	20. 33	17.53	M2	
		27.93	25.30	23.80	M3	
21.50	19.65	19. 66	16.60	15. 67	M1	S2
		20. 33	19.50	17.80	M2	
	26.83	31.01	27.60	25. 33	M3	
LSD N= 0.2114 M= 0.2114 S= 0.1726 MNS= 0.5178		23.32	20.83	19.13	Effect N	

Biological Yield (g plant^{-1})

Table (8) presents the impact of nano and mineral iron fertilization, along with soil texture, on the biological yield (g plant^{-1}). The results indicate that both types of fertilization—applied via soil and foliar methods—had a significant effect on the total biological yield. Effects of Nano-Iron Fertilization Regarding nano-fertilization, the foliar application (N3) recorded the highest value of 45.60 g plant^{-1}, representing a statistically significant increase of 24.62% over the control. In contrast, the soil application (N2) achieved a 14.18% increase compared to the non-fertilized treatment.Effects of Mineral Iron Fertilization For mineral iron treatments, the foliar application (M3) achieved a significant increase of 45.68%, while the soil application resulted in an 18.51% increase. A significant difference was also observed between the study locations (Filfil & Al-Rashidiya), with Site S2 outperforming Site S1 by 1.19%. Interaction Effects The triple interaction (application method × fertilizer type × soil texture) revealed that: At Site S2, the M3N3S2 treatment achieved the highest total seed fresh weight, with an increase of 73.51% compared to the control. At Site S1, the M3N3S1 treatment yielded the most significant response, showing an increase of 85.37% over the non-fertilized treatment. Scientific Discussion The enhancement in biological yield is attributed to the role of nano and mineral fertilizers in optimizing the utilization of Photosynthetically Active Radiation (PAR). This improvement increases the availability of essential compounds that support the development of tiller primordia, leading to a higher total seed dry weight within the cultivated area due to the increased bioavailability of iron (Fe). These findings are consistent with (Al-Jubouri et al., 2019). Furthermore, the absorption of nutrients through the stomata during foliar application led to accelerated plant growth and overall development, as noted by Al-Hayali et al. (2018).

Table 8. Effect of nano and mineral iron fertilization and soil texture on biological yield (g plant^{-1}).

Effect S	Effect M	N3	N2	N1		
41.13	34.04	37.96	31.23	28.23	M1	S1
		44. 67	40.86	35.26	M2	
	40.34	52. 33	50.63	47.96	M3	
41.62	49.59	40. 33	36. 33	30.16	M1	S2
		46.00	42. 00	33.26	M2	
		52.33	49. 67	44. 67	M3	
LSD N= 0.3709 M= 0.3709 S= 0.3028 MNS= 0.9084		45.60	41.78	36.59	Effect N	

Conclusion

This study concludes that the application of nanotechnology in iron fertilization, whether via foliar spray or soil addition, led to a significant advancement in all morphological and yield parameters of the wheat plant. The

(M3N3) treatment demonstrated exceptional efficiency in maximizing biological yield and seed weight. This success is attributed to the ability of nanoparticles to rapidly penetrate through stomata and cell membranes, subsequently activating enzymes responsible for chlorophyll biosynthesis and photosynthesis. Furthermore, the results indicated that the interaction between fertilizer type and soil texture at the Al-Rashidiya site (S2) effectively enhanced nutrient uptake efficiency. This synergy promoted the initiation of tiller primordia and mitigated oxidative stress within plant tissues, ultimately The study demonstrates that iron fertilization (both nano and mineral) significantly improved all growth and yield parameters of the wheat plant. The conclusions are summarized as follows:

1. *Superiority of Nanotechnology:* Nano-fertilizers exhibited high efficiency, particularly via foliar application (N3), in enhancing plant height, leaf area, and chlorophyll concentration. This reflects the superior penetration ability of nanoparticles into plant tissues.
2. *Enhanced Photosynthetic Efficiency***:** Improved iron uptake increased the utilization of Photosynthetically Active Radiation (PAR), which supported tiller primordia initiation and subsequently increased dry weight, shoot biomass, and biological yield.
3. *Triple Interaction Effects:* The interaction between foliar application, nano/mineral fertilizers, and soil texture at the Al-Rashidiya site (S2) yielded the highest biological yield and seed fresh weight, indicating the role of soil properties in maximizing fertilization efficiency.
4. *Protective Role:* Nano-iron contributed to reducing oxidative stress (ROS) and delaying senescence, thereby maintaining vegetative vigor for a longer duration.

Recommendations

1. *Adopting Foliar Application***:** It is recommended to utilize foliar spray techniques for nano and mineral fertilizers as an alternative or supplement to soil application to ensure rapid absorption and avoid iron fixation in the soil.
2. *Integrated Fertilization:* Implementing the (M3N3) combination is advised to achieve maximum biological yield and seed weight, especially in soils with textures similar to the Al-Rashidiya site.
3. *Economic Studies:* Conducting an economic feasibility study to compare the cost of nano-fertilizers against the qualitative increase in yield to encourage farmers to adopt these technologies.
4. *Expanding Research:* Further investigation is suggested regarding the impact of various nano-iron concentrations on grain quality (protein and starch content) across different growing seasons.

Scientific Ethics Declaration

* The authors declare that the scientific ethical and legal responsibility of this article published in EPSTEM Journal belongs to the authors.

Conflict of Interest

* The author declares that there is no conflict of interest

Funding

* This research received no external funding

Acknowledgements or Notes

* This article was presented as an oral presentation at the International Conference on Basic Sciences, Engineering and Technology (www.icbaset.net) held in Istanbul/Türkiye on September 17-18, 2026.

* The authors thank the College of Agriculture and Forestry, University of Mosul for providing laboratory facilities and technical support during this research.

* This research is extracted from the author's Master's thesis

References

Abdul-Jabbar, G. (2017). Effect of mineral compound fertilizer application and micronutrients spraying in growth and faba bean yield. *Journal of University of Babylon for Pure and Applied Sciences, 25*(6), 2078–2087.

Abobatta, W. F. (2017). Green synthesis and antimicrobial activity of iron nanoparticles. *International Journal of Current Research in Biosciences and Plant Biology, 4*(5), 1–9. Retrieved from https://www.ijcrbp.com/

Abu Batta, O. H. (2016). Nano-fertilizers and their impact on plant growth. *Journal of Agricultural Research, 34*(2), 123–135. [In Arabic]. Retrieved from https://www.agriresearch.org/

Al-Ansi, L. H. G., & Al-Maghrabi, N. M. H. (2025). Effect of adding nano-iron fertilizer and commercial fertilizer on some soil properties and the growth of carrot plants (*Daucus carota* L. var. *sativa*). *Sana'a University Journal of Applied Sciences and Technology, 3*(4), 973–989.

Ali, A., & Al-Khayri, J. M. (2014). Effect of nitrogen fertilizer on the growth of hybrid sorghum (*Sorghum bicolor* L.) and Sudan grass. *Journal of Applied Sciences Research, 3*(9), 867–872. Retrieved from https://www.aensiweb.com/old/jasr/jasr/2007/867-872

Al-Rawi, M. K. (1977). *Applied statistics in agricultural research*. [In Arabic].

Al-Sahaf, M. A. (1989). *Plant analysis techniques*. [In Arabic].

Association of Official Analytical Chemists. (1970). *Official methods of analysis* (11th ed.). AOAC International. Retrieved from https://www.aoac.org/

Black, C. A. (1965). *Methods of soil analysis: Part I—Physical and mineralogical properties*. American Society of Agronomy. Retrieved from https://www.scribd.com/document/393540059/

Bremner, J. M., & Edwards, A. P. (1965). Determination and isotope-analysis of different forms of nitrogen in soils: I. Apparatus and procedure for total nitrogen analysis. *Soil Science Society of America Journal, 29*(6), 111–116.

Brill, W. J. (1980). Nitrogenase: Structure, function, and mechanism. *Annual Review of Biochemistry, 49*, 1–15.

Cerovic, Z. G., Masdoumier, G., Ghozlen, N. B., & Latouche, G. (2012). A new optical leaf-clip meter for simultaneous non-destructive assessment of leaf chlorophyll and epidermal flavonoids. *Plant, Cell & Environment, 35*(3), 535–544. Retrieved from https://onlinelibrary.wiley.com

Chafi, M., & Bensoltan, S. (2009). *Vicia faba* (L.), a source of organic and biological manure for the Algerian arid regions. *Research Journal of Agriculture and Biological Sciences, 5*(6), 1024–1029. Retrieved fromhttps://www.researchgate.net/publication/238729322_Vicia_faba_L_A_Source_of_Organic_and_Biological_Manure_for_the_Algerian_Arid_Regions

Filipponi, L., & Sutherland, D. (2013). Green synthesis and characterization of iron oxide nanoparticles. *Journal of Nanoscience and Nanotechnology, 13*(9), 6351–6356.

Food and Agriculture Organization. (1973). *Calcareous soils* (FAO Soils Bulletin No. 21). Retrieved from https://www.fao.org/3/x5868e/x5868e00.htm

Gee, G. W., & Bauder, J. W. (1986). Particle-size analysis. In A. Klute (Ed.), *Methods of soil analysis: Part 1—Physical and mineralogical methods* (2nd ed., pp. 383–411). American Society of Agronomy. Retrieved from https://acsess.onlinelibrary.wiley.com

Goh, C. H., Tan, K. H., & Lee, S. K. (2000). Effects of iron on chlorophyll synthesis and growth of soybean. *Journal of Plant Nutrition, 23*(4–6), 621–633.

Gupta, U. C. (1999). *Handbook of reference methods for plant analysis*. PlantStress. Retrieved from https://plantstress.com/wpcontent/uploads/2020/03/Handbook_of_Reference_Methods_for_Plant_Analysis-1998

Hallmark, C. T., & Loeppert, R. H. (1985). Indigenous soil properties influencing the availability of iron in calcareous soils. *Soil Science Society of America Journal, 49*(3), 597–603.

Jones, D. L., & Kobayashi, T. (2019). Iron and chlorophyll synthesis in plants. *Plant and Soil, 435*(1–2), 1–12.

Kandil, H. (2007). Effect of cobalt fertilizer on growth, yield and nutrients status of faba bean (*Vicia faba* L.) plants. *Journal of Applied Sciences Research, 3*(9), 867–872. Retrieved from https://www.aensiweb.com/old/jasr/jasr/2007/867-872

Klute, A. (Ed.). (1986). *Methods of soil analysis: Part 1—Physical and mineralogical methods* (2nd ed.). American Society of Agronomy. Retrieved from https://books.google.com/books/about/Methods_of_Soil_Analysis.html?id=0lxRAAAAMAAJ

Lucena, J. J., & Chaney, R. L. (2007). Synthetic iron chelates as substrates of root ferric chelate reductase in green stressed cucumber plants. *Journal of Plant Nutrition, 30*(3), 413–426.

Mohammed, Z. M. (2022). Effect of spraying three types of foliar fertilizers on the growth and yield of faba bean (*Vicia faba* L.). *Journal of Kirkuk University for Agricultural Sciences, 13*(2).

Morales-Díaz, A., García, M. J., & García-Mina, J. M. (2017). Iron nutrition in plants: From the soil to the leaf. *Frontiers in Plant Science, 8*, 1380.

Natalia, S., & Alvarado, J. (2008). Seed mineral composition and protein content of faba beans (*Vicia faba* L.). *Journal of Agricultural and Food Chemistry, 56*(14), 5743–5749.

Olsen, S. R., & Sommers, L. E. (1982). Phosphorus. In A. L. Page, R. H. Miller, & D. R. Keeney (Eds.), *Methods of soil analysis: Part 2—Chemical and microbiological properties* (2nd ed., pp. 403–430). American Society of Agronomy. Retrieved from https://acsess.onlinelibrary.wiley.com

Page, A. L., Miller, R. H., & Keeney, D. R. (1982). *Methods of soil analysis: Part 2—Chemical and microbiological properties* (2nd ed., Agronomy Monograph No. 9). American Society of Agronomy. Retrieved from https://acsess.onlinelibrary.wiley.com

Quraishi, M. F., et al. (2018). Nano-fertilizers and improving nutrient use efficiency. *Journal of Agricultural Sciences, 60*(1), 78–89. [In Arabic]. Retrieved from https://www.agrisciencejournal.com/

Rabih, F. M. Y., Abdul Jalil, L. F., Ahmida, F. M., & Mansour, Z. F. (2023). Effect of nitrogen fertilization and spraying with iron, manganese, and zinc elements on the volatile oil yield of tea apple plants grown in the Al-Jabal Al-Akhdar region. *Bani Waleed University Journal of Humanities and Applied Sciences, 8*(4), 18–32.

Roosta, H. R., & Hamidpour, M. (2015). Effect of iron and zinc on photosynthetic pigments and chlorophyll fluorescence in lettuce. *Photosynthetica, 53*(2), 222–229.

Rout, G. R., & Sahoo, S. (2015). Role of iron in plant growth and metabolism. *Review in Agricultural Science, 3*, 1–24.

Rowell, D. L. (1996). *Soil science: Methods and applications*. Longman Group UK Ltd. Retrieved from https://books.google.com/books/about/Soil_Science.html?id=skG1QgAACAAJ

Saeed, M. M., & Al-Khayri, J. M. (2012). Iron deficiency and its effect on plant growth and metabolism. *International Journal of Agriculture and Biology, 14*(6), 1017–1022. Retrieved from https://www.fspublishers.org/published_papers/14216

Sajet, A. M. (2022). The role of iron in human and plant health. *Journal of Agricultural Sciences, 58*(3), 45–59. [In Arabic]. Retrieved from https://www.iasj.net/iasj/article/234567

SAS Institute Inc. (2012). *SAS/STAT® 12.1 user's guide*. SAS Institute Inc. Retrieved from https://support.sas.com/documentation/onlinedoc/stat/121/intro

Sotiropoulos, T., & Mouhtaridou, G. (2005). Use of a SPAD-502 meter to measure leaf chlorophyll concentration in *Arabidopsis thaliana*. *PubMed*. Retrieved from https://pubmed.ncbi.nlm.nih.gov/21188527/

Tandon, H. L. S. (1999). *Methods of analysis of soils, plants, waters, fertilizers & organic manures*. Fertilizer Development and Consultation Organization. Retrieved from https://scholar.google.com/citations?user=9wTTzuAAAAAJ

Tisdale, S. L., Nelson, W. L., Beaton, J. D., & Havlin, J. L. (1997). *Soil fertility and fertilizers* (5th ed.). Prentice Hall. Retrieved from https://www.amazon.com/Soil-Fertility-Fertilizers-Tisdale/dp/0134431145

United States Department of Agriculture. (2006). *Keys to soil taxonomy* (10th ed.). Natural Resources Conservation Service, USDA. Retrieved from https://www.nrcs.usda.gov/sites/default/files/2022-10/soils_keys_to_soil_taxonomy

Wylie, S. J. (2018). An overview of global leaf area index (LAI): Methods, products, and applications. *Reviews of Geophysics, 56*(4), 712–740.

Author(s) Information

Maryam Abdulkader Albadranie
University of Mosul, Department, College of Agriculture and Forestry, Soil Sciences and Water Resources, Mosul, Iraq
ORCID iD: https://orcid.org/0009-0009-9352-1174

Rana Saadallah Aziz
University of Mosul, Department of Soil Science and Water Resources College of Mosul, Iraq
ORCID iD: https://orcid.org/0009-0007-6918-2817
*Contact e-mail: rana.saadallah1979@uomosul.edu.iq

*Corresponding author(s) contact e-mail

To cite this article:

Albadranie, M.A. & Aziz, R.S. (2026). Efficiency of nano and mineral iron in sustaining faba bean (Vicia Faba L.) productivity within different soil orders. *The Eurasia Proceedings of Science, Technology, Engineering and Mathematics (EPSTEM), 42,* 211-222.

The Eurasia Proceedings of Science, Technology, Engineering and Mathematics (EPSTEM)
ISSN: 2602-3199

The Eurasia Proceedings of Science, Technology, Engineering and Mathematics (EPSTEM), 2026

Volume 42, Pages 223-228

ICBASET 2026: International Conference on Basic Sciences, Engineering and Technology

3D Printing in Shipbuilding and Ship Repair Industry: Challenges and Opportunities

Yordan Denev
Technical University of Varna

Abstract: In the article, the possibilities and challenges of using 3D printing in the shipbuilding and ship repair industry are discussed. This technology enables the fast and efficient production of spare parts, elements, and components required for these industries. To a certain extent, this leads to reduced repair time, faster deliveries, and lower dependence on maintaining permanent warehouse stock. Technology also allows the production of lighter, more efficient, and relatively complex structures. In addition, it helps reduce the generated carbon footprint. The challenges facing the shipbuilding and ship repair industry in the use of 3D printing are related to several aspects. The first is purely technological and focuses on integrating components produced by this method into the ship's hull structure. The second aspect is related to the certification of the parts and their durability throughout the ship's life cycle. The third aspect concerns the economic factors associated with equipment, consumables, and maintenance. Nevertheless, the method of 3D printing cannot completely replace traditional shipbuilding and repair processes, but it can support and facilitate these industries to a certain extent.

Keywords: Shipbuilding, Ship repair, Printing, 3D, Challenges

Introduction

The use of 3D printing has been known for more than 40 years. The first experiment with this type of printer was conducted in the United States in 1983. In its early stages of development, the technology was primarily used for rapid and cost-effective prototyping. Over the decades, this manufacturing method has undergone continuous improvement and modernization across virtually all industrial sectors. Today, 3D printing is employed to produce custom-designed components, architectural models, and large-scale parts for industrial applications. The emergence of Industry 4.0 and Industry 5.0 has placed industry in a state of transformation aimed at maintaining competitiveness. Shipbuilding and ship repair, as integral parts of the industrial sector, are also facing this transformation. In line with this trend, these two industries must adapt to fundamental technologies, artificial intelligence, reengineering throughout the product life cycle, and other related innovations.

The use of 3D printing for the production of ship models is presented in (Choi, 2024). This approach has proven to be particularly effective for models of high-speed vessels with high Froude numbers. An algorithm for the application of modular 3D printing in model manufacturing has been developed. The use of this approach reduces the time required for model production and allows significant modifications to the hull form design when necessary. In the manufacture of ship models intended for assessing the performance characteristics of the full-scale vessel, similarity is of critical importance, as it has a direct impact on the accuracy of the results. Experimental investigations have demonstrated a high level of accuracy when this method is employed.

Over the years, 3D printing has made significant advances across engineering industries. The emergence of 4D printing has further accelerated this process. This technology enables the creation of complex shapes and structures, which can be produced much more easily than through traditional manufacturing processes. The primary materials used in 4D printing include carbon fibers, wood-grain programmable materials, and

- This is an Open Access article distributed under the terms of the Creative Commons Attribution-Noncommercial 4.0 Unported License, permitting all non-commercial use, distribution, and reproduction in any medium, provided the original work is properly cited.

- Selection and peer-review under responsibility of the Organizing Committee of the Conference

© 2026 Published by ISRES Publishing: www.isres.org

programmable textiles. These materials exhibit high tensile strength and low weight, making them highly desirable for a wide range of engineering applications (Haleem,2021). The application of 3D printing as a smart manufacturing technology is presented in (Endharta,2018). This technology, together with the Internet of Things (IoT), cloud computing, and other advanced digital solutions, has been developed and implemented. Measures have been identified to improve manufacturing through optimization techniques and strategic approaches applied at various stages of the shipbuilding production process.

3D printing is a more sustainable manufacturing method compared to traditional technologies. It is not only cost-effective and efficient but also environmentally friendly, contributing to the reduction of pollution. As technology has evolved, the range of materials used has expanded significantly and is no longer limited to polymers. Different 3D printing methods have their own advantages and disadvantages, enabling the processing of both complex and simpler materials. The FDM process is among the most widely used technologies and is particularly suitable for working with polymer materials. On the other hand, one of the main challenges of SLS technology is the transportation and storage of the powdered materials used in the process (Mughir, 2022).

3D Printing in the Shipbuilding and Ship Repair Industry

The use of additive manufacturing is becoming increasingly widespread in shipbuilding and ship repair. One of the technologies included in this type of manufacturing is 3D printing. Its use enables the rapid production of components compared to traditional manufacturing methods, facilitates supply and logistics, and reduces costs. On the other hand, additive manufacturing contributes to the optimization of logistics processes by reducing the inventory of spare components for ship systems. Instead of maintaining large stocks of physical spare parts, their digital models can be stored, enabling rapid on-demand production whenever required. This approach reduces vessel downtime and improves the efficiency of repair and maintenance operations. For example, the production of a ship propeller using 3D printing technology can be completed in significantly less time compared to conventional manufacturing methods (Fig. 1).



Figure 1. 3D printed ship propeller (Ship- shape)

Current trends in the European shipbuilding industry are focused on the construction of specialized vessels designed to perform specific operational tasks. In most cases, these vessels feature more complex structural designs and components with intricate geometries, creating favorable conditions for the application of additive manufacturing technologies (Fig. 2).

The application of 3D printing in ship repair has also experienced significant development. During repair operations, this approach can be used for the rapid production of components and parts for machinery and equipment that require immediate replacement, particularly when their delivery through the conventional supply chain would involve considerable delays. Furthermore, certain stages of the 3D printing process can be carried out on board the vessel, even while it is at sea (Fig. 3).



Figure 2. Catamaran hull (CEAD group)



Figure 3. 3D printed part for ship repair (The Salty Mariner)

Challenges and Opportunities of 3D Printing in Shipbuilding and Ship Repair

The challenges and opportunities of implementing 3D printing in shipbuilding and ship repair can be classified into three main groups: technical, technological, and related to certification and regulatory compliance (Figure 4). The main challenges associated with the application of 3D printing in shipbuilding and ship repair are related to the materials employed, the scale of component production, the required manufacturing accuracy, and the certification of personnel involved in additive manufacturing processes. Regarding the materials used for component manufacturing, ferrous and non-ferrous alloys, various polymers, metal powders, and rubber are commonly employed. Their application in shipbuilding and ship repair requires certification by the classification societies responsible for the survey and certification of vessels operating within the modern commercial fleet.

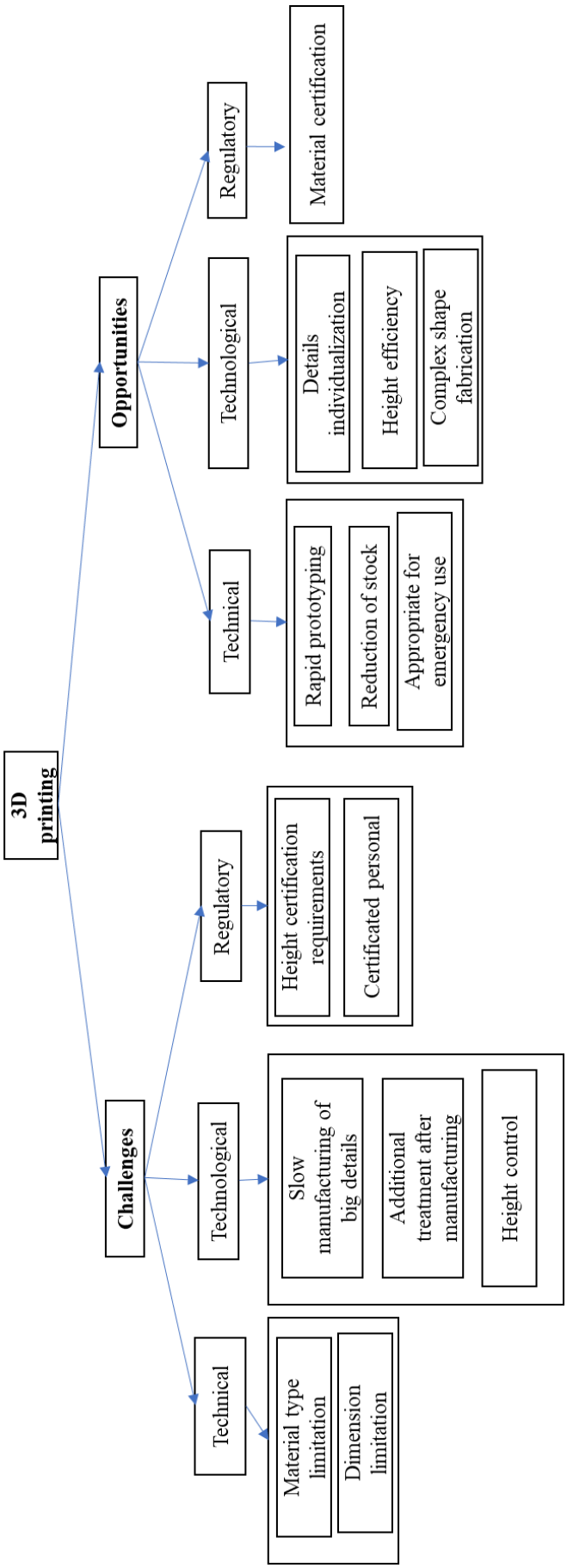

Figure 4. Challenges and opportunities of 3D printing in shipbuilding and ship repair

An important challenge for the application of 3D printing in shipbuilding and ship repair is the size and scale of the components. For this reason, this manufacturing method is currently most suitable for producing parts for marine machinery and mechanical systems. Furthermore, the manufactured components require subsequent machining to achieve the required surface roughness and dimensional tolerances where necessary. All of these requirements are met through a high level of control and precision already at the stage of designing the model for 3D printing.

A particularly important challenge is related to regulatory requirements, more specifically, those imposed by classification societies. These organizations are directly responsible for the certification of both the materials used and the operators performing the manufacturing process. The requirements are stringent, as components produced by 3D printing must satisfy all applicable mechanical strength and technological criteria to ensure their reliable and safe operation.

The potential applications of 3D printing in the maritime industry are extensive. When considered within the context of technical, technological, and regulatory aspects, these capabilities enable the implementation of this manufacturing method at various stages of shipbuilding, particularly in ship repair. From a technical perspective, the capabilities of 3D printing include rapid prototyping, reducing the need for maintaining extensive inventories of spare parts, and manufacturing components for emergency repairs.

Other significant possibilities of this manufacturing method include its high efficiency and the ability to produce customized components with complex geometries, which are commonly encountered in shipbuilding and ship repair. From a regulatory perspective, the main advantages are closely related to the certification of the materials used in the manufacturing process, ensuring the reliability, safety, and operational performance of the ship's systems.

Conclusion

The article examines the challenges and opportunities associated with the use of 3D printing in shipbuilding and ship repair. For each category, the potential challenges and opportunities are analyzed according to three criteria: technical, technological, and regulatory. The manufacturing of components involves the use of various metallic alloys, polymers, metal powders, and elastomeric materials, all of which must possess the required certifications, as this is a regulatory requirement. A significant challenge is the limitation related to the size of the manufactured components and the materials used for their production. The purpose of certification is to ensure the operational reliability and functionality of parts produced through this method. In addition, the accuracy of the digital model must be carefully controlled in accordance with the specified dimensional tolerances and the required surface quality of the finished component.

The capabilities of this manufacturing method are extensive and versatile. One of its most important advantages is the rapid production of prototypes, which significantly reduces the need to maintain large inventories of spare parts and components. High productivity is particularly valuable in dynamic industries such as ship repair, and when combined with the ability to manufacture components with complex geometries, it makes the process highly suitable for applications in the maritime sector.

Furthermore, recent amendments to the regulations of classification societies have introduced specific procedures governing the use of components manufactured through 3D printing. These developments facilitate the wider adoption of additive manufacturing technologies while ensuring compliance with safety, quality, and certification requirements.

Scientific Ethics Declaration

* The author declares that the scientific ethical and legal responsibility of this article published in EPSTEM Journal belongs to the author.

Conflict of Interest

* The author declares that there is no conflict of interest.

Funding

* The author received no financial support for the research, authorship, and publication of this article.

Acknowledgements or Notes

* This article was presented as an oral presentation at the International Conference on Basic Sciences, Engineering and Technology (www.icbaset.net) held in Istanbul/Türkiye on September 17-18, 2026.

References

CEAD Group. (n.d.). 3D printing in boat manufacturing. Retrieved from https://ceadgroup.com/resources/blog/3d-printing-in-boat-manufacturing/

Choi, L., Choi, M., Kwon, S., Youn, D., & Song, G. (2024). Modular production of small ship models using 3D printing for model tests. *Ocean Engineering, 302*.

Endharta, A., Norita, D., Singgih, I., Putra, A., Singgih, M., Setyorini, P., & Dinariyana, A. (2018). Smart manufacturing concept in shipbuilding process with related optimization issues and strategies. In *Proceeding of Marine Safety and Maritime Installation* (pp. 191–199).

Haleem, A., Javaid, M., Singh, R., & Suman, R. (2021). Significant roles of 4D printing using smart materials in the field of manufacturing. *Advanced Industrial and Engineering Polymer Research, 4*, 301–311.

Mughir, W. (2022). A review in 3D printing technique: Types, applications and process parameters. *Journal of University of Babylon for Engineering Science, 30*(3), 33–49.

Ship-shape: The world's first 3D printed marine propeller. (n.d.). Retrieved from https://www.theengineer.co.uk/content/advanced-manufacturing/ship-shape-the-worlds-first-3d-printed-marine-propeller

The Salty Mariner. (n.d.). 3D printing in maritime: Additive manufacturing for ship parts and repairs. Retrieved from https://www.thesaltymariner.com/posts/3d-printing-maritime-additive-manufacturing-ship-parts

Author(s) Information

Yordan Denev
Technical University of Varna
Studentska 1 str., Bulgaria
ORCID iD: https://orcid.org/0000-0001-7124-1600
*Contact e-mail: *y.denev@tu-varna.bg*

*Corresponding author(s) contact email

To cite this article:

Denev, Y. (2026). 3D printing in shipbuilding and ship repair industry: Challenges and opportunities. *The Eurasia Proceedings of Science, Technology, Engineering and Mathematics (EPSTEM), 42,* 223-228.

The Eurasia Proceedings of Science, Technology, Engineering and Mathematics (EPSTEM)
ISSN: 2602-3199

The Eurasia Proceedings of Science, Technology, Engineering and Mathematics (EPSTEM), 2026

Volume 42, Pages 229-236

ICBASET 2026: International Conference on Basic Sciences, Engineering and Technology

Deep Learning-Based Classification of Archaeological Artifacts Using Image Processing

Fatma Ozge Ozkok
Erciyes University

Abstract: The classification of archaeological artifacts according to their material types is important for archaeological documentation and analysis. This study evaluates five convolutional neural network (CNN) architectures for the classification of archaeological artifact images. A balanced dataset containing 1,000 images from four material classes, namely ceramic, glass, metal, and stone, was used. Five CNN architectures, SqueezeNet1.1, MNASNet0.5, RegNetX-200MF, FasterNet-T0, and InceptionNeXt-Tiny, were evaluated using stratified five-fold cross-validation. Model performance was assessed using accuracy, precision, recall, F1-score, and confusion matrices. The experimental results showed that InceptionNeXt-Tiny achieved the highest average accuracy of 90.70 ± 0.76% and F1-score of 90.66 ± 0.76%. RegNetX-200MF and FasterNet-T0 achieved average accuracies of 87.50% and 86.20%, respectively. Confusion matrix analysis showed that classification errors varied across material classes, particularly between glass and metal and between ceramic and stone. The results demonstrate the potential of CNN architectures for automated material classification of archaeological artifacts.

Keywords: Archaeological artifacts, Material classification, Convolutional neural networks, Deep learning, Image classification.

Introduction

Archaeological artifacts provide important information about past civilisations, including details of their cultural, technological and artistic developments. They are commonly examined according to their material, shape, production technique and historical period (Kowalski et al., 1972; Rouse, 1960). Ceramics, metals, stones, and glasses are among the materials frequently encountered in archaeological collections. Classifying these objects is important for archaeological research, museum documentation and organising digital collections (Mikhailova et al., 2019). The growing accessibility of digitised museum collections has given rise to opportunities for the application of image processing and machine learning techniques (Bertacchini & Morando, 2013; Li et al., 2012). Traditional classification approaches typically necessitate manual examination and expert knowledge. However, the sheer quantity of objects in museum collections means manual classification is extremely time-consuming. Automated image classification methods can support the identification and organisation of archaeological artifacts based on their visual characteristics (Mnasri & D'Andrea, 2025).

Deep learning methods, particularly convolutional neural networks (CNNs), have been widely used in image classification tasks. CNN architectures can automatically extract visual features such as edges, textures, shapes, and spatial patterns from images (Nani et al., 2025). Different CNN architectures have been developed to improve classification performance while reducing model parameters and computational requirements. Lightweight architectures provide different approaches for image classification tasks (Chen et al., 2024; Zhou et al., 2020).

In this study, five CNN architectures, including SqueezeNet1.1, MNASNet0.5, RegNetX-200MF, FasterNet-T0, and InceptionNeXt-Tiny, were employed for material-based classification of archaeological artifacts. A dataset containing 1,000 images was prepared from the publicly available iMet Open Access dataset. The artifacts were

- This is an Open Access article distributed under the terms of the Creative Commons Attribution-Noncommercial 4.0 Unported License, permitting all non-commercial use, distribution, and reproduction in any medium, provided the original work is properly cited.

- Selection and peer-review under responsibility of the Organizing Committee of the Conference

© 2026 Published by ISRES Publishing: www.isres.org

divided into four classes, including ceramic, metal, stone, and glass, with 250 images in each class. Stratified five-fold cross-validation was used to evaluate the models. Classification performance was compared using Accuracy, Precision, Recall, and F1-score.

Related Works

Artificial intelligence and deep learning have been used in archaeology to identify, classify, and digitally document artifacts. Gattiglia (2025) reviewed the applications of artificial intelligence in archaeology and discussed the problems associated with archaeological data. The main issues included data quality, classification methods, and the limitations of AI-based approaches.

Gualandi et al. (2021) developed an open system for identifying archaeological pottery using neural network algorithms. Their work focused on the shape and decoration of pottery and included two approaches for identifying archaeological ceramics. Cintas et al. (2020) used deep convolutional networks for feature extraction and classification of Iberian ceramics. Their experiments were based on profile images of wheel-made pottery vessels.

Resler et al. (2021) combined an ImageNet-pretrained EfficientNetB3 model with metric learning to classify archaeological artifacts and identify archaeological communities. Artifacts from different archaeological sites and historical periods were included in their analysis. For rock art identification, Jalandoni et al. (2022) investigated machine learning methods and developed an approach for identifying photographs containing painted rock art. Tsigkas et al. (2020) addressed a related task involving the automatic detection of ancient rock carvings using image-based recognition methods.

Grove and Blinkhorn (2020) investigated the differences between Middle and Later Stone Age lithic assemblages in eastern Africa. They used artificial neural networks for classification. Their classification was based on the presence or absence of 16 technological characteristics, and more than 94% of the assemblages were correctly classified. Mnasri and D'Andrea (2025) investigated the use of object detection and deep learning for the automatic inventory of archaeological artifacts. Their work included object identification and material-based classification. They also compared their approach with transfer learning models such as SqueezeNet and GoogLeNet.

Previous studies have investigated different applications of deep learning in archaeology, including pottery classification, rock art detection, and artifact identification. In this study, we classified archaeological artifacts into four groups based on their materials: ceramic, metal, stone, and glass. Five CNN models with different convolutional structures were evaluated using the same dataset and experimental procedure. We compared their classification results using accuracy, precision, recall, F1-score, and confusion matrices.

Method

This section describes the dataset, CNN architectures, experimental setup, and performance evaluation methods used in this study.

Dataset

The dataset used in this study was obtained from the publicly available iMet Open Access dataset, which is based on The Metropolitan Museum of Art's Open Access collection. The dataset is related to the iMet Collection 2019 Challenge Dataset described by Zhang et al. (2019). Archaeological artifacts were selected from the Ancient West Asian Art, Egyptian Art, and Greek and Roman Art departments. The first seven training files were examined, containing 4,477 records from these departments. Objects with missing end dates or end dates later than 1500 CE were excluded.

The artifacts were put into four groups based on the material they were made of, including ceramic, metal, stone, and glass, using the material information provided in the metadata. The Ceramic class included things made of terracotta, pottery, ceramic and faience. The Metal class included bronze, gold, silver, copper, iron, and lead objects. The Stone class included limestone, marble, granite, sandstone, and alabaster objects. The Glass class included objects made of glass.

After filtering, 3,293 artifacts remained, including 2,273 ceramic, 468 metal, 277 stone, and 275 glass objects. From these records, 250 artifacts were randomly selected for each class using a random seed of 42. The final dataset consisted of 1,000 images, with 250 images in each class.

Table 1. Distribution of archaeological artifacts by material

Class	Eligible artifacts	Selected artifacts
Ceramic	2,273	250
Metal	468	250
Stone	277	250
Glass	275	250
Total	3,293	1,000

The distribution of the selected artifacts is presented in Table 1. Representative images from each material class are shown in Figure 1.

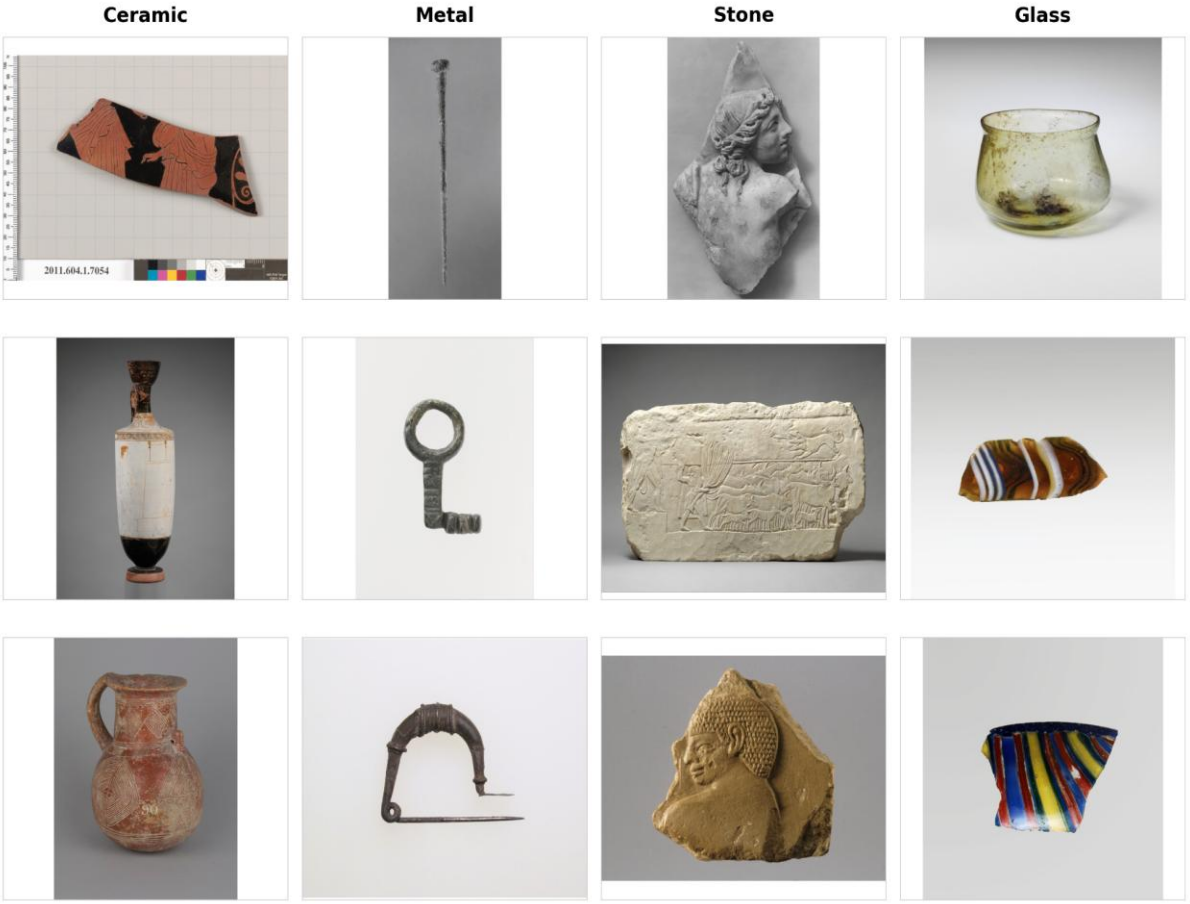

Figure 1. Sample images of archaeological artifacts from the four material classes.

CNN Architectures

Five CNN architectures were used to classify archaeological artifacts. These were SqueezeNet1.1, MNASNet0.5, RegNetX-200MF, FasterNet-T0, and InceptionNeXt-Tiny. The models have different convolutional structures, and their classification results were compared under the same experimental conditions. SqueezeNet1.1 uses Fire modules to extract image features with fewer parameters. Each Fire module contains a squeeze layer with 1 × 1 convolutions and an expand layer with both 1 × 1 and 3 × 3 convolutions (Iandola et al., 2016).

MNASNet0.5 was developed using neural architecture search. The model uses mobile inverted bottleneck blocks and depthwise separable convolutions. Compared with the standard MNASNet architecture, the 0.5 width multiplier reduces the number of channels (Tan et al., 2019). RegNetX-200MF uses grouped convolutions and a regular network structure in which channel widths increase across stages. Its network configuration is determined

using a parameterized design. The 200MF version was developed for a computational budget of approximately 200 million floating-point operations (Radosavovic et al., 2020).

FasterNet-T0 applies partial convolutions to only some of the input channels. The other channels are not processed by spatial convolutions and are later combined with the processed channels. This design aims to reduce unnecessary computations during feature extraction (Chen et al., 2023).
InceptionNeXt-Tiny uses depthwise convolutions together with an Inception-based structure. Different convolutional kernels are applied in separate branches to extract spatial information. This structure is designed to reduce computational complexity (Yu et al., 2024).

All models were initialized with ImageNet-pretrained weights. The original classification layers were replaced to classify the four material classes. The same dataset partitions, training settings, and evaluation procedure were used for all models.

Experimental Setup

The experiments were conducted using Python and PyTorch in Google Colab with an NVIDIA A100 GPU. Stratified five-fold cross-validation was used to evaluate the classification performance of the five CNN architectures. In each fold, 80% of the dataset was allocated to training and validation, while the remaining 20% was used for testing. The training and validation data were further divided into 80% training and 20% validation sets. Accordingly, each fold contained 640 training, 160 validation, and 200 test images. The same data partitions were used for all models. All images were resized to 224 × 224 pixels and normalized using ImageNet mean and standard deviation values. Random horizontal flipping, rotation, and color jittering were applied to the training images. No data augmentation was applied to the validation and test images.

All models were trained using the AdamW optimizer with an initial learning rate of 0.0001, weight decay of 0.0001, and batch size of 32. The maximum number of training epochs was set to 20. A cosine annealing learning rate scheduler was used during training. Early stopping was applied with a patience of five epochs based on validation Macro F1-score. The model weights corresponding to the highest validation Macro F1-score were selected for testing. A fixed random seed of 42 was used for data partitioning.

Performance Evaluation

The classification performance of the models was evaluated using Accuracy, Precision, Recall, and F1-score. Macro averaging was applied to Precision, Recall, and F1-score to give equal importance to the four material classes. The evaluation metrics were calculated separately for each test fold, and the results were reported as mean and standard deviation across five folds. Confusion matrices were generated using the combined test predictions from all five folds to examine the classification performance of individual material classes.

Results and Discussion

The classification performance of five CNN architectures was evaluated using stratified five-fold cross-validation. The experiments were conducted on a balanced dataset containing 1,000 archaeological artifact images from four material classes. Model performance was evaluated using accuracy, precision, recall, and F1-score. The results are presented as mean ± standard deviation across five folds. In addition, confusion matrices were generated to examine class-specific classification performance and misclassification patterns.

Table 2. Classification performance of five CNN architectures

Model	Accuracy	Precision	Recall	F1-score
SqueezeNet1.1	82.50 ± 4.02	83.13 ± 3.95	82.50 ± 4.02	82.45 ± 4.05
MNASNet0.5	73.00 ± 3.18	75.20 ± 3.52	73.00 ± 3.18	72.94 ± 3.16
RegNetX-200MF	87.50 ± 2.81	87.94 ± 2.64	87.50 ± 2.81	87.46 ± 2.81
FasterNet-T0	86.20 ± 1.92	86.52 ± 1.71	86.20 ± 1.92	86.19 ± 1.88
InceptionNeXt-Tiny	90.70 ± 0.76	91.08 ± 0.76	90.70 ± 0.76	90.66 ± 0.76

Table 2 presents the classification results of the five CNN architectures. InceptionNeXt-Tiny achieved the highest average accuracy of 90.70 ± 0.76% and F1-score of 90.66 ± 0.76%. RegNetX-200MF achieved the second-highest

accuracy of 87.50 ± 2.81%, followed by FasterNet-T0 with 86.20 ± 1.92%. SqueezeNet1.1 achieved an average accuracy of 82.50 ± 4.02%, while MNASNet0.5 showed the lowest accuracy of 73.00 ± 3.18%. InceptionNeXt-Tiny also achieved the highest precision and recall values. The lower standard deviation of this model indicates more consistent classification performance across the five folds.

Figure 2 shows the confusion matrices for the five CNN architectures. Each material class is comprised of 250 images, resulting in 1,000 predictions for each model. The confusion matrices provide a detailed comparison of classification performance across the Ceramic, Glass, Metal, and Stone classes. SqueezeNet1.1 correctly classified 197 ceramic, 207 glass, 210 metal and 211 stone images. The highest level of confusion occurred between the glass and metal classes, with 34 glass images being misclassified as metal and 26 metal images being misclassified as glass. MNASNet0.5 performed relatively poorly in terms of classification, particularly for glass and metal. The model correctly classified 169 images of glass and 161 images of metal. The highest misclassification rate was observed between metal and stone, with 58 metal images being misclassified as stone. Additionally, 46 glass images were misclassified as metal.

The RegNetX-200MF model correctly classified 207 ceramic images, 221 glass images, 221 metal images and 226 stone images. The model demonstrated relatively consistent performance across all four categories. The highest misclassification rate was observed between the ceramic and stone classes, with 23 ceramic images being misclassified as stone. The FasterNet-T0 model correctly classified 212 ceramic, 213 glass, 217 metal and 220 stone images. The model performed similarly across the material classes, although 25 glass images were misclassified as metal.

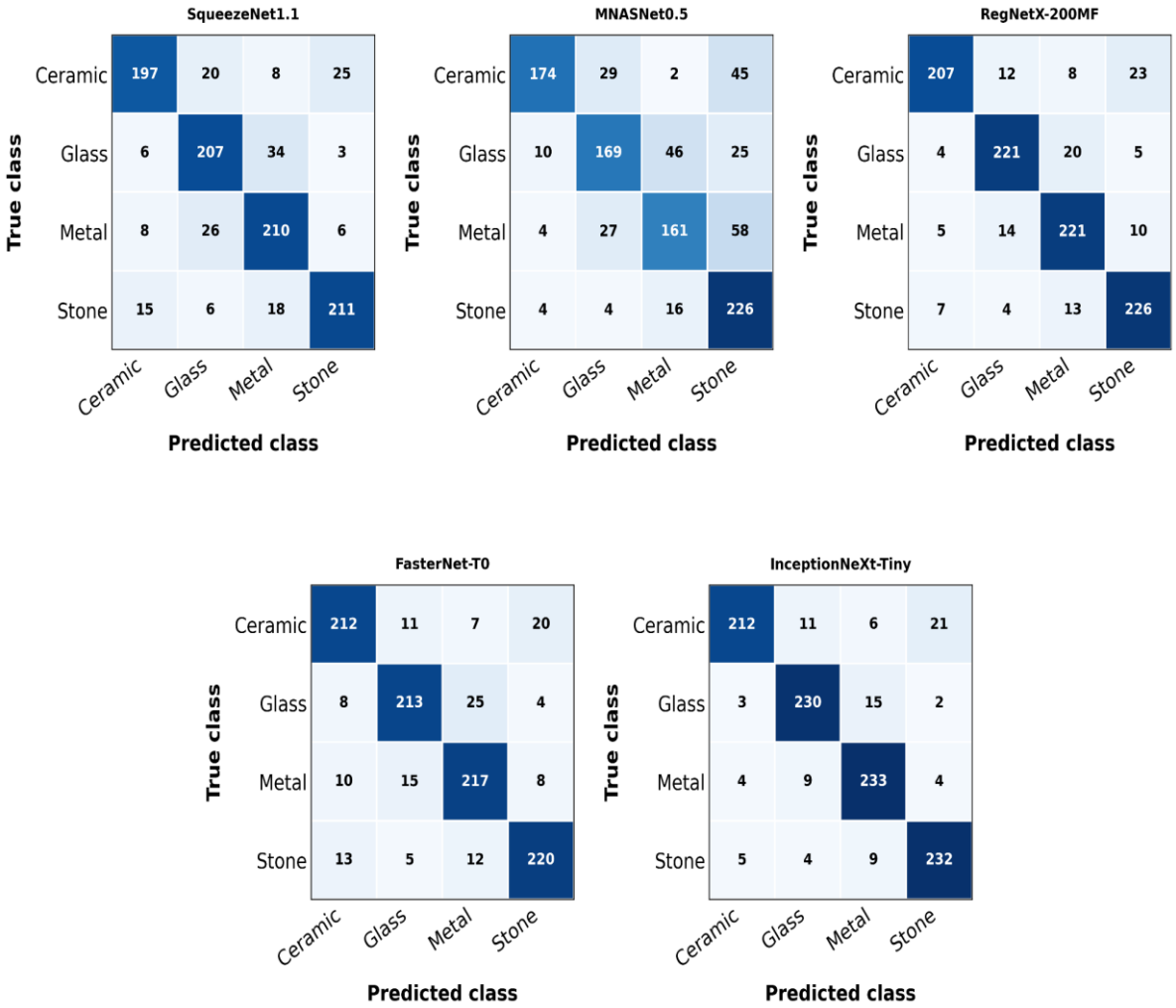

Figure 2. Confusion matrices of five CNN architectures

InceptionNeXt-Tiny achieved the highest number of correct predictions overall, correctly classifying 212 ceramic, 230 glass, 233 metal and 232 stone images. The model achieved the highest number of correct classifications for glass, metal and stone, while equalling FasterNet-T0's performance for ceramic. The highest misclassification rate

was between ceramic and stone, with 21 ceramic images being misclassified as stone. Compared with the other models, InceptionNeXt-Tiny produced fewer misclassifications, particularly for glass and metal.

Overall, InceptionNeXt-Tiny achieved the highest classification performance among the evaluated architectures. RegNetX-200MF and FasterNet-T0 also provided competitive results, while SqueezeNet1.1 and MNASNet0.5 showed lower performance. The confusion matrices revealed that classification errors were mainly observed between glass and metal and between ceramic and stone, although the error patterns differed across models. These results indicate that the evaluated CNN architectures can classify archaeological artifacts according to their material types, with differences in classification accuracy and consistency.

Conclusion

In this study, five CNN architectures were evaluated for the classification of archaeological artifacts into four material classes, namely Ceramic, Glass, Metal, and Stone. A balanced dataset containing 1,000 images was used, and the models were evaluated using stratified five-fold cross-validation. Classification performance was compared using accuracy, precision, recall, F1-score, and confusion matrices.

The experimental results showed that InceptionNeXt-Tiny achieved the highest classification performance, with an average accuracy of 90.70 ± 0.76% and F1-score of 90.66 ± 0.76%. RegNetX-200MF and FasterNet-T0 also achieved competitive results, with average accuracies of 87.50% and 86.20%, respectively. SqueezeNet1.1 and MNASNet0.5 showed lower classification performance. Confusion matrix analysis revealed that classification errors were mainly observed between Glass and Metal and between Ceramic and Stone, although the misclassification patterns varied across the models.

In summary, the results suggest that CNN architectures can be employed for the automated classification of materials in archaeological artifacts. However, the study was limited to a balanced dataset containing four material classes, so the generalisation performance on independent archaeological image collections remains to be evaluated.

Recommendations

Future studies may investigate transformer-based architectures for classifying archaeological artifacts. Additionally, lightweight CNN architectures could be optimised for deployment on mobile devices, enabling automated material classification in field applications.

Real-time image analysis could also be investigated to support archaeological documentation and material identification. Further experiments using larger datasets, additional material classes and independent image collections could provide a more comprehensive evaluation of classification performance and model generalisation.

Scientific Ethics Declaration

* The author declares that the scientific ethical and legal responsibility of this article published in EPSTEM Journal belongs to the author.

Conflict of Interest

* The author declares that there is no conflict of interest.

Funding

* Financial support was received through COST Action CA22143 – European Materials Informatics Network (EuMINe), supported by COST (European Cooperation in Science and Technology).

Acknowledgements or Notes

* This article was presented as an oral presentation at the International Conference on Basic Sciences, Engineering and Technology (www.icbaset.net) held in Istanbul/Türkiye on September 17-18, 2026.

* The author thanks the reviewers for their valuable feedback.

References

Bertacchini, E., & Morando, F. (2013). The future of museums in the digital age: New models for access to and use of digital collections. *International Journal of Arts Management, 15*(2), 60–72.

Chen, F., Li, S., Han, J., Ren, F., & Yang, Z. (2024). Review of lightweight deep convolutional neural networks. *Archives of Computational Methods in Engineering, 31*(4), 1915–1937.

Chen, J., Kao, S.-H., He, H., Zhuo, W., Wen, S., Lee, C.-H., & Chan, S.-H. G. (2023). Run, don't walk: Chasing higher FLOPS for faster neural networks. In *Proceedings of the IEEE/CVF Conference on Computer Vision and Pattern Recognition* (pp. 12021–12031).

Cintas, C., Lucena, M., Fuertes, J. M., Delrieux, C., Navarro, P., González-José, R., & Molinos, M. (2020). Automatic feature extraction and classification of Iberian ceramics based on deep convolutional networks. *Journal of Cultural Heritage, 41*, 106–112.

Gattiglia, G. (2025). Managing artificial intelligence in archeology: An overview. *Journal of Cultural Heritage, 71*, 225–233.

Grove, M., & Blinkhorn, J. (2020). Neural networks differentiate between Middle and Later Stone Age lithic assemblages in eastern Africa. *PLOS ONE, 15*(8), e0237528.

Gualandi, M. L., Gattiglia, G., & Anichini, F. (2021). An open system for collection and automatic recognition of pottery through neural network algorithms. *Heritage, 4*(1), 140–159.

Iandola, F. N., Han, S., Moskewicz, M. W., Ashraf, K., Dally, W. J., & Keutzer, K. (2016). *SqueezeNet: AlexNet-level accuracy with 50x fewer parameters and less than 0.5MB model size*. arXiv.

Jalandoni, A., Zhang, Y., & Zaidi, N. A. (2022). On the use of machine learning methods in rock art research with application to automatic painted rock art identification. *Journal of Archaeological Science, 144*, 105629.

Kowalski, B. R., Schatzki, T. F., & Stross, F. H. (1972). Classification of archaeological artifacts by applying pattern recognition to trace element data. *Analytical Chemistry, 44*(13), 2176–2180.

Li, Y. C., Liew, A. W. C., & Su, W. P. (2012). The digital museum: Challenges and solution. In *2012 8th International Conference on Information Science and Digital Content Technology (ICIDT2012)* (Vol. 3, pp. 646–649). IEEE.

Mikhailova, N., Mikhailova, E., & Grafeeva, N. (2019). The application of clustering techniques to group archaeological artifacts. In *World Conference on Information Systems and Technologies* (pp. 50–57). Springer International Publishing.

Mnasri, Z., & D'Andrea, A. (2025). Automatic inventory of archaeological artifacts based on object detection and classification using deep and transfer learning. *Digital Applications in Archaeology and Cultural Heritage, 39*, e00458.

Nani, P., Das, S., & Dey, S. (2025). Enhancing object recognition: A comprehensive analysis of CNN based deep learning models considering lighting conditions and perspectives. *Evolutionary Intelligence, 18*(4), Article 72.

Radosavovic, I., Kosaraju, R. P., Girshick, R., He, K., & Dollár, P. (2020). Designing network design spaces. In *Proceedings of the IEEE/CVF Conference on Computer Vision and Pattern Recognition* (pp. 10428–10436).

Resler, A., Yeshurun, R., Natalio, F., & Giryes, R. (2021). A deep-learning model for predictive archaeology and archaeological community detection. *Humanities and Social Sciences Communications, 8*, Article 295.

Rouse, I. (1960). The classification of artifacts in archaeology. *American Antiquity, 25*(3), 313–323.

Tan, M., Chen, B., Pang, R., Vasudevan, V., Sandler, M., Howard, A., & Le, Q. V. (2019). MnasNet: Platform-aware neural architecture search for mobile. In *Proceedings of the IEEE/CVF Conference on Computer Vision and Pattern Recognition* (pp. 2820–2828).

Tsigkas, G., Sfikas, G., Pasialis, A., Vlachopoulos, A., & Nikou, C. (2020). Markerless detection of ancient rock carvings in the wild: Rock art in Vathy, Astypalaia. *Pattern Recognition Letters, 135*, 337–345.

Yu, W., Zhou, P., Yan, S., & Wang, X. (2024). InceptionNeXt: When Inception meets ConvNeXt. In *Proceedings of the IEEE/CVF Conference on Computer Vision and Pattern Recognition* (pp. 5672–5683).

Zhang, C., Kaeser-Chen, C., Vesom, G., Choi, J., Kessler, M., & Belongie, S. (2019). *The iMet Collection 2019 Challenge Dataset* [Preprint]. arXiv.

Zhou, Y., Chen, S., Wang, Y., & Huan, W. (2020). Review of research on lightweight convolutional neural networks. In *2020 IEEE 5th Information Technology and Mechatronics Engineering Conference (ITOEC)* (pp. 1713–1720). IEEE.

Author(s) Information

Fatma Ozge Ozkok
Erciyes University, Department of Computer Engineering,
Kayseri, Türkiye
ORCID iD: https://orcid.org/0000-0002-1421-4670
*Contact e-mail: *fozgeozkok@erciyes.edu.tr*

*Corresponding author(s) contact email

To cite this article:

Ozkok, F.O. (2026). Deep learning-based classification of archaeological artifacts using image processing. *The Eurasia Proceedings of Science, Technology, Engineering and Mathematics (EPSTEM), 42,* 229-236.

The Eurasia Proceedings of Science, Technology, Engineering and Mathematics (EPSTEM)
ISSN: 2602-3199

The Eurasia Proceedings of Science, Technology, Engineering and Mathematics (EPSTEM), 2026

Volume 42, Pages 237-259

ICBASET 2026: International Conference on Basic Sciences, Engineering and Technology

Tetra Neutrosophic Alpha Star Generalized #Ψ Mappings in Tetra Neutrosophic Topological Spaces

Raja Mohammad Latif
Prince Mohammad Bin Fahd University

Abstract: In 2026, R. Radha, R. Princy, and Arokia Pratheesha S. V. introduced Tetra Neutrosophic Sets and investigated their fundamental properties. In 2024, S. Pooja, M. Vignashwaren, and L. Vidyarani introduced the concept of $\alpha^*g^{\#}\psi$-closed sets in topological spaces. In the same year, they further investigated $\alpha^*g^{\#}\psi$-continuous and irresolute maps. Motivated by these developments, we introduce the concept of Tetra Neutrosophic $\alpha^*g^{\#}\psi$-closed sets in Tetra Neutrosophic topological spaces and investigate their fundamental properties. Based on this new class of generalized closed sets, we introduce Tetra Neutrosophic $\alpha^*g^{\#}\psi$-continuous, $\alpha^*g^{\#}\psi$-irresolute, $\alpha^*g^{\#}\psi$-open, and $\alpha^*g^{\#}\psi$-closed mappings. Their basic properties and characterizations are established. Furthermore, Tetra Neutrosophic $\alpha^*g^{\#}\psi$-homeomorphisms are introduced, and some of their fundamental properties are investigated. The obtained results extend the theory of generalized mappings to the Tetra Neutrosophic topological setting and provide a systematic framework for studying generalized transformations between TN-Top-Spaces.

Keywords: TN-Top-Space, $TN\alpha^*g^{\#}\psi$-closed set, $TN\alpha^*g^{\#}\psi$-continuous Mapping, $TN\alpha^*g^{\#}\psi$-irresolute Mapping, $TN\alpha^*g^{\#}\psi$-open Mapping, $TN\alpha^*g^{\#}\psi$-homeomorphism

Introduction

Topology is one of the fundamental branches of mathematics that provides a general framework for studying continuity, convergence, connectedness, compactness, and various types of mappings. In recent years, generalized closed sets and generalized open sets have received considerable attention because they provide broader and more flexible approaches to classical topological concepts. These generalized classes have also led to the development of several types of generalized continuous, irresolute, open, closed, and homeomorphic mappings.

Neutrosophic Set Theory, introduced by Smarandache, provides an effective mathematical framework for dealing with indeterminate, incomplete, and inconsistent information. Since its introduction, neutrosophic sets and their extensions have been extensively investigated in different areas of mathematics and applied sciences. In particular, neutrosophic topological structures have been developed to extend classical topological concepts to environments involving uncertainty and indeterminacy.

Radha et al. (2026) introduced Tetra Neutrosophic Sets and investigated their fundamental properties. Tetra Neutrosophic Sets provide a generalized framework for representing information through multiple truth, indeterminacy, and falsity membership components. This development provides a suitable setting for extending various generalized topological concepts to a richer neutrosophic environment.

Pooja et al. (2024) introduced the concept of $\alpha^*g^{\#}\psi$-closed sets in topological spaces and investigated their fundamental properties. In the same year, they further studied $\alpha^*g^{\#}\psi$-ontinuous and irresolute maps associated

- This is an Open Access article distributed under the terms of the Creative Commons Attribution-Noncommercial 4.0 Unported License, permitting all non-commercial use, distribution, and reproduction in any medium, provided the original work is properly cited.
- Selection and peer-review under responsibility of the Organizing Committee of the Conference
© 2026 Published by ISRES Publishing: www.isres.org

with these generalized closed sets. These developments motivated us to investigate the corresponding concepts in the framework of $\mathrm{TN}-\mathrm{Top}-\mathrm{Spaces}$.

Motivated by the above developments, in this paper we introduce and study the concept of $\mathrm{TN}\alpha^{*}g^{\#}\psi-$closed sets in $\mathrm{TN}-\mathrm{Top}-\mathrm{Spaces}$.. We investigate their fundamental properties and establish several relationships with other generalized closed sets. We also introduce the corresponding notion of $\mathrm{TN}\alpha^{*}g^{\#}\psi-$open sets and study their basic properties.

Furthermore, based on the newly introduced class of $\mathrm{TN}\alpha^{*}g^{\#}\psi-$closed sets, we introduce $\mathrm{TN}\alpha^{*}g^{\#}\psi-$continuous mappings and $\mathrm{TN}\alpha^{*}g^{\#}\psi-$irresolute mappings. We investigate their fundamental properties, characterize these mappings under suitable conditions, and establish relationships between the different classes of generalized mappings. In addition, we introduce $\mathrm{TN}\alpha^{*}g^{\#}\psi-$open mappings and $\mathrm{TN}\alpha^{*}g^{\#}\psi-$closed mappings and study their basic properties.

Finally, we introduce the concept of a $\mathrm{TN}\alpha^{*}g^{\#}\psi-$homeomorphism and investigate some of its fundamental properties. The results obtained in this paper extend the existing theory of generalized closed sets and generalized mappings to the Tetra Neutrosophic topological setting. Thus, the present work provides a systematic mathematical framework for studying generalized transformations between Tetra Neutrosophic topological spaces and contributes to the continuing development of generalized neutrosophic topology.

2. Tetra Neutrosophic −Closed and Open Sets

Definition 2.1. Let R be a universe. A Neutrosophic set M on R can be defined as follows: $M=\{\langle r,T_M(r),I_M(r),F_M(r)\rangle : r\in R\}$ where $T_M,I_M,F_M : U\to[0.1]$ and $0\le T_M(r)+I_M(r)+F_M(r)\le 3.$ Here, $T_M(r)$ is the degree of membership, $I_M(r)$ is the degree of indeterminancy and $F_M(r)$ is the degree of non-membership. Here, $T_M(r)$ and $F_M(r)$ are dependent neutrosophic components and $I_M(r)$ is an independent component.

Definition 2.2. Let R be a universe. A Neutrosophic Pythagorean set $(\text{briefly } \mathrm{NP}-\text{set})$ M with T and F as dependent Neutrosophic Pythagorean components and U as an independent component for M on R is an object of the form $M=\{\langle r,T_M(r),U_M(r),F_M(r)\rangle : r\in R\}$ where $T_M(r)+F_M(r)\le 1,\ (T_M(r))^2+(F_M(r))^2\le 1,$ and $0\le (T_M(r))^2+(U_M(r))^2+(F_M(r))^2\le 2,$ for all $r\in R.$ We note that $T_M(r)$ is the truth membership, $U_M(r)$ is indeterminancy membership, and $F_M(r)$ is the false membership.

Definition 2.3. Let R be a non-empty set (universe). A Tetra Neutrosophic set $(\text{briefly } \mathrm{TN}-\text{set})$ M on R is an object of the form: $M=\{\langle r,T_M(r),I_M(r),F_M(r)\rangle : r\in R\}$ where $T_M(r),I_M(r),F_M(r)\in[0,1]$, $0\le (T_M(r))^4+(I_M(r))^4+(F_M(r))^4\le 1,$ for all $r\in R.$ $T_M(r)$ is the truth membership, $I_M(r)$ is an indeterminancy membership and $F_M(r)$ is the false membership.

$\mathrm{TN}(\mathrm{R})$ presents the family of all $\mathrm{TN}-$sets on R.

Definition 2.4. The complement of a $\mathrm{TN}-$set $M=\{\langle r,T_M(r),I_M(r),F_M(r)\rangle : r\in R\}$ is defined and denoted by $\mathrm{M}^{\mathrm{C}}=\{\langle \mathrm{r},\mathrm{F}_{\mathrm{M}}(\mathrm{r}),1-\mathrm{I}_{\mathrm{M}}(\mathrm{r}),\mathrm{T}_{\mathrm{M}}(\mathrm{r})\rangle : \mathrm{r}\in\mathrm{R}\}$

Definition 2.5. Let $M=\{\langle r,T_M(r),I_M(r),F_M(r)\rangle : r\in R\}$ and $Q=\{\langle r,T_Q(r),I_Q(r),F_Q(r)\rangle : r\in R\}$ be two TN−sets on the universe R. Then the union, the intersection and the difference of two TN−sets can be defined by $M\cup Q=\{\langle r,max(T_M(r),T_Q(r)),min(I_M(r),I_Q(r)),min(F_M(r)),F_Q(r)\rangle : r\in R\}$

$M\cap Q=\{\langle r,min(T_M(r),T_Q(r)),max(I_M(r),I_Q(r)),max(F_M(r)),F_Q(r)\rangle : r\in R\}$

$M-Q=\{\langle r,min(T_M(r),F_Q(r)),min(I_M(r),1-I_Q(r)),max(F_M(r)),T_Q(r)\rangle : r\in R\}$

Definition 2.6. Let $M=\{\langle r,T_M(r),I_M(r),F_M(r)\rangle : r\in R\}$ and $Q=\{\langle r,T_Q(r),I_Q(r),F_Q(r)\rangle : r\in R\}$ be two TN−sets on the universe R. Then M is contained in Q (i.e) $M\subseteq Q$ if $T_M\le T_Q$, $I_M\ge I_Q$ and $F_M\ge F_Q$.

Definition 2.7. Let R be a non-empty set. The TN−empty set on R, denoted by 0_{TN}, is defined by $0_{TN}=\{\langle r,0,1,1\rangle : r\in R\}$. The TN−universal set on R, denoted by 1_{TN}, is defined by $1_{TN}=\{\langle r,1,0,0\rangle : r\in R\}$.

Theorem 2.8. Let M, P and Q be any TN−sets on the universe R. Then

$(1)\ M\cap 0_{TN}=0_{TN}\quad 0_{FN}=\{\langle 0,1,1\rangle : r\in R\}$ $(2)\ M\cup 1_{TN}=1_{TN}\ 1_{TN}=\{\langle 1,0,0\rangle : r\in R\}$

$(3)\ M\cup P=P\cup M$ $(4)\ M\cap P=P\cap M$ $(5)\ (M\cup P)\cup Q=M\cup(M\cup Q)$

$(6)\ (M\cap P)\cap Q=M\cap(M\cap Q)$ $(7)\ (M^C)^C=M$ $(8)\ M\cup(M\cap Q)=M$ $(9)\ M\cap(M\cup Q)=M$

$(10)\ M\cup(P\cap Q)=(M\cup P)\cap(M\cup Q)$ $(11)\ M\cap(P\cup Q)=(M\cap P)\cup(M\cap Q)$

$(12)\ (M\cup Q)^C=M^C\cap Q^C$ $(13)\ (M\cap Q)^C=M^C\cup Q^C$ $(14)\ (0_{TN})^C=1_{TN}$ $(15)\ (1_{TN})^C=0_{TN}$ (16)

$M\cup 0_{TN}=M$ $(17)\ M\cup 1_{TN}=1_{TN}$ $(18)\ M\cap 0_{TN}=0_{TN}$ $(19)\ M\cap 1_{TN}=M$ $(20) M\subseteq Q\Leftrightarrow M\cap Q=M$

$(21) M\subseteq Q\Leftrightarrow M\cup Q=Q.$

Definition 2.10. A Tetra Neutrosophic topology $(\text{TN}-\text{Topology})$ on a nonempty set R is a $T_{TN}\subseteq TN(R)$ is a family T_{TN} of TN−sets on R satisfying the following axioms

(1) $0_{TN}, 1_{TN}\in T_{TN}$

(2) $K\cap L\in T_{TN}$ for any $K,L\in T_{TN}$

(3) $\bigcup_{\lambda\in\Lambda} M_\lambda\in T_{TN}$ for any $\{M_\lambda : \lambda\in\Lambda\}\subseteq T_{TN}$

The pair (R,T_{TN}) is called a TN−Top−Space.

Definition 2.11. Let (R,T_{TN}) be a TN−Top−Space. and $M\in T_{TN}$. Then M is called a TN−open set in R. The complement of a TN−open set M is called a TN−closed set in R and it is denoted by M^C.

Definition 2.12. Let (R,T_{TN}) be a TN−Top−Space and $M=\{\langle r,T_M(r),I_M(r),F_M(r)\rangle : r\in R\}$ be a TN−set in R. Then the TN−interior and the TN−closure of M are denoted by $TN-Int(M)$ and $TN-Cl(M)$ respectively and are defined as follows.

$TN-Int(M)=\bigcap\{K : K \text{ is a TN−open set and } M\subseteq K\}$ and

$TN-Cl(M)=\bigcup\{K : K \text{ is a TN−closed set and } K\subseteq M\}$

Theorem 2.13. Let (R,T_{TN}) be a TN−Top−Space and let M and K be TN−set subset of R. Then the following statements hold.

(i) $TN-Int(M)$ is a TN−open set in R.

(ii) $TN-Int(0_{TN})=0_{TN}$ and $TN-Int(1_{TN})=1_{TN}$.

(iii) $TN-Cl(M)$ is a TN−closed set in R.

(iv) $TN-Cl(0_{TN})=0_{TN}$ and $TN-Cl(1_{TN})=1_{TN}$.
(v) M is $TN-$open set if and only if $M=TN-Int(M)$
(vi) M is $TN-$closed set if and only if $M=TN-Cl(M)$
(vii) $TN-Int[TN-Int(M)]=TN-Int(M)$
$(viii)$ $TN-Cl[TN-Cl(M)]=TN-Cl(M)$
(ix) $M\subseteq K$ implies that $TN-Int(M)\subseteq TN-Int(K)$
(x) $M\subseteq K$ implies that $TN-Cl(M)\subseteq TN-Cl(K)$
(xi) $TN-Int(M\cap K)=[TN-Int(M)]\cap[TN-Int(K)]$
(xii) $TN-Cl(M\cap K)\subseteq[TN-Cl(M)]\cap[TN-Cl(K)]$
$(xiii)$ $[TN-Int(M)]\cup[TN-Int(K)]\subseteq TN-Int(M\cup K)$

Definition 2.14. Let (R,T_{TN}) be a $TN-$Top$-$Space and M be a $TN-$set. M is said to be a Tetra Neutrosophic Pre$-$open (briefly TNP$-$open) set if $M\subseteq TN-Int(TN-Cl(M))$. The family of all $TNP-$open sets in (R,T_{TN}) is denoted by $TNP-O(R,T_{TN})$. The complement of a $TNP-$open set is called a Tetra Neutrosophic Pre$-$closed (briefly $TNP-$closed) set in R. M is said to be a Fermatean Neutrosophic Pre$-$closed (briefly TNP$-$closed) set if $TN-Cl(TN-Int(M))\subseteq M$.

Definition 2.15. Let (R,T_{TN}) be a $TN-$Top$-$Space and M be a $TN-$set. M is said to be a Tetra Neutrosophic Semi$-$open (briefly TNS$-$open) set if $M\subseteq TN-Cl(TN-Int(M))$. The family of all $TNS-$open sets in (R,T_{TN}) is denoted by $TNS-O(R,T_{TN})$. The complement of a $TNS-$open set is called a Tetra Neutrosophic Semi$-$closed (briefly TNS$-$closed) set in R. M is said to be a Tera Neutrosophic Semi$-$closed (briefly TNS$-$closed) set if $TN-Int(TN-Cl(M))\subseteq M$.

Definition 2.16. Let (R,T_{TN}) be a $TN-$Top$-$Space and M be a $TN-$set. M is said to be a Tetra Neutrosophic $\alpha-$open (briefly TN$\alpha-$open) set if $M\subseteq TN-Int(TN-Cl(TN-Int(M)))$. The family of all $TN\alpha-$open sets in (R,T_{TN}) is denoted by $TN\alpha-O(R,T_{TN})$. The complement of a $TN\alpha-$open set is called a Tetra Neutrosophic $\alpha-$closed (briefly TN$\alpha-$closed) set in R. M is said to be a Tetra Neutrosophic $\alpha-$closed (briefly TN$\alpha-$closed) set if $TN-Cl(TN-Int(TN-Cl(M)))\subseteq M$.

Proposition 2.17. A $TN-$open subset M of a $TN-$Top$-$Space (R,T_{TN}) is a $TN\alpha-$open set in R if and only if M is a $TNS-$open set and $TNP-$open set.

Definition 2.18. Let (R,T_{TN}) be a $TN-$Top$-$Space and $M=\{\langle r,T_M(r),I_M(r),F_M(r)\rangle : r\in R\}$ be a $TN-$set in R. Then the $TN\alpha-$interior and the $TN\alpha-$closure of M are denoted by $TN\alpha-Int(M)$ and $TN\alpha-Cl(M)$, and are defined as follows.
$TN\alpha-Int(M)=\cup\{K: K \text{ is a } TN\alpha-\text{open set and } K\subseteq M\}$ and
$TN\alpha-Cl(M)=\cap\{L: L \text{ is a } TN\alpha-\text{closed set and } M\subseteq L\}$

Theorem 2.19. Let (R,T_{TN}) be a $TN-$Top$-$Space and M be a $TN-$set in X. Then M is a $TN\alpha-$open set in R if and only if there exists a $TN-$open set K in R such that $K\subseteq M\subseteq TN-Int(TN-Cl(K))$.

Proof. Let M be a $TN\alpha$−open set in R. Then $M \subseteq TN-Int\left[TN-Cl\left(TN-Int(M)\right)\right]$. Then this implies that $TN-Int(M) \subseteq M \subseteq TN-Int\left[TN-Cl\left(TN-Int(M)\right)\right]$. Let $K = TN-Int(M)$. Then there exists a TN−open set K such that $K \subseteq M \subseteq TN-Int\left[TN-Cl(K)\right]$.

Conversely, suppose that there is a TN−open set K such that $K \subseteq M \subseteq TN-Int\left[TN-Cl(K)\right]$. Then $K = TN-Int(K) \subseteq TN-Int(M)$. Therefore $TN-Cl(K) \subseteq TN-Cl\left(TN-Int(M)\right)$, then we obtain $TN-Int\left(TN-Cl(K)\right) \subseteq TN-Int\left[TN-Cl\left(TN-Int(M)\right)\right]$. But by hypothesis, we have $K \subseteq M \subseteq TN-Int\left[TN-Cl(K)\right]$. Then $M \subseteq TN-Int\left[TN-Cl\left(TN-Int(M)\right)\right]$. Therefore, M is a $TN\alpha$−open set in R.

Theorem 2.20. The union of any family of $TN\alpha$−open sets in a TN−Top−Space $\left(R, T_{TN}\right)$ is a $TN\alpha$−open set in R.

Proof. Let $\left\{M_j : j \in J\right\}$ be a family of $TN\alpha$−open sets in R. Then $M_j \subseteq TN-Int\left(TN-Cl\left(TN-Int\left(M_j\right)\right)\right)$, for each $j \in J$. Since $\bigcup_{j\in J} TN-Int\left(M_j\right) \subseteq TN-Int\left(\bigcup_{j\in J} M_j\right)$ and $\bigcup_{i\in I} TN-Cl\left(M_i\right) \subseteq TN-Cl\left(\bigcup_{i\in I} M_i\right)$. We have $\bigcup_{j\in J} M_j \subseteq \bigcup_{j\in J} TN-Int\left(TN-Cl\left(TN-Int\left(M_j\right)\right)\right) \subseteq TN-Int\left(\bigcup_{j\in J} TN-Cl\left(TN-Int\left(M_j\right)\right)\right)$
$\subseteq TN-Int\left(TN-Cl\left(\bigcup_{j\in J} TN-Int\left(M_j\right)\right)\right) \subseteq TN-Int\left(TN-Cl\left(TN-Int\left(\bigcup_{j\in J} M_j\right)\right)\right)$. Hence, we conclude that $\bigcup_{j\in J} M_j$ is a $TN\alpha$−open set in R.

Theorem 2.21. Let $\left(R, T_{TN}\right)$ be a TN−Top−Space. Then the following statements hold.

(i) Every TN−open (resp. TN−closed) set is a $TN\alpha$−open (resp. $TN\alpha$−closed) set.

(ii) Every $TN\alpha$−open (resp. $TNP\alpha$−closed) set is a TNS−open (resp. TNS−closed) set.

(iii) Every $TN\alpha$−open (resp. $TN\alpha$−closed) set is a TNP−open (resp. TNP−closed) set.

Lemma 2.22. Let $\left(R, T_{TN}\right)$ be a TN−Top−Space and let M be a TN−set in R.

(i) If M is a TN−open set, then $TNS-Cl(M) = TN-Int\left(TN-Cl(M)\right)$.

(*ii*) $TNS-Int\left(TN-Cl(M)\right) = TN-Cl\left(TN-Int\left(TN-Cl(M)\right)\right)$.

Definition 2.23. Let $\left(R, T_{TN}\right)$ be a TN−Top−Space and let M be a TN−set in R. Then M is called a

(i) Tetra Neutrosophic Regular−closed (briefly TN−Regular−closed) if $M = TN-Cl\left(TN-Int(M)\right)$.

(ii) Tetra Neutrosophic Regular−open (briefly TN−Regular−open) if $M = TN-Int\left(TN-Cl(M)\right)$.

(iii) Tetra Neutrosophic β−closed (briefly $TN\beta$−closed) if $TN-Int\left(TN-Cl\left(TN-Int(M)\right)\right) \subseteq M$.

(iv) Tetra Neutrosophic β−open (briefly $TN\beta$−open) if $M \subseteq TN-Cl\left(TN-Int\left(TN-Cl(M)\right)\right)$.

(v) Tetra Neutrosophic $\mathbf{b}$−closed (briefly $TN\mathbf{b}$−closed) if
$\left[TN-Cl\left(TN-Int(M)\right)\right] \cap \left[TN-Int\left(TN-Cl(M)\right)\right] \subseteq M$.

(vi) Tetra Neutrosophic $\mathbf{b}$−open (briefly $TN\mathbf{b}$−open) if
$M \subseteq \left[TN-Int\left(TN-Cl(M)\right)\right] \cup \left[TN-Cl\left(TN-Int(M)\right)\right]$

(vii) Tetra Neutrosophic π−closed (briefly $TN\pi$−closed) set if M is the union of TNR−closed sets.

(viii) Tetra Neutrosophic π−open (briefly $TN\pi$−open) if M is the union of TNR−open sets.

(ix) Tetra Neutrosophic Generalized closed (briefly TNg−closed) set if $TN-Cl(M) \subseteq H$ whenever $M \subseteq H$ and H is TN−open set in R.

(x) Tetra Neutrosophic Generalized semi-closed (briefly TNgs−closed) set if $TNS-Cl(M) \subseteq H$ whenever $M \subseteq H$ and H is TN−open set in R.

(xi) Tetra Neutrosophic α Generalized closed (briefly TNαg−closed) set if $TN\alpha-Cl(M) \subseteq H$ whenever $M \subseteq H$ and H is TN−open set in R.

(xii) Tetra Neutrosophic generalized pre-closed set (briefly TNgp−closed) if $TNP-Cl(M) \subseteq H$ whenever $M \subseteq H$ and H is TN−open set in R.

(xiii) Tetra Neutrosophic generalized α closed set (briefly TNgα−closed) if $TN\alpha-Cl(M) \subseteq H$ whenever $M \subseteq H$ and H is $TN\alpha$−open set in R.

(xiv) Tetra Neutrosophic *generalized α closed set (briefly $TN^{*}g\alpha$−closed) if $TN-Cl(M) \subseteq H$ whenever $M \subseteq H$ and H is TNgα−open set in R.

(xv) Tetra Neutrosophic semi generalized closed set (briefly TNsg−closed) if $TNs-Cl(M) \subseteq H$ whenever $M \subseteq H$ and H is TNS−open set in R.

(xvi) Tetra Neutrosophic generalized semi pre closed set (briefly TNgsp−closed) if $TNSP-Cl(M) \subseteq H$ whenever $M \subseteq H$ and H is TN−open set in R.

(xvii) Tetra Neutrosophic generalized* semi pre closed set (briefly TNg*sp−closed) if $TNSP-Cl(M) \subseteq H$ whenever $M \subseteq H$ and H is TNg−open set in R.

(xviii) Tetra Neutrosophic generalized pre regular closed set (briefly TNgpr−closed) if $TNp-Cl(M) \subseteq H$ whenever $M \subseteq H$ and H is TN−regular open set in R.

(xix) Tetra Neutrosophic ψ closed (briefly TNψ−closed) set if $TNS-Cl(M) \subseteq H$ whenever $M \subseteq H$ and H is TNsg−open set in R.

(xx) Tetra Neutrosophic ψ generalized closed (briefly TNψg−closed) set if $TN\psi-Cl(M) \subseteq H$ whenever $M \subseteq H$ and H is TN−open set in R.

(xxi) Tetra Neutrosophic $g^{\#}\psi$−closed closed (briefly TN$g^{\#}\psi$−closed) set if $TN\psi-Cl(M) \subseteq H$ whenever $M \subseteq H$ and H is TNψ−open set in R.

(xxii) Tetra Neutrosophic TN$g^{\#}\psi$−closed set (briefly TN$g^{\#}\psi$−closed) set if $TN\psi-Cl(M) \subseteq H$ whenever $M \subseteq H$ and H is TNψ−open set in R.

(xxiii) Tetra Neutrosophic TN$\alpha g^{\#}\psi$−closed set (briefly TN$\alpha g^{\#}\psi$−closed) set if $TN\alpha-Cl(M) \subseteq H$ whenever $M \subseteq H$ and H is TN$g^{\#}\psi$−open set in R.

3. Tetra Neutrosophic $\alpha^{*}g^{\#}\psi$−Closed and Open Sets

We introduce TN$\alpha^{*}g^{\#}\psi$−closed and TN$\alpha^{*}g^{\#}\psi$−open sets and explore some of their properties.

Definition 3.1. A TN−set M in a TN−Top−Space (R, T_{TN}) is said to be a Tetra Neutrosophic $\alpha^{*}g^{\#}\psi$−closed (briefly TN$\alpha^{*}g^{\#}\psi$−closed) set if $TN\alpha-Cl(M) \subseteq H$ whenever $M \subseteq H$ and H is TN$\alpha g^{\#}\psi$−open set in (R, T_{TN}). The family of all TN$\alpha^{*}g^{\#}\psi$−closed in (R, T_{FQN}) is denoted by TN$\alpha^{*}g^{\#}\psi$−$C(R, T_{TN})$.

Definition 3.2. Let (R, T_{TN}) be a TN−Top−Space and M be a TN−set in (R, T_{TN}). Then M is said to be a TN$\alpha^{*}g^{\#}\psi$−open set in (R, T_{TN}) if its complement $M^{C} = 1_{TN} - M$ is a TN$\alpha^{*}g^{\#}\psi$−closed set in (R, T_{TN}). The family of all TN$\alpha^{*}g^{\#}\psi$−open sets in (R, T_{TN}) is denoted by TN$\alpha^{*}g^{\#}\psi$−$O(R, T_{TN})$.

Definition 3.3. Let (R, T_{TN}) be a $TN-$Top$-$Space. and M be a $TN-$set in (R, T_{TN}). Then the Tetra Neutrosophic $\alpha^{*}g^{\#}\psi-$interior of M $\left(\text{briefly, } TN\alpha^{*}g^{\#}\psi-\text{Int}(M)\right)$ is defined as the union of all $TN\alpha^{*}g^{\#}\psi-$open sets contained in M i.e., $TN\alpha^{*}g^{\#}\psi-\text{Int}(M)=\bigcup\{G: G \text{ is a } TN\alpha^{*}g^{\#}\psi-\text{open set in } (R, T_{TN}) \ \& \ G\subseteq M\}$.

Theorem 3.4. Let (R, T_{TN}) be a $TN-$Top$-$Space. If M and K are $TN-$sets in R. Then the following results hold:

(i) $TN\alpha^{*}g^{\#}\psi-\text{Int}(0_{TN})=0_{TN}$.

(ii) $TN\alpha^{*}g^{\#}\psi-\text{Int}(1_{TN})=1_{TN}$.

(iii) $TN\alpha^{*}g^{\#}\psi-\text{Int}(M)\subseteq M$.

(iv) $M\subseteq K\Rightarrow TN\alpha^{*}g^{\#}\psi-\text{Int}(M)\subseteq TN\alpha^{*}g^{\#}\psi-\text{Int}(K)$.

(v) $TN\alpha^{*}g^{\#}\psi-\text{Int}\left(TN\alpha^{*}g^{\#}\psi-\text{Int}(M)\right)=TN\alpha^{*}g^{\#}\psi-\text{Int}(M)$.

(vi) $TN-\text{Int}(M)\subseteq TN\alpha^{*}g^{\#}\psi-\text{Int}(M)$.

(vii) $\left[TN\alpha^{*}g^{\#}\psi-\text{Int}(M)\right]\cup\left[TN\alpha^{*}g^{\#}\psi-\text{Int}(K)\right]\subseteq TN\alpha^{*}g^{\#}\psi-\text{Int}(M\cup K)$.

$(viii)$ $TN\alpha^{*}g^{\#}\psi-\text{Int}(M\cap K)\subseteq\left[TN\alpha^{*}g^{\#}\psi-\text{Int}(M)\right]\cap\left[TN\alpha^{*}g^{\#}\psi-\text{Int}(K)\right]$.

Definition 3.5. Let (R, T_{TN}) be a $TN-$Top$-$Space and M be a $TN-$set in (R, T_{TN}). Then the Tetra Neutrosophic $\alpha^{*}g^{\#}\psi-$closure of M $\left(\text{briefly, } TN\alpha^{*}g^{\#}\psi-\text{Cl}(M)\right)$ is defined as the intersection of all $TN\alpha^{*}g^{\#}\psi-$closed sets in (R, T_{TN}) containing M i.e., $TN\alpha^{*}g^{\#}\psi-\text{Cl}(M)=\bigcap\{H: H \text{ is a } TN\alpha^{*}g^{\#}\psi-\text{closed set in } (R, T_{TN}) \ \& \ M\subseteq H\}$.

Theorem 3.6. Let (R, T_{TN}) be a $TN-$Top$-$Space. Let M and K be $TN-$sets in R. Then the following results hold:

(i) $TN\alpha^{*}g^{\#}\psi-\text{Cl}(0_{TN})=0_{TN}$.

(ii) $TN\alpha^{*}g^{\#}\psi-\text{Cl}(1_{TN})=1_{TN}$.

(iii) $M\subseteq TN\alpha^{*}g^{\#}\psi-\text{Cl}(M)$.

(iv) $M\subseteq K\Rightarrow TN\alpha^{*}g^{\#}\psi-\text{Cl}(M)\subseteq TN\alpha^{*}g^{\#}\psi-\text{Cl}(K)$.

(v) $TN\alpha^{*}g^{\#}\psi-\text{Cl}\left(TN\alpha^{*}g^{\#}\psi-\text{Cl}(M)\right)=TN\alpha^{*}g^{\#}\psi-\text{Cl}(M)$.

(vi) $M\subseteq TN\alpha^{*}g^{\#}\psi-\text{Cl}(M)\subseteq TN-\text{Cl}(M)$.

(vii) $\left[TN\alpha^{*}g^{\#}\psi-\text{Cl}(M)\right]\cup\left[TN\alpha^{*}g^{\#}\psi-\text{Cl}(K)\right]\subseteq TN\alpha^{*}g^{\#}\psi-\text{Cl}(M\cup K)$.

$(viii)$ $TN\alpha^{*}g^{\#}\psi-\text{Cl}(M\cap K)\subseteq\left[TN\alpha^{*}g^{\#}\psi-\text{Cl}(M)\right]\cap\left[TN\alpha^{*}g^{\#}\psi-\text{Cl}(K)\right]$.

Theorem 3.7. Every $TN-$closed $(\text{resp. } TN-\text{open})$ set in a $TN-$Top$-$Space (R, T_{TN}) is a $TN\alpha^{*}g^{\#}\psi-$closed $(\text{resp. } TN\alpha^{*}g^{\#}\psi-\text{open})$ set in (R, T_{TN}).

Proof. Consider a $TN-$closed set M in a $TN-$Top$-$Space (R, T_{TN}). Assume that $M\subseteq H$ and H be a $TN\alpha g^{\#}\psi-$open set in (R, T_{TN}). Since M is a $TN-$closed set in (R, T_{TN}), $TN-\text{Cl}(M)=M$. But $TN\alpha-\text{Cl}(M)\subseteq TN-\text{Cl}(M)\Rightarrow TN\alpha-\text{Cl}(M)\subseteq H$. Therefore, M is a $TN\alpha^{*}g^{\#}\psi-$closed set in (R, T_{TN}).

Theorem 3.8. Every $\mathrm{TN}\alpha$ −closed $(\text{resp. } \mathrm{TN}\alpha$ −open$)$ set in a TN −Top −Space $(\mathrm{R}, \mathrm{T}_{\mathrm{TN}})$ is a $\mathrm{TN}\alpha^{*}g^{\#}\psi$ −closed $(\text{resp. } \mathrm{TN}\alpha^{*}g^{\#}\psi$ −open$)$ set in $(\mathrm{R}, \mathrm{T}_{\mathrm{TN}})$.

Proof. Consider a $\mathrm{TN}\alpha$ −closed set M in a TN −Top −Space $(\mathrm{R}, \mathrm{T}_{\mathrm{TN}})$. Assume that $M \subseteq H$ and H be a $\mathrm{TN}\alpha g^{\#}\psi$ −open set in $(R, \mathrm{T}_{\mathrm{TN}})$. Since M is a $\mathrm{TN}\alpha$ −closed set in $(R, \mathrm{T}_{\mathrm{TN}})$, $\mathrm{TN}\alpha$ −Cl$(\mathrm{M}) = \mathrm{M}$. Therefore $\mathrm{TN}\alpha$ −Cl$(\mathrm{M}) \subseteq \mathrm{H}$. Hence, M is a $\mathrm{TN}\alpha^{*}g^{\#}\psi$ −closed set in $(R, \mathrm{T}_{\mathrm{TN}})$.

Theorem 3.9. Every $\mathrm{TN}\alpha^{*}g^{\#}\psi$ −closed $(\text{resp. } \mathrm{TN}\alpha^{*}g^{\#}\psi$ −open$)$ set in a TN −Top −Space $(\mathrm{R}, \mathrm{T}_{\mathrm{TN}})$ is a $\mathrm{TN}gs$−closed $(\text{resp. } \mathrm{TN}gs$−open$)$ set in $(\mathrm{R}, \mathrm{T}_{\mathrm{TN}})$.

Proof. Consider a $\mathrm{TN}\alpha^{*}g^{\#}\psi$ −closed set M in a TN −Top −Space $(\mathrm{R}, \mathrm{T}_{\mathrm{TN}})$. Assume that $M \subseteq H$ and H be a TN −open set in $(R, \mathrm{T}_{\mathrm{TN}})$. As every TN −open set is $\mathrm{TN}\alpha g^{\#}\psi$ −open set, H is $\mathrm{TN}\alpha g^{\#}\psi$ −open set. Here M is a $\mathrm{TN}\alpha^{*}g^{\#}\psi$ −closed set in $(R, \mathrm{T}_{\mathrm{TN}})$, so $\mathrm{TN}\alpha$ −Cl$(\mathrm{M}) \subseteq \mathrm{H}$. But TNS −Cl$(\mathrm{M}) \subseteq \mathrm{TN}\alpha$ −Cl(M), then TNS −Cl$(\mathrm{M}) \subseteq \mathrm{H}$. Therefore, M is a $\mathrm{TN}gs$−closed set in $(R, \mathrm{T}_{\mathrm{TN}})$.

Theorem 3.10. Every $\mathrm{TN}\alpha^{*}g^{\#}\psi$ −closed $(\text{resp. } \mathrm{TN}\alpha^{*}g^{\#}\psi$ −open$)$ set in a TN −Top −Space. $(\mathrm{R}, \mathrm{T}_{\mathrm{TN}})$ is a $\mathrm{TN}sg$−closed $(\text{resp. } \mathrm{TN}sg$−open$)$ set in $(\mathrm{R}, \mathrm{T}_{\mathrm{TN}})$.

Proof. Consider a $\mathrm{TN}\alpha^{*}g^{\#}\psi$ −closed set M in a TN −Top −Space $(\mathrm{R}, \mathrm{T}_{\mathrm{TN}})$. Assume that $M \subseteq H$ and H be a TN −open set in $(R, \mathrm{T}_{\mathrm{TN}})$. As every TN −open set is $\mathrm{TN}\alpha g^{\#}\psi$ −open set, H is $\mathrm{TN}\alpha g^{\#}\psi$ −open set. Here M is a $\mathrm{TN}\alpha^{*}g^{\#}\psi$ −closed set in $(R, \mathrm{T}_{\mathrm{TN}})$, so $\mathrm{TN}\alpha$ −Cl$(\mathrm{M}) \subseteq \mathrm{H}$. Also, TNS −Cl$(\mathrm{M}) \subseteq \mathrm{TN}\alpha$ −Cl(M), then TNS −Cl$(\mathrm{M}) \subseteq \mathrm{H}$. Therefore, M is a $\mathrm{TN}sg$−closed set in $(R, \mathrm{T}_{\mathrm{TN}})$.

Theorem 3.11. Every $\mathrm{TN}\alpha^{*}g^{\#}\psi$ −closed $(\text{resp. } \mathrm{TN}\alpha^{*}g^{\#}\psi$ −open$)$ set in a TN −Top −Space $(\mathrm{R}, \mathrm{T}_{\mathrm{TN}})$ is a $\mathrm{TN}\alpha g$−closed $(\text{resp. } \mathrm{TN}ag$−open$)$ set in $(\mathrm{R}, \mathrm{T}_{\mathrm{TN}})$.

Proof. Consider a $\mathrm{TN}\alpha^{*}g^{\#}\psi$ −closed set M in a TN −Top −Space $(\mathrm{R}, \mathrm{T}_{\mathrm{TN}})$. Assume that $M \subseteq H$ and H be a TN −open set in $(R, \mathrm{T}_{\mathrm{TN}})$. As every TN −open set is $\mathrm{TN}\alpha g^{\#}\psi$ −open set, H is $\mathrm{TN}\alpha g^{\#}\psi$ −open set. Here M is a $\mathrm{TN}\alpha^{*}g^{\#}\psi$ −closed set in $(R, \mathrm{T}_{\mathrm{TN}})$, so $\mathrm{TN}\alpha$ −Cl$(\mathrm{M}) \subseteq \mathrm{H}$. Therefore, M is a $\mathrm{TN}\alpha g$−closed set in $(R, \mathrm{T}_{\mathrm{TN}})$.

Theorem 3.12. Every $\mathrm{TN}\alpha^{*}g^{\#}\psi$ −closed $(\text{resp. } \mathrm{TN}\alpha^{*}g^{\#}\psi$ −open$)$ set in a TN −Top −Space. $(\mathrm{R}, \mathrm{T}_{\mathrm{TN}})$ is a $\mathrm{TN}gsp$−closed $(\text{resp. } \mathrm{TN}gsp$−open$)$ set in $(\mathrm{R}, \mathrm{T}_{\mathrm{TN}})$.

Proof. Consider a $\mathrm{TN}\alpha^{*}g^{\#}\psi$ −closed set M in a TN −Top −Space $(\mathrm{R}, \mathrm{T}_{\mathrm{TN}})$. Assume that $M \subseteq H$ and H be a TN −open set in $(R, \mathrm{T}_{\mathrm{TN}})$. As every TN −open set is $\mathrm{TN}\alpha g^{\#}\psi$ −open set, H is $\mathrm{TN}\alpha g^{\#}\psi$ −open set. Here M is a $\mathrm{TN}\alpha^{*}g^{\#}\psi$ −closed set in $(R, \mathrm{T}_{\mathrm{TN}})$, so $\mathrm{TN}\alpha$ −Cl$(\mathrm{M}) \subseteq \mathrm{H}$. Also, TNSP −Cl$(\mathrm{M}) \subseteq \mathrm{TN}\alpha$ −Cl(M). This implies TNSP −Cl$(\mathrm{M}) \subseteq \mathrm{H}$. Therefore, M is a $\mathrm{TN}gsp$−closed set in $(R, \mathrm{T}_{\mathrm{TN}})$.

Theorem 3.13. Every $\mathrm{TN}\alpha^{*}g^{\#}\psi$ −closed $(\text{resp. } \mathrm{TN}\alpha^{*}g^{\#}\psi$ −open$)$ set in a TN −Top −Space $(\mathrm{R}, \mathrm{T}_{\mathrm{TN}})$ is a $\mathrm{TN}g^{*}sp$−closed $(\text{resp. } \mathrm{TN}g^{*}sp$−open$)$ set in $(\mathrm{R}, \mathrm{T}_{\mathrm{TN}})$.

Proof. Consider a $\mathrm{TN}\alpha^{*}g^{\#}\psi$ −closed set M in a TN −Top −Space $(\mathrm{R}, \mathrm{T}_{\mathrm{TN}})$. Assume that $M \subseteq H$ and H be a $\mathrm{TN}g$−open set in $(R, \mathrm{T}_{\mathrm{TN}})$. As every $\mathrm{TN}g$−open set is $\mathrm{TN}\alpha g^{\#}\psi$ −open set, H is $\mathrm{TN}\alpha g^{\#}\psi$ −open set. Here M

is a $\mathrm{TN}\alpha^{*}g^{\#}\psi$ −closed set in $(R,\mathrm{T}_{\mathrm{TN}})$, so $\mathrm{TN}\alpha$ −$\mathrm{Cl}(\mathrm{M})\subseteq \mathrm{H}$. Also, TNSP −$\mathrm{Cl}(\mathrm{M})\subseteq \mathrm{TN}\alpha$ −$\mathrm{Cl}(\mathrm{M})$. This implies TNSP −$\mathrm{Cl}(\mathrm{M})\subseteq \mathrm{H}$. Therefore, M is a $\mathrm{TN}g^{*}\mathrm{sp}$ −closed set in $(R,\mathrm{T}_{\mathrm{TN}})$.

Theorem 3.14. Every $\mathrm{TN}\alpha^{*}g^{\#}\psi$ −closed $(\text{resp. } \mathrm{TN}\alpha^{*}g^{\#}\psi$ −open$)$ set in a TN −Top −Space $(\mathrm{R},\mathrm{T}_{\mathrm{TN}})$ is a $\mathrm{TN}gpr$ −closed $(\text{resp. } \mathrm{TN}gpr$ −open$)$ set in $(\mathrm{R},\mathrm{T}_{\mathrm{TN}})$.

Proof. Consider a $\mathrm{TN}\alpha^{*}g^{\#}\psi$ −closed set M in a TN −Top −Space $(\mathrm{R},\mathrm{T}_{\mathrm{TN}})$. Assume that $M\subseteq H$ and H be a TN −regular open set in $(R,\mathrm{T}_{\mathrm{TN}})$. As every TN −regular open set is $\mathrm{TN}\alpha g^{\#}\psi$ −open set, H is $\mathrm{TN}\alpha g^{\#}\psi$ −open set. Here M is a $\mathrm{TN}\alpha^{*}g^{\#}\psi$ −closed set in $(R,\mathrm{T}_{\mathrm{TN}})$, so $\mathrm{TN}\alpha$ −$\mathrm{Cl}(\mathrm{M})\subseteq \mathrm{H}$. Also, TNP −$\mathrm{Cl}(\mathrm{M})\subseteq \mathrm{TN}\alpha$ −$\mathrm{Cl}(\mathrm{M})$. This implies TNP −$\mathrm{Cl}(\mathrm{M})\subseteq \mathrm{H}$. Therefore, M is a $\mathrm{TN}gpr$ −closed set in $(R,\mathrm{T}_{\mathrm{TN}})$.

Theorem 3.15. Every $\mathrm{TN}\alpha^{*}g^{\#}\psi$ −closed $(\text{resp. } \mathrm{TN}\alpha^{*}g^{\#}\psi$ −open$)$ set in a TN −Top −Space. $(\mathrm{R},\mathrm{T}_{\mathrm{TN}})$ is a $\mathrm{TN}\psi g$ −closed $(\text{resp. } \mathrm{TN}\psi g$ −open$)$ set in $(\mathrm{R},\mathrm{T}_{\mathrm{TN}})$.

Proof. Consider a $\mathrm{TN}\alpha^{*}g^{\#}\psi$ −closed set M in a TN −Top −Space $(\mathrm{R},\mathrm{T}_{\mathrm{TN}})$. Assume that $M\subseteq H$ and H be a TN −open set in $(R,\mathrm{T}_{\mathrm{TN}})$. As every TN −open open set is $\mathrm{TN}\alpha g^{\#}\psi$ −open set, H is $\mathrm{TN}\alpha g^{\#}\psi$ −open set. Here M is a $\mathrm{TN}\alpha^{*}g^{\#}\psi$ −closed set in $(R,\mathrm{T}_{\mathrm{TN}})$, so $\mathrm{TN}\alpha$ −$\mathrm{Cl}(\mathrm{M})\subseteq \mathrm{H}$. Also, $\mathrm{TN}\psi$ −$\mathrm{Cl}(\mathrm{M})\subseteq \mathrm{TN}\alpha$ −$\mathrm{Cl}(\mathrm{M})$. This implies $\mathrm{TN}\psi$ −$\mathrm{Cl}(\mathrm{M})\subseteq \mathrm{H}$. Therefore, M is a $\mathrm{TN}\psi g$ −closed set in $(R,\mathrm{T}_{\mathrm{TN}})$.

Theorem 3.16. Every $\mathrm{TN}g^{\#}$ −closed $(\text{resp. } \mathrm{TN}g^{\#}$ −open$)$ set in a TN −Top −Space $(\mathrm{R},\mathrm{T}_{\mathrm{TN}})$ is a $\mathrm{TN}\alpha^{*}g^{\#}\psi$ −closed $(\text{resp. } \mathrm{TN}\alpha^{*}g^{\#}\psi$ −open$)$ set in $(\mathrm{R},\mathrm{T}_{\mathrm{TN}})$.

Proof. Consider a $\mathrm{TN}g^{\#}$ −closed set M in a TN −Top −Space $(\mathrm{R},\mathrm{T}_{\mathrm{TN}})$. Assume that $M\subseteq H$ and H be a $\mathrm{TN}\alpha g^{\#}\psi$ −open set in $(R,\mathrm{T}_{\mathrm{TN}})$. As M is $\mathrm{TN}g^{\#}$ −closed set, then TN −$\mathrm{Cl}(\mathrm{M})\subseteq \mathrm{H}$. But $\mathrm{TN}\alpha$ −$\mathrm{Cl}(\mathrm{M})\subseteq \mathrm{TN}$ −$\mathrm{Cl}(\mathrm{M})$. This implies $\mathrm{TN}\alpha$ −$\mathrm{Cl}(\mathrm{M})\subseteq \mathrm{H}$. Therefore, M is a $\mathrm{TN}\alpha^{*}g^{\#}\psi$ −closed set in $(R,\mathrm{T}_{\mathrm{TN}})$.

Theorem 3.17. Every $\mathrm{TN}\alpha^{*}g^{\#}\psi$ −closed $(\text{resp. } \mathrm{TN}\alpha^{*}g^{\#}\psi$ −open$)$ set in a TN −Top −Space $(\mathrm{R},\mathrm{T}_{\mathrm{TN}})$ is a $\mathrm{TN}g^{\#}\psi$ −closed $(\text{resp. } \mathrm{TN}g^{\#}\psi$ −open$)$ set in $(\mathrm{R},\mathrm{T}_{\mathrm{TN}})$.

Proof. Consider a $\mathrm{TN}\alpha^{*}g^{\#}\psi$ −closed set M in a TN −Top −Space $(\mathrm{R},\mathrm{T}_{\mathrm{TN}})$. Assume that $M\subseteq H$ and H be a $\mathrm{TN}\psi$ −open set in $(R,\mathrm{T}_{\mathrm{TN}})$. As every $\mathrm{TN}\psi$ −open set is $\mathrm{TN}\alpha g^{\#}\psi$ −open set, H is $\mathrm{TN}\alpha g^{\#}\psi$ −open set. Since M is $\mathrm{TN}\alpha^{*}g^{\#}\psi$ −closed set, $\mathrm{TN}\alpha$ −$\mathrm{Cl}(\mathrm{M})\subseteq \mathrm{H}$. But $\mathrm{TN}\psi$ −$\mathrm{Cl}(\mathrm{M})\subseteq \mathrm{TN}\alpha$ −$\mathrm{Cl}(\mathrm{M})$. This implies $\mathrm{TN}\alpha$ −$\mathrm{Cl}(\mathrm{M})\subseteq \mathrm{H}$. Therefore, M is a $\mathrm{TN}g^{\#}\psi$ −closed set in $(R,\mathrm{T}_{\mathrm{TN}})$.

Theorem 3.18. Every $\mathrm{TN}\alpha g^{\#}\psi$ −closed $(\text{resp. } \mathrm{TN}\alpha g^{\#}\psi$ −open$)$ set in a TN −Top −Space $(\mathrm{R},\mathrm{T}_{\mathrm{TN}})$ is a $\mathrm{TN}\alpha^{*}g^{\#}\psi$ −closed $(\text{resp. } \mathrm{TN}\alpha^{*}g^{\#}\psi$ −open$)$ set in $(\mathrm{R},\mathrm{T}_{\mathrm{TN}})$.

Proof. Consider a $\mathrm{TN}\alpha g^{\#}\psi$ −closed set M in a TN −Top −Space $(\mathrm{R},\mathrm{T}_{\mathrm{TN}})$. Assume that $M\subseteq H$ and H be a $\mathrm{TN}\alpha g^{\#}\psi$ −open set in $(R,\mathrm{T}_{\mathrm{TN}})$. As every $\mathrm{TN}\alpha g^{\#}\psi$ −open set is $\mathrm{TN}g^{\#}\psi$ −open set, H is $\mathrm{TN}g^{\#}\psi$ −open set. Since M is $\mathrm{TN}\alpha g^{\#}\psi$ −closed set, $\mathrm{TN}\alpha$ −$\mathrm{Cl}(\mathrm{M})\subseteq \mathrm{H}$. Therefore, M is a $\mathrm{TN}\alpha^{*}g^{\#}\psi$ −closed set in $(R,\mathrm{T}_{\mathrm{TN}})$.

Theorem 3.19. The intersection (resp. union) of two $\text{TN}\alpha^{*}g^{\#}\psi$ −closed $\left(\text{resp. TN}\alpha^{*}g^{\#}\psi\text{−open}\right)$ sets in a TN −Top −Space $\left(\text{R},\text{T}_{\text{TN}}\right)$ is a $\text{TN}\alpha^{*}g^{\#}\psi$ −closed $\left(\text{resp. TN}\alpha^{*}g^{\#}\psi\text{−open}\right)$ set in $\left(\text{R},\text{T}_{\text{TN}}\right)$.

Proof. Let M and K be $\text{TN}\alpha^{*}g^{\#}\psi$ −closed sets and $\text{M}\bigcup\text{K}\subseteq\text{H}$ where H is $\text{TN}\alpha g^{\#}\psi$ −open set. Then $\text{M}\subseteq\text{H}$ and $\text{K}\subseteq\text{H}$. As M and K are $\text{TN}\alpha^{*}g^{\#}\psi$ −closed sets, $\text{TN}\alpha\text{−Cl}\left(\text{M}\right)\subseteq\text{H}$ and $\text{TN}\alpha\text{−Cl}\left(\text{K}\right)\subseteq\text{H}$. Also $\text{TN}\alpha\text{−Cl}\left(\text{M}\bigcup\text{K}\right)=\text{TN}\alpha\text{−Cl}\left(\text{M}\right)\bigcup\text{TN}\alpha\text{−Cl}\left(\text{K}\right)\subseteq\text{H}\Rightarrow\text{TN}\alpha\text{−Cl}\left(\text{M}\bigcup\text{K}\right)\subseteq\text{H}$. Thus it follows thats that $\text{M}\bigcup\text{K}$ is $\text{TN}\alpha^{*}g^{\#}\psi$ −closed set. Hence, the union of two $\text{TN}\alpha^{*}g^{\#}\psi$ −closed sets is $\text{TN}\alpha^{*}g^{\#}\psi$ −closed set.

Theorem 3.20. Let M be a TN −open set and K be a $\text{TN}\alpha^{*}g^{\#}\psi$ −open set in a TN −Top −Space. $\left(\text{R},\text{T}_{\text{TN}}\right)$. Then $\text{M}\bigcap\text{K}$ is $\text{TN}\alpha^{*}g^{\#}\psi$ −open set.

Proof. Let M be a TN −open set and K be a $\text{TN}\alpha^{*}g^{\#}\psi$ −open set in a TN −Top −Space $\left(\text{R},\text{T}_{\text{TN}}\right)$. As every TN −open set is $\text{TN}\alpha^{*}g^{\#}\psi$ −open set, M is $\text{TN}\alpha^{*}g^{\#}\psi$ −open set. Since the intersection of two $\text{TN}\alpha^{*}g^{\#}\psi$ −open sets is $\text{TN}\alpha^{*}g^{\#}\psi$ −open set. Hence $\text{M}\bigcap\text{K}$ is $\text{TN}\alpha^{*}g^{\#}\psi$ −open set.

Example 3.21. Let $R=\{a,b,c\}$. Let G,H and M be TN-sets given by
$G=\{\langle a,0.7,0.10,0.10\rangle,\langle b,0,0,1\rangle,\langle c,0,0,1\rangle\}$, $H=\{\langle a,1,0,0\rangle,\langle b,0.60,0.20,0.20\rangle,\langle c,0,0,1\rangle\}$,
$M=\{\langle a,0,0,1\rangle,\langle b,0.60,0.20,0.20\rangle,\langle c,0,0,1\rangle\}$. Clearly $(0.70)^4+(0.10)^4+(0.10)^4=0.2403\leq 1$, and $(0.60)^4+(0.20)^4+(0.20)^4=0.1328\leq 1$. Thus, all the above triples satisfy the condition $T^4+I^4+F^4\leq 1$. Consider the tetra neutrosophic Topology $T_{\text{TN}}=\{0_{\text{TN}},G,H,1_{\text{TN}}\}$. Since M is different from the corresponding TN −closed sets: $0_{\text{TN}},G^{C},H^{C},1_{\text{TN}}$. Hence M is not TN −closed. Now, $\text{TN}\text{−Int}\left(\text{M}\right)=0_{\text{TN}}$. Threefore, $\text{TN}\text{−Cl}\left(\text{TN}\text{−Int}\left(\text{M}\right)\right)=\text{TN}\text{−Cl}\left(0_{\text{TN}}\right)=0_{\text{TN}}$, and hence $\text{TN}\text{−In}\left(\text{TN}\text{−Cl}\left(\text{TN}\text{−Int}\left(\text{M}\right)\right)\right)=0_{\text{TN}}$. Furthermore, the TN −complement of M is $\text{TN}\alpha$ −open. Hence M is $\text{TN}\alpha$ −closed and consequently $\text{TN}\alpha\text{−Cl}\left(\text{M}\right)=\text{M}$.
Let H be any $\text{TN}\alpha g^{\#}\psi$ −open set such that $M\subseteq H$. Since $\text{TN}\alpha\text{−Cl}\left(\text{M}\right)=\text{M}$. We immediately obtain $\text{TN}\alpha\text{−Cl}\left(\text{M}\right)=\text{M}\subseteq\text{H}$. Therefore, by the definition of a $\text{TN}\alpha g^{\#}\psi$ −closed set, M is $\text{TN}\alpha g^{\#}\psi$ −closed. Thus, by Theorem 3.18, M is $\text{TN}\alpha^{*}g^{\#}\psi$ −closed which is not TN −closed. Hence, $\text{TN}\alpha$ −closed $\Rightarrow$ $\text{TN}\alpha^{*}g^{\#}\psi$ −closed, but the converse implication does not hold.

4. Tetra Neutrosophic $\alpha^{*}g^{\#}\psi$ −Continuous Mappings

In this section, we introduce the concepts of Tetra Neutrosophic $\alpha^{*}g^{\#}\psi$ −continuous $\left(\text{briefly, TN}\alpha^{*}g^{\#}\psi\text{−continuous}\right)$ mappings in TN −Top −Spaces. Also, we study some of the main results depending on $\text{TN}\alpha^{*}g^{\#}\psi$ −open and $\text{TN}\alpha^{*}g^{\#}\psi$ −closed sets.

Definition 4.1. Let $\xi:(R,\text{T}_{\text{TN}})\to(Z,\Gamma_{\text{TN}})$ be a mapping. Then ξ is called a $\text{TN}\alpha^{*}g^{\#}\psi$ −continuous mapping if $\xi^{-1}(H)$ is a $\text{TN}\alpha^{*}g^{\#}\psi$ −open set in R for every TN −open set H in Z.

Theorem 4.2. Every TN −continuous mapping is a $\text{TN}\alpha^{*}g^{\#}\psi$ −continuous mapping.

Proof. Let $\xi:(R,\mathrm{T}_{\mathrm{TN}})\to(Z,\Gamma_{\mathrm{TN}})$ be TN−continuous mapping. Let H be a TN−open set in (Z,Γ_{TN}). Then $\xi^{-1}(H)$ is TN−open set in $(\mathrm{R},\mathrm{T}_{\mathrm{TN}})$. Since every TN−open set is TNα*g#ψ−open, $\xi^{-1}(H)$ is TNα*g#ψ−open set in $(\mathrm{R},\mathrm{T}_{\mathrm{TN}})$. Hence ξ is a TNα*g#ψ−continuous mapping.

Theorem 4.3. Let $\xi:(R,\mathrm{T}_{\mathrm{TN}})\to(Z,\Gamma_{\mathrm{TN}})$ be a TNα*g#ψ−continuous map and $\mu:(Z,\Gamma_{\mathrm{TN}})\to(W,\Psi_{\mathrm{TN}})$ be a TN−continuous mappings. Then prove that $\mu o\xi:(R,\mathrm{T}_{\mathrm{TN}})\to(W,\Psi_{\mathrm{TN}})$ is a TNα*g#ψ−continuous mapping.

Proof. Let H be a TN−open set in W. Since $\mu:(Z,\Gamma_{\mathrm{TN}})\to(W,\Psi_{\mathrm{TN}})$ is TN−continuous, $\mu^{-1}(H)$ is TN−open set in Z. Since ξ is a TNα*g#ψ−continuous mapping, $\xi^{-1}\left[\mu^{-1}(H)\right]$ is a TNα*g#ψ−open set in R. But $\xi^{-1}\left[\mu^{-1}(H)\right]=(\mu o\xi)^{-1}(H)$. Then $(\mu o\xi)^{-1}(H)$ is a TNα*g#ψ−open set in R. Therefore, $\mu o\xi$ is a TNα*g#ψ−continuous mapping.

Theorem 4.4. Prove that $\xi:(R,\mathrm{T}_{\mathrm{TN}})\to(Z,\Gamma_{\mathrm{TN}})$ is a TNα*g#ψ−continuous mapping if and only if $\xi^{-1}(H)$ is TNα*g#ψ−closed set in R for every TN−closed set H in R.

Proof. Let H be a TN−closed set in Z. Then H^C is TN−open set in Z. Since ξ is TNα*g#ψ−continuous. Therefore $\xi^{-1}(H^C)$ is a TNα*g#ψ−open set in R. Since $\xi^{-1}(H^C)=\left[\xi^{-1}(H)\right]^C$, $\xi^{-1}(H)$ is a TNα*g#ψ−closed set in R.

Conversely, Let H be a TN−open set in Z. Then H^C is TN−closed set in Z. By assumption $\xi^{-1}(H^C)$ is TNα*g#ψ−closed set in R. Since $\xi^{-1}(H^C)=\left[\xi^{-1}(H)\right]^C$, $\xi^{-1}(H)$ is TNα*g#ψ−open set in R. Therefore, ξ is a TNα*g#ψ−continuous mapping.

The following example shows that a TNα*g#ψ−continuous function may not be a TN−continuous function.

Example 4.5. Let $R=\{p_1,p_2,p_3\}$, where $p_1=(0.80,0.20,0.20)$, $p_2=(0.60,0.40,0.20)$, $p_3=(0.40,0.30,0.30)$. Let the Tetra Neutrosophic topology on R be $\mathrm{T}_{\mathrm{TN}}=\{0_{\mathrm{TN}},\{p_1\},1_{\mathrm{TN}}\}$. Consider the set $A=\{p_1,p_2\}$. Then $\mathrm{TN}-Int(A)=\{p_1\}$, $\mathrm{TN}-Cl(\mathrm{TN}-Int(A))=1_{\mathrm{TN}}$, and $A\subseteq\mathrm{TN}-Int(\mathrm{TN}-Cl(\mathrm{TN}-Int(A)))=1_{\mathrm{TN}}$. This shows that A is a TNα−open set. Since every TNα−open set is a TNα*g#ψ−open set. Thus, A is a TNα*g#ψ−open set. But $A\notin\mathrm{T}_{\mathrm{TN}}$, therefor, A is not TN−open. Let $Z=\{q_1,q_2\}$, where $q_1=(0.70,0.20,0.20)$, $q_2=(0.40,0.40,0.30)$, and let $\Gamma_{\mathrm{TN}}=\{0_{\mathrm{TN}},\{q_1\},1_{\mathrm{TN}}\}$ be the Tetra Neutrosophic topology on Z. Define the mapping $\xi:(R,\mathrm{T}_{\mathrm{TN}})\to(Z,\Gamma_{\mathrm{TN}})$ by $\xi(p_1)=q_1$, $\xi(p_2)=q_1$, $\xi(p_3)=q_2$. Then $\xi^{-1}(\{q_1\})=\{p_1,p_2\}=A$, and $\xi^{-1}(Z)=1_{\mathrm{TN}}$. Therefore, ξ is TNα*g#ψ−continuous but not TN−continuous.

Theorem 4.6. A mapping $\xi:(R,\mathrm{T}_{\mathrm{TN}})\to(Z,\Gamma_{\mathrm{TN}})$ is a TNα*g#ψ−continuous mapping if and only if $\xi(\mathrm{TN}\alpha^*\mathrm{g}^{\#}\psi-Cl(E))\subseteq\mathrm{TN}-Cl(\xi(E))$ for every TN−set E in R.

Proof. Let E be a TN−set in R and ξ be a TNα*g#ψ−continuous mapping. We note that evidently $\xi(E)\subseteq\mathrm{TN}\alpha^*\mathrm{g}^{\#}\psi-Cl[\xi(E)]$. Then we obtain $E\subseteq\xi^{=1}[\xi(E)]\subseteq\xi^{-1}[\mathrm{TN}\alpha^*\mathrm{g}^{\#}\psi-Cl(\xi(E))]$ and $\mathrm{TN}\alpha^*\mathrm{g}^{\#}\psi-Cl(E)\subseteq\mathrm{TN}\alpha^*\mathrm{g}^{\#}\psi-Cl[\xi^{-1}(\mathrm{TN}\alpha^*\mathrm{g}^{\#}\psi-(\xi(E)))]$. Since ξ is a TNα*g#ψ−continuous mapping

and $\text{TN}\alpha^{*}\text{g}^{\#}\psi-Cl\left[\xi(E)\right]$ is a $\text{TN}\alpha^{*}\text{g}^{\#}\psi-$closed set. Therefore, $\text{TN}\alpha^{*}\text{g}^{\#}\psi-Cl\left[\xi^{-1}\left(\text{TN}\alpha^{*}\text{g}^{\#}\psi-Cl\left(\xi(E)\right)\right)\right]=\xi^{-1}\left[\text{TN}\alpha^{*}\text{g}^{\#}\psi-Cl\left(\xi(E)\right)\right]$. Hence, we have $\xi\left[\text{TN}\alpha^{*}\text{g}^{\#}\psi-Cl(E)\right]\subseteq\text{TN}-Cl\left[\xi(E)\right]$.

Conversely, let $\xi\left[\text{TN}\alpha^{*}\text{g}^{\#}\psi-Cl(E)\right]\subseteq T\text{N}-Cl\left[\xi(E)\right]$, for each $\text{TN}-\text{set}\ E$ in R. Let H be a $\text{TN}-\text{closed}$ set in Z. Then $\text{TN}\alpha^{*}\text{g}^{\#}\psi-Cl\left[\xi\left(\xi^{-1}(H)\right)\right]\subseteq\text{TN}\alpha^{*}\text{g}^{\#}\psi-Cl(H)=H$. By assumption, by taking $E=\xi^{-1}(H)$, we obtain $\xi\left[\text{TN}\alpha^{*}\text{g}^{\#}\psi-\text{Cl}\left(\xi^{-1}(\text{H})\right)\right]\subseteq\text{TN}-\text{Cl}\left[\xi\left(\xi^{-1}(\text{H})\right)\right]\subseteq\text{H}$ and hence $\text{TN}\alpha^{*}\text{g}^{\#}\psi-Cl\left[\xi^{-1}(H)\right]\subseteq\xi^{-1}(H)$. Since $\xi^{-1}(H)\subseteq\text{TN}\alpha^{*}\text{g}^{\#}\psi-Cl\left[\xi^{-1}(H)\right]$. Thus $\text{TN}\alpha^{*}\text{g}^{\#}\psi-Cl\left[\xi^{-1}(H)\right]=\xi^{-1}(H)$. This implies that $\xi^{-1}(H)$ is a $\text{TN}\alpha^{*}\text{g}^{\#}\psi-$closed set in R. Therefore, by Theorem 4.4, ξ is a $\text{TN}\alpha^{*}\text{g}^{\#}\psi-$continuous mapping.

Theorem 4.7. Let $\xi:(R,\text{T}_{\text{TN}})\to(Z,\Gamma_{\text{TN}})$ be a mapping. Then ξ is a $\text{TN}\alpha^{*}\text{g}^{\#}\psi-$continuous mapping if and only if $\text{TN}\alpha^{*}\text{g}^{\#}\psi-\text{Cl}\left[\xi^{-1}(\text{H})\right]\subseteq\xi^{-1}\left[\text{TN}-\text{Cl}(\text{H})\right]$ for each $\text{TN}-$set H in Z.

Proof. Suppose that $\xi:(R,\text{T}_{\text{TN}})\to(Z,\Gamma_{\text{TN}})$ is a $\text{TN}\alpha^{*}\text{g}^{\#}\psi-$continuous mapping. Take H be any $\text{TN}-$set in Z. Clearly $H\subseteq\text{TN}-Cl(H)$ implies $\xi^{-1}(H)\subseteq\xi^{-1}\left[\text{TN}\alpha^{*}\text{g}^{\#}\psi-Cl(H)\right]$. Then $\text{TN}\alpha^{*}\text{g}^{\#}\psi-Cl\left[\xi^{-1}(H)\right]\subseteq\text{TN}\alpha^{*}\text{g}^{\#}\psi-Cl\left[\xi^{-1}\left(\text{TN}-Cl(H)\right)\right]$. Since $\text{TN}-Cl(H)$ is $\text{TN}-$closed set in Z. So by Theorem 4.4, $\xi^{-1}\left[\text{TN}-Cl(H)\right]$ is a $\text{TN}\alpha^{*}\text{g}^{\#}\psi-$closed set in R. Therefore, $\text{TN}\alpha^{*}\text{g}^{\#}\psi-\text{Cl}\left[\xi^{-1}\left(\text{TN}-\text{Cl}(\text{H})\right)\right]=\xi^{-1}\left[\text{TN}-Cl(H)\right]$. Hence, we obtain $\text{TN}\alpha^{*}\text{g}^{\#}\psi-Cl\left[\xi^{-1}(H)\right]\subseteq\xi^{-1}\left[\text{TN}-Cl(H)\right]$.

Conversely, let $\text{TN}\alpha^{*}\text{g}^{\#}\psi-\text{Cl}\left[\xi^{-1}(\text{H})\right]\subseteq\xi^{-1}\left[\text{TN}-\text{Cl}(\text{H})\right]$ for every $\text{TN}-\text{set}\ H$ in Z. Let K be a $\text{TN}-$closed set in Z. Since every $\text{TN}-$closed set is $\text{TN}\alpha^{*}\text{g}^{\#}\psi-$closed set, $\text{TN}\alpha^{*}\text{g}^{\#}\psi-\text{Cl}\left[\xi^{-1}(\text{K})\right]\subseteq\xi^{-1}\left[\text{TN}-\text{Cl}(\text{K})\right]=\xi^{-1}(\text{K})$. This implies that $\xi^{-1}(K)$ is a $\text{TN}\alpha^{*}\text{g}^{\#}\psi-$closed set in R. Thus, by Theorem 4.4, ξ is a $\text{TN}\alpha^{*}\text{g}^{\#}\psi-$continuous mapping.

Theorem 4.8. A mapping $\xi:(R,\text{T}_{\text{TN}})\to(Z,\Gamma_{\text{TN}})$ is a $\text{TN}\alpha^{*}\text{g}^{\#}\psi-$continuous mapping if and only if $\xi^{-1}\left[\text{TN}-\text{Int}(\text{H})\right]\subseteq\text{TN}\alpha^{*}\text{g}^{\#}\psi-\text{Int}\left[\xi^{-1}(\text{H})\right]$ for every $\text{TN}-\text{set}\ H$ in Z.

Proof. Let H be any $\text{TN}-$set in Z and ξ be a $\text{TN}\alpha^{*}\text{g}^{\#}\psi-$continuous mapping. Then $\text{TN}-\text{Int}(\text{H})\subseteq\text{H}$ implies $\xi^{-1}\left[\text{TN}-\text{Int}(\text{H})\right]\subseteq\xi^{-1}(\text{H})$. Therefore then this implies that $\text{TN}\alpha^{*}\text{g}^{\#}\psi-\text{Int}\left[\xi^{-1}\left(\text{TN}-\text{Int}(\text{H})\right)\right]\subseteq\text{TN}\alpha^{*}\text{g}^{\#}\psi-\text{Int}\left[\xi^{-1}(\text{H})\right]$. Since $\text{TN}-\text{Int}(\text{H})$ is $\text{TN}-$open set in Z and ξ is $\text{TN}\alpha^{*}\text{g}^{\#}\psi-$continuous Therefore, $\xi^{-1}\left[\text{TN}-\text{Int}(\text{H})\right]$ is $\text{TN}\alpha^{*}\text{g}^{\#}\psi-$open set in R. Hence, we get $\text{TN}\alpha^{*}\text{g}^{\#}\psi-\text{Int}\left[\xi^{-1}\left(\text{TN}-\text{Int}(\text{H})\right)\right]=\xi^{-1}\left[\text{TN}-\text{Int}(\text{H})\right]\subseteq\text{TN}\alpha^{*}\text{g}^{\#}\psi-\text{Int}\left[\xi^{-1}(\text{H})\right]$.

Conversely, let $\xi^{-1}\left[\text{TN}-\text{Int}(\text{H})\right]\subseteq\text{TN}\alpha^{*}\text{g}^{\#}\psi-\text{Int}\left[\xi^{-1}(\text{H})\right]$ for every $\text{TN}-\text{set}\ H$ in Z. Let G be any $\text{TN}-$open set in Z and hence $\text{TN}-\text{Int}(\text{G})=\text{G}$. By hypothesis, we have $\xi^{-1}\left[\text{TN}-\text{Int}(\text{G})\right]\subseteq\text{TN}\alpha^{*}\text{g}^{\#}\psi-\text{Int}\left[\xi^{-1}(\text{G})\right]$. Therefore. we obtain $\xi^{-1}(\text{G})\subseteq\text{TN}\alpha^{*}\text{g}^{\#}\psi-\text{Int}\left[\xi^{-1}(\text{G})\right]$. Also $\text{TN}\alpha^{*}\text{g}^{\#}\psi-\text{Int}\left[\xi^{-1}(\text{G})\right]\subset\left[\xi^{-1}(\text{G})\right]$. Consequently, $\text{TN}\alpha^{*}\text{g}^{\#}\psi-\text{Int}\left[\xi^{-1}(\text{G})\right]=\left[\xi^{-1}(\text{G})\right]$. This implies that $\xi^{-1}(G)$ is $\text{TN}\alpha^{*}\text{g}^{\#}\psi-$open set in R. Hence we conclude that ξ is a $\text{TN}\alpha^{*}\text{g}^{\#}\psi-$continuous mapping.

Definition 4.9. Let $p_{(t,i,f)}$ be a $\text{TN}-\text{point}$ of a $\text{TN}-\text{Top}-\text{Space}\ (R,\text{T}_{\text{TN}})$. A $\text{TN}-$set M of R is called $\text{TN}-\text{neighbourhood}$ of $p_{(t,i,f)}$ if there exists a $\text{TN}-$open set G such that $p_{(t,i,f)}\in G\subseteq M$.

Theorem 4.10. Let $\xi:(R,\text{T}_{\text{TN}})\to(Z,\Gamma_{\text{TN}})$ be a mapping. Then the following assertions are equivalent.

(i) ξ is $\mathrm{TN}\alpha^{*}\mathrm{g}^{\#}\psi$ −continuous.

(ii) For each TN−point $p_{(\mathrm{t},\mathrm{i},\mathrm{f})}$ in R and every TN−neighbourhood M_p of $\xi\left(p_{(\mathrm{t},\mathrm{i},\mathrm{f})}\right)$, there exists a $\mathrm{TN}\alpha^{*}\mathrm{g}^{\#}\psi$ −open set G_p in R such that $p_{(\mathrm{t},\mathrm{i},\mathrm{f})} \in G_p \subseteq \xi^{-1}\left(M_p\right)$.

(iii) For each TN−point $p_{(\mathrm{t},\mathrm{i},\mathrm{f})}$ in R and every TN−neighbourhood H of $\xi\left(p_{(\mathrm{t},\mathrm{i},\mathrm{f})}\right)$, there exists a $\mathrm{TN}\alpha^{*}\mathrm{g}^{\#}\psi$ −open set G in R such that $p_{(\mathrm{t},\mathrm{i},\mathrm{f})} \in G$ and $\xi(G) \subseteq H$.

Proof. $(\mathrm{i}) \Rightarrow (\mathrm{ii})$: Let $p_{(\mathrm{t},\mathrm{i},\mathrm{f})}$ be a TN−point in R and let H be a TN−neighbourhood of TN−open set G in Z such that $\xi\left(p_{(\mathrm{t},\mathrm{i},\mathrm{f})}\right) \in G \subseteq H$. Since ξ is $\mathrm{TN}\alpha^{*}\mathrm{g}^{\#}\psi$ −continuous. we know that $\xi^{-1}(G)$ is a $\mathrm{TN}\alpha^{*}\mathrm{g}^{\#}\psi$ −open set in R and $p_{(\mathrm{t},\mathrm{i},\mathrm{f})} \in \xi^{-1}(G) \subseteq \xi^{-1}(H)$. This implies (ii) is true.

$(\mathrm{ii}) \Rightarrow (\mathrm{iii})$: Let $p_{(\mathrm{t},\mathrm{i},\mathrm{f})}$ be a TN−point in R and let H be a TN−neighbourhood of $\xi\left(p_{(\mathrm{t},\mathrm{i},\mathrm{f})}\right)$. The condition (ii) implies that there exists a $\mathrm{TN}\alpha^{*}\mathrm{g}^{\#}\psi$ −open set G in R such that $p_{(\mathrm{t},\mathrm{i},\mathrm{f})} \in G \subseteq \xi^{-1}(H)$. Thus $p_{(\mathrm{t},\mathrm{i},\mathrm{f})} \in G$ and $\xi(G) \subseteq \xi\left[\xi^{-1}(H)\right] \subseteq H$. Hence (iii) is true.

$(\mathrm{iii}) \Rightarrow (\mathrm{i})$: Let H be a TN−open set in Z and let $p_{(\mathrm{t},\mathrm{i},\mathrm{f})} \in \xi^{-1}(H)$. Since H is TN−open set, $\xi\left(p_{(\mathrm{t},\mathrm{i},\mathrm{f})}\right) \in H$, and so H is TN−neighbourhood of $\xi\left(p_{(\mathrm{t},\mathrm{i},\mathrm{f})}\right)$. It follows from (iii) that there exists a $\mathrm{TN}\alpha^{*}\mathrm{g}^{\#}\psi$ −open set G in R such that $p_{(\mathrm{t},\mathrm{i},\mathrm{f})} \in G$ and $\xi(G) \subseteq H$ so that $p_{(\mathrm{t},\mathrm{i},\mathrm{f})} \in G \subseteq \xi^{-1}\left[\xi(G)\right] \subseteq \xi^{-1}(H)$. This implies by definition that $\xi^{-1}(H)$ is a $\mathrm{TN}\alpha^{*}\mathrm{g}^{\#}\psi$ −open set in R. Therefore, ξ is a $\mathrm{TN}\alpha^{*}\mathrm{g}^{\#}\psi$ −continuous mapping.

Proof. Let $p_{(\mathrm{t},\mathrm{i},\mathrm{f})}$ be a TN−point in R and let H be a TN−neighbourhood of $\xi\left(p_{(\mathrm{t},\mathrm{i},\mathrm{f})}\right)$. Then there exists a TN−open set E in Z such that $\xi\left(p_{(\mathrm{t},\mathrm{i},\mathrm{f})}\right) \in E \subseteq H$. Since ξ is $\mathrm{TN}\alpha^{*}\mathrm{g}^{\#}\psi$ −continuous, we know that $G = \xi^{-1}(E)$ is a $\mathrm{TN}\alpha^{*}\mathrm{g}^{\#}\psi$ −open set in R and $p_{(\mathrm{t},\mathrm{i},\mathrm{f})} \in G = \xi^{-1}(E) \subseteq \xi^{-1}(H)$.

5. Tetra Neutrosophic $\alpha^{*}\mathrm{g}^{\#}\psi$ −Irresolute Mappings

In this section, we introduce the concept of Tetra Neutrosophic $\alpha^{*}\mathrm{g}^{\#}\psi$ −irresolute $(\text{briefly, } \mathrm{TN}\alpha^{*}\mathrm{g}^{\#}\psi\text{ −irresolute})$ mappings in TN−Top−Spaces. Also, we study some of the main results depending on $\mathrm{TN}\alpha^{*}\mathrm{g}^{\#}\psi$ −open and $\mathrm{TN}\alpha^{*}\mathrm{g}^{\#}\psi$ −closed sets in TN−Top−Spaces.

Definition 5.1. Let a mapping $\xi:\left(R,\mathrm{T}_{\mathrm{TN}}\right) \to \left(Z,\Gamma_{\mathrm{TN}}\right)$ is called $\mathrm{TN}\alpha^{*}\mathrm{g}^{\#}\psi$ −irresolute if the inverse image of every $\mathrm{TN}\alpha^{*}\mathrm{g}^{\#}\psi$ −open set in Z is $\mathrm{TN}\alpha^{*}\mathrm{g}^{\#}\psi$ −open in R.

Theorem 5.2. A mapping $\xi:\left(R,\mathrm{T}_{\mathrm{TN}}\right) \to \left(Z,\Gamma_{\mathrm{TN}}\right)$ is $\mathrm{TN}\alpha^{*}\mathrm{g}^{\#}\psi$ −irresolute if and only if the inverse image of every $\mathrm{TN}\alpha^{*}\mathrm{g}^{\#}\psi$ −closed set in $\left(Z,\Gamma_{\mathrm{TN}}\right)$ is $\mathrm{TN}\alpha^{*}\mathrm{g}^{\#}\psi$ −closed set in $\left(R,\mathrm{T}_{\mathrm{TN}}\right)$.

Proof. Let H be any $\mathrm{TN}\alpha^{*}\mathrm{g}^{\#}\psi$ −closed set in Z. Then H^{C} is $\mathrm{TN}\alpha^{*}\mathrm{g}^{\#}\psi$ −open set in Z. Since ξ is $\mathrm{TN}\alpha^{*}\mathrm{g}^{\#}\psi$ −irresolute, $\xi^{-1}\left(H^{C}\right)$ is $\mathrm{TN}\alpha^{*}\mathrm{g}^{\#}\psi$ −open set in R and $\xi^{-1}\left(H^{C}\right) = \left[\xi^{-1}(H)\right]^{C}$ which implies that $\xi^{-1}(H)$ is $\mathrm{TN}\alpha^{*}\mathrm{g}^{\#}\psi$ −closed set in R.

Conversely, Let G be any $\mathrm{TN}\alpha^{\star}\mathrm{g}^{\#}\psi-$open set in Z. Then G^{C} is $\mathrm{TN}\alpha^{\star}\mathrm{g}^{\#}\psi-$closed set in Z. Thus $\xi^{-1}\left(G^{C}\right)$ is $\mathrm{TN}\alpha^{\star}\mathrm{g}^{\#}\psi-$closed set in R and $\xi^{-1}\left(G^{C}\right)=\left[\xi^{-1}(G)\right]^{C}$ which implies that $\xi^{-1}(G)$ is $\mathrm{TN}\alpha^{\star}\mathrm{g}^{\#}\psi-$open set in R. Hence $\xi:U\to W$ is $\mathrm{TN}\alpha^{\star}\mathrm{g}^{\#}\psi-$irresolute.

Theorem 5.3. Every $\mathrm{TN}\alpha^{\star}\mathrm{g}^{\#}\psi-$irresolute mapping $\xi:\left(R,\mathrm{T}_{\mathrm{TN}}\right)\to\left(Z,\Gamma_{\mathrm{TN}}\right)$ is $\mathrm{TN}\alpha^{\star}\mathrm{g}^{\#}\psi-$continuous.

Proof. Let H be a $\mathrm{TN}-$open set in Z. Since every $\mathrm{TN}-$open set is $\mathrm{TN}\alpha^{\star}\mathrm{g}^{\#}\psi-$open, H is $\mathrm{TN}\alpha^{\star}\mathrm{g}^{\#}\psi-$open. Since ξ is $\mathrm{TN}\alpha^{\star}\mathrm{g}^{\#}\psi-$irresolute, $\xi^{-1}(H)$ is $\mathrm{TN}\alpha^{\star}\mathrm{g}^{\#}\psi-$open in R. Therefore ξ is $\mathrm{TN}\alpha^{\star}\mathrm{g}^{\#}\psi-$continuous.

Theorem 5.4. A mapping $\xi:\left(R,\mathrm{T}_{\mathrm{TN}}\right)\to\left(Z,\Gamma_{\mathrm{TN}}\right)$ is a $\mathrm{TN}\alpha^{\star}\mathrm{g}^{\#}\psi-$irresolute mapping if and only if $\xi\left(\mathrm{TN}\alpha^{\star}\mathrm{g}^{\#}\psi-Cl(M)\right)\subseteq\mathrm{TN}\alpha^{\star}\mathrm{g}^{\#}\psi-Cl\left(\xi(M)\right)$ for every $\mathrm{TN}-$set M in $\left(R,\mathrm{T}_{\mathrm{TN}}\right)$.

Proof. Let M be a $\mathrm{TN}-$set in R and ξ be a $\mathrm{TN}\alpha^{\star}\mathrm{g}^{\#}\psi-$iresolute mapping. Then evidently $\xi(M)\subseteq\mathrm{TN}\alpha^{\star}\mathrm{g}^{\#}\psi-Cl\left[\xi(M)\right]$. Then we have $M\subseteq\xi^{=1}\left[\xi(M)\right]\subseteq\xi^{-1}\left[\mathrm{TN}\alpha^{\star}\mathrm{g}^{\#}\psi-Cl\left(\xi(M)\right)\right]$ and hence $\mathrm{TN}\alpha^{\star}\mathrm{g}^{\#}\psi-Cl(M)\subseteq\mathrm{TN}\alpha^{\star}\mathrm{g}^{\#}\psi-Cl\left[\xi^{-1}\left(\mathrm{TN}\alpha^{\star}\mathrm{g}^{\#}\psi-Cl\left(\xi(M)\right)\right)\right]$. Since ξ is a $\mathrm{TN}\alpha^{\star}\mathrm{g}^{\#}\psi-$irresolute mapping and $\mathrm{TN}\alpha^{\star}\mathrm{g}^{\#}\psi-Cl\left[\xi(M)\right]$ is a $\mathrm{TN}\alpha^{\star}\mathrm{g}^{\#}\psi-$closed set. Therefore $\mathrm{TN}\alpha^{\star}\mathrm{g}^{\#}\psi-Cl\left[\xi^{-1}\left(\mathrm{TN}\alpha^{\star}\mathrm{g}^{\#}\psi-Cl\left(\xi(M)\right)\right)\right]=\xi^{-1}\left[\mathrm{TN}\alpha^{\star}\mathrm{g}^{\#}\psi-Cl\left(\xi(M)\right)\right]$. So $\xi\left[\mathrm{TN}\alpha^{\star}\mathrm{g}^{\#}\psi-Cl(M)\right]\subseteq\mathrm{TN}\alpha^{\star}\mathrm{g}^{\#}\psi-Cl\left[\xi(M)\right]$.

Conversely assume that $\xi\left[\mathrm{TN}\alpha^{\star}\mathrm{g}^{\#}\psi-Cl(M)\right]\subseteq\mathrm{TN}\alpha^{\star}\mathrm{g}^{\#}\psi-Cl\left[\xi(M)\right]$, for each $\mathrm{TN}-$set M in R. Let G be a $\mathrm{TN}\alpha^{\star}\mathrm{g}^{\#}\psi-$closed set in Z. Therefore $\mathrm{TN}\alpha^{\star}\mathrm{g}^{\#}\psi-Cl(G)=G$. By assumption, $\xi\left[\mathrm{TN}\alpha^{\star}\mathrm{g}^{\#}\psi-Cl\left(\xi^{-1}(G)\right)\right]\subseteq\mathrm{TN}\alpha^{\star}\mathrm{g}^{\#}\psi-Cl\left[\xi\left(\xi^{-1}(G)\right)\right]\subseteq\mathrm{TN}\alpha^{\star}\mathrm{g}^{\#}\psi-Cl(G)=G$ and then this implies that $\mathrm{TN}\alpha^{\star}\mathrm{g}^{\#}\psi-Cl\left[\xi^{-1}(G)\right]\subseteq\xi^{-1}(G)$. Since we also have $\xi^{-1}(G)\subseteq\mathrm{TN}\alpha^{\star}\mathrm{g}^{\#}\psi-Cl\left[\xi^{-1}(G)\right]$. Thus we conclude that $\mathrm{TN}\alpha^{\star}\mathrm{g}^{\#}\psi-Cl\left[\xi^{-1}(G)\right]=\xi^{-1}(G)$. This shows that $\xi^{-1}(G)$ is a $\mathrm{TN}\alpha^{\star}\mathrm{g}^{\#}\psi-$closed set in R. Thus, by Theorem 5.3, ξ is a $\mathrm{TN}\alpha^{\star}\mathrm{g}^{\#}\psi-$irresolute mapping.

Theorem 5.5. A mapping $\xi:\left(R,\mathrm{T}_{\mathrm{TN}}\right)\to\left(Z,\Gamma_{\mathrm{TN}}\right)$ is a $\mathrm{TN}\alpha^{\star}\mathrm{g}^{\#}\psi-$irresolute mapping if and only if $\mathrm{TN}\alpha^{\star}\mathrm{g}^{\#}\psi-Cl\left[\xi^{-1}(G)\right]\subseteq\xi^{-1}\left[\mathrm{TN}\alpha^{\star}\mathrm{g}^{\#}\psi-Cl(G)\right]$ for each $\mathrm{TN}-$set G in Z.

Proof. Let $\xi:R\to Z$ be a $\mathrm{TN}\alpha^{\star}\mathrm{g}^{\#}\psi-$irresolute mapping. Let G be any $\mathrm{TN}-$set set in Z. Since $G\subseteq\mathrm{TN}\alpha^{\star}\mathrm{g}^{\#}\psi-Cl(G)$ and therefore we get $\xi^{-1}(G)\subseteq\xi^{-1}\left[\mathrm{TN}\alpha^{\star}\mathrm{g}^{\#}\psi-Cl(G)\right]$. *So* $\mathrm{TN}\alpha^{\star}\mathrm{g}^{\#}\psi-Cl\left[\xi^{-1}(G)\right]\subseteq\mathrm{TN}\alpha^{\star}\mathrm{g}^{\#}\psi-Cl\left[\xi^{-1}\left(\mathrm{TN}\alpha^{\star}\mathrm{g}^{\#}\psi-Cl(G)\right)\right]$. Since $\mathrm{TN}\alpha^{\star}\mathrm{g}^{\#}\psi-Cl(G)$ is $\mathrm{TN}\alpha^{\star}\mathrm{g}^{\#}\psi-$closed set in Z and ξ is a $\mathrm{TN}\alpha^{\star}\mathrm{g}^{\#}\psi-$irresolute mapping. Hence, by Theorem 5.3, $\xi^{-1}\left[\mathrm{TN}\alpha^{\star}\mathrm{g}^{\#}\psi-Cl(G)\right]$ is a $\mathrm{TN}\alpha^{\star}\mathrm{g}^{\#}\psi-$closed set in R. Therefore $\mathrm{TN}\alpha^{\star}\mathrm{g}^{\#}\psi-Cl\left[\xi^{-1}\left(\mathrm{TN}\alpha^{\star}\mathrm{g}^{\#}\psi-Cl(G)\right)\right]=\xi^{-1}\left[\mathrm{TN}\alpha^{\star}\mathrm{g}^{\#}\psi-Cl(G)\right]$. Hence, we have $\mathrm{TN}\alpha^{\star}\mathrm{g}^{\#}\psi-Cl\left[\xi^{-1}(G)\right]\subseteq\xi^{-1}\left[\mathrm{TN}\alpha^{\star}\mathrm{g}^{\#}\psi-Cl(G)\right]$.

Conversely, assume $\mathrm{TN}\alpha^{\star}\mathrm{g}^{\#}\psi-Cl\left[\xi^{-1}(G)\right]\subseteq\xi^{-1}\left(\mathrm{TN}\alpha^{\star}\mathrm{g}^{\#}\psi-Cl(G)\right)$ for all $\mathrm{TN}\alpha^{\star}\mathrm{g}^{\#}\psi-$sets G in Z. Let K be a $\mathrm{TN}\alpha^{\star}\mathrm{g}^{\#}\psi-$closed set in Z. By assumption, $\mathrm{TN}\alpha^{\star}\mathrm{g}^{\#}\psi-Cl\left[\xi^{-1}(K)\right]\subseteq\xi^{-1}\left[\mathrm{TN}\alpha^{\star}\mathrm{g}^{\#}\psi-Cl(K)\right]=\xi^{-1}(K)$. This implies that $\xi^{-1}(K)$ is a $\mathrm{TN}\alpha^{\star}\mathrm{g}^{\#}\psi-$closed set in R. Thus by Theorem 5.3, ξ is a $\mathrm{TN}\alpha^{\star}\mathrm{g}^{\#}\psi-$irresolute mapping.

Theorem 5.6. Let $\xi:(R,\mathrm{T}_{\mathrm{TN}})\to(Z,\Gamma_{\mathrm{TN}})$ be a bijective mapping. Then ξ is $\mathrm{TN}\alpha^{\star}\mathrm{g}^{\#}\psi-$irresolute if and only if $\mathrm{TN}\alpha^{\star}\mathrm{g}^{\#}\psi-Int\left[\xi(M)\right]\subseteq\xi\left[\mathrm{TN}\alpha^{\star}\mathrm{g}^{\#}\psi-Int(M)\right]$ for every $\mathrm{TN}-$set M in R.

Proof. Let M be any $\mathrm{TN}-$set in R and ξ be a bijective and $\mathrm{TN}\alpha^{\star}\mathrm{g}^{\#}\psi-$irresolute mapping. Let $\xi(M)=K$. Since $\mathrm{TN}\alpha^{\star}\mathrm{g}^{\#}\psi-Int(K)\subseteq K$ and hence we obtain $\xi^{-1}\left[\mathrm{TN}\alpha^{\star}\mathrm{g}^{\#}\psi-Int(K)\right]\subseteq\xi^{-1}(K)$. Since ξ is an injective mapping, so $\xi^{-1}(K)=M$. Thus $\xi^{-1}\left[\mathrm{TN}\alpha^{\star}\mathrm{g}^{\#}\psi-Int(K)\right]\subseteq M$. Then this implies that $\mathrm{TN}\alpha^{\star}\mathrm{g}^{\#}\psi-Int\left[\xi^{-1}\left(\mathrm{TN}\alpha^{\star}\mathrm{g}^{\#}\psi-Int(K)\right)\right]\subseteq\mathrm{TN}\alpha^{\star}\mathrm{g}^{\#}\psi-Int(K)$. Since ξ is $\mathrm{TN}\alpha^{\star}\mathrm{g}^{\#}\psi-$irresolute, $\xi^{-1}\left[\mathrm{TN}\alpha^{\star}\mathrm{g}^{\#}\psi-Int(K)\right]$ is $\mathrm{TN}\alpha^{\star}\mathrm{g}^{\#}\psi-$open set in R and thus $\xi^{-1}\left[\mathrm{TN}\alpha^{\star}\mathrm{g}^{\#}\psi-Int(K)\right]\subseteq\mathrm{TN}\alpha^{\star}\mathrm{g}^{\#}\psi-Int(M)$. Hence $\xi\left[\xi^{-1}\left(\mathrm{TN}\alpha^{\star}\mathrm{g}^{\#}\psi-Int(K)\right)\right]\subseteq\xi\left[\mathrm{TN}\alpha^{\star}\mathrm{g}^{\#}\psi-Int(M)\right]$. Thus $\mathrm{TN}\alpha^{\star}\mathrm{g}^{\#}\psi-Int\left[\xi(M)\right]\subseteq\xi\left[\mathrm{TN}\alpha^{\star}\mathrm{g}^{\#}\psi-Int(M)\right]$.

Conversely, suppose that $\mathrm{TN}\alpha^{\star}\mathrm{g}^{\#}\psi-Int\left[\xi(M)\right]\subseteq\xi\left[\mathrm{TN}\alpha^{\star}\mathrm{g}^{\#}\psi-Int(M)\right]$ for every $\mathrm{TN}-$set M in R. Let K be a $\mathrm{TN}\alpha^{\star}\mathrm{g}^{\#}\psi-$open set in Z. Since ξ is surjective and therefore, by hypothesis, $K=\mathrm{TN}\alpha^{\star}\mathrm{g}^{\#}\psi-Int(K)$ $=\mathrm{TN}\alpha^{\star}\mathrm{g}^{\#}\psi-Int\left[\xi\left(\xi^{-1}(K)\right)\right]\subseteq\xi\left[\mathrm{TN}\alpha^{\star}\mathrm{g}^{\#}\psi-Int\left(\xi^{-1}(K)\right)\right]$. It follows that $\xi^{-1}(K)\subseteq\mathrm{TN}\alpha^{\star}\mathrm{g}^{\#}\psi-Int\left[\xi^{-1}(K)\right]$. Therefore $\xi^{-1}(K)$ is $\mathrm{TN}\alpha^{\star}\mathrm{g}^{\#}\psi-$open set in R. Hence ξ is a $\mathrm{TN}\alpha^{\star}\mathrm{g}^{\#}\psi-$irresolute mapping.

Theorem 5.7. A mapping $\xi:(R,\mathrm{T}_{\mathrm{TN}})\to(Z,\Gamma_{\mathrm{TN}})$ is a $\mathrm{TN}\alpha^{\star}\mathrm{g}^{\#}\psi-$irresolute mapping if and only if $\xi^{-1}\left[\mathrm{TN}\alpha^{\star}\mathrm{g}^{\#}\psi-Int(H)\right]\subseteq\mathrm{TN}\alpha^{\star}\mathrm{g}^{\#}\psi-Int\left[\xi^{-1}(H)\right]$ for every $\mathrm{TN}-$set H in Z.

Proof. Let H be any $\mathrm{TN}-$set in Z and ξ be a $\mathrm{TN}\alpha^{\star}\mathrm{g}^{\#}\psi-$irresolute mapping. Then $\mathrm{TN}\alpha^{\star}\mathrm{g}^{\#}\psi-Int(H)\subseteq H$ implies that $\xi^{-1}\left[\mathrm{TN}\alpha^{\star}\mathrm{g}^{\#}\psi-Int(H)\right]\subseteq\xi^{-1}(H)$. Thus $\mathrm{TN}\alpha^{\star}\mathrm{g}^{\#}\psi-Int\left[\xi^{-1}\left(\mathrm{TN}\alpha^{\star}\mathrm{g}^{\#}\psi-Int(H)\right)\right]\subseteq\mathrm{TN}\alpha^{\star}\mathrm{g}^{\#}\psi-Int\left[\xi^{-1}(H)\right]$. Since $\mathrm{TN}\alpha^{\star}\mathrm{g}^{\#}\psi-Int(H)$ is $\mathrm{TN}\alpha^{\star}\mathrm{g}^{\#}\psi-$open set in Z and ξ is $\mathrm{TN}\alpha^{\star}\mathrm{g}^{\#}\psi-$irresolute, $\xi^{-1}\left[\mathrm{TN}\alpha^{\star}\mathrm{g}^{\#}\psi-Int(H)\right]$ is $\mathrm{TN}\alpha^{\star}\mathrm{g}^{\#}\psi-$open set in R. Thus $\mathrm{TN}\alpha^{\star}\mathrm{g}^{\#}\psi-Int\left[\xi^{-1}\left(\mathrm{TN}\alpha^{\star}\mathrm{g}^{\#}\psi-Int(H)\right)\right]=\xi^{-1}\left[\mathrm{TN}\alpha^{\star}\mathrm{g}^{\#}\psi-Int(H)\right]$. Then we obtain $\xi^{-1}\left[\mathrm{TN}\alpha^{\star}\mathrm{g}^{\#}\psi-Int(H)\right]\subseteq\mathrm{TN}\alpha^{\star}\mathrm{g}^{\#}\psi-Int\left[\xi^{-1}(H)\right]$.

Conversely, assume that $\xi^{-1}\left[\mathrm{TN}\alpha^{\star}\mathrm{g}^{\#}\psi-Int(H)\right]\subseteq\mathrm{TN}\alpha^{\star}\mathrm{g}^{\#}\psi-Int\left[\xi^{-1}(H)\right]$ for every $\mathrm{TN}-$set H in R. Let M be any $\mathrm{TN}\alpha^{\star}\mathrm{g}^{\#}\psi-$open set in Z. Then by assumption, $\xi^{-1}(M)=\xi^{-1}\left[\mathrm{TN}\alpha^{\star}\mathrm{g}^{\#}\psi-Int(M)\right]\subseteq\mathrm{TN}\alpha^{\star}\mathrm{g}^{\#}\psi-Int\left[\xi^{-1}(M)\right]$ and therefore $\xi^{-1}(M)\subseteq\mathrm{TN}\alpha^{\star}\mathrm{g}^{\#}\psi-Int\left[\xi^{-1}(M)\right]$. This implies that $\xi^{-1}(M)$ is $\mathrm{TN}\alpha^{\star}\mathrm{g}^{\#}\psi-$open set in R. Hence ξ is a $\mathrm{TN}\alpha^{\star}\mathrm{g}^{\#}\psi-$irresolute mapping.

Theorem 5.8. Let $\xi:(R,\mathrm{T}_{\mathrm{TN}})\to(Z,\Gamma_{\mathrm{TN}})$ be a bijective mapping and $\mathrm{TN}\alpha^{\star}\mathrm{g}^{\#}\psi-$irresolute mapping. Then $\xi\left[\mathrm{TN}\alpha^{\star}\mathrm{g}^{\#}\psi-Fr(M)\right]\subseteq\mathrm{TN}\alpha^{\star}\mathrm{g}^{\#}\psi-Fr\left[\xi(M)\right]$ for every $\mathrm{TN}-$set M in R.

Proof. Let ξ be a bijective and $\mathrm{TN}\alpha^{\star}\mathrm{g}^{\#}\psi-$irresolute mapping. Let M be a $\mathrm{TN}-$set in R. By definition, $\mathrm{TN}\alpha^{\star}\mathrm{g}^{\#}\psi-Fr(M)=\mathrm{TN}\alpha^{\star}\mathrm{g}^{\#}\psi-Cl(M)\cap\mathrm{TN}\alpha^{\star}\mathrm{g}^{\#}\psi-Cl\left(M^{C}\right)$. By Theorem 5.6, $\mathrm{TN}\alpha^{\star}\mathrm{g}^{\#}\psi-Int\left[\xi(M)\right]\subseteq\xi\left[\mathrm{TN}\alpha^{\star}\mathrm{g}^{\#}\psi-Int(M)\right]$ and from Theorem 5.4, $\xi\left[\mathrm{TN}\alpha^{\star}\mathrm{g}^{\#}\psi-Cl(M)\right]\subseteq\mathrm{TN}\alpha^{\star}\mathrm{g}^{\#}\psi-Cl\left[\xi(M)\right]$. Thus

$$\xi\left[\mathrm{TN}\alpha^{\star}\mathrm{g}^{\#}\psi-Fr(M)\right]=\xi\left[\mathrm{TN}\alpha^{\star}\mathrm{g}^{\#}\psi-Cl(M)\right]\cap\xi\left[\mathrm{TN}\alpha^{\star}\mathrm{g}^{\#}\psi-Cl\left(M^{C}\right)\right]\subseteq$$

$$\mathrm{TN}\alpha^{\star}\mathrm{g}^{\#}\psi-Cl\left[\xi(M)\right]\cap\mathrm{TN}\alpha^{\star}\mathrm{g}^{\#}\psi-Cl\left[\xi(M)\right]^{C}=\mathrm{TN}\alpha^{\star}\mathrm{g}^{\#}\psi-Fr\left[\xi(M)\right].$$

Theorem 5.9. Let $\xi:(R,\mathrm{T}_{\mathrm{TN}})\to(Z,\Gamma_{\mathrm{TN}})$ be a bijective $\mathrm{TN}\alpha^{*}\mathrm{g}^{\#}\psi$-irresolute mapping. Then we have $\mathrm{TN}\alpha^{*}\mathrm{g}^{\#}\psi-Fr\left[\xi^{-1}(M)\right]\subseteq\xi^{-1}\left[\mathrm{TN}\alpha^{*}\mathrm{g}^{\#}\psi-Fr(M)\right]$ for every TN-set M in Z.

Proof. Let ξ be a bijective and $\mathrm{TN}\alpha^{*}\mathrm{g}^{\#}\psi$-irresolute mapping. Let M be a TN-set in Z. By Theorem 5.5, $\mathrm{TN}\alpha^{*}\mathrm{g}^{\#}\psi-Cl\left[\xi^{-1}(M)\right]\subseteq\xi^{-1}\left[\mathrm{TN}\alpha^{*}\mathrm{g}^{\#}\psi-Cl(M)\right]$. Now we have $\xi^{-1}\left[\mathrm{TN}\alpha^{*}\mathrm{g}^{\#}\psi-Fr(M)\right]=\xi^{-1}\left[\left(\mathrm{TN}\alpha^{*}\mathrm{g}^{\#}\psi-Cl(M)\right)\cap\mathrm{TN}\alpha^{*}\mathrm{g}^{\#}\psi-Cl\left(M^{C}\right)\right]=\xi^{-1}\left[\mathrm{TN}\alpha^{*}\mathrm{g}^{\#}\psi-Cl(M)\right]\cap\xi^{-1}\left[\mathrm{TN}\alpha^{*}\mathrm{g}^{\#}\psi-Cl\left(M^{C}\right)\right]\supseteq\mathrm{TN}\alpha^{*}\mathrm{g}^{\#}\psi-Cl\left[\xi^{-1}(M)\right]\cap\mathrm{TN}\alpha^{*}\mathrm{g}^{\#}\psi-Cl\left[\xi^{-1}\left(M^{C}\right)\right]=\mathrm{TN}\alpha^{*}\mathrm{g}^{\#}\psi-Cl\left[\xi^{-1}(M)\right]\cap\mathrm{TN}\alpha^{*}\mathrm{g}^{\#}\psi-Cl\left[\left(\xi^{-1}(M)\right)^{C}\right]=\mathrm{TN}\alpha^{*}\mathrm{g}^{\#}\psi-Fr\left[\xi^{-1}(M)\right]$. Therefore, we obtain $\mathrm{TN}\alpha^{*}\mathrm{g}^{\#}\psi-Fr\left[\xi^{-1}(M)\right]\subseteq\xi^{-1}\left[\mathrm{TN}\alpha^{*}\mathrm{g}^{\#}\psi-Fr(M)\right]$.

Theorem 5.10. If $\xi:(R,\mathrm{T}_{\mathrm{TN}})\to(W,\Gamma_{\mathrm{TN}})$ and $\mu:(W,\Gamma_{\mathrm{TN}})\to(Z,\Psi_{\mathrm{TN}})$ are $\mathrm{TN}\alpha^{*}\mathrm{g}^{\#}\psi$-irresolute, then the composition function $\mu o\xi:(R,\mathrm{T}_{\mathrm{TN}})\to(Z,\Psi_{\mathrm{TN}})$ is also $\mathrm{TN}\alpha^{*}\mathrm{g}^{\#}\psi$-irresolute.

Proof. Let M be a $\mathrm{TN}\alpha^{*}\mathrm{g}^{\#}\psi$-open set in Z. Since μ is a $\mathrm{TN}\alpha^{*}\mathrm{g}^{\#}\psi$-irresolute mapping, $\mu^{-1}(M)$ is $\mathrm{TN}\alpha^{*}\mathrm{g}^{\#}\psi$-open in W. Since ξ is a $\mathrm{TN}\alpha^{*}\mathrm{g}^{\#}\psi$-irresolute mapping, $\xi^{-1}\left[\mu^{-1}(M)\right]=(\mu o\xi)^{-1}(M)$ is $\mathrm{TN}\alpha^{*}\mathrm{g}^{\#}\psi$-open in R. Therefore $\mu o\xi$ is $\mathrm{TN}\alpha^{*}\mathrm{g}^{\#}\psi$-irresolute.

Theorem 5.11. If $\xi:(R,\mathrm{T}_{\mathrm{TN}})\to(W,\Gamma_{\mathrm{TN}})$ and is $\mathrm{TN}\alpha^{*}\mathrm{g}^{\#}\psi$-irresolute and $\mu:(W,\Gamma_{\mathrm{TN}})\to(Z,\Psi_{\mathrm{TN}})$ is $\mathrm{TN}\alpha^{*}\mathrm{g}^{\#}\psi$-continuous, then the composition function $\mu o\xi:(R,\mathrm{T}_{\mathrm{TN}})\to(Z,\Psi_{\mathrm{TN}})$ is also a $\mathrm{TN}\alpha^{*}\mathrm{g}^{\#}\psi$-continuous function.

Proof. Let M be a TN-open set in Z. Since μ is a $\mathrm{TN}\alpha^{*}\mathrm{g}^{\#}\psi$-continuous mapping, $\mu^{-1}(M)$ is $\mathrm{TN}\alpha^{*}\mathrm{g}^{\#}\psi$-open set in W. Since ξ is a $\mathrm{TN}\alpha^{*}\mathrm{g}^{\#}\psi$-irresolute function, $\xi^{-1}\left[\mu^{-1}(M)\right]=(\mu o\xi)^{-1}(M)$ is $\mathrm{TN}\alpha^{*}\mathrm{g}^{\#}\psi$-open in R. Therefore $\mu o\xi$ is $\mathrm{TN}\alpha^{*}\mathrm{g}^{\#}\psi$-conrinuous.

6. Tetra Neutrosophic $\alpha^{*}\mathrm{g}^{\#}\psi$-Closed and Open Mappings

In this section, we introduce Tetra Neutrosophic $\alpha^{*}\mathrm{g}^{\#}\psi$-closed $\left(\text{briefly } \mathrm{TN}\alpha^{*}\mathrm{g}^{\#}\psi\text{-closed}\right)$ functions and Tera Neutrosophic $\alpha^{*}\mathrm{g}^{\#}\psi$-open $\left(\text{briefly } \mathrm{TN}\alpha^{*}\mathrm{g}^{\#}\psi\text{-open}\right)$ mappings in TN-Top-Spaces and investigate certain characterizations and properties of these classes of mappings.

Definition 6.1. A mapping $\xi:(R,\mathrm{T}_{\mathrm{TN}})\to(Z,\Gamma_{\mathrm{TN}})$ is said to be $\mathrm{TN}\alpha^{*}\mathrm{g}^{\#}\psi$-closed if the image of each TN-closed set in R is $\mathrm{TN}\alpha^{*}\mathrm{g}^{\#}\psi$-closed in Z.

Definition 6.2. A function $\xi:(R,\mathrm{T}_{\mathrm{TN}})\to(Z,\Gamma_{\mathrm{TN}})$ is said to be $\mathrm{TN}\alpha^{*}\mathrm{g}^{\#}\psi$-open if the image of each TN-open set in R is $\mathrm{TN}\alpha^{*}\mathrm{g}^{\#}\psi$-open in Z.

Theorem 6.3. **A** function $\xi:(R,\mathrm{T}_{\mathrm{TN}})\to(Z,\Gamma_{\mathrm{TN}})$ is $\mathrm{TN}\alpha^{*}\mathrm{g}^{\#}\psi$-closed if and only if $\mathrm{TN}\alpha^{*}\mathrm{g}^{\#}\psi-Cl\left[\xi(A)\right]\subseteq\xi\left[\mathrm{TN}-Cl(A)\right]$ for every TN-set M of R.

Proof. Suppose $\xi:(R,\mathrm{T}_{\mathrm{TN}})\to(W,\Gamma_{\mathrm{TN}})$ is a $\mathrm{TN}\alpha^{*}\mathrm{g}^{\#}\psi$-closed function and M is any TN-set in R. Then $\mathrm{TN}-Cl(M)$ is a TN-*closed* set in R. Since ξ is $\mathrm{TN}\alpha^{*}\mathrm{g}^{\#}\psi$-closed, $\xi\left[\mathrm{TN}-Cl(M)\right]$ is a $\mathrm{TN}\alpha^{*}\mathrm{g}^{\#}\psi$-closed

set in Z. So we have $\mathrm{TN}\alpha^{\star}\mathrm{g}^{\#}\psi-Cl\left[\xi\left(\mathrm{TN}-Cl(M)\right)\right]=\xi\left[\mathrm{TN}-Cl(M)\right]$. Therefore, $\mathrm{TN}\alpha^{\star}\mathrm{g}^{\#}\psi-Cl\left[\xi(M)\right]\subseteq \mathrm{TN}\alpha^{\star}\mathrm{g}^{\#}\psi-Cl\left[\xi\left(\mathrm{TN}-Cl(M)\right)\right]=\xi\left(\mathrm{TN}-Cl(M)\right)$. Thus we obtain $\mathrm{TN}\alpha^{\star}\mathrm{g}^{\#}\psi-Cl\left[\xi(M)\right]\subseteq\xi\left(\mathrm{TN}-Cl(M)\right)$. Conversely, let M be a $\mathrm{TN}-$closed set in R. Then $\mathrm{TN}-Cl(M)=M$ and so $\xi(M)=\xi\left[\mathrm{TN}-Cl(M)\right]$. By our assumption $\mathrm{TN}\alpha^{\star}\mathrm{g}^{\#}\psi-Cl\left[\xi(M)\right]\subseteq\xi(M)$. But $\xi(M)\subseteq\mathrm{TN}\alpha^{\star}\mathrm{g}^{\#}\psi-Cl\left[\xi(M)\right]$. Thus we conclude that $\mathrm{TN}\alpha^{\star}\mathrm{g}^{\#}\psi-Cl\left[\xi(M)\right]=\xi(M)$ and hence $\xi(M)$ is $\mathrm{TN}\alpha^{\star}\mathrm{g}^{\#}\psi-$closed set in Z. Therefore eventually ξ is a $\mathrm{TN}\alpha^{\star}\mathrm{g}^{\#}\psi-$closed mapping.

Theorem 6.4. A mapping $\xi:(R,\mathrm{T}_{\mathrm{TN}})\to(Z,\Gamma_{\mathrm{TN}})$ is $\mathrm{TN}\alpha^{\star}\mathrm{g}^{\#}\psi-$closed if and only if for each $\mathrm{TN}-$set H of Z and for each $\mathrm{TN}-$open set G of R containing $\xi^{-1}(H)$ there exists a $\mathrm{TN}\alpha^{\star}\mathrm{g}^{\#}\psi-$open set V of Z such that $H\subseteq V$ and $\xi^{-1}(V)\subseteq G$.

Proof. Let ξ be a $\mathrm{TN}\alpha^{\star}\mathrm{g}^{\#}\psi-$closed mapping and let H be any $\mathrm{TN}-$set in Z and G be a $\mathrm{TN}-$open set of R such that $\xi^{-1}(H)\subseteq G$. Then $V=\left[\xi\left(G^{C}\right)\right]^{C}$ is $\mathrm{TN}\alpha^{\star}\mathrm{g}^{\#}\psi-$open in Z such that $\xi^{-1}(V)\subseteq G$. Conversely, let H be a $\mathrm{TN}-$closed of R. Then $\xi^{-1}\left[\left(\xi(H)\right)^{C}\right]\subseteq H^{C}$ and H^{C} is $\mathrm{TN}-$open in R. By assumption, there exists a $\mathrm{TN}\alpha^{\star}\mathrm{g}^{\#}\psi-$open set V of Z such that $\left[\xi(H)\right]^{C}\subseteq V$ and $\xi^{-1}(V)\subseteq H^{C}$ and this implies that $H\subseteq\left[\xi^{-1}(V)\right]^{C}$. Hence we obtain $V^{C}\subseteq\xi(H)\subseteq\xi\left[\left(\xi^{-1}(V)\right)^{C}\right]\subseteq V^{C}$, which implies $\xi(H)=V^{C}$. Since V^{C} is $\mathrm{TN}\alpha^{\star}\mathrm{g}^{\#}\psi-$closed, $\xi(H)$ is $\mathrm{TN}\alpha^{\star}\mathrm{g}^{\#}\psi-$closed and ξ is $\mathrm{TN}\alpha^{\star}\mathrm{g}^{\#}\psi-$closed mapping.

Theorem 6.5. Let $\xi:(R,\mathrm{T}_{\mathrm{TN}})\to(W,\Gamma_{\mathrm{TN}})$ be a $\mathrm{TN}-$closed mapping and $\mu:(W,\Gamma_{\mathrm{TN}})\to(Z,\Psi_{\mathrm{TN}})$ be a $\mathrm{TN}\alpha^{\star}\mathrm{g}^{\#}\psi-$closed mapping. Then their composition $\mu o\xi:(R,\mathrm{T}_{\mathrm{TN}})\to(Z,\Psi_{\mathrm{TN}})$ is a $\mathrm{TN}\alpha^{\star}\mathrm{g}^{\#}\psi-$closed mapping.

Proof. Let M be a $\mathrm{TN}-$closed set in R. Since ξ is $\mathrm{TN}-$closed, $\xi(M)$ is $\mathrm{TN}-$closed in W. Since μ is $\mathrm{TN}\alpha^{\star}\mathrm{g}^{\#}\psi-$closed, $\mu\left[\xi(M)\right]=(\mu o\xi)(M)$ is $\mathrm{TN}\alpha^{\star}\mathrm{g}^{\#}\psi-$closed in Z. Hence $\mu o\xi$ is a $\mathrm{TN}\alpha^{\star}\mathrm{g}^{\#}\psi-$closed mapping.

Theorem 6.6. Let $\xi:(R,\mathrm{T}_{\mathrm{TN}})\to(W,\Gamma_{\mathrm{TN}})$ and $\mu:(W,\Gamma_{\mathrm{TN}})\to(Z,\Psi_{\mathrm{TN}})$ be two mappings such that their composition $\mu o\xi:(R,\mathrm{T}_{\mathrm{TN}})\to(Z,\Psi_{\mathrm{TN}})$ is $\mathrm{TN}\alpha^{\star}\mathrm{g}^{\#}\psi-$closed. Then the following statements are true.

(i) If ξ is $\mathrm{TN}-$continuous and surjective, then μ is $\mathrm{TN}\alpha^{\star}\mathrm{g}^{\#}\psi-$closed.

(ii) If μ is $\mathrm{TN}\alpha^{\star}\mathrm{g}^{\#}\psi-$irresolute and injective, then ξ is $\mathrm{TN}\alpha^{\star}\mathrm{g}^{\#}\psi-$closed.

Proof. (i) Let M be a $\mathrm{TN}-$closed set of W. Since ξ is $\mathrm{TN}-$continuous, $\xi^{-1}(M)$ is $\mathrm{TN}-$closed in R. Since $\mu o\xi$ is $\mathrm{TN}\alpha^{\star}\mathrm{g}^{\#}\psi-$closed, $(\mu o\xi)\left(\xi^{-1}(M)\right)$ is $\mathrm{TN}\alpha^{\star}\mathrm{g}^{\#}\psi-$closed in Z. Since ξ is surjective, $(\mu o\xi)\left(\xi^{-1}(M)\right)=\mu(M)$ is $\mathrm{TN}\alpha^{\star}\mathrm{g}^{\#}\psi-$closed in Z. Hence μ is $\mathrm{TN}\alpha^{\star}\mathrm{g}^{\#}\psi-$closed.

(ii) Let M be any $\mathrm{TN}-$closed set of R. Since $\mu o\xi$ is $\mathrm{TN}\alpha^{\star}\mathrm{g}^{\#}\psi-$closed, $(\mu o\xi)(M)$ is $\mathrm{TN}\alpha^{\star}\mathrm{g}^{\#}\psi-$closed in Z. Since μ is $\mathrm{TN}\alpha^{\star}\mathrm{g}^{\#}\psi-$irresolute, $\mu^{-1}\left(\mu o\xi(M)\right)$ is $\mathrm{TN}\alpha^{\star}\mathrm{g}^{\#}\psi-$closed in W. Since μ is injective, $\mu^{-1}\left(\mu o\xi(M)\right)=\mu^{-1}\left(\mu\left(\xi(M)\right)\right)=\xi(M)$ is $\mathrm{TN}\alpha^{\star}\mathrm{g}^{\#}\psi-$closed in W. Hence ξ is $\mathrm{TN}\alpha^{\star}\mathrm{g}^{\#}\psi-$closed.

Theorem 6.7. A function $\xi:(R,\mathrm{T}_{\mathrm{TN}})\to(Z,\Gamma_{\mathrm{TN}})$ is $\mathrm{TN}\alpha^{\star}\mathrm{g}^{\#}\psi-$open if and only if $\xi\left[\mathrm{TN}-Int(M)\right]\subseteq\mathrm{TN}\alpha^{\star}\mathrm{g}^{\#}\psi-Int\left[\xi(M)\right]$, for every $\mathrm{TN}-$set M of R.

Proof. Suppose $\xi:(R,\mathrm{T}_{\mathrm{TN}})\to(Z,\Gamma_{\mathrm{TN}})$ is a $\mathrm{TN}\alpha^{*}\mathrm{g}^{\#}\psi$-open function and M is any TN-set in R. Then $\mathrm{TN}\text{-}Int(M)$ is a TN-open set in R. Since ξ is $\mathrm{TN}\alpha^{*}\mathrm{g}^{\#}\psi$-open, $\xi[\mathrm{TN}\text{-}Int(M)]$ is a $\mathrm{TN}\alpha^{*}\mathrm{g}^{\#}\psi$-open set. Since $\mathrm{TN}\alpha^{*}\mathrm{g}^{\#}\psi\text{-}Int[\xi(\mathrm{TN}\text{-}Int(M))]\subseteq \mathrm{TN}\alpha^{*}\mathrm{g}^{\#}\psi\text{-}Int[\xi(M)]$, $\xi[\mathrm{TN}\text{-}Int(M)]\subseteq \mathrm{TN}\alpha^{*}\mathrm{g}^{\#}\psi\text{-}Int[\xi(M)]$. Conversely, $\xi[\mathrm{TN}\text{-}Int(M)]\subseteq \mathrm{TN}\alpha^{*}\mathrm{g}^{\#}\psi\text{-}Int[\xi(M)]$ for every TN-set M in R. Let E be a TN-open set in R. Then $\mathrm{TN}\text{-}Int(E)=E$ and by hypothesis, $\xi(E)\subseteq \mathrm{TN}\alpha^{*}\mathrm{g}^{\#}\psi\text{-}Int[\xi(E)]$. But $\mathrm{TN}\alpha^{*}\mathrm{g}^{\#}\psi\text{-}Int[\xi(E)]\subseteq\xi(E)$. Therefore, $\xi(E)=\mathrm{TN}\alpha^{*}\mathrm{g}^{\#}\psi\text{-}Int[\xi(E)]$. Then $\xi(E)$ is $\mathrm{TN}\alpha^{*}\mathrm{g}^{\#}\psi$-open. Hence ξ is a $\mathrm{TN}\alpha^{*}\mathrm{g}^{\#}\psi$-open mapping.

Theorem 6.8. Let $\xi:(R,\mathrm{T}_{\mathrm{TN}})\to(Z,\Gamma_{\mathrm{TN}})$ be a $\mathrm{TN}\alpha^{*}\mathrm{g}^{\#}\psi$-open function. If for each $p_{(t,i,f)}\in\mathrm{TN}(R)$ and for each TN-neighbourhood M of $p_{(t,i,f)}$ in R, there exists a $\mathrm{TN}\alpha^{*}\mathrm{g}^{\#}\psi$-neighbourhood G of $\xi(p_{(t,i,f)})$ in Z such that $G\subseteq\xi(M)$.

Proof. Let $\xi:(R,\mathrm{T}_{\mathrm{TN}})\to(Z,\Gamma_{\mathrm{TN}})$ be a $\mathrm{TN}\alpha^{*}\mathrm{g}^{\#}\psi$-open function. Let $p_{(t,i,f)}\in\mathrm{TN}(R)$ and M be any arbitrary TN-neighbourhood of $p_{(t,i,f)}$ in R. Then there exists a TN-open set G such that $p_{(t,i,f)}\in G\subseteq M$. By Theorem 6.7, $\xi(G)=\xi[\mathrm{TN}\text{-}Int(G)]\subseteq \mathrm{TN}\alpha^{*}\mathrm{g}^{\#}\psi\text{-}Int[\xi(G)]$. But, $\mathrm{TN}\alpha^{*}\mathrm{g}^{\#}\psi\text{-}Int[\xi(G)]\subseteq\xi(G)$. Therefore, $\mathrm{TN}\alpha^{*}\mathrm{g}^{\#}\psi\text{-}Int[\xi(G)]=\xi(G)$ and hence $\xi(G)$ is $\mathrm{TN}\alpha^{*}\mathrm{g}^{\#}\psi$-open in Z. Since $p_{(t,i,f)}\in G\subseteq M$, $\xi(p_{(t,i,f)})\in\xi(G)\subseteq\xi(M)$ and so the result follows by taking $H=\xi(G)$.

Theorem 6.9. For any bijective mapping $\xi:(R,\mathrm{T}_{\mathrm{TN}})\to(Z,\Gamma_{\mathrm{TN}})$ the following statements are equivalent:
(i) $\xi^{-1}:(Z,\Gamma_{\mathrm{TN}})\to(R,\mathrm{T}_{\mathrm{TN}})$ is $\mathrm{TN}\alpha^{*}\mathrm{g}^{\#}\psi$-continuous.
(ii) ξ is $\mathrm{TN}\alpha^{*}\mathrm{g}^{\#}\psi$-open.
(iii) ξ is $\mathrm{TN}\alpha^{*}\mathrm{g}^{\#}\psi$-closed.

Proof. (i)$\Rightarrow$(ii): Let M be a TN-open set in R. By assumption, $(\xi^{-1})^{-1}(M)=\xi(M)$ is $\mathrm{TN}\alpha^{*}\mathrm{g}^{\#}\psi$-open in W and hence ξ is a $\mathrm{TN}\alpha^{*}\mathrm{g}^{\#}\psi$-open function.
(ii)$\Rightarrow$(iii): Let M be a TN-closed set of R. Then M^{C} is a TN-open set in R. By assumption $\xi(M^{C})$ is $\mathrm{TN}\alpha^{*}\mathrm{g}^{\#}\psi$-open in Z. But $\xi(M^{C})=[\xi(M)]^{C}$. Therefore $\xi(M)$ is $\mathrm{TN}\alpha^{*}\mathrm{g}^{\#}\psi$-closed set in Z. Hence, ξ is $\mathrm{TN}\alpha^{*}\mathrm{g}^{\#}\psi$-closed.
(iii)$\Rightarrow$(i): Let M be a TN-closed set of R. By assumption, $\xi(M)$ is $\mathrm{TN}\alpha^{*}\mathrm{g}^{\#}\psi$-closed set in Z. But $\xi(M)=(\xi^{-1})^{-1}(M)$ and therefore by Theorem 4.4, $\xi^{-1}:Z\to R$ is $\mathrm{TN}\alpha^{*}\mathrm{g}^{\#}\psi$-continuous.

7. Tetra Neutrosophic $\mathrm{TN}\alpha^{*}\mathrm{g}^{\#}\psi$-Homeomorphisms

In this section, we define and study the concept of Tetra Neutrosophic $\alpha^{*}\mathrm{g}^{\#}\psi$-homeomorphism (briefly, $\mathrm{TN}\alpha^{*}\mathrm{g}^{\#}\psi$-homeomorphism) in TN-Top-Space $(R,\mathrm{T}_{\mathrm{TN}})$ and obtain some of its properties and characterizations.

Definition 7.1. A mapping $\xi:(R,\mathrm{T}_{\mathrm{TN}})\to(Z,\Gamma_{\mathrm{TN}})$ is said to be TN-homeomorphism if ξ is one-to-one & onto, TN-open and TN-continuous.

Definition 7.2. A mapping $\xi:(R,\mathrm{T}_{\mathrm{TN}})\to(Z,\Gamma_{\mathrm{TN}})$ is said to be $\mathrm{TN}\alpha^{*}\mathrm{g}^{\#}\psi$ −homeomorphism if ξ is one-to-one and onto, $\mathrm{TN}\alpha^{*}\mathrm{g}^{\#}\psi$ −open and $\mathrm{TN}\alpha^{*}\mathrm{g}^{\#}\psi$ −continuous.

Theorem 7.3. Let $\xi:(R,\mathrm{T}_{\mathrm{TN}})\to(Z,\Gamma_{\mathrm{TN}})$ be a one-to-one onto mapping. Then ξ is $\mathrm{TN}\alpha^{*}\mathrm{g}^{\#}\psi$ −homeomorphism if and only if ξ is $\mathrm{TN}\alpha^{*}\mathrm{g}^{\#}\psi$ −closed and $\mathrm{TN}\alpha^{*}\mathrm{g}^{\#}\psi$ −continuous.

Proof. Let $\xi:(R,\mathrm{T}_{\mathrm{TN}})\to(Z,\Gamma_{\mathrm{TN}})$ be a $\mathrm{TN}\alpha^{*}\mathrm{g}^{\#}\psi$ −homeomorphism. Then ξ is $\mathrm{TN}\alpha^{*}\mathrm{g}^{\#}\psi$ −continuous. Let M be an arbitrary TN −closed set in $(R,\mathrm{T}_{\mathrm{TN}})$. Then $1_{\mathrm{TN}}-M$ is TN −open. Since ξ is $\mathrm{TN}\alpha^{*}\mathrm{g}^{\#}\psi$ −open, $\xi(1_{\mathrm{TN}}-M)$ is $\mathrm{TN}\alpha^{*}\mathrm{g}^{\#}\psi$ −open in (Z,Γ_{TN}). That is, $1_{\mathrm{TN}}-\xi(M)$ is $\mathrm{TN}\alpha^{*}\mathrm{g}^{\#}\psi$ −open in (Z,Γ_{TN}) for every TN −closed set M in $(R,\mathrm{T}_{\mathrm{TN}})$ implies that $\xi(M)$ is $\mathrm{TN}\alpha^{*}\mathrm{g}^{\#}\psi$ −closed in (Z,Γ_{TN}). Hence $\xi:(R,\mathrm{T}_{\mathrm{TN}})\to(Z,\Gamma_{\mathrm{TN}})$ is $\mathrm{TN}\alpha^{*}\mathrm{g}^{\#}\psi$ −closed.
Conversely, let ξ be a $\mathrm{TN}\alpha^{*}\mathrm{g}^{\#}\psi$ −closed and $\mathrm{TN}\alpha^{*}\mathrm{g}^{\#}\psi$ −continuous function. Let M be a TN −open set in $(R,\mathrm{T}_{\mathrm{TN}})$. Then $1_{\mathrm{TN}}-M$ is TN −closed in $(R,\mathrm{T}_{\mathrm{TN}})$. Since ξ is $\mathrm{TN}\alpha^{*}\mathrm{g}^{\#}\psi$ −closed, $\xi(1_{\mathrm{TN}}-M)$ is $\mathrm{TN}\alpha^{*}\mathrm{g}^{\#}\psi$ −closed in (Z,Γ_{TN}). That is, $\xi(1_{\mathrm{TN}}-M)=1_{\mathrm{TN}}-\xi(M)$ is $\mathrm{TN}\alpha^{*}\mathrm{g}^{\#}\psi$ −closed in (Z,Γ_{TN}). Hence $\xi(M)$ is $\mathrm{TN}\alpha^{*}\mathrm{g}^{\#}\psi$ −open in (Z,Γ_{TN}) for every TN −open set M in (Z,Γ_{TN}). Thus, ξ is $\mathrm{TN}\alpha^{*}\mathrm{g}^{\#}\psi$ −open and hence $\xi:(R,\mathrm{T}_{\mathrm{TN}})\to(Z,\Gamma_{\mathrm{TN}})$ is $\mathrm{TN}\alpha^{*}\mathrm{g}^{\#}\psi$ −homeomorphism.

Theorem 7.4. : Let $\xi:(R,\mathrm{T}_{\mathrm{TN}})\to(Z,\Gamma_{\mathrm{TN}})$ be a bijective and $\mathrm{TN}\alpha^{*}\mathrm{g}^{\#}\psi$ −continuous mapping. Then the following statements are equivalent.
(i) ξ is a $\mathrm{TN}\alpha^{*}\mathrm{g}^{\#}\psi$ −open mapping.
(ii) ξ is a $\mathrm{TN}\alpha^{*}\mathrm{g}^{\#}\psi$ −homeomorphism.
(iii) ξ is a $\mathrm{TN}\alpha^{*}\mathrm{g}^{\#}\psi$ −closed mapping.

Proof. $(i)\Rightarrow(ii)$. By the given hypothesis, the mapping $\xi:(R,\mathrm{T}_{\mathrm{TN}})\to(Z,\Gamma_{\mathrm{TN}})$ is bijective $\mathrm{TN}\alpha^{*}\mathrm{g}^{\#}\psi$ −continuous and $\mathrm{TN}\alpha^{*}\mathrm{g}^{\#}\psi$ −open. Hence $\xi:(R,\mathrm{T}_{\mathrm{TN}})\to(Z,\Gamma_{\mathrm{TN}})$ is $\mathrm{TN}\alpha^{*}\mathrm{g}^{\#}\psi$ −homeomorphism.
$(ii)\Rightarrow(iii)$. Let M be a TN −closed set in $(R,\mathrm{T}_{\mathrm{TN}})$ Then M^{C} is FQN −open in $(R,\mathrm{T}_{\mathrm{TN}})$. By assumption, $\xi(M^{C})$ is $\mathrm{TN}\alpha^{*}\mathrm{g}^{\#}\psi$ −open in (Z,Γ_{TN}). That is $\xi(M^{C})=(\xi(M))^{C}=Z-\xi(M)$ is $\mathrm{TN}\alpha^{*}\mathrm{g}^{\#}\psi$ −open in (Z,Γ_{TN}) and hence $\xi(M)$ is $\mathrm{TN}\alpha^{*}\mathrm{g}^{\#}\psi$ −closed in (Z,Γ_{TN}) for every TN −closed set M in $(R,\mathrm{T}_{\mathrm{TN}})$. Hence the function $\xi:(R,\mathrm{T}_{\mathrm{TN}})\to(Z,\Gamma_{\mathrm{TN}})$ is $\mathrm{TN}\alpha^{*}\mathrm{g}^{\#}\psi$ −closed mapping.
$(iii)\Rightarrow(i)$. Let M be a TN −open set in $(R,\mathrm{T}_{\mathrm{TN}})$. Then M^{C} is TN −closed set in $(R,\mathrm{T}_{\mathrm{TN}})$. By the given hypothesis, $\xi(M^{C})$ is $\mathrm{TN}\alpha^{*}\mathrm{g}^{\#}\psi$ −closed in (Z,Γ_{TN}). But $\xi(M^{C})=(\xi(M))^{C}=1_{\mathrm{TN}}-\xi(M)$ is $\mathrm{TN}\alpha^{*}\mathrm{g}^{\#}\psi$ −closed. Therefore $\xi(M)$ is $\mathrm{TN}\alpha^{*}\mathrm{g}^{\#}\psi$ −open in (Z,Γ_{TN}) for every TN −open set M in $(R,\mathrm{T}_{\mathrm{TN}})$. Hence $\xi:(R,\mathrm{T}_{\mathrm{TN}})\to(Z,\Gamma_{\mathrm{TN}})$ is $\mathrm{TN}\alpha^{*}\mathrm{g}^{\#}\psi$ −open mapping.

Theorem 7.5. Every TN −homeomorphism is $\mathrm{TN}\alpha^{*}\mathrm{g}^{\#}\psi$ −homeomorphism.

Proof. If $\xi:(R,\mathrm{T}_{\mathrm{TN}})\to(Z,\Gamma_{\mathrm{TN}})$ is TN −homeomorphism, by definition 7.1, ξ is bijective, TN −continuous and TN −open. Then $\xi:(R,\mathrm{T}_{\mathrm{TN}})\to(Z,\Gamma_{\mathrm{TN}})$ is $\mathrm{TN}\alpha^{*}\mathrm{g}^{\#}\psi$ −continuous and $\mathrm{TN}\alpha^{*}\mathrm{g}^{\#}\psi$ −open. Hence the function $\xi:(R,\mathrm{T}_{\mathrm{TN}})\to(Z,\Gamma_{\mathrm{TN}})$ is $\mathrm{TN}\alpha^{*}\mathrm{g}^{\#}\psi$ −homeomorphism. Every TN −continuous function is $\mathrm{TN}\alpha^{*}\mathrm{g}^{\#}\psi$ −continuous and every TN −open map is $\mathrm{TN}\alpha^{*}\mathrm{g}^{\#}\psi$ −open. Then ξ is bijective, $\mathrm{TN}\alpha^{*}\mathrm{g}^{\#}\psi$ −continuous and $\mathrm{TN}\alpha^{*}\mathrm{g}^{\#}\psi$ −open. Therefore ξ is $\mathrm{TN}\alpha^{*}\mathrm{g}^{\#}\psi$ −homeomorphism.

Theorem 7.6. Let $\xi:(R,\mathrm{T}_{\mathrm{TN}})\to(Z,\Gamma_{\mathrm{TN}})$ be a $\mathrm{TN}\alpha$−homeomorphism. Then prove that ξ is $\mathrm{TN}\alpha^{*}\mathrm{g}^{\#}\psi$−homeomorphism.

Proof. Let $\xi:(R,\mathrm{T}_{\mathrm{TN}})\to(Z,\Gamma_{\mathrm{TN}})$ be a $\mathrm{TN}\alpha$−homeomorphism. Then ξ is bijective, $\mathrm{TN}\alpha$−continuous and $\mathrm{TN}\alpha$−open. Let H be a TN−open set in (Z,Γ_{TN}). Since ξ is $\mathrm{TN}\alpha$−continuous, $\xi^{-1}(H)$ is $\mathrm{TN}\alpha$−open set in $(R,\mathrm{T}_{\mathrm{TN}})$. Since every $\mathrm{TN}\alpha$−open set is $\mathrm{TN}\alpha^{*}\mathrm{g}^{\#}\psi$−open set, $\xi^{-1}(H)$ is $\mathrm{TN}\alpha^{*}\mathrm{g}^{\#}\psi$−open in $(R,\mathrm{T}_{\mathrm{TN}})$ which implies that ξ is $\mathrm{TN}\alpha^{*}\mathrm{g}^{\#}\psi$−continuous. Let M be a TN−open set in $(R,\mathrm{T}_{\mathrm{TN}})$. Since ξ is $\mathrm{TN}\alpha$−open, $\xi(M)$ is $\mathrm{TN}\alpha$−open set in (Z,Γ_{TN}). Since every $\mathrm{TN}\alpha$−open set is $\mathrm{TN}\alpha^{*}\mathrm{g}^{\#}\psi$−open set, $\xi(M)$ is $\mathrm{TN}\alpha^{*}\mathrm{g}^{\#}\psi$−open set in (Z,Γ_{TN}) which implies ξ is $\mathrm{TN}\alpha^{*}\mathrm{g}^{\#}\psi$−open mapping. Therefore, consequently ξ is $\mathrm{TN}\alpha^{*}\mathrm{g}^{\#}\psi$−homeomorphism.

Theorem 7.7. Let $\xi:(R,\mathrm{T}_{\mathrm{TN}})\to(Z,\Gamma_{\mathrm{TN}})$ be a bijective and $\mathrm{TN}\alpha^{*}\mathrm{g}^{\#}\psi$−irresolute mapping. Then the following statements are equivalent.

(i) ξ is a $\mathrm{TN}\alpha^{*}\mathrm{g}^{\#}\psi$−open mapping.

(ii) ξ is a $\mathrm{TN}\alpha^{*}\mathrm{g}^{\#}\psi$−homeomorphism.

(iii) ξ is a $\mathrm{TN}\alpha^{*}\mathrm{g}^{\#}\psi$−closed mapping.

Proof. Identical to the proof of Theorem 7.4.

Theorem 7.8. Let $\xi:(R,\mathrm{T}_{\mathrm{TN}})\to(Z,\Gamma_{\mathrm{TN}})$ be a bijective function. Then prove that ξ is $\mathrm{TN}\alpha^{*}\mathrm{g}^{\#}\psi$−homeomorphism if and only if $\xi\left[\mathrm{TN}\alpha^{*}\mathrm{g}^{\#}\psi-Cl(M)\right]=\mathrm{TN}-Cl(\xi(M))$ for every subset M of $(R,\mathrm{T}_{\mathrm{TN}})$.

Proof. If $\xi:(R,\mathrm{T}_{\mathrm{TN}})\to(Z,\Gamma_{\mathrm{TN}})$ is $\mathrm{TN}\alpha^{*}\mathrm{g}^{\#}\psi$−homeomorphisms, then ξ is $\mathrm{TN}\alpha^{*}\mathrm{g}^{\#}\psi$−continuous and $\mathrm{TN}\alpha^{*}\mathrm{g}^{\#}\psi$−closed. If $M\subseteq R$. Then $\xi\left[\mathrm{TN}\alpha^{*}\mathrm{g}^{\#}\psi-Cl(M)\right]\subseteq\mathrm{TN}-Cl(\xi(M))$ since ξ is $\mathrm{TN}\alpha^{*}\mathrm{g}^{\#}\psi$−continuous. Since $\mathrm{TN}\alpha^{*}\mathrm{g}^{\#}\psi-Cl(\mathrm{A})$ is TN−closed in $(R,\mathrm{T}_{\mathrm{TN}})$ and ξ is $\mathrm{TN}\alpha^{*}\mathrm{g}^{\#}\psi$−closed mapping, $\xi\left[\mathrm{TN}\alpha^{*}\mathrm{g}^{\#}\psi-Cl(M)\right]$ is $\mathrm{TN}\alpha^{*}\mathrm{g}^{\#}\psi$−closed in (Z,Γ_{TN}). Also $\mathrm{TN}\alpha^{*}\mathrm{g}^{\#}\psi-Cl\left[\xi\left(\mathrm{TN}\alpha^{*}\mathrm{g}^{\#}\psi-Cl(M)\right)\right]=\xi\left(\mathrm{TN}\alpha^{*}\mathrm{g}^{\#}\psi-Cl(M)\right)$. Since $M\subseteq\mathrm{TN}\alpha^{*}\mathrm{g}^{\#}\psi-Cl(M)$, $\xi(M)\subseteq\xi\left[\mathrm{TN}\alpha^{*}\mathrm{g}^{\#}\psi-Cl(M)\right]$ and therefore we obtain $\mathrm{TN}-Cl(\xi(M))\subseteq\mathrm{TN}-Cl\left[\xi\left(\mathrm{TN}\alpha^{*}\mathrm{g}^{\#}\psi-Cl(M)\right)\right]=\xi\left(\mathrm{TN}\alpha^{*}\mathrm{g}^{\#}\psi-Cl(M)\right)$ Thus $\mathrm{TN}-Cl(\xi(M))\subseteq\xi\left(\mathrm{TN}\alpha^{*}\mathrm{g}^{\#}\psi-Cl(M)\right)$. Hence, $\xi\left[\mathrm{TN}\alpha^{*}\mathrm{g}^{\#}\psi-Cl(M)\right]=\mathrm{TN}-Cl(\xi(M))$ if ξ is $\mathrm{TN}\alpha^{*}\mathrm{g}^{\#}\psi$−homeomorphism.

Conversely, if $\xi\left[\mathrm{TN}\alpha^{*}\mathrm{g}^{\#}\psi-Cl(M)\right]=\mathrm{TN}-Cl(\xi(M))$ for every subset M of $(R,\mathrm{T}_{\mathrm{TN}})$, then ξ is $\mathrm{TN}\alpha^{*}\mathrm{g}^{\#}\psi$−continuous. If M is TN−closed in $(R,\mathrm{T}_{\mathrm{TN}})$, then M is $\mathrm{TN}\alpha^{*}\mathrm{g}^{\#}\psi$−closed in $(R,\mathrm{T}_{\mathrm{TN}})$. Then $\mathrm{TN}\alpha^{*}\mathrm{g}^{\#}\psi-Cl(M)=M$ which implies $\xi\left[\mathrm{TN}\alpha^{*}\mathrm{g}^{\#}\psi-Cl(M)\right]=\xi(M)$. Hence, by the given hypothesis, it follows that $\mathrm{TN}-Cl(\xi(M))=\xi(M)$. Thus $\xi(M)$ is TN−closed in Z and hence $\mathrm{TN}\alpha^{*}\mathrm{g}^{\#}\psi$−closed in Z for every TN−closed set M in R. That is, ξ is a $\mathrm{TN}\alpha^{*}\mathrm{g}^{\#}\psi$−closed mapping. Therefore $\xi:(R,\mathrm{T}_{\mathrm{TN}})\to(Z,\Gamma_{\mathrm{TN}})$ is $\mathrm{TN}\alpha^{*}\mathrm{g}^{\#}\psi$−homeomorphism.

Conclusion

We introduced and systematically investigated the concept of Tetra Neutrosophic α* generalized $g^{\#}\psi$ −closed sets in Tetra Neutrosophic topological spaces. The fundamental properties of $TN\alpha^{*}g^{\#}\psi$ −closed sets were established through a collection of results concerning their relationships with the relevant generalized closed and open sets and their associated closure properties. These results provide a systematic theoretical foundation for the subsequent development of generalized mappings in Tetra Neutrosophic topological spaces.

Based on the proposed $TN\alpha^{*}g^{\#}\psi$ −closed sets, we introduced and investigated $TN\alpha^{*}g^{\#}\psi$ −continuous, $TN\alpha^{*}g^{\#}\psi$ −irresolute, $TN\alpha^{*}g^{\#}\psi$ −open and $TN\alpha^{*}g^{\#}\psi$ −closed mappings. Their basic properties, relationships, and characterizations were established within the Tetra Neutrosophic topological framework. Furthermore, the concept of $TN\alpha^{*}g^{\#}\psi$ −homeomorphism was introduced, and fundamental properties of this homeomorphism were investigated, thereby providing a suitable notion of topological equivalence based on the proposed generalized structure.

Overall, the results obtained in this paper extend the theory of α^{*} generalized$^{\#}\psi$ −closed sets and their associated mappings from classical topological spaces to the Tetra Neutrosophic setting. The study consequently establishes a coherent framework connecting $TN\alpha^{*}g^{\#}\psi$ −closed sets with generalized continuity, irresoluteness, openness, closedness, and homeomorphisms. Thus, the present work contributes to the development of generalized mapping theory in the newly developing field of Tetra Neutrosophic topology and provides a foundation for the further study of generalized topological structures in this setting.

Recommendations

It is recommended to investigate the relationships of $TN\alpha^{*}g^{\#}\psi$ −mappings with other generalized mappings and generalized closed and open sets in Tetra Neutrosophic topology. Further research may examine separation axioms, compactness, connectedness, countability properties, and various forms of generalized compactness associated with $TN\alpha^{*}g^{\#}\psi$ −mappings.

Another promising direction is to study the preservation of these properties under composition and inverse mappings and to characterize $TN\alpha^{*}g^{\#}\psi$ −homeomophisms through suitable invariants of Tetra Neutrosophic topological spaces. The proposed framework may also be extended to other neutrosophic structures and, where appropriate, investigated for applications involving uncertain, inconsistent, and indeterminate information in intelligent systems, decision-making, and information processing.

These directions may provide further theoretical development of Tetra Neutrosophic topology and contribute to the establishment of a broader framework for generalized mappings in uncertainty-aware mathematical models.

Scientific Ethics Declaration

* The author declares that the scientific ethical and legal responsibility of this article published in EPSTEM Journal belongs to the author.

Conflict of Interest

* The author declares that there is no conflict of interest.

Funding

* This research received no specific grant from any funding agency in the public, commercial, or not-for-profit sectors.

Acknowledgements or Notes

* This article was presented as an oral presentation at the International Conference on Basic Sciences, Engineering and Technology (www.icbaset.net) held in Istanbul/Türkiye on September 17-18, 2026.

* The author is indebted to Prince Mohammad Bin Fahd University Al Khobar, Saudi Arabia, for providing the necessary research facilities during the preparation of this research paper.

References

Anto, M., & Carolinal, J. (2023). Functions in nano topological spaces. *Ratio Mathematica, 45*, 97–110.

Bhuvaneswari, K., & Ezhilarasi, A. (2016). Nano semi-generalized homeomorphisms in nano topological space. *International Journal of Mathematical Archive, 7*(7), 168–175.

Bhuvaneswari, K., & Gnanapriya, K. M. (2016, July). Nano generalized pre homeomorphisms in nano topological space. *International Journal of Scientific and Research Publications, 6*(7), 526–530.

Brindha, R. (2025). Neutrosophic nano topology: An analysis of neut.nano αg#ψ-open and closed functions and their properties. *Advances in Nonlinear Variational Inequalities, 28*(4S), 344–350.

Damodharan, K., Vigneshwaran, M., & Khalil, S. (2020). Irresolute functions in neutrosophic topological spaces. *Neutrosophic Sets and Systems, 38*, 439–452.

Deepa, M., & Kalaivanan, M. R. (2021). On nano Y**-closed and nano Y**-open functions. *IT in Industry, 9*(1), 1437–1442.

Geetha, K., & Vigneshwaran, M. (2018, April). Characterization of nano P*G-homeomorphisms in nano topological spaces. *International Journal of Advanced Research Trends in Engineering and Technology (IJARTET), 5*(Special Issue 12), 973–977.

Imran, Q. H., Smarandache, F., Al-Hamido, R. K., & Dhavaseelan, R. (2017). On neutrosophic semi alpha open sets. *Neutrosophic Sets and Systems*, 37–42.

Inthumathi, V., Abinprakash, R., & Banu, M. P. (2019). Some weaker forms of continuous and irresolute mappings in nano ideal topological spaces. *Journal of New Results in Science (JNRS), 8*(1), 14–25.

Mahdi, S. S., & Jamil, J. M. (2024). On some types of nano functions. *BIO Web of Conferences, 97*, 00144, 1–13.

Maheswari, N. R. S. (2023). On nano functions in nano topological spaces. *International Journal of Mathematics and Combinatorics, 1*, 81–86.

Malarvizhi, M., Sarankumar, T., Rajendran, V., & Satishmohan, P. (2021). On Ng^α-homeomorphisms in nano topological spaces. *Turkish Journal of Computer and Mathematics Education, 12*(10), 4707–4711.

Nandhini, T., & Vigneshwaran, M. (2019). $\mathcal{N}$αg#ψ-open map, $\mathcal{N}$αg#ψ-closed map, and $\mathcal{N}$αg#ψ-homeomorphism in neutrosophic topological spaces. *Neutrosophic Sets and Systems, 29*, 187–186.

Nandhini, T., & Vigneshwaran, M. (2019). Nαg#ψ-closed sets in neutrosophic topological spaces. *American International Journal of Research in Science, Technology, Engineering and Mathematics, Special Issue of 2nd International Conference on Current Scenario in Pure and Applied Mathematics*, 370–373.

Nandhini, T., & Vigneshwaran, M. (2019). On $\mathcal{N}$αg#ψ-continuous and $\mathcal{N}$αg#ψ-irresolute functions in neutrosophic topological spaces. *International Journal of Recent Technology and Engineering, 7*, 1097–1101.

Nandhini, T., & Vigneshwaran, M. (2020). On neutrosophic nano αg#ψ-closed sets in neutrosophic nano topological spaces. *International Journal of Neutrosophic Science (IJNS), 5*(2), 67–71.

Nandhini, T., Banu, M. N., Savithiri, D. D., Pandima, J., Rajalakshmi, R., Suganthi, G., & Brindha, R. (2025). Neutrosophic nano topology: An analysis of neut.nano αg#ψ-open and closed functions and their properties. *Advances in Nonlinear Variational Inequalities, 28*(4S), 344–350.

Parimala, M., Jeevitha, R., Jafari, S., Smarandache, F., & Karthika, M. (2018). Neutrosophic nano αψ-closed sets in neutrosophic nano topological spaces. *Journal of Advanced Research in Dynamical and Control Systems, 10*(Special Issue 10), 523–531.

Parimala, M., Arivuoli, D., & Jeevitha, R. (2018, November). Composition of functions under Niαg continuous and Niαg-irresolute functions in nano ideal topological spaces. *International Journal of Recent Technology and Engineering (IJRTE), 7*(4S), 107–110.

Pooja, S., Vigneshwaren, M., & Vidyarani, V. (2024). On sets in topological spaces. *International Journal of Natural Sciences, 15*(83), 72610–72617.

Pooja, S., Pooja, S., Vigneshwaren, M., & Vidyarani, V. (2024). On functions and irresolute maps in topological spaces. *International Journal of Natural Sciences, 15*(83), 76164–76175.

Radha, R., Princy, R., & Pratheesha, A. S. V. (2026). Tetra neutrosophic set. *International Journal of Creative Research Thoughts (IJCRT), 14*(1), 1–7.

Rajendran, V., Mohan, P. S., & Chitra, M. (2021, June). Nano g*α-continuous functions in nano topological spaces. *Turkish Online Journal of Qualitative Inquiry (TOJOI), 12*(5), 1156–1164.

Rajendran, V., Mohan, P. S., & Mangayarkarasi, R. (2021). Functions in nano topological spaces. *Turkish Journal of Computer and Mathematics Education, 12*(10), 4712–4718.

Sathya, C. J., & Richard, C. (2024). A new class of Ng*B-continuous and Ng*B-irresolute functions in NTS. *Tuijin Jishu/Journal of Propulsion Technology, 45*(2), 85–90.

Smarandache, F. (1998). *Neutrosophy: Neutrosophic probability, set, and logic: Analytic synthesis & synthetic analysis*. Rehoboth, NM: American Research Press.

Author(s) Information

Raja Mohammad Latif
Prince Mohammad Bin Fahd University, Department of Mathematics and Natural Sciences, Al Khobar, Saudi Arabia
ORCID iD: https://orcid.org/0000-0003-3140–9581
Contact e-mail: *rajamlatif@yahoo.com*

To cite this article:

Latif, R. M. (2026). Tetra neutrosophic alpha star generalized #Ψ mappings in tetra neutrosophic topological spaces *The Eurasia Proceedings of Science, Technology, Engineering and Mathematics (EPSTEM), 42,* 237-259.

ICBASET 2026: International Conference on Basic Sciences, Engineering and Technology

Mid-Infrared (FTIR) Spectroscopy for Urinary Stone Identification: Clinical Relevance in an Industrial Region

Kostyantyn BARANNIK
Dnipro State Medical University, Ukraine

Volodymyr SULYMA
Dnipro State Medical University, Ukraine

Serhij MALINOVSKYJ
Dnipro State Medical University, Ukraine

Oleksandr BALALAEV
Institute of Geotechnical Mechanics named after M.S. Polyakova of the National Academy of Sciences of Dnipro, Ukraine

Abstract: Accurate identification of urinary stone composition remains a key challenge in the management of urolithiasis, particularly in industrial regions characterized by complex environmental and metabolic influences. This study aimed to evaluate the clinical utility of mid-infrared (FTIR) spectroscopy and to improve the identification of urinary stones in patients from an industrial region. A comparative analysis of the chemical composition, morphology, and structural characteristics of 85 urinary stones obtained from patients residing in the Dnipropetrovsk region was performed using an integrated FTIR system with μ-FTIR microscopy and the NICODOM spectral database. Spectral matching demonstrated that 55% of stones exhibited semi-quantitative composition, while the remaining samples were characterized by qualitative identification only. The overall agreement with reference spectra was satisfactory, with a mean correlation coefficient of 82.7 ± 5.3%. However, significant overlap of absorption peaks in mixed-composition stones, particularly in the <1800 cm^{-1} region, and the influence of the broad O–H stretching band (2700–3700 cm^{-1}) may lead to misclassification due to masking of minor components by dominant mineral phases. μ-FTIR mapping enabled visualization of the spatial distribution of organic and mineral components, revealing microstructural heterogeneity and layered growth patterns associated with protein-rich matrices. The findings demonstrate that FTIR spectroscopy, combined with spatial analysis, provides a powerful tool for accurate stone identification. This approach enhances understanding of lithogenesis, supports personalized treatment strategies, and offers significant potential for early diagnosis and prevention of recurrence in patients with urolithiasis.

Keywords: urinary stones, infrared spectrometry, spectral monitoring.

Introduction

Urolithiasis is a complex multifactorial disease resulting from the interaction of genetic and environmental factors [1,2,5,9]. Epidemiological studies have demonstrated a strong association between urolithiasis and a range of lifestyle-related conditions, including cardiovascular diseases, arterial hypertension, chronic kidney disease, diabetes mellitus, and metabolic disorders [3, 4].

The formation of urinary stones is driven by complex physicochemical, biological, and biochemical processes that determine their mineral composition and morphostructural characteristics. This is supported by data obtained using modern analytical techniques, including spectral, X-ray, polarizing, and infrared methods [6,8]. Understanding the mechanisms underlying lithogenesis is essential for the development of effective preventive strategies for urolithiasis [8,9].

- This is an Open Access article distributed under the terms of the Creative Commons Attribution-Noncommercial 4.0 Unported License, permitting all non-commercial use, distribution, and reproduction in any medium, provided the original work is properly cited.

- Selection and peer-review under responsibility of the Organizing Committee of the Conference

© 2026 Published by ISRES Publishing: www.isres.org

Accurate determination of urinary stone composition plays a crucial role in selecting appropriate treatment strategies and preventing recurrence. In particular, identification of the metabolic type of stones enables the implementation of personalized therapeutic and metaphylactic approaches. One of the promising directions in this field is the comprehensive analysis of lithogenic metabolic factors, the prolonged influence of which contributes to the initiation, growth, and recurrence of stone formation [7, 8].

Fourier Transform Infrared (FTIR) spectroscopy is a highly informative analytical method for identifying organic and inorganic substances based on the measurement of infrared absorption spectra. It provides detailed qualitative information about the molecular composition of the analyzed material and, when appropriate standards are used, allows for quantitative analysis [6, 8,10,11].

FTIR spectroscopy is characterized by its non-destructive nature, high specificity, rapid analysis, and accuracy. It enables the study of a wide range of materials, including solids, liquids, and semi-solid samples, making it a versatile tool for the analysis of biological and mineral structures. In the context of urolithiasis, FTIR spectroscopy offers significant potential for detailed characterization of both mineral and organic components of urinary stones, which is essential for understanding disease pathogenesis and optimizing clinical management [6, 8].

Method

A comparative analysis of the chemical composition, morphology, and structural characteristics of 85 urinary stones obtained from patients residing in the Dnipropetrovsk region was performed. The patients' age ranged from 18 to 70 years; the study cohort included 34 females and 51 males.

The analyzed stones were obtained following spontaneous passage during conservative management, after contact or extracorporeal lithotripsy, or were surgically removed. The dimensions of the stones ranged from 5 to 67 mm in length, 4 to 54 mm in width, and 3 to 31 mm in thickness. Some stones exceeded these dimensions. The morphology of the stones was heterogeneous.

Despite these limitations, reflected FTIR methods demonstrated high analytical performance and were successfully applied for the identification of more than 85 urinary stones. Infrared spectra were recorded in the mid-infrared range using a Thermo Scientific Nicolet iS10 FTIR spectrometer (USA) with a spectral resolution of 8 cm^{-1} and averaging 50 scans per sample. (Fig 1).

Spectral identification was performed using OMNIC 9 software (Thermo Scientific) in combination with the specialized NICODOM IR Kidney Stones spectral library (Czech Republic), which is based on transmission spectra of 1668 reference samples. The overall agreement with reference spectra was satisfactory, with a mean correlation coefficient of 82.7 ± 5.3%.

However, significant overlap of absorption peaks in mixed-composition stones, particularly in the <1800 cm^{-1} region, and the influence of the broad O–H stretching band (2700–3700 cm^{-1}) may lead to misclassification due to masking of minor components by dominant mineral phases. μ-FTIR mapping enabled visualization of the spatial distribution of organic and mineral components, revealing microstructural heterogeneity and layered growth patterns associated with protein-rich matrices.

The findings demonstrate that FTIR spectroscopy, combined with spatial analysis, provides a powerful tool for accurate stone identification. This approach enhances understanding of lithogenesis, supports personalized treatment strategies, and offers significant potential for early diagnosis and prevention of recurrence in patients with urolithiasis.

In terms of analytical accuracy, FTIR spectroscopy is comparable only to thermogravimetric analysis and polarizing microscopy; however, both methods have significant limitations.



Figure 1. Thermo Scientific Nicolet iS10 Fourier-transform infrared (FTIR) spectrometer employed for the identification of urinary stone composition using attenuated total reflectance (ATR) technique.

Results and Discussion

Thermogravimetric analysis requires destruction of the sample during the measurement process and necessitates a relatively larger amount of material to achieve optimal resolution.

In contrast, polarizing microscopy is time-consuming due to the complexity of sample preparation, lacks sensitivity for detecting small quantities of transparent components in mixed samples, and its results are highly dependent on the operator's expertise.

Another widely used physical method for structural analysis of solid materials, powder X-ray diffraction (XRD), demonstrated relatively low identification accuracy (below 60%), which is inferior even to conventional wet chemical analysis. This limitation is primarily related to the specific interaction of X-ray radiation with the crystalline structure of urinary stones, particularly in cases involving heterogeneous or poorly crystalline components.

Calcium oxalate may crystallize in two distinct chemical and crystallographic forms: the monohydrate $CaC_2O_4 \cdot H_2O$ (whewellite) and the dihydrate $CaC_2O_4 \cdot 2H_2O$ (weddellite). These types of stones are radiopaque. In contrast, uric acid crystals, urates, amorphous calcium phosphate, and organic components such as proteins are radiolucent.

These limitations are overcome by FTIR spectroscopy, which enables the identification of crystalline, amorphous, and poorly crystalline components, including both mineral and organic molecules. This is particularly important for the analysis of urinary stones, as their formation involves a complex interplay of inorganic and organic constituents.

Infrared absorption occurs due to changes in the dipole moment of a molecule during atomic vibrations. Three main types of vibrational modes are distinguished: stretching (changes in bond length), in-plane bending, and out-of-plane deformation (changes in bond angles), along with their various combinations. These vibrational modes are distributed across the electromagnetic spectrum and generate characteristic infrared spectra.

Heteronuclear bonds are IR-active due to the absence of symmetry restrictions. Urinary stones typically contain functional groups such as OH, NH, CH, CO, CN, PO, CS, SO, and SiO, which are components of both mineral and organic phases. The simultaneous presence of multiple vibrational modes facilitates the identification of molecular functional groups.

Infrared spectra can be acquired using transmission mode, attenuated total reflectance (ATR), or diffuse reflectance (DRIFT) with appropriate spectrometer accessories, each having specific advantages and limitations. Transmission spectroscopy requires relatively small sample amounts and follows the Beer–Lambert law, allowing for quantitative analysis. However, it is limited by the time-consuming preparation of KBr pellets.

The DRIFT method enables analysis of finely dispersed stone powder without dilution in potassium bromide and provides a favorable signal-to-noise ratio. However, it requires a larger sample volume, has limitations for quantitative analysis, and may introduce spectral distortions. These artifacts may contain additional information but complicate matching with spectral libraries.

Among these techniques, ATR-FTIR spectroscopy is considered the most optimal for analyzing the molecular composition of urinary stones. It combines minimal sample preparation, spectral similarity to transmission spectra, and the potential for quantitative analysis. The main limitation of ATR-FTIR is the shift of the low-frequency boundary of the mid-infrared range from approximately 400 to 650 cm^{-1}, due to the use of infrared-transparent optical components.

However, practical measurements indicate that the effective lower limit is approximately 500 cm^{-1}, which is sufficient for accurate identification of all analyzed stones, as characteristic absorption bands are typically absent at longer wavelengths.

From a clinical perspective, accurate identification of stone composition using ATR-FTIR spectroscopy enables targeted metabolic evaluation and individualized prevention strategies.

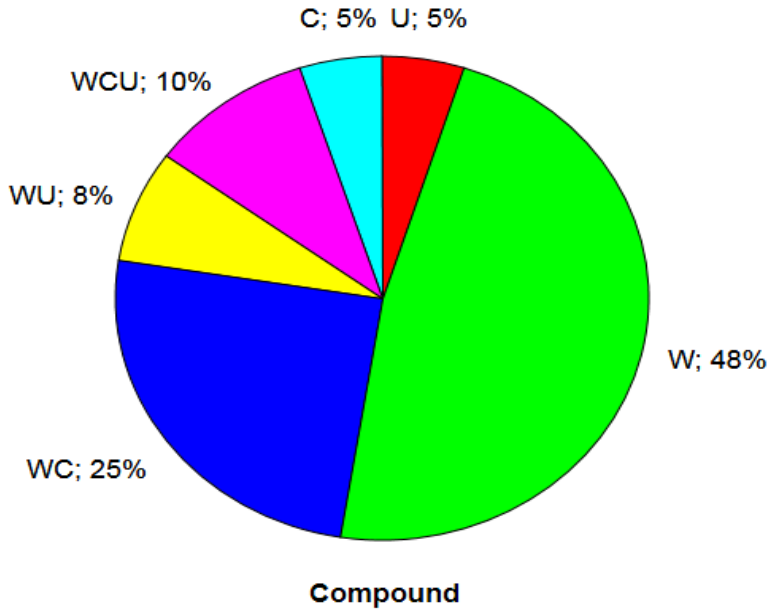

Figure 2. Distribution of urinary stone composition based on FTIR identification using the NICODOM spectral database. W – whewellite and weddellite; C – carbonate apatite and struvite; U – uric acid and urates; WC, WU, and WCU – mixed-composition stones.

The distribution of stone composition was as follows: calcium oxalate – 48% (n=41), mixed oxalate stones – 43% (n=37), urate stones – 4% (n=3), and phosphate stones – 5% (n=4). (Fig 2).

The recorded spectra generally demonstrated satisfactory agreement with reference library spectra. The mean correlation coefficient was 82.7 ± 5.3%. Slightly lower values observed in some cases may be attributed to increased noise in the initial samples during the optimization phase of measurement and spectral processing. However, this did not affect the accuracy of stone identification.

This phenomenon was reflected by a local maximum on the histogram centered at approximately 74%, indicating the presence of a subset of spectra with lower correlation values.

Spectral database matching revealed that 55% of the analyzed urinary stones exhibited a semi-quantitative composition, whereas the remaining samples were characterized by qualitative composition only (Fig. 3).

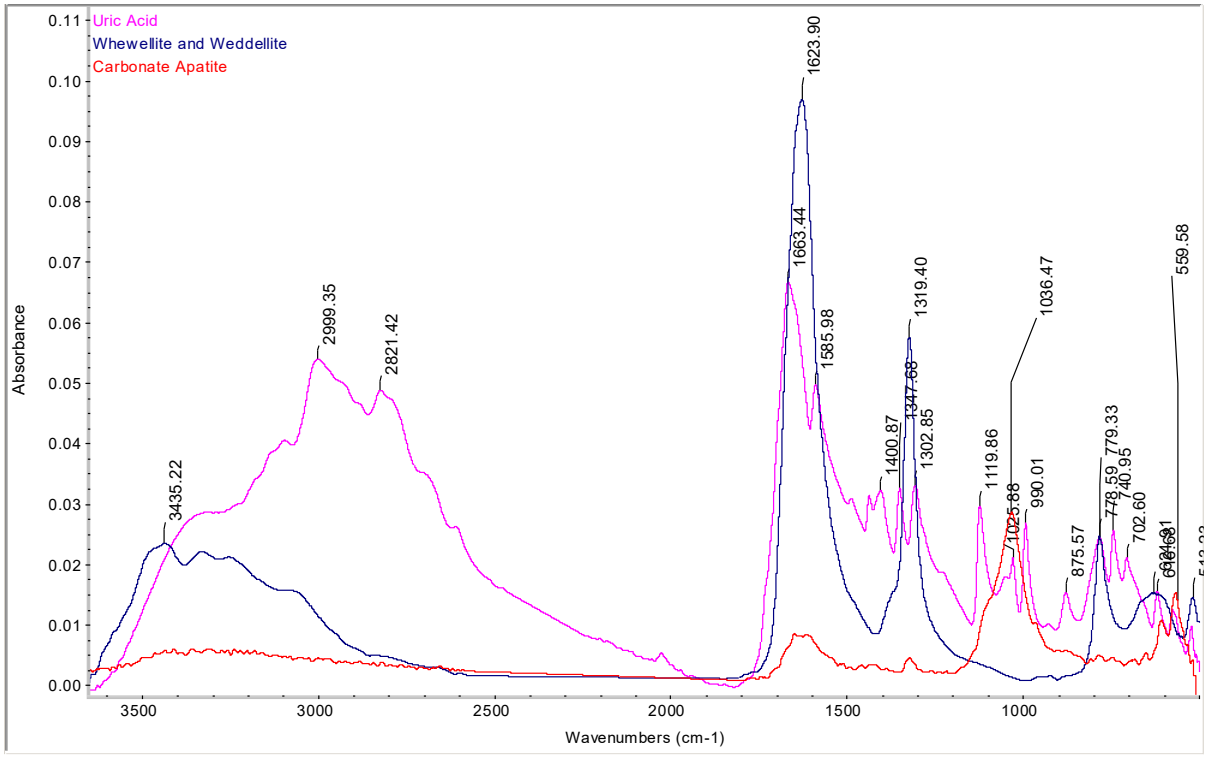

Figure 3. ATR-FTIR spectra of relatively pure oxalate, phosphate, and urate urinary stones.

Comparison of ATR-FTIR spectra from patients with predominantly pure oxalate, phosphate, and urate stones on a unified scale demonstrated that the long-wavelength region of the spectrum (<1800 cm^{-1}) is more enriched with characteristic absorption peaks. However, the peak maxima differ among these stone types, and in mixed compositions, these peaks tend to overlap, potentially leading to misidentification. Furthermore, absorption bands of the dominant mineral may mask the characteristic peaks of minor components. To address this limitation, correlation-based identification should be supplemented with additional analysis of spectral band shapes. An example of misclassification during automated spectral identification of a mixed-composition stone using a reference spectral library is presented (Fig. 4).

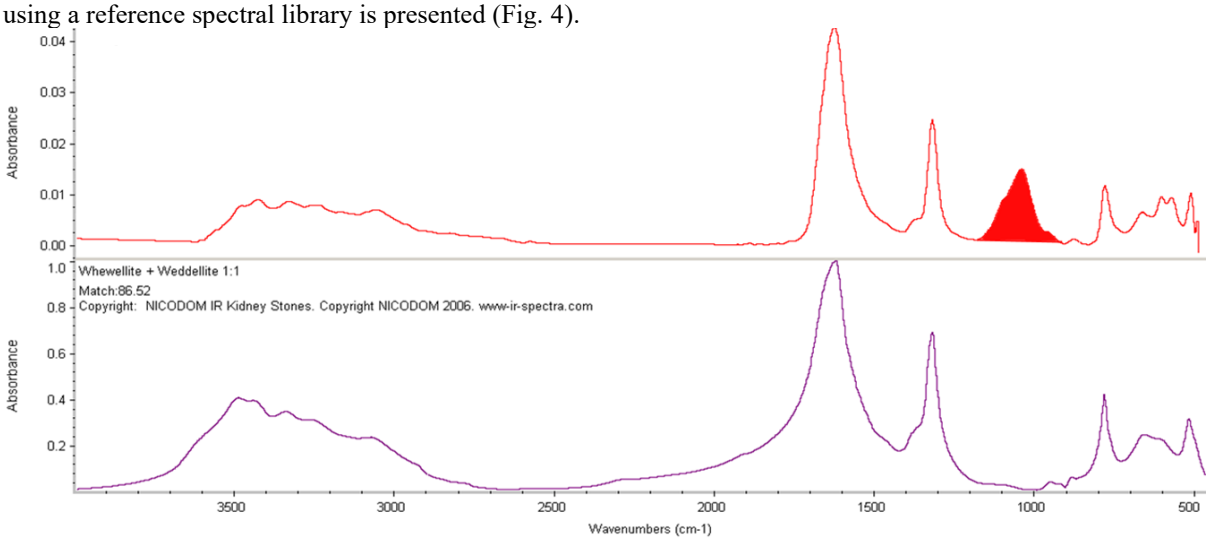

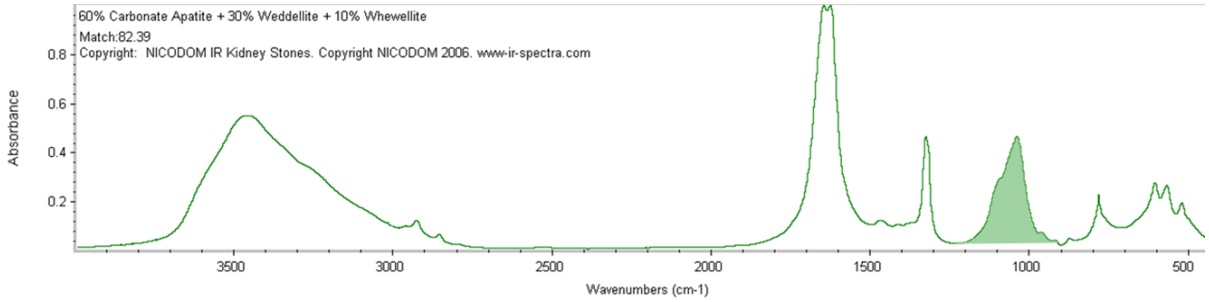

Figure 4. Example of automated misidentification of a urinary stone spectrum using the NICODOM spectral database.

Database matching indicated the highest similarity with a combination of whewellite and weddellite in approximately equal proportions. Formal comparison of the spectral curves resulted in the prominent carbonate apatite absorption band (highlighted) being assigned less significance than the similarity in the shape of the broad diffuse peak corresponding to O–H stretching vibrations in the 2700–3700 cm^{-1} range.

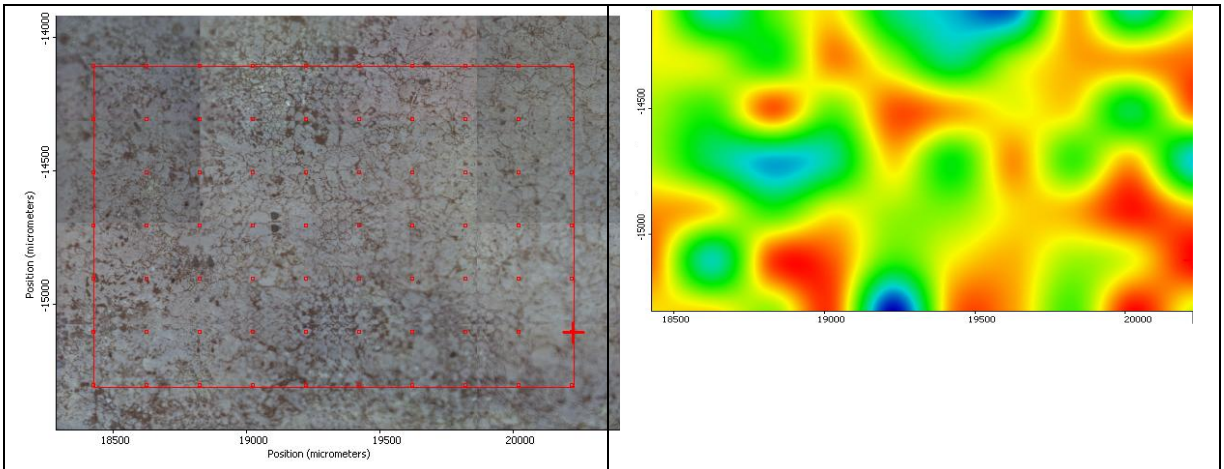

Microimage of the polished surface of a urinary stone (×150 magnification)	The corresponding μ-FTIR map of the distribution of organic CH groups (red – high concentration, blue – low concentration).

Figure 5. μ-FTIR microscopy of a polished thin section of a urinary stone.

Notably, this spectral region is more informative for urate stones than for oxalate-based compositions. Consequently, the spectrum corresponding to the actual stone composition, in which carbonate apatite accounted for more than 50% of the total content, ranked only eighth in the matching results.

The capabilities of the analytical system are not limited to conventional FTIR measurements. For intact stones that have not been fragmented, micro-scale μ-FTIR analysis is particularly advantageous (Fig. 5). This approach enables mapping and visualization of the spatial distribution of organic components and mineral phases within the stone samples.

Moreover, μ-FTIR analysis provides valuable insights into the origins of microstructural heterogeneity and the mechanisms underlying the layered deposition of constituents during stone growth.

The presented example demonstrates a μ-FTIR map of spatial heterogeneity in the redistribution of organic CH groups on the surface of the urinary stone thin section. These organic components are most likely associated with protein constituents.

Conclusion

Mid-infrared (FTIR) spectroscopy demonstrated clear advantages over conventional analytical methods for urinary stone identification and can be effectively integrated into the comprehensive evaluation of patients with urolithiasis.

Accurate determination of both primary and secondary chemical composition, together with analysis of the spatial distribution of stone components, provides deeper insight into the physicochemical mechanisms underlying lithogenesis.

Spectral monitoring of urinary composition represents a promising approach for early diagnosis, development of personalized treatment strategies, and effective prevention of stone recurrence in patients with urolithiasis.

Micro-scale μ-FTIR analysis enables detailed mapping of the spatial distribution of organic and mineral components, revealing microstructural heterogeneity and layered growth patterns, which are essential for understanding stone formation mechanisms and improving diagnostic accuracy.

Significant overlap of absorption peaks in mixed-composition stones, particularly in the <1800 cm^{-1} region, and the influence of the broad O–H stretching band (2700–3700 cm^{-1}) may lead to misclassification due to masking of minor components by dominant mineral phases. μ-FTIR mapping enabled visualization of the spatial distribution of organic and mineral components, revealing microstructural heterogeneity and layered growth patterns associated with protein-rich matrices.

The findings demonstrate that FTIR spectroscopy, combined with spatial analysis, provides a powerful tool for accurate stone identification. This approach enhances understanding of lithogenesis, supports personalized treatment strategies, and offers significant potential for early diagnosis and prevention of recurrence in patients with urolithiasis.

Among these techniques, ATR-FTIR spectroscopy is considered the most optimal for analyzing the molecular composition of urinary stones. It combines minimal sample preparation, spectral similarity to transmission spectra, and the potential for quantitative analysis. The main limitation of ATR-FTIR is the shift of the low-frequency boundary of the mid-infrared range from approximately 400 to 650 cm^{-1}, due to the use of infrared-transparent optical components.

However, practical measurements indicate that the effective lower limit is approximately 500 cm^{-1}, which is sufficient for accurate identification of all analyzed stones, as characteristic absorption bands are typically absent at longer wavelengths.

The presented example demonstrates a μ-FTIR map of spatial heterogeneity in the redistribution of organic CH groups on the surface of the urinary stone thin section. These organic components are most likely associated with protein constituents.

Recommendations

In the future, the application of the proposed complex-combined method of prevention, detection, correct diagnosis and effective treatment of effective prevention of stone recurrence in patients with urolithiasis using biophysical and biotechnological means can objectify and accelerate the determination of this pathological condition, and an in-depth study of these results can become the basis for successful surgical treatment of specialized patients.

Scientific Ethics Declaration

The authors declare that this study was conducted in accordance with established scientific, ethical, and legal standards. Full responsibility for the content of this article rests with the authors.

Conflict of Interest

The authors declare that they have no conflicts of interest.

Funding

This research received no external funding.

Acknowledgements or Notes

This article was presented as an oral presentation at the International Conference on Basic Sciences, Engineering and Technology (www.icbaset.net) held in Istanbul/Türkiye on September 17-18, 2026.

References

1. Stus VP, Moiseyenko MM, Koshtura VV, Svitlichnyy EO, Mozheyko OO, Lyulka DI. X-ray structuralanalysis of urinary stones. *Urologiya*. 2018;22(3):205.
2. Ishkov VV, Koziy ES, Trufanova MO. Features of urolith ontogenesis in residents of the Dnipropetrovsk region. *Mineralogical Journal*. 2020;42(4):50–59.
3. Barannik K, Ishkov V, Molchanov R, Barannik S. Practical significance of the composition and structure of urinary stones in residents of an industrial region. In: *Proceedings of the XXI International Scientific and Practical Conference*; 2022; Paris, France. p. 410–414.
4. Barannik K, Molchanov R, Barannik S. Lithogenesis features of urate stones in patients from an industrial region. In: *Proceedings of the II International Scientific and Theoretical Conference*; 2022; Helsinki, Finland. p. 40–44.
5. Barannik K, Molchanov R, Barannik S, Kasparova M. Chemical composition and structure of urinary stones for selecting optimal treatment strategies. In: *Proceedings of the III International Scientific Conference "Scientia"*; 2022; Lisbon, Portugal. p. 153–157.
6. Barannik K, Molchanov R, Barannik S, Kasparova M. Clinical significance of urinary stone composition and structure in treatment planning. *Grail of Science*. 2022;(20):170–177.
7. Rodriguez-Plata IT, Medina-Escobedo M, Basulto-Martinez M, Avila-Nava A, Gutierrez-Solis AL, Mendez-Dominguez N, et al. Implementation of a technique based on Hounsfield units to determine kidney stone composition. *Tomography*. 2021;7(4):606–613.
8. Wang Z, Zhang Y, Zhang J, Deng Q, Liang H. Recent advances inmechanisms of kidney stone formation. *Int J Mol Med*. 2021;48:149.
9. Khan SR, Pearle MS, Robertson WG, et al. Kidney stones. *Nat Rev Dis Primers*. 2023;9:75.
10. Daudon M, Bazin D. Analysis of urinary stones by FTIR spectroscopy: current trends and clinical relevance. *Clin Chem Lab Med*. 2023;61(7):1131–1142. Bouatia M, et al. Recent advances in FTIR spectroscopy for kidney stone analysis. *Spectrochim Acta A Mol Biomol Spectrosc*. 2024;301:122992.

Author(s) Information

Kostyantyn BARANNIK
Dnipro State Medical University
V.Vernadskyj Street, 9, Dnipro, 49000, Ukraine
ORCID iD: https://orcid.org/0000-0002-1009-4990

Volodymyr Sulyma
Dnipro State Medical University
V.Vernadskyj Street, 9, Dnipro, 49000, Ukraine
ORCID iD: https://orcid.org/0000-0002-8373-6480
*Contact e-mail: *Volodyasulyma2@gmail.com*

Serhij Malinovskyj
Dnipro State Medical University
V.Vernadskyj Street, 9, Dnipro, 49000, Ukraine
ORCID iD: https://orcid.org/0000-0002-5554-836X

Oleksandr Balalaev
Institute of Geotechnical Mechanics
Gonchar Street, 1, Dnipro, 49000, Ukraine
ORCID iD: https://orcid.org/0000-0002-9389-4562

*Corresponding authors contact email

ICBASET 2026: International Conference on Basic Sciences, Engineering and Technology

Value-Enhanced Oat Breeding for High-Quality Biscuit Production

Hayati AKMAN
Selcuk University

Aysegul SOYAKIL
Eskisehir Osmangazi University

Yasar KARADUMAN
Eskisehir Osmangazi University

Abstract: Oat (Avena sativa L.) has emerged as a strategically significant cereal, distinguished by its exceptional nutritional density and multifunctional bioactive profile. Its grains provide high-quality protein, beneficial lipids, several minerals, dietary fiber, and functional constituents such as β-glucan and avenanthramides. These compositional attributes make oat a particularly promising raw material for biscuit manufacturing, where it imparts a distinctive coarse, fibrous texture and a characteristic nutty flavor that clearly distinguish oat-based products from conventional wheat-based alternatives**.** Beyond sensory differentiation, oat-based biscuits serve as efficient delivery matrices for bioactive β-glucans, which reduce cholesterol and modulate glucose absorption, conferring cardiovascular and metabolic benefits; concurrently, their prebiotic properties support beneficial gut microbiota. The elevated fiber content further enhances satiety, rendering oat-based biscuits particularly appealing to consumers managing diabetes or obesity-related conditions. Contemporary breeding strategies therefore seek to harmonize industrial processing requirements with nutritional functionality. In addition to nutritional superiority, optimal genotypes must exhibit high yield, disease resistance, and climate adaptability to ensure agronomic viability. From a technological standpoint, biscuit production requires a low hull ratio, reduced oil and starch content, coupled with favorable physical and nutritional attributes such as dietary fiber, β-glucan, milling yield, hectoliter weight, sieve retention, and thousand-grain weight. Ultimately, biscuit quality is contingent upon achieving an optimal balance of protein content, texture, and sensory properties to guarantee consumer satisfaction. Consequently, expanding the cultivation and utilization of purpose-grown, regionally adapted biscuit-type oats through integrated breeding and food technology approaches constitutes a strategic priority for securing a reliable and sustainable raw material pipeline and meeting evolving consumer demand for nutrient-dense functional snacks without compromising industrial productivity.

Keywords: Technological quality, oat, biscuit, functionality, breeding.

Introduction

Over recent decades, food science has moved beyond the traditional paradigm that regarded nutrition merely as sustenance, adopting instead a holistic perspective that recognizes foods as agents capable of preserving and enhancing physical and mental health. This conceptual transformation has catalyzed the emergence of functional foods, defined as products that, in addition to basic nutritional requirements, provide specific health benefits and mitigate disease risk (Siró et al., 2008). The principal aim of functional food development is either to restore nutrients diminished during processing or to fortify foods with their indigenous bioactive constituents, thereby advancing public health (Siró et al., 2008).

Given their role as staple foods for vast populations, cereals occupy a strategic position in functional food development owing to their dietary fiber, β-glucan, phenolic compounds, and antioxidant content in whole grains (Liu, 2007). Within this context, oat (*Avena sativa* L.) is distinguished by its superior nutritional profile, which encompasses high-quality protein, a balanced amino acid composition, unsaturated fatty acids, β-glucan, and unique compounds termed avenanthramides (Singh et al., 2013). These characteristics have prompted the characterization of oat as a “potential therapeutic agent” (Singh et al., 2013).

- This is an Open Access article distributed under the terms of the Creative Commons Attribution-Noncommercial 4.0 Unported License, permitting all non-commercial use, distribution, and reproduction in any medium, provided the original work is properly cited.

- Selection and peer-review under responsibility of the Organizing Committee of the Conference

© 2026 Published by ISRES Publishing: www.isres.org

The functional efficacy of oat is predominantly attributable to β-glucan, a water-soluble dietary fiber localized in endosperm cell walls (Webster & Wood, 2011). Earlier study has linked β-glucan to increased gastrointestinal viscosity, reduced cholesterol absorption, beneficial effects on gut health and microbiota, improved glycaemic control, and cancer therapy (Murphy et al., 2020). Both the European Food Safety Authority (EFSA) and the United States Food and Drug Administration (FDA) have authorized health claims concerning oat β-glucan's role in reducing coronary heart disease risk and regulating postprandial blood glucose (FDA, 1997; EFSA, 2026).

While the nutritional and health-promoting attributes of oat are firmly established, its technological characteristics are of comparable importance to the food industry; these are examined in detail in the Technological Properties section below. Accordingly, this review aims to synthesize current knowledge on oat as a breeding quality and functional food ingredient, focusing in particular on: (i) its nutrient profile, bioactive constituents, and health-promoting effects; (ii) its technological functionality, biscuit manufacture, and end-product quality; and (iii) breeding, genotype × environment variation, stress adaptation, and the production/industry framework. Therefore, a comprehensive review of oat as a functional ingredient is necessary to bridge the gap between breeding material and end-product quality in biscuit production.

Nutritional Value, Bioactive Composition, and Health Effects

Among cereals, oat displays a distinctive macronutrient composition, notably higher protein and oil content relative to wheat and barley. Protein content varies between 12.4% and 24.5%, with elevated concentrations observed in the oat groat (Klose & Arendt, 2012). Such variation is governed by variety, cultivation region, and environmental conditions. The amino acid profile of oat protein is remarkably balanced, being especially rich in essential amino acids such as cysteine, methionine, and lysine (Givens et al., 2004). Oat oil content ranges from 3 to 11%, which substantially exceeds the 1.4–1.8% oil content characteristic of wheat and barley (Dikshit et al., 2025). With lipid levels far exceeding those of any other cereal grain, oat oil is an excellent source of energy and unsaturated fatty acids (Wilde et al. 2019; Zhou et al. 1999). Oat lipids consist notably oleic acid (C18:1) and linoleic acid (C18:2), which contribute substantially to the grain high energy value and nutritional quality (Givens et al., 2004).

Dietary fiber constitutes a critical component of oat functional value. The hull, which accounts for approximately 20–36% of the grain, comprises 30–35% crude fiber, 30–35% pentosans, 10–15% lignin, ~4% protein, and 5% ash (Girardet & Webster, 2011). Relative to husked cultivars, naked (hulless) genotypes exhibited lower fibre content but considerably higher levels of energy, total oil, linoleic acid, protein, starch, and essential amino acids (Givens et al., 2004; Biel et al., 2009). Among the bioactive constituents of oat, β-glucan has received the most extensive investigation. Situated within the cell walls of the endosperm and aleurone layer, β-glucan content ranges from 2.3 to 8.5 g/100 g depending upon genetic, environmental, and agronomic factors (Welch et al., 2000). The physiological relevance of β-glucan stems from its ability to form viscous solutions even at minimal concentrations (Hussein, 2022).

β-Glucan has been demonstrated to lower circulating LDL cholesterol levels (Lambo et al., 2005). Accordingly, the FDA has sanctioned a health claim indicating that consumption of at least 0.75 g of oat or barley β-glucan per serving, or 3 g per day, may lower the risk of coronary heart disease (FDA, 1997). Earlier research has demonstrated that daily consumption of 3 g of oat β-glucan can decrease plasma total and low-density lipoprotein (LDL) levels by 5–10% in normocholesterolemic or hypercholesterolemic subjects (Othman et al., 2011). Avenanthramides, the oat-specific phenolic compounds, may likewise promote cardiovascular health by reducing the risk of heart and vascular disorders linked to high cholesterol. In addition, β-glucan attenuates insulin response and prolongs satiety, thereby assisting in weight control (Beck et al., 2009). Apart from its cardiovascular and metabolic effects, β-glucan demonstrates immune-modulating properties and facilitates tissue healing (Mio et al., 2023). β-Glucan additionally supports gut health, exerts anti-diabetic and anti-tumor effects, and plays favorable roles in immune function, hypertension, insulin resistance, and obesity (Krupińska & Zegan, 2013; Du et al., 2014). Importantly, oats pose no risk to people with celiac disease, thus permitting their inclusion in gluten-free diets (Picarelli et al., 2001). Neither daily intake nor prolonged consumption of oats produced small-bowel mucosal villous damage, inflammation, or gastrointestinal symptoms in celiac patients (Kaukinen et al., 2013). This finding establishes oat as a valuable grain for individuals with gluten-related disorders, though careful consideration of contamination during processing remains essential.

Oat oil is a source of various antioxidants, including ferulic acid, caffeic acid, p-hydroxybenzoic acid, and vanillic acid, as well as tocopherols, sterols, alk(en)ylresorcinols, and flavonoids (Banaś & Harasym, 2021). Oat additionally contains unique phenolic compounds designated avenanthramides, which are unique for oat and display potent antioxidant, anti-inflammatory, and cardioprotective properties (Prats et al., 2026). Moreover, oat constitutes a good source of selenium, which participates in DNA repair and may diminish the risk of colon cancer (Comino et al., 2015). Oat is particularly rich in B complex vitamins (B1, B2, B3, and B6) and tocopherol (vitamin E) (Morcia et al., 2023). Most vitamins reside in the bran, especially the aleurone layer and embryo. Oats furthermore contain significant minerals such as selenium, copper, zinc, iron, and manganese (Flander et al., 2007). Products derived from oat exhibit higher levels of Na, Cu, Fe, Ca, K, Mg, Mn, and Zn compared to those made from rice, corn, potato, and gluten-free wheat starch (Rybicka & Gliszczyńska-Świgło, 2017). Together with its vitamin profile, this mineral content enhances oat's superior nutritional value among cereals. Overall, oat combines a favorable β-glucan, avenanthramides, vitamins, and minerals, making it a strong candidate for health-oriented bakery products.

Technological properties, biscuit production, and product quality

When compared with other cereal starches, oat starch possesses smaller granule size, while its gel proves more elastic, less firm, and less susceptible to retrogradation (Paton, 1977). Coupled with oat high lipid content, which fosters unique aroma and texture development in baked goods, these properties establish oat as a valuable raw material for both nutritional and technological functional food applications (Zhou et al., 1999). However, oat flavor and storage quality are negatively influenced by lipids, especially free fatty acids (Zhou et al., 1999). Beyond its nutritional and health-promoting functions, β-glucan performs numerous technological roles in food systems. Moreover, β-glucan has recently gained broad application in the food industry, functioning as an emulsion stabilizer, thickener, fat substitute, and bioactive ingredient, owing to its water solubility, viscosity, gelation properties, and health benefits (Sun et al., 2021). Although the high lipid content of oat contributes to nutritional value and unique flavor development, it also poses challenges regarding oxidative stability. Oat lipids are chiefly unsaturated, rendering them susceptible to oxidation during processing and storage. This vulnerability demands careful consideration of packaging strategies and antioxidant capacity in product development. The nutritional richness associated with whole-grain oat utilization thus signals significant potential for the food industry.

Biscuit production encompasses four principal stages: mixing and dough formation, shaping (rotary molding), baking and moisture transfer, and cooling and packaging. Every stage introduces specific considerations regarding oat flour utilization. The initial stage entails creating a homogeneous emulsion of fat, sugar, and water, which establishes the porous structure of the final product (Manley, 2014). Throughout baking, dough gases expand, leading the biscuit to gain volume as moisture content declines dramatically from approximately 21% to below 1.5% (Singla et al., 2023). Incorporation of oat into biscuit production constitutes not merely a nutritional substitution but rather a complex technological transformation. Advanced breeding lines, positioned at the final stage of improvement programs, exhibit different grain morphology and biochemical composition relative to standard varieties. Within biscuit technology, flour water-holding capacity and protein quality exert a direct influence on dough processability. Genotype × location interactions affect yield, starch, protein, and amylose in oat flour, thereby determining biscuit behavior during baking (expansion and spreading) (Alexander et al., 2025). These factors must be taken into account when evaluating oat genotypes for specific end-product applications.

Additional considerations include non-enzymatic browning (Maillard reaction) and lipid oxidation. Leiva-Valenzuela et al. (2018) underscored the impact of biscuit formulation and baking conditions on product structure and color development, observing that these reactions influence both visual quality and chemical safety. Oat's characteristic lipid composition may predispose it to oxidation (Zhou et al., 1999). However, the genotype-dependent fatty acid composition, together with cholesterol-lowering effects (Guo et al., 2014), necessitates optimization of process parameters to safeguard these beneficial components. Furthermore, as Dong et al. (2022) noted, the baking method plays a pivotal role in controlling thermal process-induced hazards (e.g., acrylamide) arising from Maillard reactions. Thus, optimizing formulation and baking parameters is essential to preserve oat's nutritional and bioactive advantages while achieving acceptable biscuit quality.

Oat breeding, genotypic variation, stress adaptation, and production/industry context

Quality parameter variability among oat genotypes carries substantial implications for end-product applications. Kahraman et al. (2017) demonstrated that genotypic variation generates pronounced differences in quality criteria, including protein and lipid content, in addition to grain yield. β-glucan content fluctuates according to variety (23%) and environment (42%) (Andersson & Börjesdotter, 2011). Contemporary breeding programs strive to produce genotypes with elevated levels of bioactive compounds, vitamins, and dietary fiber (Loskutov & Khlestkina, 2021; Morcia et al., 2023). Novel varieties characterized by high β-glucan content and yield, such as Neiyou 6 (Wang et al., 2026), along with investigations of the Bonaerense variety with high β-glucan content (Astiz et al., 2022), illustrate the potential inherent in genetic improvement.

Oat represents the cereal best adapted to marginal conditions such as low-fertility soils (Hoffman, 1995). Its water use efficiency exceeds that of wheat, rice, and corn by a factor of 2.33–9.69 (Yu et al., 2023). Nonetheless, diminished precipitation associated with global warming adversely affects oat yield, rendering the development of drought-tolerant varieties imperative (Petrova et al., 2024). Under irrigated conditions, oats produce roughly 1.5 times higher grain yield (2.26–4.4 t ha^{-1}) than under dry conditions (1.17–2.88 t ha^{-1}) (Mut et al., 2021). Given that a substantial proportion of Central Anatolian agricultural land relies on dry farming, developing drought-tolerant varieties adapted to rainfall conditions assumes particular importance. Stress tolerance indices, including Stress Susceptibility Index (SSI), Harmonic Mean (HM), Stress Tolerance Index (STI), Geometric Mean Productivity (GMP), Relative Stress Index (RSI), Tolerance (TOL), Mean Productivity (MP), Yield Stability Index (YSI), and Yield Index (YI) may be employed to identify drought-tolerant genotypes (Lamba et al., 2023).

Oats possess a wide range of uses, including forage, fodder, straw for bedding, hay, haylage, silage, chaff, human food, and healthcare and cosmetic products (Ahmad et al., 2014). Oats are employed in a wide range of products for human consumption, encompassing oat bread, oat cakes, oat milk, breakfast cereals, and baked goods, while oat powder is integrated into dairy products such as low-fat ice creams, yogurts, cheese, and fermented drinks (Pallavi et al., 2021). The biscuit industry, represented by companies such as Eti Inc., in Türkiye maintains specific quality criteria for oat raw materials: low hull ratio, oil and starch content with high β-glucan, protein, dietary milling yield, 1000-grain weight ≥26 g, ≥50% over 2 mm sieve, and hectoliter weight of 46 kg hl^{-1} (Kahraman et al., 2017).

Although the high oil content of oats proves advantageous in animal feed by supplying high energy, it offers fewer benefits in human food and may give rise to processing issues such as rancidity, bitter taste, and excessive browning of toasted products (Rasane et al., 2015). 10% of oat in Europe is allocated to human nutrition, pointing to substantial market potential (Andersson & Börjesdotter, 2011).

The sensory properties of oat biscuits, including texture, appearance, flavor, and consumer acceptance, are governed by ingredient ratios, structural modifications, and storage parameters (Zaki & Hussien, 2018; Marzec et al., 2025). Texture attributes such as crispness and hardness are also sensory properties of food that determine consumer acceptability (Szczesniak, 2002; Marzec et al., 2025); this indicates that consumer texture perception cannot be explained solely by hardness, as crispness and fracturability are also determining factors (Brown et al., 1998; Mosafa et al., 2017).

Developing varieties that satisfy these industry requirements is essential for reducing import dependency and ensuring domestic raw material sustainability. Consequently, breeding programs should integrate agronomic, technological, and nutritional targets to develop regionally adapted, industry-ready biscuit-type oat varieties.

Conclusion

Oat (*Avena sativa* L.) constitutes a strategically important cereal for functional food development, providing a unique combination of nutritional, health-promoting, and technological properties. Its high β-glucan content, balanced amino acid profile, unsaturated fatty acids, and oat-specific avenanthramides establish it as a valuable raw material for functional food applications. The FDA and EFSA approvals of health claims concerning benefits of β-glucan supply robust regulatory foundations for oat-based product development. In oat breeding studies, agronomic performance, grain and flour technological quality, biscuit quality, and health-benefit traits should be evaluated together as an integrated selection framework for variety improvement. This integrated approach allows breeders to identify genotypes that are not only high-yielding and stress-tolerant but also technologically suitable for biscuit production and nutritionally valuable for consumers. In addition, oat into biscuit production demands careful consideration of formulation and process parameters to optimize product quality while maximizing nutritional benefits.

Substituting oat flour in biscuit production represents a significant opportunity for developing functional snack products with functional properties. Research of this nature would yield scientific data for functional snack development, contribute to increased domestic raw material utilization, diminish import dependency, and support public health through improved nutrition. In conclusion, integrated oat breeding and food technology approaches are required to transform local oat genetic resources into sustainable, health-promoting biscuit ingredients.

Conflict of Interest

* The authors declare that they have no conflicts of interest.

Funding

No funds have been received.

Acknowledgements and Notes

* This article was presented as an oral presentation at the International Conference on Basic Sciences, Engineering and Technology (www.icbaset.net) held in Istanbul/Türkiye on September 17-18, 2026.

*We would like to thank Scientific Research Coordinator of Selçuk University to support for presentation.

References

Ahmad, M., Dar, Z. A., & Habib, M. (2014). A review on oat (*Avena sativa* L.) as a dual-purpose crop. *Scientific Research and Essays, 9*(4), 52–59.

Alexander, V., Nilsen, K. T., Joseph, S., Beta, T., & Malunga, L. N. (2025). Effects of genotype and environment on the physiochemical properties of Canadian oat varieties. *Journal of the Science of Food and Agriculture, 105*(5), 3111–3121.

Andersson, A. A., & Börjesdotter, D. (2011). Effects of environment and variety on content and molecular weight of β-glucan in oats. *Journal of Cereal Science, 54*(1), 122–128.

Astiz, V., Guardianelli, L. M., Salinas, M. V., Brites, C., & Puppo, M. C. (2022). High β-glucans oats for healthy wheat breads: Physicochemical properties of dough and breads. *Foods, 12*(1), 1–15.

Banaś, K., & Harasym, J. (2021). Current knowledge of content and composition of oat oil—Future perspectives of oat as oil source. *Food and Bioprocess Technology, 14*(2), 232–247.

Beck, E. J., Tosh, S. M., Batterham, M. J., Tapsell, L. C., & Huang, X. F. (2009). Oat β-glucan increases postprandial cholecystokinin levels, decreases insulin response and extends subjective satiety in overweight subjects. *Molecular Nutrition & Food Research, 53*(10), 1343–1351.

Biel, W., Bobko, K., & Maciorowski, R. (2009). Chemical composition and nutritive value of husked and naked oats grain. *Journal of Cereal Science, 49*(3), 413–418.

Brown, W. E., Langley, K. R., & Braxton, D. (1998). Insight into consumers' assessments of biscuit texture based on mastication analysis—Hardness versus crunchiness. *Journal of Texture Studies, 29*(5), 481–497.

Comino, I., de Lourdes Moreno, M., & Sousa, C. (2015). Role of oats in celiac disease. *World Journal of Gastroenterology, 21*(41), 11825–11831.

Dikshit, N., Syed, N., Rout, P. K., Singhal, R. K., Indu, I., Halli, H. M., ... Ahmed, S. (2025). Comparative evaluation of quantitative and qualitative attributes of oat (*Avena sativa* L.) varieties grown in semi-arid India. *Discover Plants, 2*(1), 1–12.

Doğan, İ. S., & Uğur, T. (2004). A study on the quality of wheat grown in Van region for biscuit production. *Yüzüncü Yıl University Journal of Agricultural Science, 15*, 139–148.

Dong, L., Qiu, C., Wei, F., Yu, Z., Zhang, Y., & Wang, S. (2022). The effect of microwave baking conditions on the quality of biscuits and the control of thermal processing hazards in the Maillard reaction. *Frontiers in Nutrition, 9*, 1–9.

Du, B., Bian, Z., & Xu, B. (2014). Skin health promotion effects of natural beta-glucan derived from cereals and microorganisms: A review. *Phytotherapy Research, 28*(2), 159–166.

EFSA Panel on Nutrition, Novel Foods and Food Allergens (NDA), Turck, D., Bohn, T., Cámara, M., Castenmiller, J., de Henauw, S., ... Siani, A. (2026). Oat beta-glucans and reduction of postprandial glucose peak: Evaluation of a health claim pursuant to Article 13(5) of Regulation (EC) No. 1924/2006. *EFSA Journal, 24*(2), 1–15.

Food and Drug Administration. (1997). Food labeling: Health claims; oats and coronary heart disease. Final rule. *Federal Register, 62*, 3583–3601.

Flander, L., Salmenkallio-Marttila, M., Suortti, T., & Autio, K. (2007). Optimization of ingredients and baking process for improved wholemeal oat bread quality. *LWT–Food Science and Technology, 40*(5), 860–870.

Girardet, N., & Webster, F. H. (2011). Oat milling: Specifications, storage, and processing. In F. H. Webster & P. J. Wood (Eds.), *Oats: Chemistry and technology*. American Association of Cereal Chemists.

Givens, D. I., Davies, T. W., & Laverick, R. M. (2004). Effect of variety, nitrogen fertilizer and various agronomic factors on the nutritive value of husked and naked oats grain. *Animal Feed Science and Technology, 113*(1–4), 169–181.

Guo, L., Tong, L.-T., Liu, L., Zhong, K., Qiu, J., & Zhou, S. (2014). The cholesterol-lowering effects of oat varieties based on their difference in the composition of proteins and lipids. *Lipids in Health and Disease, 13*(1), 1–10.

Hoffman, L. A. (1995). World production and use of oats. In R. W. Welch (Ed.), *The oat crop: Production and utilization*. Chapman and Hall.

Hussein, L. A. (2022). Novel prebiotics and next-generation probiotics: Opportunities and challenges. In *Functional foods and nutraceuticals in metabolic and non-communicable diseases* (pp. 431–457).

Iannucci, A., Codianni, P., & Cattivelli, L. (2011). Evaluation of genotype diversity in oat germplasm and definition of ideotypes adapted to the Mediterranean environment. *International Journal of Agronomy, 2011*, 1–8.

Kahraman, T., Kurt, C., Subaşı, A. S., Özderen, T., Yıldız, Ö., Büyükkileci, C., & Sanal, T. (2017). Determination of oat (*Avena sativa* L.) genotypes suitable for human nutrition in Trakya-Marmara region. *Journal of Field Crops Central Research Institute, 26*, 105–111.

Kaukinen, K., Collin, P., Huhtala, H., & Mäki, M. (2013). Long-term consumption of oats in adult celiac disease patients. *Nutrients, 5*(11), 4380–4389.

Klose, C., & Arendt, E. K. (2012). Proteins in oats; their synthesis and changes during germination: A review. *Critical Reviews in Food Science and Nutrition, 52*(7), 629–639.

Krupińska, P., & Zegan, M. (2013). β-glucan—Selected sanitary advantages with particular reference to lipid metabolism. *Bromatologia i Chemia Toksykologiczna, 46*, 162–170.

Lamba, K., Kumar, M., Singh, V., Chaudhary, L., Sharma, R., Yashveer, S., & Dalal, M. S. (2023). Heat stress tolerance indices for identification of the heat tolerant wheat genotypes. *Scientific Reports, 13*(1), 1–13.

Lambo, A. M., Öste, R., & Nyman, M. E. G. L. (2005). Dietary fibre in fermented oat and barley β-glucan rich concentrates. *Food Chemistry, 89*(2), 283–293.

Leiva-Valenzuela, G. A., Quilaqueo, M., Lagos, D., Estay, D., & Pedreschi, F. (2018). Effect of formulation and baking conditions on the structure and development of non-enzymatic browning in biscuit models using images. *Journal of Food Science and Technology, 55*(4), 1234–1243.

Liu, R. H. (2007). Whole grain phytochemicals and health. *Journal of Cereal Science, 46*(3), 207–219.

Loskutov, I. G., & Khlestkina, E. K. (2021). Wheat, barley, and oat breeding for health benefit components in grain. *Plants, 10*(1), 1–18.

Manley, D. (2014). *Biscuit, cracker and cookie recipes for the food industry*. Woodhead Publishing.

Marzec, A., Stępień, A., Goclik, A., Kowalska, H., Kowalska, J., & Salamon, A. (2025). Analysis of the correlation of microstructure, instrumental texture, and consumer acceptance of shortbread biscuits with selected sweeteners and fibre. *Applied Sciences, 15*(3), 1–15.

Mio, K., Togo-Ohno, M., Tadenuma, N., Ogawa, R., Yamanaka, C., & Aoe, S. (2023). A single administration of barley β-glucan and arabinoxylan extracts reduces blood glucose levels at the second meal via intestinal fermentation. *Bioscience, Biotechnology, and Biochemistry, 87*(1), 99–107.

Morcia, C., Finocchiaro, F., Delbono, S., Ghizzoni, R., Reggiani, F., Carnevali, P., ... Terzi, V. (2023). Oats: Nutritional uniqueness and breeding of a healthy superfood. In *Compendium of crop genome designing for nutraceuticals* (pp. 153–193). Singapore: Springer Nature.

Mosafa, L., Nadian, N., & Hojatoleslami, M. (2017). Investigating the effect of whole oat flour, maltodextrin and isomalt on textural and sensory characteristics of biscuits using response surface methodology. *Journal of Food Measurement and Characterization, 11*(4), 1780–1786.

Murphy, E. J., Rezoagli, E., Major, I., Rowan, N. J., & Laffey, J. G. (2020). β-glucan metabolic and immunomodulatory properties and potential for clinical application. *Journal of Fungi, 6*(4), 1–36.

Mut, Z., Demirtaş, N., & Köse, Ö. D. E. (2021). Evaluation of yield and some physical quality characteristics of different oat (*Avena sativa* L.) genotypes under supplemented irrigation and rainfall conditions. *Turkish Journal of Agriculture-Food Science and Technology, 9*(1), 197–204.

Othman, R. A., Moghadasian, M. H., & Jones, P. J. (2011). Cholesterol-lowering effects of oat β-glucan. *Nutrition Reviews, 69*(6), 299–309.

Pallavi, D., Hiremath, J. P., & Madhusudan, N. M. (2021). Oats as a functional food. *Bhartiya Krishi Anusandhan Patrika, 36*(4), 350–352.

Paton, D. (1977). Oat starch, Part I. Extraction, purification and pasting properties. *Stärke, 29*(1), 9–13.

Petrova, L. V., Novikova, L. Y., Alekseeva, A. V., & Loskutov, I. G. (2024). Climate change and crop yield of oats (*Avena sativa* L.) in Yakutia. *Труды по прикладной ботанике, генетике и селекции, 185*(1), 86–98.

Picarelli, A., Di Tola, M., Sabbatella, L., Gabrielli, F., Di Cello, T., Anania, M. C., ... De Vincenzi, M. (2001). Immunologic evidence of no harmful effect of oats in celiac disease. *The American Journal of Clinical Nutrition, 74*(1), 137–140.

Prats, E., Cañuelo, M. J., Tejero-Arroyo, C., Sghaier-Hammami, B., Hammami, S. B., & Montilla-Bascon, G. (2026). Exploring nutritional quality and bioactive compounds in oat Mediterranean landraces and cultivars. *Antioxidants, 15*(3), 1–20.

Rasane, P., Jha, A., Sabikhi, L., Kumar, A., & Unnikrishnan, V. S. (2015). Nutritional advantages of oats and opportunities for its processing as value added foods: A review. *Journal of Food Science and Technology, 52*(2), 662–675.

Rybicka, I., & Gliszczyńska-Świgło, A. (2017). Minerals in grain gluten-free products. The content of calcium, potassium, magnesium, sodium, copper, iron, manganese, and zinc. *Journal of Food Composition and Analysis, 59*, 61–67.

Singh, R., De, S., & Belkheir, A. (2013). *Avena sativa* (oat), a potential nutraceutical and therapeutic agent: An overview. *Critical Reviews in Food Science and Nutrition, 53*(2), 126–144.

Singla, M., Sharma, M., Jan, K., & Habib, M. (2023). Technology of biscuits. In *Bakery and confectionery technology* (pp. 99–115).

Siró, I., Kápolna, E., Kápolna, B., & Lugasi, A. (2008). Functional food. Product development, marketing and consumer acceptance—A review. *Appetite, 51*(3), 456–467.

Sun, L., Hu, M., Zhao, J., Lv, L., Zhang, Y., Liu, Q., ... Zhang, Y. (2021). Molecular characteristics, synthase, and food application of cereal β-glucan. *Journal of Food Quality, 2021*(1), 1–8.

Szczesniak, A. S. (2002). Texture is a sensory property. *Food Quality and Preference, 13*(4), 215–225.

Wang, T., Qin, Y., Guo, Y., Cai, Y., Kai, X., & Han, B. (2026). Neiyou 6, a high yielding and high β-glucan hulless oat variety. *Molecular Breeding, 46*(1), 1–5.

Webster, F. H., & Wood, P. J. (Eds.). (2011). *Oats: Chemistry and technology*. Woodhead Publishing and AACC International Press.

Welch, R. W., Brown, J. C. W., & Leggett, J. M. (2000). Interspecific and intraspecific variation in grain and groat characteristics of wild oat (*Avena*) species: Very high groat (1→3),(1→4)-β-D-glucan in an *Avena atlantica* genotype. *Journal of Cereal Science, 31*(3), 273–279.

Wilde, P. J., Garcia-Llatas, G., Lagarda, M. J., Haslam, R. P., & Grundy, M. M. (2019). Oat and lipolysis: Food matrix effect. *Food Chemistry, 278*, 683–691.

Yu, H., Li, S., Ding, J., Yang, T., & Wang, Y. (2023). Water use efficiency and its drivers of two typical cash crops in an arid area of Northwest China. *Agricultural Water Management, 287*, 1–11.

Zaki, H., & Hussien, A. (2018). Chemical, rheological and sensory properties of wheat-oat flour composite cakes and biscuits. *Journal of Productivity and Development, 23*(2), 287–306.

Zhou, M., Robards, K., Glennie-Holmes, M., & Helliwell, S. (1999). Oat lipids. *Journal of the American Oil Chemists' Society, 76*(2), 159–169.

Authors Information

Hayati Akman
Selcuk University
Department of Plant and Animal Production, 42430, Konya, Türkiye
ORCID ID: https://orcid.org/0000-0001-6878-3329
*Contact e-mail: hayatiakman@selcuk.edu.tr

Aysegul Soyakil
Eskisehir Osmangazi University
Department of Food Engineering, 26040, Eskişehir, Türkiye
ORCID ID: https://orcid.org/0009-0009-5174-3537

Yasar Karaduman
Eskisehir Osmangazi University
Department of Food Engineering, 26040, Eskişehir, Türkiye
ORCID ID: https://orcid.org/0000-0003-1306-3572

*Corresponding author's contact email

ICBASET 2026: International Conference on Basic Sciences, Engineering and Technology

The Impacts of Capitalism on the Transformation of Cultural Identity: The Case of the Clock Tower in Makkah

Bushra ZALLOOM
Zarqa University

Abstract: This research examines the influence of globalized capitalism through the construction of the Royal Makkah Clock Tower, which mimics London's Big Ben. It explores the project's impacts on the historical context of the city, as a sacred site with spiritual significance, and its cultural cityscape. A qualitative research method was employed to collect data from 50 participants who travelled between Makkah and London, through questionnaires and semi-structured interviews. Documentary photographs and relevant studies from the literature were used to support the findings, which indicate that the Clock Tower initiated economic revitalization and tourism development while undermining Makkah's identity and heritage. The findings also confirm that the Tower represents global interests while damaging the spiritual lure of the site, which had a profound emotional and cultural impact on visitors who felt more worried about the extinction of the traditional Islamic architectural spirit. This research exhibits the necessary relationship between economic development and cultural heritage preservation when planning religious and historic sites.

Keywords: Makkah Clock Tower, Cultural identity, Capitalism, Economic development.

Introduction

Makkah is considered a holy land for Muslims; it has an important religious value because millions of pilgrims visit the Kaaba for Hajj and Umrah every year, and it also has the lure of Islamic heritage (Alharbi, 2020; Winerman, 2011). During the last decades, Makkah's landscape has been transformed because of the large-scale constructions that emerged in the area. The Royal Makkah Clock Tower, considered the main component of the Abraj Al-Bait complex, stands out as a clear representation of how Makkah has transformed. (Alkathiri et al., 2024; Ghaleb & Juhari, 2024). This tower reflects the power of capitalism in transforming cultural identity; it is inspired by Big Ben -London's Clock Tower- where the design demonstrates the globalization of architectural styles (Figure 1), yet triggers discussions about cultural authenticity (Sklair, 2017). Cities facing global capitalism tend to pick international symbols yet fail to localize them properly, thus causing architectural disharmony.

Globally, Capitalism has impacted the urban areas and the cultural landscape, these impacts are clearly defined in cities as Dubai, Shanghai, and Makkah where the study conducted (Zalloom, 2018; Zukin, 2012). The economic power integrated with political authority controls the architectural and urban pattern; this integration exceeds the hard attempts for cultural preservation (Akcan, 2016). Makkah's shifting urban identity becomes even more concerning because of the major cultural mismatch between Big Ben and the Clock Tower. Big Ben in London reflects national history, yet the Clock Tower in Makkah deviates from traditional Islamic architecture, thus sparking debates regarding the commercialization of sacred spaces (Qurashi, 2019). This design choice represents an effort by the authorities to link Makkah with the international symbols associated with modern, proud civilization

Research on globalization's effects on urban development has accumulated substantially but lacks extensive investigation into how religious and sacred cities transform under capitalist pressures. The studies conducted by Habib (2024) and Benkherouf (2024) examine general patterns of urban transformation in Makkah without exploring the religious symbolism behind the architectural copying in sacred spaces. Little qualitative research exists to analyze how users experience the new urban environment in real terms, including their emotional and cultural reactions as visitors or pilgrims.

- This is an Open Access article distributed under the terms of the Creative Commons Attribution-Noncommercial 4.0 Unported License, permitting all non-commercial use, distribution, and reproduction in any medium, provided the original work is properly cited.

- Selection and peer-review under responsibility of the Organizing Committee of the Conference

© 2026 Published by ISRES Publishing: www.isres.org

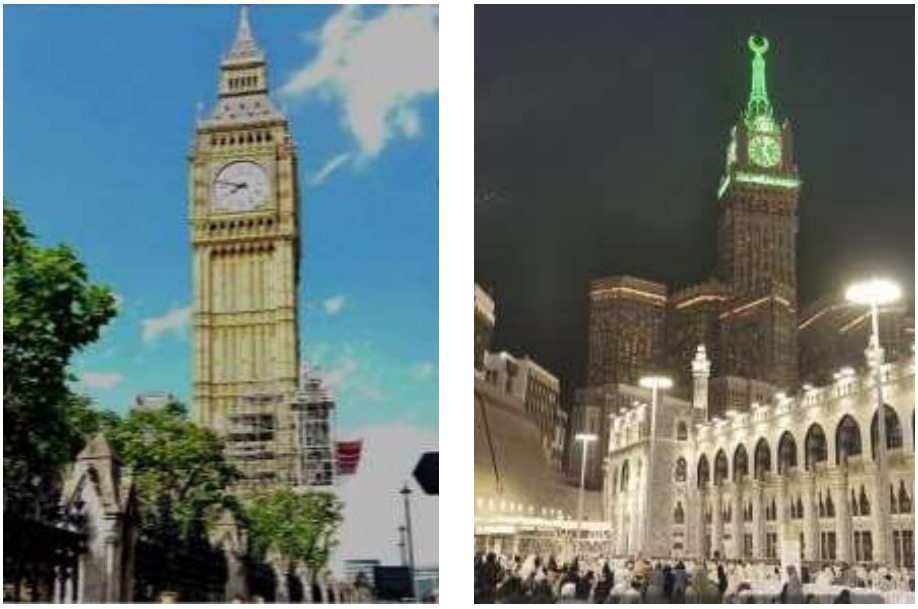

Figure 1. Makkah's Clock Tower (on right) is inspired by Big Ben -London's Clock Tower (on left) (author, Big Ben 2017 & Makkah's Tower 2025)

The evolution of historical and cultural aspects, besides the power of capitalist interests, directly shapes the development of urban identity. Today, globalization transforms cities worldwide through structural conceptual changes that frequently produce standardized architectural design and urban planning patterns (Aboutorabi & Zalloom, 2019). Cities modify their approach to bring in capital investments and tourist flows at the expense of indigenous cultural roots (Corner & Harvey, 2005). According to Southworth and Ruggeri (2011), global capitalism results in the implementation of foreign design elements that separate themselves from native contexts, thus losing city authenticity. Similarly, Musa et al. (2020) believe that economic factors and political motives served as the primary drivers for developing the Royal Clock Tower project together with its commissioning requirements. The Saudi government directed its efforts towards building glamorous projects like the Clock Tower, which served the double purpose of displaying worldwide sophistication and generating income from religious visitors.

Historic urban centers experience the detachment of historical urban dialogues because of extensive large-scale developments (Awatta, 2015). The excessive visual power of commercial buildings inside religious sites demonstrates the conflict between urban transformation projects and the preservation of the original historical city character. The Royal Makkah Clock Tower construction represents a transformative development for the traditional Islamic city of Makkah, which results from capitalist interests and global architectural styles (Musa et al., 2020). Zalloom and Tarrad (2020) identify how improper urban development in historical sites leads to a split between the city's population and their cultural heritage. However, newly constructed structures in Makkah with a purpose and design that contradict local, historical, and cultural heritage trigger a sensation of disconnect among visitors and their surroundings, and create contemporary city skylines that undermine religious settings (Lichtenwalter, 2020). Winerman (2011) shows that numerous pilgrims viewed the Royal Makkah Clock Tower as an indicator of contemporary development, which reduced their traditional pilgrim experience. According to Winerman, the luxurious amenities and improved services of the Clock Tower displaced the spiritual focal point of the city from the Kaaba and its traditional precinct.

A defining feature of megaprojects involves massive urban development expenses, which receive financial backing from political bodies and economic platforms (Söderlund et al., 2017). Despite providing economic opportunities and new infrastructure development, their effects on historic cities remain strongly disputed between experts (Alnsour et al., 2024). Osman (2016) explains that the development of megaprojects in Makkah cities poses the risk of converting spiritual areas into tourist destinations where profit goals replace core historical and sacred values. According to Altshuler and Luberoff (2004), political factors involved in megaproject commissioning and design frequently select projects for global promotion and financial gain at the cost of cultural heritage protection.

Ashworth and Kavaratzis (2010) stated that modern cities utilize place branding strategies to create specific international marketplace images. The analysis of similar urban developments in other cities. Urbanization in Dubai, through the Burj Khalifa project, faces criticism because of the emphasis on attracting the world instead of maintaining the principles of local cultures. The urbanization of Istanbul, due to the influence of the neoliberal movement, has raised controversy about the removal of Ottoman heritage to make way for the construction of buildings associated with the West. Global capitalism has also been accused of using architectural icons to represent power, which ignores the heritage of cultures, as well as traditional practices, in Makkah and Dubai. Makkah is unique compared to other cities because of the universal significance of the city to the Islamic faith.

This paper evaluates the impacts of the Clock Tower in Makkah on the skyline and the city's identity. It also explores the tower's effects on the Kaaba users during Hajj and Umrah. Moreover, the paper discusses why a Western architectural symbol was chosen for the design of a tower in the sacred area. As Hamada (2015) and Al-Naim (2014) explain, historically important cities face permanent change to collective memory and identity because of building choices. The research underscores cultural heritage preservation as an essential development factor in sacred settings.

Methodology

Study Design

The study design is based on a qualitative approach to explore the cultural identity and modifications in the urban landscape created by the Royal Makkah Clock Tower. The use of qualitative research methods was appropriate for conducting the study because it allows an in-depth examination of participants' perceptions and emotional understanding of urban landscape changes in sacred spaces. The use of qualitative methods in identity and cultural aspects and emotional studies is appropriate because it reveals descriptive information about participants' perceptions and emotions (Thompson, 2018). The study used phenomenology as an approach to understand how dual-identity visitors from Makkah and London make sense of the connection between meaning and architectural changes. It focuses on real-life experiences to unveil how the construction of the Clock Tower changed the urban identity of Makkah in terms of spirituality and aesthetics.

Study Population and Sampling

Participants in the research were chosen based on the fact that they visited both Makkah and London. This was a criterion to ensure that they experienced the Royal Makkah Clock Tower and Big Ben in London. A comprehensive comparison between the two places was required in order to obtain valuable information regarding the transformation in the urban identity of Makkah. Fifty participants were chosen through purposive sampling methods. The study adopted purposive sampling because this method enabled the researcher to select participants who possessed knowledgeable perspectives about the studied subject (Alnsour et al., 2024; Bula, 2023). Research participants joined the study using their connections in social media groups that focused on travel and Hajj

Table 1. Study design and participant demographics.

Study Component	Description
Study Design	Qualitative, phenomenological approach
Population	Visitors to both Makkah and London
Sample Size	50 participants
Sampling Method	Purposive sampling
Context	Comparison between the Clock Tower in Makkah and Big Ben in London
Data Collection Methods	Questionnaires using Google Forms, Photographic documentation
Age Range of Participants	20–65 years
Gender Distribution	28 males, 22 females
Location / Country	Participants from Saudi Arabia, Malaysia, Egypt, Jordan, and Turkey
Field of Interest	Architecture, Urban Studies, Cultural Studies, Religious Studies, Tourism
Educational Qualification	Bachelor's degree, Master's degree, Doctorate
Data Analysis	Thematic analysis following Braun & Clarke's method

Phenomenon of Interest and Context

The current study investigated how people perceived the transformation of Makkah's urban identity because of the Clock Tower's construction. The research area consisted of two sites: The environment near the Clock Tower in Makkah, adjacent to the Kaaba, alongside the Big Ben area in London. An analysis of their visual impact, together with their symbolic meaning and cultural value, took place through this comparative study.

Data Collection Methods

The researcher gathered complete information through several methods:

Questionnaires

The 50 participants received an online questionnaire through survey distribution to obtain their responses. Participants answered open-ended survey questions, which focused on their emotional responses as well as their perspectives on urban spaces and opinions regarding the Clock Tower structure. Participants evaluated how the Clock Tower represents Makkah's spiritual values along with its heritage. Google Forms served to gather responses throughout five months.

Photographic Documentation

Many photographs are provided by the researcher, who previously visited the Makkah Clock Tower in 2024 and 2025, and also visited Big Ben in London in 2017. The researcher additionally obtained publicly available images while using Google Earth and Wikimedia Commons for site analysis. The visual evidence based on architectural and urban changes served to both contextualize participant perceptions and represent structural alterations.

Ethical Considerations

This research worked with general populations who did not need review board approval, given that sensitive personal data or vulnerable groups were excluded. The study participants received information about the research objectives before they provided written approval for having their responses included. The study contained no collection of personal data, and it protected participants from identification. The experimental design omitted the use of animal testing at any point.

Results

Makkah's cultural identity, capitalist influence, and architectural contradictions within the site and its cultural effects on travelers. An analysis of themes produced results that affirmed the pre-existing code framework through its application

Demographic Profile of Participants

Multiple demographics were represented in the participant group through age distribution paired with gender, diverse national origins, educational disciplines, and areas of interest. Table 2 displays the core demographic data about the participants according to the research group.

Table 2. Participants' information analysis from the questionnaire data.

Category	Sub-category	Percentage (%)
Gender	Male	54%
	Female	46%
Age	18–30	30%

	31–45	42%
	46–60	20%
	Above 60	8%
Country/Region	Middle East	55%
	Europe	25%
	Asia	15%
	Others	5%
Field of Interest	Architecture and Urban Studies	40%
	Religious Studies	30%
	Tourism and Hospitality	15%
	General Visitors	15%
Educational Qualification	Bachelor's Degree	35%
	Master's Degree	40%
	PhD	15%
	Others	10%

The varied professional experiences of research participants enhanced the collection of numerous distinct perspectives about Makkah's urban development process.

Changes in Perception of Makkah's Spiritual Identity

Several respondents expressed their views on how the Clock Tower project resulted in Makkah losing its spiritual character Figure 2. It is clear from the study that 68% of respondents feel that the tower's height prevents the Kaaba from being visible. The respondents also stated that the presence of the large hotel building accompanied by the shopping malls resulted in maximizing the experience of consumerism over spirituality. When people gaze at the buildings around the Kaaba, which are actually commercial hotels, their spiritual attention diminishes considerably. Several respondents stated that the Clock Tower project disrupted the perceptual link between the sacred elements present in the holy site. The use of modern materials did not complement the simplicity of the sacred sites.



Figure 2. The Clock Tower led to Makkah losing its spiritual essence (Rasch, 2025)

Influence of Economic Motives and Global Capitalism

Economic motivations, together with capitalist methods, played a dominant role in developing the Clock Tower; 47% of the participants mentioned that economic factors were given priority over the preservation of cultural and religious heritage in this project. The presence of luxury hotels and shopping malls, along with restaurants inside the tower, was considered an indicator of this commercial orientation. Moreover, participants noticed how the builders of the tower pursued economic globalization strategies together with their political objectives. A vast majority of 74% of respondents reported that the Clock Tower exists mostly to attract tourism revenue and attract global attention for Saudi Arabia, instead of improving religious pilgrimages.

Participants observed how global capitalism has become the main force affecting urban development, especially in religious cities, because profit pursuits now dominate over historic and cultural preservation values. They observed that Makkah is increasingly transforming into a commercial center instead of its original purpose of worship. The architectural developments, such as skyscrapers and shopping centers, together with luxury brands, do not represent the core purpose for which pilgrims' journey to the site. People discussed how Saudi Arabia's current development targets the country to function as a rival tourist and commercial center, similar to Dubai or London, to achieve political and economic gains.

Cultural Dissonance Caused by Architectural Mimicry

The participants showed a high level of resentment because the Royal Makkah Clock Tower had adopted the design elements from London's famous Big Ben tower. A total of 62% of the participants were able to understand the design elements, while 70% of the total respondents felt a sense of cultural tension due to architectural duplication. Moreover, many participants were concerned about adopting a Western architectural style for a building that needed to reflect Islamic architectural style in the most sacred Muslim location in the world. Participants felt that Makkah's cultural hub rejected the modern Western look of the tower, as the designers had attempted to impose London's symbols in the wrong location. Participants were also disappointed with the failure of the designers to incorporate Islamic art elements with Arabian style elements and calligraphy, which could connect with their roots.

Emotional and Cultural Impacts on Visitors

People in Makkah demonstrated sadness because the city's skyline transformed into something that represents luxury instead of spiritual humility. Sixty-five percent of participants believed the Clock Tower weakened the historical and spiritual essence that defined the City of Makkah. The visitors felt dominated by the towers,which created feelings of intimidation due to the offset from traditional open spaces that focus on the Kaaba (Figure 3).

The participants who recognized benefits from the Clock Tower's construction made up around 15% of the total group. Those participants who acknowledged the practical benefits of the skyscraper first expressed their belief that these practical advantages resulted in significant cultural and emotional losses to Muslims.



Figure 3. Towers create feelings of intimidation due to the offset from traditional open spaces that focus on the Kaaba (Rasch, 2025)

Table 3. The analysis of the questionnaire responses.

Question	% Agreeing
Clock Tower affects Makkah's spiritual atmosphere negatively	68%
Economic and commercial motives dominate the Clock Tower project	74%
Architectural mimicry (Big Ben resemblance) causes cultural dissonance	70%
Makkah's traditional urban identity has been diminished	65%
Some benefits acknowledged (proximity, facilities, modern services)	15%

General Observations

The data showed in every outcome that modernization/globalization forces clashed with protecting cultural heritage. Most participants shared the view that essential infrastructure needs were justified, but they acknowledged that the symbolic, emotional, and cultural sacrifices proved unfavorable and substantial. Future projects in holy sites need to pay attention to celebrating cultural authenticity, religious importance, and emotional linkage with the worldwide faith community, instead of following international capitalist design norms.

Discussion

This paper discusses how global capitalism interacts with cultural preservation for urban spaces in the holy city of Makkah. The core research explored the Clock Tower's modifications to Makkah's identity and skyline and its religious consequences because of its adjacency to the Kaaba. The Clock Tower has caused major transformations of Makkah's characteristics visually and spiritually. Most individuals accepted the tower as a reflective symbol that represents commercial activities, thus competing with the spiritual value of the Kaaba. The benefits generated by the Clock Tower as an economic project offset its unintended disturbance of the religious and spiritual character and historical connections to the urban environment.

The debate is centered on the economic and cultural costs of constructing the Clock Tower. The Saudi government had the intention of using this development to increase its recognition worldwide, including attracting tourism interests and meeting the needs of religious tourists. Through the incorporation of hotels and shopping centers within the complex, the Clock Tower plays a vital role in promoting economic growth within the local environment. Mayer (2018) explains this through his theory on neoliberal urbanization, stating that cities that prioritize capital accumulation above anything else often face a decline in their cultural foundation and relationships with the people, in addition to losing their historical identity. This paper supports this theory through the fact that it shows how economic growth led to a decline in culture and spirituality, which is often a problem faced by modern developing cities.

The reconstruction of the Clock Tower, which mimics Big Ben, also had complex layers. Most visitors felt that the Western style of the building clashed with Islamic cultural traditions because it introduced foreign elements into the architecture of the building, which was meant to be a sacred place. The ideas presented by Maguire and Falcous (2010) and Traganou (2016) are similar to the ideas presented by the participants of the study, which highlighted that globalization causes the fundamentals of the architecture of popular landmarks to be copied from one cultural region to another, thereby losing their identity in the process. However, the Clock Tower does not meet the requirements of Islamic architecture, which are normally focused on modesty, as well as inclusion and sacredness. The replication of Big Ben was also a manifestation of the conflict between the Western capitalist culture and the traditional Islamic heritage of Makkah.

This research will make a new contribution to the field by providing a thorough assessment of visitors' feelings regarding the impact of the Clock Tower on spiritual and cultural heritage sites, with the use of the London Big Ben site for comparative analysis. While previous research by Dicks (2004) and Smith (2020) was able to show the political and economic impacts of the construction of the Clock Tower, there has been no research to date that provides a systemic assessment of visitor perceptions of these changes to cultural and spiritual sites. The use of questionnaires, along with photographs, provided a thorough insight into individual experiences with international architectural styles.

The research indicates that the participants are demanding culture-based solutions for modernization. The participants in the survey advocated for the development of a balance in modern infrastructures through Islamic architectural design elements as the basis for developing future constructions in the sacred city; this supports Jha et al. (2013) viewpoint, which highlighted that the main aspect of urban resilience is the development of cultural continuity in the process rather than using it to hinder economic development.

While the Clock Tower adds economic value to the city of Makkah, the above-mentioned discussion indicates the negative impacts of the Clock Tower on the cultural identity and spiritual integrity of the city, as well as its architectural character. The research findings confirm that the city transformation under capitalism negatively affects the participants' perception. It also validates the earlier criticisms of the Clock Tower in the context of

new cultural and emotional observations of the visitors, which provide the essential requirements that should be considered for the upcoming buildings in the holy city.

Conclusion

This paper aims to explore the impacts of capitalism on the transformation of cultural identity by studying the case of the Clock Tower in Makkah and discussing its impacts on the cultural heritage and religious setting of the city. The research outcomes revealed that the Royal Makkah Clock Tower provides economic growth and development to the city but causes disturbances and conflicts regarding historical and religious sanctity within the most sacred place of Islam. The majority of the respondents to the survey confirm that the presence of the tower and its economic nature impacts the religious lure of the place and thus leads to cultural and spiritual conflicts. Furthermore, the architectural design of the tower was criticized for its similarity to Big Ben, which considered to be inappropriate to introduce Western architectural designs to such an Islamic site. The findings from this survey have provided vital knowledge that can be used in creating future decisions in matters relating to urban planning, architecture, and practices in cultural heritage preservation. Urban developers and policymakers must ensure that there is a balance between development progress and cultural values while remaking cities that have a history and religious significance that require special attention. Economic issues must never be the sole drivers of change in a city where authenticity of the religious values and original city identity should be the main drivers in architectural developments. There is a need to ensure that there is a mix of architectural projects with elements of indigenous cultural practices and symbolic religious values, along with the historical background of the targeted community.

Accordingly, future designs of megaprojects should involve a more comprehensive planning process for locations with cultural value. Decision-making processes involved in new development projects must always include representatives from the local scholarly community together with experienced architects, religious authorities and members of the community who maintain cultural authenticity. All future projects must synchronize with current city structures while protecting the site's historical values and sacred characteristics. Future research should examine the enduring social consequences of globalization-driven architectural changes on religious sites throughout the world as it develops working methods to preserve cultural heritage.

Scientific Ethics Declaration

* The author declares that the scientific ethical and legal responsibility of this article published in EPSTEM Journal belongs to the author.

Conflict of Interest

* The author declares that there is no conflict of interest

Funding

The author acknowledges Zarqa University for funding this research.

Acknowledgements or Notes

* This article was presented as a virtual presentation at the International Conference on Basic Sciences, Engineering and Technology (www.icbaset.net) held in Istanbul/Türkiye on September 17-18, 2026.

References

Akcan, E. (2016). Global conflict and global glitter: Architecture of West Asia (1960–2010). In E. G. Haddad & D. Rifkind (Eds.), *A critical history of contemporary architecture* (pp. 339–366). London, England: Routledge.

Aboutorabi, M., & Zalloom, B. (2019). Transformation of urban identity: The case of Amman since the post-World War II. *Journal of Engineering*. Retrieved from https://scholar.google.com/scholar?oi=bibs&cluster=11163451992517849174&btnI=1&hl=en

Al-Naim, M. (2014). *Political influences and paradigm shifts in the contemporary Arab cities: Questioning the identity of urban form*. Milan, Italy: EDUCatt-Ente per il diritto allo studio universitario dell'Università Cattolica.

Alharbi, M. (2020). *Understanding multiculturalism in Saudi education: A case study of two schools in Mecca* (Doctoral dissertation). Andrews University.

Alkathiri, N., Katar, I., & Abdelhadi, A. (2024). Integration of culture in contemporary Saudi architecture: A review and survey. In *Proceedings of the International Conference on Sustainability: Developments and Innovations*.

Alnsour, M., Al-Omari, Z., Rawashdeh, T., & Oudat, A. (2024). Shaping tomorrow's community requires right decisions to be made today through investment in sustainable infrastructure: An international review. *Evergreen, 11*(3), 1508–1529.

Altshuler, A. A., & Luberoff, D. E. (2004). *Mega-projects: The changing politics of urban public investment*. Lanham, MD: Rowman & Littlefield.

Ashworth, G., & Kavaratzis, M. (2010). *Towards effective place brand management: Branding European cities and regions*. Cheltenham, England: Edward Elgar Publishing.

Awatta, H. (2015). *Whose downtown is it anyways? The urban transformation of Downtown Cairo between state and non-state stakeholders* (Master's thesis). American University in Cairo, Cairo, Egypt.

Benkherouf, A. (2024). *Ruotsin moskeijoiden kontekstualismi ja kaupunkien integraatio A*. Benkherouf.

Bula, M. Y. (2023). Research design and methodology for empirical research. In *Transnational communication and identity construction in diaspora: A comparative analysis of four diaspora communities from the Horn of Africa* (pp. 125–158). Cham, Switzerland: Springer.

Corner, J., & Harvey, S. (2005). *Enterprise and heritage: Crosscurrents of national culture*. London, England: Routledge.

Dastoor, F. Y. M. (2023). *Reading the city: Architectural sites as the interlocutors of past, present and future identity in Dubai*.

Dicks, B. (2004). *Culture on display: The production of contemporary visitability*. Maidenhead, England: McGraw-Hill Education.

Ghaleb, M. M. S., & Juhari, A. S. (2024). The role of architecture in shaping social and cultural landscapes in Saudi Arabia: A case study approach. *Rita Revista Indexada de Textos Academicos, 21*.

Habib, M. (2024). *Holy sites and sanctuaries of the pre-Islamic Near and Middle East: To what extent is there a link between pre-Islamic and Islamic notions of sacred space?* SOAS University of London.

Hamada, A. M. A. (2015). *The integration history of Kuwaiti television from 1957–1990: An audience-generated oral narrative on the arrival and integration of the device in the city* (Doctoral dissertation). Virginia Commonwealth University.

Jha, A. K., Miner, T. W., & Stanton-Geddes, Z. (2013). *Building urban resilience: Principles, tools, and practice*. Washington, DC: World Bank.

Lichtenwalter, L. L. (2020). Kaaba & sanctuary: Qur'anic and biblical cosmic centers—Ontological and existential worldviews. *Journal of the Adventist Theological Society, 31*(1), 7.

Maguire, J., & Falcous, M. (2010). *Sport and migration: Borders, boundaries and crossings*. London, England: Routledge.

Mayer, M. (2018). Neoliberalism and the urban. In D. Cahill, M. Cooper, M. Konings, & D. Primrose (Eds.), *The SAGE handbook of neoliberalism* (pp. 483–493). London, England: SAGE.

Musa, A. B., Maimagani, S. S., & Tukur, R. B. (2020). Influence of politics in the commissioning and design of projects: A case study of Royal Clock Tower (Abraj Al-Bait), Mecca, Saudi Arabia. *Kuwait Chapter of the Arabian Journal of Business and Management Review, 9*(4), 183–187.

Osman, T. (2016). *Islamism: What it means for the Middle East and the world*. New Haven, CT: Yale University Press.

Qurashi, J. (2019). Diminishing religious cultural heritage of holy Makkah and Medina due to commercialization of the sacred event. In R. Raj & K. Griffin (Eds.), *Spiritual and religious tourism: Motivations and management* (pp. 85–96). Wallingford, England: CABI.

Rasch, S. L. (2025). *Makkah Royal Clock Tower: Tallest building in Saudi Arabia*. Retrieved from https://www.re-thinkingthefuture.com/case-studies/a4579-makkah-royal-clock-tower-by-sl-rasch-gmbh-and-dar-al-handasah-architects-tallest-building-in-saudi-arabia/

Sklair, L. (2017). *The icon project: Architecture, cities, and capitalist globalization*. New York, NY: Oxford University Press.

Smith, L. (2020). *Emotional heritage: Visitor engagement at museums and heritage sites*. London, England: Routledge.

Söderlund, J., Sankaran, S., & Biesenthal, C. (2017). The past and present of megaprojects. *Project Management Journal, 48*, 5–16.

Southworth, M., & Ruggeri, D. (2011). Beyond placelessness: Place identity and the global city. In T. Banerjee & A. Loukaitou-Sideris (Eds.), *Companion to urban design* (pp. 495–509). London, England: Routledge.

Thompson, R. (2018). A qualitative phenomenological study of emotional and cultural intelligence of international students in the United States of America. *Journal of International Students, 8*(2), 1220–1255.

Traganou, J. (2016). *Designing the Olympics: Representation, participation, contestation*. London, England: Routledge.

Winerman, A. (2011). *Developing Mecca: A case study of the Royal Makkah Clock Tower*. SSRN Electronic Journal. Retrieved from https://ssrn.com/abstract=1846593

Zalloom, B. (2018). Tracing the cityscape transformation under capitalism: The case study of Amman. *Journal of Urban Regeneration and Renewal, 11*, 54–71.

Zalloom, B., & Tarrad, M. (2020). The role of public spaces in reviving the historical areas: The case study of As-Salt City in Jordan. *International Journal of Sustainable Development and Planning, 15*, 361–367.

Zukin, S. (2012). Competitive globalization and urban change: The allure of cultural strategies. In X. Chen & A. Kanna (Eds.), *Rethinking global urbanism: Comparative insights from secondary cities* (pp. 17–34). London, England: Routledge.

Author Information

Bushra Zalloom
Zarqa University Tel. +96253821100
2000 Zarqa 13110 Jordan
ORCID iD: https://orcid.org/0000-0002-3698-8132
Contact e-mail: *bzalloom@zu.edu.jo*